



# Structure nanoengineering of functional nanomaterials Advanced electron microscopy study

Reza Zamani

**ADVERTIMENT.** La consulta d'aquesta tesi queda condicionada a l'acceptació de les següents condicions d'ús: La difusió d'aquesta tesi per mitjà del servei TDX ([www.tdx.cat](http://www.tdx.cat)) i a través del Dipòsit Digital de la UB ([diposit.ub.edu](http://diposit.ub.edu)) ha estat autoritzada pels titulars dels drets de propietat intel·lectual únicament per a usos privats emmarcats en activitats d'investigació i docència. No s'autoritza la seva reproducció amb finalitats de lucre ni la seva difusió i posada a disposició des d'un lloc aliè al servei TDX ni al Dipòsit Digital de la UB. No s'autoritza la presentació del seu contingut en una finestra o marc aliè a TDX o al Dipòsit Digital de la UB (framing). Aquesta reserva de drets afecta tant al resum de presentació de la tesi com als seus continguts. En la utilització o cita de parts de la tesi és obligat indicar el nom de la persona autora.

**ADVERTENCIA.** La consulta de esta tesis queda condicionada a la aceptación de las siguientes condiciones de uso: La difusión de esta tesis por medio del servicio TDR ([www.tdx.cat](http://www.tdx.cat)) y a través del Repositorio Digital de la UB ([diposit.ub.edu](http://diposit.ub.edu)) ha sido autorizada por los titulares de los derechos de propiedad intelectual únicamente para usos privados enmarcados en actividades de investigación y docencia. No se autoriza su reproducción con finalidades de lucro ni su difusión y puesta a disposición desde un sitio ajeno al servicio TDR o al Repositorio Digital de la UB. No se autoriza la presentación de su contenido en una ventana o marco ajeno a TDR o al Repositorio Digital de la UB (framing). Esta reserva de derechos afecta tanto al resumen de presentación de la tesis como a sus contenidos. En la utilización o cita de partes de la tesis es obligado indicar el nombre de la persona autora.

**WARNING.** On having consulted this thesis you're accepting the following use conditions: Spreading this thesis by the TDX ([www.tdx.cat](http://www.tdx.cat)) service and by the UB Digital Repository ([diposit.ub.edu](http://diposit.ub.edu)) has been authorized by the titular of the intellectual property rights only for private uses placed in investigation and teaching activities. Reproduction with lucrative aims is not authorized nor its spreading and availability from a site foreign to the TDX service or to the UB Digital Repository. Introducing its content in a window or frame foreign to the TDX service or to the UB Digital Repository is not authorized (framing). Those rights affect to the presentation summary of the thesis as well as to its contents. In the using or citation of parts of the thesis it's obliged to indicate the name of the author.

Doctorate Program in Nanoscience

**STRUCTURE NANOENGINEERING OF  
FUNCTIONAL NANOMATERIALS  
ADVANCED ELECTRON MICROSCOPY STUDY**

**Reza Zamani**

Supervisors:

**Prof. Jordi Arbiol i Cobos**

**Prof. Joan Ramón Morante i Lleonart**

Department of Electronics, University of Barcelona (UB)

Catalonia Institute for Energy Research (IREC)

Institute of Materials Science of Barcelona (ICMAB-CSIC)



UNIVERSITAT DE BARCELONA



September 2013



# A CKNOWLEDGEMENT

Almost four years ago, when I started to walk in this road, with a much narrower view over my future career, I just knew that it is a hard way to go through. I was four years younger, and had four years less experience. Now I feel like everything that I experienced in this road, difficulties, problems, joy, success and failure, triumph and tragedy, glory and ruin, etc, they all made me grow up; I feel like I see the world in a different way. Anyway, many people helped me carry on, and therefore, I owe them cordial gratitude; without them it was not possible to fulfill this PhD. I hope I do not forget anybody.

First of all I would like to express my deepest gratitude to my supervisor, Prof. Jordi Arbiol for all he did for me, his excellent guidance, patience, caring and effort. During all these years he was always available for me and always helped me solve the problems and deal with critical situations. Without him this work would definitely be impossible. There were always ups and downs, moments of hope and despair; he never let me down, and he always motivated me and made me rise. I thank him not only as a great supervisor, but also as an excellent and admirable person.

I would also like to acknowledge Prof. Joan Ramon Morante, the big boss! His novel ideas and wise guidelines opened my view through the science world, and together with his financial support made this work possible.

The great people of my group (GAeN) are kindly appreciated too: Francisco, Roger, María, and Aziz. We had a fantastic time together and I learnt a lot with them. I enjoyed their friendship, as well as the coworkership. In particular, I especially thank Francisco for teaching me how to prepare TEM samples, and also preparing samples for me.

I would like to appreciate the hospitality of Prof. Anna Fontcuberta and her group as they hosted me in their group for four months. They were pretty nice to

me; I learnt quite a lot during that period and I enjoyed my time with them in Lausanne. Thank you Anna, Albertino, Daniel, Yanik, Anna (Dalmau), Sònia, Elenora, Martin, Gözde, and Prof. Dirk Grundler.

I also cordially acknowledge our collaborators:

- The Functional Nanomaterials Group in IREC, Prof. Andreu Cabot and his team: María, Wenhua, Fan, Doris, and Raquel, special thanks for their fantastic work and the profitable collaboration.
- Stutzmann Group in Walter Schottky Institute (WSI-TUM), especially Prof. Stutzmann and Fabian.
- Sensor Lab in Brescia: Prof. Elisabetta Comini, Andrea and Dario.
- People of the Group of Advanced Materials in IREC: Paco, Feng, Cristian, Cristina, Teresa and Javier; special thanks to Cristian for teaching me how to use the SEM in IREC.
- Department of Inorganic and Materials Chemistry, University of Cologne, Prof. Sanjay Mathur, Raquel and Jun.
- Department of Electronics, UB: Daniel, Nuria, and Frank.
- Dr. Aurelian Marcu from INFLPR, Bucharest.
- And the last, but not the least, Dr. Mauro Epifani from IMM-CNR, Lecce, with additional thanks for hosting me in his lab.

Moreover, I should also acknowledge the people of the microscopy centers I worked with:

- ER-C: I am very grateful to the scientists in ER-C: Prof. Rafal Dunin-Borkowsky, Dr. Martina Luysberg, Dr. Lothar Houben, Dr. Andras Kovács, Dr. Chris Boothroyd, and Mrs. Doris Meertens. Special thanks to Martina for the fantastic microscopy job as well as the arrangement of my stays in Jülich, and to Andras for the great holography work, and Doris for fast and on-time FIB sample preparation even when she had many other things to do. I should also acknowledge the invited scientists, Prof. Giulio Pozzi and Dr. Paul Voyles for worthwhile and fruitful discussions.
- CIME-EPFL: I am thankful to Prof. Cécile Hébert, Dr. Duncan Alexander, and Mrs. Danièle Laub for hosting me in their lab during my internship in Lausanne. I especially thank Duncan for the training courses and the great cathodoluminescence job, and also Danièle for the fully-detailed and perfect sample preparation training course.
- LMA-INA: I appreciate the marvelous job of Prof. César Magen, Prof. Raul Arenal, and Dr. Rodrigo Fernández-Pacheco.

- SCT-UB: Sònia, Juan and Lluís, thanks for solving the problems and permanent assistance with the TEMs.
- ICMAB: Judith, thanks for the help with resolving the complex structures, and also the SEM work.

In general, I should thank my fantastic coworkers in both ICMAB and IREC that made me feel like home. Thanks to the nice working atmosphere in these institutes, during all these years I never got homesick despite my strong dependence to my family and my land. I am grateful to Prof. Xavier Obradors and Prof. Teresa Puig for having me in their department as a guest for a pretty long time.

Some personal messages... It is not really easy to forget the effort that my parents did for me during all these thirty years of my life. From the bottom of my heart I would like to thank them for their constant support and care. I also thank my brothers for the encouragement. And finally I would like to thank my darling, Anna, for her support, help, patience, empathy, and understanding.



# Contents

<b>Acknowledgement</b>	<b>iii</b>
<b>Contents</b>	<b>vii</b>
<b>Chapter I: Introduction</b>	<b>1</b>
1.1 Let's go nano!	3
1.2 Plenty of room at the bottom to be engineered	4
1.3 Plenty of engineered room at the bottom to be observed	6
1.4 State-of-the-art	7
1.5 Description of the report	8
1.6 References	9
<b>Chapter II: Transmission electron microscopy: methodology</b>	<b>15</b>
2.1 Transmission electron microscope	17
2.2 Basic principles of TEM	18
2.2.1 Electron-matter interaction	20
2.2.2 The concept of resolution	22
2.2.3 Aberrations and aberration correction	23
2.3 Diffraction	28
2.4 TEM Imaging	31
2.4.1 Bright-field and dark-field TEM imaging	32
2.4.2 High-resolution TEM	33
2.5 STEM imaging	37
2.5.1 Annular dark-field and high-angle annular dark-field STEM	38
2.5.2 Bright-field and annular bright-field STEM	40
	vii

2.6	Spectroscopy	41
2.6.1	Electron energy-loss spectroscopy	41
2.6.2	Aberration-corrected STEM-EELS	44
2.6.3	Energy-dispersive X-ray spectroscopy	45
2.6.4	Cathodoluminescence	48
2.7	Quantitative analysis, image processing and simulation	52
2.7.1	Strain analysis by geometric phase analysis	53
2.7.2	Multivariate statistical analysis	54
2.7.3	Rhodium and Eje-Z	55
2.7.4	JEMS	56
2.8	Specimen preparation	56
2.8.1	Dispersion of nanostructured materials	57
2.8.2	Crushing	58
2.8.3	Mechanical polishing	58
2.8.4	Mechanical polishing for wedge making	59
2.8.5	Ion milling	59
2.8.6	Focused ion beam	60
2.9	Some of the key events in the history of electron microscopy	62
2.10	References	63

**Chapter III: Nanoengineering crystal structure and morphology of nanoparticles: complex copper-based chalcogenide nanocrystals** **67**

3.1	Introduction	69
3.1.1	Thermoelectrics	70
3.1.1.1	Basic principles	70
3.1.1.2	Thermoelectric devices	72
3.1.1.3	Thermoelectric materials	73
3.1.2	How to improve the efficiency: bulk vs. nano	74
3.1.3	Colloidal synthesis	76
3.1.4	Thermoelectric characterization	76
3.1.5	Structural changes in nanostructured materials	77
3.1.5.1	Twinning and polytypism	77
3.1.5.2	Copper-based chalcogenides	80
3.1.5.3	Stannite and kesterite structures	81
3.2	Experimental	82
3.2.1	Synthesis	82
3.2.2	Structural characterization	83
3.2.3	Thermoelectric characterization	83

3.3	Structure study	84
3.3.1	Single-phased structures	85
3.3.1.1	Cu <sub>2</sub> SnSe <sub>3</sub> nanocrystals	85
3.3.1.2	Cu <sub>2</sub> ZnSnSe <sub>4</sub> nanocrystals	86
3.3.1.3	Cu <sub>2</sub> ZnGeSe <sub>4</sub> nanocrystals	88
3.3.1.4	Cu <sub>2</sub> HgSnSe <sub>4</sub> nanocrystals	92
3.3.1.5	Section summary	94
3.3.2	Multi-phased structures	95
3.3.2.1	Cu <sub>2</sub> GeSe <sub>3</sub> nanocrystals	95
3.3.2.2	Cu <sub>2</sub> CdSnSe <sub>4</sub> pentatetrahedral nanocrystals	104
3.3.2.3	Cu <sub>2</sub> Cd <sub>7</sub> SnSe <sub>10</sub> polypods	112
3.3.2.4	Cu <sub>2</sub> HgGeSe <sub>4</sub> nanocrystals	126
3.3.2.5	Section summary	132
3.3.3	Core-shell structures	133
3.3.3.1	Fe <sub>3</sub> Pt@PbTe nanoparticles	134
3.3.3.2	BiTe@PbTe nanoparticles	138
3.3.3.3	PbTe@PbS nanoparticles	139
3.3.3.4	Section summary	154
3.4	Conclusion	155
3.5	References	156

## **Chapter IV: Coaxial nanojunctions: metal oxide heterostructured nanowires** **171**

4.1	Introduction	173
4.1.1	Metal oxide nanowires	174
4.1.2	Why heterostructure?	174
4.1.3	The p-n junction	176
4.1.4	Some applications	179
4.1.4.1	Photovoltaics	179
4.1.4.2	Gas sensing	181
4.1.5	Growth methods	183
4.1.5.1	Electrochemical growth	184
4.1.5.2	Thermal oxidation	185
4.1.5.3	Chemical vapor deposition	186
4.1.6	Structural changes in nanostructured materials	188
4.1.6.1	Accommodation on the base	188
4.1.6.2	Mixed oxide interface	188
4.1.6.2	Crystal structure changes in shells	189
4.1.6.3	Reduction	190
4.2	Experimental	190
4.2.1	Synthesis	190
4.2.1.1	Electrochemical growth	190

4.2.1.2 Pulsed laser deposition	191
4.2.1.3 Chemical vapor deposition	193
4.2.1.4 Thermal oxidation	194
4.2.2 Structural characterization	194
4.2.3 Experimental measurements for applications	195
4.2.3.1 Optoelectronics	195
4.2.3.2 Gas sensing	196
4.3 Structure study	196
4.3.1 ZnO nanowires and related heterostructures	197
4.3.1.1 Bare ZnO nanowires	197
4.3.1.2 ZnO:Cl@ZnS nanowires	202
4.3.1.3 ZnO:Cl@TiO <sub>2</sub> nanowires	205
4.3.1.4 Section summary	207
4.3.2 TiO <sub>2</sub> nanowires and nanorods, and related heterostructures	208
4.3.2.1 Bare TiO <sub>2</sub> nanowires and nanorods	209
4.3.2.2 TiO <sub>2</sub> @TiO nanowires	211
4.3.2.3 Section summary	215
4.3.3 SnO <sub>2</sub> nanowires and related heterostructures	215
4.3.3.1 Bare SnO <sub>2</sub> nanowires	216
4.3.3.2 SnO <sub>2</sub> @Ti <sub>2</sub> O nanowires	220
4.3.3.3 SnO <sub>2</sub> @V <sub>2</sub> O <sub>3</sub> nanowires	223
4.3.3.4 SnO <sub>2</sub> @TiVO <sub>3</sub> nanowires	225
4.3.3.5 SnO <sub>2</sub> nanowires decorated with CuO nanoparticles	229
4.3.3.6 Section summary	235
4.4 Conclusion	236
4.5 References	237

**Chapter V: Epitaxial growth and nanoengineered interfaces:  
III-V nanowires** **251**

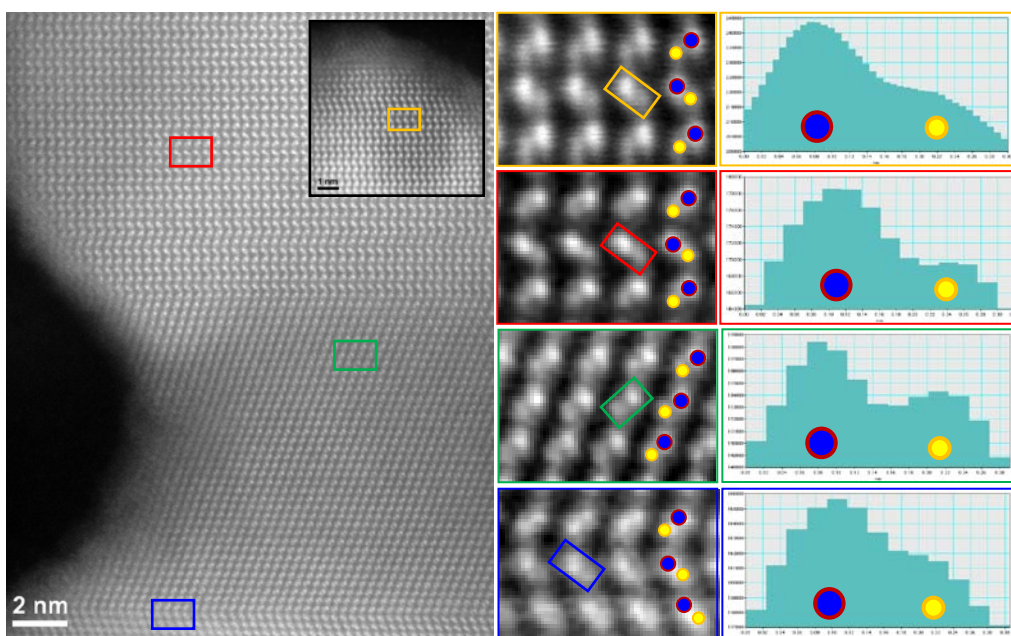
5.1 Introduction	253
5.1.1 III-V nanowires	254
5.1.2 Optoelectronics and optoelectronic devices	255
5.1.2.1 Photodiodes and solar cells	257
5.1.2.2 Light emitting diodes and laser diodes	258
5.1.3 Catalyst-free growth via molecular beam epitaxy	259
5.1.4 Structural study: polarity	260
5.2 Experimental	261
5.2.1 Synthesis	261
5.2.2 Structural characterization	262
5.2.3 Optical measurements	262

5.3	Structure study	262
5.3.1	GaN nanowires on diamond	263
5.3.2	p-GaN/n-ZnO heterostructure nanowires	275
5.4	Conclusion	286
5.5	References	287
 <b>Chapter VI: Conclusion and outlook</b>		<b>295</b>
6.1	Let's sum up!	297
6.2	Outlook	299
 <b>Appendices</b>		<b>303</b>
	Appendix A: Abbreviations and symbols	305
	Appendix B: Abstract in English	313
	Appendix C: Resumen en Español	319
	Appendix D: Resum en Català	325
	Appendix E: Publications	331
	Appendix F: Author's curriculum vitae	355



# CHAPTER I

## INTRODUCTION



CHAPTER I: INTRODUCTION

## 1.1 Let's go nano!

In recent years '*nanoscience*' as a novel scientific field has attracted a vast surge of interest due to its unique influences on physical, mechanical, chemical, and biological properties of the materials. Indeed, nanoscience and nanotechnology are revolutionizing devices, procedures, and applications which can be employed in various fields such as electronics, automotive technology, food and pharmaceutical industry, and medical world. For instance, electronic devices such as sensors, diodes, and transistors have already been produced with excessively excellent performance with extremely small dimensions.<sup>1</sup>

Nanoscience has also benefited the energy sector. More effective energy-producing, energy-absorbing, and energy storage products are being developed in smaller and more efficient devices by virtue of nanoscience.<sup>2</sup> Nowadays, energy issue is becoming problematic as on the one hand the demand for energy is skyrocketing, and on the other hand, shortage of energy sources in future is a serious concern. Besides pollution and other disadvantages, fossil fuels will be exhausted sooner or later. In addition, types like nuclear energy foundered on expensive maintenance and high risk of disaster origination. Hence, green energy sources are required.

Equally important, energy consumption and waste can be controlled. As an example, every year several thousand billion kWh of electricity is used for lighting which is roughly a portion of 7-15% of the whole electricity consumption (depending on the sector, country, etc). However, traditional lighting technologies are unduly inefficient. We need electric devices with higher efficiency in order to consume energy as less as possible. Moreover, devices that can recover wasted energy, as well as reliable energy storage devices with longer life-time, seem to be advantageous.

Therefore, novel environment-friendly high-efficient low-cost accessible methods are desired to generate/harvest/save energy. In this context, nanoscience offers some promising solutions. New generation of solar cells, fuel cells, batteries, supercapacitors, and thermoelectric devices are examples of the advancement in energy industry catered for by dint of nanoscience and nanotechnology advantages.

At nanoscale, the materials exhibit rather different properties mostly for the sake of their high surface-to-volume ratio and well-defined atomic arrangement. In this scenario, dimensionality plays a decisive role. 0-dimensional (0D) and 1-dimensional (1D) semiconductor nanocrystals, e.g. nanoparticles (NPs), nanorods (NRs), and nanowires (NWs) represent the forefront of today's solid state physics and technology. They have emerged as potential building blocks of new devices regarding their outstanding performance and remarkably high efficiency.<sup>3-5</sup>

There are always pros and cons to everything. Nanotechnology is not an exception either. Despite all the advantages, it cannot be disregarded that in general, nanotechnology is yet rather expensive. The processes of nanomaterial production are complicated and expensive, while mass production in the case of many compounds does not reach the order of few tens of grams, i.e. it is yet far from industrial scales in many cases.

### **1.2 Plenty of room at the bottom to be engineered**

“There's plenty of room at the bottom,” said Richard P. Feynman (1918-1988) in his famous speech to the American Physical Society in California Institute of Technology, 1959.<sup>6</sup> Decades after, researchers started to go through ‘the room at the bottom’ and outstanding results were obtained. Carbon nanotubes and oxide nanowires were the first examples. Afterwards, the results were further improved by ‘engineering the room at the bottom’, i.e. property modifications at atomic scale, which here will be referred to as ‘*nanoengineering*’.

Therefore, considerable functionality enhancement can occur via nanoengineering the structure, morphology, surface, interface, heterostructure, etc, which leads to changes in the intrinsic properties of the material, e.g. thermal/electrical conductivity, electronic band gap energy, carrier concentration, and optical properties. This is accessible through different approaches. Previous studies proved the effect of dimensionality on band

confinement.<sup>7</sup> Hence, morphology (shape and size) control at nanoscale is quite crucial. Moreover, each new element can act differently in the structure and cause expected/unexpected changes in the compound's properties. It can lead for instance to band gap tuning, which occurs often in nanostructured semiconductors when ternary and quaternary semiconductors are achieved. In the case of quaternaries, for example with three cations and one anion, regarding the ordering or disordering of cation arrangement, quite different properties are obtained.

This approach (introducing additional elements to the structure) quite frequently leads to formation of metastable phases (polytypism), and as a consequence, enhancement in functionality of the compounds. The simultaneous presence of two common phases of tetrahedrally-coordinated semiconductors, i.e. wurtzite (WZ) and zinc-blende (ZB) and the polytypes between them, can have a dramatic effect on physical and chemical properties of the compound. One can take advantage of this phenomenon in order to engineer the properties such as electrical/thermal conductivity or band structure, and as a consequence improve their functionality, for instance in thermoelectricity.

Another approach which can be referred to as 'surface modification' is playing around with the surface properties. In this scenario, formation of core-shell nanostructures can be definitely useful, because: (i) adequate core with predetermined properties such as carrier concentration and band gap energy can be used, while (ii) a well-designed shell modifies the general electrical/thermal properties and radial electric/magnetic field distribution of the whole structure; and furthermore, the shell can increase/decrease the density of surface chemical reaction sites if necessary.

Here the concept of '*epitaxy*' and '*epitaxial relationship*' between the two structures arises; a concept that has a remarkable influence on the final material's properties.<sup>8,9</sup> An incoherent heterointerface can deteriorate conductivity and charge mobility due to the presence of numerous structural defects. In the case of optoelectronic devices, such defects can abruptly wreck the luminescence. However, for some particular applications, defected structure can benefit the functionality of the compound, e.g. a polycrystalline shell with a rather rough surface can be quite advantageous when more surface and more chemical reaction sites are desired.

Whatsoever, epitaxial relationship in the '*nanojunctions*' is usually sought, not only in coaxial (core-shell) heterostructures, but also in axial (one on the other) ones. The latter can be wisely used for designing p-n junctions at

nanoscale; a p-type NW/NR/NP can be accommodated on an n-type base or vice versa. Such a design can be used for many applications, e.g. LEDs and gas sensors. The key point here is to choose the adequate secondary structure such that (i) it has quite low mismatch with the base, i.e. structures with not exactly the same but close cell parameters should be selected, and also (ii) it shows adequate semiconducting properties, meaning if the base is p-type, the secondary structure should be suitably n-type, and the other way around.

In addition, there is another phenomenon which plays a crucial role in physical and chemical properties of heterostructures: ‘*polarity*’,<sup>10</sup> the concepts that determines the relative charge distribution in the so-called ‘*dumbbell-units*’ comprised of a cation on one side and an anion on the other. Orientation of these dumbbell units in tetrahedrally-coordinated semiconductors determines the polarity. Further, changes in polarity have a dramatic influence on band structure and other electronic properties of the nanojunction. Therefore, the polarity should be carefully studied, as its determination has long been a challenge for physicists.

### **1.3 Plenty of engineered room at the bottom to be observed**

Now that the ‘*room at the bottom*’ is engineered, an instrument is required to reveal whether the nanoengineering is carried out properly, and thus the importance of transmission electron microscopy (TEM) arises. Unquestionably TEM is one of the most powerful tools in this scenario.

“What you (physicists) should do in order for us (biologist) to make more rapid progress is to make the electron microscope 100 times better.” Feynman said in the same lecture.<sup>6</sup> Nowadays, indeed we realize that he was right. What he expected from electron microscopes more than 50 years ago is now achieved. In late 1950s the TEM resolution limit hardly arrived to 5 nm, and now sub-0.5-Å is achieved. Such a magnificent improvement in microscopy field had a strong impact on other fields, especially materials science which is the main topic of this report.

Since construction of the first electron microscope by Ernst Ruska (1933),<sup>11,12</sup> a vast amount of effort has been carried out by many scientist and engineers around the world to improve the performance of this device, and some of them led to drastic progresses in this issue. The resolution limit was gradually pushed down such that from the first prototype electron microscope with a resolution of ~ 7 nm in 1939, eventually we reached to sub-Å and sub-0.5-Å

resolutions. Not only the resolution, but also the TEM techniques were astonishingly developed. High-resolution TEM (HRTEM) and STEM imaging techniques on the one hand, and spectroscopy methods on the other hand, opened new ways towards materials research.

As will be described in the next chapter, recently-development aberration-corrected microscopes have proven their usefulness for solving specific problems of the materials science. For instance, determination of ordering effect of the cations in ternary and quaternary compound, polarity and ionicity, doping percentage and dopant concentration profiles along the diameter of the nanostructured materials are now possible by employing novel techniques of electron microscopy.

As an example, polarity determination is a challenging issue, especially in compounds like ZnO, GaN and GaAs,<sup>13-15</sup> as previously light atoms like O and N were not observable and small differences in atomic numbers were not distinguishable by conventional microscopes. Development of STEM techniques and technologies, nevertheless, allows us to visualize the polarity directly by analyzing the ABF/HAADF-STEM micrographs.<sup>16-18</sup> On the other hand, such recognition power can be employed for determination of ordering effect when the difference of average atomic number between cation and anion is considerably small.

On the other hand, TEM is a powerful tool for studying heterointerfaces between two dissimilar structures. Epitaxial relationship is a decisive issue in the properties of the heterostructures. In nanoscale sometimes accommodation of the secondary structure on the base does not follow the rules of thermodynamics and kinetics, as the influence of epitaxial growth and surface energies interfere in the crystal and/or chemical structure and thus the formation of the conventional compounds. It is quite probable to have strain in the interfaces which is an affecting parameter. Therefore, by HRTEM micrograph processing with different methods such as geometric phase analysis (GPA) one is able to study and map the strain in the structure and determine the strain concentration points if present.

## 1.4 State-of-the-art

In one word, the state-of-the-art in this report is nothing but the solutions of the challenging points which were mentioned in the previous sections. Novel materials for advanced applications are studied by means of the latest

microscopy technologies and methodologies which have had a dramatic impact on progress in materials science.

Polytypism,<sup>19-22</sup> unusual morphologies,<sup>23,24</sup> polytypic branching,<sup>25-27</sup> band gap engineering,<sup>28-30</sup> cation ordering,<sup>31</sup> polarity determination,<sup>13-15</sup> epitaxial growth<sup>8,32</sup> and interface,<sup>33</sup> accommodation of a secondary structure on a base,<sup>34</sup> p-n junction functionality,<sup>35,36</sup> optoelectronic properties,<sup>37-39</sup> all of these are the current challenges of materials science for which TEM analyses usually have convincing solutions.

### **1.5 Description of the report**

In this report nanoengineered structures of functional materials at nanoscale are studied by means of advanced electron microscopy techniques.

Chapter 1 is the current introduction and preface to the report. In Chapter 2 the methodology is described. Chapter 3, 4, and 5 are the results, and Chapter 6 is the general conclusions and the outlook. Note that each chapter of results (Chapters 3 to 5) has its own introduction and conclusion. Therefore, Chapter 1 consists of just a short introduction to the general idea of the study and its importance and the state-of-the-art, and a preface of the thesis.

In Chapter 2 the TEM methodology is described, the advanced TEM techniques used to study the nanostructured semiconductors at atomic scale. In general, it consists of brief descriptions of basic principles of TEM, techniques, and the cons and pros to them. Note that in order to keep the report short, details are avoided, hence excellent references are provided for further details. Each section starts with conventional use of the method(s) and ends with the state-of-the-art which is applied for novel materials science studies. Mostly the experimental results are corroborated by theoretical studies and simulations. Therefore, these procedures (image processing, simulations, etc) are also described shortly.

Chapter 3 is dedicated to nanoengineering the crystal structure and morphology of nanocrystals of complex copper-based chalcogenides. Several compounds were studied from binaries to complex ternaries and quaternaries. In this chapter it is shown that there is a wide range of possibilities for engineering, as many elements can be substituted with the primary cations and anions, and each element has unique influence on the properties of the compound. Mostly these compounds are based on copper-selenide with additional cations substituting copper. They are excellent candidates for thermoelectric devices.

Advanced TEM studies are performed in order to figure out the physics behind the property modifications. Phenomena such as morphology change, polytypism, cation ordering, polarity, electronic band change, strain, etc, are elaborately studied, and correlated to the physical properties such as luminescence and thermoelectricity.

Chapter 4 is based on the study of nanojunctions in metal oxide heterostructured NWs; a strategy that can enhance the functionality of the targeted devices, such as photovoltaic cells, or gas sensors. Metal oxide semiconductors showed their promise since few decades ago, and still a considerable amount of research is dedicated to them in order to optimize their properties. Production of nanojunctions is one of the most successful approaches in this context. In Chapter 4 it is shown how coaxial heterostructuring of NWs, i.e. formation of core-shell structures and other types increase the efficiency of the solar cells or enhance the sensitivity and selectivity of the gas sensors.

Almost the same approach is followed in Chapter 5, nevertheless, this time with III-V NWs. Also there the importance of axial heterostructures and fully-epitaxial and relaxed structure are emphasized. The promising p-n junctions and the optoelectronic properties of the GaN NWs are examined. Polarity issue, as a remarkably influencing parameter, is precisely studied in practice, and its effect on electronic band structure in the heterointerface is proven by the theoretical simulations.

In the end, a general conclusion of the whole work and room for further study and future work is discussed in Chapter 6. The ample freedom of structural nanoengineering in the materials is that much that in my opinion each chapter can be a starting point for a new PhD thesis. It is a never-ending story... Also on the other side of this never-ending story, there are some other works in hand which have not arrived to the final results yet. Those works are briefly described in Chapter 6. They are still in nanoengineering road and quite feasible to be applied for novel applications in near future.

## 1.6 References

- 1 J.R. Heath, '**Nanoscale materials**', *Accounts of Chemical Research* 32, 388 (1999)
- 2 C. Flox, J. Rubio-García, R. Nafria, R. Zamani, M. Skoumal, T. Andreu, J. Arbiol, A. Cabot, J.R. Morante, '**Active nano-CuPt<sub>3</sub> electrocatalyst**

**supported on graphene for enhancing reactions at the cathode in all-vanadium redox flow batteries**', *Carbon* 50, 2372-2374 (2012)

3 J. Hu, T.W. Odom, C.M. Lieber, '**Chemistry and Physics in One Dimension: Synthesis and Properties of Nanowires and Nanotubes**', *Accounts of Chemical Research* 32, 435-445 (1999)

4 M. Nirmal L. Brus, '**Luminescence photophysics in semiconductor nanocrystals**', *Accounts of Chemical Research* 32, 407-414 (1999)

5 M. Law, J. Goldberger, P.-D. Yang, '**Semiconductor nanowires and nanotubes**', *Annual Review of Materials Research* 34, 83-122 (2004)

6 R.P. Feynman, '**Plenty of room at the bottom**', Transcript of a talk to the American Physical Society in California Institute of Technology, Pasadena (1959)

7 M. Notomi, J. Hammersberg, H. Weman, S. Nojima, H. Sugiura, M. Okamoto, T. Tamamura, M. Potemski, '**Dimensionality effects on strain and quantum confinement in lattice-mismatched InAs<sub>x</sub>P<sub>1-x</sub>/InP quantum wires**', *Physical Review B* 52, 11147-11158 (1995)

8 W. M. Yim, E. J. Stofko, P. J. Zanzucchi, J. I. Pankove, M. Ettenberg, S.L. Gilbert, '**Epitaxially grown AlN and its optical band gap**', *Journal Applied Physics* 44, 292-296 (1973)

9 G. Vogga, C.R. Miskys, J.A. Garrido, M. Hermann, M. Eickhoff, M. Stutzmann, '**High quality heteroepitaxial AlN films on diamond**', *Journal of Applied Physics* 96, 895-902 (2004)

10 M.A. Berding, A. Sher, A.-B. Chen, '**Polarity in semiconductor compounds**', *Physical Review B* 36, 7433-7436 (1987)

11 E. Ruska, '**The development of the electron microscope and of electron microscopy**', *Bioscience Reports* 7 (Nobel Lecture), 607-629 (1986)

12 F. Haguenu, P.W. Hawkes, J.L. Hutchison, B. Satiat-Jeunemaître, G.T. Simon, D.B. Williams, '**Key events in the history of electron microscopy**', *Microscopy and Microanalysis* 9, 96-138 (2003)

13 M.I.B. Utama, F.J. Belarre, C. Magen, B. Peng, J. Arbiol, Q. Xiong, '**Incommensurate van der Waals epitaxy of nanowire arrays: A case study with ZnO on muscovite mica substrates**', *Nano Letters* 12, 2146-2152 (2012)

14 F. Schuster, F. Furtmayr, R. Zamani, C. Magen, J.R. Morante, J. Arbiol, J.A. Garrido, M. Stutzmann, '**Self-assembled GaN nanowires of diamond**', *Nano Letters* 12, 2199-2204 (2012)

- 
- 15 M. de la Mata, C. Magen, J. Gazquez, M.I.B. Utama, M. Heiss, S. Lopatin, F. Furtmayr, C.J. Fernandez-Rojas, B. Peng, J.R. Morante, R. Rurali, M. Eickhoff, A. Fontcuberta i Morral, Q. Xiong, J. Arbiol, **'Polarity assignment in ZnTe, GaAs, ZnO and GaN-AlN nanowires from direct dumbbell analysis'**, *Nano Letters* 12, 2579-2586 (2012)
- 16 E. Okunishi, I. Ishikawa, H. Sawada, F. Hosokawa, M. Hori, Y. Kondo, **'Visualization of light elements at ultrahigh resolution by STEM annular bright field microscopy'**, *Microscopy and Microanalysis* 15, 164-165 (2009)
- 17 S.D. Findlay, N. Shibata, H. Sawada, E. Okunishi, Y. Kondo, Y. Ikuhara, **'Dynamics of annular bright field imaging in scanning transmission electron microscopy'**, *Ultramicroscopy* 110, 903-923 (2010)
- 18 R. Ishikawa, E. Okunishi, H. Sawada, Y. Kondo, F. Hosokawa, E. Abe, **'Direct imaging of hydrogen-atom columns in a crystal by annular bright-field electron microscopy'**, *Nature Materials* 10, 278-281 (2011)
- 19 D. Spirkoska, J. Arbiol, A. Gustafsson, S. Conesa-Boj, F. Glas, I. Zardo, M. Heigoldt, M.H. Gass, A.L. Bleloch, S. Estrade, M. Kaniber, J. Rossler, F. Peiro, J.R. Morante, G. Abstreiter, L. Samuelson, A. Fontcuberta i Morral, **'Structural and optical properties of high quality zinc-blende/wurtzite GaAs nanowire heterostructures'**, *Physical Review B* 80, 245325 (2009)
- 20 P. Caroff, K.A. Dick, J. Johansson, M.E. Messing, K. Deppert, L. Samuelson, **'Controlled polytypic and twin-plane superlattices in III-V nanowires'**, *Nature Nanotechnology* 4, 50 (2009)
- 21 H.J. Joyce, J. Wong-Leung, Q. Gao, H.H. Tan, C. Jagadish, **'Phase perfection in zinc blende and wurtzite III-V nanowires using basic growth parameters'**, *Nano Letters* 10, 908-915 (2010)
- 22 M. Ibáñez, R. Zamani, W. Li, D. Cadavid, S. Gorsse, N.A. Katcho, A. Shavel, A.M. López, J.R. Morante, J. Arbiol, A. Cabot, **'Crystallographic control at the nanoscale to enhance functionality: Cu<sub>2</sub>GeSe<sub>3</sub> nanoparticles as thermoelectric materials'**, *Chemistry of Materials* 24, 4615-4622 (2012)
- 23 M. Ibáñez, R. Zamani, W. Li, A. Shavel, J. Arbiol, J.R. Morante, A. Cabot, **'Extending the nanocrystal synthesis control to quaternary compositions'**, *Crystal Growth and Design* 12, 1085-1090 (2012)
- 24 M. Ibáñez, D. Cadavid, R. Zamani, N. Garcia-Castello, V. Izquierdo-Roca, W. Li, A. Fairbrother, J.D. Prades, A. Shavel, J. Arbiol, A. Pérez-Rodríguez, J.R. Morante, A. Cabot, **'Composition control and thermoelectric properties of quaternary chalcogenide nanocrystals: The case of stannite Cu<sub>2</sub>CdSnSe<sub>4</sub>'**, *Chemistry of Materials* 24, 562-570 (2012)

- 
- 25 D. Wang, C.M. Lieber, '**Nanocrystals branch out**', *Nature Materials* 2, 355-356 (2003)
- 26 L. Manna, D.J. Milliron, A. Meisel, E.C. Scher, A.P. Alivisatos, '**Controlled growth of tetrapod-branched inorganic nanocrystals**', *Nature Materials* 2, 382-385 (2003)
- 27 W. Qi, J. de Graaf, F. Qiao, S. Marras, L. Manna, M. Dijkstra, '**Ordered two-dimensional superstructures of colloidal octapod-shaped nanocrystals on flat substrates**', *Nano Letters* 12, 5299-5303 (2012)
- 28 L.-S. Li, J. Hu, W. Yang, A.P. Alivisatos, '**Band gap variation of size- and shape-controlled colloidal cdse quantum rods**', *Nano Letters* 1, 349-351 (2001)
- 29 F.-J. Fan, L. Wu, M. Gong, G.-Y. Liu, Y.-X. Wang, S.-H. Yu, S.Y. Chen, L.-Y. Wang, X.-G. Gong, '**Composition- and band-gap-tunable synthesis of wurtzite-derived  $\text{Cu}_2\text{ZnSn}(\text{S}_{1-x}\text{Se}_x)_4$  nanocrystals: theoretical and experimental insights**', *ACS Nano* 7, 1454-1463 (2013)
- 30 J. Arbiol, M. de la Mata, M. Eickhoff, A. Fontcuberta i Morral, '**Bandgap engineering in a nanowire: self-assembled 0, 1 and 2D quantum structures**', *Materials Today* 16, 213-219 (2013)
- 31 S.Y. Chen, A. Walsh, Y. Luo, J.H. Yang, X.G. Gong, S.-H. Wei, '**Wurtzite-derived polytypes of kesterite and stannite quaternary chalcogenide semiconductors**', *Physical Review B* 82, 195203 (2010)
- 32 C. R. Miskys, J. A. Garrido, C.E. Nebel, M. Hermann, O. Ambacher, M. Eickhoff, M. Stutzmann, '**AlN/diamond heterojunction diodes**', *Applied Physics Letters* 82, 290-292 (2003)
- 33 R. Zamani, R. Fiz, J. Pan, T. Fishcher, S. Mathur, J.R. Morante, J. Arbiol, '**Oxide-oxide nanojunctions in coaxial  $\text{SnO}_2/\text{TiO}_2$ ,  $\text{SnO}_2/\text{V}_2\text{O}_3$  and  $\text{SnO}_2/(\text{Ti}_{0.5}\text{V}_{0.5})_2\text{O}_3$  nanowire heterostructures**', *CrystEngComm* 15, 4532-4539 (2013)
- 34 M. Ibáñez, R. Zamani, S. Gorsse, J.D. Fan, S. Ortega, D. Cadavid, J.R. Morante, J. Arbiol, A. Cabot, '**Core-shell nanoparticles as building blocks for the bottom-up production of functional nanocomposites: PbTe-PbS thermoelectric properties**', *ACS Nano* 7, 2573-2586 (2013)
- 35 S.D. Carnevale, T.F. Kent, P.J. Phillips, A.T.M.G. Sarwar, C. Selcu, R.F. Klie, R.C. Myers, '**Mixed polarity in polarization-induced p-n junction nanowire light-emitting diodes**', *Nano Letters* 13, 3029-3035 (2013)

- 
- 36 F. Shao, M.W.G. Hoffmann, J.D. Prades, R. Zamani, J. Arbiol, J.R. Morante, E. Varechkina, M. Rumyantseva, A. Gaskov, I. Giebelhaus, T. Fischer, S. Mathur, F. Hernández-Ramírez '**Heterostructured p-CuO (nanoparticle) / n-SnO<sub>2</sub> (nanowire) devices for selective H<sub>2</sub>S detection**', *Sensors and Actuators B: Chemical* 181, 130-135 (2013)
- 37 F.A. Ponce, D.P. Bour, '**Nitride-based semiconductors for blue and green light-emitting devices**', *Nature* 386, 351-359 (1997)
- 38 W. Guo, M. Zhang, A. Banerjee, P. Bhattacharya, '**Catalyst-free InGaN/GaN nanowire light emitting diodes grown on (001) Si by molecular beam epitaxy**', *Nano Letters* 10, 3355-3359 (2010)
- 39 M. Heiss, Y. Fontana, A. Gustafsson, G. Wüst, C. Magen, D.D. O'Regan, J.W. Luo, B. Ketterer, S. Conesa-Boj, A.V. Kuhlmann, J. Houel, E. Russo-Averchi, J.R. Morante, M. Cantoni, N. Marzari, J. Arbiol, A. Zunger, R. J. Warburton, A. Fontcuberta i Morral, '**Self-assembled quantum dots in a nanowire system for quantum photonics**', *Nature Materials* 12, 439-444 (2013)





CHAPTER II: METHODOLOGY

## 2.1 Transmission electron microscope

When making the first sketch of his electron microscope (Figure 2.1), maybe Ernst Ruska did not imagine what a dramatic influence this device would make in the progress of materials science in future. In 1932 Knoll and Ruska published a paper in which they developed the idea of electron lenses into a practical reality and demonstrated electron images taken on the instrument. Ruska received the Nobel Prize “somewhat late” in 1986 (shortly before his death in 1988) for this crucial step. In fact, resolution limit in visible light microscopes (VLMs) on the one hand, and discovery of wave-like characteristics of the electron (with a wavelength substantially less than visible light) on the other hand, led to the idea of building an electron microscope. A couple of years after Ruska’s breakthrough, commercial transmission electron microscopes (TEMs) were developed which apparently did not work very well. In mid-1950s Bollman in Switzerland and Hirsch and co-workers in Cambridge (UK) developed the techniques of metal foil thinning to approach electron transparency and in mid-1970s commercial TEMs were already capable of resolving individual atomic columns in the crystal.<sup>1,2</sup>

TEM techniques keep being improved and nowadays TEM is undoubtedly the most efficient and versatile tool for characterization of materials over spatial ranges from atomic scale to several hundred nanometers. A somewhat recent invention was development of aberration correction of the electromagnetic lenses which caused a drastic progress in enhancement of TEM resolution. In this chapter after explain the basic principles of TEM we will briefly discuss the issue of aberration correction, and then we will move on to the methods and techniques that we utilized to perform the experiments in this report.

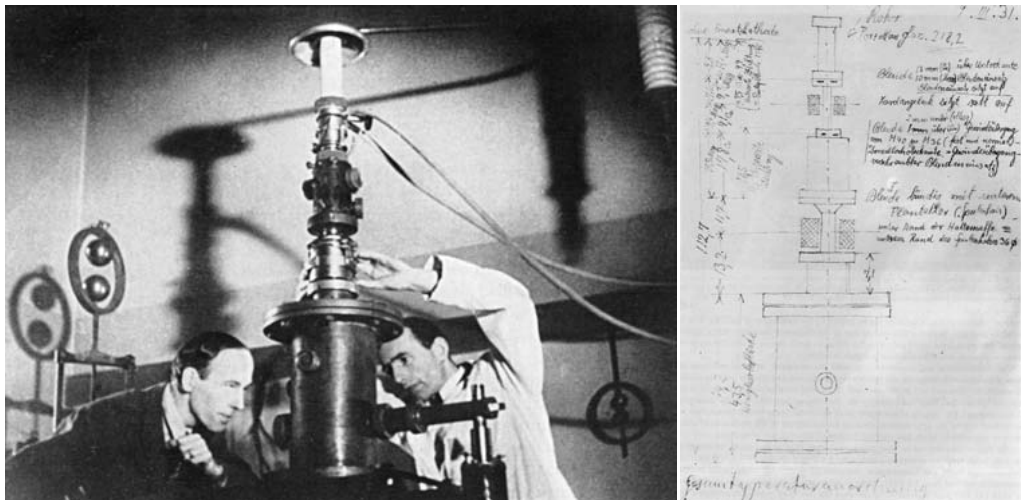


**Figure 2.1** (Left) Knoll (at left) and Ruska (in the lab coat) building up the first electron microscope, (right) Ruska’s first electron microscope sketch

## 2.2 Basic principles of TEM

Figure 2.2 schematically shows the trajectory of electrons in the TEM and how the images form (Condenser lenses and apertures are not considered). The working principle of the TEM is closely related to that of the VLM. Assume a plane wave of coherently accelerated electrons is incident on the sample under investigation. Within the sample, such a plane wave is no longer an eigenfunction of the system; it gets diffracted and generates different Bloch waves. For very thin samples it is considered that the wavefunction at the exit plane of the object is not dependent on the thickness of the sample. By means of the ‘*objective lens*’ the diffracted beams are focused onto the ‘*back focal plane*’ of this lens, where the ‘*objective aperture*’ is positioned. Note that ‘*back focal plane*’ is where the parallel beams cross. With some mathematics, if the wavefunction of the exit plane of the object (object function) is given by  $f(x,y)$ , the diffracted amplitude of the beam is given by the Fourier transform of the object function:

$$F(u,v) = \mathcal{F}[f(x,y)] \quad (2.1)$$

Then, these ‘spherical waves’ interfere in the first image plane which leads to the formation of the image. Mathematically it is the inverse Fourier transform of the waves at the back focal plane:

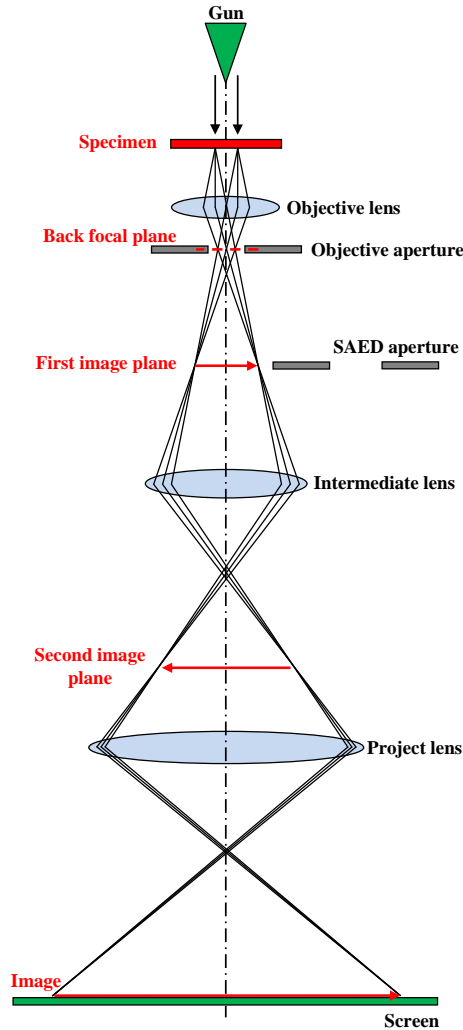


**Figure 2.2** Schematic illustration of electron trajectory in TEM and image formation

$$\psi(x,y) = \mathcal{F}^{-1}[F(u,v)] \quad (2.2)$$

and the intensity of the image plane is given by  $|\psi(x,y)|^2$ . Van Tendeloo believes that “reality is distorted by the microscope.” In a simple way all the microscope’s parameters such as spherical ( $C_s$ ) or chromatic aberrations ( $C_c$ ), coma or focus, are combined in the so-called ‘transfer function’,  $\exp[i\chi(u,v)]$ , which is considered in the image as bellow:

$$\psi(x,y) = \mathcal{F}^{-1}\{F(u,v)\exp[i\chi(u,v)]\} \quad (2.3)$$

It is shown that only the imaginary part of the transfer function affects the intensity in the image. It is plotted in Figure 2.3. It should be pointed out that this function is quite sensitive to  $C_s$ ,  $C_c$ , and focus. As an example it is shown how a small change in  $C_s$  causes a considerable change in the transfer function.<sup>3</sup> As can be seen in this figure, contrast transfer in an image has an oscillatory behavior. Transfer contrast is at maximum when transfer function is in one of the maximum points, and in the zeros no contrast is transferred to the image, meaning a considerable amount of information is lost.

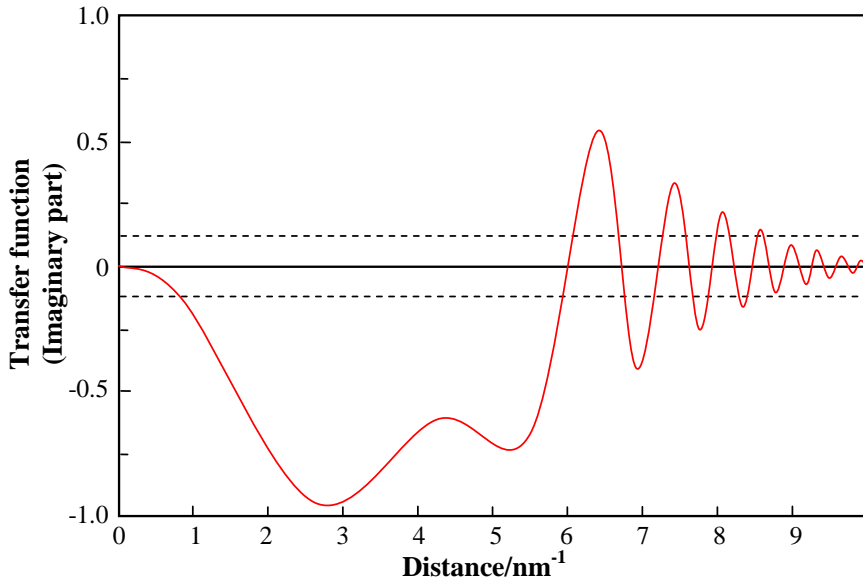


**Figure 2.3** Transfer function

### 2.2.1 Electron-matter interaction

With interaction of the electron beam with the specimen a wide range of secondary signals are produced as seen in the schematic illustration of Figure 2.4. The electron beam is an ionizing radiation, meaning it is capable of penetrating into the electron orbitals and remove the tightly-bound inner-shell electrons from the attractive field of the nucleus. The mentioned secondary signals are used in different techniques of electron microscopy. Secondary electrons (SE) and back-scattered electrons (BSE) are usually used in a scanning electron microscope (SEM) and Auger electrons in Auger electron spectroscopy (AES) which gives information of the specimen surface. In Figure 2.4 the signal that are shown in red are the ones we use in TEM. X-rays coming out from the

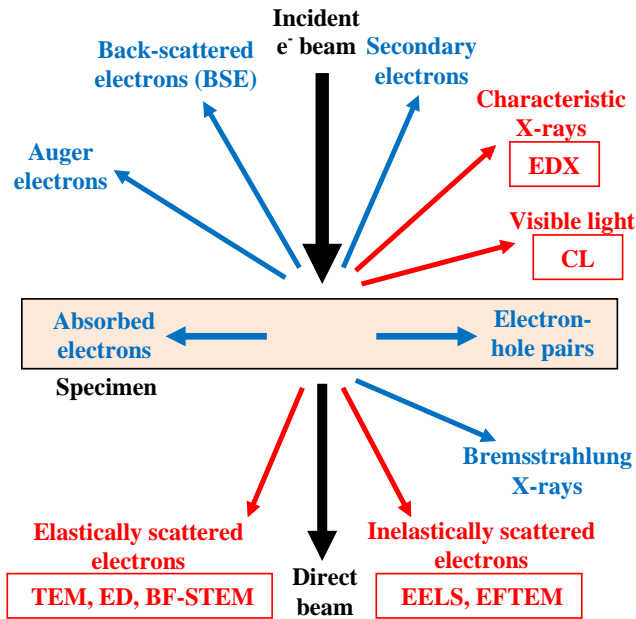


**Figure 2.4** The interaction of the electrons with matter, the signals shown in red are the ones we detect and use in TEM

upper face of the sample are collected by a detector for energy-dispersive X-ray spectroscopy (EDX and also EDS and XEDS) which is an analytical technique showing the chemical composition. Visible light (and also a part of the photons in UV-range) can be sent to a cathodoluminescence (CL) detector for chemical and optical analyses. These methods will be discussed in this chapter while their applications in materials science are shown in the next ones.

Some of the transmitting electrons continue their trajectory without being scattered (direct beam) and do not carry any information. In contrast, the scattered ones are pretty vital to TEM analyses. Scattering of the transmitted electrons can occur ‘*elastically*’ and ‘*inelastically*’ where each of them can be ‘*coherent*’ or ‘*incoherent*’ referring to their wave nature. Nevertheless, it should be taken into account that elastically scattered electrons are ‘usually’ coherent and inelastically scattered ones are ‘usually’ incoherent.

Elastically scattered electrons are the ones which create the intensity in diffraction patterns (DPs). They are also the major source of contrast in TEM images. Elastic scattering means that the electrons do not lose their energy in their interaction with the specimen. Note that the truly-elastic scattering never happens; energy loss can be neglected just for simplification. After being elastically scattered and transmitted from a crystalline specimen, the electrons

form a diffraction pattern. Such electrons provide pivotal information about the crystal structure of the specimen. Details of the mathematics behind the diffraction an elastic scattering can be found in the TEM textbooks.<sup>1,4</sup>

On the other hand, inelastically scattered electrons are equally important as they carry information about the chemistry of the specimen. Beside inelastically scattered (often referred to energy-loss) electrons, other inelastic signals such as X-rays and visible light are used for chemical techniques in TEM. However, with the term inelastic scattering we refer to the as-transmitted electrons that are used in electron energy-loss spectroscopy (EELS) which will be described in the following sections.

### 2.2.2 The concept of resolution

The smallest resolvable distance between two points is known as ‘*resolution*’ or ‘*resolving power*’ of the device. For a VLM, in terms of the classic Rayleigh criterion, this minimum distance that can be resolved,  $\delta$ , is given by:

$$\delta = \frac{0.61\lambda}{\mu \sin \beta} \quad (2.4)$$

where  $\lambda$  is the wavelength of the radiation,  $\mu$  the refractive index of the viewing medium, and  $\beta$  the semi-angle of collection of magnifying lens. Therefore, for green light for example, after applying some simplifying assumptions, the distances less than 300 nm cannot be resolved. This is indeed the resolution limit of VLMs.

In contrast, Louis de Broglie’s equation shows that the wavelength of the electron is related to its energy:

$$\lambda = \frac{1.22}{\sqrt{E}} \quad (2.5)$$

where  $\lambda$  is in nm and  $E$  in electron volts (eV). Thus one can determine that theoretically with higher electron energy, better resolution will be obtained. As an example, for 100 keV electron energy,  $\lambda \sim 4$  pm, and the resolution will be less than the diameter of an atom. However, imperfections (aberrations) in electromagnetic lenses of the TEM do not allow achieving such high resolutions.

In 1960s, high-voltage electron microscopes (accelerating potentials between 1 and 3 MV) were produced which are not used these days anymore as their aim, rather than pushing the resolution limits, was simulation of nuclear-

reactor environments. The other solution, that still is being used, is to correct the aberrations of the lenses. This will be discussed in the next section.

### 2.2.3 Aberrations and aberration correction

Invention of aberration-correctors was a breakthrough which pushed the TEM resolution below the angstrom barrier as in modern TEMs the resolution is ultimately limited by either spherical or chromatic aberrations. So in this section we briefly mention different types of aberrations and how the aberration correctors work.

Aberrations in TEM can have two main origins: the lenses and the incident beam. Lens imperfections lead to spherical aberrations ( $C_s$ ), and inequality of electrons' energies in the beam (not having a monochromatic beam) causes chromatic aberrations ( $C_c$ ). Note that the lenses can also cause  $C_c$ .

In an ideal optical system every single point on the object is supposed to be reproduced perfectly in the image, which is not the case in practice. If the angle that the rays make with the optical axis is  $\theta$ , the following approximation can be applied:

$$\sin \theta = \theta - \frac{\theta^3}{3!} + \frac{\theta^5}{5!} - \dots \quad (2.6)$$

In electromagnetic lenses as well, for very small angles the first order approximation can be applied:  $\sin \theta \sim \theta$ . At the next level, i.e. third order approximation, aberrations more obviously show up due to the distorting effect of the lenses. When the beam is not monochromated, the aberrations are due to the inherent energy spread in the electrons emitted from a source, fluctuations in the gun accelerating voltage or different losses due to interactions with the sample. In Figure 2.5 it is illustrated that the chromatic aberration in the lenses results in waves of different wavelengths and energies which leads to focuses at

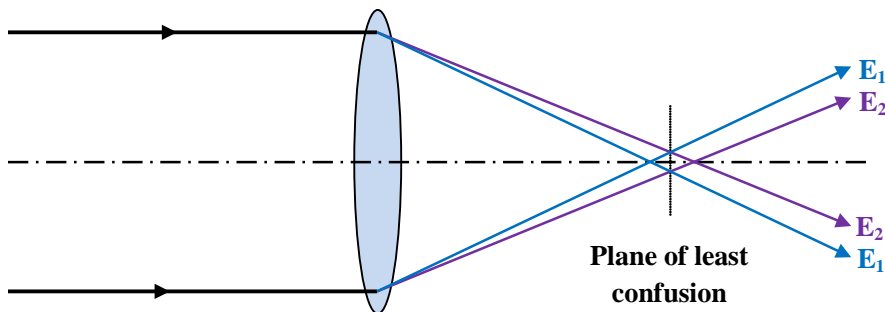


**Figure 2.5** Chromatic aberration

different points along the optical axis. Particularly, monochromatic aberrations are of five types: spherical aberrations, astigmatism, coma, field curvature, and distortion, where the first three ones are the most important and tried to be corrected by aberration correctors in the microscope. These aberrations are schematically shown in Figure 2.6 and we describe them one by one.

Spherical aberration is because the off-axis rays are not brought to a focus at the same point as paraxial rays. So a disc of least confusion can be defined which its diameter depends on the spherical aberration coefficient ( $C_s$ ) and the collection semi-angle of the lens (with the power of 3). What is illustrated in the

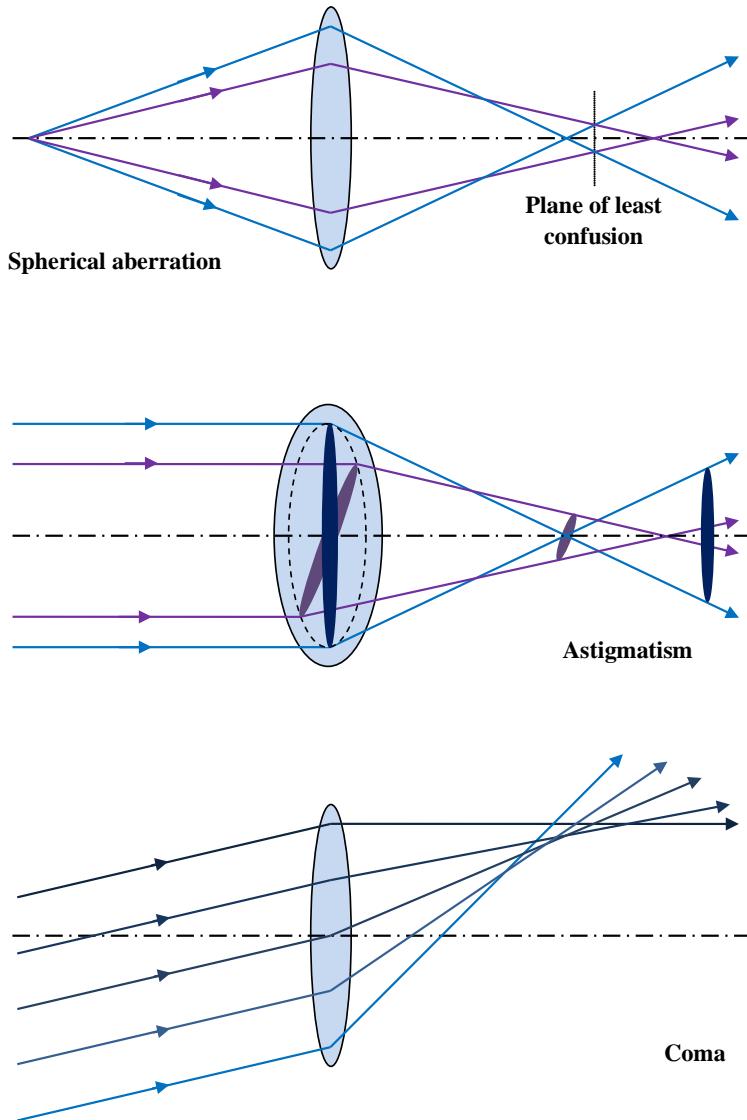


Figure 2.6 Spherical aberration, astigmatism and coma

upper scheme of Figure 2.6 is the longitudinal spherical aberration. Besides, transverse spherical aberration can also occur in which cross-over of the rays does not lie on the optical axis.

In the case of astigmatism, the cross-over of the off-axis rays is displaced along the optical axis but here the degree of displacement varies with the ‘azimuthal’ angle of the beam (see the center scheme in Figure 2.6).

Coma or comatic aberrations occurs in the case of rays that make a slight angle with the optical axis and are traveling through the center of the lens and they cannot be brought to a sharp focus point (see the lower scheme in Figure 2.6). It should be pointed out that any anisotropy in the lenses also adds additional contributions to coma, astigmatism, and distortion.<sup>5</sup>

Aforementioned lens aberrations show up in the third order approximation. In higher orders, more aberrations appear which are classified by their radial order (ray and wave) and azimuthal symmetry. Bleloch and Ramasse provide further details in their book chapter.<sup>6</sup> There it is explained how the aberration contributions are calculated and plotted. As examples, some of them are revealed in Figure 2.7. For aberration correction, it is of high importance to know how these contributions look like.

The  $C_s$ -correctors consist of a number of multipole lenses. Multipoles are named by their rotational symmetry (dipoles, quadrupoles,

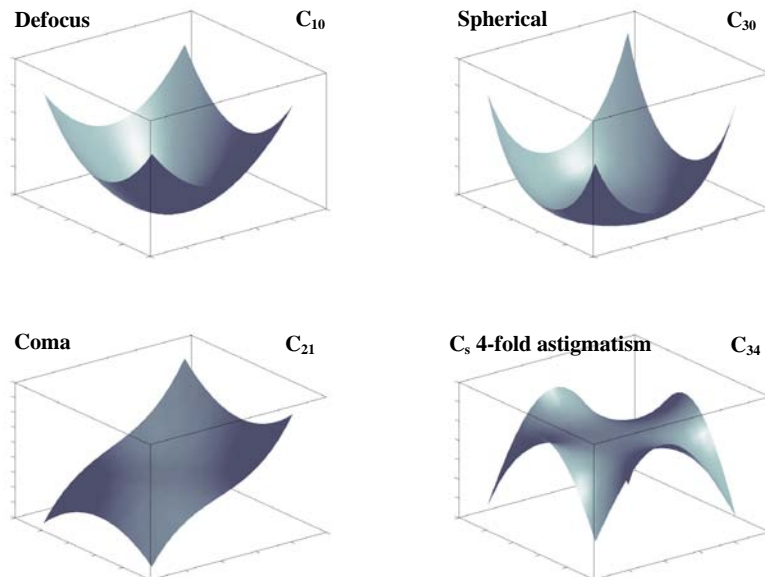


**Figure 2.7** Some aberrations<sup>6</sup>

hexapoles/sextupoles, octupoles, etc). See Figure 2.8. Usually quadrupoles and octupoles are combined (quadrupole-octupole correctors). These multipoles, like the alignment coils in the TEM, are normally magnetic; although a chromatic aberration corrector would have to have both magnetic and electrostatic poles.

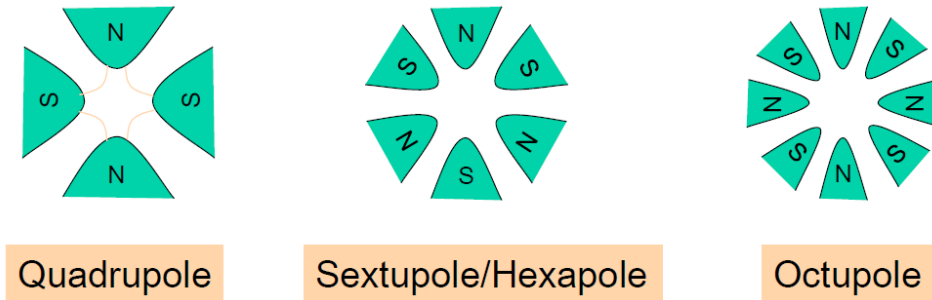


**Figure 2.8** Multipole lenses

Quadrupole-octupole correctors work because octupoles have a field that varies with distance off the optic axis in the same way as does spherical aberration but has a 4-fold rotational symmetry about this axis (with alternating sign on rotation by  $45^\circ$ ). Thus the quadrupole-octupole corrector relies on using a series of quadrupoles to distort the beam in a way that it acquires the negative spherical aberration from the octupoles and leaves the corrector as a round beam. Three octupoles are used in order to correct the round aberration in the X, Y, and  $45^\circ$  directions. In contrast, hexapole correctors rely on the fact that an extended hexapole imparts spherical aberration to a round beam in addition to the primary effect of 3-fold astigmatism. Further refinements allow the projection of one hexapole to another and then into the objective lens in such a manner as to eliminate the spherical aberration without increasing off axial or higher-order aberrations.<sup>7</sup> A miscellany of quadrupole-octupole and hexapole correctors is schematically shown in Figure 2.9.

After  $C_s$  correction up to fifth order, in many cases chromatic aberration becomes the limiting issue for further resolution improvements. Therefore it is important to have ways to minimize it. One solution is to reduce the energy spread of the electrons in the gun in order to obtain a more monochromatic beam. The second approach can be energy filtering of the beam after passing through the sample (i.e. energy-filtered transmission electron microscopy, EFTEM). The latter is more demanding than the former due to requirement of a more precise filter. The third approach to  $C_c$  correction is through the optics. First, the electrons with different energies are separated, and then their trajectory

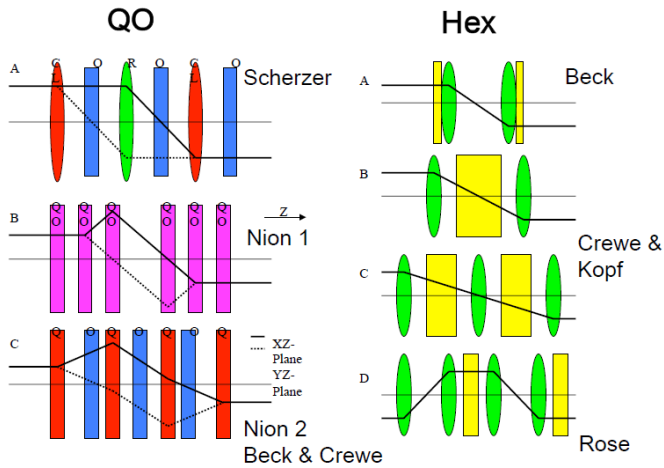


**Figure 2.9** A miscellany of correctors

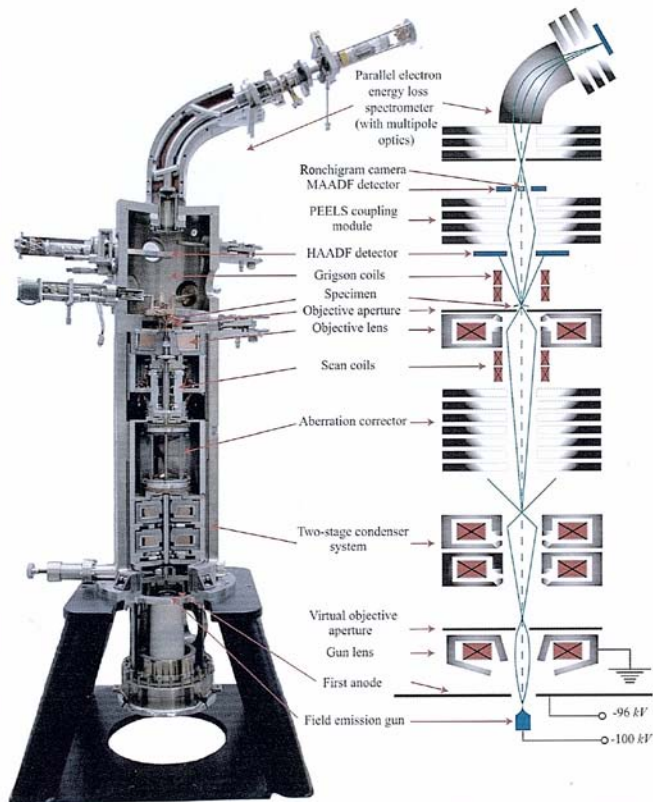


**Figure 2.10** A sectioned Nion STEM with correctors, associated with the scheme

is corrected by allowing them to pass through a field which modifies their energy.<sup>6</sup> A scheme of correctors in an aberration-corrected TEM is shown in Figure 2.10.

In summary, aberration-correction technology was a breakthrough in TEM characterization, as it pushed the resolution limits to sub-angstrom and even sub-half-angstrom,<sup>8</sup> especially in high-resolution STEM techniques<sup>9</sup> which will be discussed in the following sections.

### 2.3 Diffraction

Electron diffraction (ED) indeed is the most important phenomenon in TEM. It follows some principal rules of X-ray diffraction (XRD), e.g. Bragg's law, although they are quite different from many aspects. Here we just talk about the positions of spots, not their intensities.

The fundamental equation of diffraction, known as '*Bragg equation*' refers to reflection of an electromagnetic ray from a set of parallel planes:

$$2d \sin \theta_B = n\lambda \quad (2.7)$$

This equation was named after W.L. Bragg, who first derived it in 1912. See Figure 2.11. Bragg equation states that constructive interference from a set of consecutive parallel planes (in a crystalline structure these are atomic planes) can only take place for certain angles  $\theta$ , and that is determined by the wavelength  $\lambda$  and the interplanar spacing  $d$ . Such an angle is known as '*Bragg angle*' indicated by  $\theta_B$ .

If  $d_{hkl}$  represents the  $hkl$  planes' spacing, in reciprocal space we have:  $d_{hkl} = 1/|\mathbf{g}_{hkl}|$  where  $\mathbf{g}_{hkl}$  is the reciprocal lattice vector.  $\mathbf{g}_{hkl}$  is the reciprocal lattice

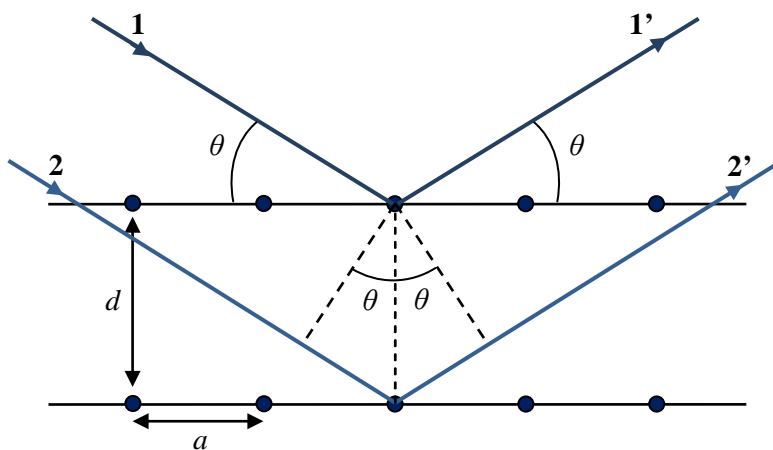


**Figure 2.11** Reflection of an electromagnetic ray from a set of parallel planes

vector,  $\mathbf{k}$  and  $\mathbf{k}'$  are the wave vectors of the incident and the diffracted waves, respectively. Therefore as can be seen in Figure 2.12:

$$\mathbf{k}' = \mathbf{k} + \mathbf{g} \quad (2.8)$$

In XRD the diffracted beam with the wave vector  $\mathbf{k}'$  will be present if and only if the endpoint of the vector  $\mathbf{k} + \mathbf{g}$  lies on the Ewald sphere (a graphical tool with radius of  $1/\lambda$  to describe diffraction events). In contrast, it is not exactly so in TEM, because due to the ‘excitation error’ even the vectors that are close to Ewald sphere appear on the screen. However, we should orient our crystal in a way that the whole plane of reciprocal lattice points is tangent to the Ewald sphere. So in general, there will be many diffracted beams close to the transmitted one simultaneously, and thus we have a ‘*diffraction pattern*’ (DP).

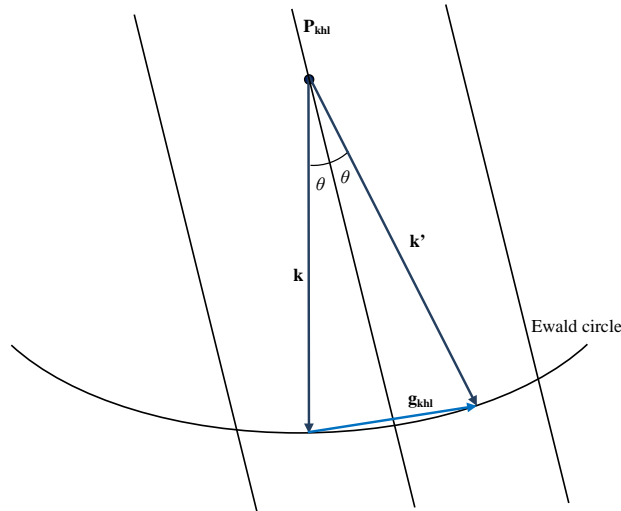


**Figure 2.12** Bragg's law in ED reciprocal space

In XRD Bragg's law predicts the geometrical conditions that need to be satisfied in order to observe diffraction from sets of lattice planes in a crystal. This is not the case in ED, because electrons are charged particles and they are not only diffracted from the interactions with the nuclei, but also the electron cloud around them. In TEM, almost from any angles diffracted spots can be seen (due to the excitation error), however, for precise crystal structure analysis it is important to find the correct zone axis.

The equation below shows that the electron wavelength depends on the accelerating voltage of the TEM:

$$\lambda = \frac{h}{mv} = \frac{h}{\sqrt{2m_0eV(1+\frac{e}{2m_0c^2}V)}} = \frac{1226.39}{\sqrt{V+0.97845 \times 10^{-6}V^2}} \quad (2.9)$$

In TEM, we seldom change the accelerating voltage. The most common voltages are 200 or 300 kV, and for some special experiments (delicate samples/experiments) 60 or 80 kV is used in order to avoid damages to the sample. On the other hand, the diffraction semi-angles are in the order of several milliradians, therefore  $\sin \theta \sim \theta$  can be considered in the Bragg's law, and thus:

$$2d_{hkl}\theta = \lambda \quad (2.10)$$

This means that the diffracted electrons are quite close to the incident beam, and hence we need to look closer in order to see the DP. In many cases we have to obscure the incident beam, because its intensity does not allow observing the rest of the spots, or it can damage the viewing screen or the charge-coupled device (CCD) camera.

Originally, in order to have the diffraction pattern (DP) on the viewing screen we use the 'diffraction mode' as in Figure 2.13. In this mode, the imaging-system lenses are adjusted so that the back focal plane (BFP) of the objective lens acts as the object plane for the intermediate lens. There are two main methods for using ED: selected-area electron diffraction (SAED), and convergent-beam electron diffraction (CBED). In SAED, the DP contains of intense spots whereas in CBED these spots are opened to some bright discs. From these discs crucial information about the crystal structure (e.g. polarity) can be obtained.<sup>10</sup> However, as CBED was not used in this thesis, here we only focus on SAED. We introduce the SAED aperture in order to select the area of interest and avoid overlap of DPs from different parts of the sample.

In a SAED pattern, the distance of a spot from the central point of the DP represents (reciprocally) the plane spacing. In other words, each spot or vector  $\mathbf{g}$  is a Bragg reflection that determines the crystal  $hkl$  plane distance. In addition, the angle between the reflections ( $\mathbf{g}$  vectors) determines the angle between atomic planes, and therefore, all together they provide vital information about the crystal structure. The diffracting planes are all in a specific zone axis  $UVW$ , which we can define as parallel to the incident beam direction. To sum up, DPs are the basis of all image formation in the TEM. They play the role of paramount importance in all crystallographic analysis as well as defect characterization.<sup>1,11</sup>

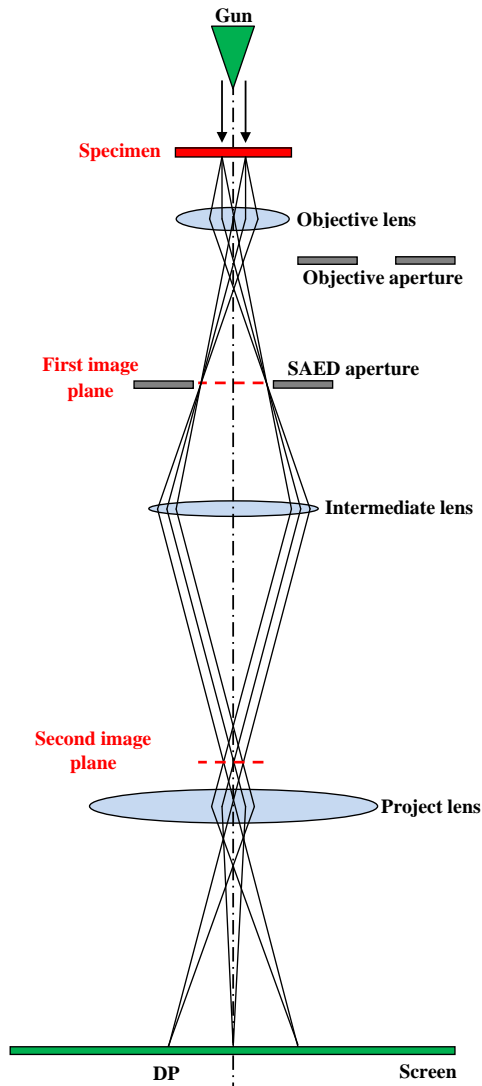


**Figure 2.13** Schematic illustration of electron trajectory in TEM in diffraction mode

## 2.4 TEM imaging

In the previous sections we showed how a TEM image is formed as the scattering of the incident beam by the specimen gives rise to the image contrast. In this section we focus on some imaging techniques. In fact images can be divided into two main groups: TEM and STEM (scanning transmission electron microscopy) images. In both cases we can have bright-field (BF) and dark-field (DF) images.

In this section we start with TEM imaging techniques, and then we will move on to STEM ones, and in each case we start with conventional TEM techniques and we finish with the state-of-the-art high-resolution techniques in aberration corrected microscopes.

### 2.4.1 Bright-field and dark-field TEM imaging

As mentioned previously, ‘contrast’ is the main task in image formation. Between amplitude contrast and phase contrast in TEM BF/DF images we only focus on the former which can be divided into two principal types: ‘mass-thickness contrast’ and ‘diffraction contrast’. Their contribution in the TEM/STEM images will be discussed in this section.

BF and DF TEM are the two basic ways to form amplitude-contrast images. TEM BF images are the ones we see in the viewing screen, and by lifting the screen we allow the electrons to arrive to the CCD. Such images are formed by diffracted beams and the contrast mostly depends on the atomic number ( $Z$ ) and the thickness.

The general contrast of a BF also depends on the size of the selected objective aperture. If you select a larger aperture, more scattered electrons are allowed to contribute to the BF image. So the contrast between scattering and non-scattering areas is lowered, although the overall image intensity increases. Figure 2.14 shows how introducing the objective aperture improves the contrast.

In TEM BF imaging the objective aperture should be centered on the center of the DP. In contrast, for TEM DF imaging the aperture should move in a way that the central beam is obscured. In fact DF images show regions of contrast that are complementary to those seen in the BF, but prepared for exceptions. In the DP usually many spots can be seen where each spot corresponds to unique

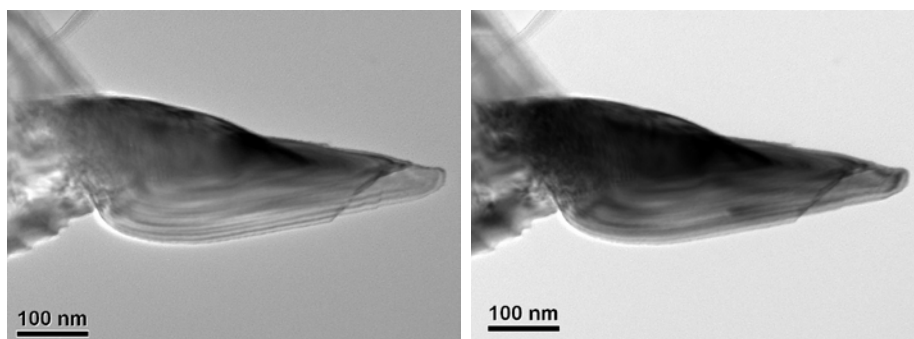


**Figure 2.14** BF-TEM images of a piece of silicon on an amorphous carbon layer (right) with and (left) without introducing the objective aperture

lattice fringes. If one moves the aperture in a way that only a few spots pass, they obtain a contrast in the image that only refers to those spots. In other words, as an advantage of this method, one can distinguish which reflections come from which parts/lattice fringes of the specimen. It is quite useful for finding the defects, or polycrystallinity in the sample. For instance, Figure 2.15 shows a BF (left) and two DF images (center and right) of a GaAs nanowire covered with a Pt shell. As Pt atoms are quite heavy, in the BF image the shell looks quite dark and it does not let the GaAs lattice fringes to be seen. To obtain the DF images, the aperture was moved to two different directions in order to reveal the polycrystalline nature of the shell. These two images in comparison show that the shell consists of Pt grains in different crystallographic directions where in each image, corresponding reflections of the bright parts were grabbed.

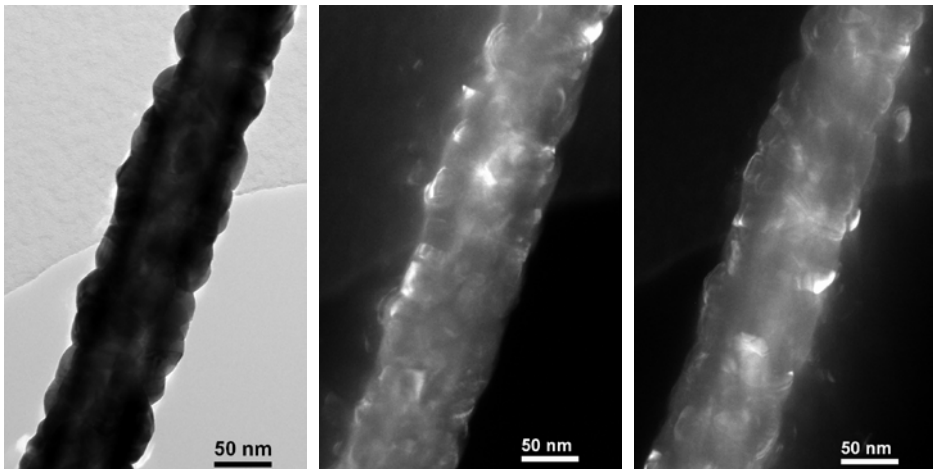


**Figure 2.15** BF and DF TEM micrographs of a GaAs@Pt core-shell nanowire, DF images with the aperture placed on different reflections

### 2.4.2 High-resolution TEM

High-resolution transmission electron microscopy (HRTEM) is a powerful technique for crystal structure analysis which takes advantage of phase contrast. In fact HRTEM is the most-used technique in this thesis.

In general, contrast in TEM images can arise due to the differences in the phase of the electron waves scattered through a thin specimen. This contrast mechanism can be difficult to interpret because it is very sensitive to many factors: the appearance of the image varies with small changes in the thickness,

orientation, or scattering factor of the specimen, and variations in the focus or astigmatism of the objective lens. However, such sensitivity is the reason phase contrast can be exploited to image the atomic structure of thin specimens. This requires a TEM with sufficient resolution to detect contrast variations at atomic dimensions and the proper control of instrument parameters that affect the phases of the electrons passing through the specimen and the lenses. Field-emission gun (FEG) in TEM was one of the advancements in electron microscopy which provided higher resolutions as it has an incident beam with lower energy dispersion compared to that of traditional filaments (W, LaB<sub>6</sub>, or CeB<sub>6</sub>).

The relationship between the lattice fringes and the spots in the DP is already described in section 2.3. In Figure 2.16 we follow a reverse approach in order to show how lattice fringes are produced in a HRTEM image. In this figure a tin dioxide nanowire with rutile structure (tetragonal symmetry) is shown from [010] zone axis.

In section 2.2 it was shown how a TEM image is formed by an inverse Fourier transform of the waves at the back focal plane. In a similar way, by applying the fast Fourier transform (FFT) on a HRTEM image, one can obtain a power spectrum which gives the same pattern as the corresponding DP. The inverse FFT (IFFT) of the power spectrum results on the initial HRTEM image. Nonetheless, we have the possibility of filtering the power spectrum before IFFT, which has some advantages. It allows us to determine the correspondence between the reflections and lattice fringes in the image, or to reduce the image noise.

From these mentioned advantages, the former is shown in Figure 2.16. Here we use the power spectrum filtering in order to simulate the appearance of lattice fringes in HRTEM images. In the upper part, the lattice fringes corresponding to the indicated reflections are shown. These reflections, and accordingly the lattice fringes, are representative of the atomic plane ((10-1) and (200)) in the rutile SnO<sub>2</sub> structure. In the center, two consecutive reflections are filtered. The important point here is that the closer spot to the center results in bigger fringes, where the farther spot gives smaller fringes. This shows the relationship between the reciprocal space and lattice planes. The lower image shows the result of the overlap of lattice fringes. In a DP, if the objective aperture is placed in a position that the reflections inside the circle can pass, we will have an image in which the atomic columns are seen as bright point, as observed in the lower-left image in this figure.

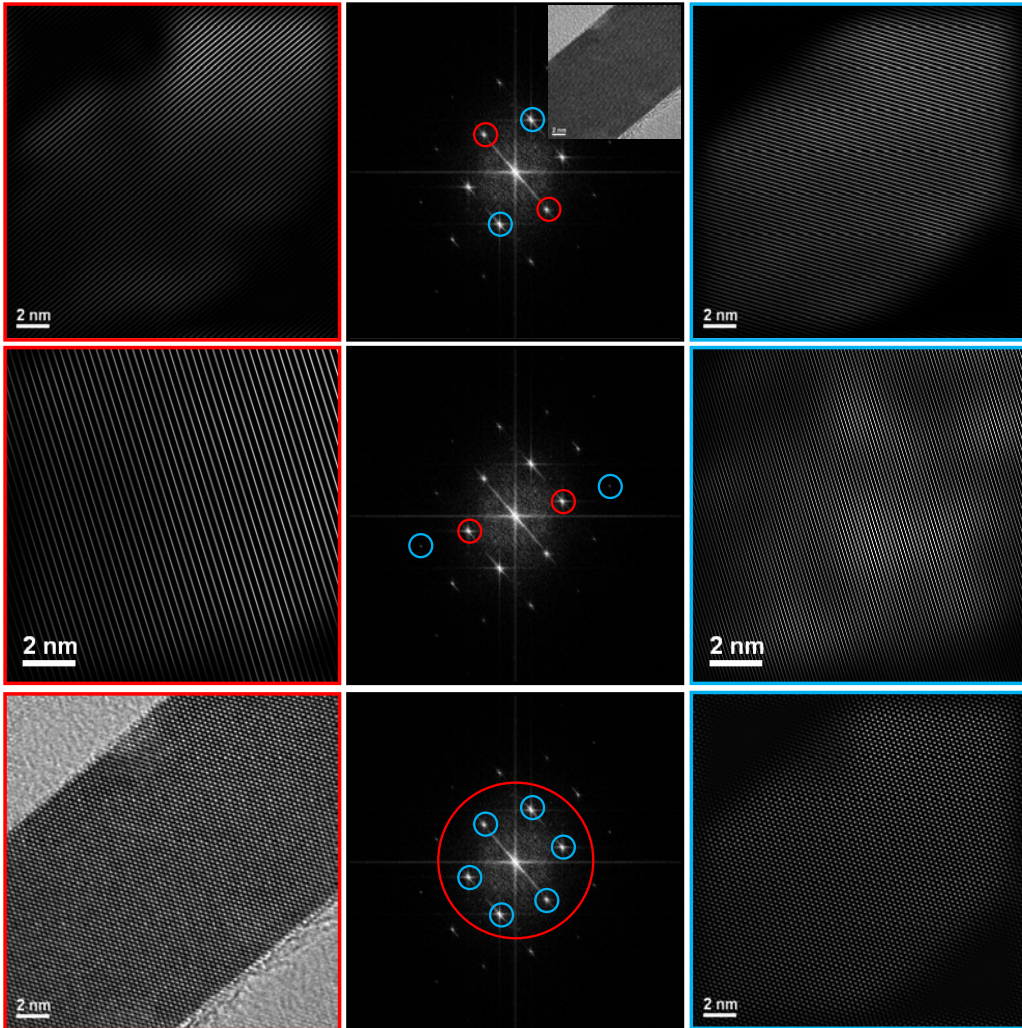


**Figure 2.16** Lattice fringes in HRTEM images and their reflections in the DF

It is worth to point out that in HRTEM images we need to be in a correct '*defocus*'. First of all we should clarify that by assuming the specimen as a '*weak-phase object*', we are using the transfer function instead of the contrast transfer function which has no contribution of amplitude phase. The presence of zeros in the imaginary part of the transfer function (see Figure 2.3) means that we have gaps in the output spectrum and important information is lost in these points. In the case of ideally perfect lenses, transfer function has the fewest zeros, which is not the case. Spherical aberration has the most considerable contribution in existence of zeros. However this effect can be minimized by a

certain negative value of defocus known as ‘*Scherzer defocus*’ ( $\Delta f_{Sch}$ ) which occurs at:

$$\Delta f_{Sch} = -1.2\sqrt{C_s\lambda} \quad (2.11)$$

At Scherzer defocus all the beams will have nearly constant phase out to the first crossover of the zero axis. This point is defined as the instrumental resolution limit which is the best performance that can be expected from a TEM.<sup>12</sup>

It should be taken into account that in HRTEM sometimes the structure is not as it appears. This especially takes place in the case of overlap of two close (but not the same) structures, as well as the case of plane defects when they are not perpendicular to the zone axis. When two different structures (with close lattice parameters) overlap, we see some periodical fringes that in fact do not exist; they just appear due to the interference of two sets of planes, and are known as ‘*moiré fringes*’. For instance, the indicated reflections close to the center of the power spectrum in Figure 2.17 do not represent any lattice planes. They can also be seen around the main reflections of the rutile SnO<sub>2</sub> structure. These reflections correspond to the moiré fringes that are indicated on the HRTEM micrograph.

Another issue that can lead to serious confusions in interpretation of HRTEM micrograph is the presence of planar defects such as twin boundaries with the plane vector non-perpendicular to the zone axis. For instance, a [111]

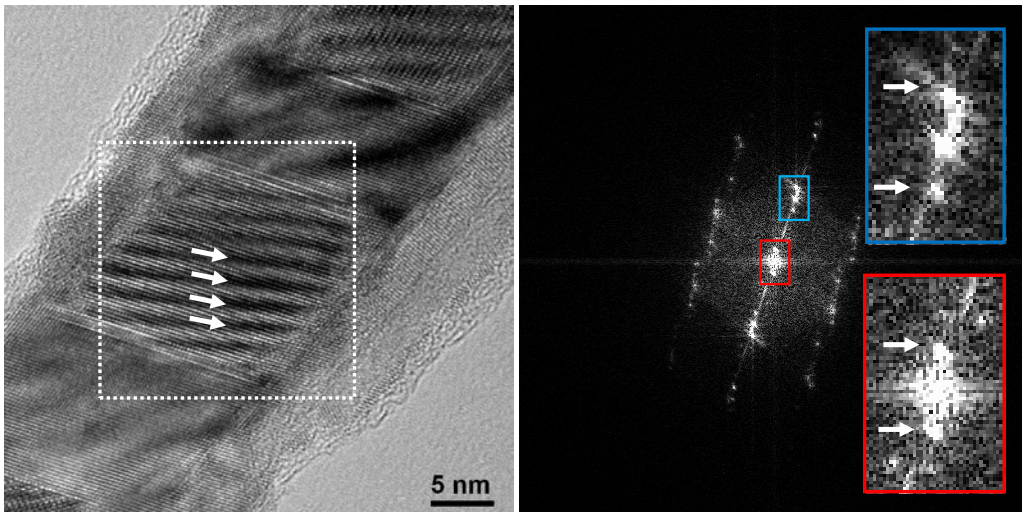


**Figure 2.17** Moiré fringes due to the overlap of two/three different structures in an SnO<sub>2</sub>@Ti<sub>2</sub>O core-shell NW

twin defect occurred in a zinc-blende (cubic) silicon nanoparticle can be seen from [110] zone axis, however, from [111] zone axis, one would be misled to this conclusion that the structure is hexagonal as they cannot figure out whether the twin has occurred. Kohno *et al.* showed this fact by simulation of HRTEM images.<sup>13</sup>

In summary, HRTEM is a powerful technique for crystal structure analysis of the materials. As mentioned before FEG-TEMs have improved the resolution limit by reducing the instrumental contribution of the chromatic aberration. During the last decade even sub-0.5-Å resolutions have been achieved by virtue of aberration correctors.

## 2.5 STEM imaging

In scanning transmission electron microscopy (STEM) imaging, unlike in SEM, the beam direction is always fixed. The beam, which is now called ‘probe’, moves on the sample without being tilted. Therefore, the objective lens optics in STEM is rather more complicated as the double deflection scan coils are introduced between the second and third condense lenses. In STEM mode we use electron detectors, in exactly the same way as we use the aperture, because the electrons diffracted with different angles can be used for different imaging techniques.

In STEM the beam scans the region of interest point by point. As the phase information was lost in such an imaging mechanism, it was regarded as ‘incoherent’. The fundamental difference between the conventional TEM (CTEM) and STEM is in the optics. In a CTEM the electron source is extended in a way that illuminates the whole object. In contrast, in STEM the true electron source is nearly a point source whose effective position is changed by the action of scanning coils.<sup>14</sup> It is shown in Figure 2.18. Furthermore, it should be simply mentioned that in CTEM the quality of the objective lens plays the key role in the resolution, whereas in STEM the key role is played by size of the probe.

Depending on the desired technique, we only allow the electrons that we want to contribute to the image to hit the particular detector. In Figure 2.19 a scheme of the STEM detectors is shown. The detectors consist of an annular (except BF detector) sensitive region that detects electrons scattered over an angular range and they follow the hollow-cone illumination (HCI) rules. The

inner and the outer radii are indicated on the figure. Now we have a brief look at STEM techniques one by one.

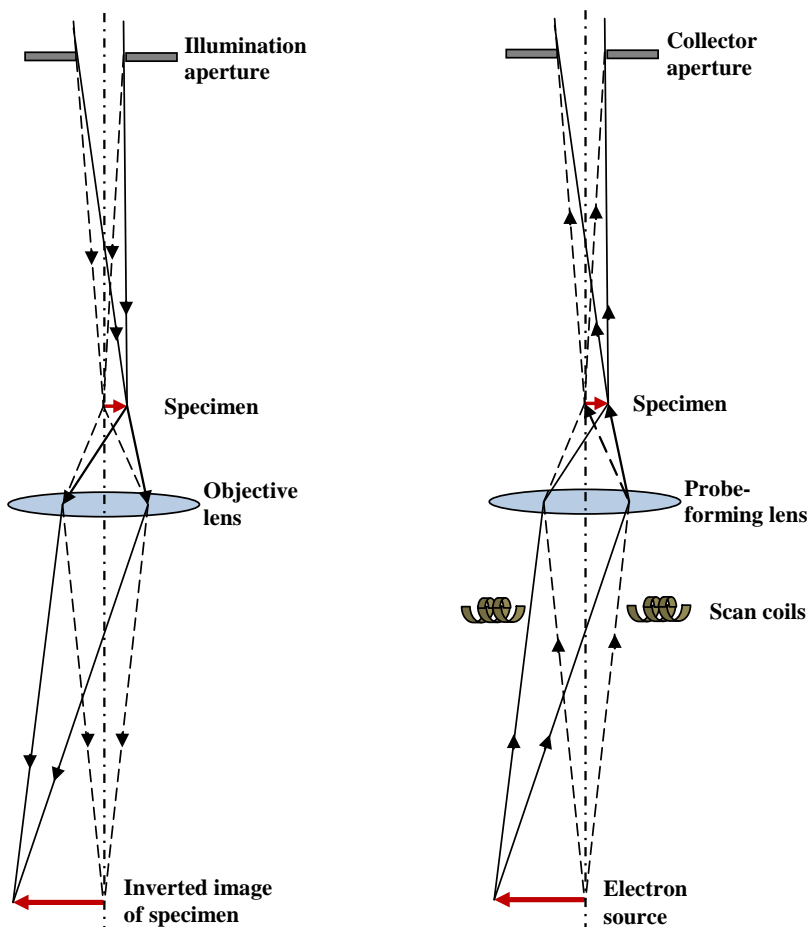


**Figure 2.18** STEM beam optics in comparison with that of CTEM<sup>14</sup>

### 2.5.1 Annular dark-field and high-angle annular dark-field STEM

The use of an annular dark-field (ADF) detector gave rise to one of the first detection modes used by Albert V. Crewe and co-workers during the initial development of the modern STEM.<sup>15</sup> The scattering comes mostly from Rutherford scattering by the atomic nuclei. Thus the intensity of the image increases by both number of the nuclei and their atomic number ( $Z$ ). By dividing the intensity in each image point by the intensity in the inelastic signal (which

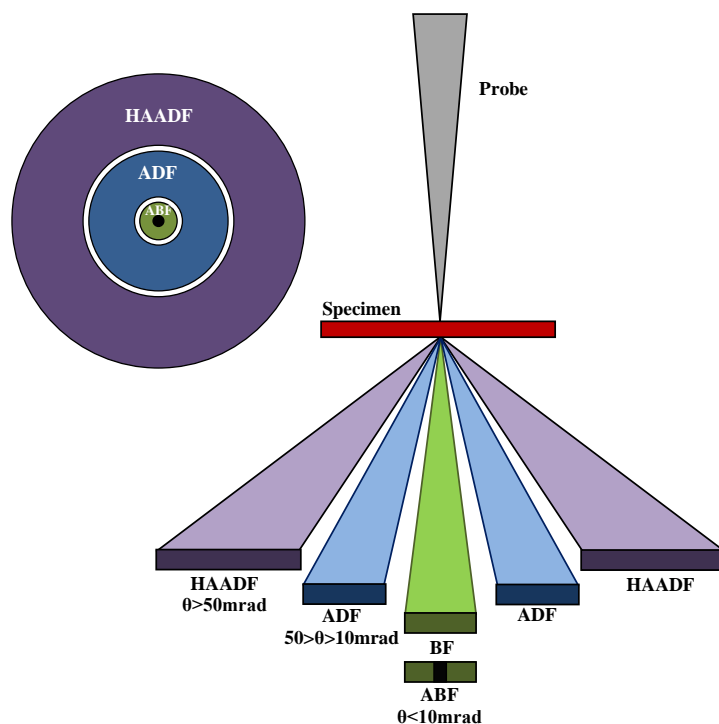


**Figure 2.19** Scheme of STEM detectors

increases with the thickness of the sample), one can obtain an image with intensity approximately proportional to the atomic number, meaning the heavier the atom, the brighter the image point. Thus the method was called by Crewe ‘*Z-contrast*’. It has remained by far the most popular STEM imaging mode. It was later proposed that high scattering angles ( $\sim 100$  mrad) would enhance the compositional contrast and that the coherent effects of elastic scattering could be neglected because the scattering was almost entirely thermally diffuse. This idea led to the use of the high-angle annular dark-field detector (HAADF) which usually collects the scattered electrons approximately over 50 mrad. A medium-angle annular dark-field (MAADF) detector is also used in some microscopes which has the collection angle in the range of 25-50 mrad. In HAADF the contrast comes from incoherent scattering (proved mathematically by Nellist), whereas in MAADF diffraction contrast contributes the most. Without going through the mathematical detail, we just point out that the HAADF image can be written as a convolution of the STEM probe intensity and an object function that represents the fraction of intensity that each atom is able to scatter to the detector.

Incoherent imaging leads to data that is much easier to interpret. The contrast reversals and delocalization usually associated with HRTEM images are absent, and generally bright features in an ADF image can be associated with the presence of atoms or atomic columns in an aligned crystal. Combined with the strong Z contrast that arises from the high-angle scattering this leads to a high-contrast, chemically sensitive imaging mode. Optimizing the conditions for incoherent imaging in STEM is simply a matter of getting the smallest, most intense probe possible.<sup>16,17</sup>

### **2.5.2 Bright-field and annular bright-field STEM**

It is already mentioned that the bright-field detector collects the electrons scattered in less than 10 mrad. By the principle of reciprocity this angular size of the detector in STEM corresponds to the illuminating aperture in CTEM, therefore, diffraction contrast can be observed. Similarly, phase contrast can also be utilized; however, it is much more efficient in CTEM than in STEM.

By blocking the center of the BF detector under the correct optical conditions, we can create an annular bright-field (ABF) detector which follows the rules of hollow-cone illumination (HCI) instead of the conventional axial one.<sup>18</sup> This enhances the contrast of light elements (such as N and O) dramatically in a way that even in the presence of heavy element, light ones can also be observed. Ishikawa *et al.* even reported on imaging of H columns by means of ABF-STEM.<sup>19</sup>

ABF phase-contrast imaging is based on wave interference, thus it is useful for detection of lighter atoms with extremely weak scattering, because this method requires the object (atoms) only to alter the phase of a wave. Note that the specimen must be thin enough to act like a weak-phase object. Characteristics of ABF imaging have been investigated on the basis of calculations of fast-electron propagations within the several compounds consisting of light atoms, and it is found that the light atoms can be visible over a wide range of specimen thickness even under strong dynamical diffraction conditions. The present phase-contrast transfer function description aims to give more fundamental insights into why ABF-STEM is able to provide enhanced phase contrast in terms of the improved lens properties.<sup>19,20</sup> Further detail is available in the literature.<sup>18-20</sup>

## 2.6 Spectroscopy

In this section we basically focus on aforementioned inelastic scattering which carry a vast amount of information and can be utilized in ‘*analytical electron microscopy*’, consisting in spectroscopy techniques such as EELS, EDX, CL, etc. The electrons from the incident beam that lose some of their energy and pass through the sample are used for electron energy-loss spectroscopy (EELS). They are accompanied with X-ray signals used for energy-dispersive X-ray spectroscopy (EDX). Additionally, cathodoluminescence (CL) signal can occur in semiconductors, where photons with energy equal to the band gap are emitted. In the following we provide more detail about these three methods and skip the rest. Also we will briefly describe the state-of-the-art aberration-corrected STEM-EELS which recently has opened new ways towards deeper materials science studies.

### 2.6.1 Electron energy-loss spectroscopy

Among all spectroscopy methods, EELS occupies a special place, as it probes the primary excitations and registers each excitation event independently of the deexcitation mechanism.

In energy loss spectra, three energy regions can be distinguished: (i) vibrational excitations, from a few meV to a few hundred meV, (ii) collective excitations (plasmons), intraband and interband transitions, from a few eV to around 40-50 eV, and (iii) inner shell excitations, above 40-50 eV. Vibrational excitations (phonons) cannot be characterized with current resolution of EELS devices. Collective excitations in ‘*low-loss EELS*’ give interesting information about the plasmonic states of the materials (especially metals). However, we do not use them in this thesis. In contrast, inner shell excitations (‘*high-loss EELS*’) are frequently used for chemical analysis of the specimen.

Energy loss ( $\Delta E$ ) of the inner shell excitations occur at:

$$\Delta E \geq E_F - E_B \quad (2.11)$$

where  $E_F$  is the Fermi level energy and  $E_B$  binding energy of the inner shell (always negative). The result is a special feature in the energy-loss spectrum, known as an ‘*inner shell loss edge*’. The threshold of the edge corresponds to the ionization energy of the particular electron shell of the atom. It is schematically shown in Figure 2.20 that each element, depending on the number of the electrons in the shells, can have various characteristic edges.<sup>21,22</sup>

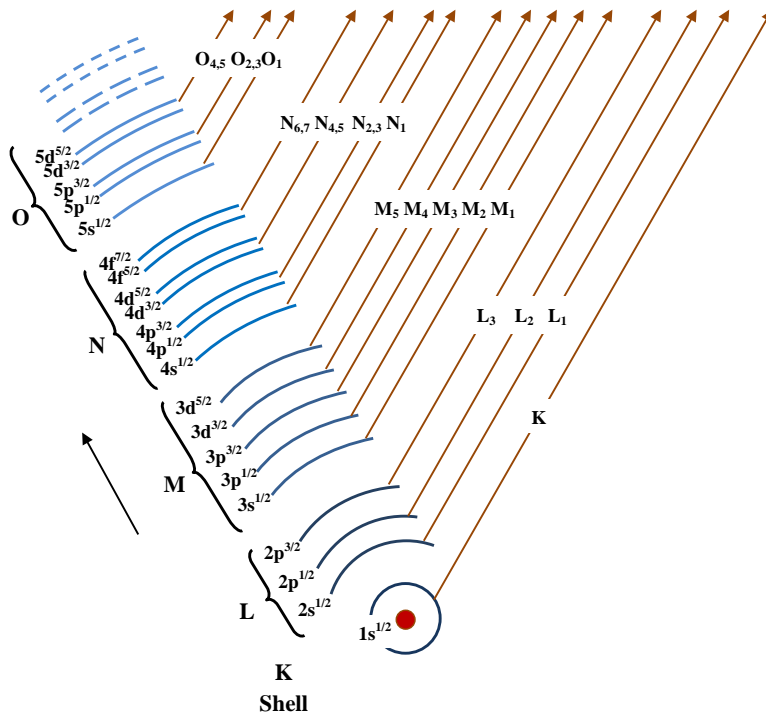


**Figure 2.20** Schematic illustration of EELS energy emission

Interestingly, sometimes changes in the chemical bonds (oxidation state) of the elements gives rise to variation of the edge shape. Therefore, the shape of the EELS shape can give an idea about the oxidation state. As an example, in Figure 2.21 Al EELS edge is shown in two different states: pure Al, and  $Al_2O_3$ . Al has a K edge with an abrupt onset at 1560 eV, i.e. the electrons that are detected by EELS detector with 1560 energy or higher, are the ones detached from the K inner shell ( $1s^{1/2}$ ) of Al atoms. A minor abrupt edge appears at 118 eV which refers to  $L_1$  inner shell. The  $L_2$  and  $L_3$  (they are the same from the aspect of bonding energy) edge appears at 73 eV which consists of a minor sharp peak at the threshold and a peak with delayed maximum. Information about the edges of the elements is gathered in an EELS atlas.<sup>21</sup>

The EELS spectrometer is shown in Figure 2.22. The magnetic prism of the EELS spectrometer creates a magnetic field which disperses the electrons due to their different energies and at the same time focuses the same-energy electrons to one point. Then the electrons pass through a ‘dispersion magnifying quadrupole’ in order to increase the energy resolution, where an energy selecting slit is placed soon after. Then the beam passes through a set of lenses

consisting of quadrupols and sextupoles for energy filtering where the signal is ready to be detected by the multi-scan camera.

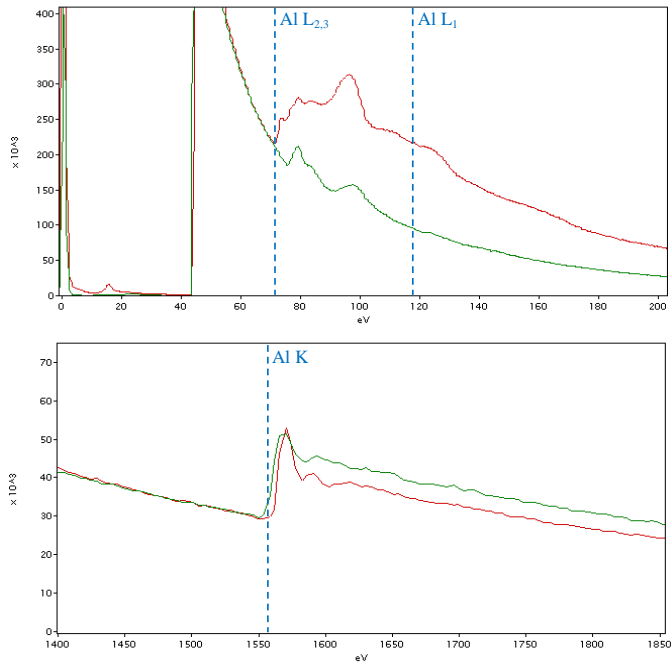


**Figure 2.21** Al EELS edge in different oxidation states: pure Al in green and Al<sub>2</sub>O<sub>3</sub> in red

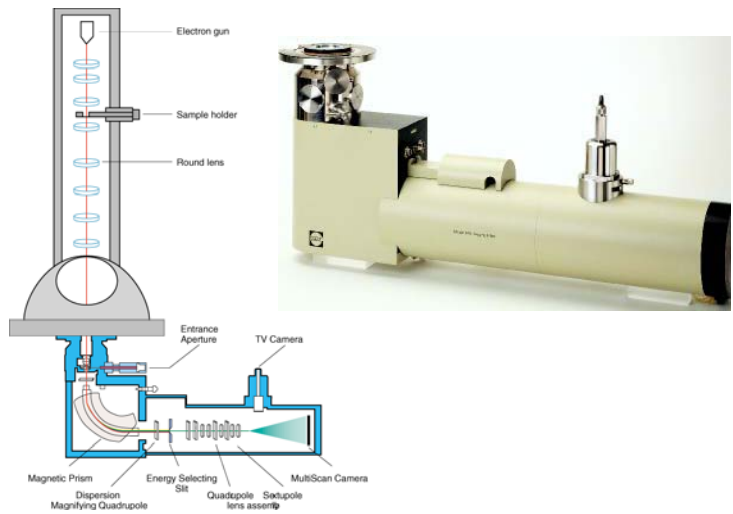


**Figure 2.22** EELS spectrometer (from Gatan Company) installed on a Jeol TEM

When the region of interest is scanned by the probe, a spectrum is acquired in each point, and therefore a ‘*data cube*’ with three coordinates  $x$ ,  $y$ , and  $E$  is recorded. By means of this data cube, one can perform elemental mapping in the

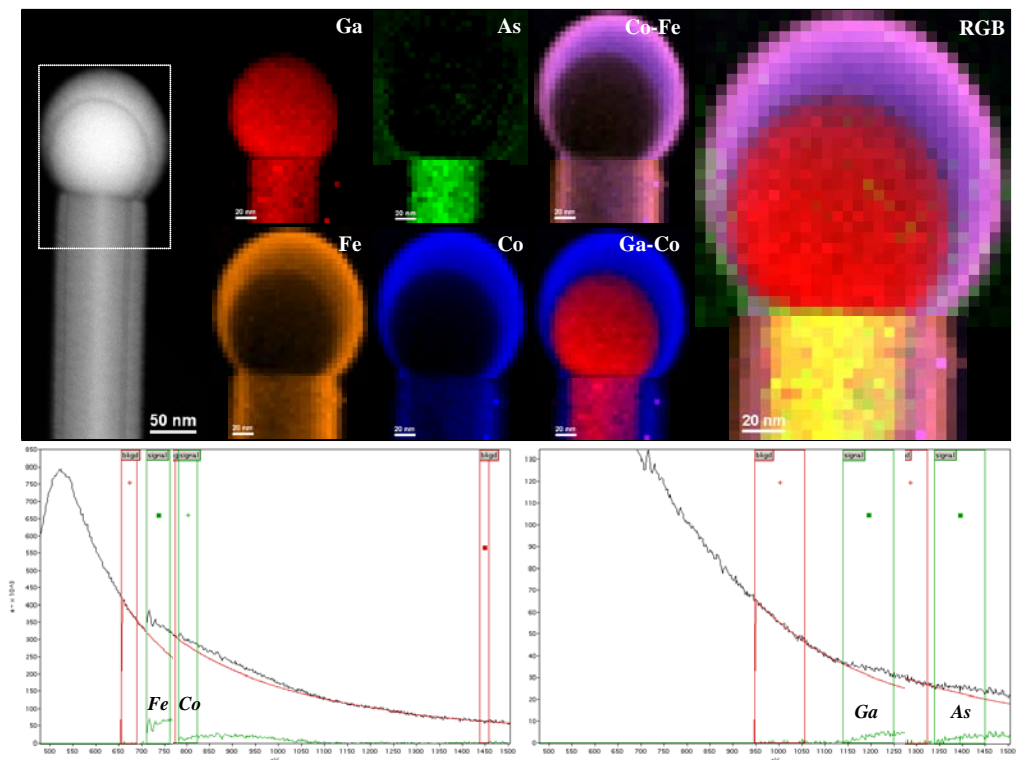


**Figure 2.23** EELS elemental mapping on a GaAs@CoFeB core-shell NW, EELS spectra showing the signals of the elements

**Figure 2.23** EELS elemental mapping on a GaAs@CoFeB core-shell NW, EELS spectra showing the signals of the elements

region of interest in the specimen. An example of elemental mapping on a GaAs nanowire covered with a CoFeB shell is revealed in Figure 2.23.

### 2.6.2 Aberration-corrected STEM-EELS

So far, aberration-corrected STEM in section 2.5.1, and EELS in section 2.6.1 have been discussed. Now we show that the combination of these two represents a powerful method to link the atomic and electronic structure of the materials to their microscopic properties at atomic scale. Aberration correction has a dramatic effect on both the distribution and the spatial localization of the intensity of the electron probe and subsequently on the resolution of STEM. As

we know, probe size is the most important parameter which limits the resolution of STEM.

Spherical aberration correction, although initially devised for conventional TEM, may have more benefits in STEM because of the reduced sensitivity of a STEM in the Z-contrast mode to chromatic aberration. Chromatic aberration correction may offer better resolution, larger pole piece gap or more flexible designs. As can be expected, a combined  $C_s$ - $C_c$  corrector would provide further benefit. The use of a monochromator would reduce chromatic aberration effects and also help improve energy resolution in EELS. The price paid for such a solution is reduced current, which then limits resolution due to an insufficient signal-to-noise ratio.<sup>7</sup> In the Chapter 3 we provide an example of aberration-corrected STEM-EELS method.

### 2.6.3 Energy-dispersive X-ray spectroscopy

X-ray is an important secondary signal generated in the specimen which is collected by an EDX (sometimes refer to as EDS) detector in TEM. By EDX one can easily find out which are the elements in the specimen. Note that here we only talk about ‘characteristic X-rays’, how they are generated and how they can be used in spectroscopy.

The high-energy electron beam penetrates to the inner shells and interacts with the electrons. As a result, an electron is ejected from the inner shells and the penetrating electron is scattered after losing that certain amount of energy that was required to eject the electron. Here an energy-loss electron is generated which will be used in EELS. On the other hand, this ionized atom needs to go back to its lowest energy, and thus an electron from the outer shell fills in the hole and this transition results in emission of either an X-ray or an Auger electron. Putting Auger electrons aside, the energy of the X-ray emission is ‘characteristic’ of the difference of energy between these two electron shells which is unique to the atom. This difference between the two shell energies equals the energy of the characteristic X-ray. The process of X-ray emission is shown schematically in Figure 2.24.<sup>1</sup>

Since characteristic X-rays typically have energies well above 1 keV, thousands of electron-hole pairs can be generated in the semiconductor detector used in EDX by a single X-ray (minimum 3.8 eV is required for Si at liquid-nitrogen temperature). The number of electrons or holes created is directly proportional to the energy of the X-ray photon. Even though all the X-ray



artifacts. Thus an electron trap is positioned right after the collimator. It comprises permanent magnets that strongly deflect the electrons. The window after the electron trap, which is tried to be transparent to low-energy X-rays, is

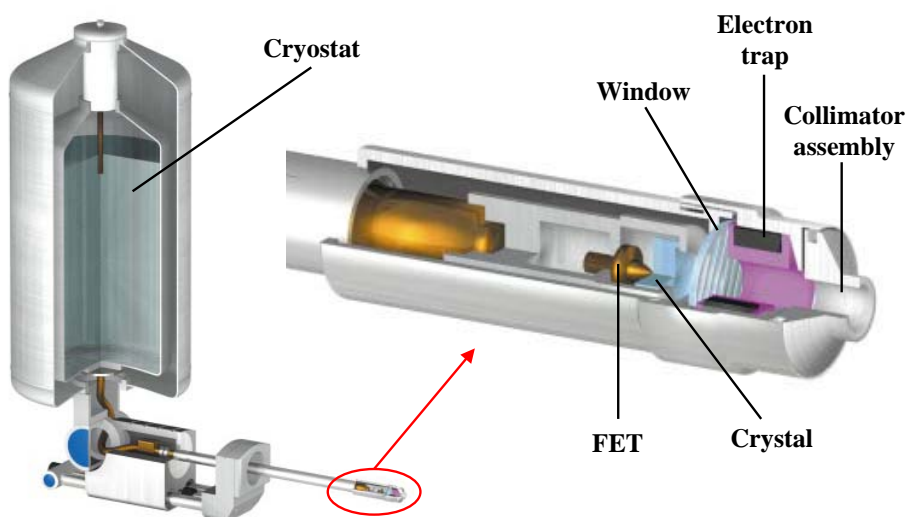


**Figure 2.25** Sectioned EDX detector and its components

just to maintain the vacuum. The crystal is the mentioned semiconductor device that converts the X-rays to proportional electric charges. Si (with some content of Li) and high-purity Ge are the most common crystals used in this context. These charges are sent to the FET for amplification and voltage output measurements. The crystal and the FET should be cooled down in order to be able to separate the generated signals from the noise.<sup>23</sup>

EDX is a powerful technique for elemental analysis and quantification. Quantification procedures may be performed using deconvolution techniques involving Fourier transformation and filtering, or alternatively both the background, escape and sum fractions may be modeled mathematically. Fortunately, such facilities are an integral part of many currently-available software packages.<sup>22</sup> As an example, an elemental line scan on a GaAs@Co core-shell NW (with a thin layer of  $\text{Al}_2\text{O}_3$ ) is shown in Figure 2.26. EDX quantification shows the presence of O in the shell with rather high quantity. Therefore we conclude that the Co shell is oxidized and we have CoO instead of a metallic shell.

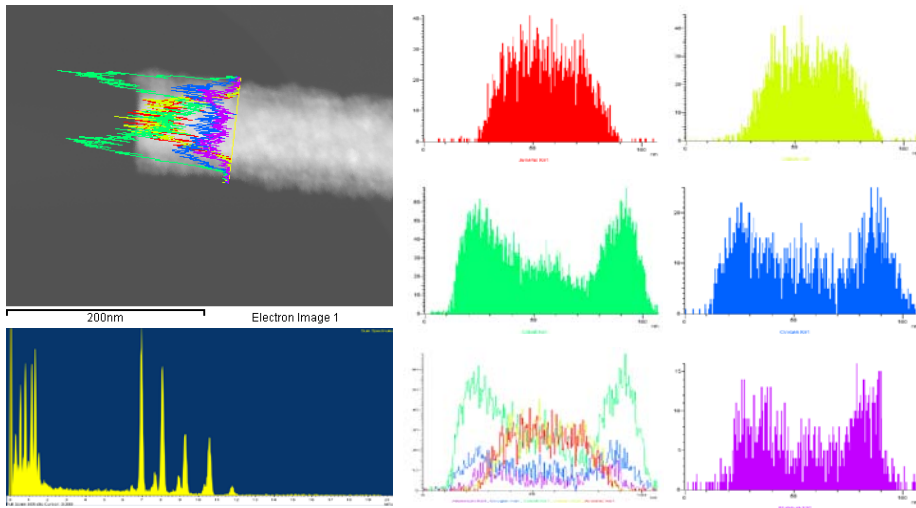


**Figure 2.26** EDX elemental line scan on a GaAs@CoO core-shell NW

### 2.6.4 Cathodoluminescence

Cathodoluminescence (CL) analysis enables one to assess various properties of the material with high spatial resolution. For instance, monochromatic imaging can be used in the identification and measurement of luminescent center concentrations and distributions or the concentration and distribution of defects, such as dislocations. In order to comprehend how CL works, one should know about ‘*luminescence*’ phenomena.

When a solid is supplied with a certain form of energy, it may emit photons in excess of thermal radiation. This process is called ‘*luminescence*’, and depending on the source of excitation of the ‘*luminescent material*’, one may categorize the process as, for example, ‘*photoluminescence*’ (photon excitation), ‘*cathodoluminescence*’ (excitation by energetic electrons, or cathode rays), ‘*chemiluminescence*’ (energy supplied by chemical reaction), and ‘*electroluminescence*’ (excitation by application of an electric field). Another distinction is commonly made between ‘*fluorescence*’ and ‘*phosphorescence*’, which differ in the time delay before the emission of photons. After the excitation is stopped, the duration of the emission is determined by the life time of the electron transition from one energy level to another. When the emission of photons is due to a direct transition from the excited to the ground state within about  $10^{-8}$  sec, the luminescence is called fluorescence. Luminescence

that persists after the excitation stops is called phosphorescence; materials exhibiting this property are called phosphors and are used as powders in fluorescent lamps, cathodoluminescent television screens, etc. The emission may persist from about  $10^{-7}$  sec to minutes and hours in long persistence phosphors. In such cases, transitions through intermediate metastable states determine the duration of the luminescence after the termination of the excitation.

Luminescence in semiconductors is generally described in terms of the radiative recombination of electron-hole pairs. This may involve transitions between states in the conduction or valence bands and those in the band gap of the material due to, for example, donors and acceptors. The emission of photons in luminescence processes is due to an electronic transition between an initial state  $E_i$  and the final state  $E_f$ . The energy, or the wavelength, of the emitted photon can be found from the relation:

$$h\nu = hc/\lambda = E_f - E_i \quad (2.12)$$

In many wide-band-gap materials, emission of photons occurs in the visible range (about 400 to 700 nm, corresponding to about 3.1 to 1.8 eV). In many luminescence phenomena light is also emitted at longer wavelengths in the near-infrared region.

Luminescence emission spectra can be divided between (i) '*intrinsic*', fundamental, or edge emission and (ii) '*extrinsic*', activated, or characteristic emission. Intrinsic luminescence, which appears at ambient temperatures as a near Gaussian-shaped band of energies with its intensity peak at a photon energy  $h\nu_p \cong E_g$  is due to recombination of electrons and holes across the fundamental energy gap, so it is an 'intrinsic' property of the material, while the emission spectra which depend on the presence of impurities are 'extrinsic' in nature. The edge emission band, arising from essentially conduction-band to valence-band transitions, is produced by the inverse of the mechanism responsible for the fundamental absorption edge. Thus, any change in  $E_g$ , due to, for instance, temperature, crystal structure in polymorphic materials, or high doping concentrations, can be monitored by measuring  $h\nu_p$ .

In indirect-band-gap semiconductors, the recombination of electron-hole pairs must be accompanied by the simultaneous emission of a photon and a phonon. Since this requires an extra particle, the probability of such a process is significantly lower compared with direct transitions. Therefore, fundamental

emission in indirect-gap semiconductors is relatively weak, especially when compared with that due to impurities or defects.

A simplified set of radiative transitions that lead to emission in semiconductors containing impurities is given in Figure 2.27. General properties of these transitions will now be discussed briefly:

- (i) Intraband transition within the conduction band: an electron excited well above the conduction-band edge dribbles down (still within the conduction band) and reaches thermal equilibrium with the lattice, more likely to lead to phonon emission only, and sometimes to phonon-assisted photon emission

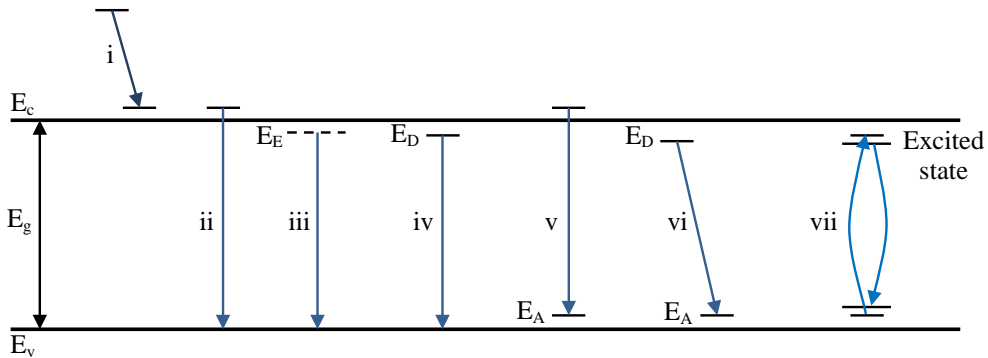


**Figure 2.27** Radiative transitions in semiconductors

- (ii) Intraband transition from the conduction band to the valence band: leading to intrinsic luminescence with the energy almost equal to  $E_g$  (Although this recombination occurs from states close to the corresponding band edges, the thermal distribution of carriers in these states will lead, in general, to a broad emission spectrum)
- (iii) Exciton decay: (observable at low temperatures) both free excitons and excitons bound to an impurity may undergo such transitions. For bound excitons, one of the charge carriers is localized at a center that can assist in conserving momentum during the transition. This will be especially important in indirect-gap materials.
- (iv) Transition starting from a localized donor state (extrinsic luminescence)
- (v) Transition finishing on a localized acceptor state (extrinsic luminescence)
- (vi) Transition starting from a donor state and finishing on an acceptor state (extrinsic luminescence)

- (vii) Excitation and radiative deexcitation of impurities with incomplete inner shell (e.g. rare-earth ions or transition metals).

Symbols:

X: free-exciton recombination, e: electron, h: hole

(D/A)<sup>(0/+/-)</sup>: neutral/ionized impurity

D: donor, A: acceptor

Examples:

D<sup>0</sup>X: recombination of an exciton bound at a neutral donor

A<sup>-</sup>X: recombination of a negatively-ionized acceptor

D<sup>0</sup>h: donor-to-free-hole transition (process iv)

eA<sup>0</sup>: free-electron-to-acceptor transition (process v)

DAP: donor-acceptor pair recombination (process vi)

Similar transitions via deep donor and deep acceptor levels can also lead to recombination emission with photon energies well below the band gap. Shallow donor or acceptor levels can be very close to the conduction and valence bands.

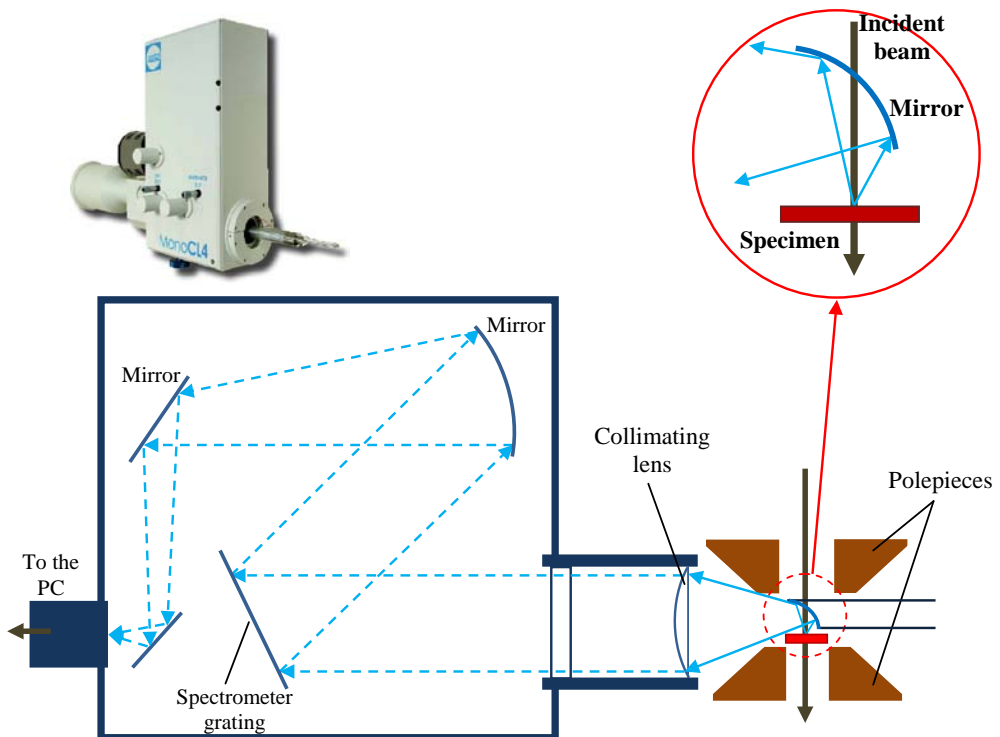


**Figure 2.28** Schematic illustration of the trajectory of light after being emitted from the sample and entering the CL detector, Gatan CL detector (upper left)

Thus, to distinguish between shallow impurity transitions and those associated with the intrinsic band-to-band transitions, we must perform measurements at very low temperatures such as liquid-helium temperature. The energy of the transition in the case of deep levels is much smaller than that of the band-to-band transition. Note that recombination of DAPs may also occur via non-radiative processes (e.g. process i).<sup>24</sup>

CL detector consists of a concave mirror. In fact when we screw the detector in, we place the mirror over the specimen holder between the pole-pieces. For better light collection, in the newly-designed CL detectors, there are two mirrors, one positioned under and the other above the specimen. In order to avoid obstructing the incident and transmitted beams, the mirrors have a hole in the middle to allow the beam to pass. There are five screws for mechanical alignment of the mirror in three directions. The scheme of a CL detector is shown in Figure 2.28. The light goes through the detector and after some processes of amplification and grating, it is sent to data storage and display system.

CL is a useful technique for characterization and even imaging of semiconductors. It can be combined with STEM imaging and provide interesting data. Some CL results will be revealed in Chapter 5.

### **2.7 Quantitative analysis, image processing and simulation**

After obtaining images and spectra from the TEM, it is time to analyze the data qualitatively and quantitatively, process them if necessary, and correlate them with theoretical models. In these contexts, appropriate software has been developed for each particular technique which provides required results without going through complicated mathematical calculations. However, it is of extremely high importance to understand the basic assumptions and methodologies behind them, in order to obtain reliable information.

Geometric phase analysis (GPA) is used for strain analysis in high-resolution TEM/STEM images. Multivariate statistical analysis (MSA) is utilized to reduce the noise of EEL spectra. Theoretical study is carried out by creating 3D atomic models by means of *'Eje-Z'* and *'Rhodius'* software and simulating HRTEM images by virtue of *'JEMS'* software. In this section we briefly describe the software we used for data analysis and complementary theoretical work in this thesis.

### 2.7.1 Strain analysis by geometric phase analysis

Geometric phase analysis (GPA) is a method based on the variation in the positions of lattice fringes that can be imaged. With this method, strain in the crystal lattices and compositional changes can be mapped. Previously some methods were developed to measure the relative lattice displacements in grain boundaries, thus one can determine whether the boundaries are relaxed.<sup>25</sup> GPA can be applied in nanocrystals, strained multilayers and antiphase boundaries. It should be pointed out that distortion in TEM lenses causes artifacts in GPA strain maps. Therefore, reliability of this analysis is increased in the case of HRTEM images obtained from aberration-corrected microscopes.

The first step in GPA is to decompose the HRTEM image according to the intensity in each point by Fourier transform, which results in a power spectrum similar to what we extract from the FFT process. The second step is '*Bragg filtering*' the power spectrum by placing a mask around the spots ( $\pm\mathbf{g}$  vectors), because there is no need to have all the Fourier components ( $H_g$ ) of the image. Now we can obtain an image of the amplitude and an image of the phase of the selected lattice fringe sets as a function of position. Amplitude images show how the strength of a set of fringes varies across an image and can be related to variations in, for example, the thickness of a crystal, the composition or local orientation. In contrast, the phase images show how regular a set of fringes is across a given image, i.e. they determine the spacing between fringes and how the fringes vary from their ideal positions.

Now by comparing the ideal situation where the amplitude and phase are no longer functions of position with the situation that displacements are present, phase directly measures the component of the displacement field, for each set of lattice planes. Combining the results for each lattice plane will give the vectorial displacement field. In a region where the lattice spacing is slightly different, due to a change in the lattice parameter for instance, the phase will have a uniform slope corresponding to the difference. The steepness of this slope is proportional to the difference in the lattice spacing.<sup>26-28</sup>

Besides mapping the fringe deformation, one can also determine the strain fields with respect to the angle they make with the phases. As well as displacement and strain field determination, local lattice distortion can be calculated by following a similar procedure.

### 2.7.2 Multivariate statistical analysis

Multivariate statistical analysis (MSA) is a family of techniques to analyze large datasets containing many known and unknown variables. It has a wide range of applications, e.g. geological remote sensing, scanning probe microscopy, and electron microscopy, especially for spectral data analysis. In the latter context, one of the most popular MSA approaches, i.e. ‘*principal component analysis*’ (PCA), is particularly used for enhancement of spectral signals. The general concept of PCA is to reduce the dimensionality of an original large dataset by finding a minimum number of variables that describe the original dataset without losing any significant information. PCA extracts the variables as mutually independent ‘abstract components’ without any prior knowledge of the dataset. It was first applied to EELS by Trebbia and Bonnet,<sup>29</sup> and now the software is available for EDX, EELS line-scans, and EEL spectrum images.

The first step is decomposition of the EEL spectrum image, by considering it as a matrix. In practice, it can be performed by applying eigenanalysis or singular value decomposition to the data matrix, with the singular values being equivalent to the square root of the eigenvalues. The relative magnitude of each eigenvalue indicates the amount of variance that the corresponding principal

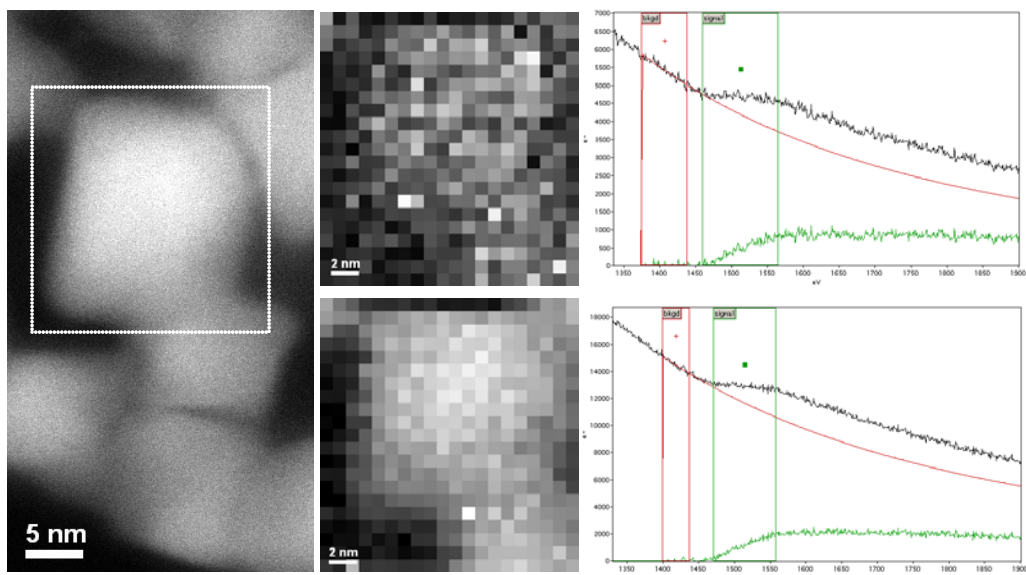


**Figure 2.29** Se EEL spectrum images and spectra of a CHTSe nanoparticle (upper) before and (lower) after applying MSA

component contributes to the dataset. Typically, the number of dominant features in the dataset is much less than the number of components of the matrix; hence the last principal components are described as experimental noise.

Therefore, the second step is determination of non-noise principal components, i.e. the dominant features which carry information. Many methods have been developed so far for this purpose, but none of them can be considered as a universal rule of thumb. In the case of EEL spectrum images, the most reliable method is the visual determination. Since the eigenvalues of subsequent, random noise-containing principal components decrease exponentially, the components that only describe experimental noise should lie on a straight line.

The next step is to remove the noise components, and reconstruct the image by keeping solely the dominant features (the first components till arriving to a straight line). In summary, we use PCA for EEL spectrum images to identify independent spectral features as abstract principal components, and reduce random noise components in a statistical manner, in order to have sharper images with clearer signals.<sup>30</sup> Figure 2.29 is a comparison of Se EEL spectra and spectrum images of a  $\text{Cu}_2\text{HgSnSe}_4$  (CHTSe) nanoparticle (upper) before and (lower) after applying MSA. One can find out how the random noise is reduced in the spectrum and the EELS Se map.

### 2.7.3 Rhodius and Eje-Z

In order to create 3D atomic models for theoretical studies, we used ‘*Rhodius*’ software package provided by the electron microscopy group of the University of Cadiz. This program is accompanied with another, ‘*Eje-Z*’ which constructs the unit cells according to the data that the user introduces which afterwards can be employed in *Rhodius*. By means of this software package one can create complicated 3D atomic models made of one or more structures. On the other hand, the created models can be used for HRTEM image simulations. They can be exported to simulation programs such as JEMS.<sup>31</sup>

In this thesis, this software has been used quite frequently in order to elucidate: (i) the unit cells and comparisons between them (Chapter 3, 4, and 5), (ii) complicated morphologies such as pentatetrahedra and tetrapods (Chapter 3), (iii) accommodation of secondary structures in heterostructures, epitaxial relationship in the interfaces, and polarity (Chapter 4 and 5).

### 2.7.4 JEMS

JEMS is a program that allows simulating HRTEM images by calculating the image following the theory of image formation under partially coherent illumination. It was previously EMS based on Fortran F77 and now most of its parts are translated in java language. The EMS package has been designed to be very modular and extendable so that new operations can be easily created and tested.

JEMS is a set of computer programs which has been developed not only for the simulation and analysis of HRTEM images, but also for the analysis of diffraction patterns. Schematically EMS can be divided into two parts. The first part is able to handle the typical calculations of crystallography encountered in electron microscopy such as automatic indexing of diffraction and Kikuchi patterns, simulation of spot and powder patterns, drawing of stereographic projections, calculation of the Bravais lattice of an unknown structure from two diffraction patterns, etc. The second part offers the possibility of the simulation of structure images of both perfect and defect structures using either a fast-Fourier-transform-based multislice approach or the Bloch wave formalism.<sup>32</sup>

In this work, JEMS is used for simulating HRTEM images of complex structures, especially when there is an overlap of two dissimilar materials and moiré fringes are formed. See Chapter 3.

## 2.8 Specimen preparation

Quality of specimen is quite vital to TEM analysis as it is one of four most important parameters that limit information extraction.<sup>33</sup> Sample preparation is a broad subject. There is a wide range of methods for sample preparation, where we should chose the ones that are the best according to the material and its stability, type of analysis to be performed, available equipments, etc. For instance, dimpling is a suitable method to thin down metallic sample, and it is useless for semiconductors. Or focused ion beam (FIB) cannot be applied for the materials sensitive to Ga ion penetration. Here we briefly describe the methods we used for preparation of specimens in this thesis, which were essentially nanostructured materials, and their interfaces with substrates.

### 2.8.1 Dispersion of nanostructured materials

In order to characterize nanostructured materials, e.g. nanowires and nanoparticle, we only need to disperse them on TEM meshed grids. For this purpose there are grids made of different material such as Cu, Ni, etc with special mesh sizes. Such grids are usually covered with a thin amorphous carbon layer. Note that the carbon layer can be continuous, with some holes within (holey), or composed of carbon laces (lacey).

In the case of nanocrystals in solution, firstly, we should make sure that the solution is sufficiently diluted, and secondly, the nanocrystals are not agglomerated. In the latter case, ultrasonication of the solution separates the agglomerated particles. Afterwards, one or two drops of the solution can be deposited on the grid. The grid should remain in rather high temperatures (60-70 °C) for some time (depending on the solution) to dry out in order to avoid contamination. For this purpose a simple lamp or a hot plate can be sufficient.

Nanoparticles in solutions usually are accompanied with organic stuff which causes contamination under the beam. Contaminated nanoparticles cannot be characterized as the images and spectra are devastated when the carbon cloud arises and covers the particles. There are a few solutions for this problem: (i) '*baking*' the sample in temperatures that do not damage the sample, (ii) leaving the sample in vacuum in medium temperatures (45-70 °C) for long times (up to a few days), and (iii) '*plasma cleaning*'. For the third option special equipment is required which produces plasma with and inert gas such as Ar to attach the sample. Note that plasma cleaning is an aggressive method which not only removes the residual organic stuff around the nanoparticles, but also destroys the amorphous carbon membrane. Therefore, in the case of carbon grids, one cannot use the plasma cleaner for more than a few seconds. Whenever further plasma cleaning is required, we can use SiN grids which are extremely robust and can be exposed to the plasma for tens of minutes.

For characterization of nanowires grown on substrates, they are supposed to be scratched from the surface and transferred to a solution like ethanol or hexane. Soon after a few seconds of ultrasonication they are ready to be deposited on the TEM grid. An easier way is to rub the grid on the substrate where the nanowires are grown, and then remove the loosely attached nanowires.

### 2.8.2 Crushing

Crushing is a suitable method for the powders that have large grains which are not transparent to the electrons. In this case the powder should be crushed in order to produce smaller grains. As an example, thermoelectric pellets made of PbTe@PbS core-shell nanoparticles (Chapter 3) were prepared with this method. The aim was to characterize the structure of the pellets to observe whether the structure of the nanoparticles changed. Therefore, the pellet was crushed to a powder; a few grains were gently crushed with a diamond polishing film, and a very soft powder of the material remained on the paper. The grains of this powder were small enough to be characterized in TEM.

### 2.8.3 Mechanical polishing

This method is used when the aim is to study the cross-section of layers, interfaces of multilayers, nanostructured materials on substrates, etc. Such experiments give crucial information about the growth, interface, as well as epitaxial relationship. In this context, the specimen should be thinned down in order to arrive to ‘*electron transparency*’.

The steps for cross-sectional sample preparation are schematically shown in Figure 2.30. Imagine a silicon substrate (grey) with nanowires (green) grown on one side, where we are interested in cross-sectional study of the interface between the substrate and the nanowires. In the first step, the sample should be

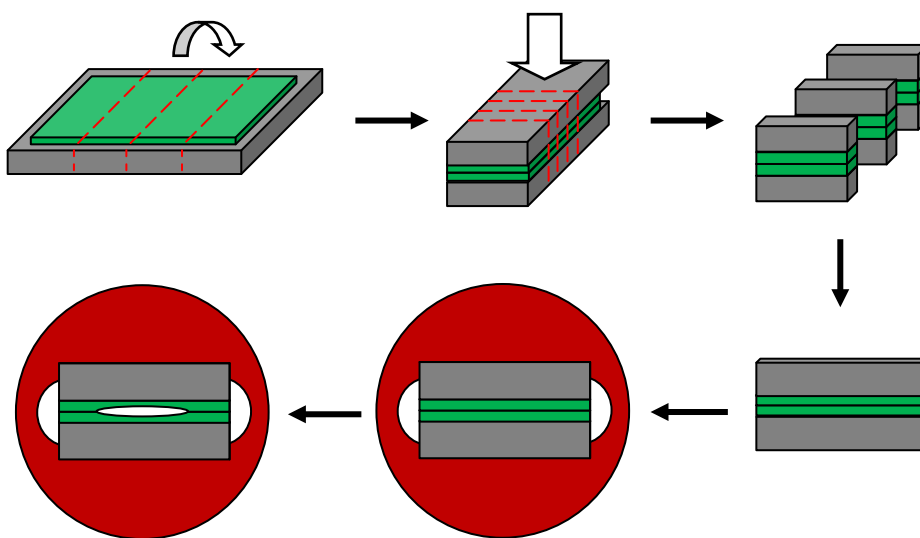


**Figure 2.30** Steps of cross-sectional TEM specimen preparation

cut by diamond or wire saw as indicated by red dash lines (cleavage is another alternative in the case of not so fragile substrates like Si). Afterwards, the two middle parts are glued face to face where the NWs remain in the middle (sandwich shape). After the glue dries out under slight pressure, the sample should be cut in the direction perpendicular to the primary cuts as shown in the scheme. These pieces are now ready for mechanical polishing.

Mechanical polishing should be done with polishing films (usually diamond) from large to small grain size. It can be done manually by pasting the sample on special holders called '*grinder*', or by putting it on automatic polishing machine. In any case, the aim is to polish one side and then the other side to achieve two shiny sides, in a way that no scratch can be seen by optical microscope. A typical thickness for the sample in this step is 20  $\mu\text{m}$ . However, Si substrate can be even thinner. Note that the sample in this step should be as thin as possible, otherwise, the next step (ion milling) will be longer, and still it hinders achieving the best sample quality. The sample in this step is attached on a copper grid with an oval hole in the middle. Afterwards, the middle of the sample, which is essentially the region of interest, is thinned by ion milling (it will be described in section 2.8.5) to be electron transparent.

#### **2.8.4 Mechanical polishing for wedge making**

This method is fundamentally the same as the previous one with the difference that in normal mechanical polishing we polish such that in the end we obtain a sample with the sides parallel. But in this method we use a slight angle for the second side in order to obtain a wedge.

Here a tripod is used instead of grinder and the last polishing steps should be performed exceedingly gently. One side of the sample will be quite thin and almost electron transparent. The advantage of this method over the previous one is that a remarkably short ion milling process is required and sometimes even without ion milling, the specimen is ready for characterization.

#### **2.8.5 Ion milling**

Precision Ion Polishing System (PIPS) is a machine dedicated to TEM sample preparation by ion milling (see Figure 2.31). Usually it is the last step of the sample preparation when the middle part of the specimen must be electron transparent. This system attacks the sample with one or two Ar ion guns with rather high energy (100 eV - 6.0 keV) and variable milling angle. With

adjustable energy and angle, one can perform the milling process in an aggressive or gent manner, depending on the specimen. Note that usually it is not recommended to use this process for a long time due to the damages that it can cause in the sample. Structural changes, morphology damage or amorphizing, are some remarkable examples of those damages.

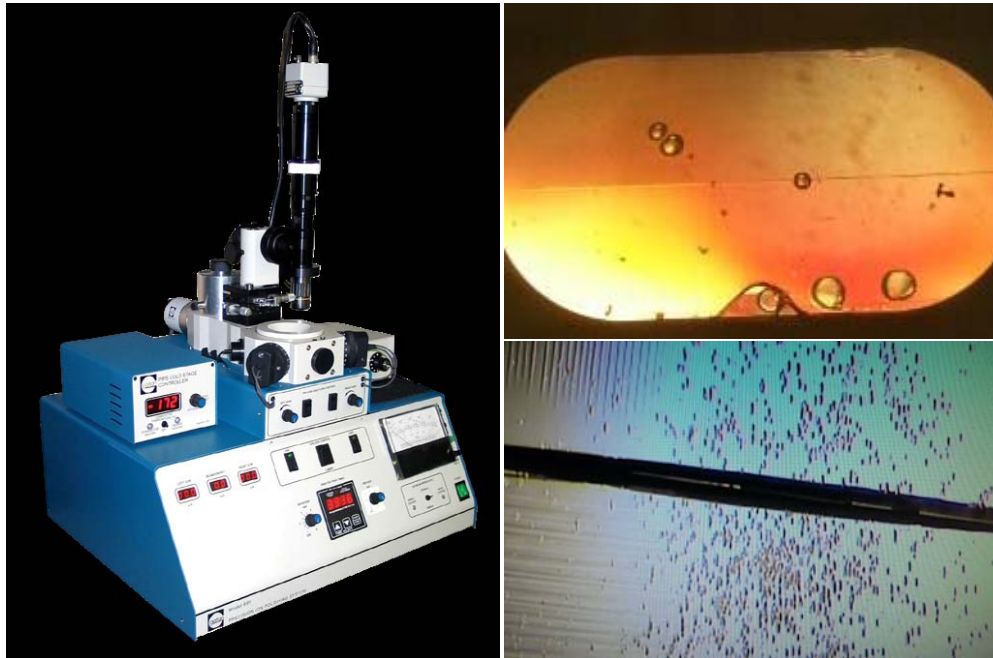


**Figure 2.31** Precision Ion Polishing System (PIPS), and a TEM specimen (upper-right) before and (lower-right) after ion milling

### 2.8.6 Focused ion beam

There is a great interest in the preparation of ‘*site-specific*’ TEM specimens, for example, examining a particular region of an integrated circuit, the microstructure of the crack tip in fracture and fatigue experiments. For these cases focused ion beam (FIB) is a very useful tool. A typical FIB uses a gallium ion beam, originating from a liquid metal ion source. This beam is accelerated (up to 30 kV). Modern FIBs (for example, FEI Helios) have dual-beam (both electron beam and ion beam) columns, gas-injection systems (GIS) and an Omniprobe (or micromanipulator) which can be used for imaging and ion-beam sectioning of a thin lamella and transfer/welding to the TEM grids.

The typical steps/conditions involved in preparing TEM specimens are:

- (i) Identification of the region of interest
- (ii) Bringing the specimen to eucentric height
- (iii) Platinum deposition using GIS (initially by the electron beam, then by the gallium ion beam)
- (iv) Ion milling (with gallium ions at ~30 kV) to make a lamella by forming trenches adjacent to the platinum coated region using cleaning cross-section mode
- (v) Lift-out of the lamella using an Omniprobe
- (vi) Transferring the lamella onto the TEM grid, and welding with platinum metal

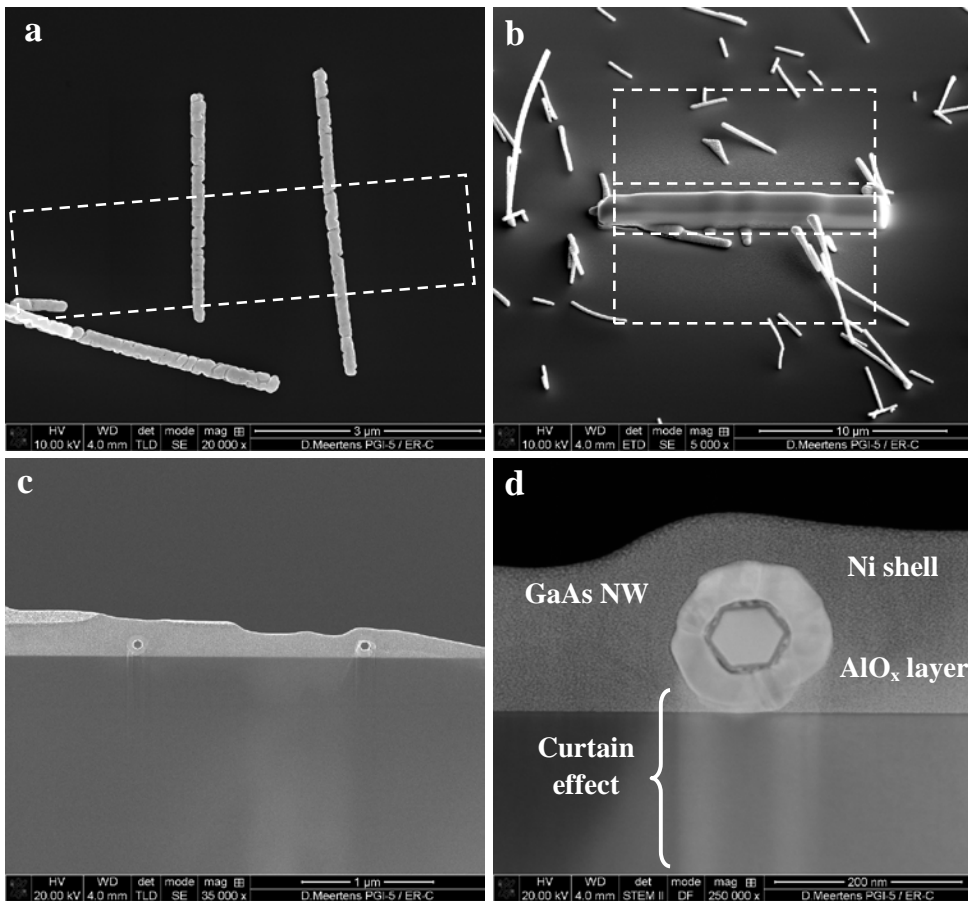


**Figure 2.32** FIB specimen preparation of GaAs@Ni core-shell NWs: (a) region of interest, to be coated with Pt, (b) Pt coated region, to be trenching and remove the lamella, (c) side view of the lamella after being welded to the grid, (d) curtain effect below the NW (upper-right) before and (lower-right) after ion milling

- (vii) Cleaning the specimen's surface with a low energy gallium beam (at 5 kV or lower) by tilting the milled surface of the specimen at  $\sim 1-2^\circ$  with respect to the beam so that the final thickness of the lamella is  $\sim 150-200$  nm.

The FIB offers rapid TEM specimen preparation, however it is necessary to note the advantages and disadvantages. Ga ions are heavier and more energetic ( $\sim 30$  keV), than the Ar ions used in PIPS (the incident energy  $\sim 4-5$  keV or lower), hence implantation damage of the lattice is higher than in PIPS. Also artifacts (such as droplets/curtaining effects on the milled surfaces) can appear, while working with a low energy (1-2 keV) Ga ion beam may not be user-friendly (due to instrumentation optics).

Although, both the ion beam and the electron beam can be used for imaging, the ion beam sputters the surface; hence electron beam is preferred and snapshots can be taken with the ion beam as and when necessary. Also, for the Pt deposition, the e-beam is suggested initially, followed by the ion-beam. A careful bonding of the lift-out lamella to the copper grid with platinum is also important, otherwise, the lamella can be lost during handling/cleaning in the PIPS. In Figure 2.32 some of the steps of FIP specimen preparation are shown.

## **2.9 Some of the key events in the history of electron microscopy**

Since construction of the first electron microscope by Ernst Ruska, a vast amount of effort has been carried out by many scientist and engineers around the world to improve the performance of this device, and some of them led to drastic progresses in it. A few of them were pointed out in this chapter; however, here a list of the most remarkable ones is presented:<sup>34</sup>

- Construction of the first electron microscope, by Ruska (1933)
- Fundamental study of the resolution limit of the device, by Scherzer (1949)
- Visibility of single atoms by invention of Z-contrast-STEM technique, by Crewe *et al.* (1970)
- Invention of  $\Omega$ -filter, by Rose and Plies (1974)
- Development of parallel EELS, Jones *et al.* (1977)
- The first spherical aberration correction of an objective lens by holography, by Tonomura *et al.* (1979)

- Intimation of Z-contrast in the STEM and later, evolution to HAADF, mostly in the hands of Pennycook and Nellist (1979-2000)
- Publication of the first EELS atlas, Ahn and Krivanek (1983)
- The start of computer-controlled microscopy, By Koster *et al.* (1989)
- Invention of field-emission gun (FEG) for TEM, by Otten and Coene (1993)
- The first successful attempts to correct spherical aberration, by Krivanek *et al.* (1997), and later by others
- Invention of ABF, by Okunishi *et al.* (2009)

## 2.10 References

- 1 D.B. Williams, C.B. Carter, '**Transmission electron microscopy, a textbook for materials science**', Second Edition (2009)
- 2 E. Ruska, '**The development of the electron microscope and of electron microscopy**', *Bioscience Reports* 7 (Nobel Lecture), 607-629 (1986)
- 3 G. Van Tendeloo, '**High resolution electron microscopy in materials research**', *Journal of Materials Chemistry* 8, 797-808 (1998)
- 4 M. De Graef, '**Introduction to conventional transmission electron microscopy**', First Edition, Ch. 5, 303-343 (2003)
- 5 G. Tatlock, '**Introduction to electron optics**', *Aberration Corrected Analytical Transmission Electron Microscopy*, Ch. 2, 21-38 (2011)
- 6 A. Bleloch, Q. Ramasse, '**Lens aberrations: diagnosis and correction**', *Aberration Corrected Analytical Transmission Electron Microscopy*, Ch. 4, 55-88 (2011)
- 7 M. Varela, A.R. Lupini, K. van Benthem, A.Y. Borisevich, M.F. Chisholm, N. Shibata, E. Abe, S.J. Pennycook, '**Materials characterization in the aberration-corrected scanning transmission electron microscope**', *Annual Review of Materials Research* 35, 539-69 (2005)
- 8 O.L. Krivanek, P.D. Nellist, N. Dellby, M.F. Murfitt, Z. Szilagy, '**Towards sub-0.5 Å electron beams**', *Ultramicroscopy* 96, 229-237 (2003)
- 9 D.A. Muller, L. Fitting Kourkoutis, M. Murfitt, J.H. Song, H.Y. Hwang, J. Silcox, N. Dellby, O.L. Krivanek, '**Atomic-Scale Chemical Imaging of Composition and Bonding by Aberration-Corrected Microscopy**', *Science* 319, 1073-1076 (2008)

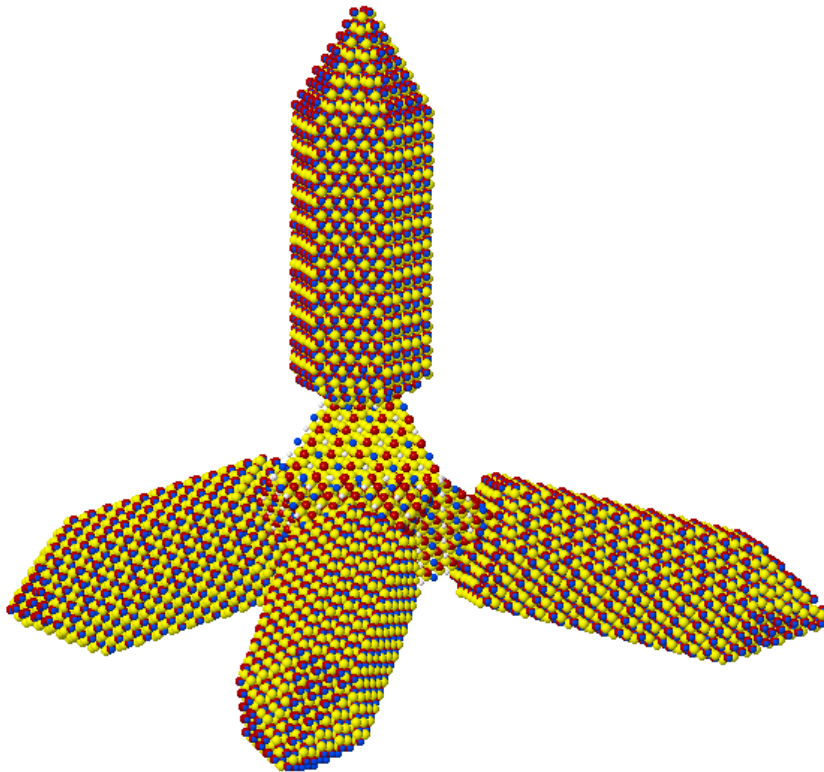
- 10 M. Tanaka, K. Tsuda, '**Convergent-beam electron diffraction**', *Journal of Electron Microscopy* 60, S245-S267 (2011)
- 11 M. De Graef, M.E. McHenry '**Structure of materials: an introduction to crystallography, diffraction, and symmetry**', First Edition, Ch. 11-13, 258-361 (2007)
- 12 O. Scherzer, '**The Theoretical Resolution Limit of the Electron Microscope**', *Journal of Applied Physics* 20, 20-29 (1949)
- 13 H. Kohno, N. Ozaki, H. Yoshida, K. Tanaka, S. Takeda, '**Misleading fringes in TEM images and diffraction patterns of Si nanocrystallites**', *Crystal Research and Technology* 38, 1082-1086 (2003)
- 14 L.M. Brown, '**Scanning transmission electron microscopy: microanalysis for the microelectronic age**', *Journal of Physics F: Metal Physics* 11, 1-26 (1981)
- 15 A.V. Crewe, J. Wall, J. Langmore, '**Visibility of single atoms**', *Science* 168, 1338-1340 (1970)
- 16 L.M. Brown, '**Development of STEM**', *Aberration Corrected Analytical Transmission Electron Microscopy*, Ch. 3, 39-54 (2011)
- 17 P.D. Nellist, '**The principles of STEM imaging**', *Scanning Transmission Electron Microscopy, Imaging and Analysis*, Ch. 2, 91-115 (2011)
- 18 E. Okunishi, I. Ishikawa, H. Sawada, F. Hosokawa, M. Hori, Y. Kondo, '**Visualization of light elements at ultrahigh resolution by STEM annular bright field microscopy**', *Microscopy and Microanalysis* 15, 164-165 (2009)
- 19 R. Ishikawa, E. Okunishi, H. Sawada, Y. Kondo, F. Hosokawa, E. Abe, '**Direct imaging of hydrogen-atom columns in a crystal by annular bright-field electron microscopy**', *Nature Materials* 10, 278-281 (2011)
- 20 S.D. Findlay, N. Shibata, H. Sawada, E. Okunishi, Y. Kondo, Y. Ikuhara, '**Dynamics of annular bright field imaging in scanning transmission electron microscopy**', *Ultramicroscopy* 110, 903-923 (2010)
- 21 C.C. Ahn, O.L. Krivanek, '**EELS atlas, a reference guide of electron energy loss spectra covering all stable elements**', *Gatan EELS Atlas* (1983)
- 22 R. Brydson, N. Hondow, '**Electron energy loss spectroscopy and energy disperse X-ray analysis**', *Aberration Corrected Analytical Transmission Electron Microscopy*, Ch. 7, 163-210 (2011)
- 23 Oxford Instruments Analytical Limited, '**Energy dispersive X-ray microanalysis hardware**', *Oxford Instruments Manual* (2002)

- 
- 24 B.G. Yacobi, D.B. Holt, '**Cathodoluminescence Microscopy of Inorganic Solids**', Ch. 3, 21-54 (1990)
- 25 M.I. Buckett, K.L. Merkle, '**Determination of grain boundary volume expansion by HREM**', *Ultramicroscopy* 56, 71-78 (1994)
- 26 M.J. Hÿtch, '**Geometric phase analysis of high resolution electron microscope images**', *Scanning Microscopy* 11, 53-66 (1997)
- 27 M.J. Hÿtch, E. Snoeck, R. Kilaas, '**Quantitative measurement of displacement and strain fields from HREM micrographs**', *Ultramicroscopy* 74, 131-146 (1998)
- 28 M.J. Hÿtch, M. Gandais, '**Quantitative criteria for the detection and characterization of nanocrystals from high-resolution electron microscopy images**', *Philosophical Magazine A* 72, 619-634 (1995)
- 29 P. Trebbia, N. Bonnet, '**EELS elemental mapping with unconventional methods: I. Theoretical basis: image analysis with multivariate statistics and entropy concepts**', *Ultramicroscopy* 34, 165-178 (1990)
- 30 M. Bosmana, M. Watanabe, D.T.L. Alexander, V.J. Keast, '**Mapping chemical and bonding information using multivariate analysis of electron energy-loss spectrum images**', *Ultramicroscopy* 106, 1024-1032 (2006)
- 31 S. Bernal, F.J. Botana, J.J. Calvino, C. Lopez-Cartes, J.A. Perez-Omil, J.M. Rodriguez-Izquierdo, '**The interpretation of HREM images of supported metal catalysts using image simulation: profile view images**', *Ultramicroscopy* 72, 135-164 (1998)
- 32 P.A. Stadelmann, '**EMS - A software package for electron diffracton analysis and hrem image simulation in materials science**', *Ultramicroscopy* 21, 131-146 (1987)
- 33 P. Goodhew, '**General introduction to transmission electron microscopy (TEM)**', *Aberration Corrected Analytical Transmission Electron Microscopy*, Ch. 1, 1-20 (2011)
- 34 F. Hagenau, P.W. Hawkes, J.L. Hutchison, B. Satiat-Jeunemaître, G.T. Simon, D.B. Williams, '**Key events in the history of electron microscopy**', *Microscopy and Microanalysis* 9, 96-138 (2003)



# CHAPTER III

## NANOENGINEERING CRYSTAL STRUCTURE AND MORPHOLOGY OF NANOPARTICLES: COMPLEX COPPER-BASED CHALCOGENIDE NANOCRYSTALS





### 3.1 Introduction

Engineering the chemical and structural changes is a crucial issue due to the effect that such changes have on the physical properties of materials. This chapter particularly deals with complex copper-based chalcogenide nanocrystals and nanoengineering their structure, morphology, and chemical composition. It starts with simple structures; then continues with complex ternary and quaternary structures. Meanwhile, a deep study on crystalline structure evolution from diamond-like structure known as ‘*zinc-blende*’ to hexagonal ‘*wurtzite*’, and their co-existence, is observed in ternary and quaternary chalcogenides. This phenomenon which occurs in many semiconductor materials and which allows the stability of many different polytypes under certain growth and composition conditions is known as ‘*polytypism*’. This kind of change is widely investigated in the case of other semiconductor nanomaterials such as III-V,<sup>1-6</sup> Si<sup>7,8</sup> and SiC,<sup>9</sup> ZnO,<sup>10</sup> and other II-VI.<sup>11,12</sup> A similar phenomenon occurs in the case of ternary and quaternary Cu-based chalcogenide nanocrystals (NCs), which can result to changes in important physical properties of the materials, which affect their application. By inducing these structural changes and combining then with the adequate morphology, one is able to manipulate the electrical and thermal conductivity, and tune the band-gap, for optoelectronics<sup>13,14</sup> and thermoelectric applications.<sup>15</sup>

On the other hand, other decisive phenomena such as polarity, cation ordering and branching are also studied. They play the key roles in the band structure of the compounds. Therefore, these issues are studied in detail and they are correlated with theoretical band structure simulations.

This chapter begins with an introduction to thermoelectrics as most of the studied materials in this chapter are used for thermoelectric applications.

Afterwards, experimental work, from synthesis to characterization and application is briefly described. Then, structural and morphological studies by means of different methodologies based on transmission electron microscopy are discussed. The methodologies are mostly HRTEM, STEM, EELS, EDX, atomic simulations, HRTEM image simulations, and GPA for strain analysis. Atomic resolution STEM and *ab-initio* simulations are also performed.

### 3.1.1 Thermoelectrics

Considering the daily-increasing demand for energy versus shortage of energy resources, thermoelectrics find a particular importance in the research world as a promising field to be used for recovering wasted energy. However, thermoelectric materials had been too inefficient previously, thus they were inhibited to be used for this application.<sup>16</sup> Newly developed thermoelectric materials, nevertheless, have improved the thermoelectric properties, meaning they exhibit significantly a higher figure of merit (ZT).

#### 3.1.1.1 Basic principles

Basically the idea of thermoelectric effect comes from a fundamental phenomenon discovered by Thomas Johann Seebeck (1770-1821) in the early 1800s. He observed that if two different materials are joined in two points and the junctions are held in different temperatures,  $T$  and  $T+\Delta T$ , a potential difference  $\Delta V$  proportional to  $\Delta T$  is generated (Figure 3.1). The  $\Delta V/\Delta T$  ratio depends on an intrinsic property of the materials called ‘Seebeck coefficient’ usually shown with  $\alpha$  or  $S$ .<sup>17</sup>

$$\alpha = \frac{\Delta V}{\Delta T} \quad (3.1)$$

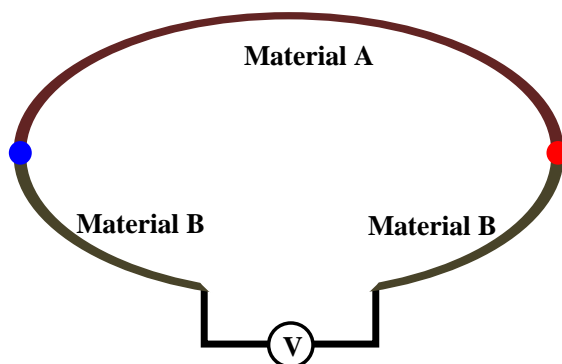


**Figure 3.1** Seebeck effect

The dimension of  $\alpha$  is  $V.K^{-1}$ , and for metals it is in order of  $\mu V.K^{-1}$  and for semiconductors typically few  $100 \mu V.K^{-1}$ . A scheme of Seebeck effect is shown in Figure 3.1.

A related effect was discovered a few years later by Jean Charles Athanase Peltier (1785-1845). He observed that when an electrical current is passed through two different materials that are joined in one point, in the junction, depending on the direction of the current, heat is either absorbed or rejected. Figure 3.2 reveals a scheme of Peltier effect. As shown in the equation 3.2, Peltier coefficient ( $\Pi$ ) and Seebeck coefficient have direct relation.

$$\Pi = \alpha T \quad (3.2)$$

The absorbed/rejected heat ( $Q_P$ ) can be calculated by equation 3.3.

$$Q_P = \alpha IT \quad (3.3)$$

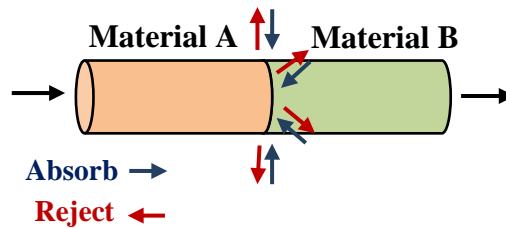


**Figure 3.2** Peltier effect

where  $I$  is the current through the junction.

Thermoelectric figure of merit ( $ZT$ ) is the parameter that determines the potential of a material for thermoelectricity. It is a dimensionless parameter calculated by the equation below:

$$ZT = \frac{\alpha^2 \sigma T}{\kappa} \quad (3.4)$$

where  $\sigma$  is the electrical conductivity, and  $\kappa$  is the total thermal conductivity (i.e. the sum of lattice thermal conductivity and electronic term). The higher the figure of merit, the better thermoelectricity is obtained from the material. Another important parameter in thermoelectric is referred to as electrical power factor (PF) determined by the numerator of the fraction of equation 3.4, i.e.:

$$PF = \alpha^2 \sigma T \quad (3.5)$$

In general all parameters  $\alpha$ ,  $\sigma$ ,  $\kappa$ ,  $ZT$  and PF depend on carrier concentration. Electrical conductivity is a reflection of charge carrier

concentration and the rest are functions of it. The electrical conductivity increases with increase in carrier concentration while Seebeck coefficient decreases. Power factor has a maximum point which lies in the range of semiconductors. Lattice thermal conductivity does not depend on carrier concentration, but electronic thermal conductivity increases with carrier concentration. Therefore, total thermal conductivity increases with carrier concentration. A scheme is shown in Figure 3.3.<sup>18</sup>

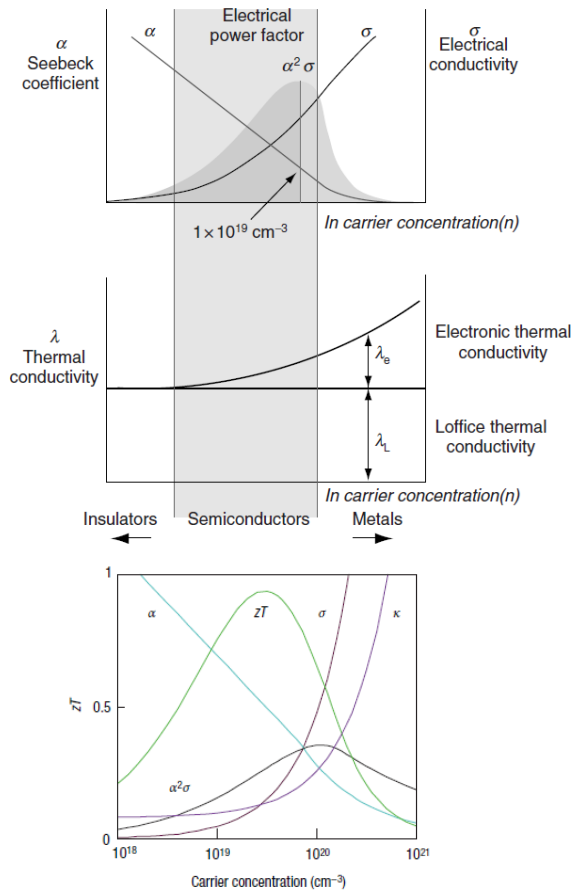


**Figure 3.3** Schematic dependence of electrical conductivity, Seebeck coefficient, power factor, and thermal conductivity on concentration of free carriers<sup>16,18</sup>

### 3.1.1.2 Thermoelectric devices

The fundamental idea of thermoelectric device is based on taking advantage of Seebeck (/Peltier) effect to generate power, meaning by temperature gradient from one joint of two materials to another, an electrostatic potential (voltage) is

created. Basically, the thermoelectric effects arise because charge carriers in metals and semiconductors are free to move and carry their charge and heat with them. When a temperature gradient is applied to a material, the mobile charge carriers at the hot end tend to diffuse to the cold end, which produces an electrostatic potential. Then, the electrostatic repulsion due to the build-up of charge and the chemical potential for diffusion reach equilibrium.<sup>16</sup>

A thermoelectric couple as shown in Figure 3.4 comprises two thermoelectric elements (semiconductors or metals), one n-type, containing free electrons, and one p-type, containing free holes (Thermoelectric materials will be discussed in section 3.1.3). As can be seen in Figure 3.4, two devices can be built from these two phenomena that can occur: (i) a ‘*thermoelectric generator*’ uses heat flow across a temperature gradient to power an electric load through the external circuit (Figure 3.4 left: Seebeck effect); (ii) a ‘*thermoelectric refrigerator*’ utilizes an electric current to cool one side down and reject the heat from the other side (Figure 3.4 right: Peltier effect). Thermoelectric devices contain many thermoelectric couples wired electrically in series and thermally in parallel as revealed in Figure 3.5.<sup>16,17</sup>

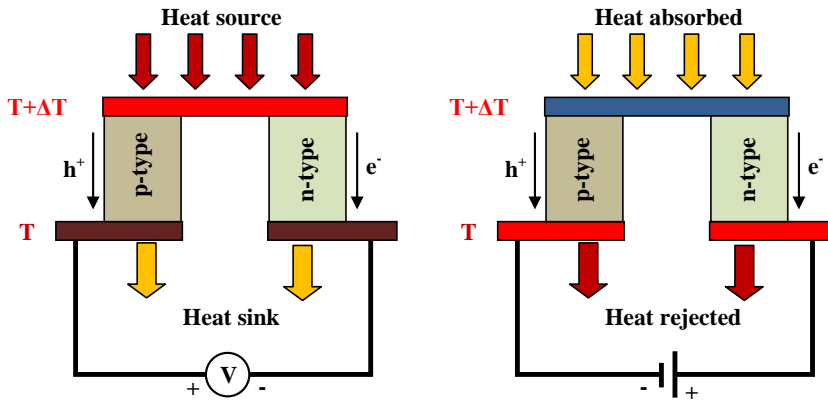


**Figure 3.4** A schematic illustration of thermoelectric effects

### 3.1.1.3 Thermoelectric materials

In general, materials with  $ZT > 0.5$  are considered as thermoelectric materials. However, other parameters such as toxicity, cost, etc can affect this definition. Figure 3.6 shows the  $ZT$  of some novel materials investigated by NASA. Although initially the thermoelectric effects were discovered in metals, few years after these effects with larger magnitude were observed in

semiconductors which facilitated their practical applications since the 1950s. Materials such as selenides and tellurides (in general, chalcogenides), antimonides, germanium and silicon alloys are good candidates for thermoelectrics.<sup>16,19</sup>

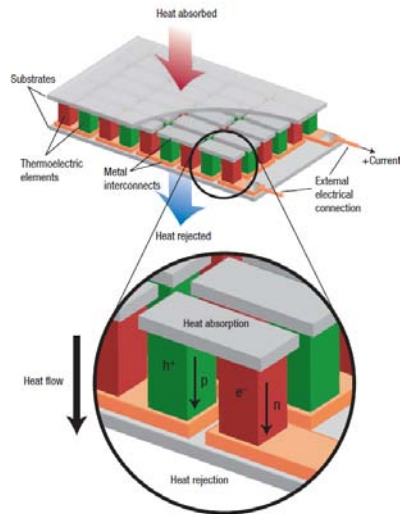


**Figure 3.5** Scheme of thermoelectric devices

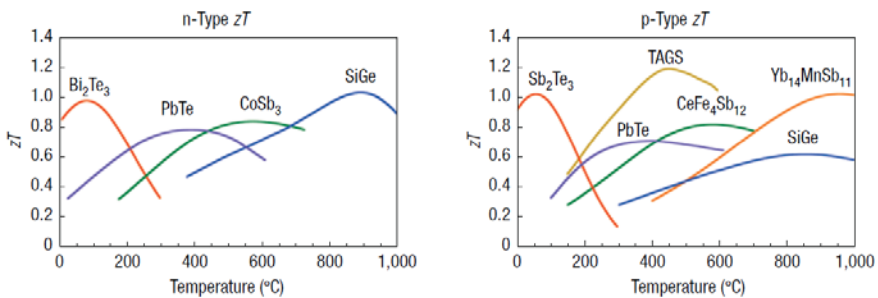


**Figure 3.6** Figure of merit of state-of-the-art commercial materials for thermoelectric power generation-type and n-type

### 3.1.2 How to improve the efficiency: bulk vs. nano

In 1990s a new wave of interest was attracted to thermoelectrics mostly due to the improvement in thermoelectric efficiency of novel complex materials, by means of nanostructuring, which creates quantum confinement of the electron charge carriers. By increases in confinement and decreases in dimensionality, the electron energy bands in a quantum confined structure are progressively

narrower. These narrow bands should produce high effective masses and as a consequence, large Seebeck coefficients. Moreover, engineered heterostructures (with similar sizes) may decouple the Seebeck coefficient and electrical conductivity that could result in high ZT.<sup>16</sup> Since mid-1990s many theoretical and experimental works revealed dramatic improvements in thermoelectrics by semiconductor quantum wells, quantum dots, superlattice structures, nanowires, nanoparticles, and other nanostructures.<sup>20-26</sup>

Therefore, it is of high importance to control the physical properties of the materials, which can be performed by controlling the size, morphology, chemical composition, and crystallographic structure of them.<sup>27,28</sup>

In this chapter, particularly, copper-based binary, ternary, and quaternary chalcogenide nanocrystals are studied. They are tetrahedrally coordinated semiconductors derived from ZnS cubic structure known as zinc-blende (ZB) as shown in Figure 3.7. These nanocrystals are synthesized by colloidal synthesis, an appropriate bottom-up process which allows a precise control on size, morphology, chemical composition, and crystal structure of the nanocrystals. As these parameters play a significant role in thermoelectric figure of merit (ZT), it

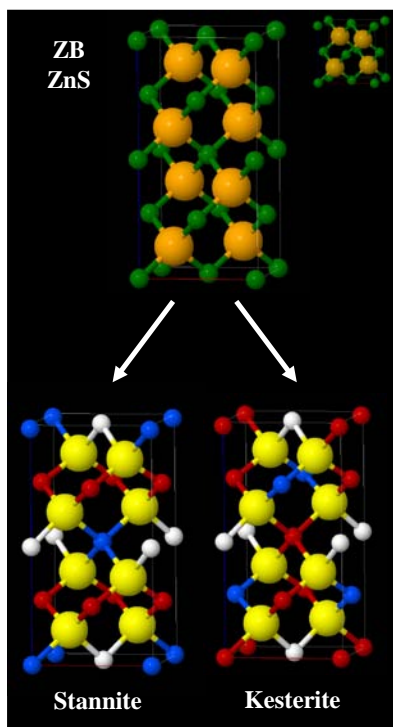


**Figure 3.7** How stannite and kesterite quaternary structures are derived from zinc-blende ZnS

is important to have them under control.<sup>29-32</sup> In the following sections of this chapter, one will see how structural changes by means of twinning mechanism affect the physical properties of the materials.

### **3.1.3 Colloidal synthesis**

Colloidal synthesis is an appropriate bottom-up approach to produce binary, ternary and quaternary nanocrystals. It offers precise control on crystal domain size, morphology, chemical composition, and crystal structure. Moreover, it is a solution-processing method which has a high potential for production of low-cost, high-yield, large-scale, and shape-adaptable devices.<sup>27,29</sup> In this method the nanocrystals are synthesized from precursor compounds dissolved in solutions, much like traditional chemical processes.

The NCs are usually prepared by reacting metal-amine complexes, heating the solutions up to certain temperatures (~200 °C) for 1 h in order to remove water and other low-boiling-point impurities. Then the solution is kept in reaction temperatures (270-300 °C) for certain times (a few minutes) to let the NCs grow, while some other pre-heated solutions are injected. Afterwards, it is quickly cooled down to the room temperature. The color of the solution shows that the NPs are obtained. In the next step Oleic acid is added to replace weakly bonded ligands. Eventually, the process ends by some purification process. There are differences in the synthesis procedures in the case of each compound. However, solely the basics of the process are described here.

### **3.1.4 Thermoelectric characterization**

Measuring the three parameters of equation 3.4: Seebeck coefficient, electrical and thermal conductivity in different temperatures, one can calculate the thermoelectric figure of merit by using equation 3.4.

The method used to measure the ZT of the materials was to make a small disk-like pellet with a press for a few minutes at relatively low temperature. Short times and low temperatures are used in order to avoid agglomeration or growth of the nanowires. The pellets are used to measure Seebeck coefficient, electrical and thermal conductivity. Nanoparticles should be free of ligands and surfactants, because presence of such organic materials increases the measurement error. So the nanoparticles should be washed thoroughly by multiple precipitation and re-dispersion steps. It should be pointed out that these

surfactants are necessary in the synthesis step, in order to control the nanoparticle size, shape, and solubility.

Seebeck coefficient and electrical conductivity can be measured simultaneously using a static direct-current (DC) method. Thermal conductivities were calculated from flash diffusivity measurements, using the mass density and Dulong-Petit approximation for the specific heat capacity. Experimental details of thermoelectric characterization will be discussed in section 3.2.3.<sup>27,29</sup>

### 3.1.5 Structural changes in nanostructured materials

#### 3.1.5.1 Twinning and polytypism

Twinning and polytypism are crucial issues in nanostructured materials since they have important effect on properties. Polytypism is a term assigned to the phenomenon that a compound crystallizes in a variety of periodic layered structures, namely polytypes. The term polytypism is different from polymorphism (the ability of a chemical compound to exist with more than one crystal structure), however, it falls, structurally, within the definition of polymorphism. In other words, polymorphism includes every possible difference encountered in the crystal structure of a substance, while polytypism considers these differences only in one dimension. The layers comprising a polytype can commonly occupy a number of lateral positions relative to their neighboring layers, e.g. A, B, C to have the closest packing. Classical ABC notation has always been used to describe close-packing of sphere since the beginning. Other notations like Hägg's and Zhdanov are not used anymore.<sup>33,34</sup>

Polytypism was first discovered in 1912 by Baumhauer in carborundum (SiC) which has a close-packed tetrahedral structure. Afterwards, several other polytypic materials such as CdI<sub>2</sub>, PbI<sub>2</sub>, CdBr<sub>2</sub>, mica, and ZnS were studied, mostly by means of X-ray diffraction (XRD).<sup>33,35,36</sup> For each material, numerous polytypes between hexagonal wurtzite (WZ) and cubic zinc-blende (ZB) were reported. Pashinkin *et al.* showed that cadmium and zinc chalcogenides also exhibit the polytypism phenomenon.<sup>37</sup>

As expected, investigation in this aspect was followed by theoretical studies trying to explain the phenomenon and eventually none of them remained uncontested. These theories can be classified into two groups: (i) dislocation theories, and (ii) thermodynamic theories. For instance, Frank's theory

explained that polytypism occurs due to occurrence of screw dislocations. Basically, he extended his celebrated screw dislocation theory of crystal growth to explain the formation of polytypes in a direct and simple way. Further experiments on different materials by others did not correlate with the theory.

Jagodzinski's disorder theory, which was based on thermodynamic considerations, criticized Frank's theory and explained the existence of structure-temperature relationship in SiC and ZnS.

One year after in 1955 Schmeer proposed his theory based on second- or higher-order phase transformation. According to his theory, the polytypes are supposed to represent intermediate states in the phase transition, proceeding by infinitesimal steps over a given range, from cubic close-packed ('sphalerite' or zinc-blende) to hexagonal close-packed (wurtzite) structure. This theory, as well as the previous ones, encounters many difficulties compared with experimental results. Apparently, a temperature-structure relationship exists only for small-period SiC polytypes.

In 1963 Peibst proposed a theory based on mutual action of lattice vibrations during growth. Indeed, no experimental observation confirmed the theory. Afterwards, Vand and Hanoka suggested a modification of Frank's screw dislocation theory, removing some difficulties associated with it, but it was still based on formation of screw dislocations. Shortly before, in 1966, another modification of Frank's screw dislocation theory was published by Mardix and Steinberger. They proposed a mechanism in which polytypism occurred due to introduction of stacking faults and their subsequent regular expansion over atomic planes inside the crystal after its growth.<sup>36</sup>

It should be taken to account that, electron microscopes and electron microscopy techniques that time were not sufficiently developed yet. Verma<sup>38</sup> was the first who claimed observation of dislocations by means of multiple-phase interference and phase-contrast microscopy. In his papers, as shown in Figure 3.8, he proved the presence of screw dislocations in SiC after growth, referring to Frank's theory on crystal growth. Years after, he utilizes the same technique on the same compound for existence of polytypes.<sup>34</sup> Notice that beside XRD, during 1950s and 1960s, multiple-phase interference and phase-contrast microscopy were the most common microscopy methods in materials science. Evidently, their resolution is limited, as well as of other optical microscopy techniques. One of the first uses of transmission electron microscopy for observing dislocations in chalcogenides was performed by

Dekkers and coworkers in 1962. However, the resolution of their microscopes yet needed to be improved.

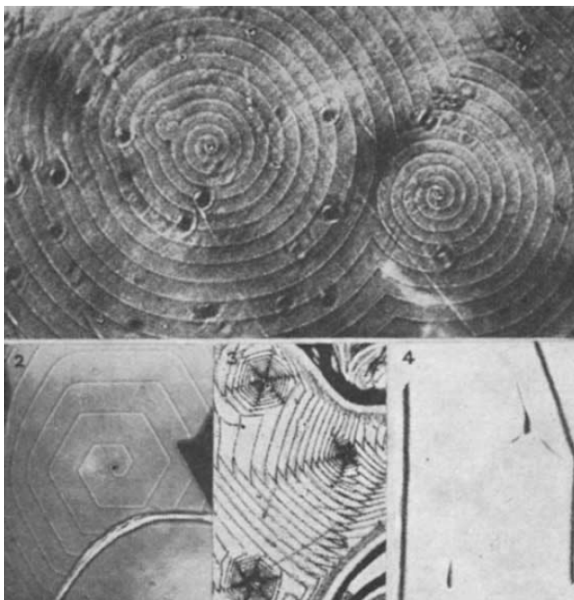


**Figure 3.8** Screw dislocations in SiC observed by multiple-phase interference<sup>38</sup>

Development of TEM techniques facilitated the study of structural changes. For instance, Sato and Shinozaki used electron diffraction patterns and dark-field electron micrographs to study ‘*Microsyntaxy and polytypism in SiC.*’ See Figure 3.9.<sup>39</sup> After development of high-resolution electron microscopy in 1970s,<sup>40</sup> it was not so difficult to see the structural defects in the compounds. For example, Buseck and Iijima used this technique to visualize polytypes (Figure 3.10 (a)), twins and anti-phase boundaries (Figure 3.10 (b)), stepped twins (Figure 3.10 (b)), ‘parting’ (cleavage in a certain direction) and cleavage in monoclinic enstatite (clinoenstatite, CLEN) and orthorhombic enstatite (orthoenstatite, OREN).<sup>41</sup>

Nowadays, electron microscopy goes even further and allows measuring the polarity directly from the micrographs. With atomic resolution scanning transmission electron microscopy (STEM) and annular bright-field (ABF) techniques, one can even visualize light atoms such as N and O.<sup>42-44</sup> These techniques are discussed in Chapter 2. Likewise, one can find example of applications in this chapter and Chapter 4.

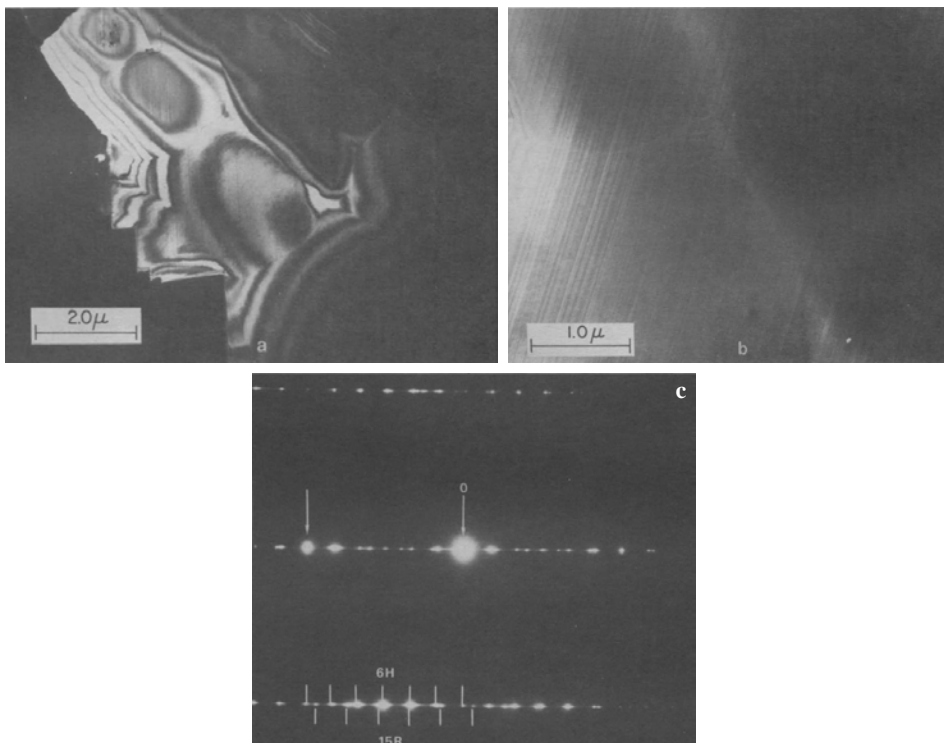


**Figure 3.9** (a), (b) Dark-field electron micrographs on a SiC grain in [010] orientation showing the stripes perpendicular to the c-direction, (c) corresponding electron diffraction pattern<sup>39</sup>

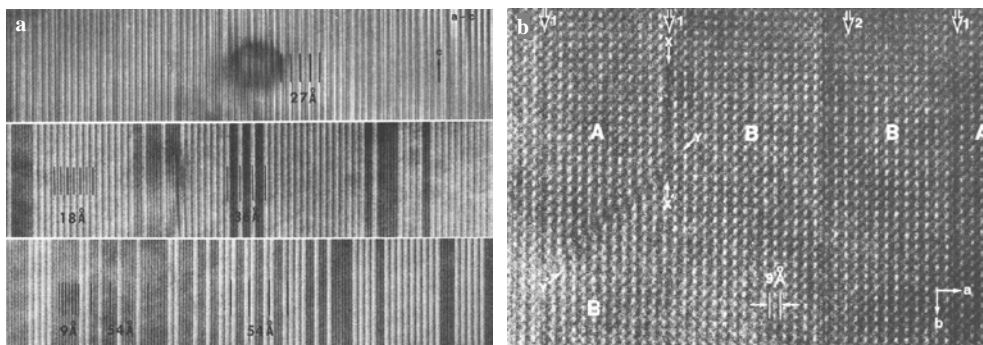


**Figure 3.10** (a) Polytypes, (b) twins (right) and stepped twins (left) in enstatite<sup>41</sup>

### 3.1.5.2 Copper-based chalcogenides

Since 1950s complex chalcogenides semiconductors generated great interest due to their optoelectronic, optics, and thermoelectrics. Relative to binary II-VI

chalcogenides, ternary I-III-VI<sub>2</sub> and I<sub>2</sub>-IV-VI<sub>3</sub> compounds can be generated through cross-substituting of related cations for the group II atoms, with the octet rule still obeyed. The former forms by substitution of a pair of group I and group III cations, and the latter, by substitution of two group I and one group IV cation. Going even further, by substituting one group II and one group IV cation for the group III atom in the I-III-VI<sub>2</sub> ternary system, one can obtain quaternary chalcogenides in form of I<sub>2</sub>-II-IV-VI<sub>4</sub> systems. Another possible quaternary system is I-III-II<sub>2</sub>-VI<sub>4</sub> which forms by replacing one group I cation and one group III cation by two group II cations.<sup>45</sup> Here is a list of possible atoms in the binary, ternary and quaternary systems:

I:	K, Cu, Ag
II:	Fe, Zn, Cd, Hg
III:	Al, Ga, In, La
IV:	Si, Ge, Sn, Pb
VI:	S, Se, Te

With combination of these elements the mathematic possibility of over 200 different ternary and quaternary compounds can be calculated. The experimental possibility of existence of all these combinations cannot be proved, however, numerous ternary and quaternary chalcogenides are already synthesized, and still many others are physically and thermodynamically possible to come to existence. This ample range of compounds can even expand larger by having two atoms of the same group in the same atomic position in the unit cell, e.g. I-(III,III')-VI<sub>2</sub> and I-III-(VI,VI')<sub>2</sub>, namely 'pseudo-quaternary' compounds.<sup>46</sup> Quinaries are out of the scope of this study.

Here in this work we just consider the copper-based compounds as the group I cation. Silver-based compounds have been studied by other groups.<sup>47,48</sup> Also from ternary and quaternary compounds we only consider I<sub>2</sub>-IV-VI<sub>3</sub> and I<sub>2</sub>-II-IV-VI<sub>4</sub> systems in which Se plays the role of the anion.

### 3.1.5.3 Stannite and kesterite structures

By replacing the Zn atoms with group I and III atoms in zinc-blende ZnS, chalcopyrite I-III-VI<sub>2</sub> structure is obtained. In the next step, by substitution of group II and IV atoms for the group III, one can obtain I<sub>2</sub>-II-IV-VI<sub>4</sub> system with three possibilities: (i) kesterite (KS), (ii) stannite (ST), and (iii) PMCA. These structures are determined by the ordering of the three cations in the atomic positions of Zn in the unit cell, as can be seen in Figure 3.11.<sup>45,49</sup>

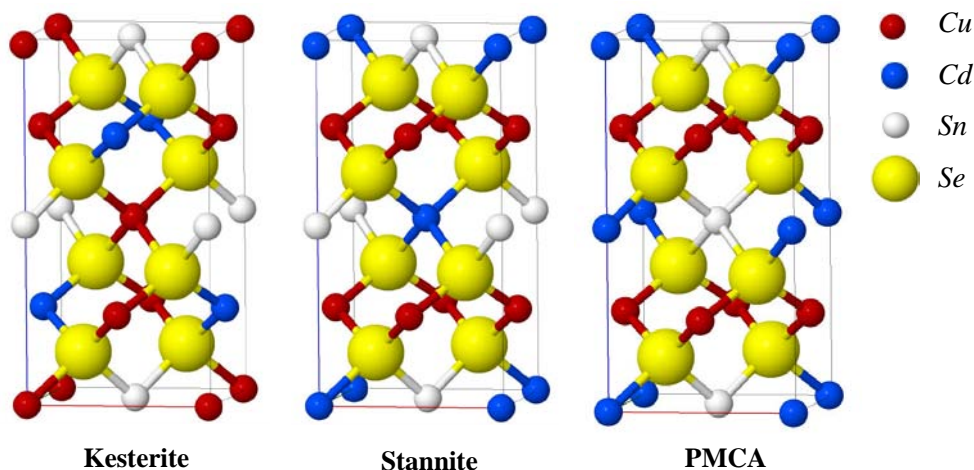


**Figure 3.11** Quaternary ( $\text{Cu}_2\text{CdSnSe}_4$ ) chalcogenide structures: (a) kesterite (KS), (b) stannite (ST), and (c) PMCA

## 3.2 Experimental

### 3.2.1 Synthesis

All the nanoparticles are synthesized by colloidal synthesis method. They are usually prepared by reacting metal-amine complexes, heating the solutions up to certain temperatures, keeping them in high temperatures for certain times to let the NCs grow, then cool them down to the room temperature, following by purification process.

The NCs are usually prepared by reacting metal-amine complexes, heating the solutions up to certain temperatures ( $\sim 200$  °C) for approximately 1 h in order to remove water and other low-boiling-point impurities. Then the solution is kept in reaction temperatures (270-300 °C) for certain times (a few minutes) to let the NCs grow, while some other pre-heated solutions are injected. Afterwards, it is quickly cooled down to the room temperature. The color of the solution shows that the NPs are obtained. In the next step ligand substitution is carried out. Oleic acid is added to replace weakly bonded ligands. Eventually, the process ends by some purification process. There are differences in the synthesis procedures in the case of each compound. However, solely the basics of the process are described here.

### 3.2.2 Structural characterization

The chemical and structural characterization of the nanowires was carried out by high-resolution transmission electron microscopy (HRTEM), electron energy loss spectroscopy (EELS), and with the extracted data we generated 3D atomic supercell models. High-resolution TEM images were obtained by means of a Jeol 2010F field-emission gun (FEG) microscope with a 0.19 nm point-to-point resolution at 200 keV with an embedded Gatan image filter (GIF) for EELS analyses. Some of the high-angle annular dark-field (HAADF) images and EELS spectra were obtained by an FEI Titan 50-300 PICO microscope operated at 200 keV. This microscope is a unique fourth generation field-emission gun TEM equipped with a high-brightness electron gun, a monochromator unit, and a  $C_s$  probe corrector, a  $C_s$ - $C_c$  achro-aplanat image corrector and a post-column energy filter system.. 3D atomic models were created by using Rhodius software package<sup>50</sup> which allows creating complex atomic models.<sup>12,51</sup> For the *ab-initio* calculations SIESTA code was used which combines density functional theory (DFT) with normconserving pseudopotentials and local basic set functions.

### 3.2.3 Thermoelectric characterization

As mentioned in the previous section, the method used to measure the ZT of the compounds was to make a small disk-like pellet (for example 10-13 mm diameter and 2 mm thick) with a press (around 2 tones pressure) for 5 minutes at room temperature. The pellets are used to measure Seebeck coefficient, electrical and thermal conductivity. First the nanoparticles were washed thoroughly by multiple precipitation and re-dispersion steps, until they could not be re-dispersed in organic solvents, meaning most of the surfactants initially used to control the nanoparticle size, shape, and solubility had already been removed. Then the nanoparticles were dried under an argon atmosphere. Afterwards, they were annealed by heating to relatively high temperatures (e.g. 500 °C) for two hour under an argon flow inside a tube furnace, and finally they were pressed to the small pellet.

The Seebeck coefficient was measured using a static direct-current (DC) method. Electrical conductivity data were obtained by a standard four-probe method. Both the Seebeck coefficient and electrical conductivity were measured simultaneously.

Thermal conductivities were calculated from flash diffusivity measurements, using the mass density and Dulong-Petit approximation for the specific heat capacity ( $C_p = 0.34 \text{ Jg}^{-1}\text{K}^{-1}$ ). The thermal conductivity was calculated as  $\kappa = DC_p d$ , where  $D$  is the thermal diffusivity,  $C_p$  is the heat capacity, and  $d$  is the density.

Eventually, by using equation 3.4,  $ZT$  is calculated in different temperatures and the graphs are plotted.

### 3.3 Structure study

The materials studied in this chapter can be classified by the number of elements in the alloy: (i) binary systems: CuSe, CuTe, PbTe and PbS; (ii) ternary systems:  $\text{Cu}_2\text{SnSe}_3$ ,  $\text{Cu}_2\text{GeSe}_3$ ; and (iii) quaternary systems:  $\text{Cu}_2\text{CdSnSe}_4$ ,  $\text{Cu}_2\text{ZnSnSe}_4$ ,  $\text{Cu}_2\text{ZnGeSe}_4$ ,  $\text{Cu}_2\text{HgGeSe}_4$ ,  $\text{Cu}_2\text{HgSnSe}_4$ . However, a different approach is considered for classification: phase complexity. First the single-structured compounds are briefly discussed. Then we move on to multi-phased structures that consist of wurtzite and zinc-blende-like compounds, and finally we study heterostructures of core-shell type which are quite interesting from the aspect of functionality.

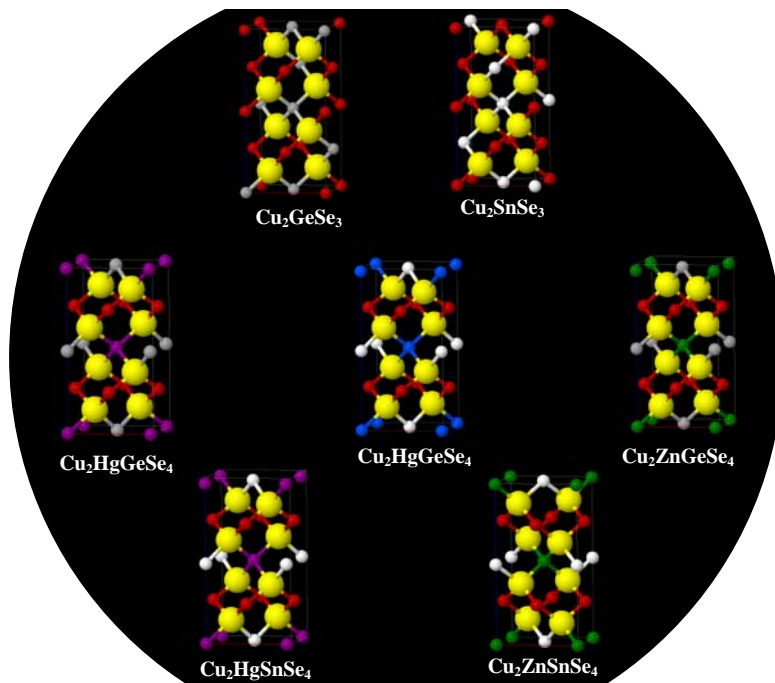


**Figure 3.12** Unit cells of ternary and quaternary copper-based selenides

Binary, ternary and quaternary copper-based chalcogenides are tetrahedrally coordinated semiconductors derived from ZnS cubic structure known as zincblende (ZB) as shown in Figure 3.7. All unit cells are revealed in Figure 3.12. In the case of some compounds we use a doubled unit cell to keep the coherency between the cells in order to facilitate the structure comparison of the compounds.

### 3.3.1 Single-phased structures

#### 3.3.1.1 $\text{Cu}_2\text{SnSe}_3$ nanocrystals

$\text{Cu}_2\text{SnSe}_3$  (CTSe) is a p-type diamond-like semiconductor with a narrow band gap (0.84 eV).<sup>52</sup> It is also a promising material for thermoelectric properties with relatively high ZT. In this compound it seems that the cations, Cu and Sn, are randomly distributed in the crystal structure, as it is shown in Figure 3.13. The structure has cubic symmetry in F43m space group (no. 216) with cell parameter  $a = 5.685 \text{ \AA}$ . The dumbbell stacking is visible from [011] zone axis. HRTEM image in Figure 3.14 shows a CTSe NP with this cubic structure visualized from [110] zone axis. Although the NP is not completely faceted, left side of the NP terminates with (1-1-1) plane family. Another important point is the existence of twin boundaries. As seen in this figure, a twinned section across (1-11) plane is observed in the middle part of the NP.

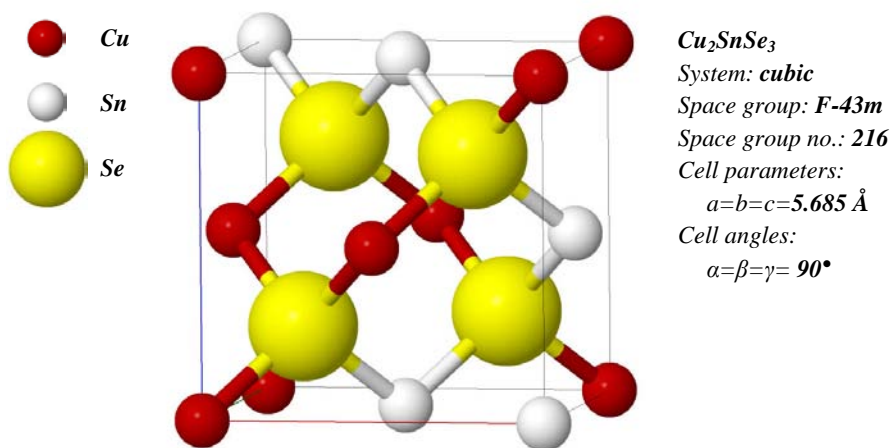


**Figure 3.13**  $\text{Cu}_2\text{SnSe}_3$  (CTSe) unit cell, cubic symmetry in F-43m (No. 216) space group with  $a=5.685 \text{ \AA}$

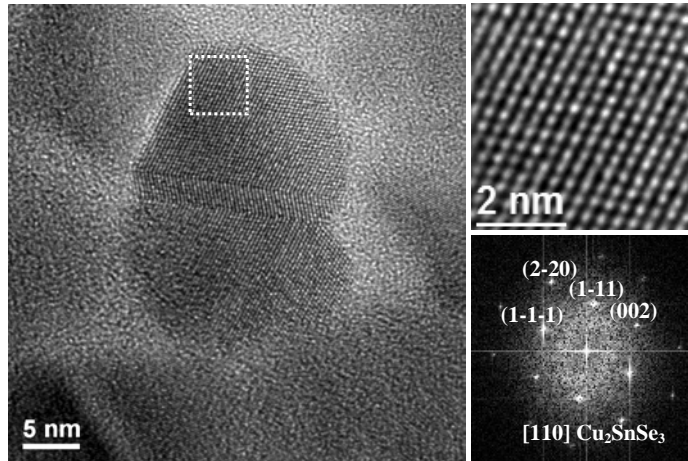


**Figure 3.14** HRTEM analysis on a  $\text{Cu}_2\text{SnSe}_3$  NC with cubic structure

### 3.3.1.3 $\text{Cu}_2\text{ZnSnSe}_4$ nanocrystals

Shavel *et al.*<sup>30</sup> reported on synthesis of  $\text{Cu}_2\text{ZnSnSe}_4$  (CZTSe) NCs which are quite similar to  $\text{Cu}_2\text{ZnSnSe}_4$  from the aspect of crystal structure. The unit cell is shown in Figure 3.15. It is the same as the one of CZGSe with slight differences in the cell parameters because of the substitution of Sn with Ge. Sn is heavier than Ge, thus, the cell parameters are slightly larger. HRTEM

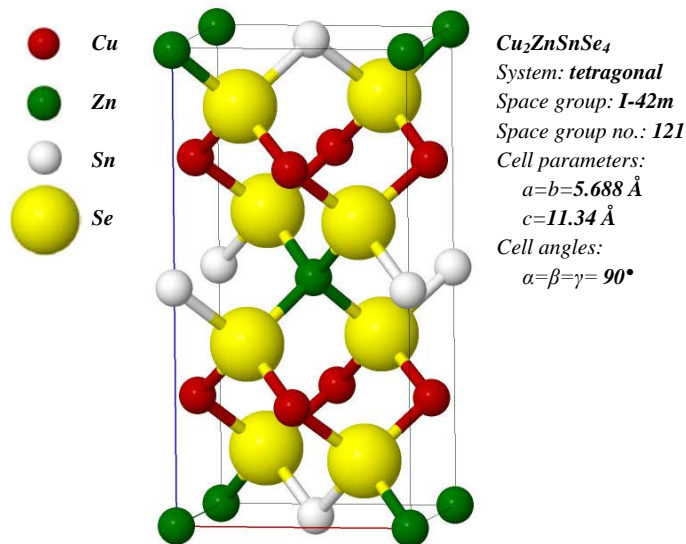


**Figure 3.15**  $\text{Cu}_2\text{ZnSnSe}_4$  (CZTSe) unit cell, tetragonal symmetry in *I-42m* (No. 121) space group with  $a=b=5.688 \text{ \AA}$  and  $c=11.34 \text{ \AA}$

structural analysis is shown in Figure 3.16, and EELS chemical composition maps are exhibited in Figure 3.17. EELS maps confirm the CZTSe structure, while XRD cannot distinguish between ZnSe, Cu<sub>2</sub>Se, Cu<sub>2</sub>SnSe<sub>4</sub>, and CZTSe. Their XRD patterns are too close. Moreover, the difference in cell constants of the mentioned structure is within the error of electron diffraction patterns. On the one hand, HRTEM could provide a reliable structural analysis, however, extensive image simulation should be required and the result could not be easily obtained straight forward. On the other hand the EELS and EDX analyses provide information about the material stoichiometry.

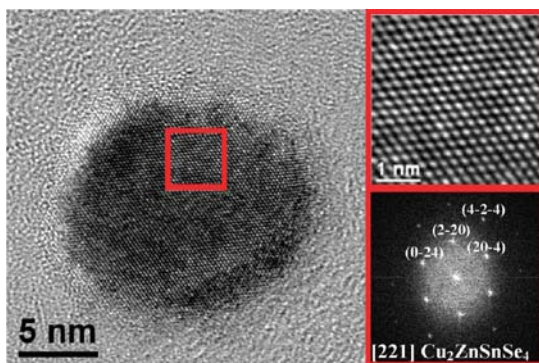


**Figure 3.16** HRTEM micrograph of a CZTSe NC with a power spectrum (lower-right) corresponding to the magnified IFFT-filtered zone (upper-right) indicated with the red square<sup>30</sup>

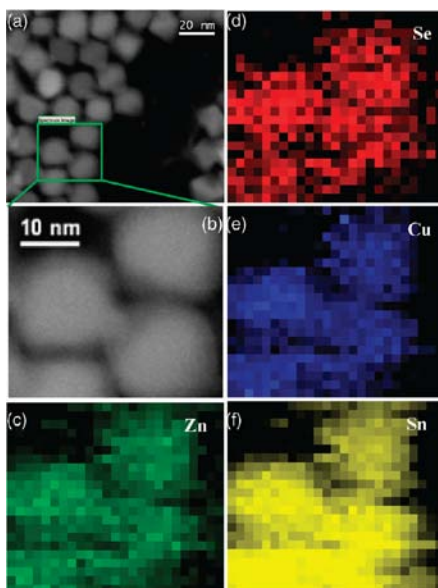


**Figure 3.17** HAADF images (left) with EELS chemical composition maps on a CZTSe NC

### 3.3.1.3 $\text{Cu}_2\text{ZnGeSe}_4$ nanocrystals

Between copper-selenide-based quaternaries  $\text{Cu}_2\text{ZnGeSe}_4$  (CZGSe) is the lightest we dealt with, as II can be Zn, Cd, or Hg, and IV can be Si, Ge, Sn, Pb, and we did not include Si. However,  $\text{Cu}_2\text{ZnSiSe}_4$  and  $\text{Cu}_2\text{Zn}(\text{Sn},\text{Si})\text{Se}_4$  are promising materials for photovoltaic devices. It has a larger band gap (2.33 eV) comparing to  $\text{Cu}_2\text{ZnGeSe}_4$  and  $\text{Cu}_2\text{ZnSnSe}_4$  (CZTSe).<sup>53</sup>

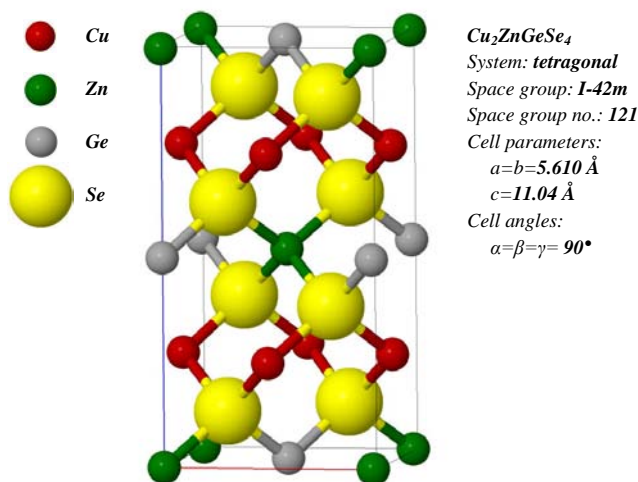


**Figure 3.18**  $\text{Cu}_2\text{ZnGeSe}_4$  (CZGSe) unit cell, tetragonal symmetry in  $I-42m$  (No. 121) space group with  $a=b= 5.610 \text{ \AA}$  and  $c= 11.04 \text{ \AA}$

CZGSe is p-type tetrahedrally coordinates semiconductor with a direct band gap between 1.21 and 1.63 eV determined theoretically and experimentally.<sup>45,53-56</sup> CZGSe crystallizes with tetragonal symmetry in space group  $I-42m$  (no. 121). The unit cell is shown in Figure 3.18. The structure shown in this figure is stannite CZGSe which indeed is a doubled cubic unit cell along  $c$ -axis with Cu, Zn and Ge atoms in cation positions, ordered as revealed in the cell.

In Figure 3.19 and 3.20 one can see Z-contrast images with EELS compositional maps of the indicated NCs. Figure 3.19 refers to two sample that had shorter reaction times (10 s and 50 s) comparing with the ones of Figure Figure 3.20 (5 min). By comparison between these three elemental maps, we realize that in the beginning of synthesis Zn and Ge do not enter the crystal structure of the particles. In the NCs shown in Figure 3.19, the amount detected by EELS of Ge in the middle is almost 0% and Zn is less than expected; it is 4%

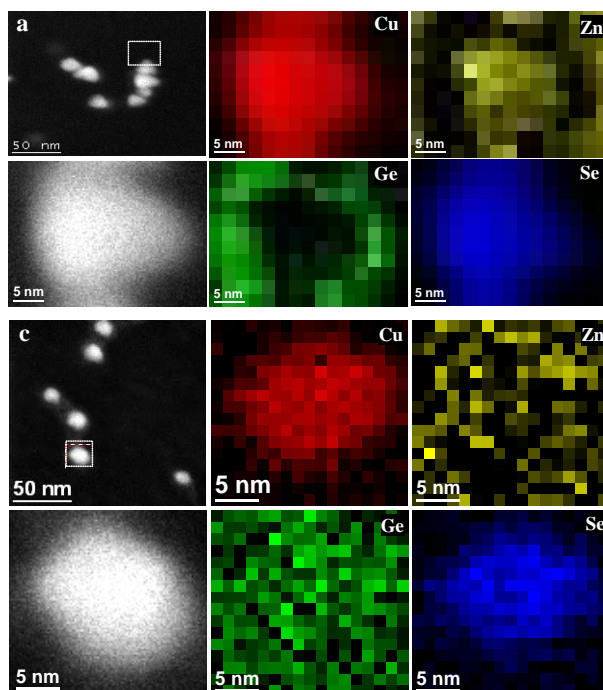


**Figure 3.19** EELS analysis on CZGSe NCs after (a) 10 s and (b) 50 s of reaction time, approximate chemical composition in the center of the NC: (a) Cu: 46%, Zn: 4%, Ge: 0%, Se: 50%, and (b) Cu: 31%, Zn: 5%, Ge: 15%, Se: 49%

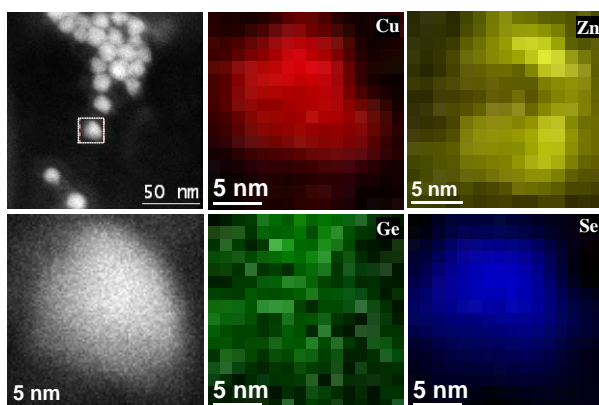


**Figure 3.20** EELS analysis on CZGSe NCs after 5 min of reaction time, approximate chemical composition in the center of the NC: Cu: 26%, Zn: 15%, Ge: 12%, Se: 47%

in Figure 3.19(a), which should be 12.5% in order to keep the stoichiometry of  $\text{Cu}_2\text{ZnGeSe}_4$ . In some cases a kind of structure is observed which could be considered as core-shell. Longer reaction time makes Ge and Zn diffuse to the

NCs' structure. Figure 3.19(b) refers to a sample which had 50 s of reaction time. Zn and Ge percentages have not arrived to the stoichiometry yet, but they are considerably higher than what was seen in Figure 3.19(a). As shown in Figure 3.19(b), Zn percentage in the NC is still too low. Ge has arrived to the stoichiometry, but in the case of many other NCs we analyzed, it was still lower. Therefore, longer reaction time is needed to reach the desired stoichiometry of  $\text{Cu}_2\text{ZnGeSe}_4$ . Figure 3.20 shows HAADF images (left) with corresponding EELS compositional maps on the indicated NC, revealing that the desired chemical composition is obtained.

HRTEM analyses in Figure 3.21 show the morphology and crystal structure

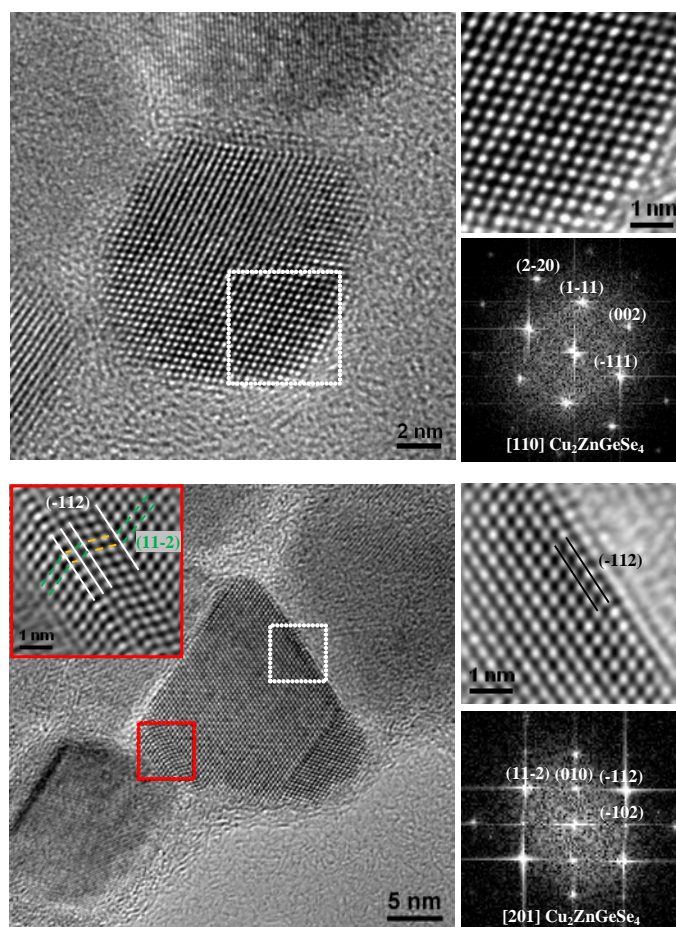


**Figure 3.21** (Upper) HRTEM micrograph of a CZGSe NC in the early stages of the growth (lower) HRTEM micrograph of a CZGSe NC with a power spectrum (lower-right) corresponding to the magnified IFFT-filtered zone (upper-right) which shows the faceting (-112) planes. The inset in the red square shows the twin defects in one of the sides of the NC around (-112) planes

of CZGSe NCs in early stages of growth (upper) and later (lower). In the early stages, before complete diffusion of Ge and Zn to the structure, the NCs have almost spherical shape, or start to have tetrahedral facets (HAADF image of Figure 3.19(a)) and they are smaller in size comparing to the NCs obtained from longer reaction times. The difference in the crystal structure of this compound with  $\text{Cu}_2\text{ZnGeSe}_4$  is within the error of power spectrum taken by fast Fourier transform (FFT) on the HRTEM image. Thus, it cannot be considered.

Longer reaction times make the NCs grow and inside many of the particles twin defects can be observed. Figure 3.21 (lower) reveals the HRTEM analysis of a NC with tetrahedral shape and twin defects. The upper-right image is the magnified part of the NC showing (-112) planes as the facet. The left side of the NC has (1-12) planes as facet which is from the same plane family. These plane families, indeed, are equivalent to (111) plane family of a cubic structure, because the  $c$  cell parameter is approximately twice of  $a$  and  $b$ . The inset in the red square shows the twin defects in one side of the NC around (-112) planes. The twins occur in (112) plane family and leg-like parts are attached to the main NC. The shape of the NCs is almost the same as what will be described in  $\text{Cu}_2\text{CdSnSe}_4$  (CCTSe) NCs with all details in the next section.

Finally, some Cu atoms were substituted intentionally with Zn. Due to their different valences electrical conductivity of the compound was increased. EELS compositional maps, this time on a NC that has more Cu atoms and less Zn. The approximate chemical composition measured by EELS is: Cu: 32%, Zn: 11%, Ge: 13%, and Se: 44%, which is roughly  $\text{Cu}_{2.15}\text{Zn}_{0.85}\text{GeSe}_{3.9}$ . This stoichiometry is confirmed by XRD.

It is proved that Cu-doping improves the thermoelectric figure of merit. The unit cell contains two tetragonal slabs:  $[\text{Cu}_2\text{Se}_4]$  and  $[\text{ZnGeSe}_4]$ . According to Liu *et al.* the former is an electrically conducting unit (ECU) and slabs analogous to the latter such as  $[\text{ZnSnSe}_4]$  and  $[\text{CdSnSe}_4]$  are electrically insulating units (EIU). Modifying the conducting unit by proper doping can enhance the electrical conductivity without any significant increase in thermal conductivity. Moreover, such doping can create structure disorder in the insulating unit, and provide connections between this unit and  $[\text{Cu}_2\text{Se}_4]$  and thus offers more hole conducting paths. Therefore, higher electrical conductivity in the whole structure is expected.<sup>57</sup>

A comparison of physical properties between  $\text{Cu}_2\text{ZnGeSe}_4$  and  $\text{Cu}_{2.15}\text{Zn}_{0.85}\text{GeSe}_{3.9}$  reveals the better thermoelectric performance of the latter. Thermoelectric characterization was performed in different temperatures and the

results are summarized in the diagrams of Figure 3.22.  $\text{Cu}_{2.15}\text{Zn}_{0.85}\text{GeSe}_{3.9}$  has higher electrical conductivity and lower thermal conductivity which both enhance the ZT (see equation 3.4), but a deteriorating lower Seebeck effect. However, figure of merit increases dramatically in total, and the highest ZT value of 0.55 is obtained at 450 °C. In the case of  $\text{Cu}_2\text{ZnGeSe}_4$ , the highest ZT is less than 0.1.

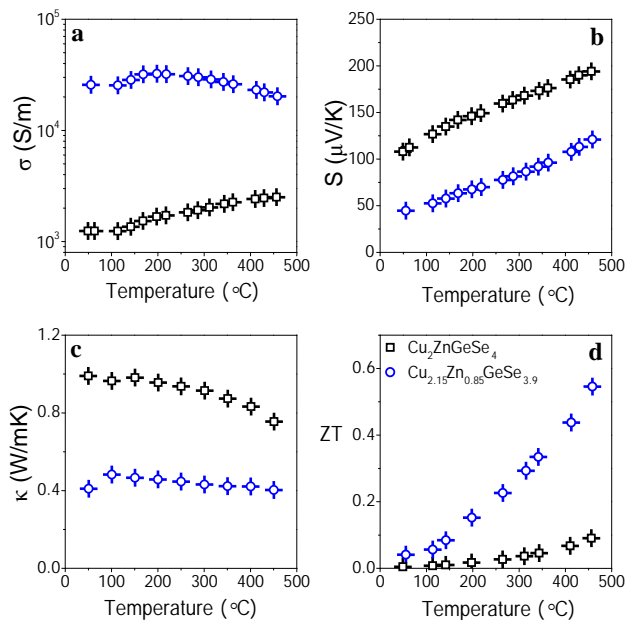


**Figure 3.22** Thermoelectric characterization of  $\text{Cu}_2\text{ZnGeSe}_4$  and  $\text{Cu}_{2.15}\text{Zn}_{0.85}\text{GeSe}_{3.9}$ : (a) electrical conductivity, (b) Seebeck coefficient, (c) thermal conductivity, and (d) thermoelectric figure of merit (ZT); Highest ZT of 0.55 at 450 °C was obtained with  $\text{Cu}_{2.15}\text{Zn}_{0.85}\text{GeSe}_{3.9}$  NCs<sup>31</sup>

### 3.3.1.4 $\text{Cu}_2\text{HgSnSe}_4$ nanocrystals

$\text{Cu}_2\text{HgSnSe}_4$  (CHTSe) is another interesting semiconducting compound from this family with a very narrow band gap of 0.17 eV, and it has a high potential as a thermoelectric material. Here CHTSe NCs are synthesized and used for thermoelectric applications. As well as the previously mentioned quaternary copper-selenide-based compounds, CHTSe has a tetragonal structure in  $I-42m$  space group (no. 121). As shown in Figure 3.23 its cell constants are:  $a = b = 5.829 \text{ \AA}$  and  $c = 11.42 \text{ \AA}$ ; the cell volume is  $0.388 \text{ nm}^3$  with totally 16

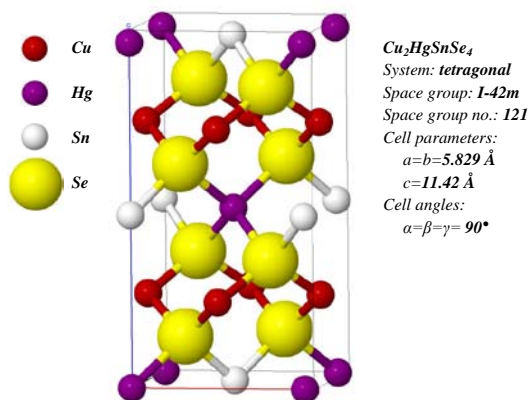


**Figure 3.23**  $\text{Cu}_2\text{HgSnSe}_4$  (CHTSe) unit cell, tetragonal symmetry in  $I-42m$  (No. 121) space group with  $a=b=5.746 \text{ \AA}$  and  $c=11.08 \text{ \AA}$

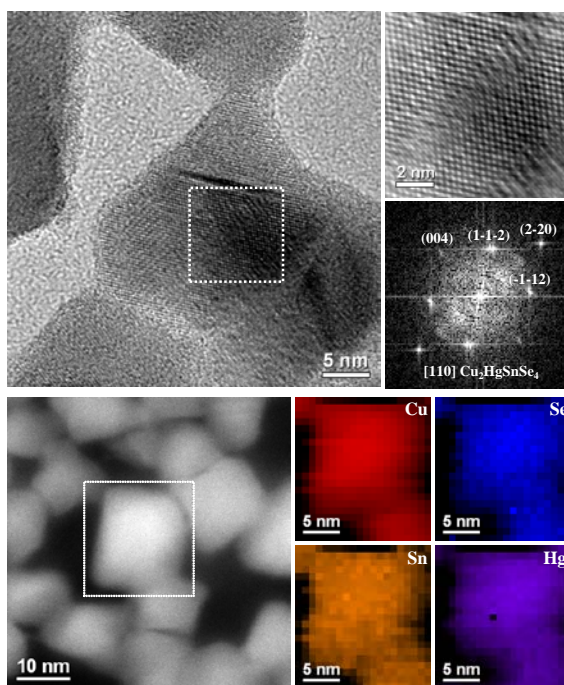


**Figure 3.24** (Upper) HRTEM micrograph of a CHTSe NC associated with (lower) EELS elemental map revealing the chemical homogeneity of the NCs

atoms in the cell, Se atoms distributed in anion sites, Cu, Hg, and Sn atoms in cation sites.<sup>58</sup>

Figure 3.24 shows HRTEM and EELS analysis of the as-grown CHTSe NCs. HRTEM analysis confirms the aforementioned crystal structure and EELS

elemental maps reveal the homogeneous chemical composition of the NCs. Here one can see that the NCs have pentatetrahedral morphology which will be described in detail in the next section.

This material, as well as the previous one, was highly Cu-doped (playing around with Se content at the same time) in order to enhance the thermoelectricity. Different compounds were examined, and the optimum situation was obtained by NCs with  $\text{Cu}_{2.8}\text{Hg}_{0.7}\text{SnSe}_{3.8}$  stoichiometry. As shown in Figure 3.25, the highest ZT of 0.20 was obtained at 450 °C.<sup>59</sup>

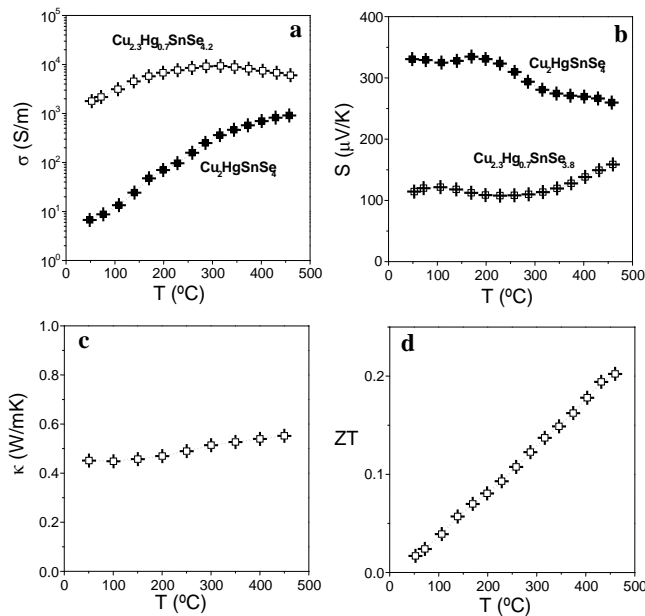


**Figure 3.25** Thermoelectric characterization of  $\text{Cu}_2\text{HgSnSe}_4$  and  $\text{Cu}_{2.8}\text{Hg}_{0.7}\text{SnSe}_{3.8}$ : (a) electrical conductivity, (b) Seebeck coefficient, (c) thermal conductivity, and (d) thermoelectric figure of merit (ZT); Highest ZT of 0.20 at 450 °C was obtained with  $\text{Cu}_{2.8}\text{Hg}_{0.7}\text{SnSe}_{3.8}$  NCs<sup>59</sup>

### 3.3.1.5 Section summary

In summary, in this section we proved the potential of the ternary and quaternary copper-selenide-based NCs for thermoelectric applications. First of all, the similar ZB/ZB-like structures of the ternary and quaternary compounds, and their homogeneous chemical composition were confirmed by HRTEM and EELS analyses, respectively. Secondly, it was shown that the distortion induced to the structure can improve the thermoelectric functionality of the compounds

as it causes reduction in thermal conductivity sometimes associated with an increase in electrical conductivity. Therefore the thermoelectric figure of merit considerably increases. In the case of CHTSe, CTSe, and CZGSe, the best ZT at 450 °C is 0.20, 0.3, and 0.55, respectively.

In fact this section is an introduction to further nanoengineering which will be revealed in the following sections. Although the chemical composition was engineered and sometimes twin defects emerged, still we have not touched the crystallographic structure of the compounds. With all the changes they still keep their ZB/ZB-like structure. However, in the next section we will study further nanoengineering issues which have remarkable influences on several properties of the materials.

### 3.3.2 Multi-phased structures

In this section, we mainly study some phenomena that dramatically change the properties of the compounds: morphology changes, polytypism, branching issue, and cation ordering. These tasks are considered in the case of different ternary and quaternary compounds.

#### 3.3.2.1 $\text{Cu}_2\text{GeSe}_3$ nanocrystals

$\text{Cu}_2\text{GeSe}_3$  (CGSe), as well as CTSe, is a p-type semiconductor with a direct band gap. Its band gap, 0.78 eV, lies in infrared (IR) range. It is a promising thermoelectric material in the form of nanostructure, due to the prompted phonon scattering which results in thermal conductivity reduction.<sup>28</sup>

The  $\text{Cu}_2\text{GeSe}_3$  (CGSe) NCs have been analyzed by HRTEM finding that the crystal structure that fits better is an orthorhombic (OTR) structure with space group  $Imm2$ .<sup>60,61</sup> This crystal structure is close to the well-known cubic diamond-like structure (zinc-blende (ZB), space group:  $F-43m$ ) in which many other semiconductors crystallize (Ge, Si and many other  $A^{II}B^{VI}$  binary compounds). The lattice constants of the orthorhombic phase found are  $a = 11.86 \text{ \AA}$ ,  $b = 3.96 \text{ \AA}$ , and  $c = 5.485 \text{ \AA}$ , presenting crystallographic ordered cations and anions on their respective sites<sup>62</sup> while cation disordering creates a similar structure that has cubic symmetry in  $F-43m$  space group (ZB). It has been further reported by several researchers that  $\text{Cu}_2\text{GeSe}_3$  undergoes a phase transformation caused by site-exchange order/disorder near its melting temperature.<sup>63</sup> As mentioned, this high temperature phase is a disordered face-centered cubic (fcc) structure (space group  $F-43m$ ), and the low temperature

structure is the ordered orthorhombic  $Imm2$  phase. In addition, as the Ge content is increased in  $Cu_2Ge_{1+x}Se_3$ , a structural phase transition takes place, resulting in conversion of the orthorhombic cell to the fcc structure with a unit cell parameter of  $\sim 0.555$  nm. The relationship between both phases corresponds to multiplying the  $a$ -axis of the orthorhombic cell by  $(2/3)^{1/2}$  and the  $b$  axis by  $(2)^{1/2}$ . The  $c$ -axis remains the same in both structures aside from a small expansion. Figure 3.26 shows the crystal relationship between these two phases, and the related wurtzite (WZ) one with hexagonal close-packed (hcp) symmetry in  $P6_3mc$  (no. 186) space group.

The first point to understand these crystal structures is to take into account the dumbbell unit as the minimum repeatable unit in the structure. Every dumbbell is composed of a cation (in this case Cu or Ge) and an anion (Se). These dumbbell units are oriented perpendicular to  $(00-1)$  planes, in both OTR and ZB structures. In the case of the cubic ZB structure, the cations are not ordered, meaning that in cation site one has a random distribution of Cu or Ge indistinctly, with a proportion of 2 to 1. However, in the orthorhombic phase

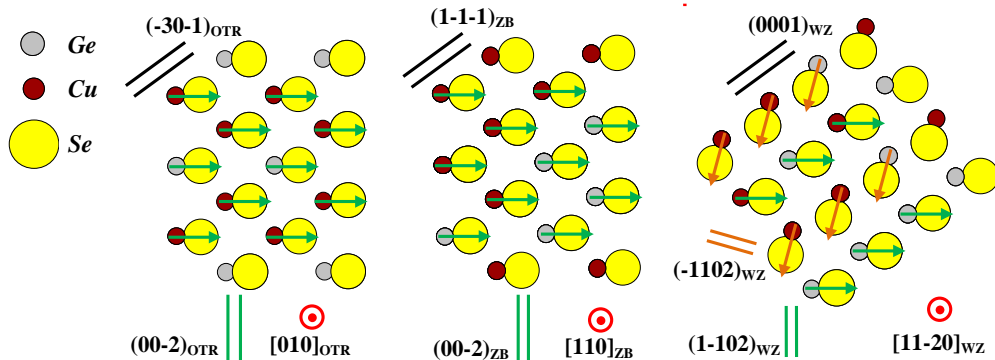


**Figure 3.26** CGSe crystallographic structures from left to right: orthorhombic (OTR), zinc-blende (ZB), and wurtzite (WZ)

(OTR) cations are ordered along the  $(200)$  planes, meaning all the cation positions in every plane are occupied by the same element, following an ordered sequence of two  $(200)_{OTR}$  planes with Cu cations between every two  $(200)_{OTR}$  planes of Ge cations. Green arrows on the OTR and ZB phases scheme of Figure 3.26 are pointing the dumbbell orientation on the  $(200)$  planes. In the OTR and ZB structures the all dumbbells are parallel, always perpendicular to  $(002)$  planes, whereas in WZ structure they alternate in each  $(0001)$  plane. In one

plane they are perpendicular to (1-102) planes (green arrows), and in the next one they are perpendicular to (-1102) planes (orange arrows).

In addition to these first phases, in some of the NCs studied, a different crystal polytype was found. Mainly in the body of these NCs, many twin-like defects appear, creating regions where the high density and periodicity of the twins was changing the atomic planes stacking, in a similar way as in other semiconductor materials. These changes mainly occur when forming nanostructures such as nanoparticles and nanowires. As none of the structures in literature for CuGeSe were matching the ones found in the body, induced by the periodic twinning, we assumed that there was a phase transformation forming a new polytype (see the regions in red on the structural maps in the HRTEM figures). In order to create the new structure we took as a model a similar phase transformation widely reported in the case of other semiconductors such as Si,<sup>7,8,64,65</sup> GaAs,<sup>1,2</sup> InP,<sup>3,4,66</sup> GaP,<sup>67,68</sup> GaN,<sup>5</sup> etc. So by following the same crystal ratio that in those well-known materials, from the original orthorhombic (OTR) or cubic (ZB) structures, we created a new crystal cell polytype with the hexagonal wurtzite (WZ) structure (space group:  $P6_3/mc$ ), not reported before for this material, to the best of our knowledge.

The new crystal structure information is as following:

- Crystal system: hexagonal
- Space group:  $P6_3mc$  (wurtzite-like crystal), no. 186
- Cell parameters:  $a=b= 3.840 \text{ \AA}$ ;  $c=6.320 \text{ \AA}$ ;
- Non-equivalent atomic positions equal to: Cu  $1/3, 2/3, 0$  (with occupancy 0.9); Ge  $1/3, 2/3, 0$  (with occupancy 0.1); Se  $1/3, 2/3, 0.374$  (with occupancy 1.0). The occupancy of Cu and Ge was calculated by taking an upper limit ratio obtained by EELS quantification (Ge atomic content equal to 5%)

In Figure 3.27 ZB and WZ structures are compared. It can be comprehended that a  $180^\circ$  rotation of the upper part of the ZB structure (Figure 3.27(a)), i.e. one Se with three directly bonded cations on top of it, results in wurtzite structure (3.27(b)). One can follow the dash-lined triangle on top and at the bottom of the structure. From the top view (Figure 3.27(c) and 3.27(d)), these two triangles overlap in the case of WZ, while in ZB they cross and create the hexagram. Side view of ZB and WZ structures (Figure 3.27(e) and 3.27(f)) give the same information as in the previous figure. Green arrows in ZB (Figure 3.27(e)) are perpendicular to (002) planes, as the only dumbbell direction, while

in WZ (Figure 3.27(f)) the green and orange arrows show the direction of the dumbbell perpendicular to (1-102) and (-1102) planes, respectively.

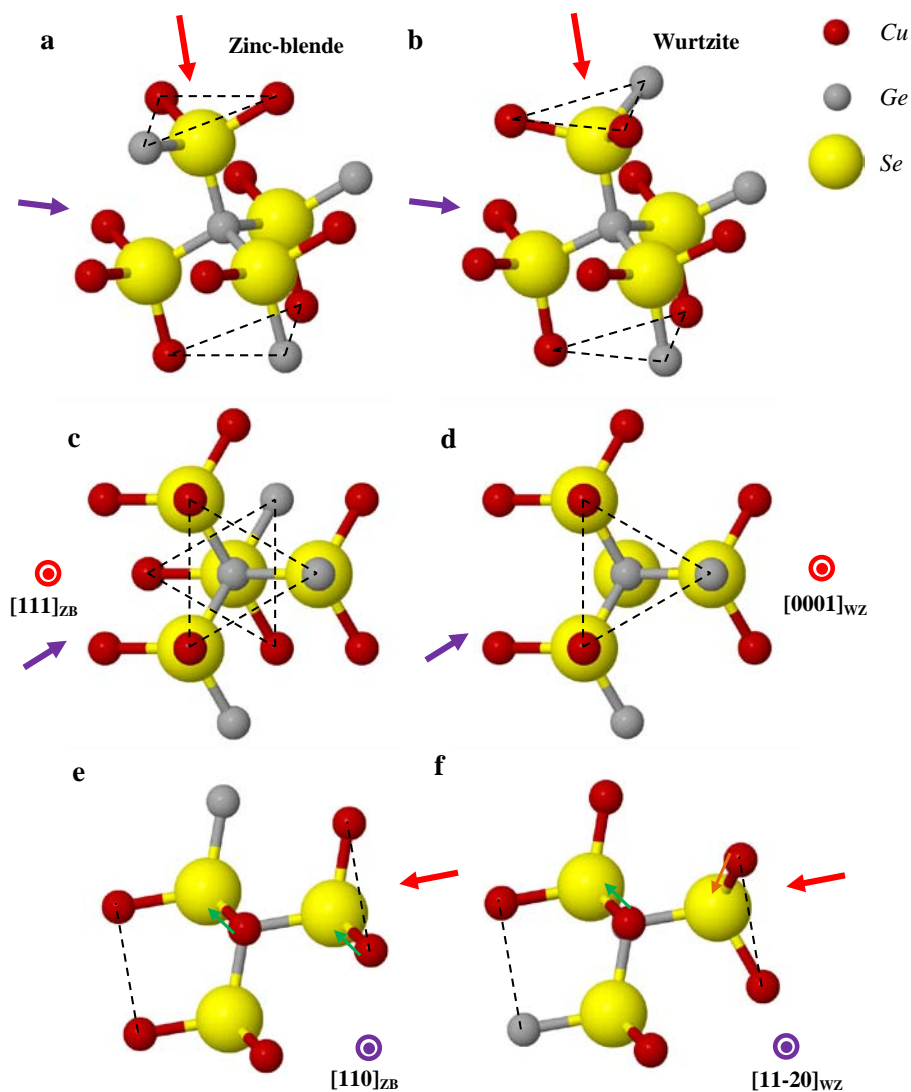


**Figure 3.27** Comparison between zinc-blende (ZB) and wurtzite (WZ) structures of CGSe: (a) ZB, (b) WZ, (c) ZB top view, (d) WZ top view, (e) ZB side view, (f) WZ side view

The new generated WZ cell matches perfectly the polytype structure we find in the NCs. Notice that in the model, Ge atoms have been considered as substitution on the Cu sites, and they are randomly distributed without cation

ordering. In some of the HRTEM figures we showed the change in the atomic stacking when moving from the OTR structure to the WZ. Both phases are intimately related, and create a kind of dumbbell system similar to that found in III-V and group IV semiconductor materials in their cubic and hexagonal polytypes.

In the present case, we have already mentioned the intimate relationship between the OTR and ZB phases, which corresponds to a cation ordering and a slight cell expansion. It is important to remark that these structures have a strong polarity, with Cu-Ge pointing up and Se down (or vice-versa). The OTR and the ZB structures have an *abcabc* stacking along the  $(30-1)_{\text{OTR}}$  or  $(1-11)_{\text{ZB}}$  planes, while the wurtzite presents an *ababab* stacking on the  $(0001)$  planes. The presence of a twin defect in the OTR or ZB structure (corresponding to a  $180^\circ$  rotation of the structure along the  $(30-1)_{\text{OTR}}$  or  $(1-11)_{\text{ZB}}$  axes) may form one

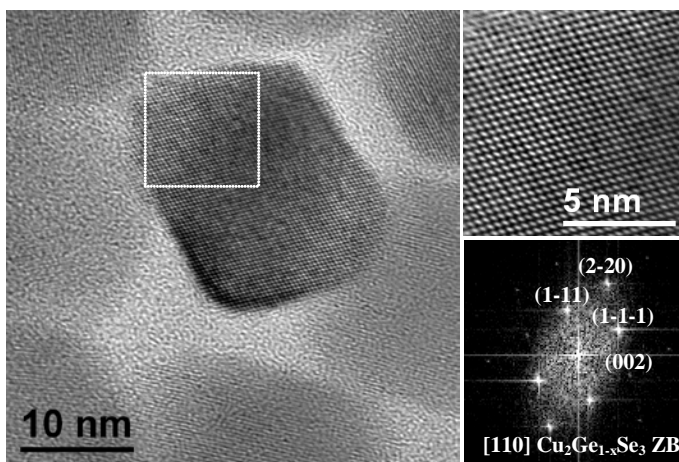


**Figure 3.28** HRTEM micrograph of a  $\text{Cu}_2\text{Ge}_x\text{Se}_3$  NC with Ge deficiency

monolayer of wurtzite. Then several consecutive twins create the pure hexagonal phase (WZ polytype). The epitaxial relationship between the 3 phases is as follows:  $(30-1)[010]_{\text{OTR}} // (1-11)[110]_{\text{ZB}} // (0001)[11-20]_{\text{WZ}}$ .

In CGSe by increasing the concentration of Ge in the solvent during the synthesis, the number of twins increases. In some cases some legs are grown as well. HRTEM study in figure 3.28 shows a NC synthesized with low concentration of Ge. Mostly there is no twin boundary in the NPs of this sample. Increasing the concentration of Ge, as shown in Figures 3.29, 3.30 and 3.31 the number of twin boundaries increases as well, and in some cases, high concentration of the twin defects causes appearance of a WZ structure. Indeed,

some theoretical studies by Chen *et al.*<sup>45</sup> justify the presence of wurtzite structure (in quaternary structures) by calculating Madelung and strain energy, as two main parameters that have significant influence on the relative-energy stability of each structure. However, they did not consider the case of  $\text{Cu}_2\text{GeSe}_3$ .

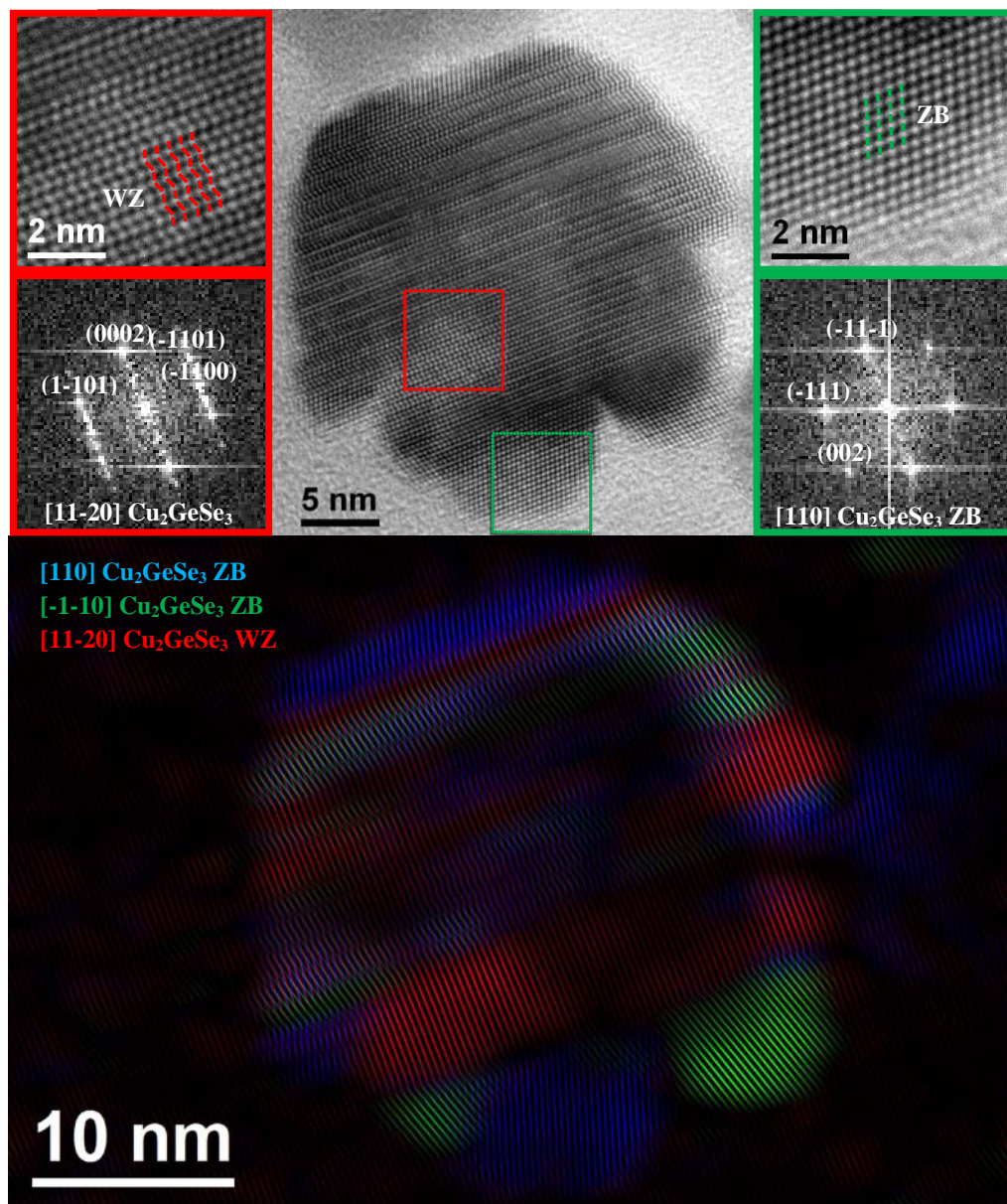


**Figure 3.29** HRTEM micrograph of a  $\text{Cu}_2\text{GeSe}_3$  NC, with magnified zones of the WZ (red squared) and ZB (green squared) and corresponding power spectra; correlated with the IFFT-filtered image showing WZ in red, and ZB in green and blue

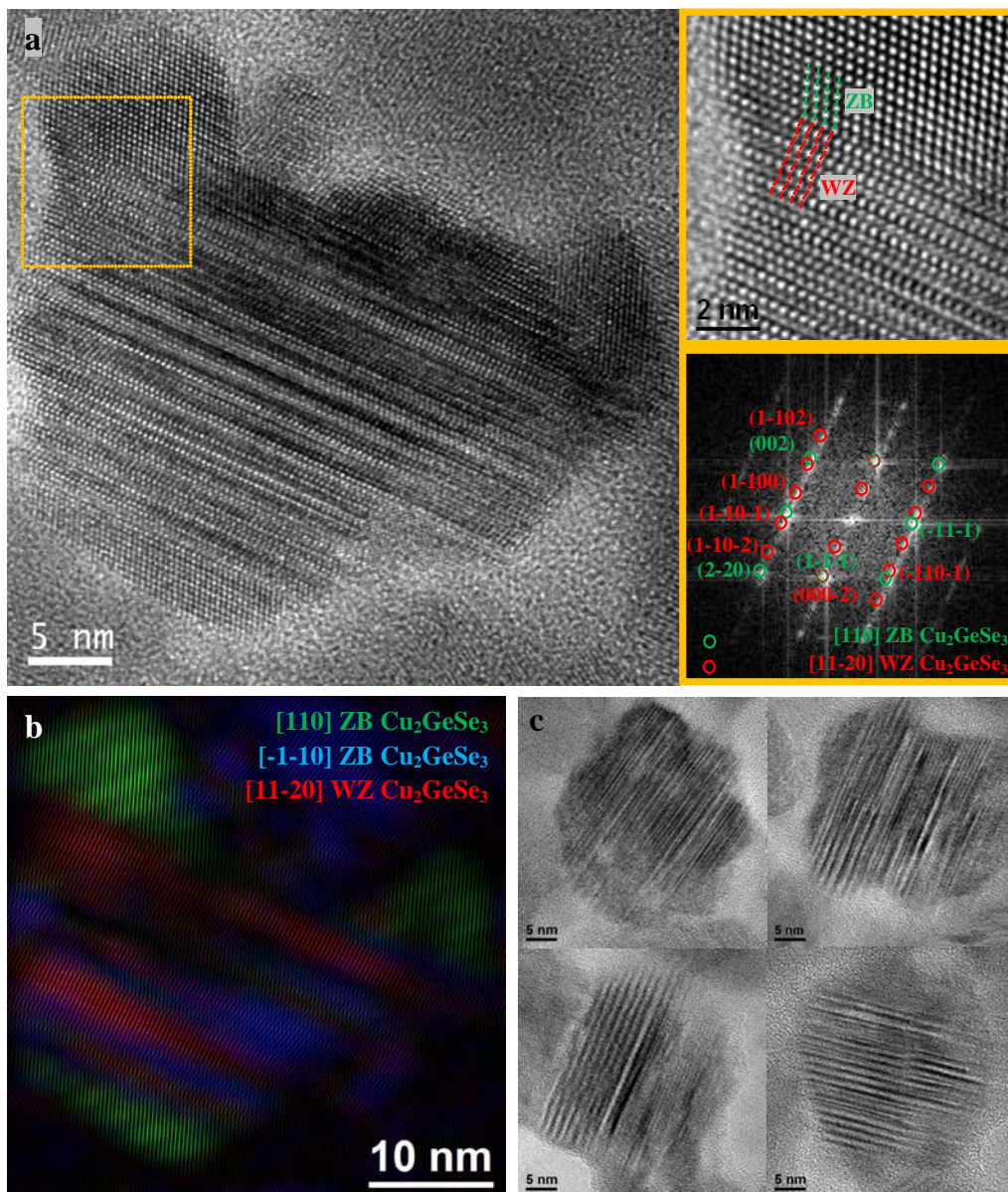


**Figure 3.30** (a) HRTEM micrograph of a  $\text{Cu}_2\text{GeSe}_3$  NC, with a magnified zone of the WZ and ZB, and the corresponding indexed power spectrum showing the planes of each structure with the related colors (green for ZB and red for WZ); (b) the correlated IFFT-filtered image showing WZ in red, and ZB in green and blue; (c) HRTEM micrographs on some other multi-phase NCs with various twin defects

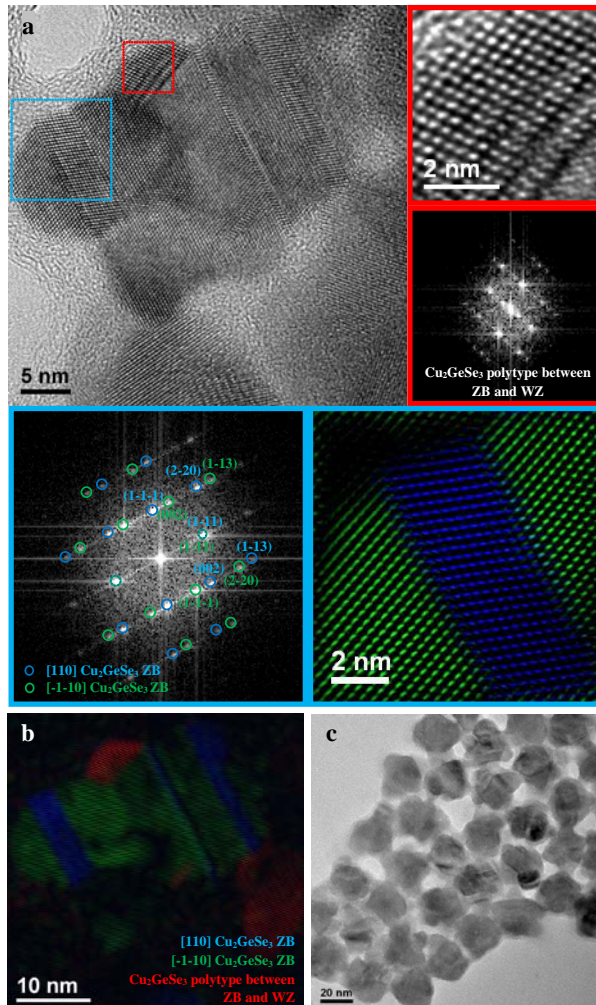


**Figure 3.31** (a) HRTEM micrograph of a  $\text{Cu}_2\text{GeSe}_3$  NC, with magnified zones on the legs of the NC and corresponding power spectra; the zone in the red square is a polytype between ZB and WZ structures, and the zone in the blue square shows a ZB leg with two twin boundaries; (b) the IFFT-filtered image showing the polytype in red, and ZB in green and blue, (c) low-magnification TEM micrograph showing a bunch of NPs which seem to have a similar structure

In Figures 3.29, 3.30 and 3.31 HRTEM micrographs of  $\text{Cu}_2\text{GeSe}_3$  NCs with high number of twin defects are revealed. In Figure 3.29 WZ and ZB structures are clearly seen in the magnified zones in the red and green square, respectively, with the corresponding indexed power spectra. The same HRTEM image is filtered (IFFT) and different structures are shown in different colors, i.e. WZ in

red, and ZB in green and blue (lower image). Figure 3.30 also gives the same information. The magnified zone of the orange square reveals both WZ and ZB structures and the epitaxial relationship between them.  $(-111)$  planes of ZB lie on  $(0002)$  ones of WZ. IFFT-filtered image in Figure 3.30(b) shows WZ in red and ZB in green and blue. Figure 3.30(c) consists of four HRTEM images on four other multi-phased NCs with abundant presence of twins which creates a mixture of ZB and WZ. In the red square of Figure 3.31(a) an extension of the NC is shown. This extension presents a polytypic structure in between ZB and WZ. It is also shown with red color in IFFT-filtered image of Figure 3.31(b). Figure 3.31(c) reveals a low-magnification TEM micrograph of a few NPs which have the same morphology and structure. Twin boundaries in the legs (extensions) of the NPs are visible even in such low magnifications. EELS chemical composition maps are shown in Figure 3.32. In the NCs with deficiency of Ge almost no twinning was observed. These NCs have simple ZB phase. See Figure 3.28.

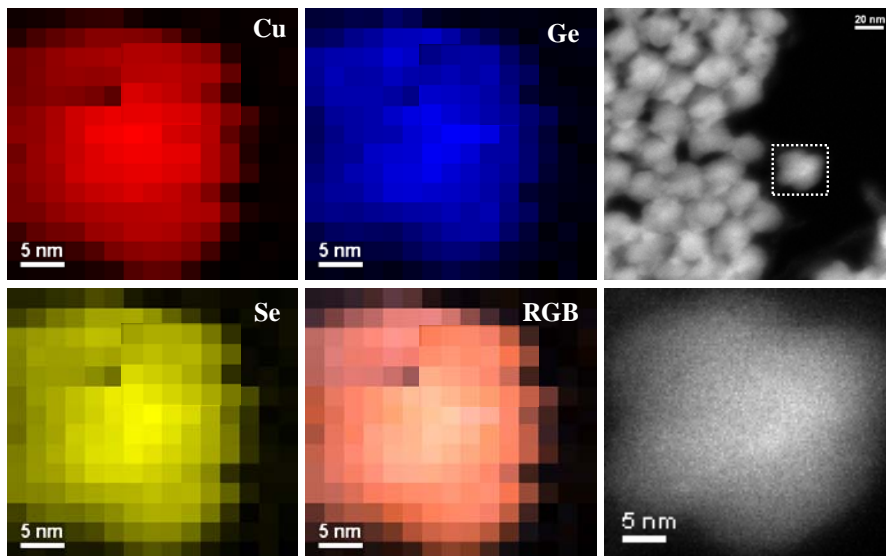


**Figure 3.32** HAADF images (right) with EELS chemical composition maps on a CGSe NC

To prove the influence of structure engineering on physical properties of these NCs, thermoelectric characterization was performed as can be seen in Figure 3.33. It is a comparison between the single-phased ZB-like NPs and multi-phased NPs consisting of a mixture of both ZB and WZ phases. As desired, thermoelectric conductivity considerably decreases, but in contrast,

electrical conductivity is reduced as well which has a negative influence on ZT. However, with the increasing Seebeck coefficient, the final figure of merit is enhanced about 2.5 folds.

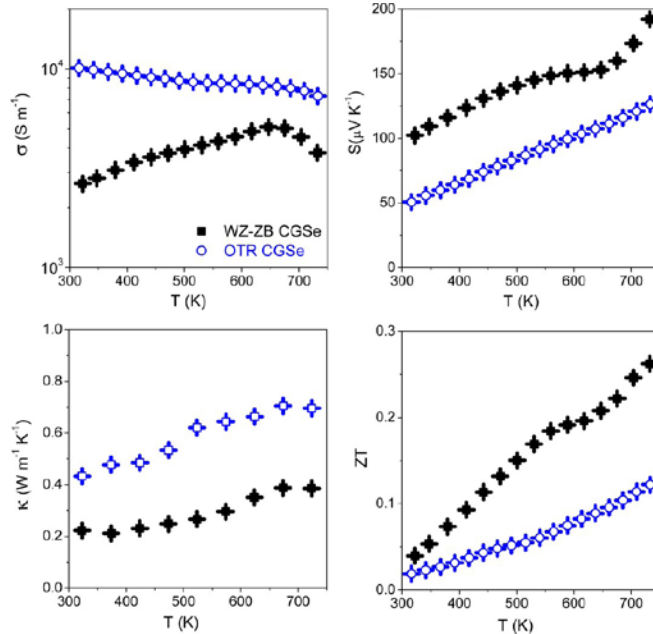


**Figure 3.33** Thermoelectric characterization of CGSe NCs, comparison between ZB-like NCs and mixed WZ-ZB NCs<sup>28</sup>

### 3.3.2.2 $\text{Cu}_2\text{CdSnSe}_4$ pentatetrahedral nanocrystals

$\text{Cu}_2\text{CdSnSe}_4$  (CCTSe) is another promising material for thermoelectrics, a p-type semiconductor with 0.96 eV band gap. In this case also it is shown that Cu-doping improves the thermoelectric properties, whereas electrical conductivity decreases and thermal conductivity is suppressed.<sup>57,69</sup> NCs nucleate and create small spherical nanoparticles (NPs) in the beginning of the growth with  $\text{Cu}_{2-x}\text{Se}$  chemical composition. In the following few minutes Sn and Cd diffuse to the structure gradually and spherical NPs change their shape to almost tetrahedral with four {112} facets.<sup>27,29</sup> The structure has tetragonal symmetry in I-42m space group. As well as in other  $\text{I}_2\text{-II-IV-VI}_4$  quaternaries, Cu, Cd, Sn and Se have oxidation states of +1, +2, +4 and -2, respectively.<sup>70</sup> The tetrahedral coordination can be seen in the unit cell revealed in Figure 3.34. Same as in CZGSe, CZTSe, CHGSe, and CHTSe, this tetragonal structure is indeed a

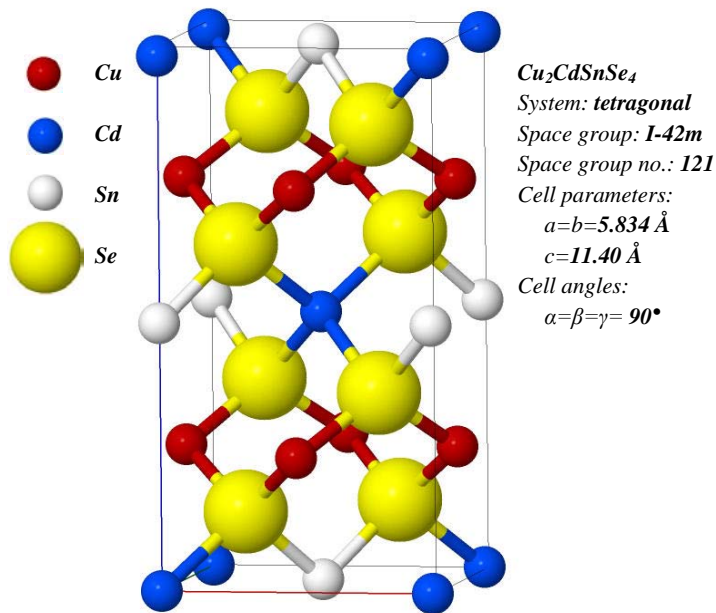


**Figure 3.34**  $\text{Cu}_2\text{CdSnSe}_4$  (CCTSe) unit cell, tetragonal symmetry in *I-42m* (No. 121) space group with  $a=b=5.834 \text{ \AA}$  and  $c=11.40 \text{ \AA}$

doubled cubic structure along  $c$  axis (with a slight difference), and this doubling is due to ordering of Cu, Cd and Sn in cation sites.

As mentioned above, these NCs have  $\{112\}$  faceting, where  $\{112\}$  plane family is equivalent to  $\{111\}$  plane family in an fcc structure. This faceting can be correlated to the fact that these planes have the most compact atomic arrangement, hence they have the minimum surface energy. The two angles of  $(112) // (-1-12)$ , and  $(-11-2) // (1-1-2)$  facets are  $108.23^\circ$  and the four angles of  $(112)$ ,  $(-1-12) // (1-1-2)$ ,  $(-11-2)$  facets are  $110.09^\circ$ . These angles are quite close to the one between the tetrahedral extensions of a perfect tetrahedron, i.e.  $109.47^\circ$ . The slight difference is due to the slight difference between  $c$  and  $2a$  in the unit cell.

Nevertheless, growth of the tetrahedra continues until the NCs arrive to a certain size. Afterwards with one twin defect the particle shape changes and on each facet of the seed another tetrahedron grows and ‘*pentatetrahedral*’ morphology forms. This kind of switching the facets of the growth is commonly observed in semiconductor nanostructures especially nanowires (NWs).<sup>3,66</sup> In the case of the tetrahedral extensions also the same  $\{112\}$  plane family forms the facets, in which three of them are free and one of them is connected to the seed tetrahedron.

Figure 3.35 shows BF-TEM images of a tetrahedral-shaped NP (Figure 3.35(a)) and the corresponding atomic model from different angles which give the same results. In Figure 3.35(b) pentatetrahedral NPs in different angles are shown with corresponding atomic models which are basically the same NP but visualized in appropriate angles that correspond to the BF-TEM images. Nonetheless, one can be confused as in 2D TEM images from each angle they look different, like in Figure 3.35(b). However, by understanding the 3D structure of the pentatetrahedra we figure out that the morphology of the NPs is not as various.

Figure 3.36 shows how a pentatetrahedron is grown. In the beginning (Figure 3.36(a)) the CCTSe sphere-like NPs nucleate. They change to faceted tetrahedral ‘seeds’ with for {112} facets (Figure 3.36(b)) as described above. Then the other four secondary tetrahedra as ‘extensions’ grow on these four

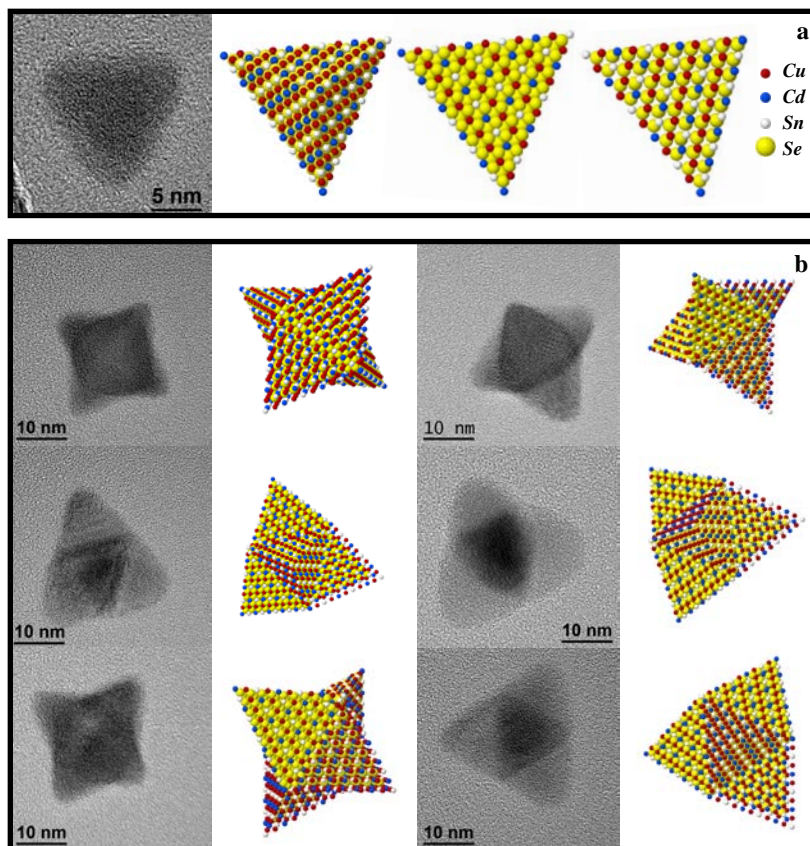


**Figure 3.35** HRTEM images of CCTSe NCs with (a) tetrahedral and (b) pentatetrahedral shape associated atomic models shown in appropriate angles

facets as shown in Figure 3.36(c). The atoms of the extensions are shown smaller in this figure, just to make the seed visible in order to give a better understanding about the growth. Afterwards, pentatetrahedra are formed (Figure 3.36(d)).

Figures 3.37 and 3.38 respectively show HRTEM analyses on NPs in the early and later stages of the growth. In both figures HRTEM is associated with EDX analyses to confirm the chemical compositions. As briefly mentioned above, the growth starts with nucleation of sphere-like NPs with  $\text{Cu}_{2-x}\text{Se}$  chemical composition. Figure 3.37(a) shows them. Their structure matches the cubic-symmetry structure with (220) plane distance of 2.04 Å, which is equivalent to (220) and (204) plane families of tetragonal CCTSe. Associated EDX chemical composition in Figure 3.37(b) exhibits the scarcity of Cd and Sn in the NPs. Afterwards, simultaneous with tetrahedral (and pentatetrahedral) faceting of the NCs, Cd and Sn diffuse to the structure gradually. This diffusion is schematically shown in the atomic models of Figure 3.36(e). Figure 3.38(a), analogous to Figure 3.37(a), shows an HRTEM micrograph of some pentatetrahedral NCs, one of them structurally analyzed and shown with details

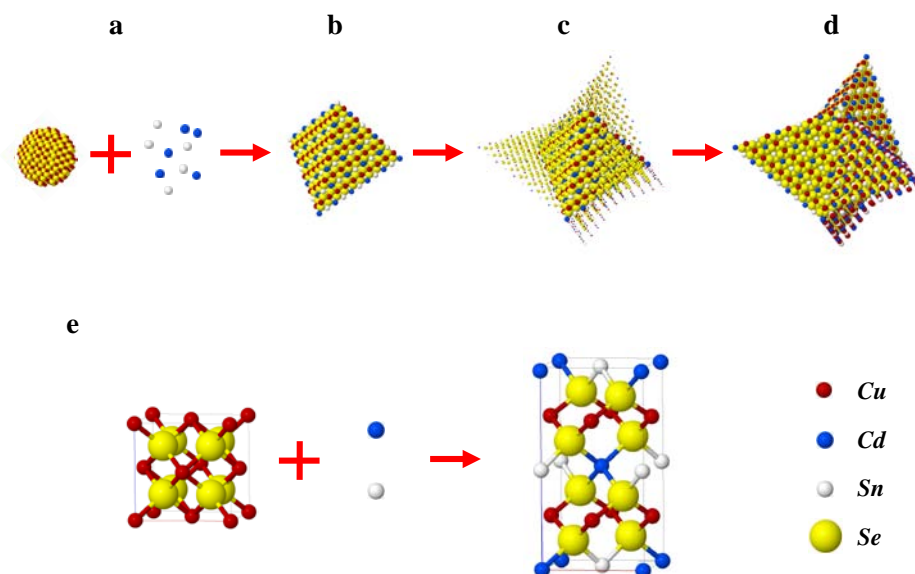


**Figure 3.36** 3D atomic models of the growth steps of NCs from (a)  $\text{Cu}_{2-x}\text{Se}$  spheres to (b) CCTSe tetrahedra, and then (c), (d) pentatetrahedra. In (c) the atoms of the legs are shown smaller in order to see how they grow on the initial tetrahedral seed. (e) How unit cell changes from  $\text{Cu}_{2-x}\text{Se}$  to CCTSe

at right. This HRTEM analysis associated with EDX chemical composition confirms the correct stoichiometry of  $\text{Cu}_2\text{CdSnSe}_4$ .

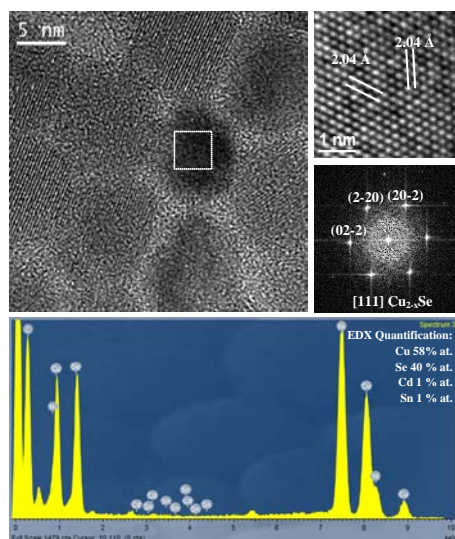


**Figure 3.37** (a) HRTEM analysis of  $\text{Cu}_{2-x}\text{Se}$  NCs with a magnified image showing the atomic planes (top-right) and the corresponding indexed power spectrum (bottom-right), associated with (b) EDX quantification showing the scarcity of Cd and Sn in the chemical composition

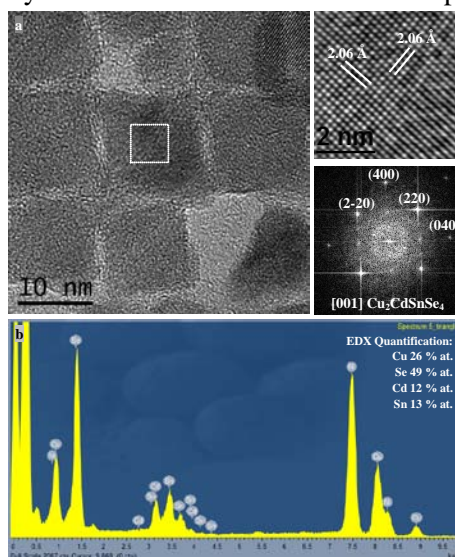


**Figure 3.38** (a) HRTEM analysis of CCTSe pentatetrahedral NCs with a magnified image showing the atomic planes (top-right) and the corresponding indexed power spectrum (bottom-right), associated with (b) EDX quantification showing that the chemical composition is almost at the perfect stoichiometry

In Figure 3.39 EDX and EELS quantifications are compared. EDX was performed in several regions similar to the one shown with the blue circle in Figure 3.39(a) which contain a few NCs on the carbon grid. The chemical quantification is written on the corresponding EDX pattern, Figure 3.39(b). Neglecting the Ni peak, which is due to the Ni TEM grid, EDX quantification shows almost the correct stoichiometry of  $\text{Cu}_2\text{CdSnSe}_4$ . It should be pointed out that Ni TEM grids are used instead of Cu grids, because taking into account that we have Cu in the structure, the Cu signal that comes out from the grid causes a high error in EDX quantification. EELS analysis (Figure 3.39(c)) presents the same results with a slight difference in atomic percentages. It is noticed that Se percentage in EELS is less than in EDX quantification. It can be due to the overlap of Cu signal with the eliminated Se background in EELS. Cu has an  $L_3$  principal edge at 931 eV and an  $L_2$  edge at 951 eV which continue hundreds of eV and overlap with the beginning of Se principle edge of  $L_3$  at 1436 eV. This overlap causes an error in Se background elimination, meaning a part of Se signal can be eliminated. Thus, in EELS quantification we can underestimate the Se atomic percentage. In general, EDX quantification error is less than the one of EELS. However, in our available TEM facilities, EELS has the advantage of high spatial resolution which in the case of core-shell NPs, or compositional variations from the center to the sides can be useful, and sometimes the unique

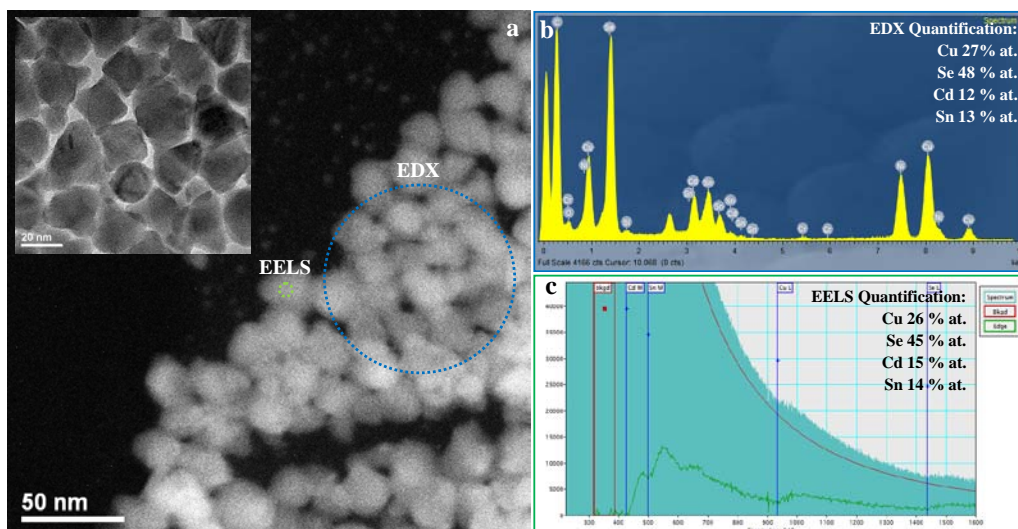


**Figure 3.39** (a) HAADF-STEM image of CCTSe pentatetrahedral NCs with a TEM image as inset, associated with (b) average EDX quantification of a few NCs, and (c) punctual EELS quantification, showing that the chemical composition is almost at the perfect stoichiometry

solution to study such structures. An example was presented in the previous section, when Ge cannot diffuse to the CZGSe NPs and create a Ge-rich shell-like layer around the NP. See Figure 3.19.

The CCTSe NCs, grown like pentatetrahedra, showed relatively high ZT, in thermoelectric characterizations, especially when they were doped with Cu. Samples with different dopant concentrations,  $\text{Cu}_{2+x}\text{Cd}_{1-x}\text{SnSe}_4$  with  $x = 0.05, 0.15, 0.3$  were examined in order to find the optimum situation, i.e. highest ZT. As shown in graphs of Figure 3.40, the best thermoelectric performance was achieved from  $\text{Cu}_{2.15}\text{Cd}_{0.85}\text{SnSe}_{3.9}$  compound,  $ZT = 0.71$  at 685 K. It is observed that by increasing the concentration of Cu the electrical conductivity increases till  $x = 0.15$ . With further doping, it falls down again. Seebeck coefficient is constantly deteriorated by Cu-doping, but thermal conductivity decreases and arrives to its minimum for  $x = 0.15$ . In conclusion, ZT remains the highest in the case of  $x = 0.15$ , which is almost four folds higher than the undoped material, and twice higher than the same compound in bulk which was previously reported.<sup>57</sup>

In fact the idea is to substitute Cu(I) for Cd(II) atoms which by creating disorder changes the band gap and displaces the Fermi level of the compound.

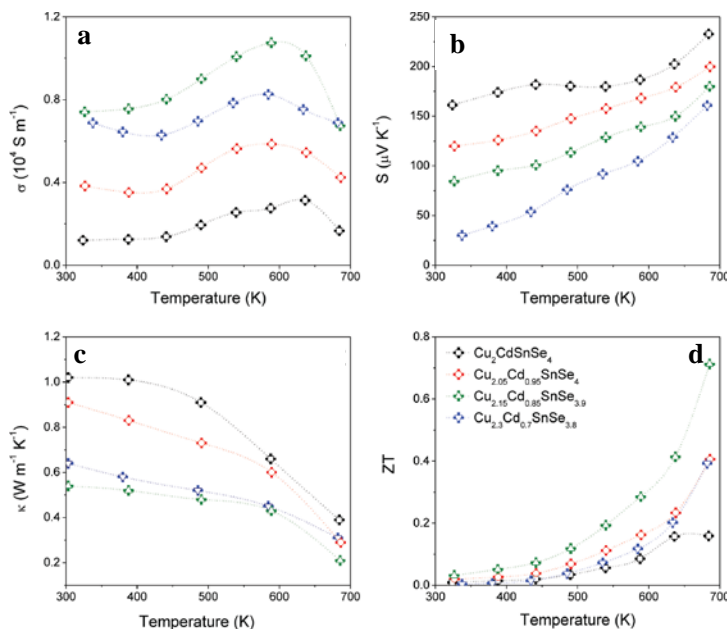


**Figure 3.40** Thermoelectric characterization: comparison between four CCTSe compounds with different Cu-doping concentration, (a) electrical conductivity, (b) Seebeck coefficient, (c) thermal conductivity, and (d) figure of merit<sup>29</sup>

*Ab-initio* theoretical study was performed to calculate the density of state by measuring the valence band maximum (VBM) and the conduction band minimum (CBM). It showed a gradual downshift of the Fermi level towards the valence band when replacing Cd by Cu. The disorder introduced by small amounts of Cu-doping increases the phonon scattering and, as a consequence, decreases the thermal conductivity. Moreover, it should not perturb the mobility of the holes while kept low. Nonetheless, large degrees of doping result in homogenization of slab composition, diminution of the structural complexity and phonon scattering centers, thus increase of the thermal conductivity, which is not desired. Details of the theoretical study can be found elsewhere.<sup>29</sup>

Moreover, a limit exists while further substitution gives rise to changes in Sn and Se content in the NCs. It is observed that increasing Cu:Cd ratio decreases the content of Se. If the compound is considered as  $\text{Cu}_{2+x}\text{Cd}_{1-x}\text{SnSe}_{4-y}$ , with  $x = 0.15$ , we reach to  $y = 0.1$  and with more Cu-doping,  $x = 0.3$ , we reach to lower Se content decreases  $y = 0.2$ , meaning there are more Se vacancies in

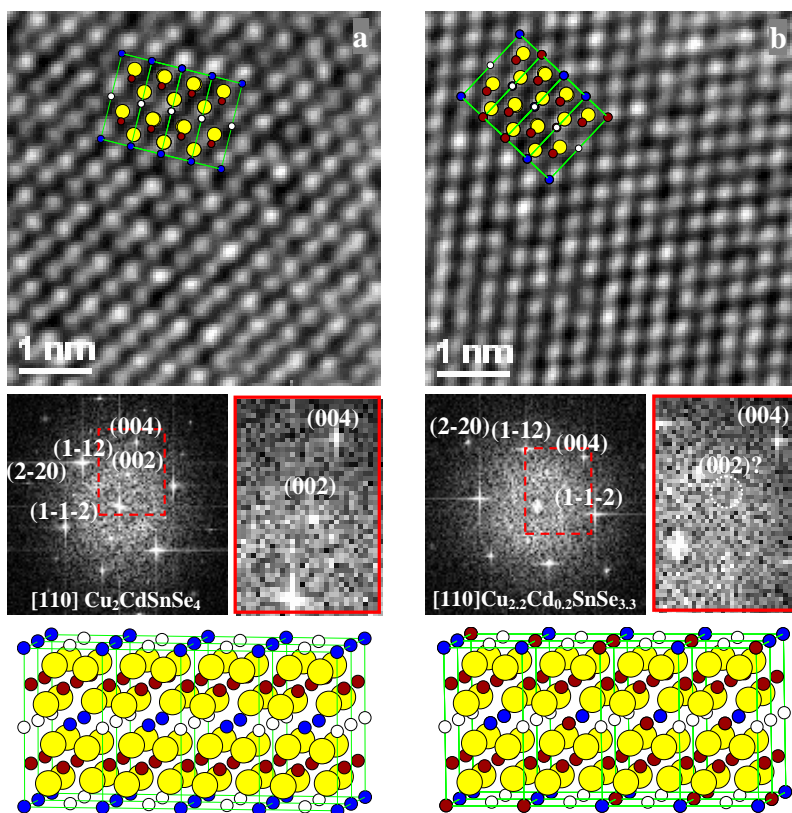


**Figure 3.41** HRTEM analysis of (a)  $\text{Cu}_2\text{CdSnSe}_4$  and (b)  $\text{Cu}_2\text{Cd}_{0.2}\text{SnSe}_{3.3}$  compounds with corresponding power spectra and crystal structures

the structure that can be attributed to the charge compensation in saturation of electrical conductivities.<sup>29</sup>

Interestingly, the structural disorder caused by Cu substitution for Cd (introducing less Cd as well) is clearly observed by HRTEM analysis in Figure 3.41. In this figure  $\text{Cu}_2\text{CdSnSe}_4$  and  $\text{Cu}_{2.2}\text{Cd}_{0.2}\text{SnSe}_{3.3}$  compounds are compared. In the power spectrum that corresponds to the former (Figure 3.41(a)), (002) plane reflection appears as it is supposed to, due to the tetragonal structure in  $I-42m$  space group. Although the latter has the same tetragonal structure, (002) plane reflection vanishes as a result of disorder in the crystal structure. See Figure 3.41(b). (002) reflection in  $\text{Cu}_2\text{CdSnSe}_4$  refers to the two different tetrahedral units in the  $c$  axis:  $[\text{Cu}_2\text{Se}_4]$  and  $[\text{SnCdSe}_4]$ , whereas in  $\text{Cu}_{2.2}\text{Cd}_{0.2}\text{SnSe}_{3.3}$  intermixing of the cations creates undistinguishable tetrahedral units.<sup>29,57</sup> In Figure 3.41, atomic columns are determined with 2D atomic models. The 3D atomic structures are shown in the lower images. The difference in these models is the random presence of Cu atoms in Cd atomic columns.

### 3.3.2.3 $\text{Cu}_2\text{Cd}_7\text{SnSe}_{10}$ polypods

In this section, control of branching, polytypism, polarity and cation ordering in CCTSe NCs, as four independent issues are studied that can give rise to remarkable changes in various properties of these nanomaterials.

Branching in NCs shows unique influence on the functionality of the compounds,<sup>71</sup> for instance electronic state.<sup>72,73</sup> Hierarchically organized branched nano-structures find various applications,<sup>74,75</sup> providing higher surface area in dye sensitized solar cells<sup>76</sup> and lithium ion batteries,<sup>77</sup> self-aligning on a substrate providing a direct path for charge transport between planar electrodes, or providing heterostructures with precise contacts at the nanoscale for nanodevices.<sup>78,79</sup>

Branching is intimately related to polytypism,<sup>71,73</sup> which additionally allows us to engineer the physical properties, for example band structure, while valence and conduction bands vary for different polytypes.<sup>1</sup> Occurrence of these two phenomena causes ‘*polytypic branching*’ in which generally WZ extensions of the nanoparticle branch out from a ZB seed. In the case of branched binary chalcogenide NCs such as CdS,<sup>80</sup> CdTe,<sup>81</sup> CuTe,<sup>82</sup> some works have been published. Even recently Wang *et al.* reported on ternary  $\text{Cu}_2\text{SnSe}_3$ .<sup>83</sup> However, to the best of our knowledge, there is no report on quaternary  $\text{Cu}_2\text{Cd}_x\text{SnSe}_y$  (CCTSe) branched NCs or any other quaternary chalcogenides.

Polytypism indeed is a phenomenon which regularly takes place in tetrahedrally-coordinated semiconductors, especially Si,<sup>8,64,84</sup> groups III-V<sup>51,85-87</sup> and II-VI<sup>12,42</sup> nanostructures. It has even been observed in ternary and quaternary copper-based chalcogenides.<sup>88</sup> In these materials, the (111) atomic planes of the cubic structure, well-known as zinc-blende are equivalent to the (0001) atomic planes of the hexagonal structure which has WZ structure in  $P6_3mc$  space group. The difference between both crystal phases lies in the different stacking of the atoms along the (111) or (0001) planes, being *abcabc* and *ababab* for ZB and WZ, respectively.

As mentioned in the previous section, in CCTSe, as the structure is tetragonal with *c* almost twice of *a* and *b*, (112) plane families are equivalent to (111) of cubic structures. Therefore, we consider the tetrahedral seed structure as zinc-blende-like (ZB-like) with (112) facets. In this material, interestingly, the structural change from ZB to WZ is associated with chemical composition changes, as the only stable CCTSe compound with hexagonal symmetry reported in the literature is  $\text{Cu}_2\text{Cd}_7\text{SnSe}_{10}$ .<sup>89</sup> Thus, the stoichiometry of the compound changes from  $\text{Cu}_2\text{CdSnSe}_4$  in ZB to  $\text{Cu}_2\text{Cd}_7\text{SnSe}_{10}$  in WZ.

Polytypism is usually accompanied with changes in the properties of the material. In this regard, for instance, Li and Wang<sup>72</sup> theoretically studied the electronic states in CdTe WZ and ZB structures. Furthermore, in section 3.3.2.1 we provided some experimental results showing that polytypism has a considerable effect on physical properties of ternary  $\text{Cu}_2\text{GeSe}_3$  NCs, and thus, causes a dramatic enhancement in its thermoelectricity.<sup>28</sup>

On the other hand, polarity, the concept of relative charge residing on cation and anion sites in the lattice,<sup>90</sup> also has a remarkable influence on physical properties of the compounds.<sup>44,91</sup> The orientation of the dumbbell units which comprise a pair of atoms, a cation on one side and an anion on the other side, determines the internal electric field of the crystal. Recently it has been shown that in some semiconductors the growth direction of one-dimensional nanostructures such as nanowires<sup>51</sup> and in general non-planar structures such as tripods and tetrapods are driven by polarity.<sup>12</sup>

Another important point is the ordering of the cations. The CCTSe structure is believed to be ordered as discussed in the previous section,<sup>29</sup> meaning the Cu, Cd, and Sn atoms occupy the cation sites as a stannite structure. In these NCs, the ordering effect creates conducting and insulating units at atomic scale within the unit cell,<sup>57</sup> whereas random distribution of the cation eliminates this effect. It is therefore challenging to determine the existence of ordering in the crystal

structures composing the NCs seed and branches and how this ordering effect may influence the electronic properties and the band structure of the material. In this context, as reported by Yang *et al.*,<sup>92</sup> the band structure and energy gap in CGSSe NCs depends on the chemical composition as stoichiometry variations cause distortion in the structure. Fan *et al.*<sup>93</sup> also showed that the band gap is tunable by composition changes in CZTSSe. However, Liu *et al.*<sup>57</sup> reported that Cu-doping in CCTSe does not cause a significant change in the band structure. CCTSe band gap is reported experimentally as 0.96 eV<sup>69</sup> and theoretically as 0.98 eV.<sup>57</sup> **Error! Marcador no definido.** Nevertheless, no band gap energy has been yet reported on hexagonal Cu<sub>2</sub>Cd<sub>7</sub>SnSe<sub>10</sub>, neither the ordering effect.

Therefore, branching, polytypism, polarity and cation ordering can be used independently to engineer the physical properties of semiconductors (e.g. chalcogenides). In the following, we will show how controlling all these properties, the morphology of our NCs can be designed at will and the properties modulated.

In the present case, the formation of the Cu<sub>2</sub>Cd<sub>x</sub>SnSe<sub>y</sub> (CCTSe) branched NCs follows a rather complicated mechanism which is different from the formerly reported ones.<sup>94-96</sup> By taking advantage of colloidal routes, we will show a multistep growth process that can be terminated at each step of the growth. Firstly, the initial ‘tetrahedral’ seed nucleates. Then, on each facet another tetrahedron forms and the morphology of the NC changes from a simple tetrahedron to a ‘pentatetrahedron’.<sup>27</sup> Till here the material of the previous section is obtain. Afterwards, the secondary tetrahedra branch out from the top, and therefore monopods, bipods, tripods and tetrapods form, depending on the number of branches (from 1 to 4). We will study the influence of polytypism in the branching process and we present theoretical studies via *ab-initio* simulations revealing the impact of this phenomenon on the electronic properties of CCTSe NCs. Furthermore, the pivotal role of the polarity in morphology and growth mechanism of the branched NCs will be also shown. As a matter of fact, polarity is considered as the reason that the seed forms like a tetrahedron with four cation-polar facets and branch out with cation-polar extensions. Finally, the presence/absence of cation ordering in our complex systems will be correlated with the *ab-initio* simulations allowing us to understand the final electronic band structure configuration of the branched CCTSe NCs (tetrapods).

It is worth to point out that still there are few methods for polarity determination. Previously developed methods such as homoepitaxy, convergent beam electron diffraction (CBED), or scanning tunneling microscopy (STM), beside inconvenience and relatively low reliability, do not have enough spatial resolution to determine the polarity at atomic scale or changes in polarity if there is any. In contrast, newly-developed aberration-corrected transmission electron microscopes (TEMs) offer the possibility of direct polarity measurement as they can reach sub-angstrom resolutions. By means of atomic-resolution scanning transmission electron microscopy (STEM) techniques such high-angle annular dark-field (HAADF) or the recently developed annular bright-field (ABF) STEM,<sup>97-99</sup> we can even visualize light atoms within the dumbbells (e.g. H, N and O)<sup>42,44,100,101</sup> or distinguish between two atoms with close atomic numbers (e.g. Ga and As).<sup>12,44</sup> In this part we take advantage of HAADF-STEM imaging which due to the comparatively small difference between the average atomic number of the cations (Cu, Cd, Sn) and the anion (Se), polarity determination is rather challenging.

Our newly synthesized CCTSe polypod structures are the result of the polytypic branching on the previously reported pentatetrahedral NCs (acting

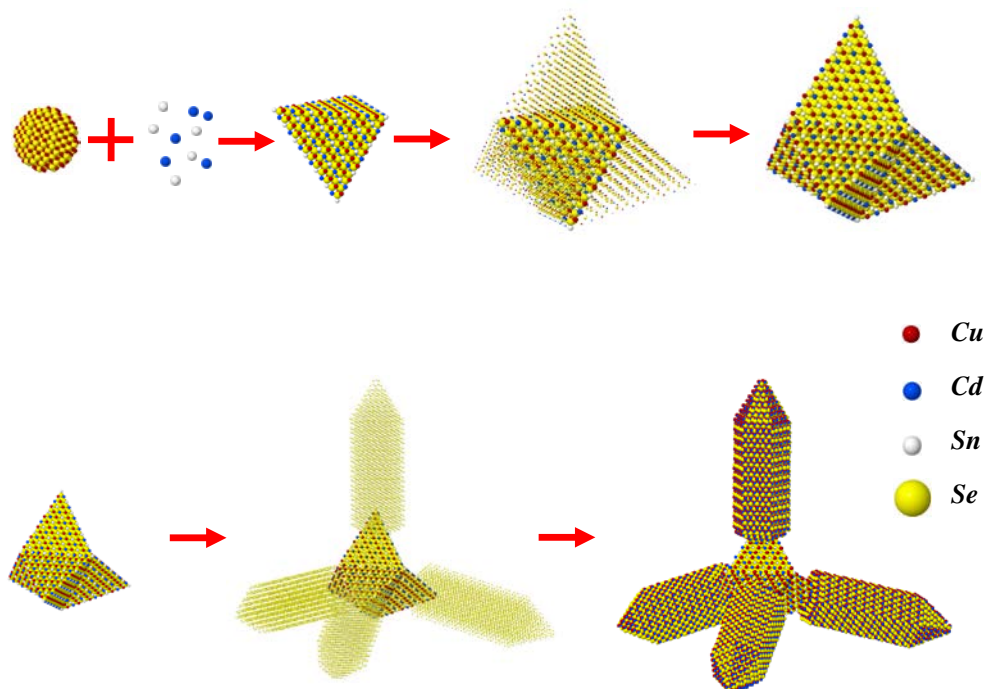


**Figure 3.42** Simulation of CCTSe tetrapod growth steps with 3D atomic model

here as seeds) in section 3.3.2.2. The NC growth, as shown in the scheme of Figure 3.36 and 3.42, initiates with nucleation of quasi-spherical  $\text{Cu}_x\text{Se}$  particles and continues with diffusion of Cd and Sn cations which gives rise to the formation of tetrahedrally-faceted CCTSe NCs with four  $\{112\}$  facets. Afterwards, the secondary tetrahedra grow on the seed and create the pentatetrahedral morphology, which later on by branching mechanism they form polypods. As shown in Figure 3.43, depending on the number of the branches we will have monopods, bipods, tripods, and tetrapods (Figure 3.43(a), (b), (c), and (d), respectively)

There are eight different planes from  $\{112\}$  family, four of them are cation terminated (cation-polar) while the other four are anion terminated (anion-polar). As a matter of fact, polarity is the reason that the seed forms as a tetrahedron (with four  $\{112\}$  facets), although there are eight possible facets from  $\{112\}$  family. It seems that the cation polar surfaces are of preferential during the growth, and thus the seed forms as tetrahedron. If the NCs could grow equally along all eight possible  $\{112\}$  facets, they would have octahedral shape, which does not occur in CCTSe, as only one of the terminations is energetically favorable for the growth in the solution. This latter fact explains why the former seeds adopt tetrahedral morphology instead of octahedral.<sup>27</sup> As we will see in the atomic resolution HAADF-STEM analysis, the NCs grow preferentially along the four  $\{112\}$  cation terminated facets, meaning the growth is cation polar, as mainly observed for example in the case of ZnO.<sup>100,102</sup> It is

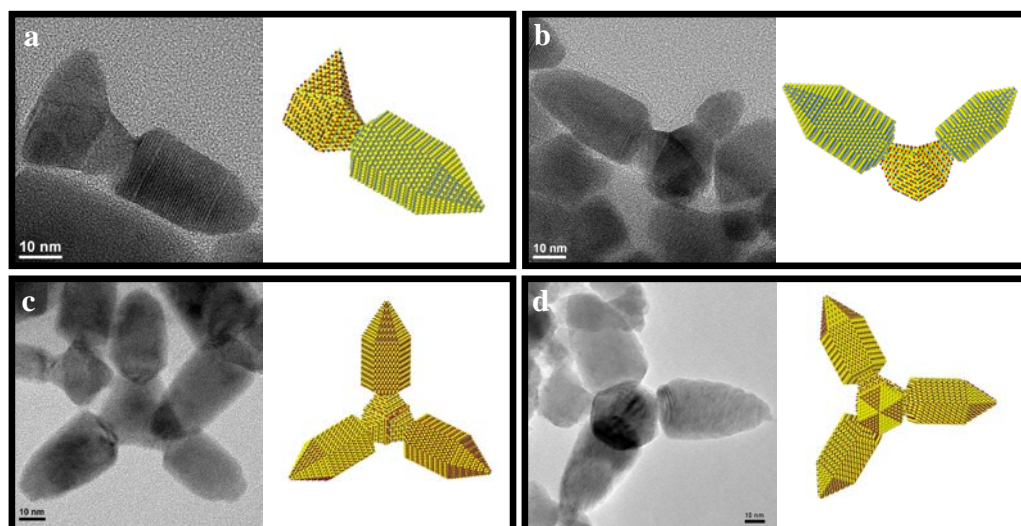


**Figure 3.43** CCTSe polypod NCs: (a) monopod, (b) bipod, (c) tripod, and (d) tetrapod

important to remark that most of the semiconductor binary systems when growing as non-planar nanostructures are anion-polarized, instead.<sup>12,44,101</sup>

At a given reaction time, a twin occurs in every one of the four cation polarized {112} facets of the initial tetrahedron seed. This twinning mechanism, consisting in a 180° rotation of the structure along the {112} axis, suddenly occurs on the four facets of the initial seed and abruptly limits the NC expansion to pentatetrahedral shape. In other words, the growth continues by formation of secondary tetrahedra on top of every triangular {112} facet of the initial one which leads to emergence of pentatetrahedral NCs. Therefore, the nanocrystal morphology changes from tetrahedral to pentatetrahedral, with 12 free facets, all from {112} plane family and anion-polar.

The addition of an excess of Cd-rich precursor leads to the formation of polypod structures from the penta-tetrahedral NCs. The formation of branches in tripods and tetrapods is usually accompanied by the change in the crystal structure. Most of the known polypod branches are composed of hexagonal WZ structure, or equivalently a highly twinned polytype.<sup>103</sup> In order to obtain a quaternary WZ structure and promote the branching, the solution needs to be Cd-rich. Figure 3.43 reveals high-resolution TEM (HRTEM) images of all these structures, associated with 3D atomic models in order to lucidly visualize them. A simple video can also be found in reference.<sup>104</sup> As expected, the branches have WZ structure with hexagonal symmetry in  $P6_3mc$  space group.

As described before, CCTSe tetragonal (ZB-like) and hexagonal (WZ) phases are intimately related, as (112) planes of ZB are equivalent to (0001) planes of WZ where the only difference is their stacking order, analogous to the system observed in group IV,<sup>84</sup> II-VI,<sup>12,42</sup> and III-V<sup>85-87</sup> polytypic semiconductors. However, the WZ structure in this material is slightly different from the common WZ that occurs in the aforementioned semiconductors; the chemical composition of WZ CCTSe is not exactly the same as the one of ZB phase, and the cell parameters are also slightly different from those of the expected WZ.

Figure 3.44 reveals HRTEM analysis on a CCTSe bipod. Due to the 3D structure of tripods and tetrapods it is quite unlikely to have them in an appropriate zone axis for HRTEM analysis while they lay on TEM carbon/graphene grids. Therefore, for all the studies of this report we choose monopods and bipods which have 2D structures that give all crucial crystallographic information we require. The result can be then correlated to tripod and tetrapod morphologies.

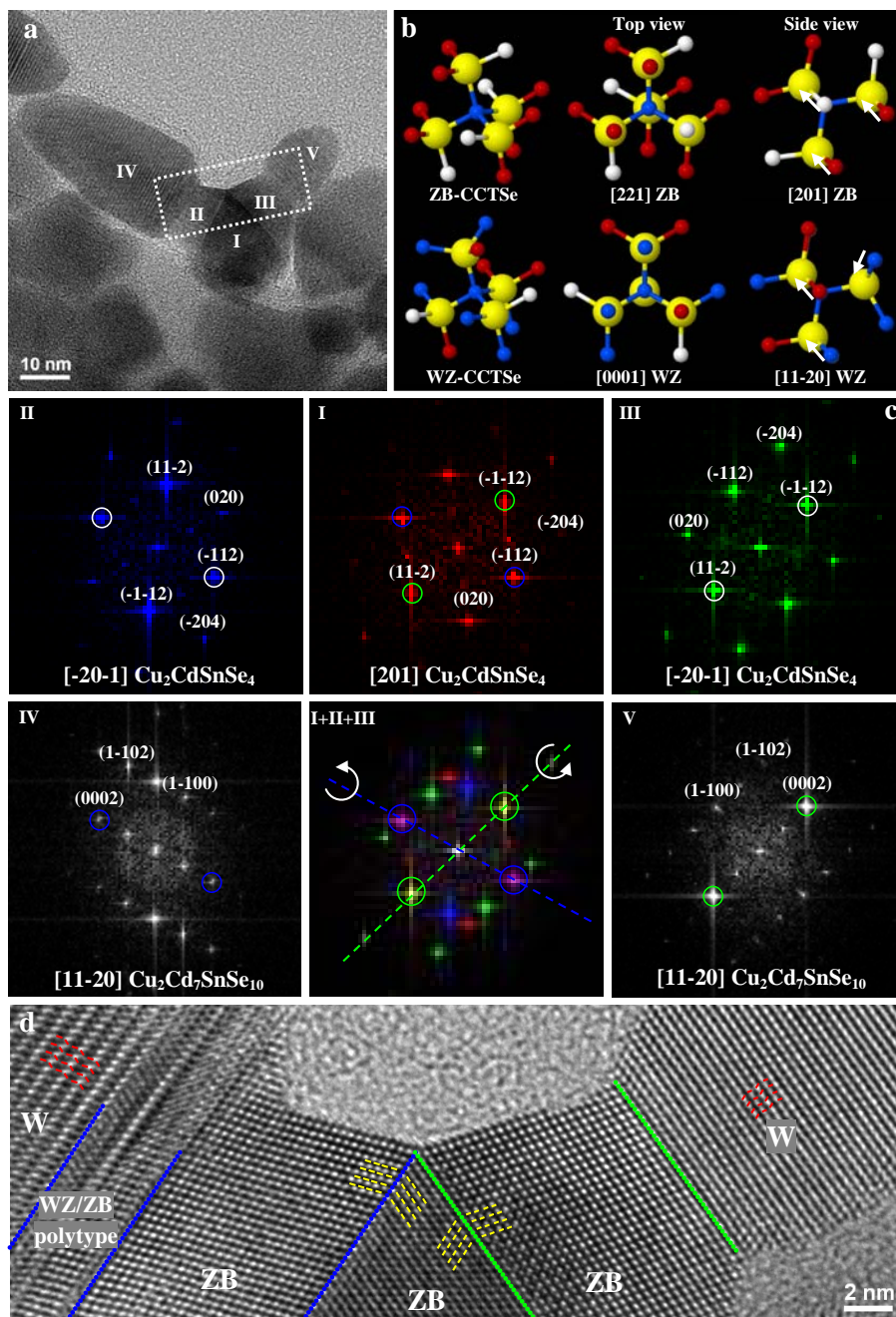


**Figure 3.44** HRTEM analysis on a bipod: (a) TEM micrograph showing the whole bipod and indicating the zones with Greek numbers: (I) the ZB initial tetrahedron, (II), (III) the secondary ZB tetrahedra, and (IV),(V) the WZ branches. (b) atomic models showing the structural difference between ZB and WZ, (c) FFTs corresponding to each zone from I to V, and (d) HRTEM micrograph showing the atomic planes and twinning in the bipod

As indicated on the HRTEM image of Figure 3.44(a) and 3.44(d), a twin defect occurs at the border of the initial tetrahedral seed and the tetrahedral extensions, where both have ZB-like structure. In the corresponding power spectra (fast Fourier transform (FFT) of the image) in Figure 3.44(c) one can see how the structure is mirrored along (-112) and (11-2) planes in the left and the right extensions, respectively. Dot lines show the twin boundaries, and dash lines correspond to the (11-2) and (-112) planes. These lines also show the dumbbell units in each atomic plane, which find a different arrangement when it arrives to the WZ structure of the branches. The zigzag form of the red lines corresponds to dumbbell orientation in WZ flipping from one atomic layer to the other. This can be seen in the side view of the atomic models in Figure 3.44(b) where the dumbbell orientation is indicated by white arrows in each structure. In Figure 3.44(a) different regions are indicated by Roman numerals to which the power spectra of Figure 3.44(c) correspond. Region I is the initial tetrahedral seed with ZB-like structure. Region II and III are two of the secondary tetrahedra which form the pentatetrahedral NCs. They also have ZB-like structure. Region IV and V are the branches with WZ structure as observed in the corresponding power spectra. The lower-center power spectrum in Figure 3.44(c) is indeed taken from Regions I, II, and III together showing the reflections of the different zones in different colors. This power spectrum reveals how the reflections are mirrored along the dash line. The blue and green dash lines indicate the direction of twinning (perpendicular to the twin planes) in the left and right tetrahedra, respectively. Afterwards, multiplicity of twin boundaries gives rise to occurrence of WZ branches. At the beginning of the left branch a kind of polytype between ZB and WZ takes place as the number of twins is not yet sufficient to reach WZ structure.

Details of the chemical composition analysis can be found in the supplementary information. Figure 3.45 shows an annular dark-field (ADF)-STEM image with EELS compositional maps. Notably, the chemical composition of the branch is not the same as the one of the seed. The seed has the stoichiometry of  $\text{Cu}_2\text{CdSnSe}_4$  structure, but the content of Cd in the branch is considerably higher. This chemical composition matches perfectly with the CCTSe hexagonal structure that exists in the literature:  $\text{Cu}_2\text{Cd}_7\text{SnSe}_{10}$ <sup>89</sup>. The EELS compositional maps in Figure 3.45 reveal that Cd content (blue color) in the branch is much higher than in the seed, whereas the seed contains more Cu (red color). These results of EELS analysis are in agreement with the ones of HRTEM.

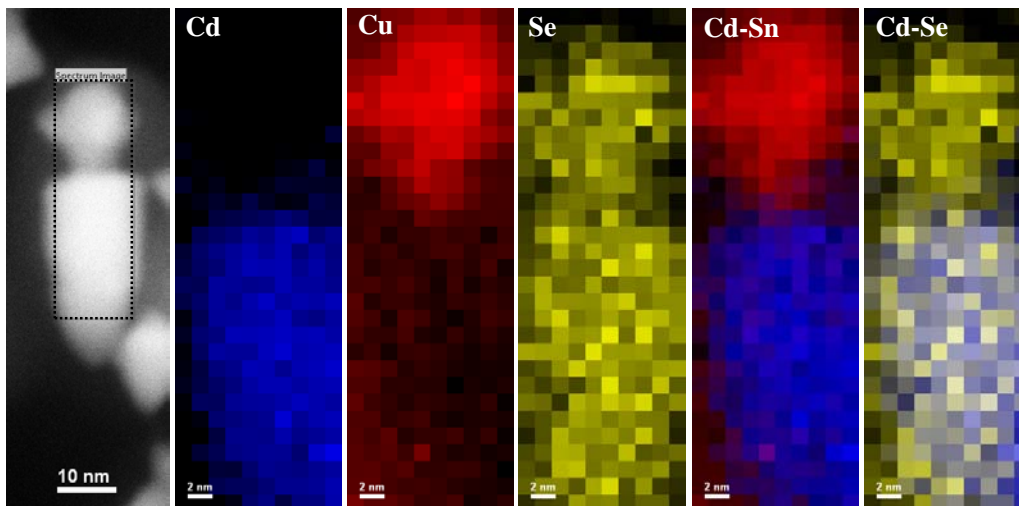


**Figure 3.45** EELS elemental map of the indicated rectangle on a CCTSe monopod

The cell parameters of this structure are slightly different from the predicted WZ. Following the common rules of WZ/ZB polytypism  $a_{WZ} = (0.70 \pm 0.03) \times a_{ZB}$  and  $c_{WZ} = (0.87 \pm 0.03) \times a_{ZB}$  we expected to have a hexagonal structure with  $a = b \sim 4.0 \text{ \AA}$  and  $c \sim 6.6 \text{ \AA}$  roughly, however, the experimentally obtained structure, matching the one of ref.<sup>89</sup>, is slightly bigger:  $a = b = 4.302 \text{ \AA}$  and  $c = 7.026 \text{ \AA}$ . This expansion in the cell parameter can be attributed to the higher concentration of Cd which is a heavier element than Cu.

As mentioned, it is evidenced that the faceting of the seed and the growth direction of branches in the tetrapods are cation-polar. Instead, the polarity of the surface facets changes from tetrahedron to pentatetrahedron. The external facets of the tetrahedra are cation-polar, while those of the pentatetrahedra are anion-polar. Lateral surfaces of the branches are non-polar, nonetheless, the start of branching comes from a plane which has the same polarity as initial tetrahedra and inverse polarity respect to the external facets of the pentatetrahedra.

Apparently the polarity of the surface of the pentatetrahedron is contrary to the one of tetrahedron. Taking into consideration that polarity inversion is not energetically favorable,<sup>12,44,51</sup> only an anion-polar surface tetrahedron can grow on a cation-polar surface seed in order to form the pentatetrahedral morphology. It is evidenced that polarity is maintained in the next steps. The secondary tetrahedra start to grow on the cation-polar facets of the initial seed after a twin

occurs. In the growth direction cation-polarity is kept, however, due to the twin boundary, lateral facets change from cation-polar to anion-polar ones, and this can be an adequate explanation for growth confinement with these new facets. Cation-polar facets are  $\{112\}$ ,  $\{-1-12\}$ ,  $\{1-1-2\}$  and  $\{-112\}$ , while anion-polar facets are  $\{1-12\}$ ,  $\{-112\}$ ,  $\{11-2\}$  and  $\{-1-1-2\}$ . For example, a secondary tetrahedron accommodates on  $\{112\}$  facet of the initial seed with  $\{-1-1-2\}$  facet, and the other three anion-polar facets are free. These facets are confined to their joining point which forms the peak of the tetrahedron. Therefore, the NCs have no possibility to grow more if they only follow this mechanism. However, branching mechanism plays the key role in order to allow the NCs grow more. Here, nevertheless, by assistance of twinning mechanism the structure changes from tetrahedral (ZB-like) to WZ. Prismatic WZ branches comprise six non-polar lateral facets and a cation-polar growth direction where theoretically has no limit for growing. It seems that non-polar surfaces have the freedom to grow further, but not as fast as the cation-polar one. Therefore, while the branches grow longer, they also thicken laterally.

In Figure 3.46 polarity is determined of the HAADF-STEM micrograph in different parts of a monopod from  $[201]_{\text{ZB}}/[11-20]_{\text{WZ}}$  zone axis ( $[201]_{\text{ZB}}$  in our ordered tetragonal structure is the same as  $[101]$  in cubic ZB) are magnified and shown at right: twinned interface between the initial and the secondary tetrahedra in blue, secondary tetrahedron in green, start of the branch in red, and the tip of the branch in yellow. Figure 3.46(a) is a high-resolution STEM image, the bottom inset shows the whole monopod and the top inset shows the top part. The zones indicated by colored rectangles are magnified in Figure 3.46(b) in order to see the polarity clearly. The corresponding intensity profiles are revealed in Figure 3.46(c). It is observed that the first tetrahedral seed (in blue) is cation-polar with ZB-like structure. Afterwards, as can be seen in the same micrograph, a twin occurs and the secondary tetrahedron grows, but still the cation is on top, thus the polarity is kept (see Figure 3.46(b) in blue and green). Note that this part is the one that has anion-polar external facets. Later on, the branch starts to grow with WZ structure as a consequence of twinning mechanism. Although the structure changes from ZB-like to WZ, the branch is still cation-polar (Figure 3.46(b) in red) and it keeps the cation-polarity till the end (Figure 3.46(b) in yellow).

In addition, we should point out that the polarity determination in the seed is more difficult than in the branch. The intensity difference between the anion and the cation is less in the ZB-like seed, which is due to the stoichiometry of the

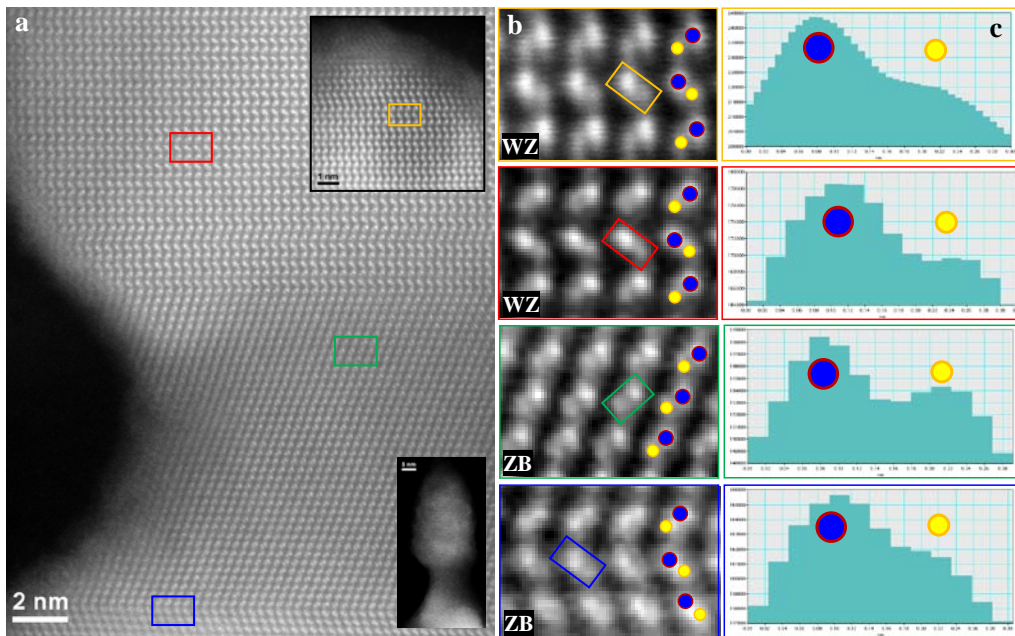


**Figure 3.46** Polarity: (a) HAADF-STEM from  $[201]_{\text{ZB}}/[11-20]_{\text{WZ}}$  zone axis, (b) magnified zones indicated on image (a) by colored rectangles, and (c) the intensity profile on one dumbbell units in (yellow) the top part of the branch, (red) the beginning of the branch, (green) the secondary tetrahedron, and (blue) the border of the initial and the secondary tetrahedra

structure. Intensity in STEM is proportional to atomic number square ( $Z^2$ ) of the elements in each point. In anion sites we only have Se ( $Z_{\text{Se}} = 34$ ), whereas in cation sites Cu ( $Z_{\text{Cu}} = 29$ ), Cd ( $Z_{\text{Cd}} = 48$ ), and Sn ( $Z_{\text{Sn}} = 50$ ) are positioned. Therefore, the average  $Z^2$  of the cations ( $Z_{\text{cat}}^2 = 1622$ , regarding the stoichiometry of  $\text{Cu}_2\text{CdSnSe}_4$ ) is relatively close to the one of anion ( $Z_{\text{Se}}^2 = 1156$ ). On the other hand, higher content of Cu ( $\text{Cu}_{2+x}\text{Cd}_{1-x}\text{SnSe}_4$  as discussed above), further reduces this difference. However, still the polarity is distinguishable from the intensity profiles. As a matter of fact, in the literature, even smaller differences in compounds like GaAs were utilized for polarity determination.<sup>44,51</sup> In the branch the Cd content is much higher, and consequently, as Cd is much heavier than Se, polarity determination is quite straightforward. With  $\text{Cu}_2\text{Cd}_7\text{SnSe}_{10}$  stoichiometry,  $Z_{\text{cat}}^2 = 2031$  which is almost twice of the one of the anion.

Another important difference between the structure of the seed and the branch is the ordering of the cations. It is observed that in the seed the cations, Cu, Cd and Sn, keep the stannite ordering while in the branches they are randomly distributed in the cation sites. The HAADF (Z-contrast) micrograph of Figure 3.47(a) reveals the ordering of the cations in the seed. Basically,  $[201]$  zone axis which is the best for visualization of the dumbbell units does not allow us to see the cation ordering, because in each cation column all Cu, Cd and Sn atoms overlap. To facilitate the comprehension, 3D atomic model of this structure is shown from different angles in Figure 3.47(f) and, as a contrast, we

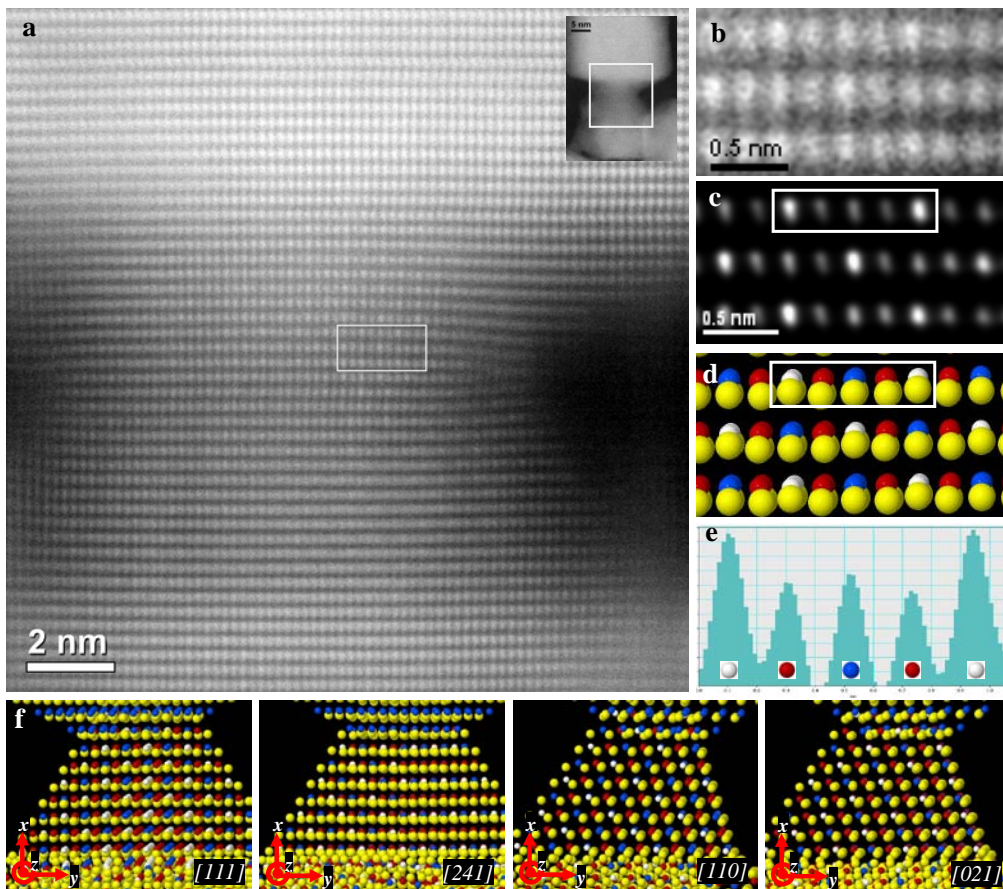


**Figure 3.47** (a) Atomic-resolution HAADF-STEM image from  $[111]_{\text{ZB}}$  zone axis of CCTSe tetragonal (ZB), (b) a magnified part of the image (a), and (c) filtered in order to show lucidly the ordering effect which is correlated with (d) the 3D atomic model. (e) the intensity profile taken from image (c). (f) 3D atomic models of a secondary ZB tetrahedron from four different zone axes showing why the ordering effect can only be seen from  $[111]_{\text{ZB}}$  zone axis

define the viewing coordination as x: horizontal, y: vertical, and z: viewing axis coming out from the screen.

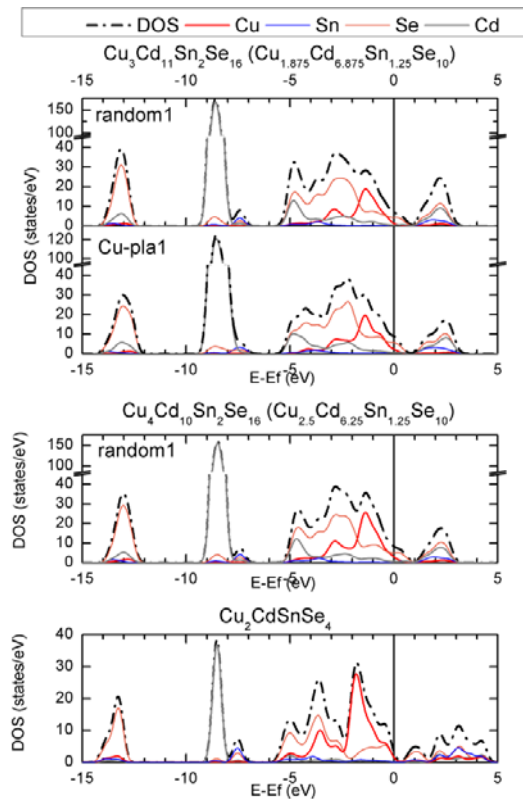
In fact in the ZB-like structure, three zone axes are proper for dumbbell visualization: [201], [021], and [110]. From [201] and [021] axes, each atomic column related to cation sites in HRTEM/STEM micrographs (in z direction) contains all Cu, Cd and Sn atoms. From [110], nevertheless, Cu columns get separated from the other two elements. Hence, ordering effect should be partially visible. However, Cd and Sn columns are still superposed along the z direction. In contrast, [111] is the only zone axis that allows observing the stannite ordering as none of these elements are superposed with the others. It can be seen in Figure 3.47(f) that from this zone axis, in x direction, vertical Cu columns and Cd-Sn columns alternate and further, Cd columns and Sn columns alternate in y direction. Note that from [241] and [421] zone axes which are the same as [111], ordering effect cannot be seen either. Therefore [111] zone axis is the only possibility for visualization of cation ordering.

Figure 3.47(a) is the HAADF-STEM image of the narrowest part of the seed (indicated in the inset) of a monopod where the structure is still ZB-like. For better visualization one part is magnified (Figure 3.47(b)) and frequency-filtered (Figure 3.47(c)). In the intensity profile in Figure 3.47(e), taken from the filtered image (Figure 5(c)), one can determine the position of cations with Sn-Cu-Cd-Cu-Sn stannite ordering which is in good agreement with the atomic model (Figure 3.47(d)). However, the intensity of Cd columns is closer to the one of Cu columns than Sn columns, i.e. less than what is expected in stannite structure. This is attributed to Cu-doping in the seed, as it was also confirmed by EELS maps. In the EELS maps of Figure 3.45 we observed that the content of Cd in the seed is low. So the stoichiometry is  $\text{Cu}_{2+x}\text{Cd}_{1-x}\text{SnSe}_4$ .

We have already proven by atomic resolution HAADF-STEM that the ZB-like show consistence in ordering, whereas, the WZ branches consist of disordered compound with random distribution of Cu, Cd, and Sn in cation sites, no stannite or kesterite cation-ordering is followed in this structure; and additionally Cd content is by far higher than in the pentatetrahedral seeds. The  $[\text{Cu}_2\text{Se}_4]$  and  $[\text{CdSnSe}_4]$  tetrahedral slabs that the ZB-like stannite CCTSe structure is comprised, are considered as electrically conducting and electrically insulating units, respectively.<sup>57</sup> It was experimentally proved the influence of distortion (as a result of Cu-doping) caused significant changes in electrical and thermal resistance of the compound, and thus its thermoelectric figure of merit.<sup>29</sup> The experimental results were in good agreement with *ab-initio* simulations of

the electronic band structure. Here we have also calculated the valence band maximum (VBM) and conduction band minimum (CBM) of both WZ and ZB distorted structures in order to compare the electronic band structures of these compounds with that of the ZB-like stannite CCTSe. It is worth to point out that in the case of random distribution of cations, keeping the stoichiometry, various 2x2x2 cells were created in order to assure that the specific local distributions do not affect the final results. See the density of state (DOS) graphs in Figure 3.48.

These simulations revealed that in the case of the WZ CCTSe, Fermi energy lies within the conduction band and the band gap shrinks to zero, thus, this compound has a quasi-metallic character (see Figure 3.48). Accordingly, we have branched NCs with a narrow-band-gap seed and metallic pods, which makes them quite promising for novel applications. These metallic branches can be used as perfect epitaxial Schottky contacts while the seed with the semiconducting nature can be used for several applications such as thermoelectrics, photovoltaics and sensing. On the other hand, such morphology-modulated poly-pods with metallic branches may have enhanced



**Figure 3.48** Density of state (DOS) in three structures

plasmonic applications, as copper vacancies in such materials, give rise to composition-dependent localized surface plasmon resonance (LSPR).<sup>82,105-108</sup>

In summary, we report on control of polytypic branching in complex quaternary chalcogenide (CCTSe) NCs, which their chemical and crystallographic structure changes from the seed to the branches and leads to dramatic changes in the physical properties. The initial seeds with ZB-like stannite structure have pentatetrahedral morphology, and branch out giving rise to formation of polytypic polypods with WZ legs while keeping the cation polarity till the end. Simulation of the electronic band structures shows that as a result of polytypism, the chemical composition change, and lack of cation ordering in the pods, the energy band gap shrinks, the Fermi energy goes inside the conduction band and the branches change from semiconductor to metal. Such an interesting combination forms a 100% epitaxial interface between the metallic pods and the semiconducting seeds which can be used for novel applications such as plasmonic devices (regarding the surface properties) and Schottky barriers (due to the vicinity of the metallic pods with the semiconducting seeds). Performance of the accurate experiments for polarity and ordering determination was possible only by dint of the novel microscopy techniques, i.e. aberration-corrected STEM imaging and spectroscopy. This work indeed proves the potential of growth nanoengineering by controlling the branching, polytypism, polarity and cation ordering, and how it may dramatically influence on the final physical properties of nanomaterials.<sup>109</sup>

### 3.3.2.4 $\text{Cu}_2\text{HgGeSe}_4$ nanocrystals

In the previous sections we proved that the crystal structure, size, and morphology of the NCs have considerable influence on their physical properties. An appropriate example of such effects is the case of  $\text{Cu}_2\text{HgGeSe}_4$  (CHGSe) NCs which were grown in two different forms: (i) single-crystal sphere-like NCs, (ii) defected structure, or polycrystalline pentatetrahedral-shaped NCs.

As well as the previously mentioned quaternary copper-selenide-based compound, CHGSe has a tetragonal structure in  $I-42m$  space group (no. 121). As shown in Figure 3.49 its cell constants are:  $a = b = 5.746 \text{ \AA}$  and  $c = 11.08 \text{ \AA}$ ; the cell volume is  $0.318 \text{ nm}^3$  with totally 16 atoms in the cell, Se atoms distributed in anion sites, Cu, Hg, and Ge atoms in cation sites. This compound has a different crystal structure in high temperatures. It changes from tetragonal to orthorhombic symmetry in  $Pmn2_1$  space group (no. 31).<sup>110</sup>

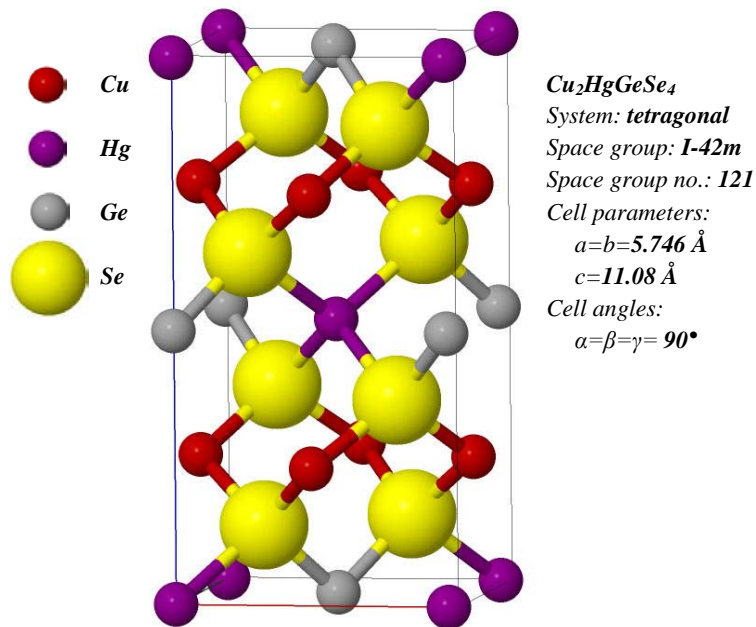


**Figure 3.49**  $Cu_2HgGeSe_4$  (CHGSe) unit cell, tetragonal symmetry in I-42m (No. 121) space group with  $a=b=5.746 \text{ \AA}$  and  $c=11.08 \text{ \AA}$

HRTEM analysis of Figure 3.50 reveals the tetragonal symmetry of the structure. In Figure 3.50(a) indicated particle is oriented in  $[221]$  zone axis which can exhibit the cation ordering of the compound. In the magnified squared-zone one can see that from each two consecutive  $(-110)$  planes, one is brighter as indicated by the red dot lines, and between each two bright planes, there is one atomic plane which is relatively darker (indicated by the blue dot line). This periodicity which gives rise to appearance of  $(-110)$  reflection in the corresponding power spectrum, shows that Cu, Hg, and Se atoms are not randomly distributed in the cation sites. In the same figure, the atomic model of the structure seen from  $[221]$  zone axis is shown at right.

Moreover, some NCs with few twin defects were observed. One of such NCs with two twin defects is analyzed in Figure 3.50(b). In the colored IFFT-filtered image at right the mirrored structures are shown in different colors. In the power spectrum below also the reflections are indicated by corresponding colors.

In the second sample, from two aspects, the NCs are different: (i) crystal structure, and (ii) morphology. Figure 3.51 shows some NCs with complex

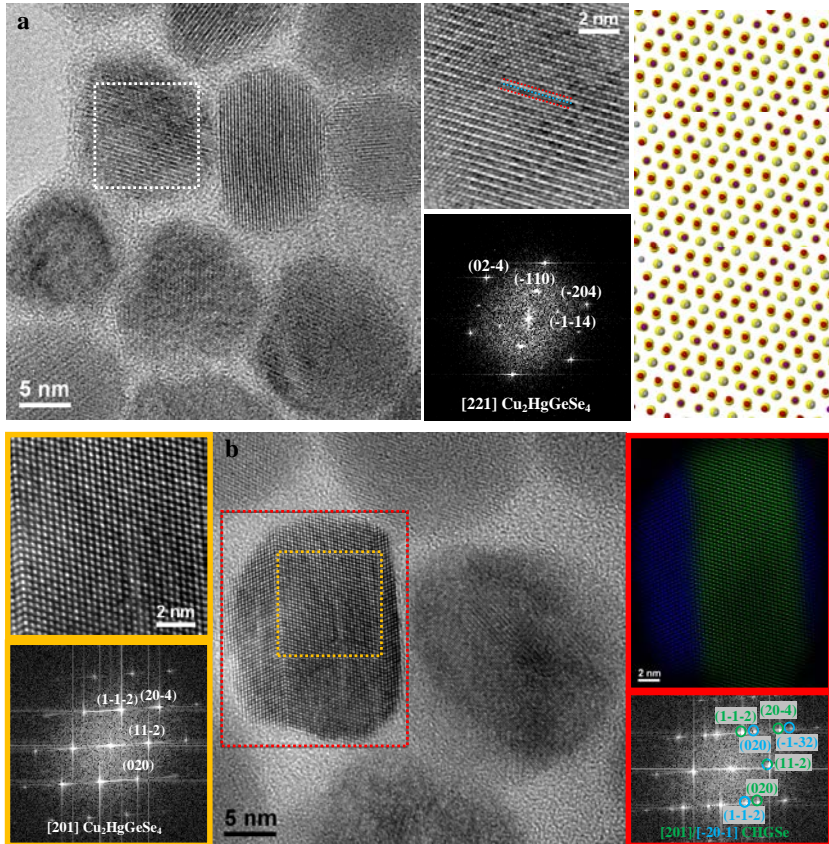


**Figure 3.50** HRTEM analysis of  $\text{Cu}_2\text{HgGeSe}_4$  (CHGSe) sphere-like NCs (a) showing cation ordering, and (b) few twin defects within the NC body

nature: polycrystalline, polytype, abundance of twins, and quasi-pentatetrahedral morphology.

Regardless of twinning, the crystal structure is still the same. However, multiplicity of twin defects in some NCs creates a structure which can be considered as a polytype between tetragonal (similar to ZB) and hexagonal (similar to WZ) structures. Figure 3.52 shows one of such particles. The top part of the particle as shown in the green square is pure tetragonal with no visible defects. But the middle of the particle as shown in the red square is a mixture of this initial tetragonal structure (ZB-like which we mark them with ZB'), with some monolayers of hexagonal (WZ-like marked as WZ') and some transition polytypes between ZB' and WZ'. In the lower part of the figure, IFFT-filtered images are placed. From the green square it can be deduced that likewise the top part of the particle, tetragonal structure can be seen in the rest of the NC, whereas hexagonal part also can be found; meaning a big part of the particle

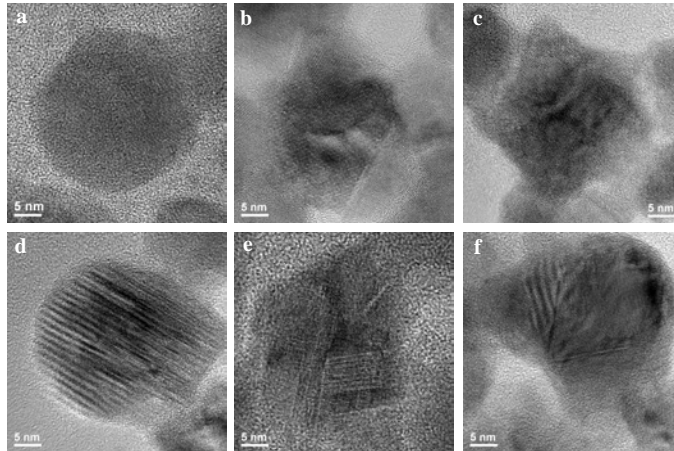


**Figure 3.51** CHGSe NCs with complex nature: (a), (b) polycrystalline, (c) polycrystalline with multiple extensions, (d) polytype, (e) twinned in two directions, (f) single-crystalline with quasi-pentatetrahedral morphology

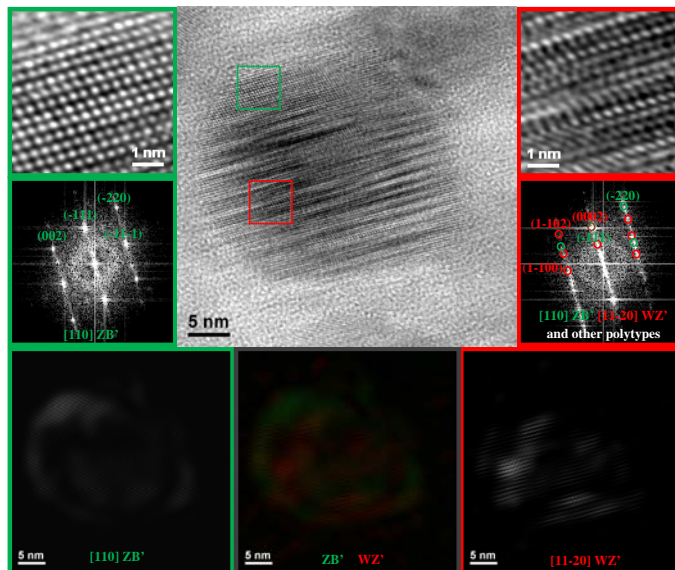


**Figure 3.52** A fully-defected CHGSe NC, tetragonal structure with the corresponding FFT in green squares (right) and defected polytype and the corresponding FFT in red squares (left), associated with IFFT-filtered images (below) which indicate the location of ZB' and WZ' structures in corresponding colors

consists of the polytype between ZB' and WZ'. It can be clearly seen in the gray square which is an overlap of the two other images in color.

Furthermore, twin defects in some NCs occur in two directions. If the part indicated with the green square in Figure 3.53 is considered as reference,

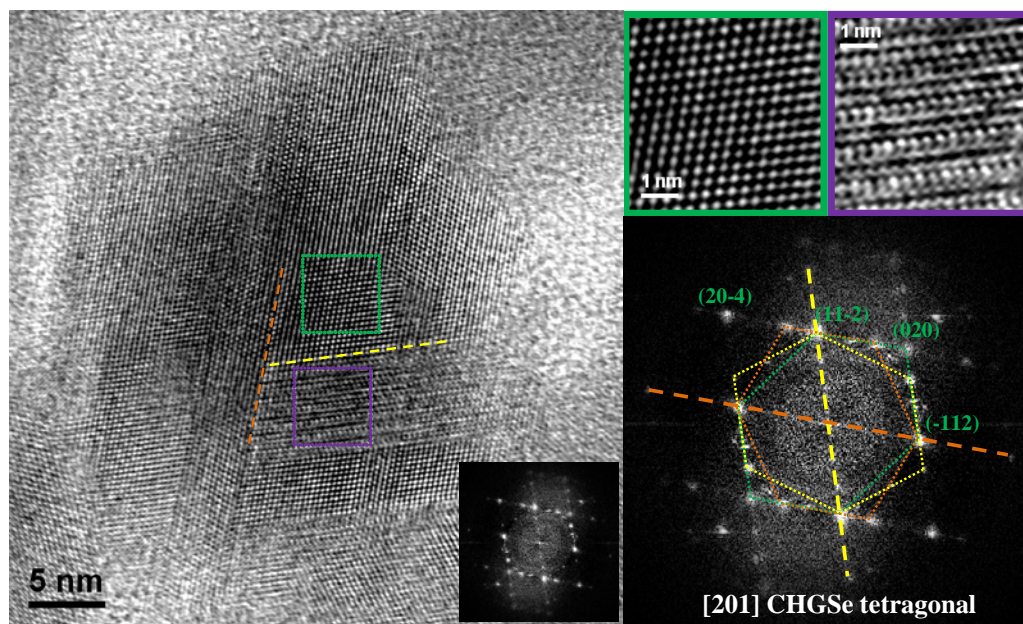


**Figure 3.53** HRTEM micrograph of a CHGSe NC with twinning along two different planes:  $(-111)$  and  $(1-11)$ . The purple square points up a zone that has many twins giving rise to the formation of a polytype between tetragonal and hexagonal structures

twinning in the following directions is seen: along  $(-112)$  planes indicated with an orange dash line, and along  $(11-2)$  planes indicated with a yellow dash line. The colors also correspond on the related power spectrum at right. The green dot lines which create a hexagon mark the reference diffraction pattern. The orange and the yellow hexagons refer to the zones after twinning along  $(-112)$  and  $(11-2)$  planes, respectively. The purple square points up a zone that has many twins giving rise to the formation of a polytype between tetragonal structures. If we consider that the periodicity of atomic layers in tetragonal is  $abcabcabc$ , and in hexagonal is  $abababab$ , this polytype, almost has the periodicity of  $abcbcababc$ .

Finally, by controlling the parameters of the colloidal synthesis, e.g. the reaction temperature, concentration of the metallic precursors, and selection of the stabilizing agent, NCs with quasi-pentatetrahedral morphology were obtained. Stoichiometric amount of  $\text{HgCl}_2$  leads to formation of NCs with this morphology, while higher concentrations of Hg give rise to formation of sphere-like NPs. The same as in CCTSe NCs, as shown in Figure 3.54, the initial tetrahedral seed is surrounded by four almost-tetrahedral extensions which are

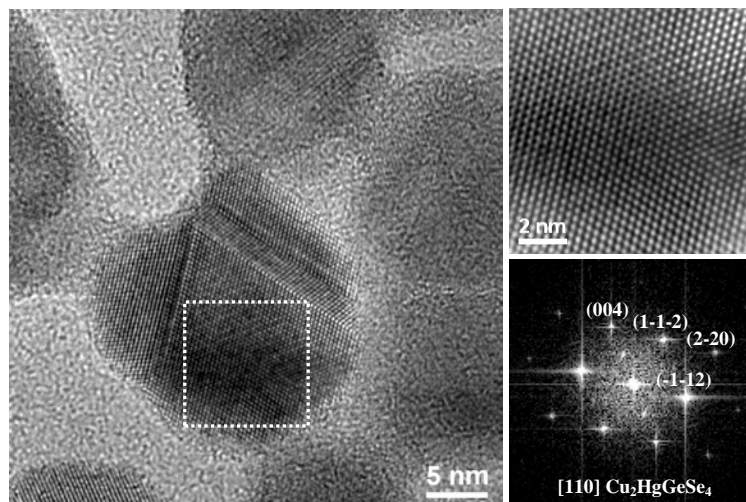


**Figure 3.54** HRTEM micrograph of a  $\text{Cu}_2\text{HgGeSe}_4$  (CHGSe) NC with pentatetrahedral shape

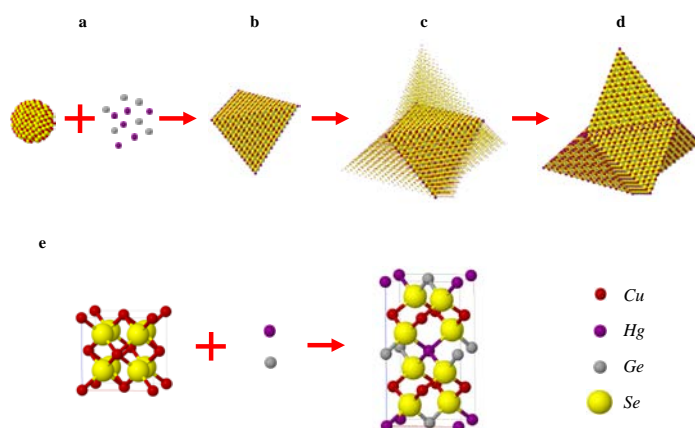


**Figure 3.55** 3D atomic models of the growth steps of NCs from (a)  $\text{Cu}_{2-x}\text{Se}$  spheres to (b) CHGSe tetrahedra, and then (c), (d) pentatetrahedra. In (c) the atoms of the legs are shown smaller in order to see how they grow on the initial tetrahedral seed. (e) How the unit cell changes from  $\text{Cu}_{2-x}\text{Se}$  to CHGSe

attached with a twin boundary along  $\{112\}$  plane family. In fact in this material, not all of the extensions grow. Moreover, they are not as sharply-faceted as CCTSe NCs.

In a first step of the synthesis, binary spherical crystals with the  $\text{Cu}_{2-x}\text{Se}$  composition are evidenced. Depending on the reaction conditions, such binary

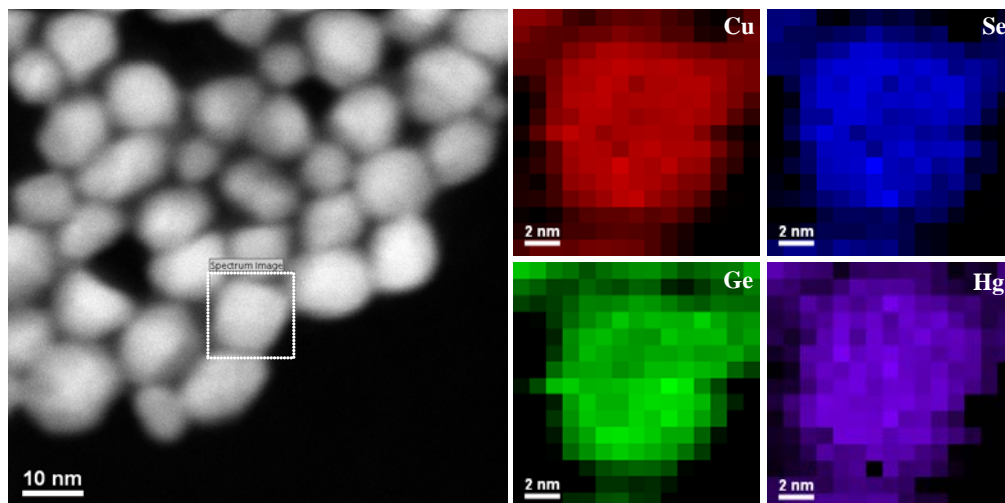


**Figure 3.56** EELS analyses on CHGSe quasi-pentatetrahedral NCs

nuclei permit the incorporation of the other elements at preferential reaction sites. In the cases in which such reactions occur at a moderate rate, isolation of tetrahedral particles is possible. However, with the use of longer reaction times or faster kinetics, the initial tetrahedral structure evolves towards the formation of pentatetrahedra.<sup>111</sup>

Figure 3.55 schematically shows how the NCs nucleate and form the pentatetrahedra. Basically, it is the same as the growth of CCTSe pentatetrahedra shown in Figure 3.36.

DF-STEM image of Figure 3.56, associated with EELS compositional maps, reveal the homogeneity of elemental distribution. Although Hg and Ge did not enter the initial spherical nuclei, they diffuse gradually to the structure and the NCs obtained in the end are stoichiometric.

### ***3.3.2.5 Section summary***

In summary, we report on control of many structural and chemical issues, such as doping, morphology, polytypism, polytypic branching, cation ordering, and polarity in different complex ternary/quaternary chalcogenide NCs. Playing around with these issues we are led to dramatic changes in the physical properties of the compound especially thermoelectricity which is the main purpose of these modulations. Simulation of the electronic band structures shows that as a result of polytypism, the chemical composition change, and lack of cation ordering in the pods, the energy band gap shrinks, the Fermi energy

goes inside the conduction band and the branches change from semiconductor to metal.

Performance of the accurate experiments for polarity and ordering determination was possible only by dint of the novel microscopy techniques, i.e. aberration-corrected STEM imaging and spectroscopy. This work indeed proves the potential of growth nanoengineering, and how it may dramatically influence on the final physical properties of nanomaterials.

The comparison between the single-phased materials (Section 3.3.1) and multi-phased ones (Section 3.3.2), one can find out that the properties of the compounds in the latter are dramatically improved. The highest ZT in single-phased compounds was 0.55 (the case of CZGSe NCs), whereas in the multi-phased ones, it increased up to 0.71 at lower temperatures. On the other hand, interesting characteristics of CCTSe polyiods were discussed, which proved how the electronic band structure can be engineered by control of the structural issues, i.e. branching, polytypism, cation ordering, and polytypism.

### 3.3.3 Core-shell structures

So far we studied how to modulate the structure of some compounds, but in each case it was only on bare NCs. Now we move one step further and try to improve the functionality by creating core-shell structures. Essentially, the aim of producing core-shell structures is to create nanocomposites in order to enhance the functional properties in any possible way.<sup>112</sup> For instance, Lee *et al.* studied magnetic material (FePt) in semiconductors (PbS and PbSe) and explored their optical, electrical, magnetic, and magnetotransport properties.<sup>113</sup> As another example, Murray and coworkers created binary superlattices by assembling PbTe@Ag<sub>2</sub>Te core-shell NCs. These nanocomposites showed strongly enhanced p-type electronic conductivity (around 100-fold increased), comparing to the ones of single-component PbTe or Ag<sub>2</sub>Te films.<sup>114</sup> It is proved that bottom-up assembly has a high potential to create the building blocks of nanoheterostructures, while their size, shape, position, and even crystal structure can be precisely controlled.<sup>115,116</sup>

Three core-shell systems were intended to be produced in which crystal structures of the cores and the shells are quite similar: FePt@PbTe, BiTe@PbTe, and PbTe@PbS. The first heterostructure did not show the expected behavior. The second one experimentally failed due to miscibility of the shell material with the one of the core. And the last one showed outstanding

functional properties in thermoelectric applications which in this material had never been achieved before.

### 3.3.3.1 $Fe_3Pt@PbTe$ nanoparticles

PbTe is an IV-VI compound semiconductor with the rock salt structure and a narrow band gap ( $E_g = 0.32$  eV). PbTe as an important thermoelectric material<sup>117,118</sup> exhibits high figure of merit, i.e. maximum ZT of about 1.1 at around 700K for p-type PbTe and 425K for n-type PbTe.<sup>119,120</sup> Moreover, it has good chemical stability, low vapor pressure, and high melting point (924 °C). The large exciton Bohr radius of PbTe ( $a_B = 152$  nm) makes it an ideal candidate for understanding its thermoelectric behavior under quantum confined conditions.<sup>121,122</sup> PbTe crystalline structure with cubic symmetry in  $Fm\bar{3}m$  space group (no. 225) is called ‘altaite’ and has cell parameter of  $a = 6.46$  Å.<sup>123,124</sup>

FePt is a magnetic material that has appropriate properties for microelectronic applications. FePt in the form of NP is chemically stable and it has large uniaxial magnetocrystalline anisotropy which determines how strongly the NP can hold its magnetic information.<sup>125,126</sup> According to Fe-Pt phase diagram in Figure 3.57 Fe can alloy with Pt in the form of  $Fe_3Pt$ , FePt, and  $FePt_3$ , depending on its mole fraction.<sup>127</sup> Here we realized that our FePt

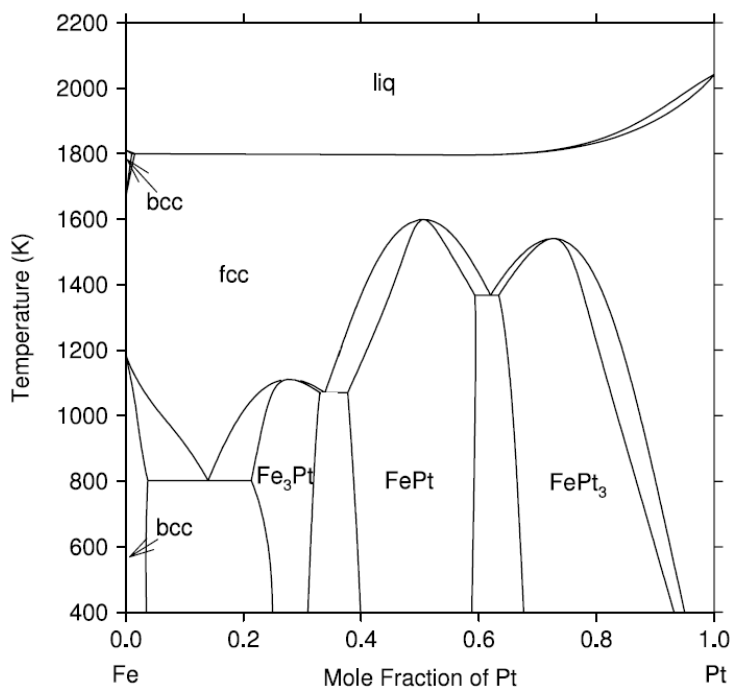


**Figure 3.57** Fe-Pt phase diagram<sup>127</sup>

structure is compatible with a cubic  $Im\bar{3}m$  structure, similar to that of the metal Iron, thus meaning that the Iron content should be high. In fact, in literature we have found  $Fe_xPt_{1-x}$  binary phases with the present structure (for  $x \geq 0.75$ ).<sup>128</sup>

Talpin and the coworkers<sup>113</sup> created  $FePt@PbS$  and  $FePt@PbSe$  structures. The  $PbS$  shells resulted in significant changes in the magnetic properties, which are correlated to the formation of  $Fe-S$  bonds in the surface of the  $FePt$  NPs. A thin interfacial layer of  $FeS$  forms in the interface of the magnetic core and semiconducting shell. Similar behavior was observed in the case of the second shell in  $FePt@PbSe$  structure.

Figure 3.58 consists of two TEM micrographs showing a general view of the  $Fe_3Pt@PbTe$  NPs; and Figure 3.59 reveals some TEM analyses associated with structural simulations.

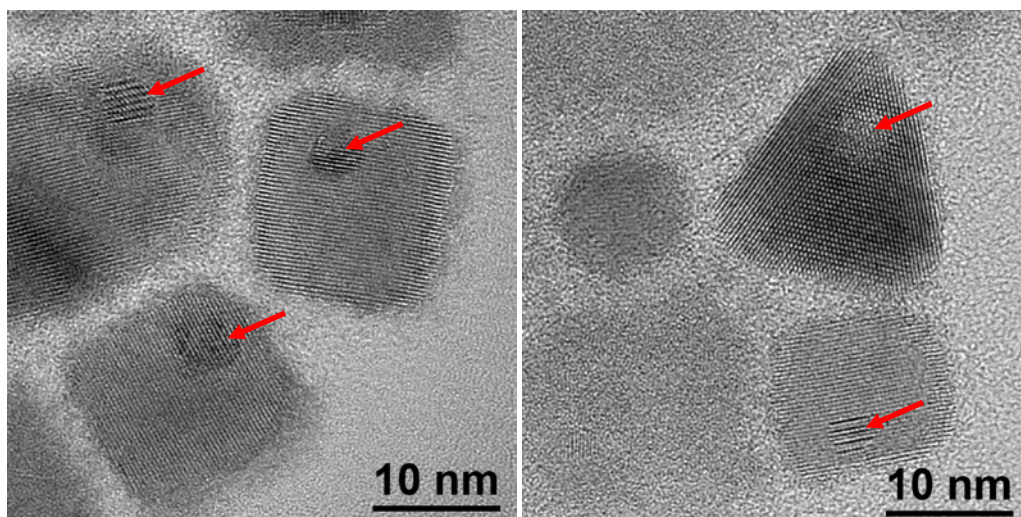


**Figure 3.58** TEM micrograph showing a general view of  $Fe_3Pt@PbTe$  NPs

The  $Fe-Pt$  crystal phase we have used for the simulation is  $Fe_3Pt$ . The analysis has been performed by obtaining the power spectrum of the HRTEM image, and then masking the frequencies corresponding to every phase (see the spots marked with red and green circles in the power spectrum for the  $FePt$  and  $PbTe$ , respectively). The next step was performing an inverse FFT (IFFT) on the masks in order to obtain the atomic plane distribution for every one of the phases. Finally a color RGB map has been obtained showing the perfect core@shell matching. All these analyses have been possible thanks to the differences on the cell parameter between  $PbTe$  and  $Fe_3Pt$  crystal structures. The result is shown in Figure 3.59 upper and center images. In addition we could

simulate the core-shell structure, by creating a model composed of a PbTe cube with 13.6 nm side facets, and an embedded Fe<sub>3</sub>Pt sphere (4 nm diameter). The 3D atomic model was used in the JEMS software package in order to obtain the HRTEM image simulation, obtained with the same microscope parameters as the ones of the experiment, e.g.:  $C_s = 0.5$ ;  $d_f = 43.4$  nm (equivalent to the experimental Scherzer defocus). An inset of the simulated image has been placed on the experimental HRTEM micrograph (upper left) in order to observe

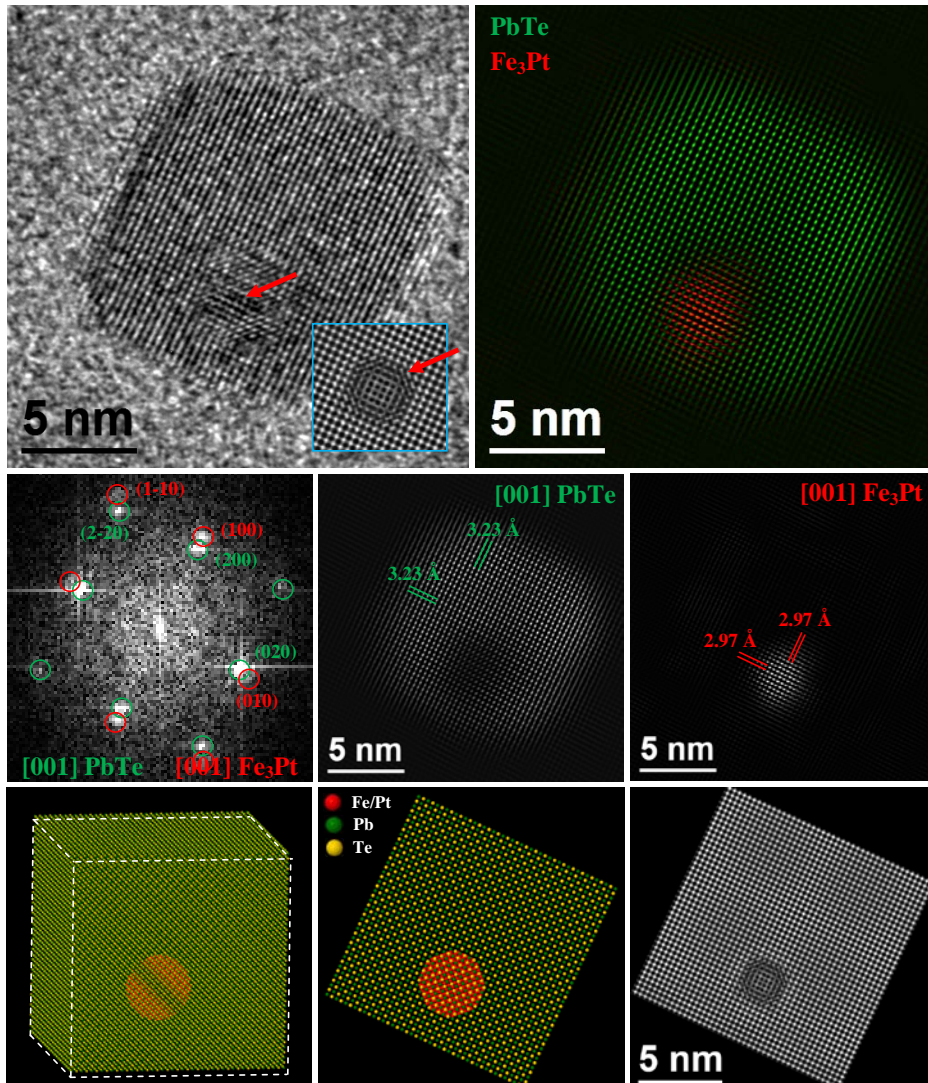


**Figure 3.59** Structural analysis of Fe<sub>3</sub>Pt@PbTe NPs, the case of epitaxial core-shell structure; HRTEM micrograph associated with IFFT-filtered images and the corresponding power spectrum (upper and middle), and simulated crystal structure (lower)

the perfect plane continuity and validate the model. The full 3D atomic supercell model as well as the complete simulated image can be observed on the bottom row of the figure.

However, not always the  $\text{Fe}_3\text{Pt}$  NPs are embedded epitaxially inside the PbTe shells. As an example, in the core-shell NP of Figure 3.60, as seen in the power spectrum, no epitaxial relationship between the  $\text{Fe}_3\text{Pt}$  core and the PbTe shell is observed. The only relation is a fiber-like orientation relationship being the (001) PbTe plane parallel to the (111)  $\text{Fe}_3\text{Pt}$ . As there was no control on epitaxial growth of the shell around the  $\text{Fe}_3\text{Pt}$  core, we did not continue the study further.

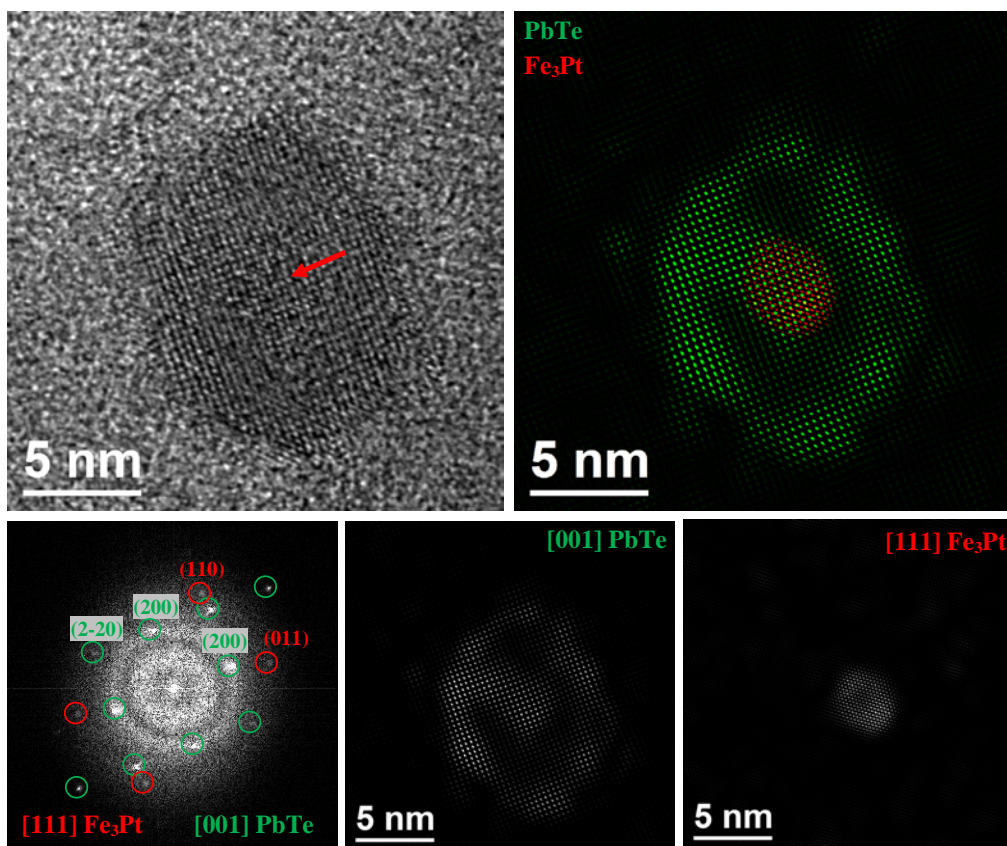


**Figure 3.60** Structural analysis of  $\text{Fe}_3\text{Pt}@$ PbTe NPs, the case of non-epitaxial core-shell structure; HRTEM micrograph associated with IFFT-filtered images and the corresponding power spectrum

### 3.3.3.2 BiTe@PbTe nanoparticles

Figure 3.61 shows all unit cells of the binary chalcogenide materials that have been used in this section. PbSe as a closely-related material is shown as well. Obviously, all of them are NaCl-type *fcc* in *Fm3m* space group (no. 225) and their cell parameters are quite close to each other. Comparing these cells, one can realize that the only difference between these four structures is the cell parameter, which in the case of PbTe and BiTe this difference is  $\sim 0.01$  Å. Therefore, it is impossible to distinguish these two structures by means of HRTEM analysis, as  $0.01$  Å lies within the error of the measurement. In this case, EELS analysis cannot be a proper solution due to closeness of energy edges of Pb and Bi and their placement in high energy ranges. Lead and bismuth have  $M_5$  delayed edge at 2484 eV and 2580 eV and  $M_4$  delayed edges at 2584 eV and 2688 eV, respectively. In such high energy ranges it is almost impossible to be sure about existence of Bi  $M_5$  edge, as it can be buried under the signal of Pb. EDX with high spatial resolution can be a proper solution, however, Pb and

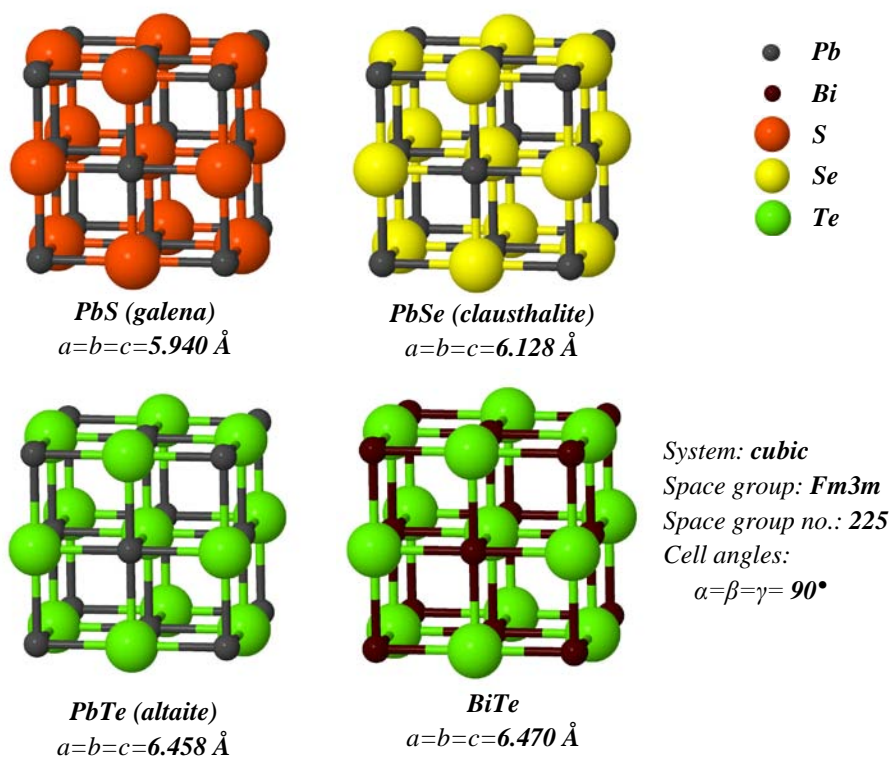


**Figure 3.61** Unit cells of PbS, PbSe, PbTe, and BiTe with fcc structure in *Fm3m* (no. 225) space group

Bi peaks in EDX are quite close as well. HRTEM analysis on one of these NPs is shown in Figure 3.62.

On the other hand, Bi-Te system crystallizes in two other structures, both with hexagonal symmetry, which are more commonly observed:  $\text{Bi}_2\text{Te}_3$  called ‘tellurobismuthite’,<sup>129,130</sup> and BiTe called ‘Tsumoite’.<sup>131,132</sup> As no hexagonal structure was detected in this sample, we assume that we have a solid solution of BiTe-PbTe system or Bi is doped in the PbTe NPs. Both cases can be found in the literature. According to previous works, solubility of BiTe and PbTe is high. Therefore, Bi can diffuse to the structure and create a Bi-Pb-Te solid solution. Lower concentrations of Bi can lead to NaCl-type *fcc* structure,<sup>133</sup> while higher percentages of Bi results in hexagonal structures similar to the ones of tellurobismuthite and Tsumoite.<sup>134,135</sup> Also, bismuth as a donor impurity in PbTe can create an n-type semiconductor and change electron concentration, and thus, thermoelectric figure of merit.<sup>136-138</sup>

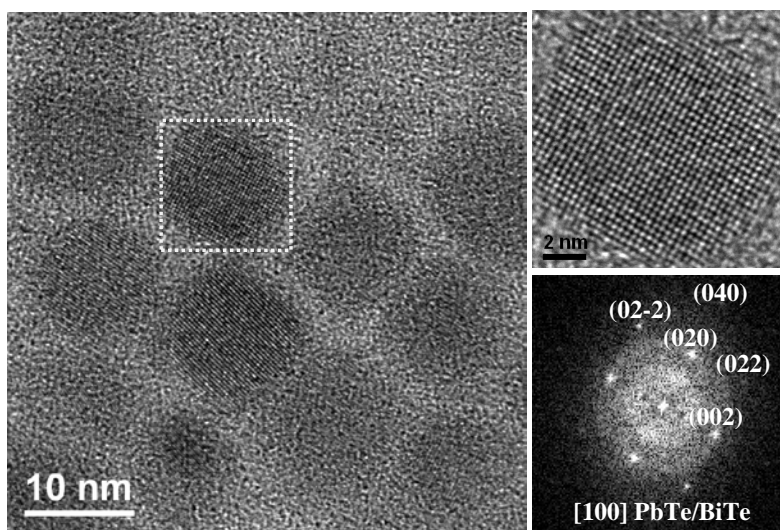


**Figure 3.62** HRTEM micrograph of PbTe/BiTe NPs

### 3.3.3.3 *PbTe@PbS nanoparticles*

The main goal in this section is to study PbTe@PbS core-shell NPs which were used for assembling proper nanocomposites as shown in the scheme of Figure 3.63. The first step of this approach is core-shell NP preparation (Figure 3.63(a)), then NP assembly as the second step (Figure 3.63(b)), and finally annealing the NPs to produce a dense nanocomposite (Figure 3.63(c)). Here,

unprecedented narrow size distribution of NPs is achieved. Size and shape of the PbTe core, and the same of PbS shell and also its crystallographic nature have been controlled by adjusting the synthesis parameters. Production process of PbTe-PbS core-shell NPs comprises two steps. In the first step, PbTe NPs are prepared by colloidal synthesis. These NPs can be designed to have cubic or spherical morphologies, by controlling the parameters of the experiment. In the second step, sulfur precursor is added to the solution without purification or exposure of PbTe NPs to the air. Then, by increasing the temperature gradually,

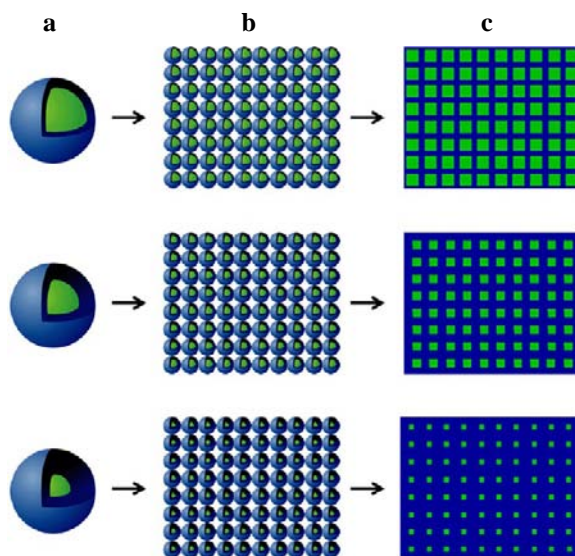


**Figure 3.63** Steps for the production of nanocomposites from the bottom-up assembly of core-shell nanoparticles showing how different core sizes and shell thicknesses affects the final result. (a) core-shell nanoparticle preparation; (b) nanoparticle assembly; and (c) annealing to produce a dense nanocomposite<sup>115</sup>

PbS shell is formed. Heating rate, reaction temperature, and sulfur source reactivity determine the mechanism of the PbS shell formation. Even the crystallinity of the shell can be controlled by reaction kinetics. Amorphous PbS shells were produced by boosting PbS nucleation at multiple PbTe surface sites by injecting the S precursor at relatively high temperatures, e.g. 80 °C.<sup>115</sup>

PbTe@PbS NPs are used to produce  $(\text{PbTe})_{1-x}(\text{PbS})_x$  nanocomposites where  $x$  is a determining parameter for the final physical properties. Different  $(\text{PbTe})_{1-x}(\text{PbS})_x$  compositions, meaning different  $x$ , were prepared to obtain the highest ZT.

Figure 3.64 reveals HRTEM micrographs obtained on  $(\text{PbTe})_{0.25} @ (\text{PbS})_{0.75}$  NPs with amorphous shell. PbTe cores are small, 9-12 nm, quasi-cubic-shaped with slightly rounded corners, and the amorphous shell is relatively thick with a round shape, forming final  $(\text{PbTe})_{0.25} @ (\text{PbS})_{0.75}$  rounded NPs. In this figure, the power spectrum reveals the crystal structure of the core of the NP in the blue square. The core has NaCl-type *fcc* structure (space group: *Fm3m*, no. 225) with

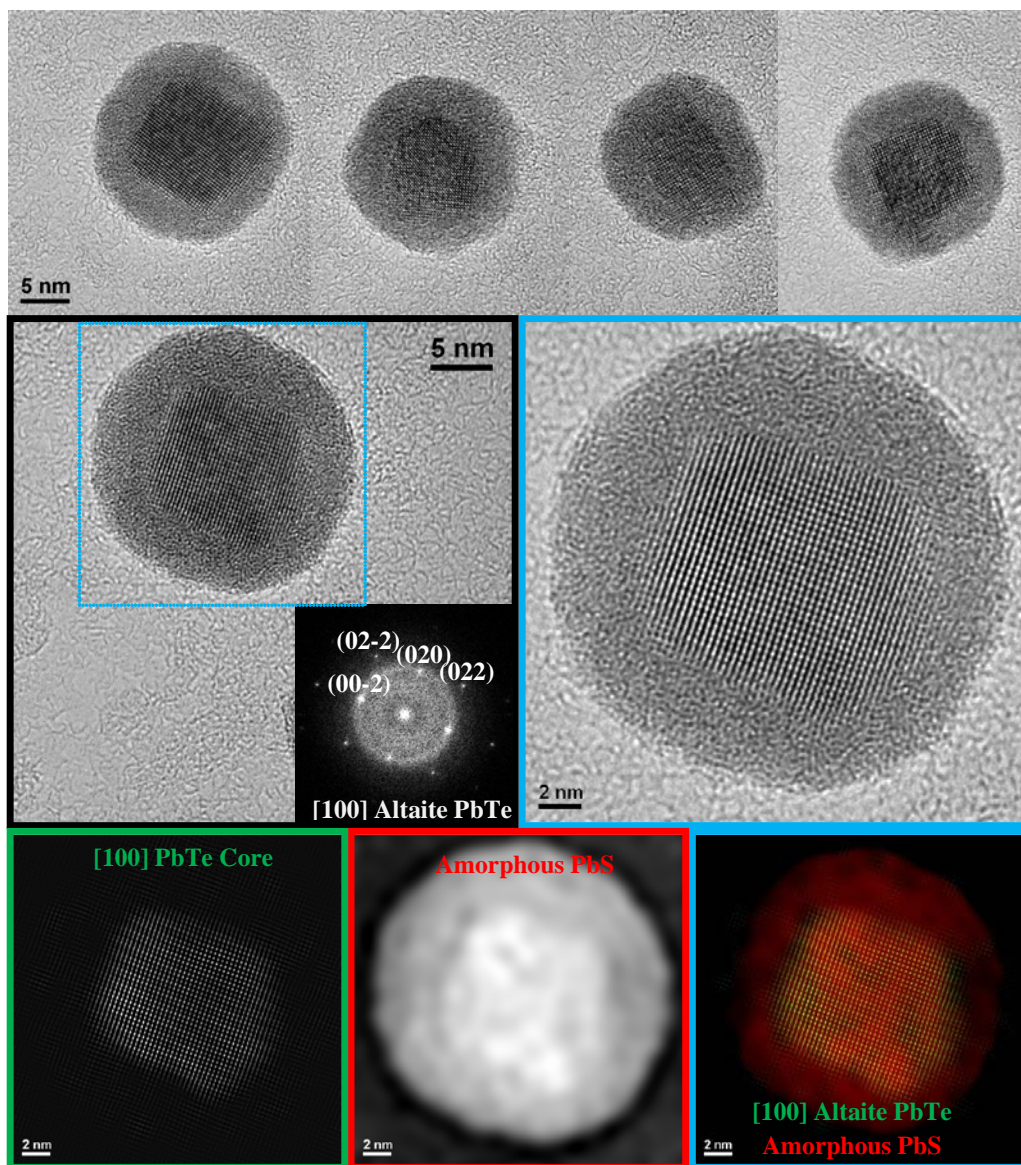


**Figure 3.64** HRTEM micrographs of  $(\text{PbTe})_{0.25} @ (\text{PbS})_{0.75}$  NPs with quasi-cubic-shaped PbTe cores, and PbS amorphous shell, associated with the corresponding FFT, and IFFT-filtered images (bottom)

cell parameter of  $a = 6.458 \text{ \AA}$  (altaite) as shown in Figure 3.61. By inverse FFT (IFFT) filtering of the HRTEM image, amorphous nature of the shell is explicitly shown. In the lower images of Figure 3.64, crystalline PbTe core is shown in the green square, amorphous PbS shell in the red square, and overlap of both colored structures, as they really are, in the blue square.

$(\text{PbTe})_{0.60} @ (\text{PbS})_{0.40}$  NPs can be seen in Figure 3.65. As expected, we used

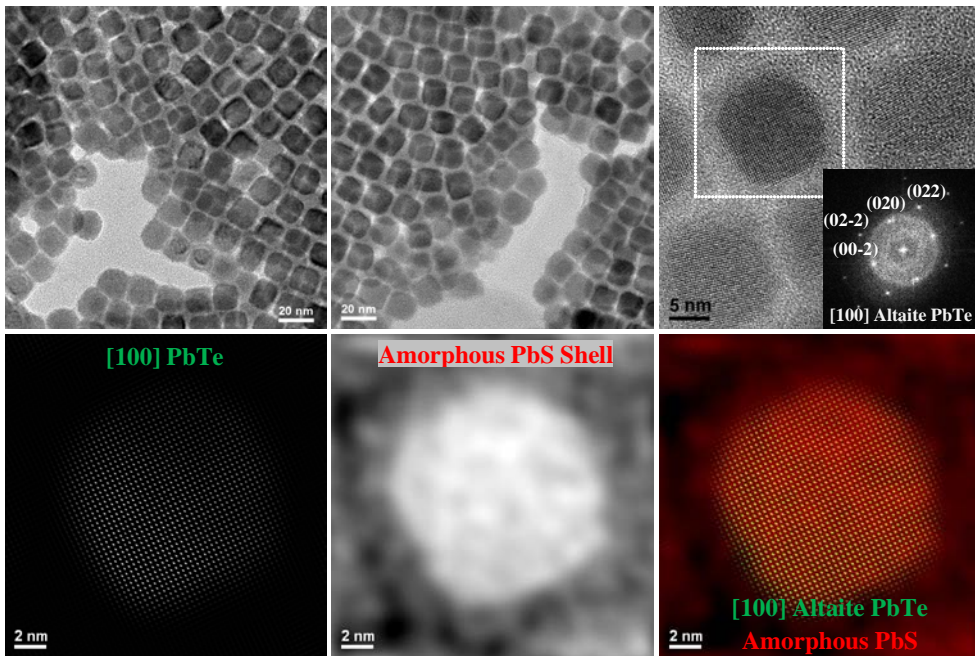


**Figure 3.65** HRTEM analyses of  $(\text{PbTe})_{0.60} @ (\text{PbS})_{0.40}$  NPs with quasi-cubic-shaped PbTe core, and PbS amorphous shell (top), associated with the corresponding FFT, and IFFT-filtered images (bottom)

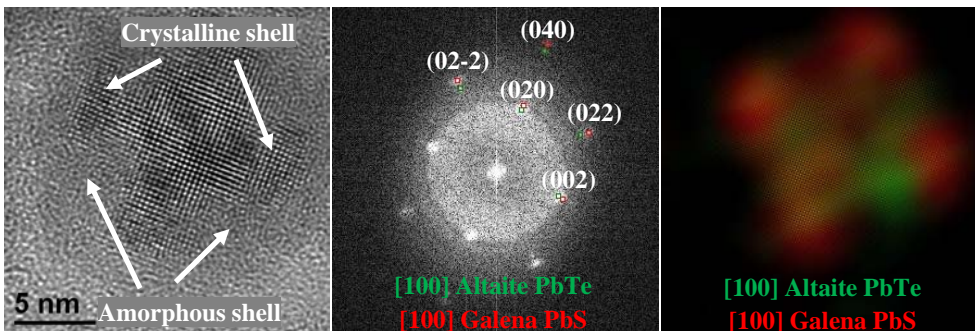


**Figure 3.66** HRTEM micrograph of  $\text{PbTe} @ \text{PbS}$  NPs with partially crystalline PbS shell (left), associated with the corresponding FFT (middle), and IFFT-filtered images (right)

bigger cubic PbTe cores with thinner PbS shells. Initial PbTe NPs had the size of 11-15 nm, and the final  $(\text{PbTe})_{0.60} @ (\text{PbS})_{0.40}$  NPs had the size of 14-18 nm. The same IFFT frequency filter was applied in this figure in order to clarify the presence, crystallinity and the exact location of the each compound. Low-magnification TEM images in this figure (upper images) show the homogeneity of the size and shape of the NPs.

In the next attempt, as shown in Figure 3.66, partially crystalline PbS shells were obtained. Amorphous and crystalline parts of the shell are indicated by arrows (left). The double points in the corresponding FFT (middle) mean that there are two different crystal structures with quite close cell parameters, which frequency filtering (IFFT) facilitates distinguishing them (right).

Finally, fully-crystalline PbS shells were obtained by playing with the parameters that affect the kinetics of the experiment. As can be seen in Figure 3.67, PbS crystallizes in an *fcc* NaCl-type system (Fm3m space group, no. 225) called ‘galena’ in the literature.<sup>139-141</sup> The unit cell is shown in Figure 3.61. The cell constant is 5.940 Å which is 0.52 Å smaller than the one of PbTe altaite. Therefore, a mismatch of 8.0% between the core and the shell is expected.

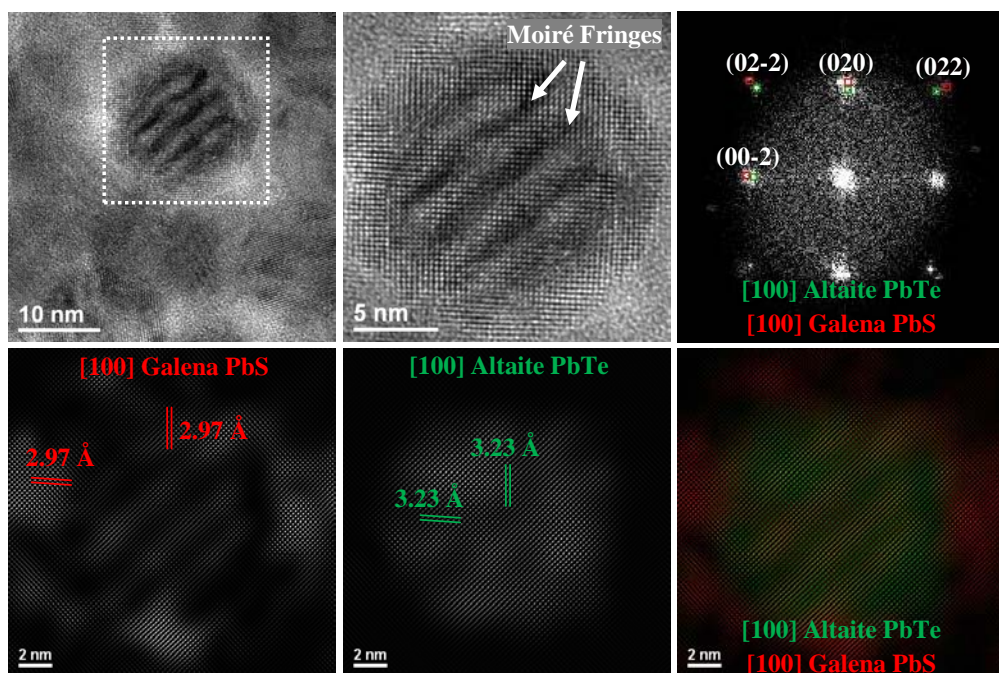


**Figure 3.67** HRTEM micrograph of PbTe@PbS NPs with crystalline galena PbS shell (top), associated with the corresponding FFT (top-right), and IFFT-filtered images (bottom)

Power spectrum of Figure 3.67 confirms the epitaxial relationship between the core and the shell. The indicated reflections related to  $\{002\}$  and  $\{022\}$  plane families are doubled. In other words, there is epitaxy; however, the slight difference in the cell parameters still exists. Thanks to this slight difference, we were able to frequency-filter the image by IFFT and show the PbTe core in green and PbS shell in red. See the lower row of Figure 3.67.

As we pointed out, these two structures, theoretically, have 8.0% of mismatch, meaning approximately 13 (020) planes of PbS covers 12 of PbTe, thus, one misfit dislocation appears with periodicity of 13 (020) atomic planes of PbS. It is explicitly visualized in the 3D atomic models of Figure 3.68. In this

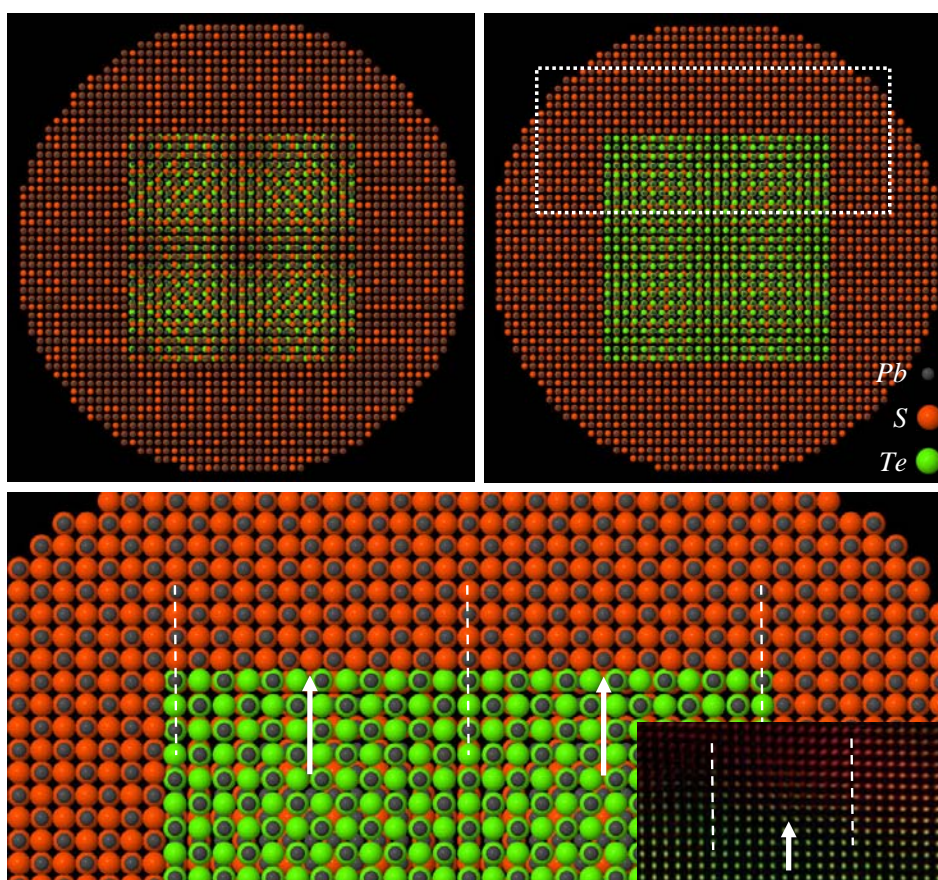


**Figure 3.68** 3D atomic models of a PbTe@PbS core-shell NP with cubic-shaped altaite PbTe core and sphere-shaped galena PbS shell (top-left), cross-sectioned (top-right), and magnified interface between the core and the shell showing the epitaxial relationship indicating the misfit dislocations and the coinciding atomic planes with IFFT-filtered of an HRTEM image as inset (bottom)

figure, a PbTe@PbS core-shell NP with cubic PbTe core and crystalline spherical PbS shell is simulated (top-right). Then it is cross-sectioned in order to see the interface between the core and the shell (top-right), and the interface is magnified in the (bottom). In this last image, misfit dislocations of PbS are indicated by white arrows. The (020) coincidence planes of PbS and PbTe are indicated by dash lines. The distance between two coinciding planes of PbTe and PbS is 12 and 13 atomic planes, respectively. In the colored IFFT-filtered image of Figure 3.69 (bottom-right) same result is observed which confirms that the experiment matches the theoretical study.

By means of geometric phase analysis (GPA) key we performed strain analysis on the last PbTe@PbS NP with crystalline PbS Shell. In the strain maps of the Figure 3.70 (lower raw) one can see when the first phase ((002) planes) is considered (002) misfit dislocations of PbS are seen as strain concentration points, while in the second phase ((020) phase) the same happens with (020) misfit dislocations. For this analysis ‘Cosine Mask’ with the size of 0.02 /pixel and spatial resolution of 1.95 nm was chosen. As a matter of fact, GPA shows that there is no strain within the PbTe core of the NP, likewise a very small

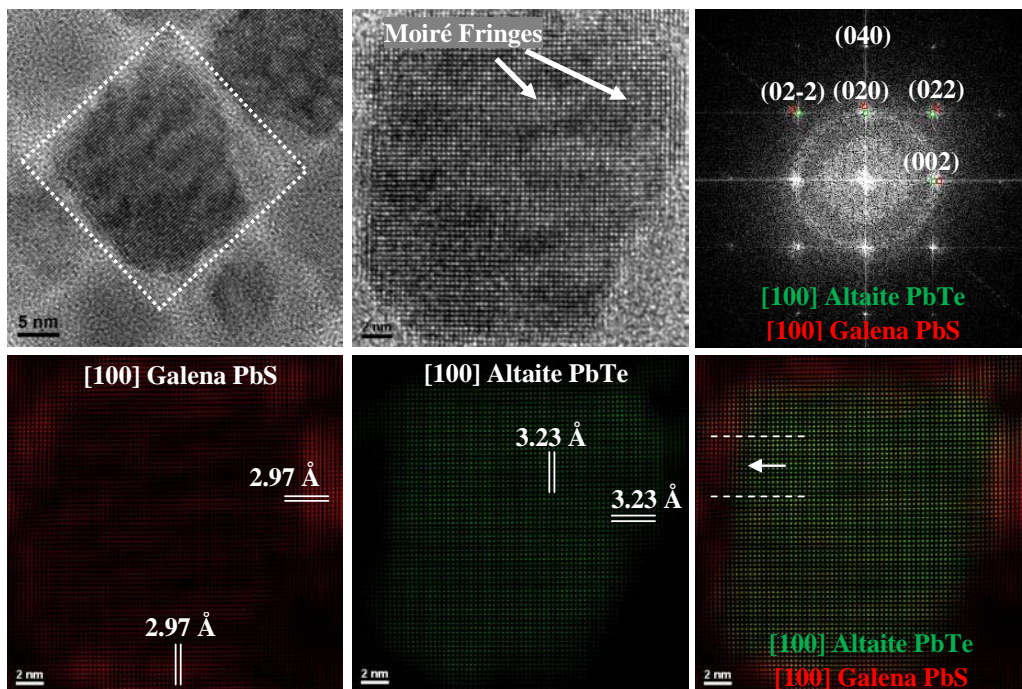


**Figure 3.69** HRTEM micrograph of PbTe@PbS NPs with crystalline galena PbS shell (top), associated with the corresponding FFT (top-right), and IFFT-filtered images (bottom)

amount of strain can be assigned to the first PbS atomic layers of the shell. The different color (intensity related) of the shell represents the different crystal structure, whereas in the core smooth green/red map is observed which means that the structure is devoid of strain.

Another important point to be mentioned is the appearance of moiré fringes in HRTEM images and the atomic models. Essentially, moiré (pronounced mwa-ray) patterns are formed by interfering two sets of lines that have nearly common periodicities. Two fundamentally different types of interference can be demonstrated: (i) rotational moiré and (ii) translational moiré. The latter is often referred to as ‘misfit moiré’. When the misorientation or the misfit is small, the moiré fringe spacing is much coarser than that of the lines themselves.<sup>142</sup>

In all NPs with crystalline shell moiré fringes are clearly seen which are pointed up in the images. In HRTEM analysis of Figure 3.69 also they are observed, especially in the IFFT-filtered image related to the shell structure in red. However, if one compares the magnified HRTEM image of Figure 3.67 with the one of Figure 3.69, they can doubt whether the core, the shell, and/or the accommodation of the shell on the core is always the same, because a difference in moiré fringe spacing angle respecting the atomic planes of the structure is observed. Even in low-magnification TEM micrographs of Figure 3.71 one notices the different moiré patterns in different NPs. It should be pointed out that in this figure in most of the NPs no moiré patterns are visible. However, one cannot assure that there is a difference in NP structure only by

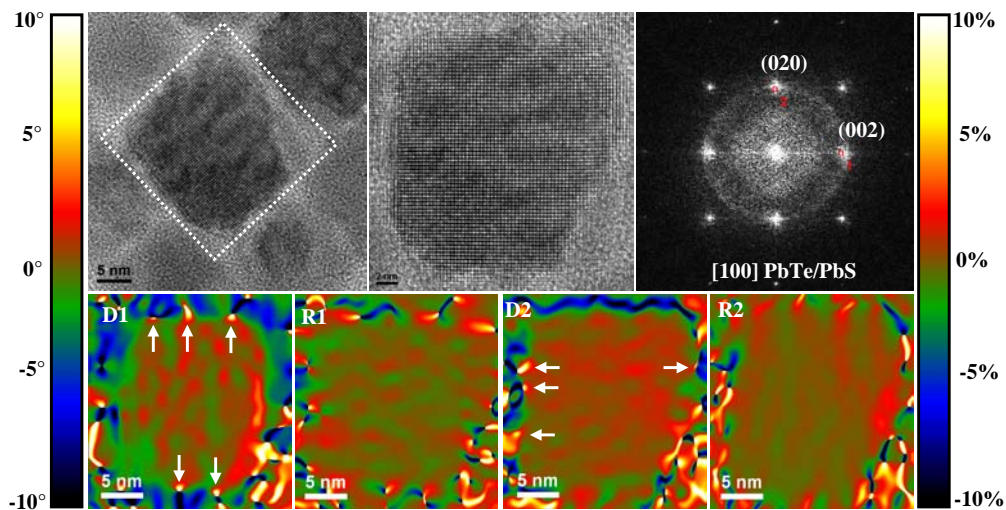


**Figure 3.70** Geometric phase analysis (GPA) of a PbTe@PbS NPs with crystalline PbS shell

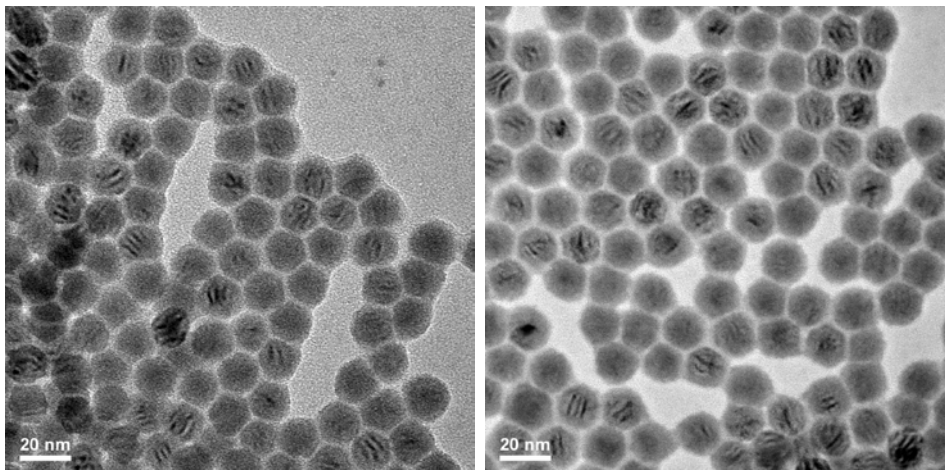


**Figure 3.71** TEM micrographs showing different moiré patterns

presence or absence of these moiré patterns in low-magnification TEM images.

HRTEM image simulations of Figure 3.72 show how slight diversions from the zone axis can result in differently visualized moiré patterns. The previously prepared 3D atomic model was used in the JEMS software package in order to obtain the HRTEM image simulation, obtained with the same microscope parameters as the ones of the experiment, e.g.:  $C_s = 0.5$ ;  $d_f = 43.4$  nm (equivalent to the experimental Scherzer defocus). When the NP is perfectly oriented along the [100] zone axis, the moiré fringes create some particular interference contrasts, circle-like patterns (see Figure 3.72(a)) which is the result of the overlap of two structures with close cell parameters in two directions, [010] and [001]. When the particle is on the perfect zone axis interferences (moiré fringes) occur along both x and y axes, giving rise to the formation of such circle-like patterns. According to random orientation of the spherical NPs on the holey-carbon TEM grids, it is not likely to find NPs in perfect zone axis.

However, in the TEM images we mostly see stripes of moiré fringes like the ones that are shown in Figures 3.72(b) and 3.72(c). Usually this kind of moiré fringes appears in the case that the two materials have the same cell parameter in one direction and a slight difference in another. But this is not the case here, because both structures of the core and the shell are cubic and difference of the cell parameters in x and y directions must be exactly the same. Hence, such fringes are explained by the slight diversion of the NPs from the exact zone axis. Figures 3.72(b) and 3.72(c) show the experimental and simulated core-shell NP

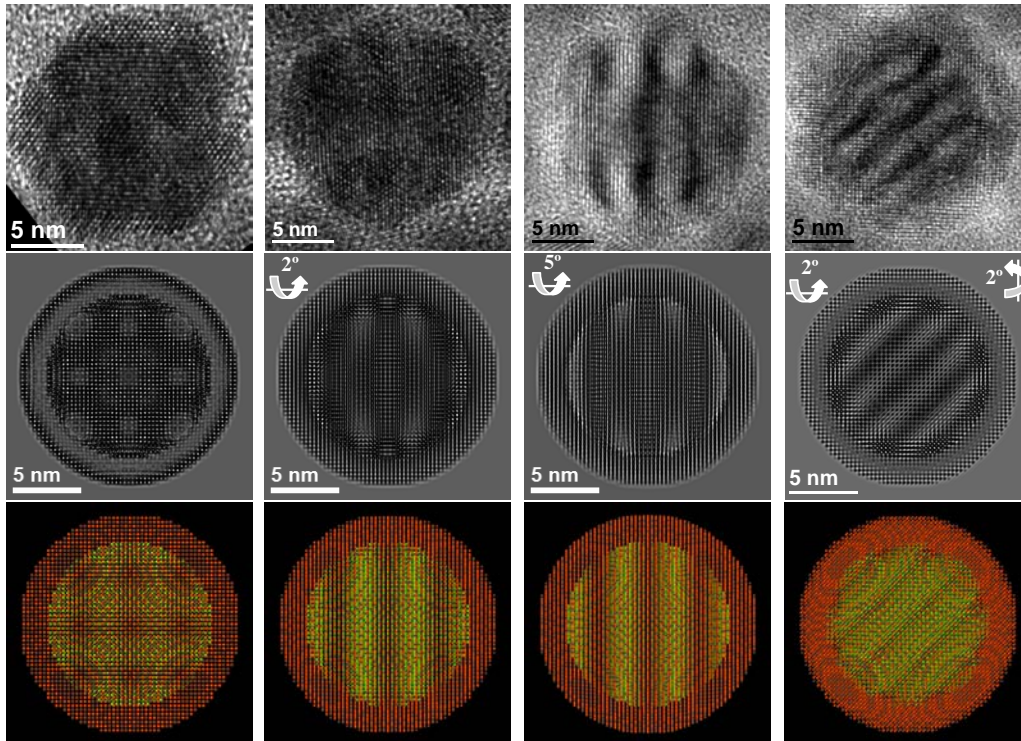


**Figure 3.72** HRTEM micrographs of PbTe@PbS core-shell NPs associated with JEMS HRTEM simulations and 3D atomic models, showing how moiré fringes can change with slight diversions from the exact zone axis

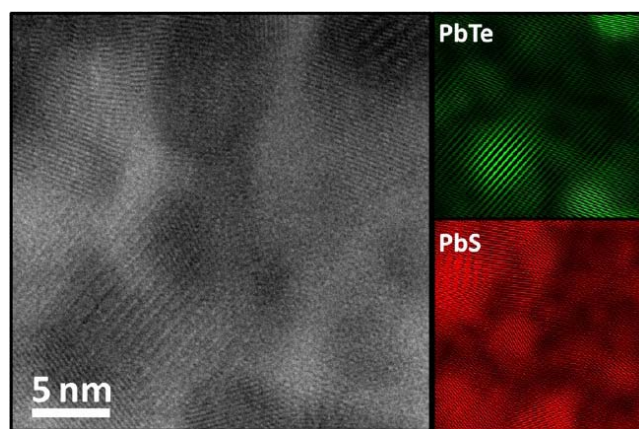
rotated  $2^\circ$  and  $5^\circ$  along the [010]-axis from [100] view direction, respectively. In these two figures, moiré fringes are vertically aligned with different contrasts.

Figure 3.72(d) explains moiré patterns that have an angle with the atomic planes.  $2^\circ$  rotation along [010] plus  $2^\circ$  along [001] results in appearance of diagonal moiré patterns. Our results demonstrate that the all the cores and shells keep the same orientation or epitaxial relationship, i.e.  $(010)[100]_{\text{PbTe}} // (010)[100]_{\text{PbS}}$ , and different moiré patterns are due to diversion from the exact zone axis.

After obtaining crystalline shells with desired thicknesses, they should be assembled and the annealed in order to create proper nanocomposites for thermoelectric devices. A set of PbTe@PbS core-shell NPs with similar overall size but different PbTe/PbS ratios was used to produce  $(\text{PbTe})_{1-x}(\text{PbS})_x$  nanocomposites with  $x = 0.32, 0.40, 0.49,$  and  $0.72$ . As references, pure PbTe and PbS nanomaterials were also produced. Once prepared,  $(\text{PbTe})_{1-x} @ (\text{PbS})_x$

NPs were purified by multiple precipitation and redispersion steps until no redispersion was possible. At this point, most of the organic ligands used to control the size and shape of the NPs during synthesis had been removed. Purified  $(\text{PbTe})_{1-x} @ (\text{PbS})_x$  NPs were dried under vacuum to obtain a dark gray nanopowder. This nanopowder was annealed at 500 °C for 1 h under a dry argon flow to completely remove residual organics.<sup>115</sup>

The annealing effect on the nanocomposite structure had to be studied by characterization of the materials in order to understand their thermoelectric performance. As proven by HRTEM (Figure 3.73 and 3.74), the composition of the final nanomaterials was highly homogeneous at the micrometer scale but contained a uniform distribution of compositional inhomogeneities at the nanometer scale. HRTEM analysis of the nanocomposite revealed that they contain PbS and PbTe crystal nanodomains with sizes in the range 10-20 nm (Figure 3.73). In Figure 3.74, one can see the structure of the  $(\text{PbTe})_{0.28}(\text{PbS})_{0.72}$  nanocomposite pellet after thermoelectric characterizations.



**Figure 3.73** HRTEM of the  $(\text{PbTe})_{0.28}(\text{PbS})_{0.72}$  nanocomposite

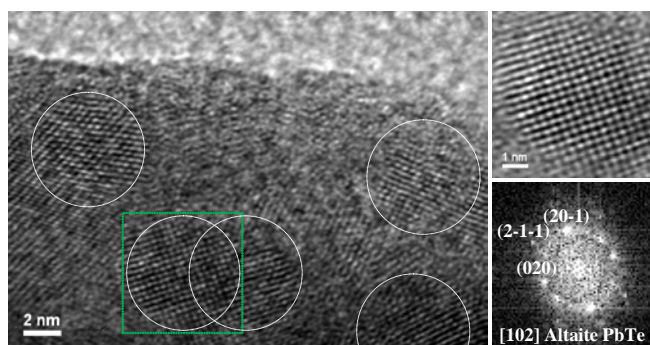


**Figure 3.74** HRTEM of the  $(\text{PbTe})_{0.28}(\text{PbS})_{0.72}$  nanocomposite in the pellet

**Table 3.1** Thermoelectric characterization of  $(\text{PbTe})_{1-x}@\text{(PbS)}_x$  nanocomposites<sup>115</sup>

$x$ $(\text{PbTe})_{1-x}$ $(\text{PbS})_x$	$E_a$ (meV)	$\sigma$ (S/m)		$S$ ( $\mu\text{V}/\text{K}$ )		$\kappa^*$ (W/mK)		$ZT$	
		320 K	710 K	320 K	710 K	320 K	710 K	320 K	710 K
0	83	55	2370	362	-270	2.2	1.20	$10^{-3}$	0.18
0.32	78	51	5510	184	-247	1.8	1.15	$10^{-4}$	0.37
0.40	81	9	4380	1	-259	1.5	0.91	$10^{-4}$	0.34
0.49	75	76	7730	-89	-232	0.85	0.61	$10^{-4}$	0.86
0.72	71	12	12530	-89	-185	0.69	0.53	$10^{-4}$	1.03
1	66	260	1180	-279	-306	1.2	0.77	$10^{-2}$	0.18

In XRD results two new peaks were observed. They were identified as the (101) and (110) plane reflections of PbO. Surprisingly, only in pure PbTe sample these peaks were not present. A significant amount of oxygen is usually observed at the surface of PbTe NPs when exposed to air even during very short periods of time.<sup>143,144</sup> Therefore, we tentatively associated the absence of the PbO phase reflections from the pure PbTe nanomaterial with the amorphous nature of the thin oxide layer potentially formed.<sup>115</sup>

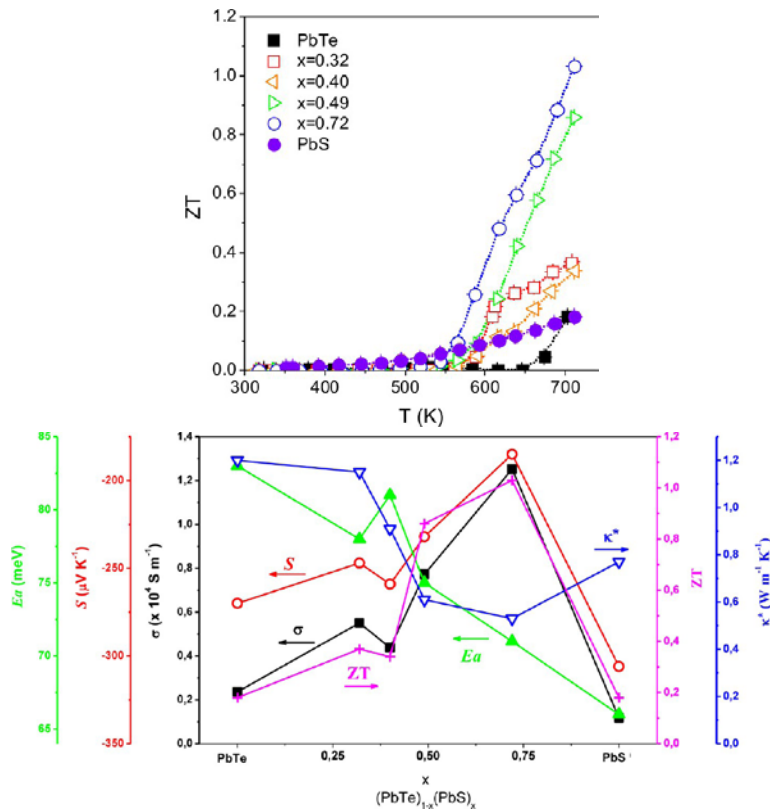
The electrical conductivity ( $\sigma$ ), Seebeck coefficient ( $S$ ), and thermal conductivity ( $\kappa$ ) of the  $(\text{PbTe})_{1-x}(\text{PbS})_x$  ( $x = 0, 0.32, 0.40, 0.49, 0.72, 1$ ) nanomaterials was measured in the temperature range from 320 to 710 K. The summary of the thermoelectric characterization of  $(\text{PbTe})_{1-x}(\text{PbS})_x$  nanomaterials is given in Table 3.1. The results are also plotted in Figure 3.75 and 3.76.

Figure 3.75(a) displays the figure of merit ( $ZT$ ) of the  $(\text{PbTe})_{1-x}(\text{PbS})_x$  nanocomposites in the temperature range from 320 to 710 K. It can be seen that the highest  $ZT$  occurs in the case of  $(\text{PbTe})_{0.28}(\text{PbS})_{0.72}$  nanocomposite at 710 K which is 1.07, a  $ZT$  that can be considered a record for these materials.  $ZT$  values of the pure PbS and pure PbTe are much lower.

Figure 3.75(b) displays the electrical conductivity ( $\sigma$ ), Seebeck coefficient ( $S$ ) porosity-corrected thermal conductivity ( $\kappa^*$ ), and thermoelectric figure of merit ( $ZT$ ) of the  $(\text{PbTe})_{1-x}(\text{PbS})_x$  nanocomposites at 710 K.

In the low-temperature regime, majority carriers in PbTe and PbS had opposite signs. While PbTe displayed p-type conductivity, PbS had an n-type character. When both phases were intermixed within  $(\text{PbTe})_{1-x}(\text{PbS})_x$  nanocomposites, holes from PbTe and electrons from PbS compensated each other, resulting in lower electrical conductivities and lower absolute Seebeck coefficients than those of pure PbTe and PbS nanomaterials. In this low-temperature range, charge transport was dominated by holes in  $(\text{PbTe})_{1-x}(\text{PbS})_x$  nanocomposites with  $x < 0.4$  and by electrons in  $(\text{PbTe})_{1-x}(\text{PbS})_x$  nanocomposites with higher PbS contents ( $x > 0.4$ ).<sup>115</sup>

In nanomaterials with energy-activated charge carrier mobility, the increase



**Figure 3.75** (a) Thermoelectric figure of merit (ZT) of  $(\text{PbTe})_{1-x}(\text{PbS})_x$  nanocomposites with  $x = 0, 0.32, 0.40, 0.49, 0.72, 1$ ; (b) electrical conductivity ( $\sigma$ ), Seebeck coefficient ( $S$ ), porosity-corrected thermal conductivity ( $\kappa^*$ ), and thermoelectric figure of merit (ZT) at 710 K and activation energy for electrical transport in the low-temperature range ( $E_a$ ), as a function of the PbS concentration in  $(\text{PbTe})_{1-x}(\text{PbS})_x$  nanomaterials<sup>115</sup>

of the average carrier kinetic energy with temperature eventually enables charge carriers to overcome the potential barrier. At this temperature, electrical conductivity is largely enhanced. At around 520 K a strong decrease of the Seebeck coefficient, from positive to negative values, starts to take place in PbTe. This is associated with an increasingly higher density of electrons participating in the charge transport within this material. At around 650 K the electron contribution to the Seebeck coefficient compensated the hole contribution. Negative Seebeck coefficients were obtained at higher temperatures. In  $(\text{PbTe})_{1-x}(\text{PbS})_x$  nanocomposites, charge carrier compensation occurred at lower temperatures. For  $(\text{PbTe})_{0.68}(\text{PbS})_{0.32}$ , the sign inversion in the Seebeck coefficient took place at around 550 K and for  $(\text{PbTe})_{0.60}(\text{PbS})_{0.40}$  at just 450 K. In  $(\text{PbTe})_{1-x}(\text{PbS})_x$  with  $x > 0.4$  a step change of the Seebeck coefficient toward more negative values was also obtained in this temperature range. This sign inversion or step change in the Seebeck coefficient was accompanied by an increase in electrical conductivity in the temperature range from 450 to 650 K for all nanocomposites. At relatively high temperature ( $T > 650$  K), both PbTe and PbS displayed n-type conductivity. In this regime a synergistic contribution of the majority charge carriers of both phases was observed, and much higher electrical conductivities were obtained for nanocomposites than for pure PbTe and PbS nanomaterials. In the high-temperature regime measured, the electrical conductivity of  $(\text{PbTe})_{1-x}(\text{PbS})_x$  nanocomposites increased with the PbS content. The highest electrical conductivities were obtained for  $(\text{PbTe})_{0.28}(\text{PbS})_{0.72}$ . For this material electrical conductivities up to 10-fold larger than PbS were measured. While the present work PbTe and PbS phases were not intentionally doped, a doping-like effect occurred when mixing both semiconductors at the nanometer scale. This nanocrystal-based doping translated into larger electrical conductivities but slightly lower absolute values of the Seebeck coefficient.<sup>115</sup>

Thermal conductivity values were calculated from thermal diffusivities obtained using flash diffusivity measurements. In nanomaterials, when calculating thermal conductivity from thermal diffusivity data, the surface contribution to the molar heat capacity needs to be taken into account.<sup>145</sup> Heat capacities were measured by a relaxation method. Surprisingly lower heat capacity values were obtained for nanocomposites when compared to pure nanomaterials. These low thermal conductivity values were in part associated with the material porosity. The porosity contribution could be roughly estimated and removed from the calculated thermal conductivities using Maxwell-

Eucken's equation.<sup>146</sup> Therefore, in Figure 3.75 and 3.76 the porosity-corrected thermal conductivities ( $\kappa^*$ ) are plotted instead of  $\kappa$ .

After porosity correction, thermal conductivities were still exceptionally low. Thermal conductivity monotonically decreased with the concentration of PbS in  $(\text{PbTe})_{1-x}(\text{PbS})_x$  nanocomposites. These low thermal conductivities obtained were associated with the efficient scattering of phonons at the high density of grain boundaries and crystal interfaces within the  $(\text{PbTe})_{1-x}(\text{PbS})_x$  nanomaterials. Another parameter that may contribute to phonon scattering is the partial phase alloying detected. Alloying or replacement of Te by S ions in PbTe and of S by Te ions in PbS introduced high densities of point defects. Taking into account the large difference in size between Te and S ions, such replacement may effectively scatter short-wavelength phonons and thus contribute to further reduce the nanocomposite thermal conductivity. Phase alloying was stronger the larger the concentration of sulfur in the nanocomposite.<sup>115</sup>

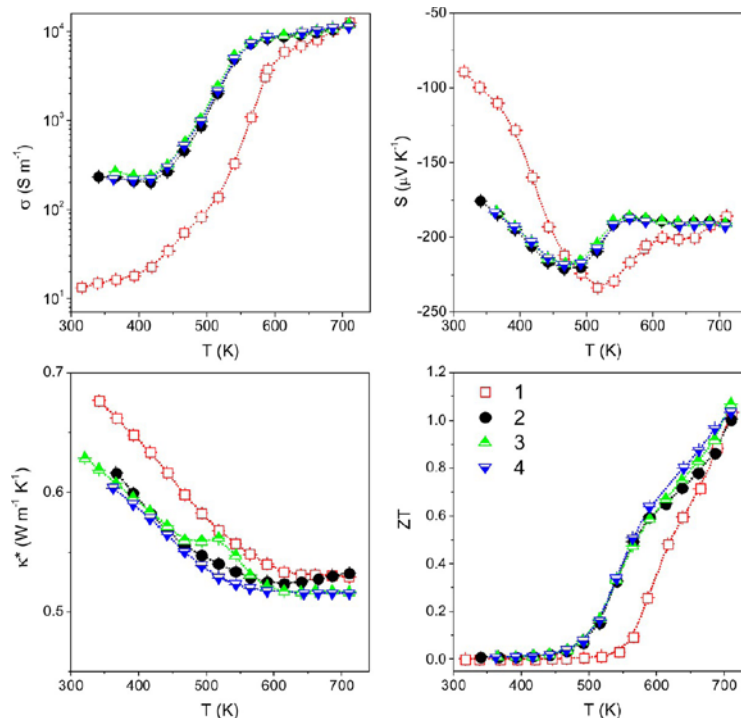


**Figure 3.76** Multiple measurements of the electrical conductivity ( $\sigma$ ), thermopower ( $S$ ), porosity-corrected thermal conductivity ( $\kappa^*$ ), and thermoelectric figure of merit ( $ZT$ ) from the same  $(\text{PbTe})_{0.28}(\text{PbS})_{0.72}$  pellet<sup>115</sup>

Figure 3.75(a) displays the thermoelectric figure of merit calculated for the different  $(\text{PbTe})_{1-x}(\text{PbS})_x$  nanocomposites. The maximum ZT value for pure PbTe and PbS nanostructured material obtained was 0.18 at 700 K. Nanocomposites obtained from core-shell NPs were characterized by figures of merit substantially higher than those of pure PbTe and PbS nanomaterials. From the compositions studied here, the nanocomposite with the largest figure of merit was  $(\text{PbTe})_{0.28}(\text{PbS})_{0.72}$ . For this nanocomposite a figure of merit ZT up to 1.07 at 700 K was calculated. The larger figures of merit obtained for nanocomposites when compared to pure nanomaterials were attributed to two main effects: (i) a synergic effect between the charge carriers of each phase resulted in nanocomposites with electrical conductivities up to 1 order of magnitude higher than pure materials; (ii) enhanced phonon scattering at multiple length scales provided nanocomposites with significantly lower thermal conductivities.

As stability of the nanomaterials and measurement reproducibility are major concerns, especially in bottom-up-assembled nanocomposites, we tested the thermoelectric performance stability of the nanocomposites by repeating the measurements different days. Figure 3.76 displays data obtained from measuring the thermoelectric properties of  $(\text{PbTe})_{0.28}(\text{PbS})_{0.72}$  four times. We observed that after the first measurement higher electrical conductivities and Seebeck coefficients and lower thermal conductivities were obtained in the low-temperature range. After the second measurement, thermoelectric properties remained unchanged.<sup>115</sup>

### 3.3.3.4 Section summary

Further to single-phased and multi-phased chalcogenide NCs, it was shown in this section that creating heterostructures can also improve some particular properties of the materials as desired. The heterostructuring approach that was chosen in this section was coaxial, i.e. production of core-shell NPs. In this context three different systems were examined, which the most successful was the case of PbTe@PbS NPs. This system was used to create  $(\text{PbTe})_{1-x}(\text{PbS})_x$  nanocomposites for thermoelectric applications, and they showed a dramatic enhancement in thermoelectric figure of merit comparing to the one of bare PbTe or PbS. The highest ZT of 1.1 at 700 K was obtained which is a record for such compounds. Precise characterization experiments were performed in order to justify the behavior of the materials.

### 3.4 Conclusion

In this chapter we proved the importance of chemical, structural, and morphological nanoengineering in the case of complex chalcogenide structures. In section 3.3.1 the influence of chemical composition was studied. A few copper-based ternary and quaternary selenide NCs were synthesized, characterized and examined for thermoelectric devices. These compounds were all keeping their ZB-like structure. Chemical composition and size of the NCs were important issues that affected their properties. Afterwards, in section 3.3.2, we studied different issues playing around with the crystal structure, chemical composition and morphology through synthetic routes, which may have influence on various properties of the compounds. Polytypism, branching, and ‘polytypic branching’, cation ordering, and polarity were the different aspects of our structural analyses. We proved how polarity determines the morphology and drives the branching mechanism. On the other hand, the influence of polytypism and cation ordering on the electronic band structure was studied. *Ab-initio* studies showed that the WZ branches which do not have cation ordering are metallic as the band gap energy from 0.98 eV in ordered ZB-like CCTSe shrinks to 0.0 eV while Fermi level lies inside the conduction band. Therefore, the CCTSe polypods consisted of a semiconducting pentatetrahedral seed and metallic pods.

Finally, the coaxial heterostructuring approach was utilized to produce core-shell NPs with two materials which are dissimilar but have close crystal structures. In this way, epitaxial relationship can be achieved while taking advantage of chemical stability of the core and surface properties of the shell. PbTe@PbS core-shell NPs were used to create PbTe-PbS nanocomposites for thermoelectric devices and they showed dramatic improvement in the thermoelectric figure of merit comparing to bare PbTe and PbS structures.

In fact, production of heterostructures is a promising approach that can be used in other types of nanostructured materials. In the next chapter we apply this idea on metal oxide NWs for different applications and we will observe the efficiency enhancement.

### 3.5 References

- 1 D. Spirkoska, J. Arbiol, A. Gustafsson, S. Conesa-Boj, F. Glas, I. Zardo, M. Heigoldt, M.H. Gass, A.L. Bleloch, S. Estrade, M. Kaniber, J. Rossler, F. Peiro, J.R. Morante, G. Abstreiter, L. Samuelson, A. Fontcuberta i Morral, **'Structural and optical properties of high quality zinc-blende/wurtzite GaAs nanowire heterostructures'**, *Physical Review B* 80, 245325 (2009)
- 2 M. Heiss, S. Conesa-Boj, J. Ren, H.-H. Tseng, A. Gali, A. Rudolph, E. Uccelli, F. Peiró, J.R. Morante, D. Schuh, E. Reiger, E. Kaxiras, J. Arbiol, A. Fontcuberta i Morral, **'Direct correlation of crystal structure and optical properties in wurtzite/zinc-blende GaAs nanowire heterostructures'**, *Physical Review B* 83, 045303 (2011)
- 3 P. Caroff, K.A. Dick, J. Johansson, M.E. Messing, K. Deppert, L. Samuelson, **'Controlled polytypic and twin-plane superlattices in III-V nanowires'**, *Nature Nanotechnology* 4, 50 (2009)
- 4 J. Bao, D.C. Bell, F. Capasso, J.B. Wagner, T. Martensson, J. Tragardh, L. Samuelson, **'Optical properties of rotationally twinned InP nanowire heterostructures'**, *Nano Letters* 8, 836 (2008)
- 5 J. Arbiol, S. Estradé, J.D. Prades, A. Cirera, F. Furtmayr, C. Stark, A. Laufer, M. Stutzmann, M. Eickhoff, M.H. Gass, A.L. Bleloch, F. Peiró, J.R. Morante, **'Triple-twin domains in Mg doped GaN wurtzite nanowires: Structural and electronic properties of this zinc-blende-like stacking'**, *Nanotechnology* 20, 145704 (2009)
- 6 H.J. Joyce, J. Wong-Leung, Q. Gao, H.H. Tan, C. Jagadish, **'Phase perfection in zinc blende and wurtzite III-V nanowires using basic growth parameters'**, *Nano Letters* 10, 908-915 (2010)
- 7 A. Fontcuberta i Morral, J. Arbiol, J.D. Prades, A. Cirera, J.R. Morante, **'Synthesis of silicon nanowires with wurtzite crystalline structure by using standard chemical vapor deposition'**, *Advanced Materials* 19, 1347-1351 (2007)
- 8 J. Arbiol, A. Fontcuberta i Morral, S. Estradé, F. Peiró, B. Kalache, P. Roca i Cabarrocas, J.R. Morante, **'Influence of the (111) twinning on the formation of diamond cubic/diamond hexagonal heterostructures in Cu-catalyzed Si nanowires'**, *Journal of Applied Physics* 104, 064312 (2008)
- 9 X.-H. Sun, C.-P. Li, W.-K. Wong, N.-B. Wong, C.-S. Lee, S.-T. Lee, B.-K. Teo, **'Formation of silicon carbide nanotubes and nanowires via reaction of silicon (from disproportionation of silicon monoxide) with**

---

**carbon nanotubes**', *Journal of the American Chemical Society* 124, 14464-14471 (2002)

10 Y. Ding, Z.L. Wang, T. Sun, J. Qiu, '**Zinc-blende ZnO and its role in nucleating wurtzite tetrapods and twinned nanowires**', *Applied Physics Letters* 90, 153510 (2007)

11 B. Gilbert, B.H. Frazer, H. Zhang, F. Huang, J.F. Banfield, D. Haskel, J.C. Lang, G. Srajer, G. De Stasio, '**X-ray absorption spectroscopy of the cubic and hexagonal polytypes of zinc sulfide**', *Physical Review B* 66, 245205 (2002)

12 M.I.B. Utama, M. de la Mata, C. Magen, J. Arbiol, Q. Xiong, '**Twining-, polytypism-, and polarity-induced morphological modulation in nonplanar nanostructures with van der Waals epitaxy**', *Advanced Functional Materials* 23, 1636-1646 (2013)

13 D.K. Ghosh, P.S. Ghosh, L.K. Samanta, '**Characterization of some quaternary defect chalcopyrites as useful nonlinear optical and solar-cell materials**', *Physical Review B* 41, 5126-5130 (1990)

14 Y. Cui, G. Wang, D. Pan, '**Synthesis and photoresponse of novel Cu<sub>2</sub>CdSnS<sub>4</sub> semiconductor nanorods**', *Journal of Materials Chemistry* 22, 12471-12473 (2012)

15 F.-J. Fan, B. Yu, Y.-X. Wang, Y.-L. Zhu, X.-J. Liu, S.-H. Yu, Z. Ren, '**Colloidal synthesis of Cu<sub>2</sub>CdSnSe<sub>4</sub> nanocrystals and hot-pressing to enhance the thermoelectric figure-of-merit**', *Journal of the American Chemical Society* 133, 15910-15913 (2011)

16 G.J. Snyder, E.S. Toberer, '**Complex thermoelectric materials**', *Nature Materials* 7, 105 (2008)

17 T.M. Tritt, '**Thermoelectric materials: principles, structure, properties, and applications**', *Encyclopedia of Materials: Science and Technology*, Ch 1, 1-11 (2002)

18 D.M. Rowe, '**General principles and basic considerations**', *Thermoelectrics Handbook: Micro to Nano*, Ch 1, 1-1 - 1-14 (2006)

19 P. Pichanusakorn, P. Bandaru, '**Nanostructured thermoelectrics**', *Materials Science and Engineering R* 67, 19-63 (2010)

20 B. Poudel, Q. Hao, Y. Ma, Y. Lan, A. Minnich, B. Yu, X. Yan, D. Wang, A. Muto, D. Vashaee, X. Chen, J. Liu, M.S. Dresselhaus, G. Chen, Z. Ren, '**High-thermoelectric performance of nanostructured bismuth antimony telluride bulk alloys**', *Science* 320, 634-637 (2008)

21 R. Venkatasubramanian, E. Siivola, T. Colpitts, B. O'Quinn, '**Thin-film thermoelectric devices with high room-temperature figures of merit**', *Nature* 413, 597-602 (2001)

22 A.I. Hochbaum, R. Chen, R. Diaz Delgado, W. Liang, E.C. Garnett, M. Najarian, A. Majumdar, P.-D Yang, '**Enhanced thermoelectric performance of rough silicon nanowires**', *Nature* 451, 163-167 (2008)

23 L.D. Hicks, T.C. Harman, M.S. Dresselhaus, '**Use of quantum-well superlattices to obtain a high figure of merit from nonconventional thermoelectric materials**', *Applied Physics Letters* 63, 3230-3232 (1993)

24 L.D. Hicks, T.C. Harman, X. Sun, M.S. Dresselhaus, '**Experimental study of the effect of quantum-well structures on the thermoelectric figure of merit**', *Physical Review B* 53, R10493-R10496 (1996)

25 T.C. Harman, P.J. Taylors, M.P. Walsh, B.E. LaForge, '**Quantum dot superlattice thermoelectric materials and devices**', *Science* 297, 2229-2232 (2002)

26 J. Androulakis, C.-H. Lin, H.-J. Kong, C. Uher, C.-I. Wu, T. Hogan, B.A. Cook, T. Caillat, K.M. Paraskevopoulos, M.G. Kanatzidis, '**Spinodal decomposition and nucleation and growth as a means to bulk nanostructured thermoelectrics: enhanced performance in  $Pb_{1-x}Sn_xTe-PbS$** ', *Journal of American Chemical Society* 129, 9780-9788 (2007)

27 M. Ibáñez, R. Zamani, W. Li, A. Shavel, J. Arbiol, J.R. Morante, A. Cabot, '**Extending the nanocrystal synthesis control to quaternary compositions**', *Crystal Growth and Design* 12, 1085-1090 (2012)

28 M. Ibáñez, R. Zamani, W. Li, D. Cadavid, S. Gorsse, N.A. Katcho, A. Shavel, A.M. López, J.R. Morante, J. Arbiol, A. Cabot, '**Crystallographic control at the nanoscale to enhance functionality:  $Cu_2GeSe_3$  nanoparticles as thermoelectric materials**', *Chemistry of Materials* 24, 4615-4622 (2012)

29 M. Ibáñez, D. Cadavid, R. Zamani, N. Garcia-Castello, V. Izquierdo-Roca, W.H. Li, A. Fairbrother, J.D. Prades, A. Shavel, J. Arbiol, A. Pérez-Rodríguez, J.R. Morante, A. Cabot, '**Composition control and thermoelectric properties of quaternary chalcogenide nanocrystals: The case of stannite  $Cu_2CdSnSe_4$** ', *Chemistry of Materials* 24, 562-570 (2012)

30 A. Shavel, J. Arbiol, A. Cabot, '**Synthesis of quaternary chalcogenide nanocrystals: stannite  $Cu_2Zn_xSn_ySe_{1+x+2y}$** ', *Journal of American Chemical Society* 132, 4514-4515 (2010)

31 M. Ibáñez, R. Zamani, A. LaLonde, D. Cadavid, W.H. Li, A. Shavel, J. Arbiol, J.R. Morante, S. Gorsse, G. Snyder, A. Cabot, ' **$Cu_2ZnGeSe_4$**

---

**nanocrystals: synthesis and thermoelectric properties**', *Journal of American Chemical Society* 134, 4060-4063 (2012)

32 M. Ibáñez, D. Cadavid, U. Anselmi-Tamburini, R. Zamani, S. Gorsse, W.H. Li, A.M. López, J.R. Morante, J. Arbiol, A. Cabot, '**Colloidal synthesis and thermoelectric properties of Cu<sub>2</sub>SnSe<sub>3</sub> nanocrystals**', *Journal of Materials Chemistry A* 1, 1421 (2013)

33 S. Mardix, '**Polytypism: a controlled thermodynamic phenomenon**', *Physical Review B* 33, 8677-8684 (1986)

34 P. Krishna, A.R. Verma, '**Crystal-polytypism in one dimension**', *Physica Status Solidi B* 17, 437-477 (1966)

35 E. Alexander, Z.H. Kalman, S. Mardix, I.T. Steinberger, '**The mechanism of polytype formation in vapour-phase grown ZnS crystals**', *Philosophical Magazine* 21, 1237-1246 (1970)

36 G.C. Trigunayat, G.K. Chadha, '**Progress in the study of polytypism in crystals (I)**', *Physica Status Solidi A* 4, 9-42 (1971)

37 A.S. Pashinkin, G.N. Tishchenko, I.V. Korneeva, B.N. Ryzhenko, '**Concerning the polymorphism of some chalcogenides of zinc and cadmium**', *Kristallografiya* 5, 261-267 (1960)

38 A.R. Verma, '**Spiral growth on carborundum crystal faces**', *Nature* 167, 939 (1951)

39 S. Sato, S. Shinozaki, '**Microsyntax and polytypism in SiC**', *Materials Research Bulletin* 9, 679-684 (1974)

40 F. Haguenu, P.W. Hawkes, J.L. Hutchison, B. Satiat-Jeunemaître, G.T. Simon, D.B. Williams, '**Key events in the history of electron microscopy**', *Microscopy and Microanalysis* 9, 96-138 (2003)

41 P.R. Buseck, S. Iijima, '**High-resolution electron-microscopy of enstatite II: geological application**', *American Mineralogist* 70, 771-784 (1975)

42 M.I.B. Utama, F.J. Belarre, C. Magen, B. Peng, J. Arbiol, Q. Xiong, '**Incommensurate van der Waals epitaxy of nanowire arrays: a case study with ZnO on muscovite mica substrates**', *Nano Letters* 12, 2146-2152 (2012)

43 F. Schuster, F. Furtmayr, R. Zamani, C. Magen, J.R. Morante, J. Arbiol, J.A. Garrido, M. Stutzmann, '**Self-assembled GaN nanowires on diamond**', *Nano Letters* 12, 2199-2204 (2012)

---

44 M. de la Mata, C. Magen, J. Gazquez, M.I.B. Utama, M. Heiss, S. Lopatin, F. Furtmayr, C.J. Fernandez-Rojas, B Peng, J.R. Morante, R. Rurali, M. Eickhoff, A. Fontcuberta i Morral, Q. Xiong, J. Arbiol, **'Polarity assignment in ZnTe, GaAs, ZnO and GaN-AlN nanowires from direct dumbbell analysis'**, *Nano Letters* 12, 2579-2586 (2012)

45 S.Y. Chen, X.G. Gong, A. Walsh, S.-H. Wei, **'Electronic structure and stability of quaternary chalcogenide semiconductors derived from cation cross-substitution of II-VI and I-III-VI<sub>2</sub> compounds'**, *Physical Review B* 79, 165211 (2009)

46 D. Aldakov, A. Lefrançois, P. Reiss, **'Ternary and quaternary metal chalcogenide nanocrystals: synthesis, properties and applications'**, *Journal of Materials Chemistry C* 1, 3756-3776 (2013)

47 I. Tsuji, Y. Shimodaira, H. Kato, H. Kobayashi, A. Kudo, **'Novel stannite-type complex sulfide photocatalysts A<sup>I</sup><sub>2</sub>-Zn-A<sup>IV</sup>-S<sub>4</sub> (A<sup>I</sup> = Cu and Ag; A<sup>IV</sup> = Sn and Ge) for hydrogen evolution under visible-light irradiation'**, *Chemistry of Materials* 1402-1409 (2010)

48 K. Zhangab, L. Guo, **'Metal sulphide semiconductors for photocatalytic hydrogen production'**, *Catalysis Science & Technology* 3, 1672-1690 (2013)

49 S.Y. Chen, A. Walsh, Y. Luo, J.H. Yang, X.G. Gong, S.-H. Wei, **'Wurtzite-derived polytypes of kesterite and stannite quaternary chalcogenide semiconductors'**, *Physical Review B* 82, 195203 (2010)

50 S. Bernal, F.J. Botana, J.J. Calvino, C. Lopez-Cartes, J.A. Perez-Omil, J.M. Rodriguez-Izquierdo, **'The interpretation of HREM images of supported metal catalysts using image simulation: profile view images'**, *Ultramicroscopy* 72, 135-164 (1998)

51 E. Uccelli, J. Arbiol, C. Magen, P. Krogstrup, E. Russo-Averchi, M. Heiss, G. Mugny, F. Morier-Genoud, J. Nygard, J.R. Morante, A. Fontcuberta i Morral, **'Three-dimensional multiple-order twinning of self-catalyzed GaAs nanowires on Si substrates'**, *Nano Letters* 11, 3827-3832 (2011)

52 Y.T. Zhai S.Y. Chen, J.-H. Yang<sup>1</sup>, H.-J. Xiang<sup>1</sup>, X.-G. Gong, A. Walsh, J. Kang, S.-H. Wei, **'Structural diversity and electronic properties of Cu<sub>2</sub>SnX<sub>3</sub> (X=S, Se): a first-principles investigation'**, *Physical Review B* 84, 075213 (2011)

53 Q. Shu, J.-H. Yang, S.Y. Chen, B. Huang, H.J. Xiang, X.G. Gong, S.-H. Wei, **'Cu<sub>2</sub>Zn(Sn,Ge)Se<sub>4</sub> and Cu<sub>2</sub>Zn(Sn,Si)Se<sub>4</sub> alloys as photovoltaic**

---

**materials: structural and electronic properties**', *Physical Review B* 87, 115208 (2013)

54 D.M. Schleich, A. Wold, '**Optical and electrical properties of quarternary chalcogenides**', *Materials Research Bulletin* 12, 111-114 (1977)

55 C. Lee, C.-D. Kim, '**Optical properties of undoped and Co<sup>2+</sup>-doped Cu<sub>2</sub>ZnGeSe<sub>4</sub> crystals**', *Journal of the Korean Physical Society* 37, 364-367 (2000)

56 H. Matsushita, T. Ichikawa, A. Katsui, '**Structural, thermodynamical and optical properties of Cu<sub>2</sub>-II-IV-VI<sub>4</sub> quaternary compounds**', *Journal of Materials Science* 40, 2003-2005 (2005)

57 M.-L. Liu, I.-W. Chen, F.-Q. Huang, L.-D. Chen, '**Improved thermoelectric properties of Cu-doped quaternary chalcogenides of Cu<sub>2</sub>CdSnSe<sub>4</sub>**', *Advanced Materials* 21, 3808-3812 (2009)

58 L. Dan, Z. Xinghong, Z. Zhenye, Z. Huayu, L. Furi, '**Ab-initio calculations of structural, electronic, and optical properties of Cu<sub>2</sub>HgSnSe<sub>4</sub>**', *Solid State Sciences* 14, 890-893 (2012)

59 W.-H. Li, M. Ibáñez, R. Zamani, N. García-Castelló, S. Gorsse, D. Cadavid, J.D. Prades, J. Arbiol, A. Cabot, '**I<sub>2</sub>-II-IV-VI<sub>4</sub> Nanoparticles: the case of Cu<sub>2</sub>HgSnSe<sub>4</sub>**', Submitted 2013

60 .Y. Cho, X. Shi, J.R. Salvador, G.P. Meisner, J. Yang, H. Wang, A.A. Wereszczak, X. Zhou, C. Uher, '**Thermoelectric properties and investigations of low thermal conductivity in Ga-doped Cu<sub>2</sub>GeSe<sub>3</sub>**', *Physical Review B* 84, 085207 (2011)

61 G. Marcano, C. Rincon, G. Marin, G.E. Delgado, A.J. Mora, J.L. Herrera-Perez, J.G. Mendoza-Alvarez, P. Rodriguez, '**Raman scattering and X-ray diffraction study in Cu<sub>2</sub>GeSe<sub>3</sub>**', *Solid State Communications* 146, 65-68 (2008)

62 E. Parthé, J. Garin, '**Zinkblende- und wurtzitüberstrukturen bei ternären chalcogeniden der zusammensetzung 1<sub>2</sub>46<sub>3</sub>**', *Monatshefte für Chemie* 102, 1197-1208 (1971)

63 L.I. Berger, V.D. Prochukhan, '**Ternary two-cation compounds**', *Ternary Diamond-like Semiconductors*, Ch. 4, 47-78 (1969)

64 S. Conesa-Boj, I. Zardo, S. Estradé, L. Wei, P.J. Alet, P. Roca i Cabarrocas, J.R. Morante, F. Peiró, A. Fontcuberta i Morral, J. Arbiol, '**Defect formation in Ga-catalyzed silicon nanowires**', *Crystal Growth and Design* 10, 1534-1543 (2010)

- 
- 65 F.J. Lopez, E.R. Hemesath, L.J. Lauhon, '**Ordered stacking fault arrays in silicon nanowires**', *Nano Letters* 9, 2774-2779 (2009)
- 66 R.E. Algra, M.A. Verheijen, M.T. Borgstrom, L.-F. Feiner, G. Immink, W.J.P. van Enckevort, E. Vlieg, E.P.A.M. Bakkers, '**Twinning superlattices in indium phosphide nanowires**', *Nature* 456, 369 (2008)
- 67 J. Johansson, L.S. Karlsson, K. A. Dick, J. Bolinsson, B. A. Wacaser, K. Deppert, L. Samuelson, '**Effects of supersaturation on the crystal structure of gold seeded IHV nanowires**', *Crystal Growth and Design* 9, 766-773 (2009)
- 68 J. Johansson, L.S. Karlsson, C. Patrik, T. Svensson, T. Martensson, B.A. Wacaser, K. Deppert, L. Samuelson, W. Siefert, '**Structural properties of <111> B-oriented III-V nanowires**', *Nature Materials* 5, 574-580 (2006)
- 69 H. Matsushita, T. Maeda, A. Katsui, T. Takizawa, '**Thermal analysis and synthesis from the melts of Cu-based quaternary compounds Cu-III-IV-VI<sub>4</sub> and Cu<sub>2</sub>-II-IV-VI<sub>4</sub> (II=Zn, Cd; III=Ga, In; IV=Ge, Sn; VI=Se)**', *Journal of Crystal Growth* 208, 416-422 (2000)
- 70 I.D. Olekseyuk, L.D. Gulay, I.V. Dydchak, L.V. Piskach, O.V. Parasyuk, O.V. Marchuk, '**Single crystal preparation and crystal structure of the Cu<sub>2</sub>Zn/Cd,Hg/SnSe<sub>4</sub> compounds**', *Journal of Alloys and Compounds* 340, 141-145 (2002)
- 71 H. Li, A.G. Kanaras, L. Manna, '**Colloidal branched semiconductor nanocrystals: state of the art and perspectives**', *Accounts of Chemical Research* 46, 1387-1396 (2013)
- 72 J. Li, L.-W. Wang, '**Shape effects on electronic states of nanocrystals**', *Nano Letters* 3, 1357-1363 (2003)
- 73 D.J. Milliron, S.M. Hughes, Y. Cui, L. Manna, J. Li, L.-W. Wang, A.P. Alivisatos, '**Colloidal nanocrystal heterostructures with linear and branched topology**', *Nature* 430, 190-195 (2004)
- 74 A. Fiore, R. Mastria, M.G. Lupo, G. Lanzani, C. Giannini, E. Carlino, G. Morello, M. De Giorgi, Y. Li, R. Cingolani, L. Manna, '**Tetrapod-shaped colloidal nanocrystals of II-VI semiconductors prepared by seeded growth**', *Journal of the American Chemical Society* 131, 2274-2282 (2009)
- 75 I. Gur, N.A. Fromer, C.-P. Chen, A.G. Kanaras, A.P. Alivisatos, '**Hybrid solar cells with prescribed nanoscale morphologies based on hyperbranched semiconductor nanocrystals**', *Nano Letters* 7, 409-414 (2007)

---

76 S.H. Ko, D. Lee, H.W. Kang, K.H. Nam, J.Y. Yeo, S.J. Hong, C.P. Grigoropoulos, H.J. Sung, '**Nanoforest of hydrothermally grown hierarchical ZnO nanowires for a high efficiency dye-sensitized solar cell**', *Nano Letters* 11, 666-671 (2011)

77 B. Liu, J. Zhang, X. Wang, G. Chen, D. Chen, C. Zhou, G. Shen, '**Hierarchical three-dimensional ZnCo<sub>2</sub>O<sub>4</sub> nanowire arrays/carbon cloth anodes for a novel class of high-performance flexible lithium-ion batteries**', *Nano Letters* 12, 3005-3011 (2012)

78 Y. Cui, U. Banin, M.T. Bjork, A.P. Alivisatos, '**Electrical transport through a single nanoscale semiconductor branch point**', *Nano Letters* 5, 1519-1523 (2005)

79 W. Fu, S. Qin, L. Liu, T.-H. Kim, S. Hellstrom, W. Wang, W. Liang, X. Bai, A.-P. Li, E. Wang, '**Ferroelectric gated electrical transport in CdS nanotetrapods**', *Nano Letters* 11, 1913-1918 (2011)

80 Y.-W. Jun, S.-M. Lee, N.-J. Kang, J. Cheon, '**Controlled synthesis of multi-armed CdS nanorod architectures using monosurfactant system**', *Journal of the American Chemical Society* 123, 5150-5151 (2001)

81 G. Morello, A. Fiore, R. Mastroia, A. Falqui, A. Genovese, A. Cretì, M. Lomascolo, I.R. Franchini, L. Manna, F. Della Sala, R. Cingolani, M. De Giorgi, '**Temperature and size dependence of the optical properties of tetrapod-shaped colloidal nanocrystals exhibiting type-II transitions**', *Journal of Physical Chemistry C* 115, 18094-18104 (2011)

82 I. Kriegel, J. Rodriguez-Fernandez, A. Wisnet, H. Zhang, C. Waurisch, A. Eychmuller, A. Dubavik, A.O. Govorov, J. Feldmann, '**Shedding light on vacancy-doped copper chalcogenides: shape-controlled synthesis, optical properties, and modeling of copper telluride nanocrystals with near-infrared plasmon resonances**', *ACS Nano* 7, 4367-4377 (2013)

83 J. Wang, A. Singh, P. Liu, S. Singh, C. Caughlan, Y. Guo, K.M. Ryan, '**Colloidal synthesis of Cu<sub>2</sub>SnSe<sub>3</sub> tetrapod nanocrystals**', *Journal of the American Chemical Society* 135, 7835-7838 (2013)

84 F.J. Lopez U. Givan, J.G. Connell, L.J. Lauhon, '**Silicon nanowire polytypes: identification by Raman spectroscopy, generation mechanism, and misfit strain in homostructures**', *ACS Nano* 5, 8958-8966 (2011)

85 M. Ek, B.M. Borg, J. Johansson, K.A. Dick, '**Diameter limitation in growth of III-Sb-containing nanowire heterostructures**', *ACS Nano* 7, 3668-3675 (2013)

---

86 D. Kriegner, C. Panse, B. Mandl, K.A. Dick, M. Keplinger, J.M. Persson, P. Caroff, D. Ercolani, L. Sorba, F. Bechstedt, J. Stangl, G. Bauer, **'Unit cell structure of crystal polytypes in InAs and InSb nanowires'**, *Nano Letters* 11, 1483-1489 (2011)

87 B. Ketterer, M. Heiss, E. Uccelli, J. Arbiol, A. Fontcuberta i Morral, **'Untangling the electronic band structure of wurtzite GaAs nanowires by resonant Raman spectroscopy'**, *ACS Nano*, 5, 7585-7592 (2011)

88 F.-J. Fan, L. Wu, M. Gong, S.Y. Chen, G.Y. Liu, H.-B. Yao, H.-W. Liang, Y.-X. Wang, S.-H. Yu, **'Linearly arranged polytypic CZTSSe nanocrystals'**, *Scientific Reports* 2, 952-957 (2012)

89 E.G. Zhukov, S.A. Mkrtchyan, K.O. Davletov, V.T. Kalinnikov, O.A. Ashirov, **'The CdSe - Cu<sub>2</sub>SnSe<sub>3</sub> system'**, *Russian Journal of Inorganic Chemistry* 27, 426-427 (1982)

90 M.A. Berding, A. Sher, A.-B. Chen, **'Polarity in semiconductor compounds'**, *Physics Review B* 36, 7433-7436 (1987)

91 S. Nakamura, **'Current status of GaN-based solid-state lighting'**, *MRS Bulletin* 34, 101-107 (2009)

92 C. Yang, B. Zhou, S. Miao, C. Yang, B. Cai, W.-H. Zhang, X. Xu, **'Cu<sub>2</sub>Ge(S<sub>3-x</sub>Se<sub>x</sub>) colloidal nanocrystals: synthesis, characterization, and composition-dependent band gap engineering'**, *Journal of the American Chemical Society* 135, 5958-5961 (2013)

93 F.-J. Fan, L. Wu, M. Gong, G.-Y. Liu, Y.-X. Wang, S.-H. Yu, S.Y. Chen, L.-Y. Wang, X.-G. Gong, **'Composition- and band-gap-tunable synthesis of wurtzite-derived Cu<sub>2</sub>ZnSn(S<sub>1-x</sub>Se<sub>x</sub>)<sub>4</sub> nanocrystals: theoretical and experimental insights'**, *ACS Nano* 7, 1454-1463 (2013)

94 D. Wang, C.M. Lieber, **'Nanocrystals branch out'**, *Nature Materials* 2, 355-356 (2003)

95 L. Manna, D.J. Milliron, A. Meisel, E.C. Scher, A.P. Alivisatos, **'Controlled growth of tetrapod-branched inorganic nanocrystals'**, *Nature Materials* 2, 382-385 (2003)

96 W. Qi, J. de Graaf, F. Qiao, S. Marras, L. Manna, M. Dijkstra, **'Ordered two-dimensional superstructures of colloidal octapod-shaped nanocrystals on flat substrates'**, *Nano Letters* 12, 5299-5303 (2012)

97 E. Okunishi, I. Ishikawa, H. Sawada, F. Hosokawa, M. Hori, Y. Kondo, **'Visualization of light elements at ultrahigh resolution by STEM annular bright field microscopy'**, *Microscopy and Microanalysis* 15, 164-165 (2009)

---

98 S.D. Findlay, S. Azuma, N. Shibata, E. Okunishi, Y. Ikuhara, '**Direct oxygen imaging within a ceramic interface, with some observations upon the dark contrast at the grain boundary**', *Ultramicroscopy* 111, 285-289, (2011)

99 S.D. Findlay, N. Shibata, H. Sawada, E. Okunishi, Y. Kondo, Y. Ikuhara, '**Dynamics of annular bright field imaging in scanning transmission electron microscopy**', *Ultramicroscopy* 110, 903-923 (2010)

100 R. Ishikawa, E. Okunishi, H. Sawada, Y. Kondo, F. Hosokawa, E. Abe, '**Direct imaging of hydrogen-atom columns in a crystal by annular bright-field electron microscopy**', *Nature Materials* 10, 278-281 (2011)

101 J. Arbiol, C. Magen, P. Becker, G. Jacopin, A. Chernikov, S. Schäfer, F. Furtmayr, M. Tchernycheva, L. Rigutti, J. Teubert, S. Chatterjee, J.R. Morante, M. Eickhoff, '**Self-assembled GaN quantum wires on GaN/AlN nanowire templates**', *Nanoscale* 4, 7517-7524 (2012)

102 F. Schuster, B. Laumer, R. Zamani, C. Magen, J.R. Morante, J. Arbiol, M. Stutzmann, '**p-GaN/n-ZnO heterojunction nanowires for UV-LEDs and laser diodes**', *Nano Letters* 13, Submitted (2013)

103 L. Carbone, S. Kudera, E. Carlino, W.J. Parak, C. Giannini, R. Cingolani, L. Manna, '**Multiple wurtzite twinning in CdTe nanocrystals induced by methylphosphonic acid**', *Journal of the American Chemical Society* 128, 748-755 (2006)

104 <http://departments.icmab.es/gaen/research>

105 J.M. Luther, P.K. Jain, T. Ewers, A.P. Alivisatos, '**Localized surface plasmon resonances arising from free carriers in doped quantum dots**', *Nature Materials* 10, 361-366 (2011)

106 W.-H. Li, R. Zamani, M. Ibáñez, D. Cadavid, A. Shavel, J.R. Morante, J. Arbiol, A. Cabot, '**Metal ions to control the morphology of semiconductor nanoparticles: Copper selenide nanocubes**', *Journal of the American Chemical Society* 135, 4664-4667 (2013)

107 W.-H. Li, R. Zamani, P. Rivera Gil, B. Pelaz, M. Ibáñez, D. Cadavid, A. Shavel, R.A. Alvarez-Puebla, W.J. Parak, J. Arbiol, A. Cabot, '**CuTe nanocrystals: Shape and size control, plasmonic properties, and use as SERS probes and photothermal agents**', *Journal of the American Chemical Society* 135, 7098-7101 (2013)

108 I. Kriegel, C. Jiang, J. Rodríguez-Fernández, R.D. Schaller, D.V. Talapin, E. da Como, J. Feldmann, '**Tuning the excitonic and plasmonic**

---

**properties of copper chalcogenide nanocrystals**, *Journal of the American Chemical Society* 134, 1583-1590 (2012)

109 R.R. Zamani, M. Ibáñez, M. Luysberg, N. Garcia-Castello, L. Houben, J.D. Prades, R. Dunin-Borkowski, J.R. Morante, A. Cabot, J. Arbiol, '**Polytypic and polarity-directed branching in Cu-based quaternary nanostructures**', To be submitted, (2013)

110 I.D. Olekseyuk, O.V. Marchuk, L.D. Gulay, O.Y. Zhibankov, '**Isothermal section of the Cu<sub>2</sub>Se-HgSe-GeSe<sub>2</sub> system at 670 K and crystal structures of the compounds Cu<sub>2</sub>HgGeSe<sub>4</sub> and HT-modification of Cu<sub>2</sub>HgGeSe<sub>4</sub>**', *Journal of Alloys and Compounds* 398, 80-84 (2005)

111 W.-H. Li, M. Ibáñez, D. Cadavid, R. Zamani, J. Rubio-Garcia, S. Gorsse, J.R. Morante, J. Arbiol, A. Cabot, '**Colloidal synthesis and functional properties of quaternary Cu-based semiconductors: Cu<sub>2</sub>HgGeSe<sub>4</sub>**', Submitted (2013)

112 R. Zamani, R. Fiz, J. Pan, T. Fishcher, S. Mathur, J.R. Morante, J. Arbiol, '**Oxide-oxide nanojunctions in coaxial SnO<sub>2</sub>/TiO<sub>2</sub>, SnO<sub>2</sub>/V<sub>2</sub>O<sub>3</sub> and SnO<sub>2</sub>/(Ti<sub>0.5</sub>V<sub>0.5</sub>)<sub>2</sub>O<sub>3</sub> nanowire heterostructures**', *CrystEngComm* 15, 4532-4539 (2013)

113 J.-S. Lee, M.I. Bodnarchuk, E.V. Shevchenko, D.V. Talapin, '**"Magnet-in-the-semiconductor" FePt-PbS and FePt-PbSe nanostructures: magnetic properties, charge transport, and magnetoresistance**', *Journal of the American Chemical Society* 132, 6382-6391 (2010)

114 J.J. Urban, D.V. Talapin, E.V. Shevchenko, C.R. Kagan, C.B. Murray, '**Synergism in binary nanocrystal superlattices leads to enhanced p-type conductivity in self-assembled PbTe/Ag<sub>2</sub>Te thin films**', *Nature Materials* 6, 115-121 (2007)

115 M. Ibáñez, R. Zamani, S. Gorsse, J.D. Fan, S. Ortega, D. Cadavid, J.R. Morante, J. Arbiol, A. Cabot, '**Core-shell nanoparticles as building blocks for the bottom-up production of functional nanocomposites: PbTe-PbS thermoelectric properties**', *ACS Nano* 7, 2573-2586 (2013)

116 W. Ma, J.M. Luther, H. Zheng, Y. Wu, A.P. Alivisatos, '**Photovoltaic devices employing ternary PbS<sub>x</sub>Se<sub>1-x</sub> nanocrystals**', *Nano Letters* 9, 1699-1703 (2009)

117 M.S. Dresslhaus, Y.M. Lin, S.B. Cronin, O. Rabin, M.R. Black, G. Dresslhaus, T. Koga '**Chapter 1: Quantum wells and quantum wires for potential thermoelectric applications**', *Semiconductors and Semimetals* 71, 1-121 (2001)

---

118 E.I. Rogacheva, I.M. Krivulkin, O.N. Nashchekina, Y. Sipatov, V.V. Volobuev, M.S. Dresselhaus, **‘Effect of oxidation on the thermoelectric properties of PbTe and PbS epitaxial films’**, *Applied Physics Letters* 78, 1661-1663 (2001)

119 G.D. Mahan, **‘Good thermoelectrics’**, *Solid State Physics* 51, 81-157 (1997)

120 L. Peng-Xian, Q. Ling-Bo, **‘Electronic structure, lattice dynamics and thermoelectric properties of PbTe from first-principles calculation’**, *Chinese Physics Letters* 30, 017101 (2013)

121 J.E. Murphy, M.C. Beard, A.G. Norman, S.P. Ahrenkiel, J.C. Johnson, P. Yu, O.I. Micic, R.J. Ellingson, A.J. Nozik, **‘PbTe colloidal nanocrystals: synthesis, characterization, and multiple exciton generation’**, *Journal of the American Chemical Society* 128, 3241-3247 (2006)

122 L. Kungumadevi, R. Sathyamoorthy, **‘Structural, optical and electrical properties of solvothermally synthesized PbTe nanodisks’**, *Advanced Powder Technology* 24, 218-223 (2013)

123 N.M. Ravindra, V.K. Srivastava, **‘Properties of PbS, PbSe, and PbTe’**, *Physica Status Solidi A* 58, 311-316 (1980)

124 V. Leute, H.J. Köller, **‘The four quasibinary phase diagrams of the quasiternary system (Hg,Pb) (Se,Te)’**, *Zeitschrift für Physikalische Chemie* 149, 213-227 (1986)

125 K.S. Sun, C.B. Murray, D. Weller, L. Folks, A. Moser, **‘Monodisperse FePt nanoparticles and ferromagnetic FePt nanocrystal superlattices’**, *Science* 287, 1989-1992 (2000)

126 K. Aissou, T. Alnasser, G. Pecastaings, G. Goglio, O. Toulemonde, S. Mornet, G. Fleury, G. Hadziioannou, **‘Hierarchical assembly of magnetic L1<sub>0</sub>-ordered FePt nanoparticles in block copolymer thin films’**, *Journal of Materials Chemistry C* 1, 1317-1321 (2013)

127 Y. Liu, J. Wang, Y. Du, L. Zhang, D. Liang, **‘Mobilities and diffusivities in fcc Fe-X (X= Ag, Au, Cu, Pd and Pt) alloys’**, *Calphad* 34, 253-262 (2010)

128 A.P. Miodownik, **‘The Invar behaviour of iron-nickel-platinum alloys’**, *Journal of Magnetism and Magnetic Materials* 10, 126-135 (1979)

129 S. Nakajima, **‘The crystal structure of Bi<sub>2</sub>Te<sub>3-x</sub>Se<sub>x</sub>’**, *Journal of Physics and Chemistry of Solids* 24, 479-485 (1963)

---

130 Y. Feutelais, B. Legendre, N. Rodier, V. Agafonov, 'A study of the phases in the bismuth - tellurium system', *Materials Research Bulletin* 28, 591-596 (1993)

131 R.F. Brebrick, 'Characterization of phases in the 50-60 at. % Te region of the Bi-Te system by X-ray powder diffraction patterns', *Journal of Applied Crystallography* 1, 241-246 (1968)

132 K. Yamana, K. Kihara, T. Matsumoto, 'Bismuth tellurides: BiTe and Bi<sub>4</sub>Te<sub>3</sub>', *Acta Crystallographica B* 35, 147-149 (1979)

133 R. Chami, G. Brun, J.C. Tedenac, M. Maurin, 'Contribution to the study of the ternary-system lead-bismuth-tellurium - study of the PbTe-Bi<sub>2</sub>Te<sub>3</sub> section', *Revue de Chimie Minerale* 20, 305-313 (1983)

134 I.I. Petrov, R.M. Imamov, 'Electron-diffraction analysis of PbTe-Bi<sub>2</sub>Te<sub>3</sub> system phases', *Kristallografiya* 14, 699-703 (1969)

135 T.B. Zhukova, A.I. Zaslavskii, 'Crystal structures of the compounds PbBi<sub>4</sub>Te<sub>7</sub>, PbBi<sub>2</sub>T<sub>4</sub>, SnBi<sub>4</sub>Te<sub>7</sub>, SnBi<sub>2</sub>Te<sub>4</sub>, SnSb<sub>2</sub>Te<sub>4</sub>, and GeBi<sub>4</sub>Te<sub>7</sub>', *Soviet Physics, Crystallography* 16, 796-796 (1972)

136 A. Popescu, A. Datta, G. S. Nolas, L. M. Woods, 'Thermoelectric properties of Bi-doped PbTe composites', *Journal of Applied Physics* 109, 103709 (2011)

137 E. Rogacheva, O. Vodoretz, V. Pinegin, O. Nashchekina, 'Evidence for self-organization processes in PbTe-Bi<sub>2</sub>Te<sub>3</sub> semiconductor solid solutions', *Journal of Materials Research* 26, 1627-1633 (2011)

138 W. Tamura, A. Yasuda, K. Suto, M. Hosokawa, O. Itoh, J.-I. Nishizawa, 'Properties of Bi-doped PbTe layers grown by liquid phase epitaxy under controlled Te vapor pressure', *Journal of Electronic Materials* 32, 1079-1084 (2003)

139 Y. Noda, K. Matsumoto, S. Ohba, Y. Saito, K. Toriumi, Y. Iwata, I. Shibuya, 'Temperature dependence of atomic thermal parameters of lead chalcogenides, PbS, PbSe and PbTe', *Acta Crystallographica C* 43, 1443-1445 (1987)

140 T.K. Chattopadhyay, H.G. von Schnering, W. Grosshans, W.B. Holzapfel, 'High pressure X-ray diffraction study on the structural phase transitions in PbS, PbSe and PbTe with synchrotron radiation', *Physica B+C* 139, 356-360 (1986)

---

141 H. Berger, H.H. Niebsch, A. Szczerbakow, '**Lattice parameters in the solid-solution system  $\text{PbS}_x\text{Se}_{1-x}$** ', *Crystal Research and Technology* 20, K8-K10 (1985)

142 D.B. Williams, C.B. Carter, '**Transmission Electron Microscopy, A Textbook for Materials Science**', Second edition (2009)

143 M. Scheele, N. Oeschler, I. Veremchuk, S.O. Peters, A. Littig, A. Kornowski, C. Klinke, H. Weller, '**Thermoelectric properties of lead chalcogenide core-shell nanostructures**', *ACS Nano* 5, 8541-8551 (2011)

144 E.J.D. Klem, D.D. MacNeil, L. Levina, E.H. Sargent, '**Solution processed photovoltaic devices with 2% infrared monochromatic power conversion efficiency: performance optimization and oxide formation**', *Advanced Materials* 20, 3433-3439 (2008)

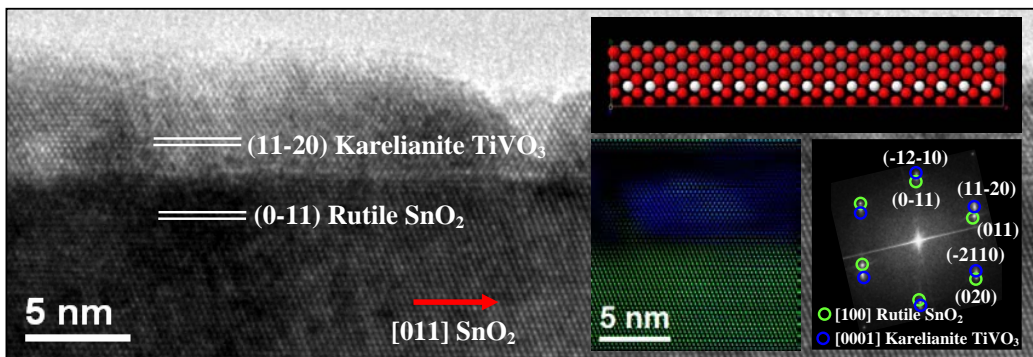
145 J. Rupp, R. Birringer, '**Enhanced specific-heat-capacity ( $c_p$ ) measurements (150-300 K) of nanometer-sized crystalline materials**', *Physical Review B* 36, 7888-7890 (1987)

146 J. Adachi, K. Kurosaki, M. Uno, S. Yamanaka, '**Effect of porosity on thermal and electrical properties of polycrystalline bulk ZrN prepared by spark plasma sintering**', *Journal of Alloys and Compounds* 432, 7-10 (2007)



# CHAPTER IV

## COAXIAL NANOJUNCTIONS: METAL OXIDE HETEROSTRUCTURED NANOWIRES





## 4.1 Introduction

Metal oxide (MOX) nanowires (NWs) and nanorods (NRs) have attracted a dramatic surge of interests in recent years. Their novel properties, which are distinctive from conventional bulk and thin film materials, carry promising potential for new applications<sup>1</sup> such as piezoelectrics,<sup>2-4</sup> thermoelectrics,<sup>5</sup> electronics and photonics,<sup>6-14</sup> sensing devices<sup>15-20</sup> and especially gas sensors.<sup>21-25</sup>

Usually, the use of 1-dimensional (1D) structures in nanodevices provides a more efficient charge carrier transfer due to their unique geometry. The direct electrical pathways provided along the axial direction ensure the rapid and efficient transfer to the external electrical contact. On the other hand, holes move across the radial direction towards their surface and/or interface under the effects of the electrical field associated with the surface depletion zone, despite the short diffusion length. Therefore, the surface properties of nanostructures become especially important to the overall charge collection efficiency since they can influence the recombination rate and the chemical reaction dynamics taking place at the surface.

Additionally, nanojunctions created by different structure nanoengineering, such as attaching nanoparticles (NPs) or quantum dots (QDs) on the NWs,<sup>26-28</sup> or adding overlayers (shells) in order to produce coaxial heterostructures,<sup>29-31</sup> open new ways towards achieving enhanced physical and functional properties.

Advanced electron microscopy techniques have thus a preeminent role in state-of-the-art materials science. Recent developments in electron microscopy, such as aberration correctors and monochromators are allowing us to reach sub-angstrom and sub-eV, spatial and energy resolutions, respectively. In addition to these advances, the possibility to obtain 3D models of our nanostructures by

means of electron tomography, have shown that electron microscopy related techniques are the most promising to fully characterize complex nanostructures even at atomic scale. In the present chapter we show how advanced electron microscopy techniques can be applied to obtain a deeper characterization of complex structures in heterostructured nanowires.

### 4.1.1 Metal oxide nanowires

Among all, metal oxide (MOX) nanowires are versatile nanostructured materials with diverse yet unique properties. Potentially, they can be widely used in various applications of electrical, chemical and semiconductor technologies.<sup>32-36</sup> Research interests in metal oxide nanowires commenced in 1990s. Considerable number of reports can be found by now on various 1D nanocrystalline structured nanowires of various metal oxides, such as CuO,<sup>37</sup> MgO,<sup>38</sup> ZnO,<sup>39-42</sup> SnO<sub>2</sub>,<sup>43,44</sup> TiO<sub>2</sub>,<sup>45-49</sup> V<sub>2</sub>O<sub>5</sub>,<sup>50,51</sup> Al<sub>2</sub>O<sub>3</sub>,<sup>52,53</sup> Ga<sub>2</sub>O<sub>3</sub>,<sup>54</sup> In<sub>2</sub>O<sub>3</sub>,<sup>55</sup> Sb<sub>2</sub>O<sub>5</sub>,<sup>56</sup> BaTiO<sub>3</sub>,<sup>57</sup> etc. The methodology of synthesis is now well developed. Reported techniques mostly include vapor-solid phase technique, chemical solution deposition (sol-gel), template etching, precipitation, micro-emulsion, flux growth and others. Growth mechanisms are out of the scope of this work, however, one can find important information about them in literature.<sup>58</sup>

### 4.1.2 Why heterostructure?

Firstly, we should clarify the reasons to produce heterostructured NWs. Basically, most of the aforementioned NWs have novel properties by themselves, yet improved by creating nanojunctions. Nanojunctions can take advantage of surface properties. As an example, coating SnO<sub>2</sub> NWs with an overlayer shell of titanium/vanadium oxide provides outstandingly efficient charge performances related to the heterostructure properties: allowing the control over the surface recombination as well as the chemical reaction kinetics and the charge transfer through the coaxial formed junction.<sup>59</sup>

In this scenario, core-shell coaxial 1D nanostructures of metal oxides, based on adequate cores and suitable shells, allow:

- (i) The use of cores with predetermined properties, mainly related to free carrier concentration and optical band gap of nano-SnO<sub>2</sub>.
- (ii) The control over core and/or shell doping, which determines, on the one hand, the global electrical properties of the coaxial heterostructure formed and, on the other hand, the radial electric

field distribution.<sup>60</sup> Moreover, band discontinuities also contribute to the control over the effective electrical mobility and crystallographic quality of the interface.

- (iii) The design of an adequate shell with high density of surface chemical reaction sites and required lattice matching with the core, which facilitate their interaction.<sup>14,30</sup>

As another example of advantages of heterostructures in nanoscale, production of p-n junctions is remarkable. The schematic illustration of Figure 4.1 reveals radial and axial p-n junctions and how the band gap and Fermi level can be engineered. These heterostructures, especially coaxial ones, have been used widely in photovoltaic devices.<sup>61-64</sup>

Furthermore, in the case of NPs on NWs (one n-type and the other p-type semiconductor) for gas sensing, selectivity and sensibility of the device to particular gases are improved, because after exposure to this gas, the function of the p-n junction effectively changes the conduction section in the nanowire, leading to a significant improvement of the conductivity, and as a result, enhancement of the sensor signal.<sup>26</sup>

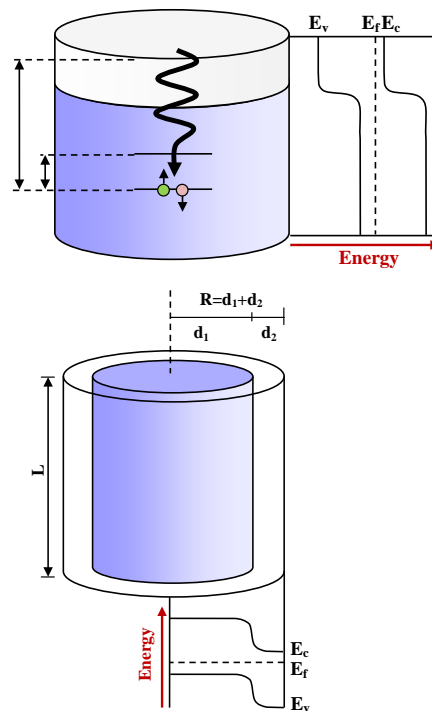


**Figure 4.1** Schematic illustration of (a) radial and (b) coaxial heterostructures which create p-n junctions

### 4.1.3 The p-n junction

A p-n junction (Figure 4.2), essential to most semiconductor devices, is a single semiconductor crystal that has been selectively doped so that one region is n-type material and the adjacent region is p-type material. If we assume that the junction has been formed mechanically by jamming together a bar of n-type semiconductor and a bar of p-type semiconductor, thus, the transition from one region to the other is perfectly sharp, occurring at a single junction plane.

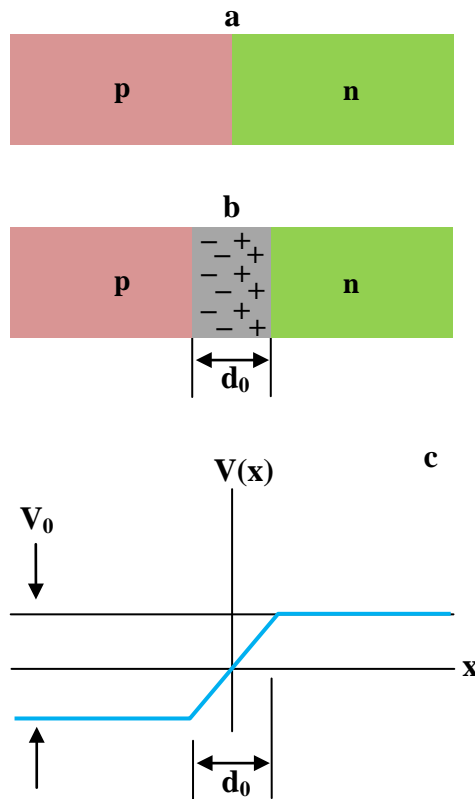


**Figure 4.2** A p-n junction

However, a ‘*depletion zone*’ (sometimes called as membrane) usually occurs in the junction. Electrons on the n side, that are close to the junction plane tend to diffuse across it (from right to left in the figure) and into the p side, where there are very few free electrons. Similarly, holes on the p side that are close to the junction plane tend to diffuse across that plane (from left to right) and into the n side, where there are very few holes. The motions of both the electrons and the

holes contribute to a ‘diffusion current’  $I_{\text{diff}}$ , conventionally directed from left to right as indicated in Figure 4.2.

Recall that the n-side is studded throughout with positively charged donor ions, fixed firmly in their lattice sites. Normally, the excess positive charge of each of these ions is compensated electrically by one of the conduction-band electrons. When an n-side electron diffuses across the junction plane, however, the diffusion ‘uncovers’ one of these donor ions, thus introducing a fixed positive charge near the junction plane on the n side. When the diffusing electron arrives on the p side, it quickly combines with an acceptor ion (which lacks one electron), thus introducing a fixed negative charge near the junction plane on the p side.

In this way electrons diffusing through the junction plane from right to left in Figure 4.2 result in a buildup of space charge on each side of the junction plane, as indicated. Holes diffusing through the junction plane from left to right have exactly the same effect. The motions of both majority carriers, electrons and holes, contribute to the buildup of these two space charge regions, one positive and one negative. These two regions form a depletion zone, so named because it is relatively free of mobile charge carriers.

The buildup of space charge generates an associated contact potential difference  $V_0$  across the depletion zone, as Figure 4.2(c) shows. This potential difference limits further diffusion of electrons and holes across the junction plane. Negative charges tend to avoid regions of low potential. Thus, an electron approaching the junction plane from the right in Figure 4.2(b) is moving toward a region of low potential and would tend to turn back into the n side. Similarly, a positive charge (a hole) approaching the junction plane from the left is moving toward a region of high potential and would tend to turn back into the p side. Nevertheless, in p-type material there are minorities of opposite charges in each side. Although the potential difference  $V_0$  in Figure 4.2(c) acts as a barrier for the majority carriers, it is a downhill trip for the minority carriers. Positive charges (holes) tend to seek regions of low potential; negative charges (electrons) tend to seek regions of high potential. Thus, both types of minority carriers are swept across the junction plane by the contact potential difference and together constitute a ‘drift current’  $I_{\text{drift}}$  across the junction plane from right to left. Thus, an isolated p-n junction is in an equilibrium state in which a contact potential difference  $V_0$  exists between its ends. At equilibrium, the average diffusion current  $I_{\text{diff}}$  that moves through the junction plane from the p side to the n side is just balanced by an average drift current  $I_{\text{drift}}$  that moves in

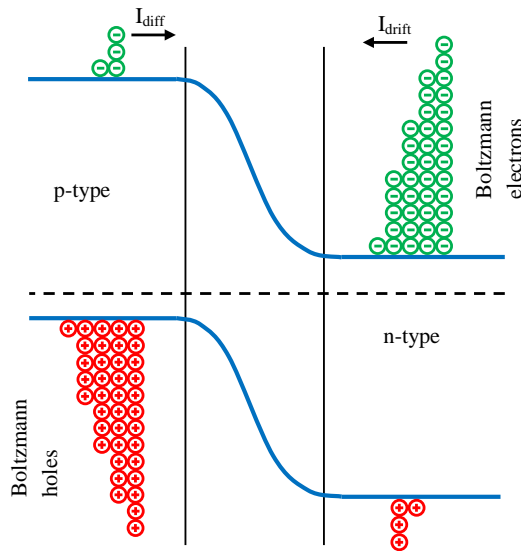


**Figure 4.3** The band structure in a p-n junction

the opposite direction. These two currents cancel because the net current through the junction plane must be zero; otherwise charge would be transferred without limit from one end of the junction to the other.<sup>65,66</sup>

In Figure 4.3 the ‘band-bending’ which occurs in the transition region (depletion zone) of a p-n junction is analyzed. If the flux of incident electrons is presented by a current  $J_0$ , and the thermal fraction is given by Boltzmann factor  $\exp(-\phi_B/kT)$ , and the electron current to the p side is given by:

$$I_{diff} = I_0 \exp(-\phi_B/kT) \quad (4.1)$$

$\phi_B$  is the barrier height,  $k$  is the Boltzmann constant, and  $T$  is the temperature. In the absence of an external bias, no current flows across the junction, which is due to the opposite current ( $I_{drift}$ ), arisen by thermal excitation or generation of the small amount of electrons in the p-type region sliding down the barrier from right to left. Meanwhile, the electrons give their kinetic energy to the lattice in the heat.

$$I_{diff} = I_{drift} \quad (4.2)$$

Now if a positive voltage is applied to the p side and a negative voltage to the n side, chemical potentials will have the following equilibrium:

$$\mu_n = \mu_p + eV \quad (V > 0) \quad (4.3)$$

and the barrier height reduces to  $\phi_B - eV$ :

$$I_{\text{diff}}(V>0) = I_0 \exp[-(\phi_B - eV)/kT] = I_{\text{diff}}(0) \exp(eV/kT) \quad (4.4)$$

while the backflow current remains unchanged:

$$I_{\text{drift}}(V>0) = I_{\text{drift}}(0) \quad (4.5)$$

Therefore, the total current ( $I = I_{\text{drift}} + I_{\text{diff}}$ ) is given by:

$$I(V>0) = I_0[\exp(eV/kT) - 1] \quad (4.6)$$

where  $I_0$  is a constant characteristic of the p-n junction. However, equation (4.6) describes the behavior of an ideal p-n junction, which is not always the case in practice.<sup>67</sup>

The p-n junction represents a system of charged particles in diffusive equilibrium in which the electrochemical potential is constant and independent of position. The electrochemical potential describes an average energy of electrons and is represented by the Fermi energy ( $E_f$ ). It means that under equilibrium conditions the Fermi level has constant position in the band diagram of the p-n junction (the blue dash line in Figure 4.3).

#### 4.1.4. Some applications

MOX NWs, as fantastic candidates for creating p-n junctions, are widely used for many different applications such as electronics, optoelectronics, thermoelectrics, sensing, etc. Due to the main point of the nanostructure study of this chapter, we only give a brief introduction on two of them: photovoltaics and gas sensing.

##### 4.1.4.1 Photovoltaics

Concerning the daily-increase of demand for energy and limits of the traditional energy sources such as fossil fuels, on the one hand, and our duty to conserve the environment, on the other hand led many researchers for decades to dedicate their effort to discovering new sources of energy which do not harm the ecosystem.

The working principle of today solar cells is essentially the same, based on the '*photovoltaic effect*' which means generation of a potential difference at the junction of two different materials in response to visible or other radiation. The basic processes behind the photovoltaic effect are:

(i) Generation of the charge carriers due to the absorption of photons in the materials that form a junction

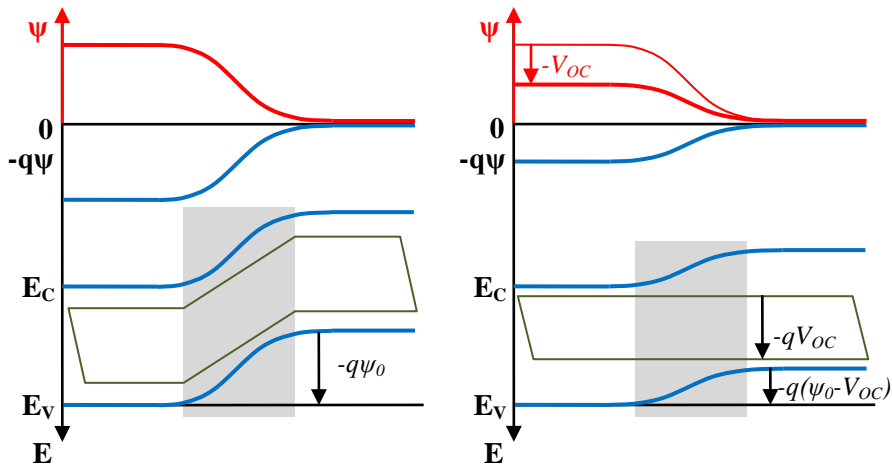


**Figure 4.4** The band structure in a p-n junction (left) in normal situation and (right) when illuminated

- (ii) Subsequent separation of the photo-generated charge carriers in the junction
- (iii) Collection of the photo-generated charge carriers at the terminals of the junction.

When a p-n junction is illuminated, additional electron-hole pairs are generated in the semiconductor. The concentration of minority carriers (electrons in the p-type region and holes in the n-type region) strongly increases. This increase in the concentration of minority carriers leads to the flow of the minority carriers across the depletion region into the quasi-neutral regions. Electrons flow from the p-type into the n-type region and holes from the n-type into the p-type region. The flow of the photo-generated carriers causes the so-called ‘photo-generation current’,  $I_{ph}$ , which adds to the ‘thermal-generation current’,  $I_{gen}$ . When no external contact between the n-type and the p-type regions is established, which means that the junction is in the open-circuit condition, no net current can flow inside the p-n junction; meaning that the current resulting from the flux of photo-generated and thermally-generated carriers has to be balanced by the opposite recombination current. The recombination current will increase through lowering of the electrostatic potential barrier across the depletion region.

This situation of the illuminated p-n junction under open-circuit condition using the band diagram is presented in Figure 4.4(a). The electrostatic-potential

barrier across the junction is lowered by an amount of  $V_{oc}$ . We refer to  $V_{oc}$  as the open-circuit voltage. Under nonequilibrium conditions the concentrations of electrons and holes are described by the quasi-Fermi energy levels. It is illustrated in Figure 4.4(a) that the electrochemical potential of electrons, denoted by  $E_{FC}$ , is higher in the n-type region than in the p-type region by an amount of  $q V_{oc}$ . This means that a voltmeter will measure a voltage difference of  $V_{oc}$  between the contacts of the p-n junction. Under illumination, when the n-type and p-type regions are short circuited, the photo-generated current will also flow through the external circuit. This situation is illustrated in Figure 4.4(b). Under the short-circuit condition the electrostatic potential barrier is not changed, but from a strong variation of the quasi-Fermi levels inside the depletion region one can determine that the current is flowing inside the semiconductor.

When a load is connected between the electrodes of the illuminated p-n junction, only a fraction of the photo-generated current will flow through the external circuit. The electrochemical potential difference between the n-type and p-type regions will be lowered by a voltage drop over the load. This in turn lowers the electrostatic potential over the depletion region which results in an increase of the recombination current. The net current flowing through the load is determined as the sum of the photo- and thermal generation currents and the recombination current (the superposition approximation). The voltage drop at the load can be simulated by applying a forward-bias voltage to the junction, therefore equation 4.6, which describes the behavior of the junction under applied voltage, is included to describe the net current of the illuminated p-n junction.<sup>68</sup>

$$I(V>0) = I_0[\exp(eV/kT) - 1] - I_{ph} \quad (4.7)$$

#### 4.1.4.2 Gas sensing

Essentially, three points are of paramount importance in gas sensing: (i) stability, (ii) selectivity, and (iii) sensibility. Long-term stability had been an issue for many years in gas sensing industry. Moreover, the device should show response only to the specific gases to which the response is desired. Also the sensibility of the device, in some critical situations, is considered as a limiting issue in their applications. During the last decade, nanostructured materials have dramatically improved the performance of gas sensors, by exhibiting longer lifetime, enhancing the selectivity, and/or being more sensible.

The fundamental sensing mechanism of metal oxide-based gas sensors relies on changes in electrical conductivity due to the interaction process between the surface complexes such as  $O^-$ ,  $O_2^-$ ,  $H^+$ , and  $OH^-$  reactive chemical species and the gas molecules to be sensed. Göpel<sup>69</sup> discussed in detail the charge transfer in chemisorptions which is the basic principle of gas sensing mechanism. Briefly, when a molecule adsorbs at the surface electrons can be transferred to this molecule if the lowest lying unoccupied molecular orbitals of the adsorbate complex lie below the Fermi level (acceptor levels) of the solid, and vice versa, electrons are donated to the solid if the highest occupied orbitals lie above the Fermi-level of the solid (donor levels). Thus, molecular adsorption may result in a net charge at the surface causing an electric field. This electrostatic field causes a bending of the energy bands in the solid. A negative surface charge bends the bands upward, i.e. pushes the Fermi level into the band gap of the solid, effectively reducing the charge carrier concentration and resulting in an electron depletion zone. Depleting electrons causes a positive space charge region that compensates for the negative surface charge. This is illustrated in Figure 4.5 on the example of negatively charged chemisorbed adsorbate.<sup>70</sup>

The first gas sensors based on 1D MOX were fabricated by Comini and coworkers in 2002.<sup>71</sup> They made gas sensors based on  $SnO_2$  nanobelts (Figure 4.6) with extremely high sensitivity to polluting gaseous species such as CO and

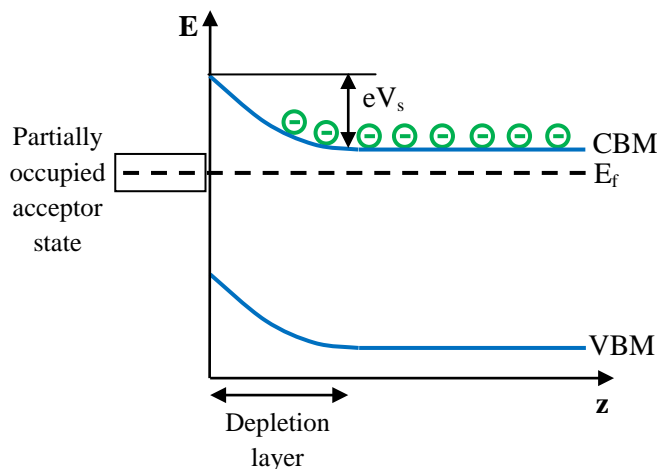


**Figure 4.5** Schematic representation of band bending in the near surface region of an n-type semiconductor induced by a (partially) filled donor state of an adsorbed molecule

$\text{NO}_2$  for environmental applications, as well as for ethanol for breath analyzers and food control applications. Years after, Hernández-Ramírez *et al.* produced single  $\text{SnO}_2$  NWs gas sensors (Figure 4.7) which were able to detect CO gas and humidity with high sensibility.<sup>72</sup>

In this scenario, p-n junctions in nanoscale, for instance p-NPs on n-NWs (Figure 4.8), are expected to exhibit enhanced sensibility, while the depletion zone with proper Fermi level can be the clue to such enhancement.<sup>26</sup> This will be explained in section 4.3.

#### 4.1.5 Growth methods and mechanisms

There are many growth methods for metal oxide NWs in the literature, including wet chemical/electrochemical methods,<sup>14,73,74</sup> templating methods,<sup>75</sup>

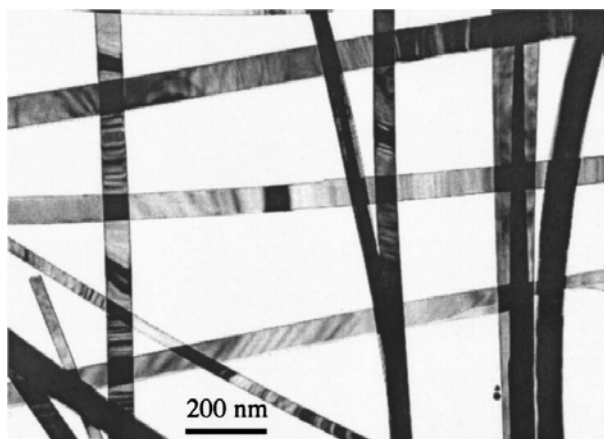


**Figure 4.6** TEM micrograph of  $\text{SnO}_2$  nanobelts<sup>71</sup>

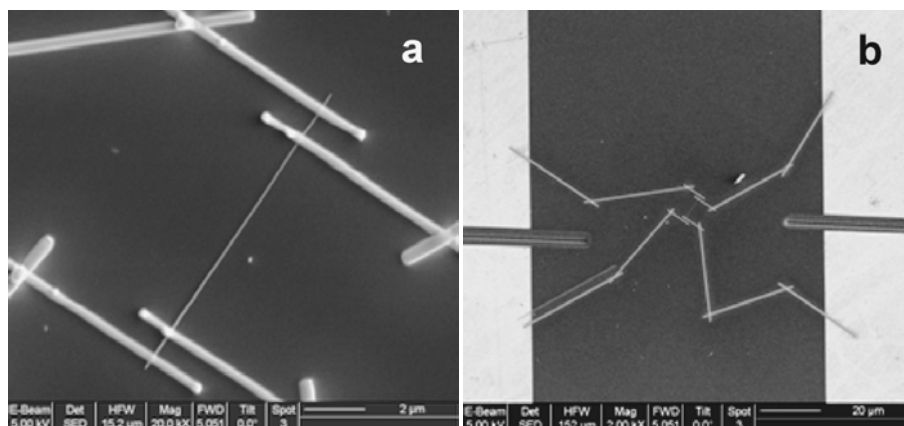


**Figure 4.7** SEM micrographs of a single- $\text{SnO}_2$ -NW gas sensor<sup>72</sup>

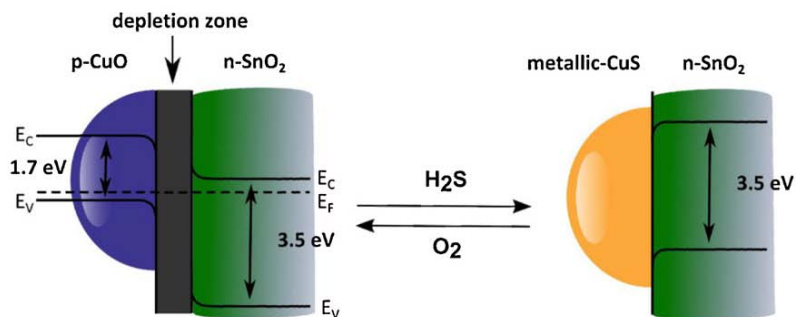


**Figure 4.8** p-n junction function in a gas sensor

thermal decomposition,<sup>76</sup> anodization,<sup>77</sup> thermal oxidation,<sup>78,79</sup> and electrospinning.<sup>80</sup> In this section, we give a brief introduction to some of these methods which have been used to prepare the NWS of this chapter: electrochemical growth, thermal oxidation, and chemical vapor deposition (CVD) as a thermal decomposition method.

Concerning the presence of catalysts, growth mechanism can be divided into two categories: (i) catalyst-free, and (ii) catalyst assisted growth. On the other hand, concerning the growth environments, they can be classified as: (i) solution phase growth, and (ii) vapor phase growth. Each of the mechanisms has its advantages and disadvantages, which will be discussed briefly in the following. Depending on both mentioned parameters, i.e. presence of catalyst and growth environment, different growth mechanisms occur: solution-liquid-solid (SLS), vapor-solid (VS), and vapor-liquid-solid (VLS).

#### 4.1.5.1 Electrochemical growth

Electrochemical growth is the method that we used to produce ZnO NWS. ZnO NWS can also be prepared by vapor-phase transport,<sup>81</sup> pulsed laser deposition (PLD)<sup>82,83</sup> and CVD.<sup>84</sup> But among all, electrochemical growth, as a solution phase method, is low-cost and scalable. As additional advantages, in this method one does not require seeds neither high temperatures (80-90 °C) while the growth rate is relatively fast.<sup>14</sup>

The solution-based growth with presence of catalyst mostly follows SLS mechanism which is similar to the VLS, in this case a nanometer-scale metallic droplet catalyze the precursors decomposition and crystalline nanostructure growth. SLS mechanism was first discovered in the mid-1990 and years after it was utilized to produce nanowires and nanotubes.<sup>85</sup> Lee and Geer reported on details of SLS growth of Si NWS.<sup>86</sup> However, in electrochemical growth of this

work no catalyst or seed has been used, thus, the mechanism does not seem to be SLS. The applied potential separates the anion and cation. ZnO NWs grow at the cathode from the preferential  $\text{Zn}(\text{OH})_2$  decomposition at the polar {0001} surfaces of the ZnO.

#### ***4.1.5.2 Thermal oxidation***

In this study, CuO NWs were prepared grown by thermal oxidation of metallic Cu thin layer deposited by sputtering on various substrates. This approach has many advantages. It mainly consists in a tubular furnace working in atmospheric pressure, without the need of vacuum equipment. It has a high yield with no risk of cross contamination due to the low temperature processing (from 300 °C to 400 °C). It is even possible to selectively pattern the nanowire area on the device substrate.<sup>87</sup> Moreover, the reproducibility of the devices is increased, because all the deposition steps could be done automatically without the operator contribution, and all these steps can be easily scaled up and integrated in a large-scale production.

Thermal oxidation of CuO NWs follows vapor-solid (VS) mechanism.<sup>88</sup> In a typical VS process, the vapor species is generated by evaporation, oxidation, reduction or other gaseous reactions. These species are then condensed onto the surface of a solid substrate in a temperature zone lower than that of the source material. 1D nanostructures growth will proceed without the need of a metal nanoparticle catalyst if the supersaturation is kept at a controlled low level.

The VS transformation growth occurs in many catalyst-free growth processes. Under high temperature condition, source materials are vaporized and then directly condensed on the substrate placed in the low temperature region. Generally, once the condensation process happens, the initially condensed molecules form seed crystals serving as the nucleation sites. As a result, they facilitate directional growth to minimize the surface energy. This self-catalytic growth associated with many thermodynamic parameters is a rather complicated process that needs quantitative modeling. For example, Sberveglieri and coworkers reported on indium oxide.  $\text{In}_2\text{O}_3$  nanowires were synthesized through thermal evaporation of pure  $\text{In}_2\text{O}_3$  powders and the effect of substrate seeding was studied for controlling density distribution and lateral dimensions of the nanowires. The nanowires exhibited uniform section, atomically sharp lateral facets, and pyramidal termination, typical of a VS growth mechanism assisted by oxidized nanocrystalline seeds.<sup>89</sup>

### 4.1.5.3 Chemical vapor deposition

Chemical Vapor Deposition (CVD) is an appropriate method for 1D metal oxide nanostructure synthesis due to its impressive advantages, such as capability of producing highly pure materials with high adhesion to the substrate, fast growth, high control on crystal structure, morphology and orientation (for nanostructures), ability of using a wide range of chemical precursors, reasonable process cost, and reproducibility of the syntheses.<sup>90</sup>

Beside conventional CVD, so called thermally activated CVD (TACVD), there are some other methods which use initiating energies other than heat and can activate the chemical reactions and help the deposition process, e.g. plasma-enhanced CVD (PECVD), photo-assisted CVD (PACVD), and laser-assisted CVD (LACVD) which instead of thermal energy use plasma, light, and laser energy, respectively. Flame-assisted CVD (FACVD) and electrochemical vapor deposition (EVD) are other types of CVD which have succeeded as well as the other ones.

A schematic image of the CVD process is shown in figure 4.9. The incoming atoms from the gas phase (adatoms) interact with the surface and surface adsorption takes place which depending on interaction type, van der Waals or covalent, it can be physical or chemical, respectively. The number of the atoms adsorbing to the sites of the surface is proportional to the partial pressure of the gas.

In particular, molecule-based chemical vapor deposition (MB-CVD) is an

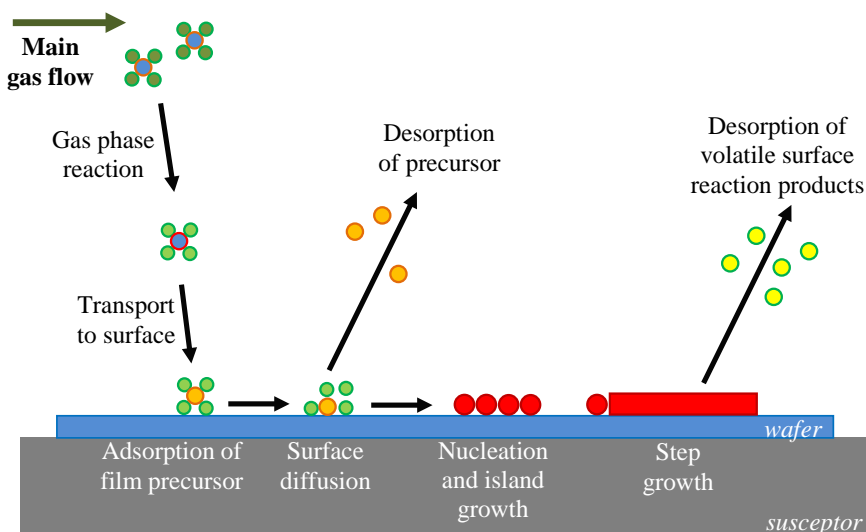


**Figure 4.9** Fundamental processes active in CVD process

efficient technique for synthesizing 1D metal oxide nanostructures. The vapor-liquid-solid (VLS) growth is assisted by presence of catalyst, which causes decomposition of the molecular precursor. In this method chemical composition, size, and morphology of the 1D nanostructures can be controlled precisely. Moreover, the process occurs in relatively low temperatures.<sup>90</sup>

In vapor-liquid-solid (VLS) mechanism, as firstly proposed by Wagner and Ellis in 1964 for growth of Si whiskers on Si substrate (Figure 4.10),<sup>91</sup> three phases are involved: (i) the vapor phase precursor, (ii) the liquid catalyst droplet (in the case of presence of catalyst) or the liquid phase of one of the compound (in the case of catalyst-free growth), and (iii) the solid crystalline product. Note that in the next chapter we will discuss catalyst-free growth; however, in this chapter we only consider the growth with the presence of metallic catalysts. In addition, three growth regimes can be considered. In the first one, a nanoscaled metallic particle forms a eutectic alloy (liquid) with the wire material (supplied as vapor). In the second one the vapor of the source material is further absorbed by the liquid catalyst until supersaturation occurs; and in the third regime, the vapor atoms diffuse and condense at the liquid/solid interface which will be

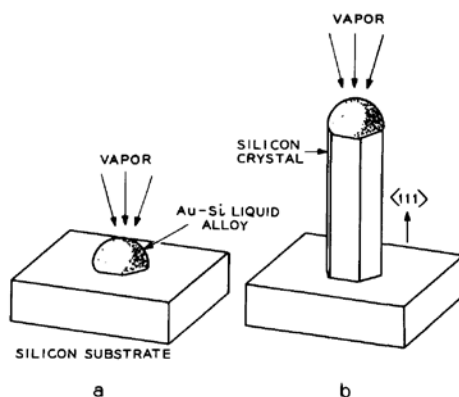


**Figure 4.10** Scheme of the Si 1D single-crystal growth by VLS mechanism<sup>91</sup>

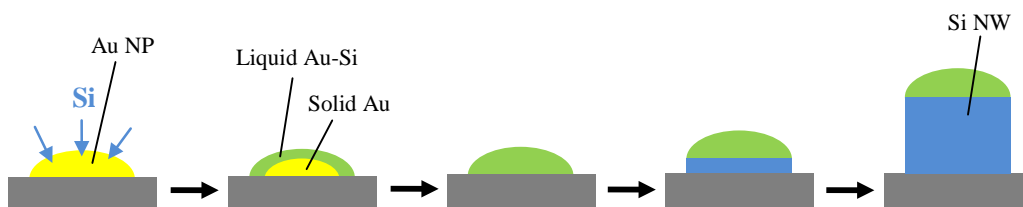


**Figure 4.11** NW growth with VLS mechanism<sup>92</sup>

pushed forward to form a nanowire, as shown in Figure 4.11.<sup>92,93</sup>

#### **4.1.6 Structural changes in nanostructured materials**

It is important to take into account that energy equilibriums of heterostructures are not the same as the ones single structures. Single structures find equilibrium with a substrate with/without presence of a catalyst. However, the secondary structure accommodates on the initial structure which is usually different from the substrate. Some phenomena can occur in this process:

- While accommodating on the base, the secondary structure can grow as single crystalline or polycrystalline, which can whether have epitaxial relationship with the base or not.

- When the secondary phase is deposited, it can diffuse into the crystalline structure of the base and form mixed oxide interfaces.

- Depending on the growth conditions, some phases of the material are more favorable and they are expected to appear on the base. However, the existence of some other phases is evidenced to be substituted although kinetically they were not favorable as a single structure.

- Analogous to the previous point, some reduced structures are observed, only because of the accommodation issue.

These points are briefly described in this section and the results are shown in the section 4.3.

##### ***4.1.6.1 Accommodation on the base***

In some cases when the mismatch between the cell parameters of the core and the shell are higher than a certain amount, the shell follows ‘*Stranski-Krastanov*’ (SK) growth. In this growth mode, the shell grows epitaxially on the core, however, the strain caused by difference in atomic plane distances gives rise to appearance of some 3D islands within 2D monolayers. An example of this growth mode is shown in Figure 4.12(a). In this image, the base is an SnO<sub>2</sub> NW covered with a TiVO<sub>3</sub> shell.

##### ***4.1.6.2 Mixed oxide interface***

Diffusion of the secondary structure into the base or vice versa, can create new phases, whether in the whole structure or only in the interface. This phenomenon highly depends on the materials, and the growth conditions. In Figure 4.12(b) a ZnO NW with TiO<sub>2</sub> shell is shown which was annealed and the

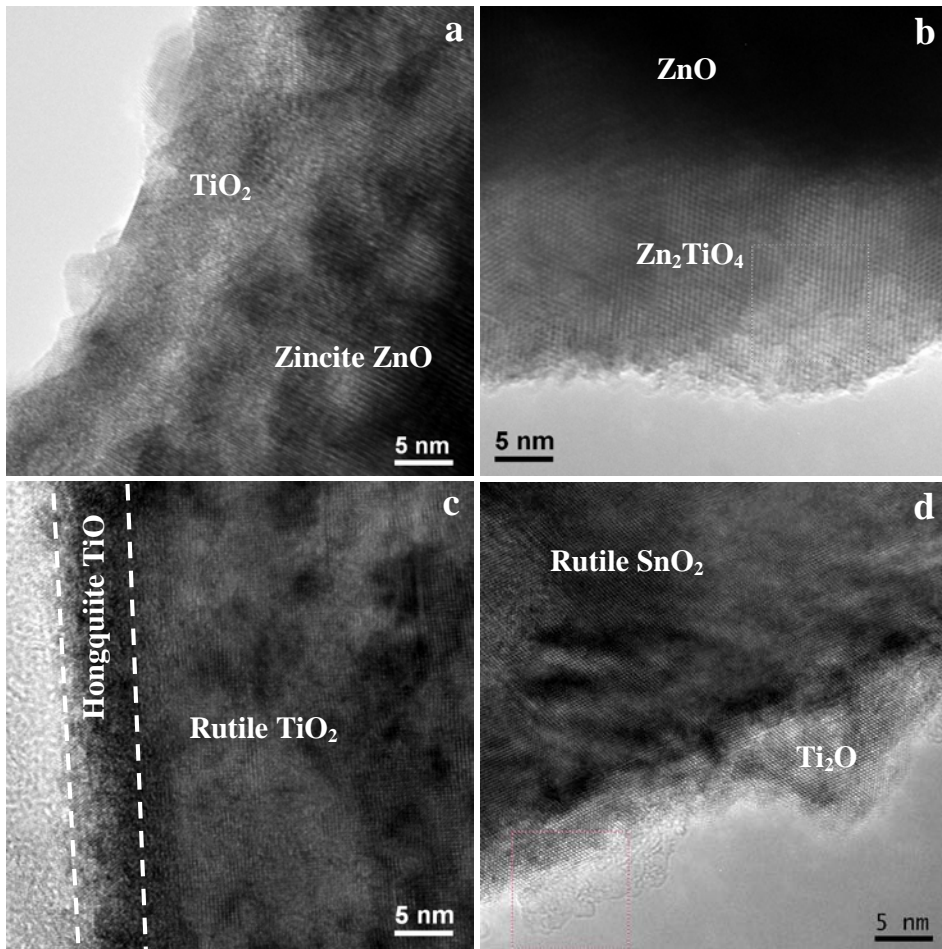


**Figure 4.12** The structural change of the secondary phase after being accommodated on the base NW: (a) polycrystallinity, (b) diffusion of the two oxide structures in the interface, (c) crystal structure change, and (d) reduction of the shell

Zn diffused to the shell structure and  $Zn_2TiO_4$  structure was produced. This mixed oxide interface can enhance the efficiency of the photovoltaic devices.

#### 4.1.6.3 Crystal structure changes in shells

In some cases one can change the growth conditions in order to obtain a particular structure. For example it is possible to apply some changes in order to have anatase  $TiO_2$  structure instead of rutile. Trying to do the same in the case of the secondary structure, nevertheless, can fail while different energy

parameters are engaged. Figure 4.12(c) shows a hongquite TiO shell on a rutile TiO<sub>2</sub> NW, whereas the shell was expected to have anatase TiO<sub>2</sub> structure.

#### ***4.1.6.4 Reduction***

In the same scenario, structural changes can give rise to chemical composition changes. As seen in Figure 4.12(d), a reduced Ti<sub>2</sub>O structure accommodates on SnO<sub>2</sub> NWs, although this phase is seldom observed in bulk. In other words, titanium oxide in the form of rutile, anatase, or brookite is more stable and more likely to occur, however, epitaxy and mismatch minimization while accommodating on SnO<sub>2</sub> base leads to formation of another phase.

## **4.2 Experimental**

### **4.2.1 Synthesis**

As mentioned above, many different synthesis methods were employed for NW growth in this chapter. The experimental details of the main ones are described here.

#### ***4.2.1.1 Electrochemical growth***

Arrays of vertically aligned and single-crystal ZnO:Cl NWs were electrochemically grown in an aqueous solution inside a three-electrode cell. The NWs thickness, length, doping concentration and tip morphology could be controlled by adjusting the growth potential and the concentration of the growth solution. Moreover, ZnO:Cl NWs could be grown in a large variety of conducting substrates, from glass covered with a transparent conducting oxide to metal foils.<sup>14</sup>

Electrodeposited ZnO:Cl NWs grown on indium tin oxide (ITO)-covered glass substrates were used to obtain ZnO:Cl@TiO<sub>2</sub> core-shell NWs. TiO<sub>2</sub> shells with controlled thickness were grown by multiple successive adsorption-activation-decomposition steps as schematized in Figure 4.13. In a first step, titanium isopropoxide [Ti(OC<sub>3</sub>H<sub>7</sub>)<sub>4</sub>] was adsorbed on the ZnO:Cl surface by immersing the NW array on an anhydrous isopropanol solution of titanium isopropoxide (0.08M) for 30 s. In the second successive step, excess titanium isopropoxide was removed by immersing the layer in anhydrous isopropanol. In a third step, titanium isopropoxide was hydrolyzed by introducing the NW array

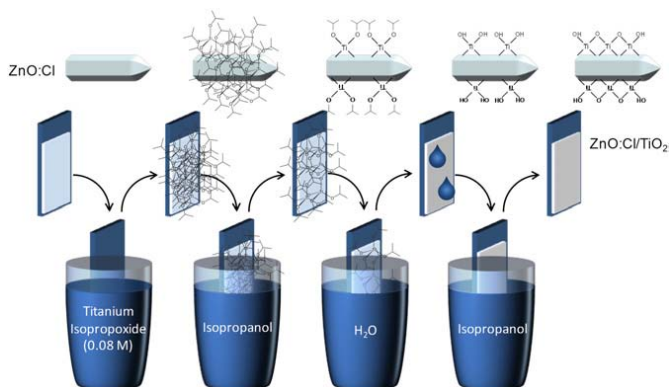


**Figure 4.13** Scheme of the successive coating and reaction steps used to produce ZnO:Cl/TiO<sub>2</sub> core-shell NWs with controlled thickness<sup>31</sup>

in water. In one last step excess of water was removed with anhydrous isopropanol. This 4-step cycle was repeated up to 100 times. The final samples were dried by means of a N<sub>2</sub> flow and annealed at 450 °C for 30 min to improve crystallinity.<sup>31</sup>

The ZnS shell was prepared by successive ionic layer adsorption and reaction (SILAR) method. In particular, the obtained ZnO NW arrays were successively immersed in two different aqueous solutions for 30 s, one containing Zn<sup>2+</sup> cations (25 mM Zn(NO<sub>3</sub>)<sub>2</sub>) and the other containing S<sup>2-</sup> anions (25 mM Na<sub>2</sub>S). Between each immersion step, the samples were rinsed with deionized water for 30 s to remove excess ions that were weakly bound to the NW surfaces. Same as in TiO<sub>2</sub> shell preparation, this two-step procedure was repeated 100 cycles. After cycles 10, 30, 60 and 100 the obtained samples were dried by means of a N<sub>2</sub> flow. These intermediate samples were used to characterize the influence of the ZnS thickness on the optoelectronic and photoelectrochemical properties of ZnO@ZnS NWs.<sup>30</sup>

#### 4.2.1.2 Pulsed laser deposition

Pulsed laser deposition (PLD) system used for growth of ZnO NWs consisted of a picosecond Nd:YAG pulsed laser and a vacuum chamber. Laser wavelength was 355 nm, frequency 500 kHz and laser power 1.5W. The target was a sintered ZnO material and the substrate an 11-20 single crystal Al<sub>2</sub>O<sub>3</sub>. Gold droplets were used as liquid catalyst. The catalyst was deposited on the substrate surface by sputtering. The substrate conditions were specific to PLD/VLS ZnO NW growing process, substrate temperature ~800 °C and

ambient oxygen pressure  $\sim 1$  Pa. Substrate pre-annealing time at the working temperature was in the range of several minutes.

The particularity of the experimental setup, as shown in the scheme of Figure 4.14 is the presence of a plane reflector between target and substrate in a so-called pulsed laser deposition (PLD) with plasma reflector. The main role of the reflector is to filter the big particles and cluster from the ablation plume and stop them from reaching the substrate area, while the big particles hinder the VLS mechanism. A second role of this reflector was to provide different particle fluxes on different substrate zones, and allow investigating the influence of the particle flux variation on the VLS growing process on the same sample surface and experimental conditions. Thus, the system will have a ‘low-flux’ (Zone L) substrate zone corresponding to high reflection angles of the reflected particles, a ‘high-flux’ (Zone H) corresponding to low reflection angles of the reflected particles, and a zone accessible to the particles coming straight from the target marked as ‘droplet-zone’ (Zone D) where small droplets or clusters might arrive. The substrate size was about  $5 \times 5$  mm, the target-reflector distance was about 2 cm, while the mask-substrate distance only several millimeters.

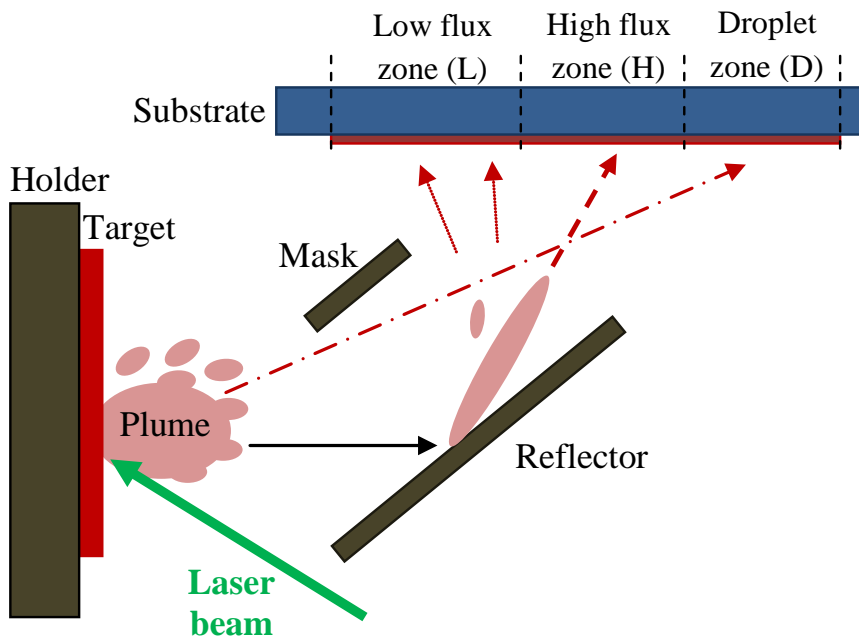


**Figure 4.14** Scheme of the PLD experimental setup

### 4.2.1.3 Chemical vapor deposition

Cassiterite SnO<sub>2</sub> nanowires were grown by decomposition of Sn(O<sup>t</sup>Bu)<sub>4</sub> in a low pressure chemical vapor deposition (LPCVD) reactor at 650-750 °C on silicon (001) substrates.<sup>94</sup>

Multistep CVD processes enable the design of layered core-shell nanoarchitectures with the desired composition by varying the precursor source used. Ti(O<sup>i</sup>Pr)<sub>4</sub> was used as single source precursor in a second CVD process and decomposed at 550-750 °C onto the as-grown SnO<sub>2</sub> NWs, resulting in the formation of SnO<sub>2</sub>/TiO<sub>x</sub> core-shell heterostructures.<sup>95</sup> Similarly, SnO<sub>2</sub>/VO<sub>x</sub> nanowires were formed when VO(O<sup>i</sup>Pr)<sub>3</sub> was used instead. It should be remarked that the variation of process parameters such as substrate temperature, precursor flux and deposition time influences the effective availability of the oxygen atoms during the material growth, and defines the oxidation state of the final metal oxide. Therefore, the controlled deposition of different vanadium oxides with defined V:O stoichiometries (V<sub>2</sub>O<sub>5</sub>, V<sub>3</sub>O<sub>7</sub>, V<sub>6</sub>O<sub>13</sub>, V<sub>7</sub>O<sub>13</sub>, VO<sub>2</sub> and V<sub>2</sub>O<sub>3</sub>) can easily be achieved by this synthetic method.<sup>96</sup>

Titanium-vanadium oxide (TVO) shells were likewise formed by sequential decomposition of Ti(O<sup>i</sup>Pr)<sub>4</sub> and VO(O<sup>i</sup>Pr)<sub>3</sub> onto the pristine SnO<sub>2</sub> NWs at higher temperatures 700-800 °C. The amount of Ti and V present in the shell can be easily defined by controlling the amount of precursor in the gas phase, which is directly related to the precursor temperature used during the process. A mass spectrometer (Pfeiffer QMG 220) attached directly to the exhaust of the CVD reactor chamber allowed the time-resolved in-situ mass spectrometric analysis of the precursor by products, after thermal decomposition took place.

p-CuO (NP)/n-SnO<sub>2</sub> (NW) heterostructures were produced following a two step CVD of corresponding metal precursors. The initial step was to produce SnO<sub>2</sub> NWs as described above. In a subsequent step, copper particles were deposited on pre-grown SnO<sub>2</sub> NWs by the CVD of [Cu<sup>II</sup>((C<sub>5</sub>H<sub>4</sub>N)(CHCOCF<sub>3</sub>))<sub>2</sub>]<sub>2</sub>, with substrate temperature of 780 °C and precursor temperature of 155 °C, for 40 min. The resulting SnO<sub>2</sub> nanowires decorated with copper particles of an average size of 200 nm were annealed in air at 300 °C for 24 h producing p-CuO (NP)/n-SnO<sub>2</sub> (NW) heterostructures. After annealing, a size-increase of particles was evident due to the volume expansion associated to the transformation of Cu to CuO.<sup>26</sup>

#### ***4.2.1.4 Thermal oxidation***

Thermal oxidation process used for CuO NW growth mainly consists in a tubular furnace working in atmospheric pressure, without the need of vacuum equipment, in relatively low temperatures (from 300-400 °C). Growth process consisted of four main steps: (1) substrates cleaning, (2) metallic layer deposition, (3) metal layer etching and (4) thermal oxidation. Cleaning is necessary in order to remove dust and most organic compounds from the substrate. Samples were cleaned in acetone using ultrasounds for 10 min and afterwards dried with a synthetic air flow. A thin layer of metallic copper was deposited on target substrates by radio-frequency (RF) magnetron sputtering, using argon plasma. Different metal layers were deposited at room temperature, 200 °C, 300 °C and 400 °C, while layer thickness ranged from 300 nm (30 min deposition) to about 3 μm (5 h deposition). Copper is very reactive in environmental atmosphere, and the interaction with oxygen (always presents in air) spontaneously produces a thin layer of copper oxide. This thin layer of native oxide is detrimental for NWs growth, so it has to be removed before the thermal oxidation. Two different methods were used to remove this layer: wet chemical etching and plasma etching.

After the copper oxide layer removal, samples were undergone to a forced oxidation in a Carbolite tubular furnace. Gas flow was set at 300 SCCM and oxidation time was fixed at 15 h, in order to reduce the number of parameters to investigate. In particular, the duration of the oxidation process mainly influences the length of NWs. The selected duration (15 h) was enough to synthesize several-micrometer long NWs. The oxidation process firstly consists of the oxidation of metallic Cu into a Cu<sub>2</sub>O film ( $\text{Cu} + \text{O}_2 \rightarrow \text{Cu}_2\text{O}$ ). Afterwards, the Cu<sub>2</sub>O film further oxidizes into CuO ( $\text{Cu}_2\text{O} + \text{O}_2 \rightarrow \text{CuO}$ ), producing CuO NWs and leading to a complete oxidation.<sup>20</sup>

#### **4.2.2 Structural characterization**

The chemical and structural characterization of the nanowires has been carried out by high-resolution transmission electron microscopy (HRTEM), electron energy loss spectroscopy (EELS), and with the extracted data we have generated 3D atomic supercell models. High-resolution TEM images have been obtained by means of a Jeol 2010F field-emission gun (FEG) microscope with a 0.19 nm point-to-point resolution at 200 keV with an embedded Gatan Image Filter (GIF) for EELS analyses. Some of the high-angle annular dark-field

(HAADF) images and EELS spectra have been obtained in a FEI Titan 60-300 kV TEM operated at 300 keV. 3D atomic models were created by using Rhodius software package<sup>97</sup> which allows creating complex atomic models.<sup>98</sup> In Chapter 2 all the experimental methodologies of structural characterizations are discussed in detail.

### 4.2.3 Experimental measurements for applications

Depending on the predetermined applications of the NWs, different electrical measurements were performed in order to examine their functionality and justify their relevance to the featured application.

#### 4.2.3.1 Optoelectronics

Electrochemical impedance spectroscopy (EIS) measurements were carried out on ZnO:Cl and ZnO:Cl@TiO<sub>2</sub> NWs both in dark and under AM 1.5 simulated solar radiation at different applied potentials. For these measurements, an electrochemical system (PARSTAT 2273) and a typical three-electrode setup with an Ag/AgCl electrode in saturated KCl (3M) as the reference electrode, a Pt wire as counter electrode and 0.1M Na<sub>2</sub>SO<sub>4</sub> aqueous solutions as electrolytes were employed. The frequency range tested was 0.1 Hz - 1 MHz and the amplitude of the alternating signal was 1mV. In the case of ZnO:Cl@ZnS core-shell NWs, 0.1 M Na<sub>2</sub>SO<sub>4</sub> or 0.5 M Na<sub>2</sub>S aqueous solutions were used as electrolytes to study the photoelectrochemical (PEC) properties of photoelectrodes.

Room-temperature photoluminescence (PL) measurements were obtained using a Kimmon IK Series HeCd CW laser (325 nm and 40 mW). Fluorescence was dispersed through an Oriel Corner Stone 1/8 74000 monochromator, detected with a Hamamatsu R928 photomultiplier, and amplified through a Stanford Research Systems SR830 DSP lock-in amplifier.

A double beam spectrophotometer (Perkin Elmer Lambda 950) equipped with an integrated sphere was used for the UV-visible transmission measurements in the range from 250 to 800 nm.

Raman measurements were made using a micro-Raman spectrometer Labram HR 800. Excitation was provided by a diode laser at 532 nm or a He-Cd laser at 325 nm. Measurements were performed in backscattering configuration. I-V characteristics of ZnO NWs were obtained by scanning probe microscopy (SPM) using a Park XE-100 Advanced Scanning Probe Microscope.

### 4.2.3.2 Gas sensing

Gas sensing experiments were performed with bundled and individual structures. Bundled bare SnO<sub>2</sub> nanowires and p-CuO/n-SnO<sub>2</sub> heterostructures were characterized after depositing sensing layers in form of thick films onto substrates with pre-patterned Pt contacts on the front side and a Pt-meander on the back-side acting as a heater and temperature probe as can be seen in Figure 4.15.<sup>99</sup> Deposited thick films of MOXs mixed with solvents were dried at relatively low temperatures (~50 °C) for some hours and then sintered at higher temperatures for some days. Sensor test were performed in DC mode, and atmosphere compositions were precisely produced with mass-flow controllers and certified gas bottles.

Individual CuO/SnO<sub>2</sub> heterostructures were electrically contacted to Pt nanoelectrodes by means of FIB assisted lithography<sup>72</sup> and they were evaluated as gas sensors inside a customized chamber especially designed to minimize the external noise. Electrical characterization was carried out by I-V measurements; the sensor was biased by 1 V and film resistance was measured by a picoammeter.



**Figure 4.15** Scheme of alumina resistive sensor<sup>99</sup>

## 4.3 Structure study

In this chapter the results and discussion section is classified based on core material. Each section starts with the bare NW, and then heterostructures based on the same bare NW. Mostly the core-shell approach is followed; however, other type of heterostructures such as NP on NW are studied. Results on enhancement of functionality are provided which prove the success of heterostructuring approach.

Core-shell NWs of this chapter are produced by depositing a crystalline overlayer on bare NWs. The overlayers can be divided into two categories: (i)

polycrystalline shells, and (ii) epitaxially grown shells. The epitaxial relationship between the core and the shell can be completely useful for many applications. Nonetheless, polycrystalline shells provide other unique advantages that can be utilized for particular applications.

### 4.3.1 ZnO nanowires and related heterostructures

We start the structure study with bare NWs, their crystal structures, shapes, and properties. Afterwards, we move to the heterostructures, i.e. coaxial nanojunctions which dramatically enhance the materials properties.

#### 4.3.1.1 Bare ZnO nanowires

Zinc oxide is a wide band gap n-type semiconductor which has appropriate specifications for a wide range of applications. It is abundant, stable, biocompatible, and relatively cheap. In the form of wurtzite (WZ) it has a direct band gap,  $E_g = 3.35$  eV,<sup>41,100,101</sup> and a large excitation binding energy (60 meV), and exhibits near UV emission. ZnO NWs have been used in many applications such as in acoustic wave devices (as piezoelectric),<sup>4</sup> solar cells,<sup>102</sup> transistors,<sup>103</sup> biological and chemical sensors.<sup>18</sup>

ZnO can occur in both wurtzite (WZ) and zinc-blende (ZB) structures. The unit cells are shown in Figure 4.16. The ZB structure has cubic symmetry in  $F-43m$  space group (No. 186) with  $a = 4.616$  Å. The WZ structure which is known as ‘zincite’ has hexagonal symmetry in  $P6_3mc$  space group (No. 186) with  $a = b = 3.265$  Å and  $c = 5.219$  Å. Both structures are considered as tetrahedrally-coordinated semiconductors. For ZnO, WZ structure is predominant and ZB-

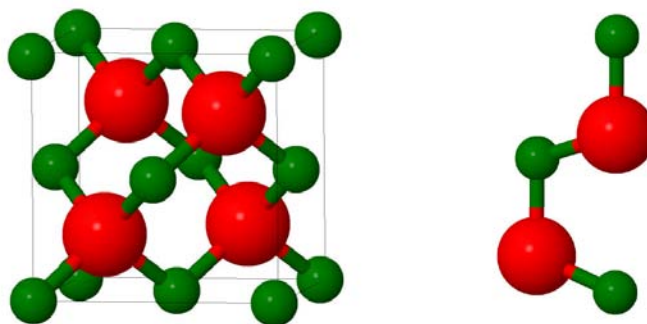


**Figure 4.16** ZnO unit cells: (a) zinc-blende (ZB) with cubic symmetry, and (b) wurtzite (WZ) with hexagonal symmetry

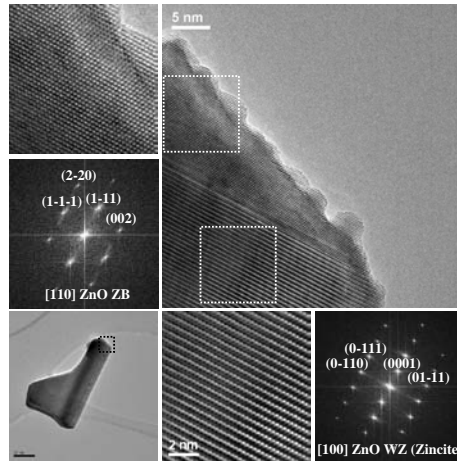


**Figure 4.17** HRTEM micrograph of a ZnO NR with WZ structure in the body of the rod (grown in [0001] direction) and ZB structure in the tip

ZnO is hardly reported. Nevertheless, it has been observed that the band gaps of these two structures are different. As mentioned, band gap energy value of 3.35-3.37 eV is reported for WZ-ZnO, whereas for ZB-ZnO this value is 3.27 eV.<sup>104</sup>

All of the ZnO NWs and NRs that we have in this chapter have WZ structure and they are mostly grown in (0001) direction. However, in some samples we observed ZB structure. See Figure 4.17. The NR consists of a body with WZ structure and a tip with ZB structure. ZB-ZnO accommodates on WZ-ZnO with  $(1-11)_{ZB}$  on  $(0001)_{WZ}$  as these two plane families are always identical

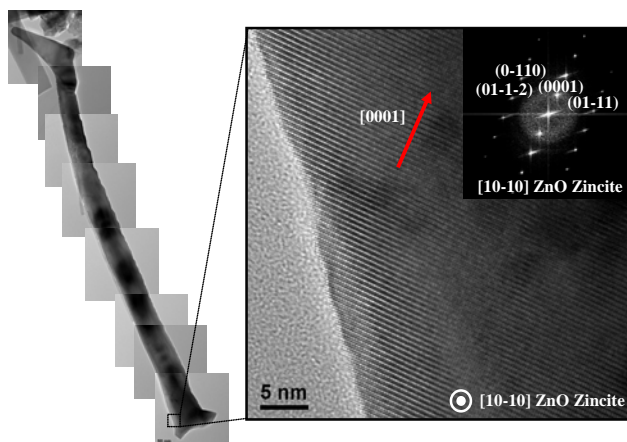


**Figure 4.18** HRTEM micrographs of a ZnO NWs grown by vapor-transport synthesis

in WZ-ZB systems.

There are also NWs that do not grow in  $[0001]$  direction. For instance, the NWs shown in Figure 4.18 do not have any special growth direction. These NWs were grown on ZnO particles by means of vapor-transport synthesis. In another attempt to grow NWs, it was observed that they were grown in  $[0-110]$  direction. Nevertheless, these NWs vertically branch out and some secondary NWs in  $[0001]$  grow from the  $[0-110]$ -grown body. Therefore, it can still prove that  $[0001]$ -growth is energetically favorable. See Figure 4.19. In fact these NWs emerged when the deposition rate in PLD process was high.

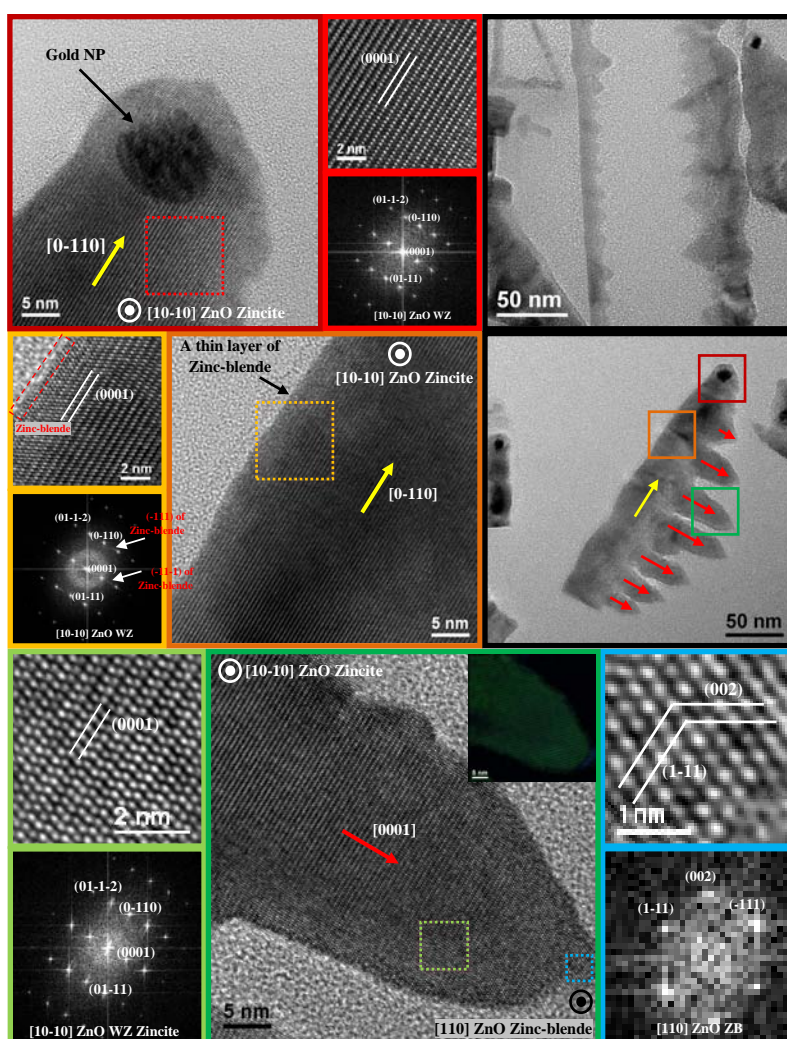


**Figure 4.19** HRTEM micrographs of ZnO branched NWs grown by PLD, the NW with  $[0-110]$  growth direction and branches with  $[0001]$  direction

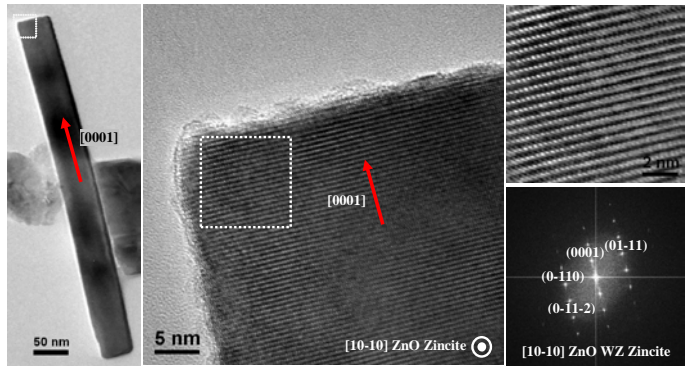


**Figure 4.20** A ZnO NW with WZ structure grown in [0001] direction

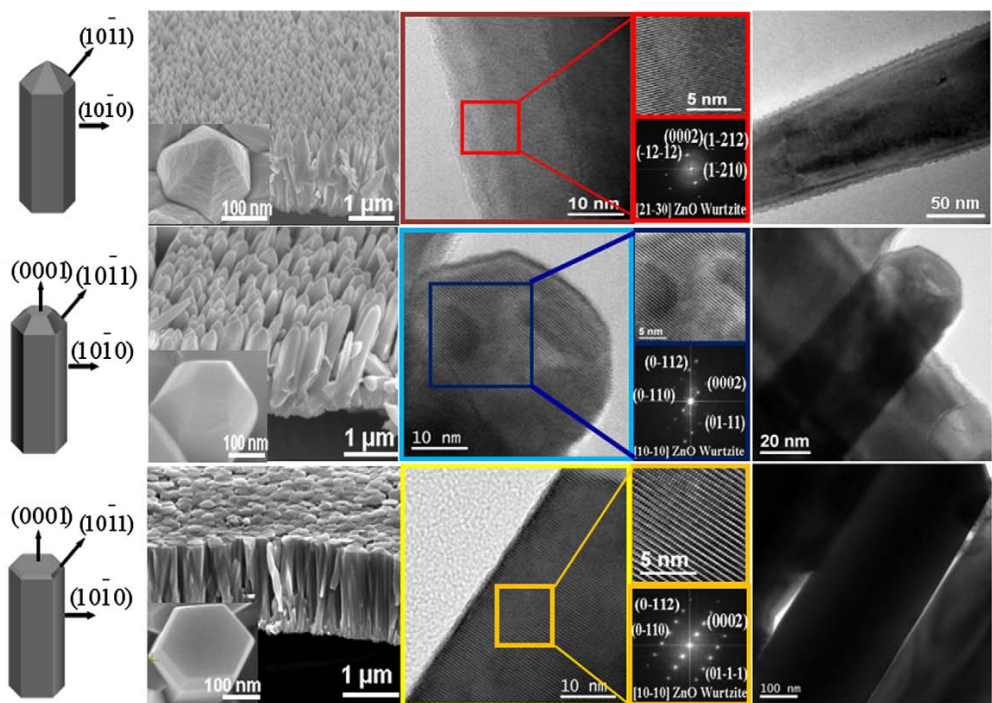


**Figure 4.21** ZnO NWs with different Cl concentration increasing from (a) to (c) causing the change in the tip shape<sup>14</sup>

On the other hand, most of the ZnO NWs grow in [0001] direction with WZ structure as shown in Figure 4.20. As an example, these NWs were grown on ZnO thin films. The electrochemically grown NWs of Figure 4.21 also have the same characteristics.

In addition, the influence of Cl-doping in ZnO NWs is studied. By changing the concentration of Cl ( $\text{NH}_4\text{Cl}$  concentration in the growth solution) and

electrodeposition potential, we observed some differences in growth rate, morphology, crystal structure, and optoelectronic properties. It was also observed how the roughness of the lateral NW surfaces decreased with the  $\text{NH}_4\text{Cl}$  concentration in the growth solution. The higher the  $\text{NH}_4\text{Cl}$  concentration, the slower the growth rate in the [0001] direction and thus the smoother the lateral surfaces obtained (Figure 4.21). Also the tips of the NWs differ as shown in the same figure. At the same time, the ZnO XRD pattern shifted to lower angles with the incorporation of Cl, which is consistent with an expansion of the ZnO lattice due to the replacement of  $\text{O}^{2-}$  ions with the larger  $\text{Cl}^-$  ones (Figure 4.22). Furthermore, transmittance spectra of the Cl-doped ZnO NWs determine the optical band gap of the ZnO:Cl NWs with different Cl concentrations (Figure 4.23(a)), while the photoluminescence (PL) spectra (at room temperature) of Figure 4.23(b) reveal the expansion of band-to-band transition by increase in Cl concentration associated with a blue shift. The band-to-band emission extends from the reduced band-gap energy, which is the difference between the top of the valence band and the bottom of the conduction band, to the energy of the optical gap, which blue-shifts with the  $\text{NH}_4\text{Cl}$  concentration due to the band filling.<sup>14</sup>

To sum up, we showed how growth conditions can change the crystal structure, morphology, growth rate, and optical properties of ZnO NWs. It is of high importance to be able to engineer these parameters as ZnO is widely utilized in a large range of applications as mentioned previously.

ZnO NWs can be used as an adequate base for core-shell structures. In this section two polycrystalline shells are accommodated on ZnO single-crystalline NWs. As mentioned, polycrystalline shells present unique advantages that can be useful for special application. The two heterostructures that will be studied in

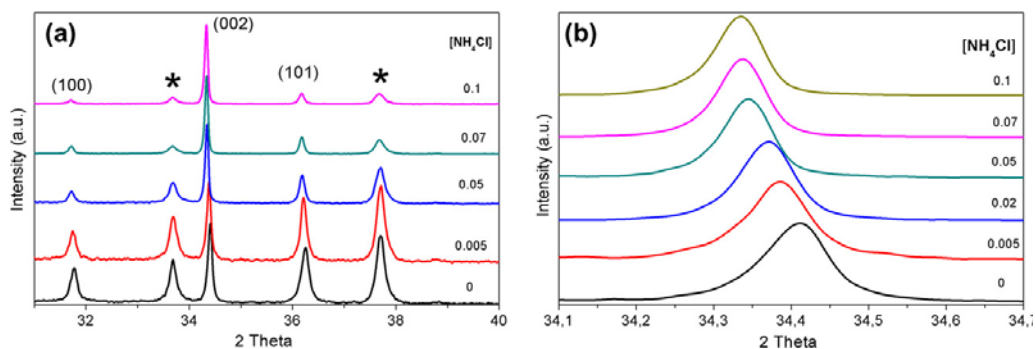


**Figure 4.22** XRD patterns showing the peak shift related to Cl-doping concentration<sup>14</sup>

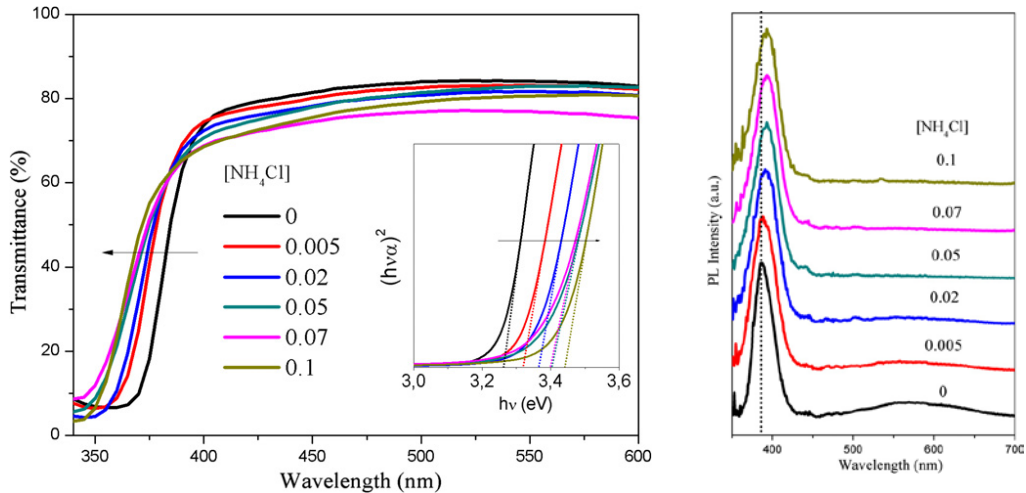


**Figure 4.23** (Left) Transmittance spectra showing the optical band, and (right) PL spectra<sup>14</sup>

the following are: ZnO:Cl@ZnS and ZnO:Cl@TiO<sub>2</sub> NWs.

#### 4.3.1.2 ZnO:Cl@ZnS nanowires

Electrochemically grown ZnO NWs of section 4.3.1.1, which were doped with chlorine, are now covered with a ZnS shell. This shell was prepared by successive ionic adsorption and reaction method.<sup>30</sup> Figure 4.24(a) shows the transversal SEM image of the ZnO:Cl NWs before being covered with ZnO shell, and Figure 4.24(b) shows these ZnO:Cl@ZnS core-shell NWs. EDX maps of Figure 4.24(c) were performed in SEM on a single NW. In these maps one can see the presence of Zn everywhere, while O is present only in the middle, and S map reveals a kind of hollow structure. EELS maps (Figure 4.24(g)) also prove the core-shell structure, nonetheless with higher spatial resolution. Although the S is not mapped here, required information can be obtained from the Zn and O maps and their overlap. Thickness of ZnS shell (the green shell where O is absent) can be approximately measured in the RGB map, which is in good agreement with the TEM image of Figure 4.24(d).

The results obtained from the XPS characterization of the NW arrays are shown in Figure 4.24(e) and 4.24(f). The Zn binding energy was slightly shifted to lower energies for the ZnS shell when compared with the ZnO core. This shift is attributed to the different binding energy of the Zn-O and the Zn-S bond due to the dissimilar anion electronegativity.<sup>105</sup> The thickness of the shell is basically proportional to the number of the cycles.

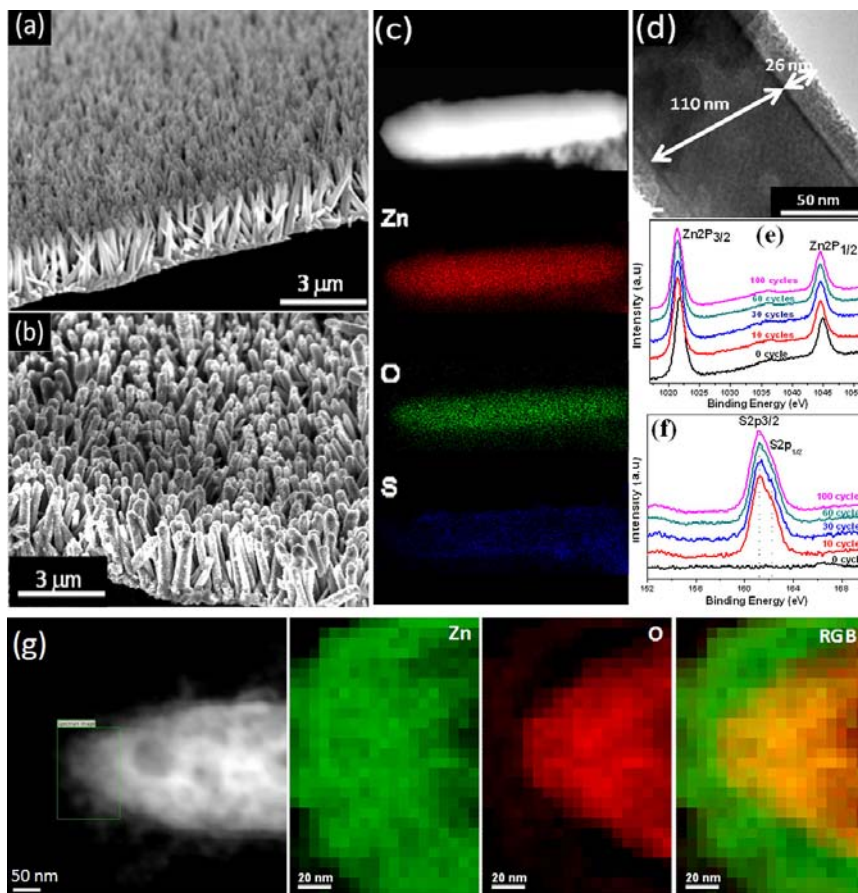


**Figure 4.24** ZnO:Cl@ZnS NWs, SEM images of (a) bare ZnO NWs and (b) ZnO:Cl@ZnS NWs, (c) EDX maps, (d) TEM image showing the thickness of the core and the shell, (e), (f) XPS analysis, and (g) Z-contrast image associated with EELS elemental maps<sup>30</sup>

The optimization of semiconductor photoelectrochemical (PEC) properties requires very large surface areas to maximize the semiconductor/electrolyte interface, and very high electrical conductivities to facilitate charge carrier transport between oxidation and reduction sites. This property can be employed in photoelectrolysis of water in order to generate  $H_2$  which occurs in the interface of the NWs and the electrolyte. The results of the characterization of the PEC properties of the core-shell ZnO@ZnS NWs in a  $Na_2SO_4$  aqueous solution are shown in Figure 4.25(a). The measurements have been performed on NW arrays with different shell thicknesses. Note that for these measurements of the evolution of photocurrent density with the thickness of ZnS shell, the exact same NW array was measured before the ZnS growth and after each

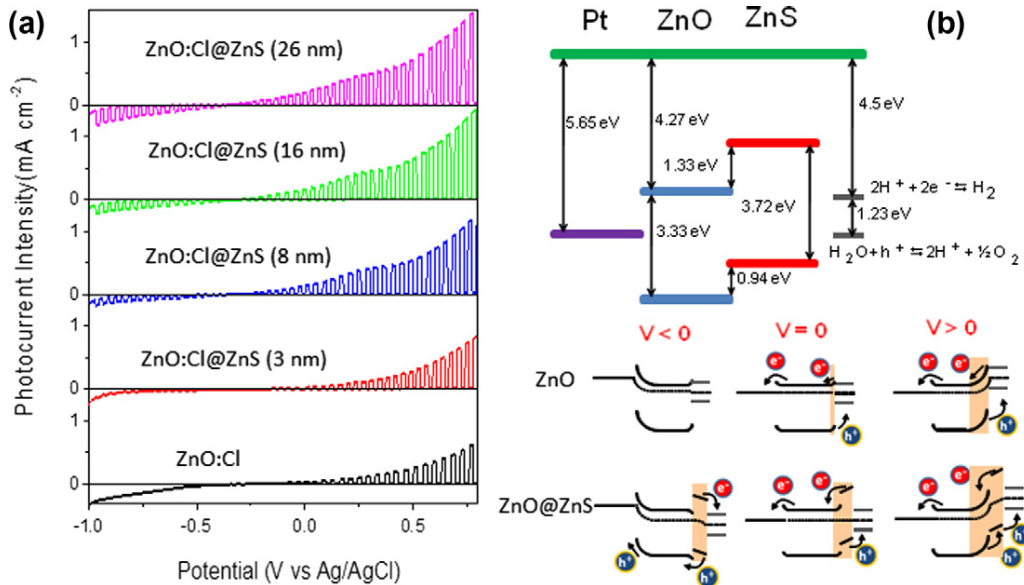


**Figure 4.25** (a) Photocurrent density vs. applied potential (V vs. Ag/AgCl) from ZnO:Cl NWs and ZnO:Cl@ZnS core-shell NWs with increasingly thicker shells, (b) Schematic representation of the energy band alignment, the depletion regions created in the formed hetero-nanostructures and the charge transfer for bare ZnO:Cl NWs and ZnO:Cl@ZnS core-shell NWs at different applied potential ( $V < 0$ ,  $V = 0$  and  $V > 0$ )<sup>30</sup>

successive set of SILAR cycles. It is clearly observed that the presence of ZnS shell prompts the collected photocurrent, as in the NWs with 26-nm-thick shells it reached up to a factor 2.5.

In particular, ZnS shells promoted photocurrent at lower voltages comparing to the bare ZnO:Cl NWs. We believe this enhancement of the PEC properties to be related with the extension of the depletion layer region with the ZnS shell growth. The highly doped ZnO:Cl NWs are able to screen the charge accumulated at the surface by means of thin depletion layers. Therefore, surface depletion regions extend just a few nanometers from the surface. On the other hand, the depletion layer expands over the whole intrinsic ZnS shell in ZnO:Cl@ZnS core-shell NWs (Figure 4.25(b)). Thus, the region within the core-shell NWs with a built in electric field able to split the photogenerated electron-hole pairs significantly increases with the presence of the ZnS shell. This increase of the volume of materials with a built in electric field promotes the separation of photogenerated charge carriers, as represented in the cartoon of Figure 4.25(b). Thus, higher PEC currents are obtained in the presence of the

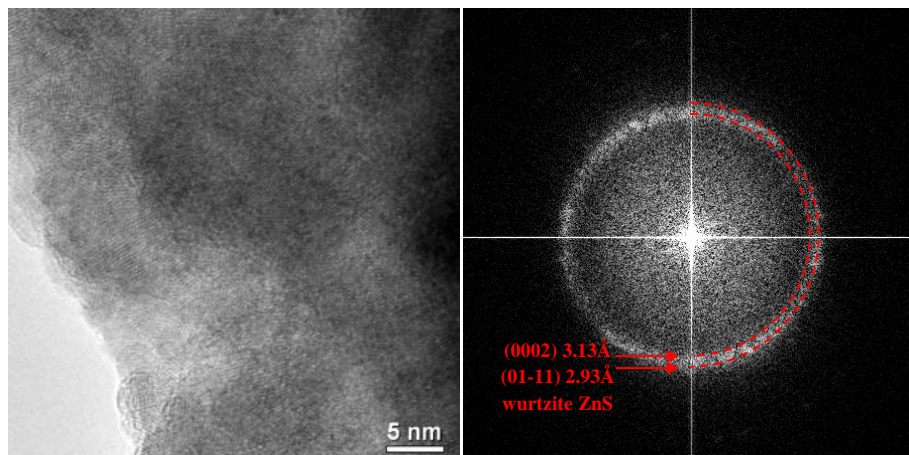


**Figure 4.26** HRTEM micrograph of ZnO:Cl@ZnS core-shell NW with polycrystalline WZ ZnS shell as indicated in the corresponding power spectrum

ZnS shell. An alternative explanation for such a PEC increase is the enhancement of the absorption of photons with energy below the ZnO and ZnS band gap by an electron transition from the ZnS valence band to the ZnO conduction band. However, this mechanism must have a very small influence as no signal of such low probability transition was obtained from the UV-Vis and PL characterization of the materials.<sup>30</sup>

Finally, it is also proven that annealing of the ZnO:Cl@ZnS NW arrays at 450 °C for 1 h in Ar atmosphere increases the PEC current significantly which can be attributed to improvement in crystallinity of ZnS shell causing a reduction in the density of trapping states and an increase in charge carrier mobility and thus an increase in charge carrier transport and collection efficiencies.<sup>30</sup> The polycrystalline nature of the WZ ZnS shell is explicitly revealed in Figure 4.26.

#### 4.3.1.3 ZnO:Cl@TiO<sub>2</sub> nanowires

TiO<sub>2</sub> shells with controlled thicknesses were grown on electrodeposited ZnO:Cl NWs by means of multiple successive adsorption-activation-decomposition steps. These steps were repeated for up to 100 times in order to obtain thicker shells. However, the shells were partially amorphous after the growth. An annealing process therefore was added at different temperatures (450 °C and above) for 30 min in order to improve the crystallinity. The NWs that were annealed at 450 °C show adequate crystallinity of the shell which

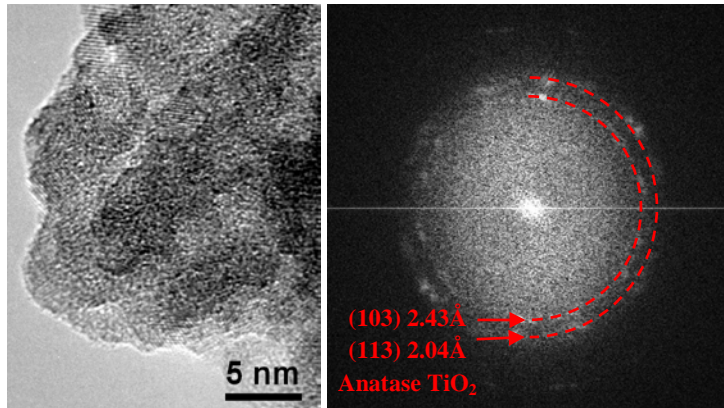


**Figure 4.27** HRTEM micrograph of TiO<sub>2</sub> anatase shell with the corresponding power spectrum

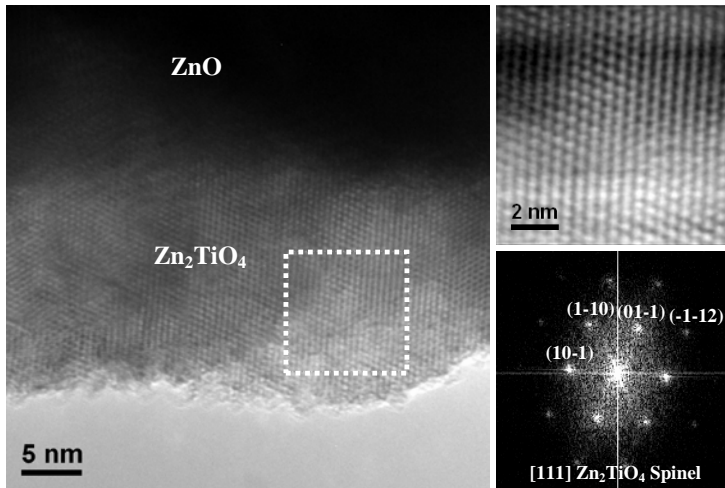


**Figure 4.28** HRTEM micrograph of core-shell structure where interdiffusion of the atoms creates Zn<sub>2</sub>TiO<sub>4</sub> compound in the shell

consists of polycrystalline anatase TiO<sub>2</sub> structure as shown in Figure 4.27. Two of the most visible rings corresponding to (103) and (113) atomic planes are indicated on the power spectrum. Different structures of titanium oxide will be discussed in section 4.3.2.

By increasing the annealing temperature, an interdiffusion of the two phases takes place in the interface of the ZnO core and the TiO<sub>2</sub> shell and Zn<sub>2</sub>TiO<sub>4</sub> phase occurs. HRTEM analysis (Figure 4.28) shows that the shell has the structure of Zn<sub>2</sub>TiO<sub>4</sub> ‘spinel’ with cubic symmetry belonging to *Fd3m* space group. Zn<sub>2</sub>TiO<sub>4</sub> spinel shells are also polycrystalline, however, in some parts as

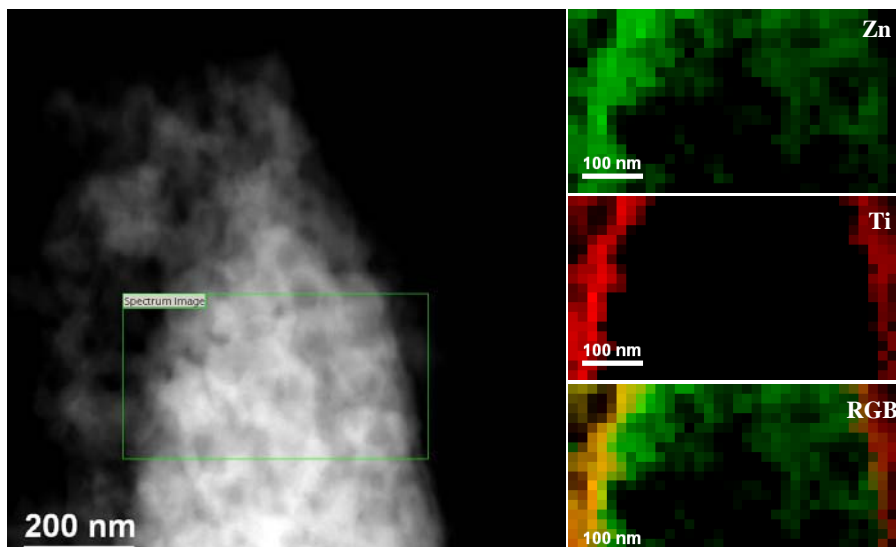


**Figure 4.29** HAADF-STEM image associated with EELS elemental maps

in Figure 4.28 the shell seems to have an epitaxial relationship with the ZnO core.

Interdiffusion of ZnO to the shell is also confirmed by EELS analysis. In Figure 4.29 a HAADF-STEM image is associated with EELS elemental maps where core-shell structure can be seen clearly. Ti can only be observed in the borders. The middle part is too thick decreasing dramatically the EELS signal-to-noise ratio, so not letting the elemental analysis. Therefore it is almost black, meaning no signal can be received. Zn is also present in the shell, i.e. the shell has a structure of a mixed oxide, which is in a good agreement with the HRTEM results.

#### **4.3.1.4 Section summary**

In this section we studied the properties of bare ZnO NWs and heterostructures based on them. The two heterostructures with ZnO:Cl NWs as cores, i.e. ZnO:Cl@ZnS and ZnO:Cl@TiO<sub>2</sub> with polycrystalline shells exhibited significant improvement in device efficiency. By annealing processes the crystallinity of the shell and thus their functionality was improved. At the same time, it should be taken into account that high annealing temperatures may cause interdiffusion of the two compounds. HRTEM and EELS analyses provided sufficient explanations for the different behavior of the material in this case, as a mixed oxide structures may form between the core and the shell.

### 4.3.2 TiO<sub>2</sub> nanowires and nanorods and related heterostructures

Titanium dioxide is a very commonly used photocatalytic material with unique characteristics such as easy handling, low cost, low toxicity, high chemical stability<sup>106</sup> and it is also robust under UV illumination. These advantages make TiO<sub>2</sub> a useful material in environmental purification,<sup>107</sup> gas sensors,<sup>108</sup> paints, pigments, air-cleaning devices, removal of NO, and SO, in controlling pollution, etc.<sup>109</sup> TiO<sub>2</sub> generally exhibits three different polymorphs namely anatase, rutile and brookite. The anatase and rutile phases have tetragonal symmetry, anatase has body centered tetragonal structure, and rutile possesses simple tetragonal structure, whereas brookite possesses rhombohedral structure. In both structures, slightly distorted octahedra are the basic building blocks, which consist of a titanium atom surrounded by six oxygen atoms in a more or less distorted octahedral configuration.

Rutile belongs to  $P4_2/mnm$  space group with lattice constant  $a = b = 4.60 \text{ \AA}$ ,  $c = 2.96 \text{ \AA}$ , and  $c/a = 2.51$ , while anatase belongs to  $I4_1/amd$  space group with lattice constant  $a = b = 3.78 \text{ \AA}$ ,  $c = 9.50 \text{ \AA}$ , and  $c/a = 2.51$ . Brookite belongs to  $Pbca$  space group with lattice constant  $a = 9.18 \text{ \AA}$ ,  $b = 5.43 \text{ \AA}$ ,  $c = 5.16 \text{ \AA}$ . These unit cells are shown in Figure 4.30. Additional phases of TiO<sub>2</sub> are also known to exist. Amongst, antase phase exhibits the best photocatalytic activity.<sup>110</sup> The photocatalytic activity of TiO<sub>2</sub> depends on several factors including the

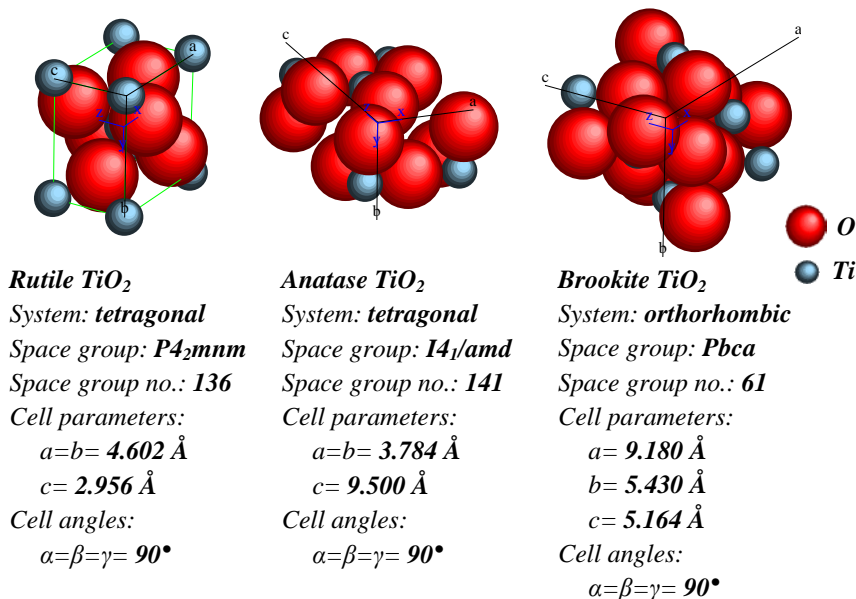


**Figure 4.30** TiO<sub>2</sub> cells with cell data, rutile, anatase, and brookite

crystallite size, crystallinity of the phase and specific surface area. Photocatalytic activity of  $\text{TiO}_2$  is high for powder with high surface area because of increased active sites,<sup>109</sup> which improves absorbance capability on surface, and thus, nanostructured materials, e.g. NPs, NRs, and NWS are appropriate for this purpose.

$\text{TiO}_2$  photocatalyst can only be excited by near-UV light. The photocatalytic activity of  $\text{TiO}_2$  is due to photo-induced electrons and the corresponding positive holes that are formed. These species are responsible for initiating the photocatalytic reactions. Furthermore, it is believed that the photocatalytic activity of  $\text{TiO}_2$  is low, because the generated photoinduced holes easily recombine with photoinduced electron thus decreasing the photocatalytic efficiency.<sup>111</sup> If the recombination rate is very fast, there is not enough time for photoreaction, which results in little or no photocatalytic effect. The band gaps of pure anatase and rutile phases are 3.2 eV and 3.05 eV, respectively, which both are quite large. Thus, one proper solution is to narrow this band gap energy by loading  $\text{TiO}_2$  with other metal ions. Several efforts were made by various researchers to improve the photocatalytic efficiency of  $\text{TiO}_2$  through metal ion loading such as Pd, Pt, Au, Ni,<sup>112-114</sup> Cu,<sup>115</sup> Cr,<sup>116</sup> Ce,<sup>117</sup> Bi.<sup>118</sup> The deposited metal ions on  $\text{TiO}_2$  surface trap and capture the photoinduced electrons or holes, leading to reduction of electron-hole recombination, thereby improving the photocatalytic efficiency.<sup>119</sup>

Another solution can be production of coaxial heterostructures which can occur by using a metal oxide NW as the base, and cover it with another structure, for example TiO hongiite shell on  $\text{TiO}_2$  rutile NW as core. As another example, one can see the mixed V-Ti oxide which was created for structural reasons. Both of these examples will be discussed in the next section.

#### ***4.3.2.1 Bare $\text{TiO}_2$ nanowires and nanorods***

In Figure 4.31 small anatase  $\text{TiO}_2$  NRs (with a mean size of  $4.0 \pm 1.4$  nm) prepared with sol-gel method are shown. These NRs were solvothermally crystallized from amorphous titanium oxide with Pt NPs. The presence of Pt NPs facilitated the crystallization process and thus better anatase crystallinity led to better photocatalytic activity and gas-sensing response of the material.<sup>120,121</sup>

On the other hand, rutile  $\text{TiO}_2$  NWS are also studied. These NWS, which can also be considered as NRs, have tetragonal structure and grow along [001]

direction. The structure of these NRs seems to be composed of thin fibers; every NR is in fact a bunch of narrow crystalline stripes (fibers) which are laterally attached. As can be seen in Figure 4.32, they seem to be separated in the direction of the growth as they do not have the same length and end up in different points. The low-magnification TEM image at left shows the end of a NR. The red arrows in the center HRTEM image indicate the [001] growth direction. On the corresponding power spectrum (FFT) atomic planes are indicated.

These TiO<sub>2</sub> NRs are used as photoanodes in photoelectrochemical (PEC) devices after annealing. It is shown that photocatalytic properties of these NRs are dramatically improved after the chlorine contamination was removed by

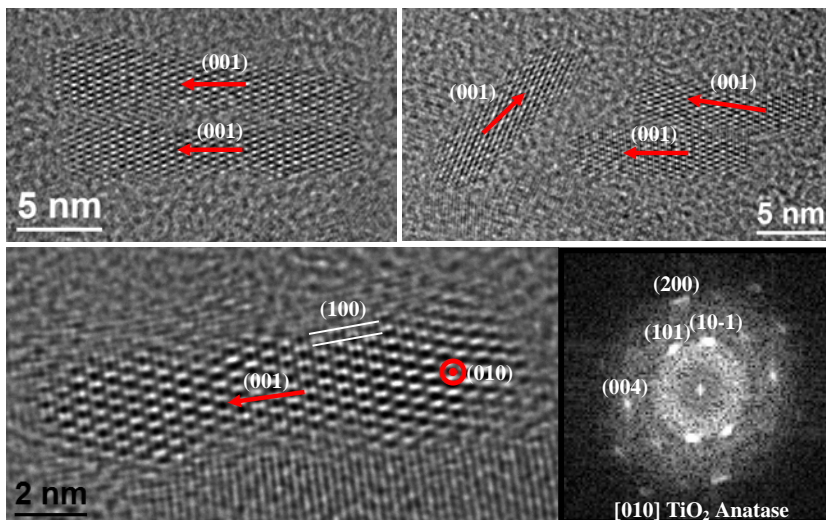


**Figure 4.31** TEM micrographs of TiO<sub>2</sub> anatase NRs with the corresponding power spectrum

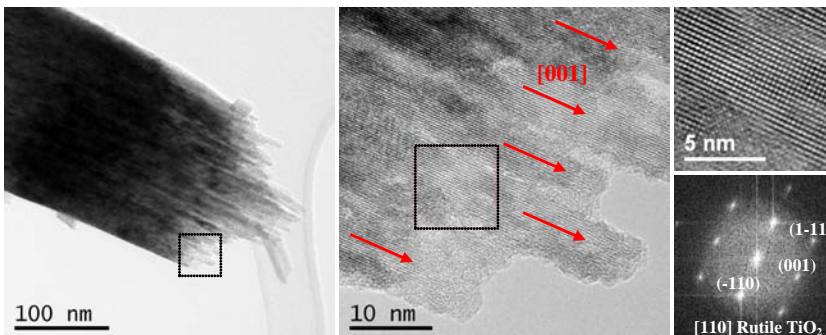


**Figure 4.32** TEM micrographs of TiO<sub>2</sub> rutile striped NRs with the corresponding power spectrum

annealing. Chlorine contamination that emerged during the growth process hinders the photocatalytic activity of the NRs in water splitting devices. Therefore, the presence of residual chlorine at a surface level has a remarkable effect on the performance of PEC devices based on TiO<sub>2</sub> NWs since it blocks water oxidation sites. An annealing treatment above 250 °C is proposed as a simple solution for overcoming the dramatic reduction of photo-current in PEC devices due to chlorine contamination.<sup>122</sup>

#### 4.3.2.2 TiO<sub>2</sub>@TiO nanowires

The use of metal oxides with a lattice parameter adaptable to that of the core and with the required electrical, optical and thermochemical properties allows the design of heterostructures with the desired functionalities. Therefore, investigations on mixed metal oxide junctions are of significant interest to overcome these crystallographic, electrical, optical or thermochemical stability requirements. A plausible strategy is the use of the metal oxide belonging to the same metal oxide group to produce binary metal oxide compounds with the required properties relative to the parent oxides and getting the adequate lattice parameters while avoiding any problem concerning thermodynamic stability.

As shown previously in this section, compositional graded and core-shell nanostructures are interesting architectures able to provide higher levels of control over the functional properties of the material.<sup>123</sup> Shells can provide higher chemical stability and surface passivation to prevent recombination, and they can extend the electric field region for charge carrier separation. Shells of lower band gap materials are also able to extend the core optical absorption to lower energies, thus promoting charge carrier photogeneration. The lattice mismatch is the main limitation to grow coaxial heterojunctions. Lattice mismatches generally introduce a significant density of interface defects and deteriorate the optoelectronic properties of the formed heterostructure. However, we were able to epitaxially grow a cubic TiO shell on rutile TiO<sub>2</sub> NWs for dye-synthesized solar cells (DSCs), where the core-shell structure caused a considerable change in the efficiency of the device.<sup>124</sup>

Indeed, the shell was expected to have anatase TiO<sub>2</sub> structure, but analyses on the power spectra (Figures 4.33(b) and 4.33(c)) show that it has a cubic TiO structure called '*hongquiite*'.<sup>125-127</sup> In the literature a reduced type of hongquiite also exists, with stoichiometry Ti-O: 0.91-1<sup>128</sup>. This phenomenon can be explained by considering the perfect epitaxial relationship between the core and

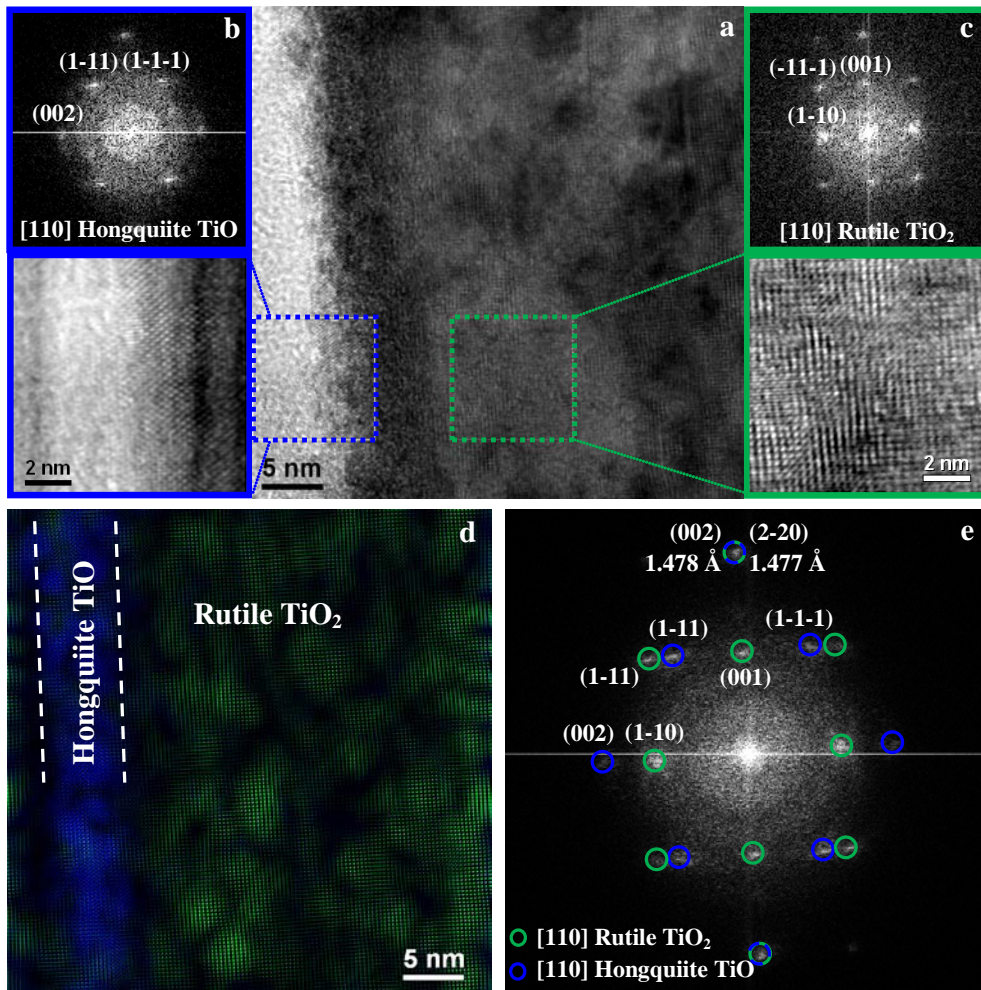


**Figure 4.33** HRTEM analysis of  $\text{TiO}_2@ \text{TiO}$  core-shell NWs, (a) HRTEM micrograph, (b) magnified zone of the shell shown in the blue square with corresponding power spectrum (c) magnified zone of the core shown in the green square with corresponding power spectrum (d) HRTEM filtered image obtained by filtering (e) the general power spectrum of the HRTEM micrograph (a)

the shell. See the power spectrum (FFT) of the whole HRTEM image (Figures 4.33(a)) in Figure 4.33(e). In this FFT, where the reflections of both structures appear, one can see that (2-20) plane family of hongquiite lie exactly on (002) plane family of rutile structure. Plane distance difference between rutile (001), 2.956 Å, and hongquiite (1-10), 2.953 Å, is only 0.003 Å (about 0.1%).

Therefore, there is perfect epitaxy between the two structures. This can be the reason for reduction of the phase from  $\text{TiO}_2$  to  $\text{TiO}$  whereas other titanium oxide structures such as anatase and brookite more commonly occur. In the filtered HRTEM image of Figure 4.33(d), the two structures are lucidly exhibited. Blue and green color is assigned to hongquuite  $\text{TiO}$  and rutile  $\text{TiO}_2$  structures, respectively. It is constructed by masking the power spectrum of Figure 4.33(e) which is the FFT of the whole HRTEM micrograph of Figure 4.33(a).

EELS analysis of Figure 4.34 confirms the results obtained with HRTEM. As seen in the EELS, the percentage of Ti vs. O increases in the borders (indicated with circles), which matches the existence of  $\text{TiO}$  hongquuite shell ( $\text{Ti}^{2+}$  instead of  $\text{Ti}^{4+}$ ). The green arrows show the direction of the scanning line, from upper border to the lower one. In the middle relative composition is Ti:  $33\pm 4\%$  - O:  $66\pm 4\%$ , and in the borders Ti percentage increase up to 41% which is in good agreement with  $\text{TiO}$  composition while the adjacency of  $\text{TiO}_2$  affects the real chemical composition due to the probe size and STEM/EELS spatial resolution.

With the presence of the hongquuite  $\text{TiO}$  shell,  $\text{TiO}_2@/\text{TiO}$  NW-based DSCs showed significantly higher  $J_{sc}$  values. A 3-fold increase in  $J_{sc}$ , up to values

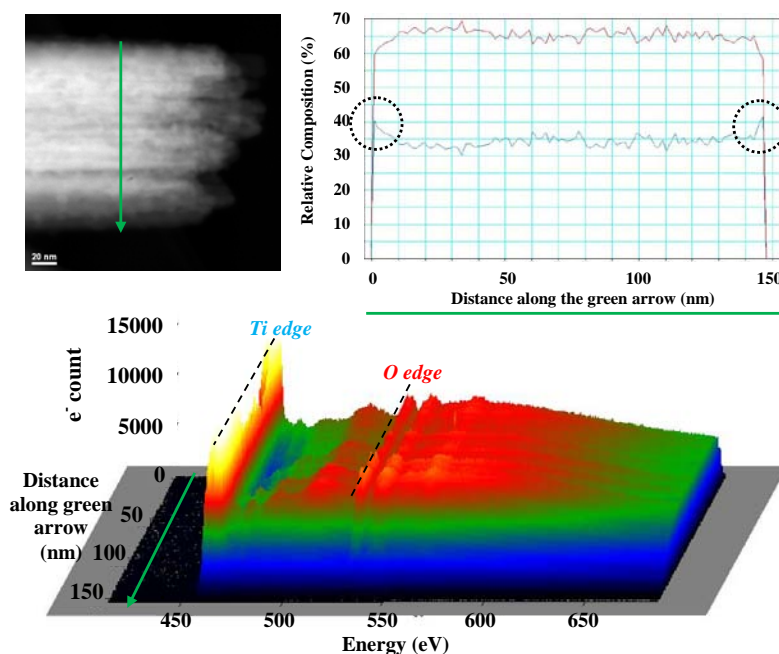


**Figure 4.34** EELS analysis on  $\text{TiO}_2@/\text{TiO}$  NWs showing the O deficiency in the borders

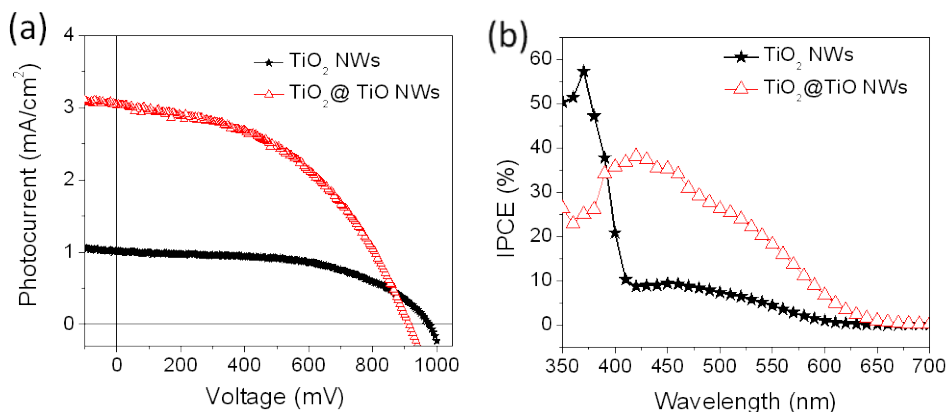


**Figure 4.35** (a) J-V characteristic and (b) spectra of incident photon to current efficiency under AM1.5G illumination of DSCs using bare rutile TiO<sub>2</sub> NWs and TiO<sub>2</sub>@TiO core-shell NWs

above 3.0 mA/cm<sup>2</sup>, was systematically obtained. On the other hand,  $V_{oc}$  values were just slightly reduced. Overall, with the presence of the TiO shell, the total DSC conversion efficiency increased by a factor 2.5, up to 1.3 %. Notable incident photon to current conversion efficiency (IPCE) enhancement was observed in the visible part of the spectra with the use of coaxial TiO<sub>2</sub>@TiO core-shell NWs (Figure 4.35(b)). Up to a 1.5 absorbance increase was obtained with the presence of the TiO shell which can be attributed to the higher surface roughness introduced with the TiO shell, which provided larger surface areas for dye loading and thus allowed to increase the dye concentration.

The amount of adsorbed dye is the main limitation in NW-based DSCs. Note that the relative density of the 3  $\mu\text{m}$  -long and 150 nm-thick TiO<sub>2</sub> NW arrays used in the present study was around 0.01 %, which contrasts with values close to 50 % in nanoparticle-based mesoporous films. TiO<sub>2</sub> NW arrays had surface areas 15-fold larger than the flat substrate where they were grown. This value is more than one order of magnitude lower than the surface areas of nanoparticle-based films commonly used for DSCs. Such lower surface areas translated into highly reduced dye concentrations, and therefore photocurrents. This is the main limitation behind the relatively low overall efficiencies measured from TiO<sub>2</sub> NW-based DSCs when compared with nanoparticle-based TiO<sub>2</sub> DSCs. Higher efficiencies require the use of longer NWs or hierarchical nanostructures.<sup>124</sup>

#### 4.3.2.3 Section summary

A thin TiO hongquuite shell on rutile TiO<sub>2</sub> NRs provided a significant improvement in functionality of the system. Aside from the increased roughness and thus surface area for dye loading, we believe that the TiO shell plays an active electronic role on the DSC performance enhancement. TiO is an n-type semiconductor with a slightly lower band gap than TiO<sub>2</sub>, between 2.9 and 3.5 eV.<sup>129-131</sup> While not much information regarding the relative position of the valence and conduction band edge is found in the literature, our results are consistent with a type-II band alignment between rutile TiO<sub>2</sub> and hongquuite TiO. This band alignment would favor the injection of electrons from the dye to the NW conduction band, thus leading to increased photocurrents.<sup>124</sup>

#### 4.3.3 SnO<sub>2</sub> nanowires and related heterostructures

Tin dioxide (SnO<sub>2</sub>) was one of the first considered, and still is the most frequently used, material for solid state gas sensors and many other applications. There is an obvious close relationship between the gas sensitivity of oxides and their surface chemical activity and thus gas sensing applications and catalytic properties should be considered jointly. This material is also utilized as transparent conductor and catalyst in many devices. Tin oxide is special in the respect that tin possesses a dual valency, within preferably attaining an oxidation state of 2+ or 4+. This dual valence facilitates a variation of the surface oxygen composition.<sup>70</sup>

SnO<sub>2</sub> belongs to the important family of oxide materials that combine low electrical resistance with high optical transparency in the visible range of the electromagnetic spectrum. These properties are notably useful for electrode materials in solar cells, light emitting diodes, flat panel displays, and other optoelectronic devices where an electric contact needs to be made without obstructing photons from either entering or escaping the optical active area and in transparent electronics such as transparent field effect transistors. Another property of SnO<sub>2</sub> and other transparent conducting oxides (such as ZnO and In<sub>2</sub>O<sub>3</sub>) is that although they are transparent in the visible they are highly reflective for infrared light which can be used as an energy conserving material.<sup>132,133</sup>

The most stable tin oxide structure is SnO<sub>2</sub> with mineral name ‘*cassiterite*’ with rutile crystal structure (tetragonal in  $P4_2mnm$  space group). It is a wide

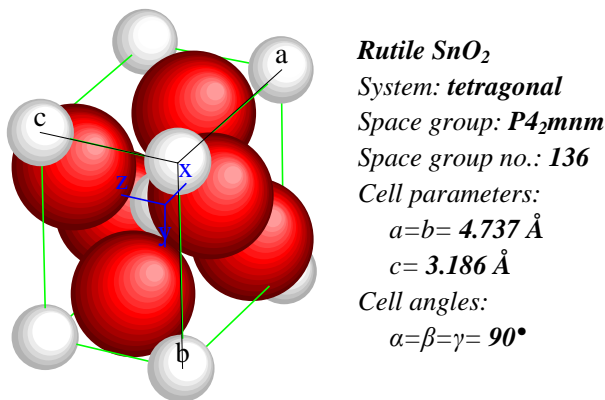


**Figure 4.36** Rutile tin dioxide ( $\text{SnO}_2$ ) unit cell and cell data

band gap semiconductor ( $E_g = 3.6 \text{ eV}$ ) and it melts at  $232 \text{ }^\circ\text{C}$ . The unit cell structure with corresponding data is shown in Figure 4.36.

Tin-oxide based catalysts exhibit good activity towards  $\text{CO/O}_2$  and  $\text{CO/NO}$  reactions.<sup>134,135</sup> It is shown that for different oxygen chemical potentials surfaces with  $\text{Sn}^{4+}$  or  $\text{Sn}^{2+}$  are stable. This indicates that an easy reduction and reoxidation of  $\text{SnO}_2$  surfaces can be expected in catalytic oxidation reactions. The activity and selectivity of tin-oxide catalysts can be substantially improved by incorporation of other elements such as V, Cu, Pd,<sup>136</sup>Cr,<sup>137</sup> etc.

All these metal oxides are suitable for gas sensing:  $\text{Cr}_2\text{O}_3$ ,  $\text{Mn}_2\text{O}_3$ ,  $\text{Co}_3\text{O}_4$ , NiO, CuO, CdO, MgO, SrO, BaO,  $\text{In}_2\text{O}_3$ ,  $\text{WO}_3$ ,  $\text{TiO}_2$ ,  $\text{V}_2\text{O}_3$ ,  $\text{Fe}_2\text{O}_3$ ,  $\text{GeO}_2$ ,  $\text{Nb}_2\text{O}_5$ ,  $\text{MoO}_3$ ,  $\text{Ta}_2\text{O}_5$ ,  $\text{La}_2\text{O}_3$ ,  $\text{CeO}_2$ ,  $\text{Nd}_2\text{O}_3$ , ZnO and  $\text{SnO}_2$ . Among all, ZnO and  $\text{SnO}_2$  are the most commonly used oxides for this purpose.  $\text{SnO}_2$  sensing mechanism is through the surface. Essentially, sensing response occurs when electrons are trapped in adsorbed molecules and the induced band bending in the surface causes a change in conductivity. It is previously described in section 4.1.4.2.

In the following, analogous to the previous sections, we start with bare NWS, and then we will study heterostructures, which in this case do not only consist of core-shell systems, but also NP-on-NW which form p-n nanojunctions comprising CuO NPs on  $\text{SnO}_2$  NWS.

#### 4.3.3.1 Bare $\text{SnO}_2$ nanowires

According to the properties mentioned in the previous section,  $\text{SnO}_2$  NWS are good candidates due to their high surface/volume ratio, high sensitivity and stability. Since the first synthesis of 1D tin oxide nanostructures,<sup>138</sup> considerable

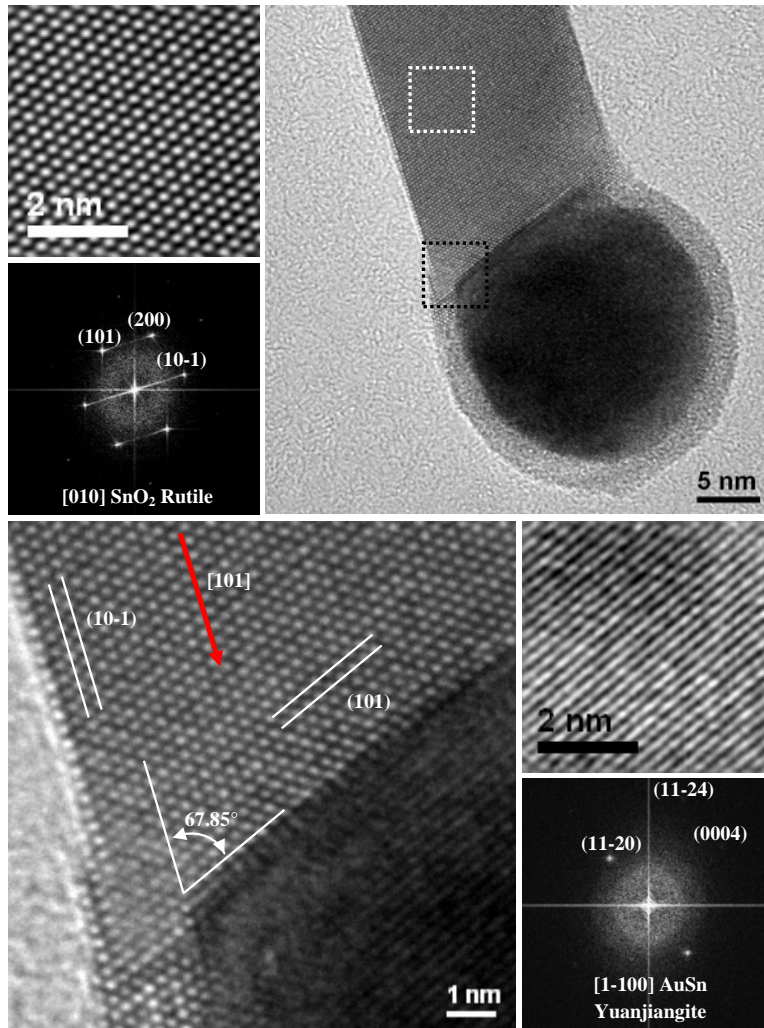


**Figure 4.37** HRTEM analysis of a rutile  $\text{SnO}_2$  NW showing the growth direction and the droplet

efforts have been carried out to investigate and improve their applications. In addition to their physical characteristics, their surface activity driven by the presence of residual groups such as dangling bonds and defects make them interesting systems to implement in nanodevices. For instance Hernandez-Ramirez *et al.* produced a gas sensor of a single  $\text{SnO}_2$  NW with high sensitivity to CO and humidity.<sup>6,72</sup>

In Figure 4.37 HRTEM micrographs of  $\text{SnO}_2$  NWs are shown. The tip matches the structure of hexagonal AuSn ‘yuanjiangite’ belonging to  $P6_3mmc$

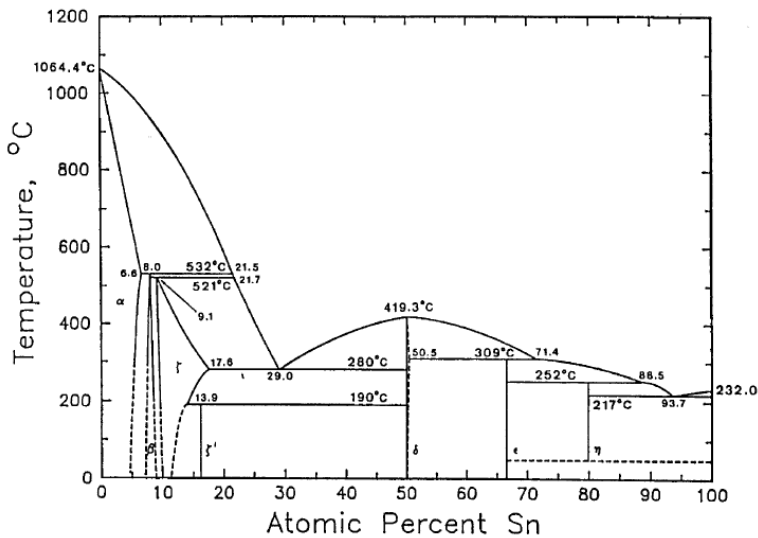
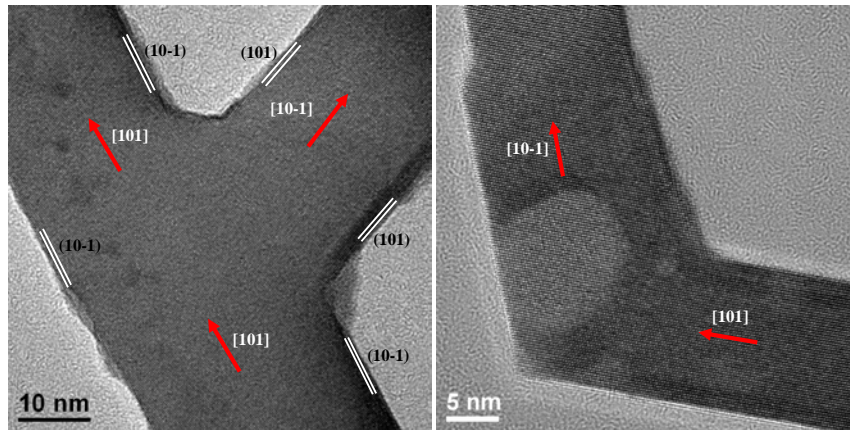


**Figure 4.38** Au-Sn phase diagram<sup>140</sup>

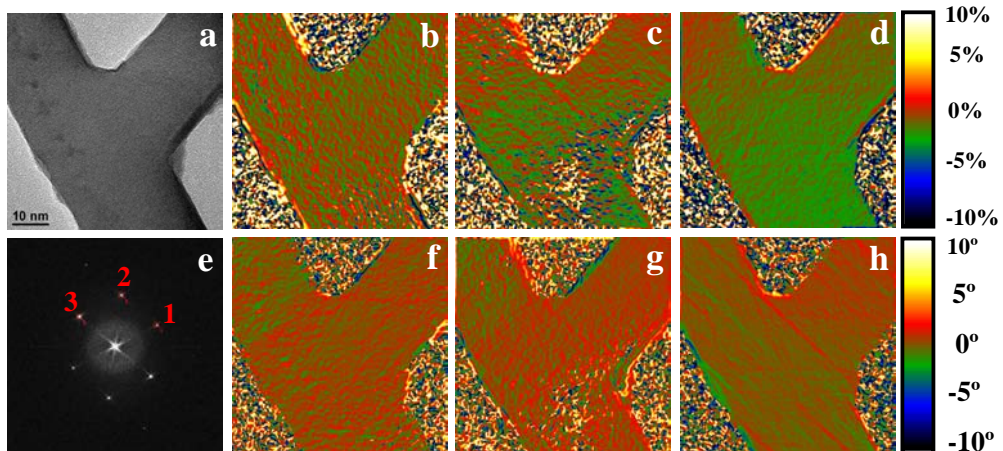
space group<sup>139</sup> as it could be predicted that during the growth process, the gold NPs melt and make an alloy with Sn, and saturation of this droplet with Sn with presence of oxygen gives rise to NW growth. Moreover, Phase diagram of Au-Sn system (Figure 4.38) confirms the existence of Au-Sn solid solution.<sup>140,141</sup> Interestingly, in SnO<sub>2</sub> NWs the interface between the droplet and the NW is never perpendicular to the growth direction. As indicated in Figure 4.37, the NWs grow in [101] direction, and the planes lying under (11-20) planes of the droplet are (101) as well. However, as the structure is tetragonal, (101) planes are not perpendicular to [101] direction, i.e. there is a 22.15° angle between them.

Further, in SnO<sub>2</sub> NWs kinks and branches were observed as shown in Figure 4.39. In the kinks the growth direction changes from [101] to [10-1] which are essentially from the same plane family. In the branched NWs, the NW continues in [101] direction likewise it branches out from [10-1] direction.

It was interesting to investigate whether branching causes any strain in the NW. Therefore, we performed geometric phase analysis (GPA), in order to locate the strain if there is any. The results can be seen in Figure 4.40 and Table 4.1. The first zone located in the upper part of the main wire is considered as the reference. Therefore, fringe deformation and rotation is zero in this case. The second zone is taken from the branch. The third zone is in the lower part of the main wire, and the fourth zone is located in junction point in the center, where



**Figure 4.39** Kinks and branches in SnO<sub>2</sub> NWs

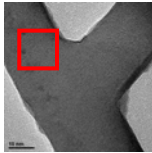
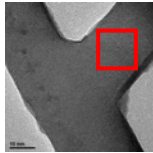
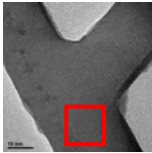
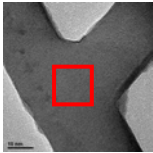


**Figure 4.40** GPA on a branched SnO<sub>2</sub> NW

the branch starts to sprout. The results in Table 4.1 show that the branched NWs are acceptably relaxed as almost in all the cases the deformation is less than 1%. The important point here is that no strain can be seen in the junction of the branch from the GPA maps of Figure 4.40. The junction is the critical zone from which the strain was expected to be high, however, the GPA maps reveal that there is no strain in this zone.

SnO<sub>2</sub> NWs with such excellent properties can be good candidates for core structure in the heterostructuring approach. Therefore, in the following, various core-shell and NP-on-NW systems are studied. Titanium oxide, vanadium oxide, and a mixture of them are accommodated on SnO<sub>2</sub> NWs as shells, and afterwards in the other approach SnO<sub>2</sub> NWs are decorated with CuO NPs.

**Table 4.1** Results of GPA on a branched  $\text{SnO}_2$  NW

<i>Position</i>	<i>1</i>	<i>2</i>	<i>3</i>	<i>4</i>
<i>Fringe Def. Result</i>				
<i>D1</i>	0% ( <i>ref.</i> )	-0.10%	0.07%	-0.04%
<i>R1</i>	0° ( <i>ref.</i> )	0.39°	0.38°	0.24°
<i>D2</i>	0% ( <i>ref.</i> )	0.11%	-0.07%	-0.75%
<i>R2</i>	0° ( <i>ref.</i> )	0.57°	0.91°	0.53°
<i>D3</i>	0% ( <i>ref.</i> )	-0.38%	-1.24%	-0.92%
<i>R3</i>	0° ( <i>ref.</i> )	0.48°	-0.04°	-0.004°

#### 4.3.3.2 $\text{SnO}_2@Ti_2O$ nanowires

HRTEM analysis and simulation investigations of the titania coated  $\text{SnO}_2$  nanowires confirms epitaxial growth of a thin trigonal  $Ti_2O$  shell on the  $\text{SnO}_2$  surface (Figure 4.41). In the case of  $TiO_2$  rutile on  $\text{SnO}_2$  we should expect the following mismatches: 3.03% in the front views from  $[100]_{TiO_2}$  rutile// $[100]_{SnO_2}$  zone axis, and 5.90% in the side view from  $[011]_{TiO_2}$  rutile// $[011]_{SnO_2}$  direction. Although the decomposition of  $Ti(O^iPr)_4$  by LPCVD was reported to form  $TiO_2$  deposits at temperatures in the range of 400-600 °C, the low-pressure CVD processes are in general well-suited for the synthesis of metastable phases due to non-equilibrium conditions prevalent in the CVD reactor.<sup>142</sup>

Nonetheless, time-resolved in-situ mass spectrometric analysis of its decomposition products proved the existence of reducing agents such as  $H_2$  during the deposition process (see Figure 4.42). The intriguing formation of  $Ti_2O$  in contrast to the expected  $TiO_2$  coating in such a thin layer can be explained in terms of non-equilibrium thermodynamics and the minimization of the Gibbs' free energy of the system.

Above a certain critical thickness, the formation of the shell is driven by thermodynamically favored processes. Thus, the minimum energy state necessary to overcome the strain created at the interface between core and shell materials is reached for example by the formation of defects such as

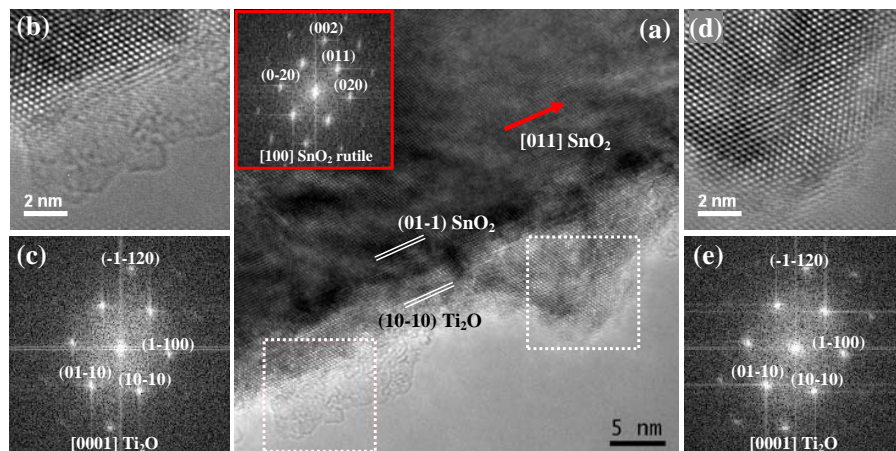


**Figure 4.41** HRTEM image of a  $\text{SnO}_2$  core NW with a  $\text{Ti}_2\text{O}$  shell showing the zone axis and growth directions. Power spectra show the crystallographic structure in (c) the layer and (e) the island, which are the same. The zones indicated by squares are magnified and frequency filtered in images (b) and (d). This comparison shows that the layer and the island have the same crystallographic structure. The power spectrum shown in the inset refers to the rutile  $\text{SnO}_2$  core.

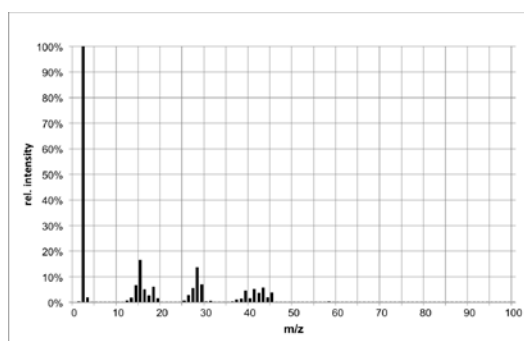


**Figure 4.42** In-situ mass spectrometrical analysis of the gas phase during the deposition process of  $\text{Ti}(\text{OPr})_4$ :  $m/z=2$  ( $\text{H}_2^+$ ), 18 ( $\text{H}_2\text{O}^+$ ), 15 ( $\text{CH}_3^+$ ), 42 ( $\text{C}_3\text{H}_5^+$ ), 45 ( $\text{C}_2\text{H}_6\text{O}^+$ ), 59 ( $\text{C}_3\text{H}_7\text{O}^+$ )<sup>59</sup>

dislocations. However, in the first stages of film growth, the crystal lattice of the shell tries to match the one of the core to create defect-free structures. In this case, the system needs to adjust the intrinsic strain created at the interface, and the minimum energy state is governed by searching the best epitaxial relationship between the crystal lattices.

In this context, thin  $\text{Ti}_2\text{O}$  layers grow at the surface of the  $\text{SnO}_2$  nanowires up to a certain critical thickness, in which the lattice mismatch is adjusted in

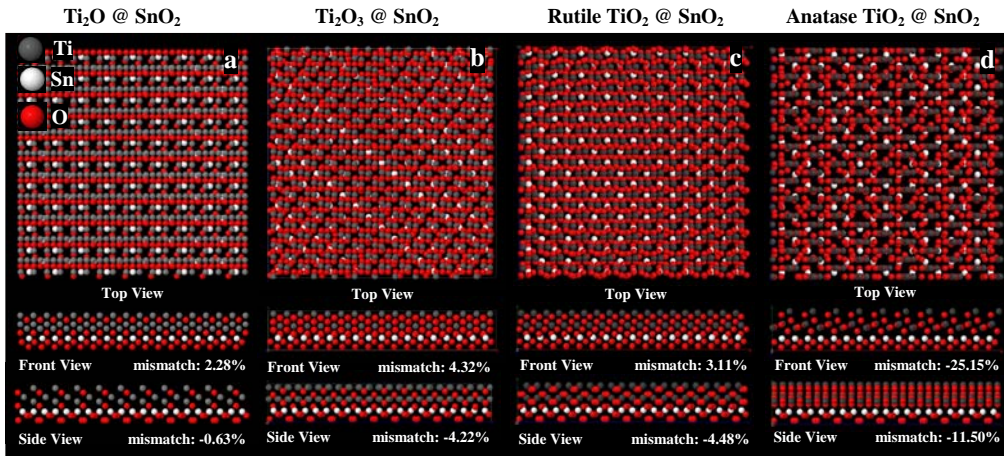


**Figure 4.43** Atomic simulation of the interfaces between rutile  $\text{SnO}_2$  NW core and different shells: (a)  $\text{Ti}_2\text{O}$ , (b)  $\text{Ti}_2\text{O}_3$ , (c)  $\text{TiO}_2$  rutile and (d)  $\text{TiO}_2$  anatase. Top views show the  $[10\text{-}10]_{\text{Ti}_2\text{O}} // [0\text{-}11]_{\text{SnO}_2}$  in the case of  $\text{Ti}_2\text{O}$  on  $\text{SnO}_2$ ,  $[11\text{-}20]_{\text{Ti}_2\text{O}_3} // [0\text{-}11]_{\text{SnO}_2}$  zone axis in the case of  $\text{Ti}_2\text{O}_3$  on  $\text{SnO}_2$  and  $[0\text{-}11]_{\text{TiO}_2} // [0\text{-}11]_{\text{SnO}_2}$  in the case of  $\text{TiO}_2$  rutile and anatase on  $\text{SnO}_2$ . Front views are visualized along the  $[0001]_{\text{Ti}_2\text{O}/\text{Ti}_2\text{O}_3} // [100]_{\text{SnO}_2}$  zone axis in the case of  $\text{Ti}_2\text{O}$  and  $\text{Ti}_2\text{O}_3$  on  $\text{SnO}_2$ , and along the  $[100]_{\text{TiO}_2} // [100]_{\text{SnO}_2}$  zone axis in the case of  $\text{TiO}_2$  rutile and anatase on  $\text{SnO}_2$ . Finally, the side view corresponds to the  $[-12\text{-}10]_{\text{Ti}_2\text{O}} // [011]_{\text{SnO}_2}$ ,  $[-1100]_{\text{Ti}_2\text{O}_3} // [011]_{\text{SnO}_2}$  and  $[011]_{\text{TiO}_2 \text{ anatase/rutile}} // [011]_{\text{SnO}_2}$  directions. In each case mismatch percentage is indicated under the model.

order to reach epitaxial growth. Epitaxial growth of  $\text{TiO}_2$  onto  $\text{SnO}_2$  presents serious problems due to the larger mismatch between both materials which is presented in Table 4.2. It is well-known that there exist three polymorphs of  $\text{TiO}_2$ : anatase (tetragonal), rutile (tetragonal) and brookite (orthorhombic). Anatase and rutile phases are expected from the chemical vapor decomposition of  $\text{Ti}(\text{O}^i\text{Pr})_4$  because they are more stable and thermodynamically most favorable.

Furthermore, the tetragonal symmetry is isostructural with rutile  $\text{SnO}_2$  NWs, which in principle minimizes the enthalpy of mixing. However, according to the computer simulations, the lattice mismatch between rutile  $\text{TiO}_2$  and  $\text{SnO}_2$  is still considerable reaching values of 23.11% in the front views from  $[100]_{\text{TiO}_2 \text{ rutile}} // [100]_{\text{SnO}_2}$  zone axis, and 24.48% in the side view from  $[011]_{\text{TiO}_2 \text{ rutile}} // [011]_{\text{SnO}_2}$  direction. In the case of anatase  $\text{TiO}_2$  on  $\text{SnO}_2$ , the mismatch dramatically increases reaching values up to 225.15% in the front views from

$[100]_{\text{TiO}_2 \text{ anatase}} // [100]_{\text{SnO}_2}$  zone axis, and 211.50% in the side view from  $[011]_{\text{TiO}_2 \text{ anatase}} // [011]_{\text{SnO}_2}$  direction (see Figure 4.43).

**Table 4.2** Mismatch values (%) between cassiterite  $\text{SnO}_2$  core and different  $\text{TiO}_x$  shell systems

	$\text{SnO}_2 @ \text{Ti}_2\text{O}$	$\text{SnO}_2 @ \text{Ti}_2\text{O}_3$	$\text{SnO}_2 @ \text{TiO}_2$ (rutile)	$\text{SnO}_2 @ \text{TiO}_2$ (anatase)
Front	+2.28	+4.32	+3.03	+20.10
Side	-0.63	-4.22	+5.9	-33.02

In contrast, Figure 4.41(a) shows a homogeneous  $\text{Ti}_2\text{O}$  shell covering the surface of the  $\text{SnO}_2$  NWs after few seconds of deposition. Two areas were investigated in detail corresponding to a region of the monolayer; and an island in the first stage of nucleation formed in the shell. Figures 4.41(c) and 4.41(e) show the indexed power spectra corresponding to the areas Figures 4.41(d) and 4.41(d), respectively. The  $\text{Ti}_2\text{O}$  shell formed in both cases a crystalline structure with trigonal symmetry in  $P-3m1$  space group (no. 164).<sup>143,144</sup> HRTEM analysis confirms the epitaxial growth of the (10-10) planes of trigonal  $\text{Ti}_2\text{O}$  on the (01-1) planes of rutile  $\text{SnO}_2$ , orthogonal to the NW growth direction [011]. The reduced Ti phase found experimentally ( $\text{Ti}_2\text{O}$ ), showed a significantly lower mismatch than the expected for  $\text{TiO}_2$  in its rutile phase, in particular 2.28% in the front views from  $[0001]_{\text{Ti}_2\text{O}} // [100]_{\text{SnO}_2}$  zone axis, and 20.63% in the side view from  $[-12-10]_{\text{Ti}_2\text{O}} // [011]_{\text{SnO}_2}$  direction. Simulations of this interface, associated with the two other interfaces of  $\text{SnO}_2 @ \text{V}_2\text{O}_3$  and  $\text{SnO}_2 @ \text{TiVO}_3$  are brought in section 4.3.3.4 in Figure 4.43.

#### 4.3.3.3 $\text{SnO}_2 @ \text{V}_2\text{O}_3$ nanowires

HRTEM images shown in Figure 4.44 reveal a homogeneous  $\text{V}_2\text{O}_3$  shell layer epitaxially grown on the  $\text{SnO}_2$  NW core. Several  $\text{VO}_x$  crystal structures with different stoichiometries were simulated in order to unambiguously identify the structure of the shell present in the  $\text{SnO}_2 / \text{VO}_x$  heterostructure. Among all different phases of vanadium oxide, karelianite  $\text{V}_2\text{O}_3$  (with trigonal structure) exhibits the best epitaxial relationship with  $\text{SnO}_2$ , and consequently the lowest mismatch. In previous works, the thermal decomposition of  $\text{VO}(\text{O}^i\text{Pr})_3$  at such

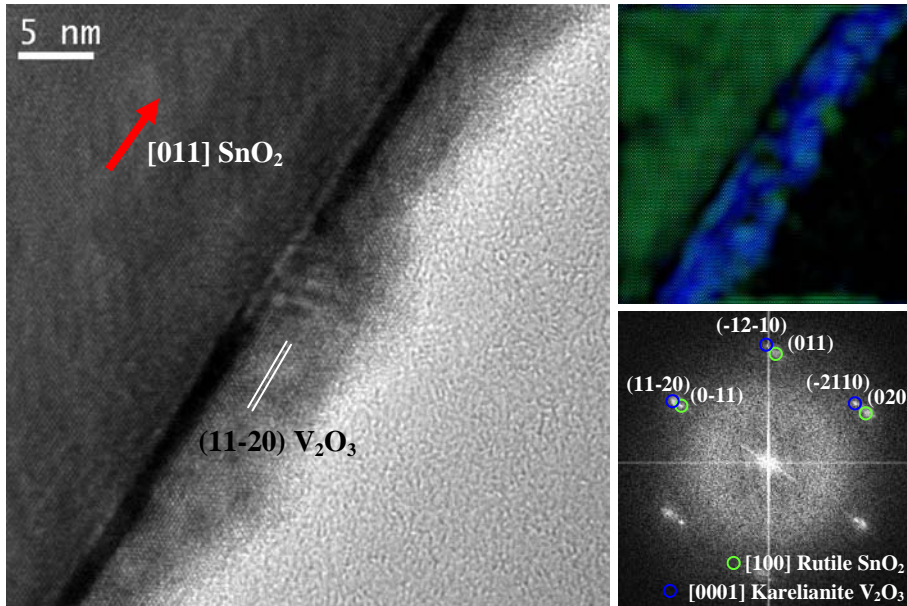


**Figure 4.44** HRTEM image of a  $\text{SnO}_2$  core NW with  $\text{V}_2\text{O}_3$  shell associated with the frequency-filtered image in color (green and blue colors correspond to  $\text{SnO}_2$  and  $\text{V}_2\text{O}_3$ , respectively as well as on the power spectrum) and the indexed power spectrum (FFT)

temperatures resulted in the formation of  $\text{VO}_2$  deposits.<sup>30</sup> However, the formation of  $\text{H}_2$  during the decomposition process of this precursor, followed by time resolved in situ mass spectrometry measurements, might also facilitate the formation of partially reduced overlayers. Therefore, the formation of a thin  $\text{V}_2\text{O}_3$  film on the  $\text{SnO}_2$  surface can be explained similarly to the case of the  $\text{TiO}_x$  system. On the one hand, when the layer is too thin, the expected  $\text{VO}_2$  deposits might be reduced to  $\text{V}_2\text{O}_3$  in the presence of reducing agents in the gas phase ( $\text{H}_2$ ) that interact with the surface of the deposited materials. Furthermore, the structure of  $\text{V}_2\text{O}_3$  adapts to the  $\text{SnO}_2$  lattice with the lowest mismatch. On the HRTEM micrograph of Figure 4.44 shows the growth directions and epitaxial relationship at the interface of the  $\text{SnO}_2/\text{V}_2\text{O}_3$  core-shell heterostructure are indicated.

Although the shell has a homogeneous structure, the presence of 2D monolayers and 3D islands in the shell is notable (as well as in the case of  $\text{Ti}_2\text{O}$  shell in previous part). The  $\text{SnO}_2$  nanowire grows along the [011] direction and exhibits (0-11) planes facing the surface, which are continued by (11-20) planes corresponding to the trigonal  $\text{V}_2\text{O}_3$  shell. In Figure 4.44 displays the colored

frequency filtered (IFFT) HRTEM image of the system is revealed which shows the rutile  $\text{SnO}_2$  core (green) and the karelianite  $\text{V}_2\text{O}_3$  shell (blue). The power spectrum (FFT) in this figure confirmed that (11-20) planes of karelianite  $\text{V}_2\text{O}_3$  shell were grown parallel to the (0-11) planes of rutile  $\text{SnO}_2$  with a slight difference in cell parameter. In other words, (11-20) plane series of karelianite  $\text{V}_2\text{O}_3$  grows epitaxially on (0-11) plane series of rutile  $\text{SnO}_2$  facing the surface of the NW. The remaining plane series shown in the power spectrum are slightly different in angle and size. Comparing the crystallographic structure of bulk karelianite  $\text{V}_2\text{O}_3$  with the one found on the shell, some differences are noticed. These variations can be interpreted as the result of the strain that the layer suffers to decrease the mismatch between  $\text{V}_2\text{O}_3$  shell and  $\text{SnO}_2$  core. The trigonal  $\text{V}_2\text{O}_3$  shell trying to match with the core causes a  $+2.2^\circ$  deformation on the (-2110) planes and a  $+0.1 \text{ \AA}$  crystal expansion on the (1-210) plane distance. The final theoretical mismatch in this case is 0.06% in the front views from  $[0001]_{\text{V}_2\text{O}_3}/[100]_{\text{SnO}_2}$  zone axis, and 21.48% in the side view from  $[-1100]_{\text{V}_2\text{O}_3}/[011]_{\text{SnO}_2}$  direction (see also simulations in Figure 4.48). Moreover, no intermixing of cations is observed in these core-shell nanostructures, corroborating the good compatibility of these two materials.

#### 4.3.3.4 $\text{SnO}_2@ \text{TiVO}_3$ nanowires

Since the ionic radius of the 6-coordinated  $\text{V}^{4+}$  in  $\text{VO}_2$  (0.072 nm) is very close to that of  $\text{Ti}^{4+}$  in a rutile  $\text{TiO}_2$  crystal (0.0745 nm) a large feasibility is expected in the formation of mixed metal  $\text{TiVO}_x$  phase. Rutile  $\text{TiO}_2$  is a stable material with a band gap larger than 3 eV (3.75 eV direct and 3.05 indirect) and, hence, a combination of  $\text{TiO}_2$  and  $\text{VO}_2$  seems to satisfy the requirements for formation of a solid solution with a band gap narrower than  $\text{TiO}_2$  and fulfilling the whole thermochemical stability requirement. Although  $\text{VO}_2$  with band gap energy of 0.62 eV is a well-known rutile type crystal, the multiple chemical valences offered by the vanadium can cause variation in the V:O stoichiometry and phase structure of the final material depending upon the synthesis conditions.

Figure 4.45 shows the titanium-vanadium oxide (TVO) shells on  $\text{SnO}_2$  NWS at different growth levels. The shell formation via CVD follows a general trend in all cases. Initially, monolayers are formed (2D layer-by-layer growth) and beyond a critical layer thickness, due to the accumulated stress energy, growth continues through the nucleation of 3D islands. Figure 4.45 from left to right

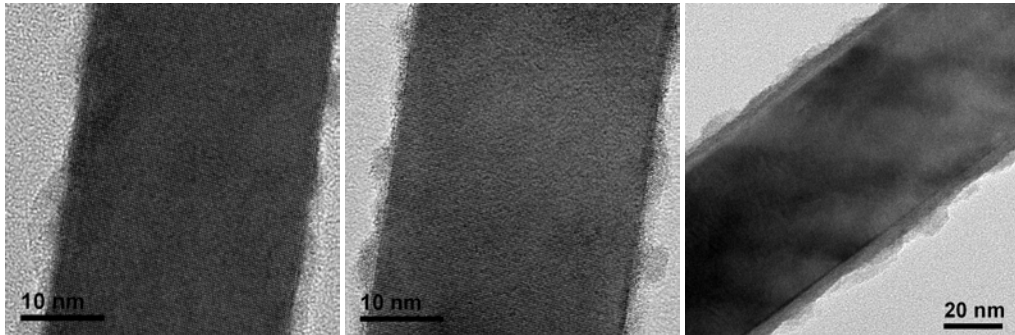


**Figure 4.45** TVO shell growth on SnO<sub>2</sub> NWs at different stages from left to right

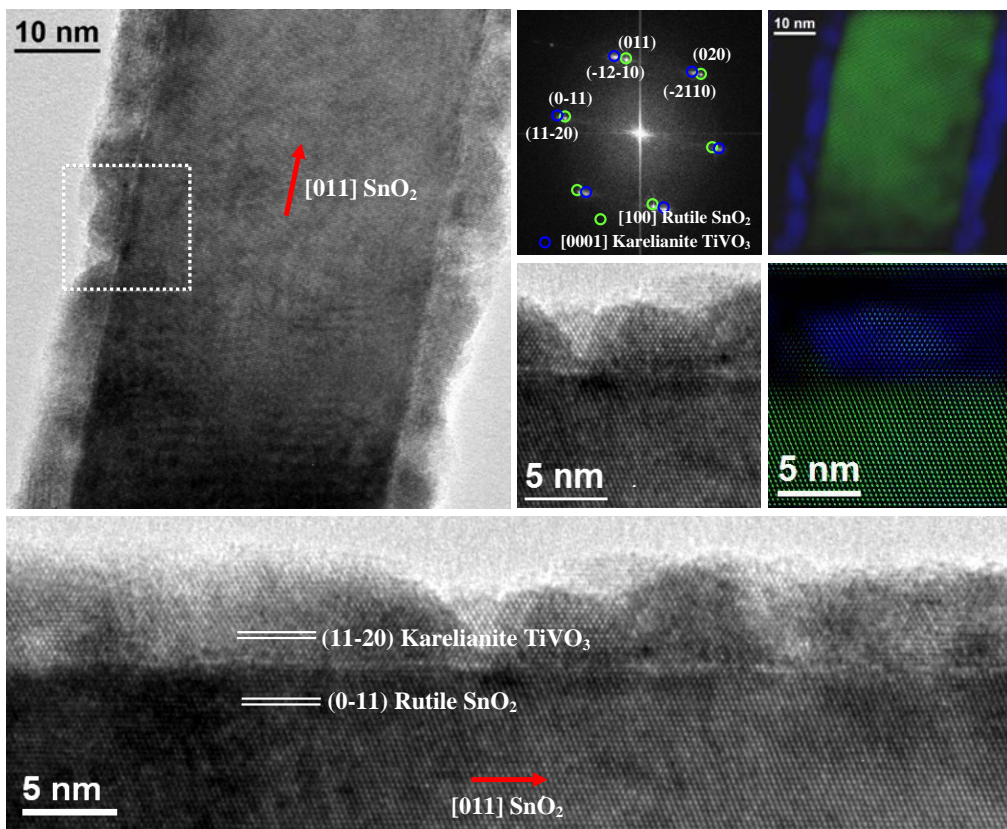


**Figure 4.46** HRTEM image of a SnO<sub>2</sub> core nanowire with a TVO type shell associated with frequency-filtered images obtained from the indexed power spectrum (green and blue correspond to SnO<sub>2</sub> and TiVO, respectively)

shows how the shell grows. The image at left reveals the first stage of growth. First, a homogeneous TVO monolayer with a thickness of few nanometers

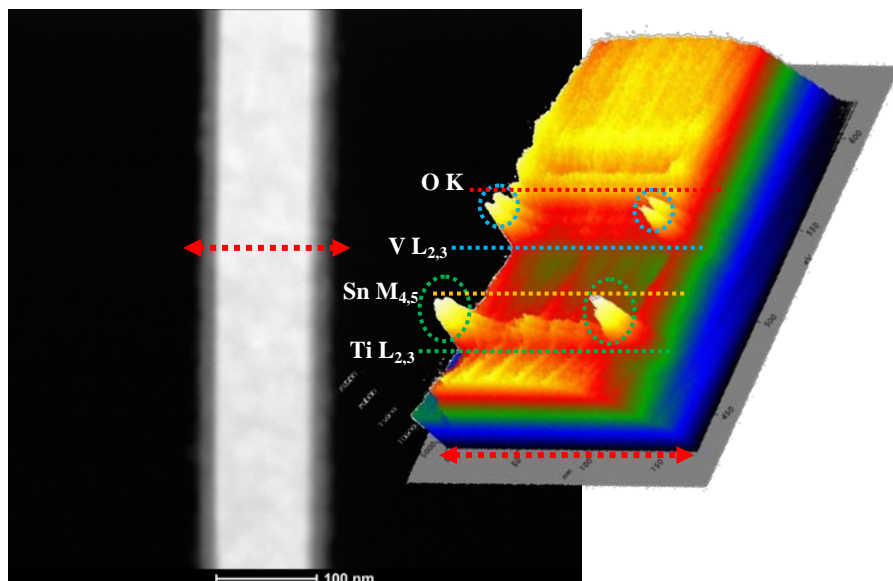


**Figure 4.47** Z-contrast STEM image with line-scan EELS along the diameter of an  $\text{SnO}_2$ @TVO core-shell NW

grows uniformly and epitaxially on the NW surface reaching a critical thickness, after which island nucleation and coalescence occurs. In the next image the layer is thicker and more islands appear to nucleate and grow. Finally, in the image at right the monolayers increase the thickness and nucleated islands cover the whole surface. Such growth mechanism is well-known as ‘*Stranski-Krastanov*’ (SK).<sup>145</sup>

Figure 4.46 shows the HRTEM analysis of the titanium-vanadium (TVO) shell, which is composed of both monolayer and islands formed at the  $\text{SnO}_2$  surface. The  $\text{SnO}_2$  NW grows along the [011] direction. In this Figure the magnified view of the TVO shell and its corresponding power spectrum are shown, in which slight differences between the cell parameters of the core and the shell can be found. To confirm the heterostructure composition, the power spectrum was frequency filtered (IFFT) where a clear interface between the  $\text{SnO}_2$  core (green) and the TVO (blue) shell is easily observed. The lower image exhibits (11-20) planes of karelianite  $\text{TiVO}_3$  lying on (01-1) planes of rutile  $\text{SnO}_2$ .

Figure 4.47 shows the Z-contrast or high-angle annular dark-field (HAADF) image of the  $\text{SnO}_2$ /TVO core-shell heterostructure, in which an EELS spectrum profile was performed. EELS analyses revealed that the relative

content of Ti and V on the shell is 50 at%, respectively. Computer simulations suggest that the TVO shell presents a crystal structure equivalent to the previously analyzed karelianite  $V_2O_3$  shell structure (trigonal), which so far showed the best epitaxial relation with the cassiterite  $SnO_2$  NWs (tetragonal). According to literature, Ti atoms can substitute the position of the V atoms maintaining the karelianite structure.<sup>146,147</sup> As the relative content of V and Ti is equal (50%), the formation of rhombohedral  $(Ti_{0.5}V_{0.5})_2O_3$  structure is proposed (Table 4.3).

**Table 4.3** Mismatch values (%) between cassiterite  $SnO_2$  core and different shells:  $Ti_2O_3$ , TVO, and  $V_2O_3$

	$SnO_2@Ti_2O_3$	$SnO_2@(Ti_{0.5}V_{0.5})_2O_3$	$SnO_2@V_2O_3$
Front	+2.28	+1.47	+0.06
Side	-0.63	-1.55	-1.48

The epitaxial relationship between the proposed  $(Ti_{0.5}V_{0.5})_2O_3$  shell and the  $SnO_2$  core was modeled. Values of +1.47% and -1.55% were obtained for the mismatch in front and side views, respectively (Figure 4.48), which is in good agreement with the HRTEM results. Although the mismatch is not as low as in the case of pure trigonal  $V_2O_3$ , the epitaxial relationship has been improved comparing to pure trigonal  $Ti_2O_3$  titanium oxide. The atomic models simulated reveal that by increasing the percentage of vanadium in the shell, the mismatch between the  $SnO_2$  core and TVO shell decreases. Even though  $Ti_2O_3$  with trigonal structure was not empirically formed, atomic simulations were still performed to understand more clearly the formation of the TVO shell (see Figure 4.43).

The theoretical mismatch calculated in the simulated model for  $Ti_2O_3$  on  $SnO_2$  was found to be +4.32% in the front views from  $[0001]_{Ti_2O_3}/[100]_{SnO_2}$  zone axis, and -4.22% in the side view from  $[-1100]_{Ti_2O_3}/[011]_{SnO_2}$  direction (Figure 4.43). Therefore, trigonal  $Ti_2O_3$  evidently showed the best matching on  $SnO_2$  among all the studied titanium oxides, which supported its formation by CVD. However, the stabilization of this subvalent Ti phase is rather intriguing and is currently the subject of further investigations within our research.

Summarizing,  $\text{SnO}_2@V_2O_3$  core-shell heterostructures show the best epitaxial relationship at the heterojunction. Although the  $\text{Ti}_2O$  shell shows a partially good epitaxy with the  $\text{SnO}_2$  core, it does not show a smooth and homogeneous surface, as it is chemically unstable. Meanwhile, the mixed oxide shell which leads to the formation of  $\text{SnO}_2@(\text{Ti}_{0.5}\text{V}_{0.5})_2O_3$  heterostructures shows a smooth structure with low mismatch in the heterojunction (+1.47% and -1.55% of mismatch in front and side view respectively), and it is expected to be more chemically and structural stable.

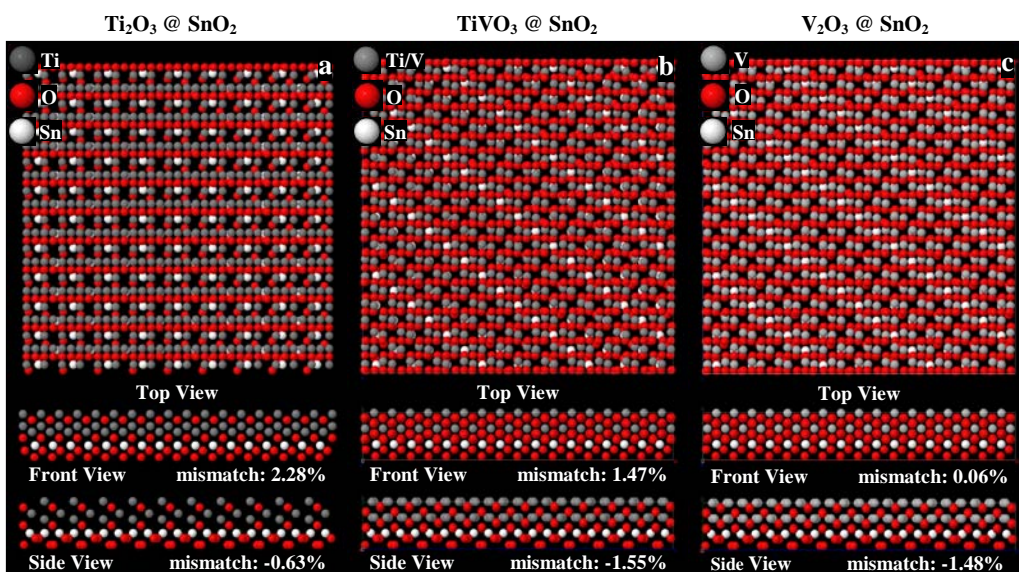


**Figure 4.48** Atomic simulation of the interfaces between rutile  $\text{SnO}_2$  NW core and different shells: (a)  $\text{Ti}_2O$ , (b)  $(\text{Ti}_{0.5}\text{V}_{0.5})_2O_3$ , and (c)  $V_2O_3$ . Top views show the  $[10-10]_{\text{Ti}_2O} // [0-11]_{\text{SnO}_2}$  in the case of  $\text{Ti}_2O$  on  $\text{SnO}_2$  and  $[11-20]_{(\text{Ti}_{1-x}\text{V}_x)_2O_3} // [0-11]_{\text{SnO}_2}$  zone axis in the case of TVO and  $V_2O_3$  on  $\text{SnO}_2$ . Front views are visualized along the  $[0001]_{\text{Ti}_2O/(\text{Ti}_{1-x}\text{V}_x)_2O_3} // [100]_{\text{SnO}_2}$  zone axis in all the cases. Finally, the side view corresponds to the  $[-12-10]_{\text{Ti}_2O} // [011]_{\text{SnO}_2}$  and  $[-1100]_{(\text{Ti}_{1-x}\text{V}_x)_2O_3} // [011]_{\text{SnO}_2}$  direction. In each case mismatch percentage is indicated under the model.

#### 4.3.3.5 $\text{SnO}_2$ nanowires decorated with CuO nanoparticles

On the one hand,  $\text{SnO}_2$  NWs were proved to be good candidates for gas sensing due to their suitable thermal and chemical stability, low electrical conductivity, and high selectivity. On the other hand, CuO is a suitable material

for  $\text{H}_2\text{S}$  detection. In addition  $\text{SnO}_2$  is an n-type semiconductor, while  $\text{CuO}$  is a p-type. Therefore, a wise idea can be creating a heterostructure in order to take advantage of the properties of both materials, as their interface forms a p-n junction.  $\text{CuO}$  NP acts like a p-type semiconductor and  $\text{SnO}_2$  NW as an n-type, where a depletion zone appears in the interface.

Before studying this heterostructure, it is worth to mention a few words about the behavior of  $\text{CuO}$  in gas sensing. Copper oxide which is the product of interaction of oxygen with copper has two different structures:  $\text{CuO}$  and  $\text{Cu}_2\text{O}$ . Copper (II) oxide, or cupric oxide ( $\text{CuO}$ ), is an intrinsically p-type semiconductor mainly due to Cu vacancies<sup>148</sup> with a narrow band gap of 1.2 eV. Copper (I) oxide or cuprous oxide ( $\text{Cu}_2\text{O}$ ) is a p-type semiconductor as well, and has an energy gap of 2.1 eV and a cubic crystal structure.

In the n-type semiconductors that follow surface sensing mechanism (such

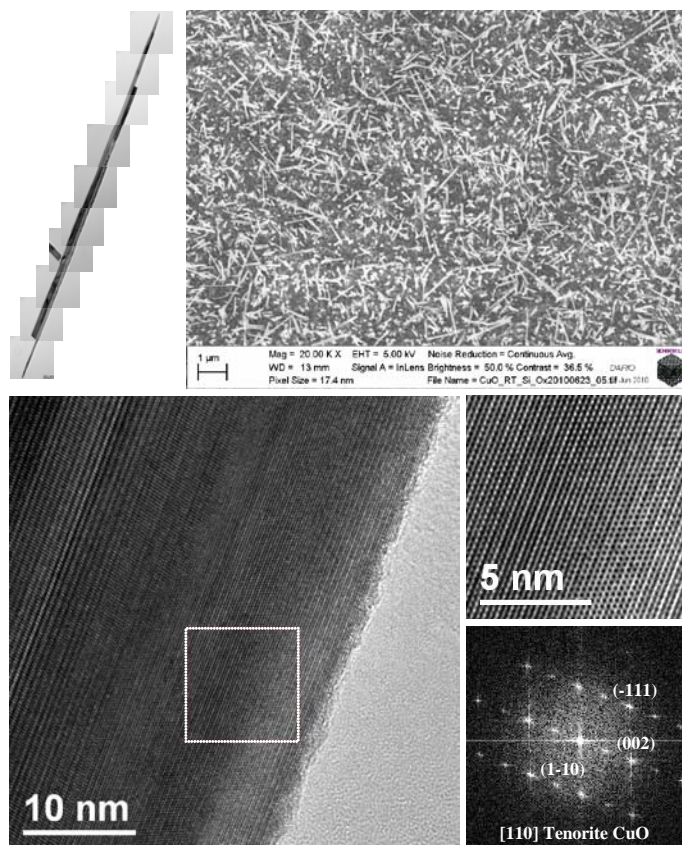
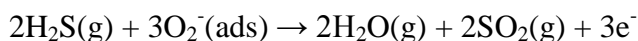


**Figure 4.49**  $\text{CuO}$  NWs, BF-TEM micrograph (top-left), SEM micrograph (top-right), and HRTEM analysis (bottom) associated with indexed power spectrum (bottom-right)

as ZnO, SnO<sub>2</sub>, In<sub>2</sub>O<sub>3</sub>), there is a decrease in conductance while they are exposed to oxidizing gases (e.g. NO<sub>2</sub> or O<sub>3</sub>). Additionally in p-type semiconductors like CuO, electrical conductivity decreases in the similar condition, which is attributed to a decrease in the charge carrier (hole) concentration upon reaction between the oxidizing gas and the adsorbed oxygen species.<sup>149,150</sup> For copper oxide NWS (shown in Figure 4.49), as it is a p-type oxide semiconductor, the measured current decreased in presence of reducing gases (e.g. ethanol and methane) as shown in Figure 4.50. Their interaction with the metal oxide surface produces similar effect on the conductance of the sensing layer i.e. a reduction in the conductance. This phenomenon is due to a reduction of charge carrier (holes) concentration upon reaction between the target gas and the adsorbed oxygen species.<sup>151</sup> However, sensing mechanism of CuO exposed to H<sub>2</sub>S gas is different. In Figure 4.50 (right) the behavior of CuO NWS towards various concentrations of H<sub>2</sub>S at different working temperatures is revealed. H<sub>2</sub>S interacts with CuO according to two different mechanisms<sup>152,153</sup> depending on the gas concentration:

(i) At low concentration adsorbed oxygen on the surface causes the oxidation of H<sub>2</sub>S via reaction:



Released electrons recombine with holes on the semiconductor surface, resulting in an increase of the resistance. This process is easily recovered removing the gas and exposing the semiconductor surface to synthetic air flow.

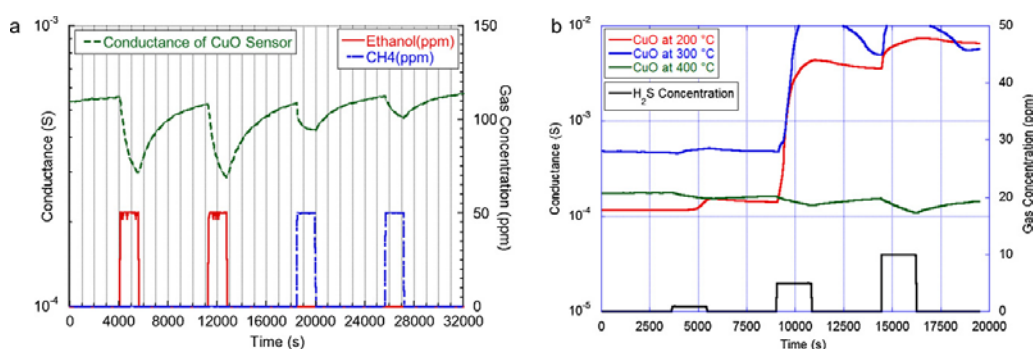
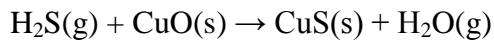


**Figure 4.50** (Left) Dynamic response of CuO NWs at a working temperature of 400 °C towards 50 ppm square concentration pulses of Ethanol and Methane, (Right) Dynamic response towards 1, 5 and 10 ppm of H<sub>2</sub>S at 200, 300 and 400 °C<sup>20</sup>

(ii) At high concentration another reaction occurs together with the previous one:



In the case of CuO NWs, this reaction causes the formation of CuS compound which covers the surface of CuO NWs. CuS, being metallic, enhances the connectivity between the neighboring NWs and the conductivity of the surface of each NW, which results in a decrease of the overall resistance of the samples and an increase of the conductance. This second mechanism is also reversible but it is much slower than the first one, and the reversibility is thermally activated. In the case of CuO NPs on SnO<sub>2</sub> NWs, H<sub>2</sub>S absorption to the surface of CuO NPs/SnO<sub>2</sub> NWs with the second mechanism, changes the CuO to metallic CuS. A schematic illustration of this mechanism is shown in Figure 4.51. In this figure, it is proposed that the main underlying sensing mechanism of p-CuO NP/n-SnO<sub>2</sub> NW heterostructures upon exposure to H<sub>2</sub>S is the chemical transformation from p-CuO to metallic CuS which modifies the depleted region that is formed at the p-CuO/n-SnO<sub>2</sub> interface and strangles the conduction channel inside the NWs in oxygen-rich atmosphere. After exposure to H<sub>2</sub>S, the breakup of the p-n junction effectively enlarges the conduction

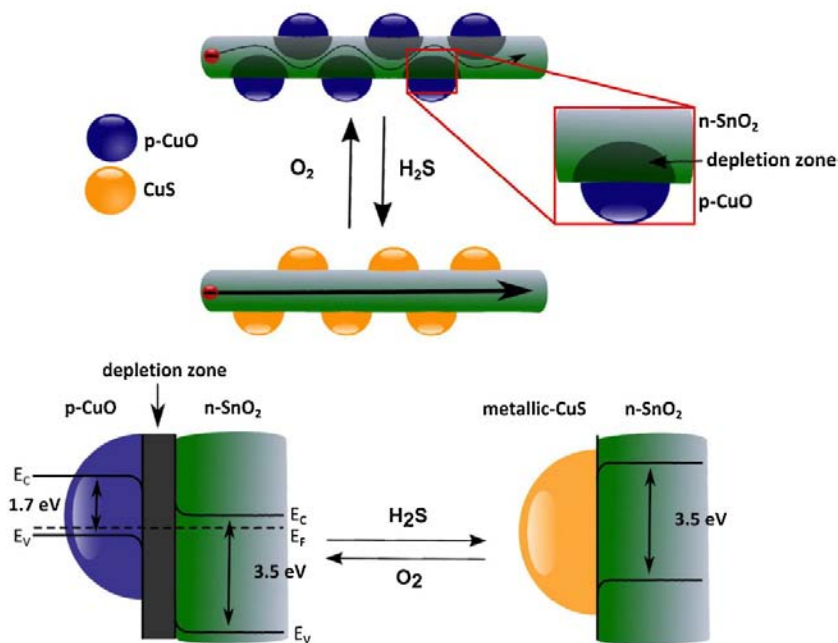


**Figure 4.51** Scheme of p-CuO NPs on n-SnO<sub>2</sub> NWs showing the sensing mechanism<sup>28</sup>

section in the NW, leading to a significant improvement of the conductivity. Second order effects like the oxidation of  $H_2S$  by adsorbed oxygen on CuO NPs may also contribute to the p-n junction modulation.<sup>20,26,154,155</sup>

In Figure 4.52 HAADF-STEM images of p-CuO NP/n-SnO<sub>2</sub> NW heterostructure with an EDX elemental map are shown. One can see how the NPs decorate the NWs. The NPs, compared to the NW are relatively large and they have an interface which cannot be studied by HRTEM due to the big size of the NPs which cover the interface and the NW.

Figure 4.53 shows the response of an individual p-CuO NP/n-SnO<sub>2</sub> NW heterostructure to  $H_2S$  pulses. Note that the dynamic response of the device is convoluted with the dynamic response of the gas chamber. The inset in this figure is an SEM image of the single NW sensor setup. It was prepared by focused ion beam (FIB) lithography. Pt is deposited in the two ends of the NW

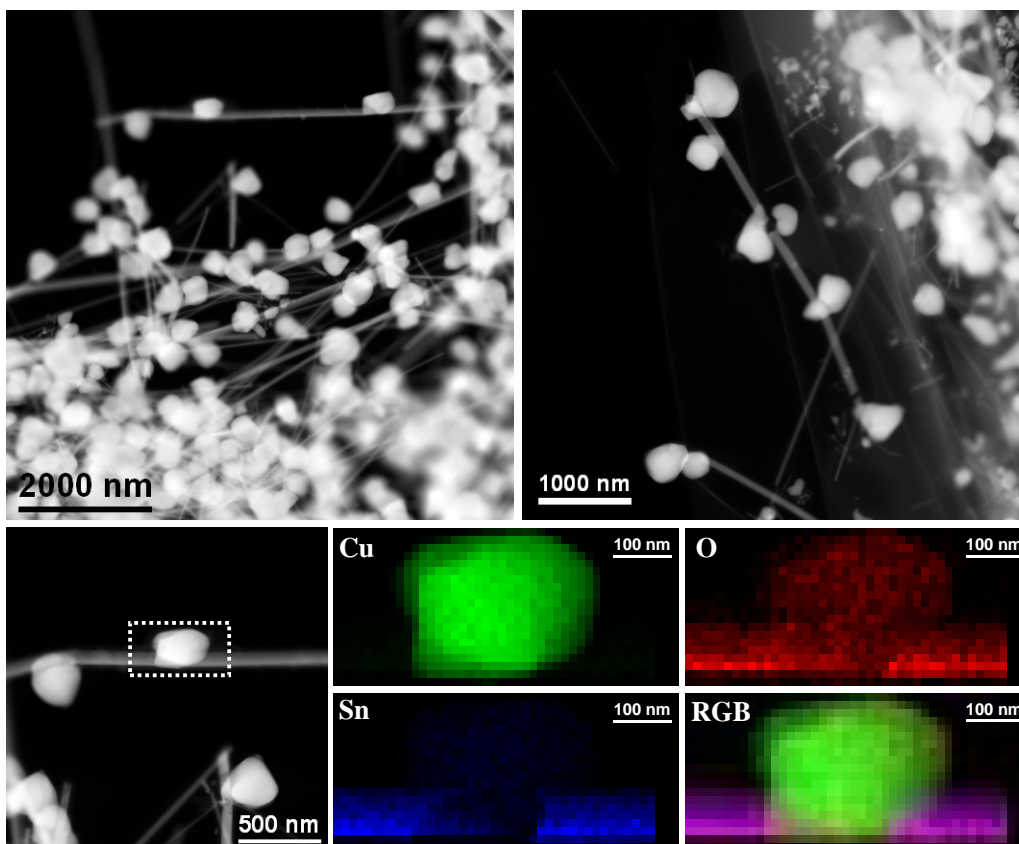
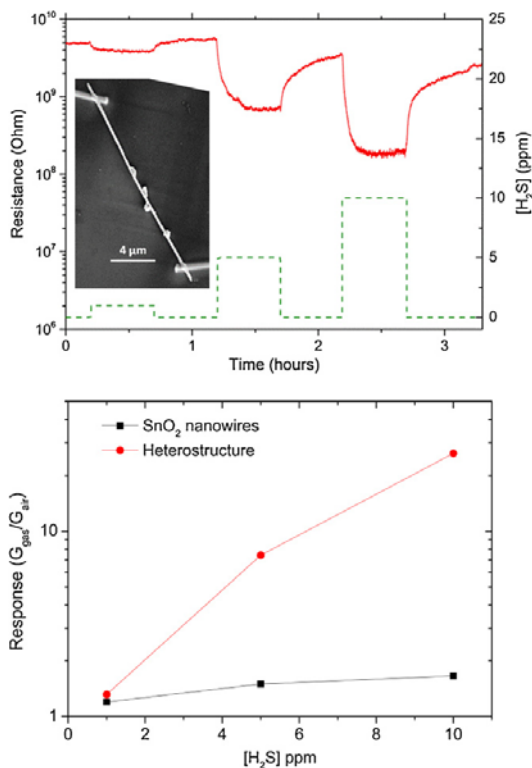


**Figure 4.52** HAADF-STEM images of the p-CuO NP/n-SnO<sub>2</sub> NW heterostructures, associated with EDX maps showing the positions of the elements: Cu (green), Sn (blue), and O (red)

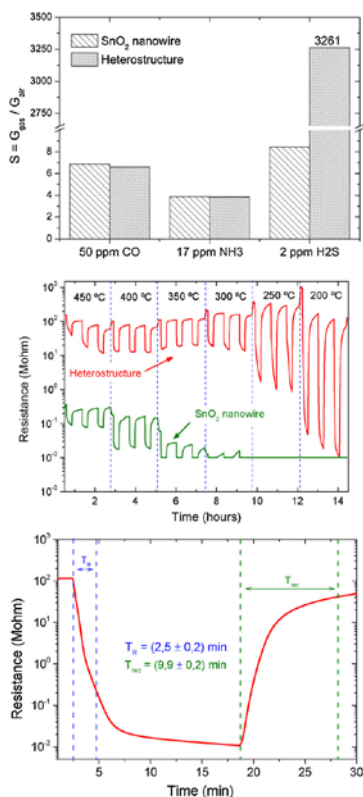
for connecting the NW to the rest of the circuit. In the lower image of this figure, response of the above setup as a function of  $H_2S$  concentration can be seen. This fact confirms the selectivity of the device in the case of  $H_2S$ .

Figure 4.54 (top) reveals the responses of the bare  $SnO_2$  NW and the p-CuO NP/n- $SnO_2$  NW heterostructure to different gases, i.e. CO,  $NH_3$ , and  $H_2S$ . The response,  $S$ , is defined by  $G_{gas}/G_{air}$  where  $G_{gas}$  is conductance of the NW while exposed to the gas and  $G_{air}$  is the NW conductance in the air. A dramatic enhancement in sensing response to  $H_2S$  gas is observed in the case of the heterostructure which is attributed to the aforementioned sensing mechanism which is different from the redox reactions that occur in the case of  $NH_3$  or CO.

In all cases, gas responses were reversible since sensors completely recovered the initial conductance baseline in synthetic air for the applied  $H_2S$  pulses with response and recovery time constants below 3 and 10 min,



**Figure 4.53** (Top) Response of an individual p-CuO NP/n- $SnO_2$  NW heterostructure to  $H_2S$  pulses (dynamic response of the device is convoluted with the dynamic response of the gas chamber, and the inset is an SEM image of the single NW sensor setup), (bottom) response of the above setup as a function of  $H_2S$  concentration<sup>28</sup>



**Figure 4.54** (Top) Response of an individual p-CuO NP/n-SnO<sub>2</sub> NW heterostructure to different gases, (center) comparison between sensing response of bare SnO<sub>2</sub> NW and the one of p-CuO NP/n-SnO<sub>2</sub> NW heterostructure to a 2 ppm H<sub>2</sub>S gas at different temperatures, and (bottom) enlarged response of the heterostructure to 2 ppm H<sub>2</sub>S at 200 °C. (response time:  $T_R$ , recovery time:  $T_{rec}$ )<sup>28</sup>

respectively (see Figure 4.54 (bottom)). Optimal working conditions were observed between 200 °C and 250 °C, whereas smaller response values towards H<sub>2</sub>S were monitored at lower and higher temperatures (Figure 4.54 (center)). At high temperatures ( $T > 250$  °C), a partial and fast regeneration of the thermodynamically more stable p-CuO from CuS during H<sub>2</sub>S pulses cannot be discarded, avoiding a complete breakup of the p-n junction.<sup>26</sup>

#### 4.3.3.6 Section summary

In section 4.3.3 we used SnO<sub>2</sub> NWs as reliable bases for different heterostructures. Both core-shell and NP-on-NW systems approaches were followed to improve the efficiency of the devices.

Titanium oxide, vanadium oxide and the mixture of both was accommodated. Amongst,  $\text{SnO}_2@V_2O_3$  core-shell heterostructures show the best epitaxial relationship at the heterojunction.  $\text{Ti}_2\text{O}$  shell shows a partially good epitaxy with the  $\text{SnO}_2$  core, but it does not show a smooth and homogeneous surface. Meanwhile, the mixed oxide shell which leads to the formation of  $\text{SnO}_2@TiVO_3$  heterostructures shows a smooth structure with low mismatch in the heterojunction, and it is expected to be more chemically and structural stable, while taking advantage of photocatalytic activity of the titanium oxide.

On the other hand, p-CuO NP/n- $\text{SnO}_2$  NW heterostructure dramatically enhanced sensitivity and selectivity of  $\text{H}_2\text{S}$  gas sensing response as a dissimilar sensing mechanism is employed. The breakup of these p-n junctions at nanoscale gave rise to this improvement. It was another example for taking advantage of oxide-oxide nanojunctions which in this case were engineered for gas sensing devices. In general, both core-shell and NP-on-NW approaches showed their promise in functionality enhancement.

### 4.4 Conclusion

In this chapter we proved the importance of oxide-oxide nanojunction engineering which can make considerable changes in their properties. There is an ample range of semiconductor metal oxides synthesized in the form of NPs, NRs, NWs, etc utilized in different applications. Further, the possibility of having heterostructures, e.g. coaxial, heteroaxial, NP-on-NW, NW-on-NW can increase it exponentially. Therefore, a good understanding of the physics behind these structures associated with precise structural study leads us to better functionality, lower cost, higher yield, and higher reliability of the devices. Such approach is likely to end up with the next step, i.e. industrial mass production of high-tech devices which are relatively inexpensive to be utilized in daily life.

In this chapter, oxide NWs were studied. After studying bare metal oxide NWs, their properties and advantages, we moved on to heterostructures in order to improve them. Three important 1D oxides were employed in the heterostructures as the core: ZnO,  $\text{TiO}_2$ , and  $\text{SnO}_2$ . ZnO NWs as appropriate core were covered with ZnS and  $\text{TiO}_2$  polycrystalline shells. Surface area of the NWs was increased and they revealed considerably better PEC properties. On the other hand, a thin hongqiite TiO shell on  $\text{TiO}_2$  NWs enhanced the photovoltaic efficiency of the material as DSCs.

Furthermore, a precise study was conducted on crystal structure of titanium, vanadium, and titanium-vanadium oxides as shells on SnO<sub>2</sub> NWs. Here, epitaxial relationship between the core and the shell played a paramount role in formation of structures that were seldom reported before. Formation of Ti<sub>2</sub>O shell was observed which in bulk is not chemically stable. Also, TiVO<sub>3</sub> mixed oxide with karelianite structure was found which can be justified by mismatch study of TiVO<sub>3</sub>-SnO<sub>2</sub> interface.

Finally, p-CuO NP/n-SnO<sub>2</sub> NW heterostructures were created in order to have p-n junctions at nanoscale. These nanojunctions exhibited a dramatic enhancement in H<sub>2</sub>S gas sensing response as they take advantage of two sensing mechanisms simultaneously. In the case of the second mechanism which is due to the formation of the heterostructure, breakup of the p-n junction causes the considerable change in electrical resistivity of the NW and thus sensing response.

#### 4.5 References

- 1 S. Conesa-Boj, S. Estrade, J.M. Rebled, J.D. Prades, A. Cirera, J.R. Morante, F. Peiro, J. Arbiol, '**Advanced electron microscopy techniques on semiconductor nanowires: from atomic density of states analysis to 3D reconstruction models**', *Nanowires*, Ch. 10, 185-214 (2010)
- 2 M. Alexe, S. Senz, M.A. Schubert, D. Hesse, U. Gosele, '**Energy harvesting using nanowires?**' *Advanced Materials* 20, 4021-4026 (2008)
- 3 Y.F. Lin, J. Song, Y. Ding, S. Y. Lu, Z.L. Wang, '**Piezoelectric nanogenerator using CdS nanowires**', *Applied Physics Letters* 92, 022105 (2008),
- 4 Z.L. Wang, J. Song, '**Piezoelectric nanogenerators based on zinc oxide nanowire arrays**', *Science* 312, 242-246 (2006)
- 5 A.I. Hochbaum, R. Chen, R. Diaz Delgado, W. Liang, E.C. Garnett, M. Najarian, A. Majumdar, P. Yang, '**Enhanced thermoelectric performance of rough silicon nanowires**', *Nature* 451, 163-167 (2008)
- 6 F. Hernandez-Ramirez, J.D Prades, A. Tarancon, S. Barth, O. Casals, R. Jimenez-Diaz, E. Pellicer, J. Rodriguez, M.A. Juli, A. Romano-Rodriguez, J.R. Morante, S. Mathur, A. Helwig, J. Spannhake, G. Mueller, '**Portable microsensors based on individual SnO<sub>2</sub> nanowires**', *Nanotechnology* 18, 495501 (2007)

- 
- 7 X. Duan, Y. Huang, R. Agarwal, C.M. Lieber, '**Single-nanowire electrically driven lasers**', *Nature* 421, 241-245 (2003)
  - 8 M.S. Gudiksen, L.J. Lauhon, J. Wang, D.C. Smith, C.M. Lieber, '**Growth of nanowire superlattice structures for nanoscale photonics and electronics**', *Nature* 415, 617-620 (2002)
  - 9 M.H. Huang, S. Mao, H. Feick, H. Yan, Y. Wu, H. Kind, E. Weber, R. Russo, P. Yang, '**Room-temperature ultraviolet nanowire nanolasers**', *Science* 292, 1897-1899, (2001)
  - 10 D. Moore, J.R. Morber, R.L. Snyder, Z.L. Wang, '**Growth of ultralong ZnS/SiO<sub>2</sub> core-shell nanowires by volume and surface diffusion VLS process**', *Journal of Physical Chemistry C* 112, 2895-2903 (2008)
  - 11 D.F. Moore, Y. Ding, Z.L. Wang, '**Crystal orientation-ordered ZnS nanowire bundles**', *Journal of the American Chemical Society* 126, 14372-14373 (2004)
  - 12 C.S. Lao, P.-X. Gao, L. Zhang, D. Davidovic, R. Tummala, Z.L. Wang, '**ZnO nanobelt/nanowire schottky diodes formed by dielectrophoresis alignment across Au electrodes**', *Nano Letters* 6, 263-266 (2006)
  - 13 J. Zhou, S. Z. Deng, L. Gong, Y. Ding, J. Chen, J. X. Huang, J. Chen, N. S. Xu, Z. L. Wang, '**Growth of large-area aligned molybdenum nanowires by high temperature chemical vapor deposition: synthesis, growth mechanism, and device application**', *Journal of Physical Chemistry B* 110, 10296-10302 (2006)
  - 14 J.D. Fan, A. Shavel, R. Zamani, C. Fábrega, J. Rousset, S. Haller, F. Güell, A. Carreté, T. Andreu, J. Arbiol, J.R. Morante, A. Cabot, '**Control of the doping concentration, morphology and optoelectronic properties of vertically aligned chlorine-doped ZnO nanowires**', *Acta Materialia* 59, 6790-6800 (2011)
  - 15 X. Wang, J. Zhou, J. Song, J. Liu, N. Xu, Z.L. Wang, '**Piezoelectric field effect transistor and nanoforce sensor based on a single ZnO nanowire**', *Nano Letters* 6, 2768-2772 (2006)
  - 16 J. Zhou, P. Fei, Y. Gao, Y. Gu, J. Liu, G. Bao, Z.L. Wang, '**Mechanical-electrical triggers and sensors using piezoelectric microwires/nanowires**', *Nano Letters* 8, 2725-2730 (2008)
  - 17 A. Liu, '**Towards development of chemosensors and biosensors with metal-oxide-based nanowires or nanotubes**', *Biosensors and Bioelectronics* 24, 167-177 (2008)

- 
- 18 Y. Cui, Q. Wei, H. Park, C.M. Lieber, '**Nanowire nanosensors for highly sensitive and selective detection of biological and chemical species**', *Science* 293, 1289-1292 (2001)
- 19 F. Patolsky, B.P. Timko, G. Yu, Y. Fang, A.B. Greytak, G. Zheng, C.M. Lieber, '**Detection, stimulation, and inhibition of neuronal signals with high-density nanowire transistor arrays**', *Science* 313, 1100-1104 (2006)
- 20 D. Zappa, E. Comini, R. Zamani, J. Arbiol, J.R. Morante, G. Sberveglieri, '**Preparation of copper oxide nanowire-based conductometric chemical sensors**', *Sensors and Actuators B: Chemical* 182, 7-15, (2013)
- 21 A. Ponzoni, E. Comini, G. Sberveglieri, J. Zhou, S.Z. Deng, N.S. Xu, Y. Ding, Z.L. Wang, '**Ultrasensitive and highly selective gas sensors using three-dimensional tungsten oxide nanowire networks**', *Applied Physics Letters* 88, 203101 (2006)
- 22 J. Liu, X. Wang, Q. Peng, Y. Li, '**Preparation and gas sensing properties of vanadium oxide nanobelts coated with semiconductor oxides**', *Sensors and Actuators B: Chemical* 115, 481-487 (2006)
- 23 E. Comini, G. Faglia, M. Ferroni, A. Ponzoni, A. Vomiero, G. Sberveglieri, '**Metal oxide nanowires: Preparation and application in gas sensing**', *Journal of Molecular Catalysis A: Chemical* 305, 170-177 (2009)
- 24 J. Arbiol, A. Cirera, F. Peiro, A. Cornet, J.R. Morante, J.J. Delgado, J.J. Calvino, '**Optimization of tin dioxide nanosticks faceting for the improvement of palladium nanocluster epitaxy**', *Applied Physics Letters* 80, 329-331 (2002)
- 25 J. Arbiol, E. Comini, G. Faglia, G. Sberveglieri, J.R. Morante, '**Orthorhombic Pbcn SnO<sub>2</sub> nanowires for gas sensing applications**', *Journal of Crystal Growth* 310, 253-260 (2008)
- 26 E. Uccelli, J. Arbiol, J.R. Morante, A. Fontcuberta i Morral, '**InAs quantum dot arrays decorating the facets of GaAs nanowires**', *ACS Nano* 4, 5985-5993 (2010)
- 27 M. Heiss, Y. Fontana, A. Gustafsson, G. Wüst, C. Magen, D.D. O'Regan, J.W. Luo, B. Ketterer, S. Conesa-Boj, A.V. Kuhlmann, J. Houel, E. Russo-Averchi, J.R. Morante, M. Cantoni, N. Marzari, J. Arbiol, A. Zunger, R. J.Warburton, A. Fontcuberta i Morral, '**Self-assembled quantum dots in a nanowire system for quantum photonics**', *Nature Materials* 12, 439-444 (2013)
- 28 F. Shao, M.W.G. Hoffmann, J.D. Prades, R. Zamani, J. Arbiol, J.R. Morante, E. Varechkina, M. Rumyantseva, A. Gaskov, I. Giebelhaus, T. Fischer,

---

S. Mathur, F. Hernández-Ramírez '**Heterostructured p-CuO (nanoparticle) / n-SnO<sub>2</sub> (nanowire) devices for selective H<sub>2</sub>S detection**', *Sensors and Actuators B: Chemical* 181, 130-135 (2013)

29 Y.-L. Chueh, C.-H. Hsieh, M.-T. Chang, L.-J. Chou, C.S. Lao, J.H. Song, J.-Y. Gan, Z.L. Wang, '**RuO<sub>2</sub> nanowires and RuO<sub>2</sub>/TiO<sub>2</sub> core/shell nanowires: from synthesis to mechanical, optical, electrical, and photoconductive properties**', *Advanced Materials* 19, 143-149 (2007)

30 J.D. Fan, C. Fábrega, R. Zamani, A. Shavel, F. Güell, A. Carrete, T. Andreu, A.M. López, J.R. Morante, J. Arbiol, A. Cabot, '**Solution-growth and optoelectronic properties of ZnO:Cl@ZnS core-shell nanowires with tunable shell thickness**', *Journal of Alloys and Compounds* 555, 213-218 (2013)

31 J.D. Fan, R. Zamani, C. Fábrega, A. Shavel, C. Flox, M. Ibáñez, T. Andreu, A.M. López, J. Arbiol, J.R. Morante, A. Cabot, '**Solution-growth and optoelectronic performance of ZnO:Cl/TiO<sub>2</sub> and ZnO:Cl/Zn<sub>x</sub>TiO<sub>y</sub>/TiO<sub>2</sub> core-shell nanowires with tunable shell thickness**', *Journal of Physics D: Applied Physics* 45, 415301 (2012)

32 L. Dai, C.H. Sow, C.T. Lim, V.B.C. Tan, '**Metal oxide nanowires - structural and mechanical properties**', *Nanowires - Fundamental Research*, Ch. 9, 183-202 (2011)

33 P.-D. Yang, Y.-Y. Wu, R. Fan, '**Inorganic semiconductor nanowires**', *International Journal of Nanoscience* 1, 1-41 (2002)

34 C.N.R Rao, F.L Deepak, Gautam Gundiah, A Govindaraj, '**Inorganic nanowires**', *Progress in Solid State Chemistry* 31, 5-147 (2003)

35 M. Law, J. Goldberger, P.-D. Yang, '**Semiconductor nanowires and nanotubes**', *Annual Review of Materials Research* 34, 83-122 (2004)

36 W. Lu, C.M. Lieber, '**Semiconductor nanowires**', *Journal of Physics D: Applied Physics* 39, R387-R422 (2006)

37 W.-Z. Wang, Y.-J. Zhan, G.-G. Wang, '**One-step, solid-state reaction to the synthesis of copper oxide nanorods in the presence of a suitable surfactant**', *Chemical Communications* 2001, 727-728 (2001)

38 R.-Z. Ma, Y.-S. Bando, '**Uniform MgO nanobelts formed from in situ Mg<sub>3</sub>N<sub>2</sub> precursor**', *Chemical Physics Letters* 370, 770-773 (2003)

39 Z.R. Tian, J.A. Voigt, J. Liu, B. McKenzie, M.J. Mcdermott, M.A. Rodriguez, H. Konishi, H. Xu, '**Complex and oriented ZnO nanostructures**', *Nature Materials* 2, 821-826 (2003)

- 
- 40 L. Vayssieres, '**Growth of arrayed nanorods and nanowires of ZnO from aqueous solutions**', *Advanced Materials* 15, 464-466 (2003)
- 41 Y.W. Heo, D.P. Norton, L.C. Tien, Y. Kwon, B.S. Kang, F. Ren, S.J. Pearton, J.R. LaRoche, '**ZnO nanowire growth and devices**', *Materials Science and Engineering R: Reports* 47, 1-47 (2004)
- 42 X.D. Wang, J.H. Song, Z.L. Wang, '**Nanowire and nanobelt arrays of zinc oxide from synthesis to properties and to novel devices**', *Journal of Materials Chemistry* 17, 711-720 (2007)
- 43 Z.R. Dai, Z.W. Pan, Z.L. Wang, '**Ultra-long single crystalline nanoribbons of tin oxide**', *Solid State Communications* 118, 351-354 (2001)
- 44 J. Arbiol, A. Cirera, F. Peiró, A. Cornet, J.R. Morante, J.J. Delgado, J.J. Calvino, '**Optimization of tin oxide nanosticks faceting for the improvement of palladium nanoclusters epitaxy**', *Applied Physics Letters* 80, 329-331 (2002)
- 45 B.B. Lakshmi, C.J. Partissi, C.R. Martin, '**Sol-gel template synthesis of semiconductor oxide micro- and nanostructures**', *Chemistry of Materials* 9, 2544-2550 (1997)
- 46 G.L. Li, G.H. Wang, '**Synthesis and characterization of rutile TiO<sub>2</sub> nanowhiskers**', *Journal of Materials Research* 14, 3346-3354 (1999)
- 47 D. Li, Y.-N. Xia, '**Fabrication of titania nanofibers by electrospinning**', *Nano Letters* 3, 555-560 (2003)
- 48 J.-M. Wu, H.-C. Shih, W.-T. Wu, Y.-K. Tseng, I.-C. Chen, '**Thermal evaporation growth and the luminescence property of TiO<sub>2</sub> nanowires**', *Journal of Crystal Growth* 281, 384-390 (2005)
- 49 J.-M. Wu, H.-C. Shih, W.-T. Wu, '**Formation and photoluminescence of single-crystalline rutile TiO<sub>2</sub> nanowires synthesized by thermal evaporation**', *Nanotechnology* 17, 105-109 (2006)
- 50 X. Chen, X.-M. Sun, Y.-D. Li, '**Self-assembling vanadium oxide nanotubes by organic molecular yemplates**', *Inorganic Chemistry* 41, 4524-4530 (2002)
- 51 C.-R. Xiong, A.E. Aliev, B. Gnade, K.J. Balkus Jr., '**Fabrication of silver vanadium oxide and V<sub>2</sub>O<sub>5</sub> nanowires for electrochromics**', *ACS Nano* 2, 293-301 (2008)
- 52 V. Valcarcel, A. Souto, F. Guitian, '**Development of single-crystal  $\alpha$ -Al<sub>2</sub>O<sub>3</sub> fibers by vapor-liquid-solid deposition (VLS) from aluminum and powdered silica**', *Advanced Materials* 10, 138-140 (1998)

---

53 Z.L. Xiao, C.Y. Han, U. Welp, H.H. Wang, W.K. Kwok, G.A. Willing, J.M. Hiller, R.E. Cook, D.J. Miller, G.W. Crabtree, '**Fabrication of alumina nanotubes and nanowires by etching porous alumina membranes**', *Nano Letters* 2, 1293-1297 (2002)

54 X.C. Wu, W.H. Song, W.D. Huang, M.H. Pu, B. Zhao, Y.P. Sun, J.J. Du, '**Crystalline gallium oxide nanowires: intensive blue light emitters**', *Chemical Physics Letters* 328, 5-9 (2000)

55 C. Li, D. Zhang, S. Han, X. Liu, T. Tang, C. Zhou, '**Diameter-controlled growth of single-crystalline In<sub>2</sub>O<sub>3</sub> nanowires and their electronic properties**', *Advanced Materials* 2, 143-146 (2003)

56 L. Guo, Z.-H. Wu, T. Liu, W.-D. Wang, H.-S. Zhu, '**Synthesis of novel Sb<sub>2</sub>O<sub>3</sub> and Sb<sub>2</sub>O<sub>5</sub> nanorods**', *Chemical Physics Letters* 318, 49-52 (2000)

57 J.J. Urban, J.E. Spanier, L. Ouyang, W.S. Yun, H. Park, '**Single-crystalline barium titanate nanowires**', *Advanced Materials* 15, 423-426 (2003)

58 K. Shantha Shankar, A.K. Raychaudhuri, '**Fabrication of nanowires of multicomponent oxides: Review of recent advances**', *Materials Science Engineering C* 25, 738-751 (2005)

59 R. Zamani, R. Fiz, J. Pan, T. Fischer, S. Mathur, J.R. Morante, J. Arbiol, '**Oxide-oxide nanojunctions in coaxial SnO<sub>2</sub>/TiO<sub>2</sub>, SnO<sub>2</sub>/V<sub>2</sub>O<sub>3</sub> and SnO<sub>2</sub>/(Ti<sub>0.5</sub>V<sub>0.5</sub>)<sub>2</sub>O<sub>3</sub> nanowire heterostructures**', *CrystEngComm* 15, 4532-4539 (2013)

60 J.D. Fan, F. Güell, C. Fábrega, A. Shavel, A. Carrete, T. Andreu, J.R. Morante, A. Cabot, '**Enhancement of the photoelectrochemical properties of Cl-doped ZnO nanowires by tuning their coaxial doping profile**', *Applied Physics Letters* 99, 262102 (2011)

61 B.M. Kayes, H.A. Atwater, N.S. Lewis, '**Comparison of the device physics principles of planar and radial p-n junction nanorod solar cells**', *Journal of Applied Physics* 97, 114302 (2005)

62 A.I. Hochbaum, P. Yang, '**Semiconductor nanowires for energy conversion**', *Chemical Reviews* 110, 527-546 (2010)

63 Y. Tak, S.J. Hong, J.S. Lee, K.-J. Yong, '**Fabrication of ZnO/CdS core/shell nanowire arrays for efficient solar energy conversion**', *Journal of Materials Chemistry* 19, 5945-5951 (2009)

64 J.A. Czaban, D.A. Thomson, R.R. LaPierre, '**GaAs core-shell nanowires for photovoltaic applications**', *Nano Letters* 9, 148-154 (2009)

- 
- 65 D. Halliday, R. Resnick, J. Walker '**Fundamentals of Physics**', Ninth edition, Ch. 41, 1142-1164 (2011)
- 66 B. Van Zeghbroeck, '**Principles of Semiconductor Devices**', (online book) Ch. 4 (2011)
- 67 J.C. Phillips, '**Bonds and Bands in Semiconductors**', Ch. 10, 256-260 (1973)
- 68 P. Würfel, '**Physics of Solar Cells: From Principles to New Concepts**', Ch. 6, 109-136 (2005)
- 69 W. Göpel, '**Chemisorption and charge transfer at ionic semiconductor surfaces: implications in designing gas sensors**', *Progress in Surface Science* 20 9-103 (1985)
- 70 M. Batzill, U. Diebold, '**The surface and materials science of tin oxide**', *Progress in Surface Science* 79, 47-154 (2005)
- 71 E. Comini, G. Faglia, G. Sberveglieri, Z.W. Pan, Z.L. Wang, '**Stable and highly sensitive gas sensors based on semiconducting oxide nanobelts**', *Applied Physics Letters* 81, 1869-1871 (2002)
- 72 F. Hernández-Ramírez, A. Tarancón, O. Casals, J. Arbiol, A. Romano-Rodríguez, J.R. Morante, '**High response and stability in CO and humidity measures using a single SnO<sub>2</sub> nanowire**', *Sensors and Actuators B: Chemical* 121, 3-17 (2007)
- 73 Z.S. Hong, Y. Cao, J.F. Deng, '**A convenient alcohothermal approach for low temperature synthesis of CuO nanoparticles**', *Materials Letters* 52, 34-38 (2002)
- 74 W. Wang, Z. Liu, Y. Liu, C. Xu, C. Zheng, G. Wang, '**A simple wet-chemical synthesis and characterization of CuO nanorods**', *Applied Physics A: Materials Science & Processing* 76, 417-420 (2003)
- 75 X.G. Wen, Y.T. Xie, C.L. Choi, K.C. Wan, X.Y. Li, S.H. Yang, '**Copper-based nanowire materials: templated syntheses, characterizations, and applications**', *Langmuir* 21, 4729-4737 (2005)
- 76 C.K. Xu, Y.K. Liu, G.D. Xu, G.H. Wang, '**Preparation and characterization of CuO nanorods by thermal decomposition of CuC<sub>2</sub>O<sub>4</sub> precursor**', *Materials Research Bulletin* 37, 2365-2372 (2002)
- 77 X.F. Wu, H. Bai, J.X. Zhang, F.E. Chen, G.Q. Shi, '**Copper hydroxide nanoneedle and nanotube arrays fabricated by anodization of copper**', *Journal of Physical Chemistry B* 109, 22836-22842 (2005)

---

78 C.H. Xu, C.H. Woo, S.Q. Shi, '**Formation of CuO nanowires on Cu foil**', *Chemical Physics Letters* 399, 62-66 (2004)

79 M. Kaur, K.P. Muthe, S.K. Deshpande, S. Choudhury, J.B. Singh, N. Verma, S.K. Gupta, J.V. Yakhmi, '**Growth and branching of CuO nanowires by thermal oxidation of copper**', *Journal of Crystal Growth* 289, 670-675 (2006)

80 H. Wu, D.D. Lin, W. Pan, '**Fabrication, assembly, and electrical characterization of CuO nanofibers**', *Applied Physics Letters* 89, 133125 (2006)

81 M.H. Huang, Y. Wu, H. Feick, N. Tran, E. Weber, P. Yang, '**Catalytic growth of zinc oxide nanowires by vapor transport**', *Advanced Materials* 13, 113-116 (2001)

82 Y. Sun, G.M. Fuge, M.N.R. Ashfold, '**Growth of aligned ZnO nanorod arrays by catalyst-free pulsed laser deposition**', *Chemical Physics Letters* 396, 21-26 (2004)

83 A. Marcu, L. Trupina, R. Zamani, J. Arbiol, C. Grigoriu, J.R. Morante, '**Catalyst size limitation in vapor-liquid-solid ZnO nanowire growth using pulsed laser deposition**', *Thin Solid Films* 520, 4626-4631 (2012)

84 W.I. Park, D.H. Kim, S.W. Jung, G.C. Yi, '**Metalorganic vapor-phase epitaxial growth of vertically well-aligned ZnO nanorods**', *Applied Physics Letters* 80, 4232-4234 (2002)

85 F. Wang, A. Dong, J. Sun, R. Tang, H. Yu, W.E. Buhro, '**Solution-liquid-solid growth of semiconductor nanowires**', *Inorganic Chemistry* 45, 7511-7521 (2006)

86 J.H. Lee, R.E. Geer, '**Templated Si-based nanowires via solid-liquid-solid (SLS) and vapor-liquid-solid (VLS) growth: Novel growth mode, synthesis, morphology control, characteristics, and electrical transport**', *Cutting Edge Nanotechnology*, Ch. 8, 167-192 (2010)

87 Y.S. Kim, I.S. Hwang, S.J. Kim, C.Y. Lee, J.H. Lee, '**CuO nanowire gas sensors for air quality control in automotive cabin**', *Sensors and Actuators B: Chemical* 135, 298-303 (2008)

88 X.-C. Jiang, T. Herricks, Y.-N. Xia, '**CuO nanowires can be synthesized by heating copper substrate in air**', *Nano Letters* 2, 1333-1338 (2002)

- 
- 89 A. Vomiero, S. Bianchi, E. Comini, G. Faglia, M. Ferroni, G. Sberveglieri, '**Controlled growth and sensing properties of In<sub>2</sub>O<sub>3</sub> nanowires**', *Crystal Growth and Design* 7, 2500-2504 (2007)
- 90 J. Pan, '**Chemical vapor deposition of one dimensional tin oxide nanostructures: Structural studies, surface modifications and device applications**', *PhD Thesis*, University of Cologne, Ch. 2, 5-52 (2010)
- 91 R.S. Wagner, W.C. Ellis, '**Vapor-liquid-solid mechanism of single crystal growth**', *Applies Physics Letters* 4, 89-90 (1964)
- 92 A. Fontcuberta i Morral, '**Synthesis and fundamental properties of semiconductor nanowires**', *Habilitation*, Walter Schottky Institut - Technische Universität München (2009)
- 93 K.W. Kolasinski, '**Catalytic growth of nanowires: vapor-liquid-solid, vapor-solid-solid, solution-liquid-solid and solid-liquid-solid growth**', *Current Opinion in Solid State & Materials Science* 10, 182-191 (2006)
- 94 S. Mathur, S. Barth, H. Shen, J.C. Pyun, U. Werner, '**Size-dependent photo-conductance in SnO<sub>2</sub> nanowires**', *Small* 1, 713-717 (2005)
- 95 J. Pan, S. V. Huhne, H. Shen, L. Xiao, P. Born, W. Mader, S. Mathur, '**SnO<sub>2</sub>-TiO<sub>2</sub> core-shell nanowire structures: investigations on solid state reactivity and photocatalytic behavior**', *Journal of Physical Chemistry C* 115, 17265-17269 (2011)
- 96 S. Mathur, T. Ruegamer, I. Grobelsek, '**Phase-selective CVD of vanadium oxide nanostructures**', *Chemical Vapor Deposition* 13, 42-47 (2007)
- 97 S. Bernal, F.J. Botana, J.J. Calvino, C. Lopez-Cartes, J.A. Perez-Omil, J.M. Rodriguez-Izquierdo, '**The interpretation of HREM images of supported metal catalysts using image simulation: profile view images**', *Ultramicroscopy* 72, 135-164 (1998)
- 98 M.I.B. Utama, F.J. Belarre, C. Magen, B. Peng, J. Arbiol, Q. Xiong, '**Incommensurate van der Waals epitaxy of nanowire arrays: a case study with ZnO on muscovite mica substrates**', *Nano Letters* 12, 2146-2152 (2012)
- 99 T. Andreu, J. Arbiol, J.R. Morante, '**Mesoporous indium oxide for gas sensor applications**', *Sensors for Environment, Health and Security*, Ch. 4, 67-76 (2009)
- 100 D.C. Look, J.W. Hemsky, J.R. Sizelove, '**Residual native shallow donor in ZnO**', *Physical Review Letters* 82, 2552-2555 (1999)

---

101 A.R. Hutson, '**Hall effect studies of doped zinc oxide single crystals**', *Physical Review* 108, 222-230 (1957)

102 M. Law, L.E. Greene, J.C. Johnson, R. Saykally, P.-D. Yang, '**Nanowire dye-sensitized solar cells**', *Nature Materials* 4, 455-459 (2005)

103 N.J. Stone, H. Ahmed, '**Silicon single electron memory cell**', *Applied Physics Letters* 73, 2134-2136 (1998)

104 G.H. Lee, T. Kawazoe, M. Ohtsu, '**Difference in optical bandgap between zinc-blende and wurtzite ZnO structure formed on sapphire (0001) substrate**', *Solid State Communications* 124, 163-165 (2002)

105 H.-C. Liao, P.-C. Kuo, C.-C. Lin, S.-Y. Chen, '**Synthesis and optical properties of ZnO-ZnS core-shell nanotube arrays**', *Journal of Vacuum Science and Technology B* 24, 2198-2201 (2006)

106 L. Zhang, T. Kanki, N. Sano, A. Toyoda, '**Development of TiO<sub>2</sub> photocatalyst reaction for water purification**', *Separation and Purification Technology* 31, 105-110 (2003)

107 A. Hagfeldt, M. Gratzel, '**Light-induced redox reactions in nanocrystalline systems**', *Chemical Reviews* 95, 49-68 (1995)

108 Y.-C. Yeh, T.-Y. Tseng, D.-A. Chang, '**Electrical properties of porous titania ceramic humidity sensors**', *Journal of the American Ceramic Society* 72, 1472-1475 (1989)

109 A.K. Menon, S.J. Kalita, '**Efficient photocatalytic degradation of methylene blue with CuO loaded nanocrystalline TiO<sub>2</sub>**', *Nanostructured Materials and Nanotechnology III*, 77-87 (2010)

110 M.V. Rao, K. Rajeshwar, V.R. Pai Verneker, J. DuBow, '**Photosynthetic production of hydrogen and hydrogen peroxide on semiconducting oxide grains in aqueous solutions**', *Journal of Physical Chemistry* 84, 1987-1991 (1980)

111 Z.H. Yuan, J.H. Jia, L.D. Zhang, '**Influence of co-doping of Zn(II)+Fe(III) on the photocatalytic activity of TiO<sub>2</sub> for phenol degradation**', *Materials Chemistry and Physics* 73, 323-326 (2002)

112 M. Jakob, H. Levanon, P.V. Kamat, '**Charge distribution between UV-irradiated TiO<sub>2</sub> and gold nanoparticles: determination of shift in the Fermi level**', *Nano Letters* 3, 353-358 (2003)

113 E.-Y. Bae, W.-Y. Choi, '**Highly enhanced photoreductive degradation of perchlorinated compounds on dye-sensitized metal/TiO<sub>2</sub> visible light**', *Environmental Science and Technology* 37, 147-152 (2003)

---

114 Y.R. Uhm, S.H. Woo, W.W. Kim, S.J. Kim, C.K. Rhee, '**The characterization of magnetic and photo-catalytic properties of nanocrystalline Ni-doped TiO<sub>2</sub> powder synthesized by mechanical alloying**', *Journal of Magnetism and Magnetic Materials* 304, e781-e783 (2006)

115 Xu, Y.H., Liang, D.H., Liu, M.L., Liu, D.Z., '**Preparation and characterization of Cu<sub>2</sub>O-TiO<sub>2</sub>: Efficient photocatalytic degradation of methylene blue**', *Materials Research Bulletin* 43, 3474-3482 (2008)

116 X. Fan, X. Chen, S. Zhu, Z. Li, T. Yu, J. Ye, Z. Zou, '**The structural, physical and photocatalytic properties of the mesoporous Cr-doped TiO<sub>2</sub>**', *Journal of Molecular Catalysis A: Chemical* 284, 155-160 (2008)

117 Y.-H. Xu, H.-R. Chen, Z.-X. Zeng, B. Lei, '**Investigation on mechanism of photocatalytic activity enhancement of nanometer cerium-doped titania**', *Applied Surface Science* 252, 8565-8570 (2006)

118 J.-X. Yu, S. Liu, Z.-L. Xiu, W. Yu, G.-J. Feng, '**Combustion synthesis and photocatalytic activities of Bi<sup>3+</sup>-doped TiO<sub>2</sub> nanocrystals**', *Journal of Alloys and Compounds* 461, L17-L19 (2008)

119 B.-F. Xin, L.-Q. Jing, Z.-Y. Ren, B.-Q. Wang, H.-G. Fu, '**Effects of simultaneously doped and deposited Ag on the photocatalytic activity and surface states of TiO<sub>2</sub>**', *Journal of Physical Chemistry B* 109, 2805-2809 (2005)

120 M. Epifani, R. Diaz, J. Arbiol, E. Comini, N. Sergent, E. Pagnier, P. Siciliano, G. Faglia, J.R. Morante, '**Nanocrystalline metal oxides from the injection of metal oxide sols in coordinating solutions: synthesis, characterization, thermal stabilization, device processing, and gas-sensing properties**', *Advanced Functional Materials* 16, 1488-1498 (2006)

121 M. Epifani, T. Andreu, R. Zamani, J. Arbiol, E. Comini, P. Siciliano, G. Faglia, J.R. Morante, '**Pt doping triggers growth of TiO<sub>2</sub> nanorods. Nanocomposite synthesis and gas-sensing properties**', *CrystEngComm* 14, 3882-2887 (2012)

122 C. Fabrega, T. Andreu, A. Tarancon, C. Flox, A. Morata, L. Calvo-Barrio, J.R. Morante, '**Optimization of surface charge transfer processes on rutile TiO<sub>2</sub> nanorods photoanodes for water splitting**', *International Journal of Hydrogen Energy* 38, 2979-2985 (2013)

123 J. Schrier, D.O. Demchenko, L.-W. Wang, A.P. Alivisatos, '**Optical properties of ZnO/ZnS and ZnO/ZnTe heterostructures for photovoltaic applications**', *Nano Letters* 7, 2377-2382, (2007)

---

124 J.D. Fan, C. Fabrega, R. Zamani, Y. Hao, A. Parra, T. Andreu, J. Arbiol, G. Boschloo, A. Hagfeldt, J.R. Morante, A. Cabot, '**Enhanced photovoltaic performance of nanowire dye-sensitized solar cells based on coaxial TiO<sub>2</sub>@TiO heterostructures with a cobalt (II/III) redox electrolyte**', *ACS Applied Materials and Interfaces*, DOI: 10.1021/am402344d, (2013)

125 E.S. Bumps, H.D. Kessler, M. Hansen, '**The titanium-oxygen system**', *Transactions of the American Society for Metals* 45, 1008-1028 (1953)

126 M.E. Straumanis, '**Absorption correction in precession determination of lattice parameters**', *Journal of Applied Physics* 30, 1965-1969 (1959)

127 D. Taylor, '**Thermal expansion data .I. Binary oxides with the sodium chloride and wurtzite structures, Mo**', *Transactions and Journal of the British Ceramic Society* 83, 5-9 (1984)

128 A.N. Christensen, '**A neutron-diffraction investigation on single-crystals of titanium oxide, zirconium carbide and hafnium nitride**', *Acta Chemica Scandinavica* 44, 851-852 (1990)

129 E.M. Assim, '**Optical constants of titanium monoxide TiO thin films**', *Journal of Alloys and Compounds* 465, 1-7 (2008)

130 P. Simon, B. Pignon, B. Miao, S. Coste-Leconte, Y. Leconte, S. Marguet, P. Jegou, B. Bouchet-Fabre, C. Reynaud, N.H. Boime, '**N-doped titanium monoxide nanoparticles with TiO rock-salt structure, low energy band gap, and visible light activity**', *Chemistry of Materials* 22, 3704-3711 (2010)

131 S. Bartkowski, M. Neumann, A. Winiarski, D.C. Rubie, '**Electronic structure of titanium monoxide**', *Physical Review B* 56, 10656-10667 (1997)

132 R.E. Presley, C.L. Munsee, C.-H. Park, D. Hong, J.F. Wager, D.A. Keszler, '**Tin oxide transparent thin-film transistors**', *Journal of Physics D: Applied Physics* 37, 2810-2813 (2004)

133 J.F. Wager, '**Transparent electronics**', *Science* 300, 1245-1246 (2003)

134 G. Croft, M.J. Fuller, '**Water-promoted oxidation of carbon monoxide over tin(IV) oxide-supported palladium**', *Nature* 269, 585-586 (1977)

135 P.W. Park, H.H. Kung, D.-W. Kim, M.C. Kung, '**Characterization of SnO<sub>2</sub>/Al<sub>2</sub>O<sub>3</sub> lean NO<sub>x</sub> catalysts**', *Journal of Catalysis* 184, 440-454 (1999)

136 T. Takeguchi, O. Takeoh, S. Aoyama, J. Ueda, R. Kikuchi, K. Eguchi, '**Strong chemical interaction between PdO and SnO<sub>2</sub> and the influence on catalytic combustion of methane**', *Applied Catalysis A: General* 252, 205-214 (2003)

- 
- 137 P.G. Harrison, N.C. Lloyd, W. Daniell, C. Bailey, W. Azelee, **'Evolution of microstructure during thermal activation of chromium-promoted tin(IV) oxide catalysts: an FT-IR, FT-Raman, XRD, TEM and XANES/EXAFS study'**, *Chemistry of Materials* 11, 896-909 (1999)
- 138 Z.W. Pan, Z.R. Dai, Z.L. Wang, **'Nanobelts of semiconducting oxides'**, *Science* 291, 1947-1949 (2001)
- 139 J.P. Jan, W.B. Pearson, A. Kjekshus, S.B. Woods, **'On the structural, thermal, electrical, and magnetic properties of Au Sn'**, *Canadian Journal of Physics* 41, 2252-2266 (1963)
- 140 J. Ciulik, M.R. Notis, **'The Au-Sn phase diagram'**, *Journal of Alloys and Compounds* 191, 71-78 (1993)
- 141 L. Yin, S.J. Meschter, T.J. Singler, **'Wetting in the Au-Sn system'**, *Acta Materialia* 52, 2873-2888 (2004)
- 142 S. Mathur, M. Veith, H. Shen, S. Hüfner, M.H. Jilavi, **'Structural and optical properties of NdAlO<sub>3</sub> nanocrystals embedded in an Al<sub>2</sub>O<sub>3</sub> matrix'**, *Chemistry of Materials* 14, 568-582 (2002)
- 143 I.I. Kornilov, V.V. Vavilova, L.E. Fykin, R.P. Ozerov, S.P. Solovev, V.P. Smirnov, **'Neutron diffraction investigation of ordered structures in titanium-oxygen system'**, *Metallurgical Transactions* 1, 2569-& (1970)
- 144 B. Holmberg, **'Disorder and order in solid solutions of oxygen in alpha-titanium'**, *Acta Chemica Scandinavica* 16, 1245-& (1962)
- 145 J. Venables, **'Introduction to Surface and Thin Film Processes'**, Ch. 5, 144-183 (2000)
- 146 J. Dumas, C. Schlenker, J.L. Tholence, R. Tournier, **'Spin-glass properties of a crystalline transition-metal oxide: (Ti<sub>1-x</sub>V<sub>x</sub>)<sub>2</sub>O<sub>3</sub>'**, *Physical Review B* 20, 3913-3925 (1979)
- 147 M.E. Sjostrand, P.H. Keesom, **'Low-temperature specific heat of metallic V-doped Ti<sub>2</sub>O<sub>3</sub>'**, *Physical Review B* 7, 3558-3568, (1973)
- 148 D.X. Wu, Q.M. Zhang, M. Tao, **'LSDA+U study of cupric oxide: electronic structure and native point defects'**, *Physical Review B* 73, 235206 (2006)
- 149 D. Barreca, E. Comini, A. Gasparotto, C. Maccato, A. Pozza, C. Sada, G. Sberveglieri, E. Tondello, **'Vapor phase synthesis, characterization and gas sensing performances of Co<sub>3</sub>O<sub>4</sub> and Au/Co<sub>3</sub>O<sub>4</sub> nanosystems'**, *Journal of Nanoscience and Nanotechnology* 10, 8054-8061 (2010)

150 A.M. Ruiz, A. Cornet, K. Shimano, J.R. Morante, N. Yamazoe, **‘Transition metals (Co, Cu) as additives on hydrothermally treated TiO<sub>2</sub> for gas sensing’**, *Sensors and Actuators B: Chemical* 109, 7-12 (2005)

151 A.M. Ruiz, A. Cornet, K. Shimano, J.R. Morante, N. Yamazoe, **‘Transition metals (Co, Cu) as additives on hydrothermally treated TiO<sub>2</sub> for gas sensing’**, *Sensors and Actuators B: Chemical* 109 7-12 (2005)

152 H. Kim, C. Jin, S. Park, S. Kim, C. Lee, **‘H<sub>2</sub>S gas sensing properties of bare and Pd-functionalized CuO nanorods’**, *Sensors and Actuators B: Chemical* 161 594-599, (2012)

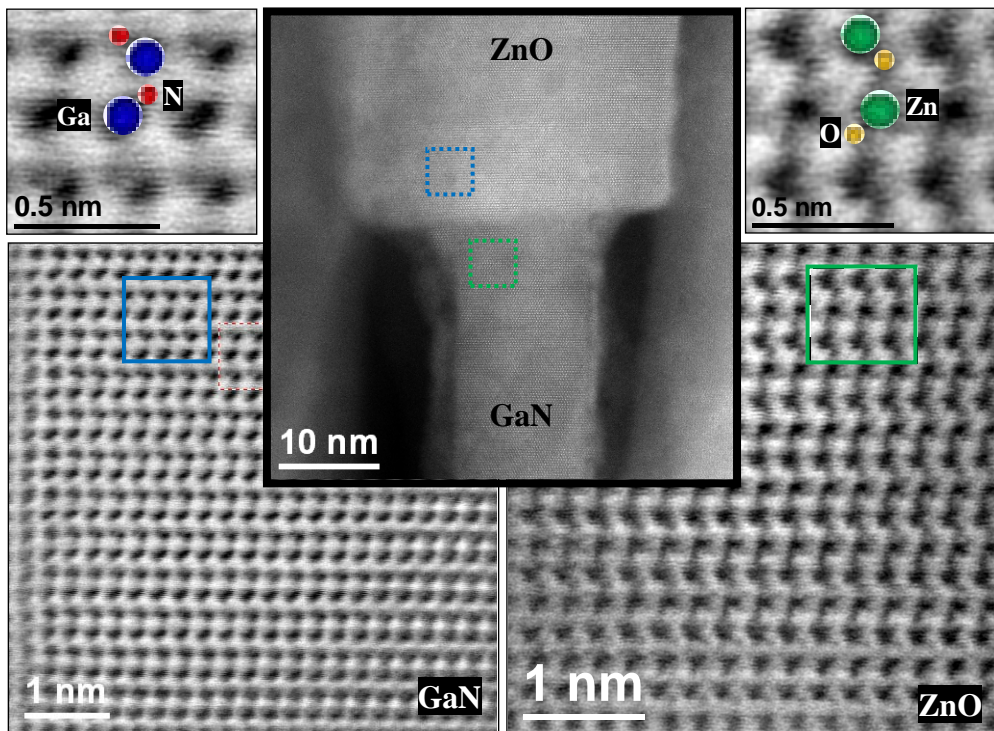
153 N.S. Ramgir, S.K. Ganapathi, M. Kaur, N. Datta, K.P. Muthe, D.K. Aswal, S.K. Gupta, J.V. Yakhmi, **‘Sub-ppm H<sub>2</sub>S sensing at room temperature using CuO thin films’**, *Sensors and Actuators B: Chemical* 151, 90-96 (2010)

154 H. Kim, C. Jin, S. Park, S. Kim, C. Lee, **‘H<sub>2</sub>S gas sensing properties of bare and Pd-functionalized CuO nanorods’**, *Sensors and Actuators B: Chemical* 161, 594-599 (2012)

155 I. Giebelhaus, E. Varechkina, T. Fischer, M. Rumyantseva, V. Ivanov, A. Gaskov, J.R. Morante, J. Arbiol, W. Tyrra, S. Mathur, **‘One-dimensional CuO-SnO<sub>2</sub> p-n heterojunctions for enhanced detection of H<sub>2</sub>S’**, *Journal of Materials Chemistry A* 1, 11261-11268 (2013)

# CHAPTER V

## EPITAXIAL GROWTH AND NANOENGINEERED INTERFACES: III-V NANOWIRES





## 5.1 Introduction

In the previous chapters we studied different ways of nanoengineering, from chemical and structural manipulations to morphology changes and coaxial heterostructuring. In this chapter we play around with axial heterostructures in order to complete our nanoengineering study in functional nanostructured materials. In this context, III-V nanowires (NWs) are chosen as they are widely used in different devices.

According to the importance of III-V NWs for many application especially optoelectronics, we will have an insight to these materials, particularly GaN NWs. Since early 1960s that III-V nitrides attracted the attention of the researchers, many efforts have been done so far to develop and control their growth, morphology, structure, and properties.<sup>1</sup> Still there is room for further improvement of these semiconductors as they still show their promise for novel applications.

An important issue in this scenario is polarity determination, as polarity has a strong influence on the properties of the materials and heterostructures, e.g. electronic, optical properties, morphology, etc.<sup>2-5</sup> For instance, Kawaguchi *et al.*<sup>5</sup> show the influence of polarity on carrier transport in multi-quantum-well light-emitting diodes (LEDs), and de la Mata *et al.*<sup>6</sup> studied the influence of polarity inversions on the carrier transport in the ballistic regime in twinned NWs. Nowadays, aberration-corrected transmission electron microscopes (TEMs) allow us to determine the polarity directly from the micrographs while they even visualize the small differences in atomic number of the elements (e.g. Ga and As) or light atoms (e.g. N and O).<sup>6</sup>

In this chapter we study GaN NWs which are mostly used for optoelectronic applications. Therefore, we start with an introduction to III-V

NWs, optoelectronics as their main application, and growth mechanism. Then we will study two novel key systems in detail based on GaN NWs. These two systems consist on (i) GaN NWs grown on diamond, and (ii) GaN/ZnO axial heterostructure NWs. The former is an excellent platform in two ways: On the one hand, high-quality GaN NWs can be used for optoelectronic devices in UV range. On the other hand, the diamond in this heterostructure can be used for quantum computation<sup>7</sup> and magnetometry.<sup>8,9</sup> The latter system, nevertheless, provides an intrinsic polarity inversion, as we will see in this chapter, which may enrich the study of their resulting electronic band structures as p-n junctions.

### 5.1.1 III-V nanowires

III-V semiconductors have been used for many applications in optoelectronics<sup>10,11</sup> and microelectronics<sup>12,13</sup> as they usually have wide band gaps. These materials, especially GaN, offer novel properties that can be used in devices such as white/color light emitting diodes (LEDs) for color displays or traffic lights, blue/violet laser diodes (LDs) for optical data storage or laser printing, UV detectors, and high power-high frequency transistors for radars and communication devices.

On the other hand, the form of one-dimensional (1D) structures like a NW offers further advantages due to their geometry, e.g. superior mechanic toughness, higher carrier mobility and luminescence efficiency, and lower lasing threshold.<sup>14</sup> In recent years, III-V NWs with binary and ternary compounds such as GaAs,<sup>15,16</sup> InGaAs,<sup>17</sup> GaSb,<sup>18</sup> InAs,<sup>19</sup> InSb,<sup>20</sup> InAsSb,<sup>21</sup> GaP,<sup>22</sup> InP,<sup>23</sup> GaN,<sup>24</sup> InN,<sup>25</sup> AlGaIn,<sup>26</sup> and different heterostructures<sup>27,28</sup> comprising two or more of them, and also their quantum structures<sup>29,30</sup> are widely investigated and employed for many different applications especially optoelectronics.

In particular GaN in the form of NW is a quite promising material for optoelectronics as its wide band gap ( $E_g = 3.4$  eV) can be tuned by impurities and heterostructuring in order to have emission with different wavelengths and colors from yellow to UV. GaN is capable of being doped with n-type and p-type impurities,<sup>31</sup> and additionally it can also be heterostructured. For instance, by introducing Al in GaN structure we create ternary  $\text{Al}_{1-x}\text{Ga}_x\text{N}$  where the band gap can be modulated by changing the Al content. This allows, for example, an enhancement of the green emission in AlGaIn LEDs (previously the green-emission efficiency of bare GaN was poor).<sup>32</sup>

In this chapter we focus on two novel approaches obtained by engineering the GaN-based heterostructures. In a first example, we will study the growth of GaN NWs on diamond substrates, and secondly, new axial p-n heterojunction of n-doped ZnO on top of a p-GaN NW will be studied. In this latter case, the polarity inversion observed across the GaN-ZnO junction will give interesting properties to the devices.

### 5.1.2 Optoelectronics and optoelectronic devices

Optoelectronic devices mostly consist of a p-type and n-type region, just like a regular p-n diode. The key difference is that there is an additional interaction between the electrons and holes in the semiconductor and light. This interaction is not restricted to optoelectronic devices. Regular diodes are also known to be light sensitive and in some cases also emit light. The key difference is that optoelectronic devices such as photodiodes, solar cells, LEDs and laser diodes are specifically designed to optimize the light absorption and emission, resulting in a high conversion efficiency.

Light absorption and emission in a semiconductor is known to be heavily dependent on the detailed band structure of the semiconductor. Direct band gap semiconductors, i.e. semiconductors for which the minimum of the conduction band occurs at the same wavevector,  $k$ , as the maximum of the valence band, have a stronger absorption of light as characterized by a larger absorption coefficient. They are also the favored semiconductors when fabricating light emitting devices. Indirect band gap semiconductors, (semiconductors for which the minimum of the conduction band does not occur at the same wavevector as the maximum of the valence band), are known to have a smaller absorption coefficient. This striking difference is illustrated in Figure 5.1 and can be explained based on the energy and momentum conservation required in the electron-photon interaction. In the direct band gap semiconductor, which has a vertically aligned conduction and valence band, (Figure 5.1(a)), absorption of a photon is obtained if an empty state in the conduction band is available for which the energy and momentum equals that of an electron in the valence band plus that of the incident photon. Photons have little momentum relative of their energy since they travel at the speed of light. The electron therefore makes an almost vertical transition on the E-k diagram. However, for an indirect band gap semiconductor, as the conduction band is not vertically aligned to the valence band (Figure 5.1(b)), a simple interaction of an incident photon with an electron

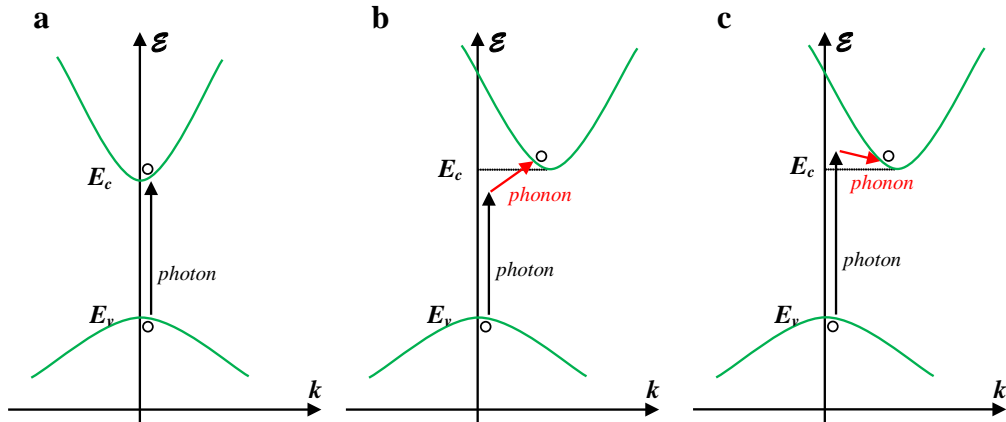


**Figure 5.1** Schematic illustration of (a) direct and (b), (c) indirect band gap, (b) photon absorption in an indirect band gap semiconductor assisted by phonon absorption and (c) photon absorption in an indirect band gap semiconductor assisted by phonon emission

in the valence band will not provide the correct energy and momentum corresponding to that of an empty state in the conduction band. As a result absorption of light requires the help a phonon. Since a phonon, has a relatively low velocity close to the speed of sound in the material, it has a small energy and large momentum compared to that of a photon. Conservation of both energy and momentum can therefore be obtained in the absorption process if a phonon is created or an existing phonon participates. The phonon assisted absorption processes are illustrated with Figure 5.1(b) and (c). Figure 5.1(b) illustrates the absorption of a photon aided by the simultaneous absorption of a phonon, while Figure 5.1(c) depicts the absorption of a photon, which results in the emission of a phonon. The minimum photon energy that can be absorbed is slightly below the band gap energy in the case of phonon absorption and has to be slightly above the band gap energy in the case of phonon emission. Since the absorption process in an indirect band gap semiconductor involves a phonon in addition to the electron and photon, the probability of having an interaction take place involving all three particles will be lower than a simple electron-photon interaction in a direct band gap semiconductor. As a consequence, one finds that absorption is much stronger in a direct band gap material.<sup>33</sup>

The most important optoelectronic devices which take advantage of photon absorption/emission are: photodiodes, solar cells, LEDs, and laser diodes (LD). In the following we briefly describe each one of them.

### 5.1.2.1 Photodiodes and solar cells

Photodiodes and solar cells are fundamentally the same as normal p-n diodes, with this difference that exposure of the photodiode to light results in an additional photocurrent due to photo-generation of electrons and holes as illustrated in Figure 5.2. The electrons and holes are pulled into the region where they are majority carriers by the electric field in the depletion region. The photo-generated carriers cause a photo-current, thus, the device can be used as a photo-detector as its resistivity changes when a photon is absorbed.

Likewise, solar cells follow the same principles, but they are typically illuminated with sunlight and are intended to convert the solar energy into electrical energy. The solar energy is in the form of electromagnetic radiation, more specifically 'black-body'. The spectrum of the sun is consistent with that of a black body at a temperature of 5800 K. The radiation spectrum has a peak at 0.8 eV where a significant part of the spectrum is in the visible range of the spectrum (400-700 nm). The power density is approximately  $100 \text{ mW/cm}^2$ . Even so, only part of the solar spectrum actually makes it to the surface of the earth. Scattering and absorption in the atmosphere, and the incident angle affect the incident power density. Therefore, the available power density depends on the time of the day, climate conditions, the season and the latitude of a specific location. Of the solar light, which reaches a solar cell, only photons with energy larger than the energy band gap of the semiconductor generate electron-hole pairs. In addition, one finds that the voltage across the solar cell at the point where it delivers its maximum power is less than the band gap energy in electron volt. The overall power-conversion efficiency of single-crystalline solar

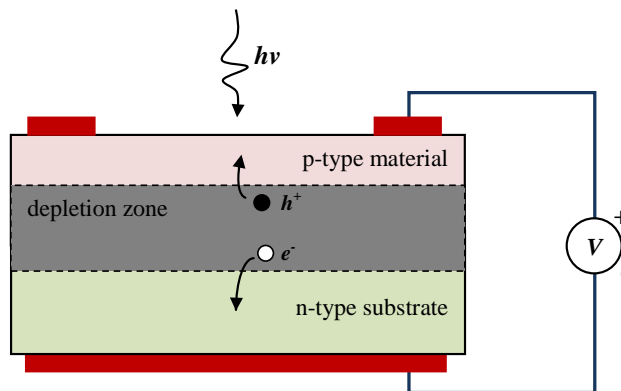


**Figure 5.2** Schematic illustration of photo-generated carrier motion in a photodiode

cells ranges from 10 to 30 % yielding 10 to 30 mW/cm<sup>2</sup>. So it is important to enhance the absorption coefficient of the device in order to take maximum advantage of the solar energy.

### 5.1.2.2 Light emitting diodes and laser diodes

Light emitting diodes (LEDs) are p-n diodes in which the recombination of electrons and holes yields a photon (see Figure 5.3). This radiative recombination process occurs primarily in direct band gap semiconductors (such as GaAs, InP, and GaN) where the lowest conduction band minimum and the highest valence band maximum occur at  $k = 0$ , where  $k$  is the wavenumber. In indirect band gap semiconductors such as Si, Ge, and SiC,  $k \neq 0$ .

The radiative recombination process is in competition with non-radiative recombination processes such as trap-assisted recombination. Radiative recombination dominates at high minority-carrier densities. Using a quantum well, a thin region with a lower band gap, positioned at the junction, one can obtain high carrier densities at low current densities. These quantum well LEDs have high internal quantum efficiency as almost every electron injected in the quantum well recombines with a hole and yields a photon. On the other hand, the external quantum efficiency of planar LEDs is much lower than unity due to total internal reflection. As the photons are generated in the semiconductor, which has a high refractive index, only photons traveling normal to the semiconductor-air interface can exit the semiconductor. InGaN/GaN quantum well are typical compounds for this purpose.<sup>34,35</sup> For GaAs with a refractive index of 3.5, the angle for total internal reflection equals 17° so that only a few percent of the generated photons can escape the semiconductor. This effect can be avoided by having NW semiconductor shape, which ensures that most

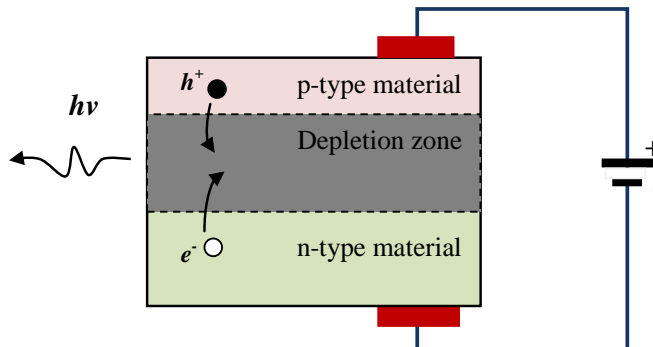


**Figure 5.3** Schematic illustration of photon generation in a LED

photons travel normal to the interface. The external quantum efficiency can thereby be increased to larger values.

Laser diodes, as a matter of fact, are very similar to LEDs since they also consist of a p-n diode with an active region where electrons and holes recombine resulting in light emission. However, a laser diode also contains an optical cavity where stimulated emission takes place. The laser cavity consists of a waveguide terminated on each end by a mirror. Photons, which are emitted into the waveguide, can travel back and forth in this waveguide provided they are reflected at the mirrors.

The light in the waveguide is amplified by stimulated emission. Stimulated emission is a process where a photon triggers the radiative recombination of an electron and hole thereby creating an additional photon with the same energy and phase as the incident photon as illustrated with Figure 5.4. This ‘cloning’ of photons results in a coherent beam. The stimulated emission process yields an increase in photons as they travel along the waveguide.

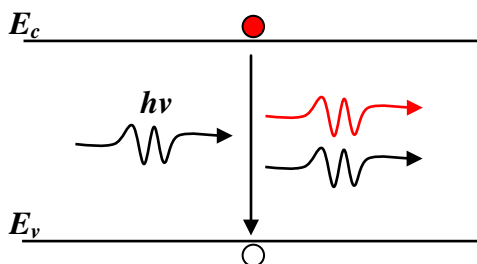


**Figure 5.4** Schematic illustration of stimulated emission in an LD

### 5.1.3 Catalyst-free growth via molecular beam epitaxy

Different NW growth methods and mechanisms were discussed in Chapter 4. However it is important to point up the advantages of catalyst-free growth, as metallic impurities deteriorate the optical properties of the NWs. Catalyst-assisted NW growth through VLS mechanism is a successful method. Gold as a catalyst plays an important role: it gathers the precursors which leads to higher sticking probability, and decomposes them preferentially. In contrast, it can be significantly harmful for the properties of the semiconductor, as it diffuses to the structure quite fast. In addition, gold is prohibited in semiconductor fabrication

facilities. Although in this case some other metals, e.g. Al and Ti can be used as catalysts, catalyst-free NW growth methods seem to be more promising.<sup>36</sup>

Molecular beam epitaxy (MBE) is an ultrahigh vacuum technique appropriate for NW growth. Soon after it was invented in 1960s it was used mostly for deposition of single crystal and thin film growth with high quality.<sup>37</sup> Nowadays it is used for growing III-V NW<sup>38</sup> and creating heterostructures and quantum structures within the NWs.<sup>39</sup> For GaN NW growth plasma-assisted molecular beam epitaxy (PAMBE) is used, because N<sub>2</sub> is an inert gas and requires excitation to react with Ga<sub>2</sub>O<sub>3</sub>. It was also evidenced that for NW growth a very low III/V ratio is needed, otherwise GaN films show up instead of NWs.<sup>40</sup> Therefore, plasma excitation of nitrogen is crucial for GaN NW growth.

#### 5.1.4 Structural study: polarity

Polarity is the concept of determining the relative charge residing on cation and anion sites in the lattice.<sup>41</sup> It has a considerable influence on physical and chemical properties of the compounds which was observed decades ago.<sup>42</sup> The so-called ‘*dumbbell units*’, which comprise a pair of atoms, a cation on one side and an anion on the other side, are important for polarity determination. The orientation of these dumbbell units causes ionicity in some surfaces and also determines the internal electric field of the crystal. For instance, in a prismatic GaN NW grown in [0001]<sub>B</sub> direction with (10-10), (1-100), and (01-10) lateral facets, the top and bottom surfaces, (0001)<sub>B</sub> and (0001)<sub>A</sub>, are N-polar and Ga-polar, respectively, whereas the lateral surfaces are all non-polar. Recently it has been shown that in some semiconductors the growth direction of one-dimensional nano structures such as NWs<sup>43</sup> and other non-planar structures such as tripods and tetrapods<sup>6,44</sup> is driven by polarity (See also in Chapter 3 the growth mechanism of CCTSe quaternary chalcogenide tetrapods).

Because of their polar axis, III-V crystals grown on a heterosubstrate can have two inequivalent orientations along *c*-axis. In the specific case of GaN, these two orientations are referred to as Ga-/N-polarity, depending on whether the Ga atoms (N atoms) of the Ga-N bilayers forming the crystal are facing towards the sample surface. In Ga-polar samples, the crystallographic *c*-axis and the internal electric field point away from the substrate towards the surface, whereas the polarization has the opposite direction. The polarization-induced fixed lattice charges are negative at the surface and positive at the substrate

interface. For N-polar materials, all charges and directions are inverted.<sup>2</sup> This concept will be further described in section 5.3.

## 5.2 Experimental

### 5.2.1 Synthesis

Self-assembled GaN NWs were grown on diamond/silicon substrates by means of PAMBE. In the case of diamond substrates, they were single crystals grown by high-pressure/high-temperature (HPHT) synthesis. They had a (111) surface orientation and an offcut angle of about 5°. The surface was polished to an atomically flat level and the backside of the substrates was metallized with Ti (200 nm) and Pt (70 nm) to improve heat transfer from the radiative MBE substrate heater. Prior to growth, the diamond substrates were exposed to an oxygen plasma at 200 W for 5 min in order to ensure a well-defined and reproducible surface termination. Afterwards, they were immediately transferred into the ultrahigh vacuum (UHV) environment of the MBE system. A very low III/V flux ratio of about 0.01 was applied, as well as a high substrate temperature of 930 °C to ensure high adatom mobility.<sup>45</sup>

In the case of Si substrates for the p-GaN/n-ZnO NW heterostructures, the native oxide layer of low-resistive p-type Si (111) substrates was removed by a HF etching step advance. Subsequently, the nanowire growth was performed in an UHV environment, where Ga and Mg (for p-type doping of GaN)<sup>46</sup> were provided by standard effusion cells and nitrogen radicals were supplied by an Oxford Applied Research RF plasma source operated at 425 W. Additionally, a Mg dopant flux was applied to ensure a high acceptor concentration in the GaN NWs. The substrate temperature was adjusted to 775°C according to pyrometer measurement. The growth process was started by a nitridation of the silicon substrates for 10 minutes.

In the case of p-GaN/ZnO heterostructures, as a second step, the Mg-doped GaN NWs were transferred to another PAMBE system for ZnO overgrowth, where UHV conditions had to be left for several minutes. A double-zone effusion cell was used for evaporating Zn while oxygen radicals were provided by an Oxford Applied Research RF plasma source operated at 400 W. The Zn and O fluxes were fixed. An elevated substrate temperature of 540°C was applied to ensure a high quality of the ZnO.<sup>47</sup>

### 5.2.2 Structural characterization

The crystal quality, epitaxy, and faceting of the NWs were investigated by high-resolution transmission electron microscopy (HRTEM) and atomic resolution aberration-corrected high-angle annular dark-field (HAADF or Z-contrast) scanning transmission electron microscopy (STEM) imaging. HRTEM was performed in a Jeol 2010F microscope, equipped with a field emission gun and operated at 200 keV, while HAADF-STEM was performed on a probe corrected FEI Titan 60-300 keV microscope operated at 300 keV. The latter was employed to carry out electron energy loss spectroscopy (EELS) and energy-dispersive X-ray spectroscopy (EDX) with high spatial resolution.

In parallel, we also performed direct polarity measurements on the grown GaN NWs, by means of the newly developed aberration-corrected annular bright-field (ABF) STEM imaging technique, which allows visualization of light elements. For cross-section analyses we prepared the samples by means of focused ion beam (FIB). Geometric phase analysis (GPA) was performed for strain analysis.<sup>48</sup> 3D atomic models were created by using Rhodius software package<sup>49</sup> which allows creating complex atomic models.<sup>50</sup>

### 5.2.3 Optical measurements

Photoluminescence was performed with a setup containing a continuous wave frequency-doubled Argon ion laser operating at 244 nm excitation wavelength and a DILOR double spectrometer with a helium cryostat for low-temperature measurements. All spectra were recorded at an excitation power of 20 mW/cm<sup>2</sup>. Cathodoluminescence (CL) analysis was carried out by means of a Jeol 2200FS microscope with Gatan CL detector at room temperature and liquid nitrogen temperature. Cryostat was used to cool down the samples to liquid nitrogen temperature (-182 °C) inside the microscope.

## 5.3 Structure study

In this chapter, as mentioned, we study interfaces and epitaxial relationships with GaN NWs. We will study two novel systems in detail: (i) GaN NWs grown on diamond, and (ii) p-GaN/n-ZnO axial heterostructure NWs. The former shows perfect epitaxial interface which is necessary for aforementioned applications. The latter provides an intrinsic polarity inversion further to the excellent epitaxy. It will be shown that the polarity inversion has a significant

influence on the electronic band structure of the interface. Optoelectronic properties of both systems are examined.

### 5.3.1 GaN nanowires on diamond

The first question that pops out from the mind is: “why diamond?” as it can be one of the most expensive substrates for GaN NW growth. Indeed it has many advantages. The paramount advantage is the high quality of GaN NWs which were obtained. The amount of structural defects is significantly less than the NWs grown on conventional substrates e.g. Si. At the same time, the growth is catalyst-free and no buffer layer forms in the interface between GaN NWs and diamond substrate. In the case of Si substrates, usually a relatively thick buffer layer (1-3 nm) made of amorphous SiN occurs,<sup>51</sup> however, in the case of diamond, GaN NWs grow directly on the substrate with epitaxial relationship subsequent to the possibility of some applications, for instance, UV-LEDs.

Diamond has an excellent thermal conductivity and is considered as a wide-band-gap semiconductor with a band gap  $E_g = 5.47$  eV<sup>52</sup> which is sometimes considered as an insulator. However, it can be p-doped with boron, which in the vicinity of any n-type semiconductors forms a p-n junction useful for optoelectronic devices. Previously Stutzmann and coworkers<sup>53,54</sup> grew heteroepitaxial AlN thin films on diamond in order to fabricate heterobipolar diodes emitting in UV spectral range. Nevertheless, the performance of the device foundered on the numerous structural imperfections in the AlN especially in the interface. Moreover, the difference between the thermal expansion coefficient of AlN/GaN and the one of diamond, gives rise to cracking of the epitaxial film during the cooling-down process (800-930 °C to room temperature). Therefore, one can take advantage of NW morphology in order to avoid this problem. NWs do not suffer from thermal mismatch as they have smaller connecting surface with the substrate and there is some room between the NWs which allows the thermal strain to be released and let the heterostructure be relaxed.

Other possible applications of this p-diamond/n-GaN NW heterostructure can be single-spin magnetometry<sup>8,9</sup> and quantum computation. Neumann *et al.*<sup>7</sup> show that diamond is a suitable material for hosting robust solid-state quantum registers, owing to their spin-free lattice and weak spin-orbit coupling. In fact, quantum logic elements can be realized by exploring long-range magnetic dipolar coupling between individually addressable single electron spins

associated with separate color centers in diamond. The strong distance dependence of this coupling was used to characterize the separation of single qubits ( $98 \pm 3 \text{ \AA}$ ) with accuracy close to the value of the crystal-lattice spacing. As both electron spins are optically addressable, this solid-state quantum device can operate at ambient conditions and low temperatures. On the one hand, it is possible to introduce defects by ion implantation in order to create nitrogen-vacancy defects in the diamond lattice,<sup>55,56</sup> and on the other hand, photo-assisted single-spin readout techniques<sup>57,58</sup> are available. Therefore, the charge of the nitrogen-vacancy defect (neutral or negative) can be optically read out.<sup>59</sup> To electrically control single nitrogen-vacancy centers, GaN NWs are ideal local contacts for applying electric fields or for electrical read-out. To this end, the same lithography mask can be used for both position-controlled implantation of the nitrogen-vacancy centers and self-aligned selective area epitaxy of single NWs.

Figure 5.5 shows SEM images of the substrate after 20 minutes (Figure 5.5(a)), 40 minutes (Figure 5.5(b)) and 180 minutes (Figure 5.5(c)). The highest

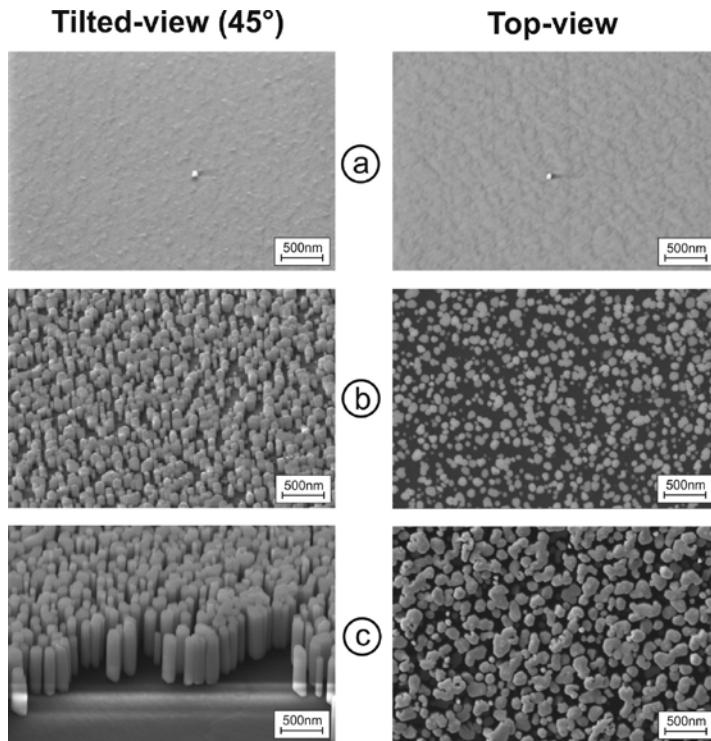
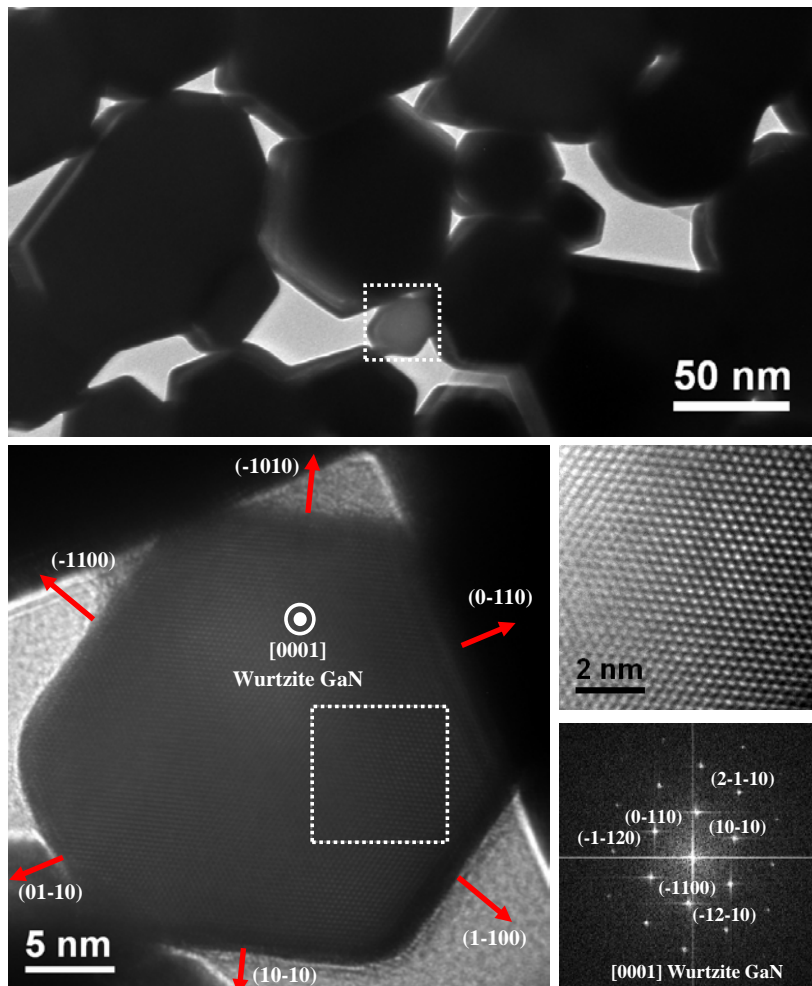


**Figure 5.5** SEM images of as-grown GaN NWs on diamond substrate after (a) 20 minutes, (b) 40 minutes, and (c) 180 minutes<sup>45</sup>

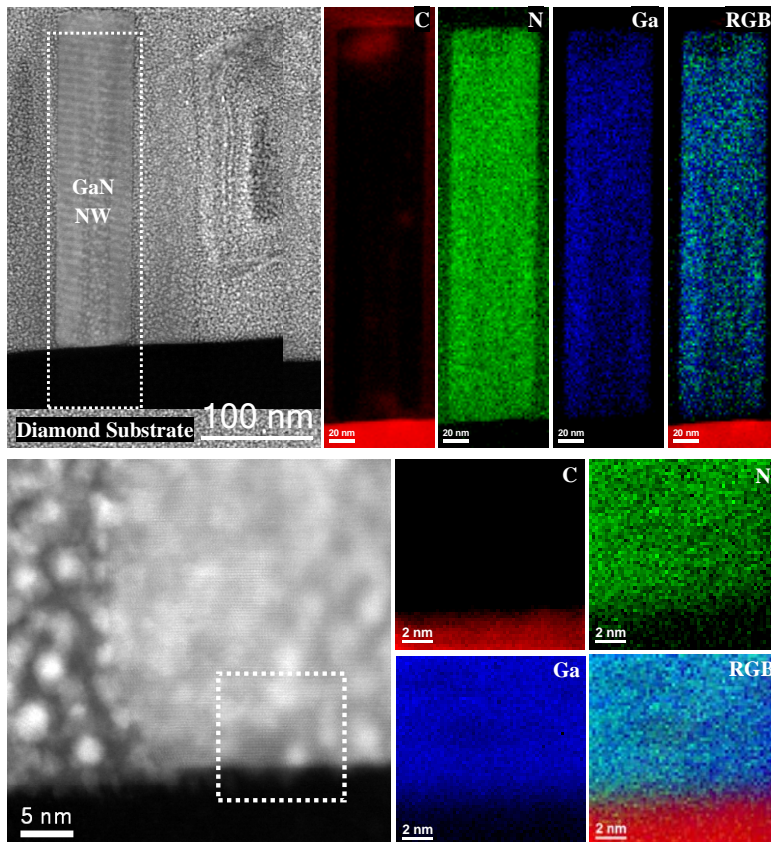
NW intensity was obtained at 40 minutes, as after that the coalescence between them takes place. After 180 minutes the substrate is almost fully covered with NWs.

Figure 5.6 reveals top view TEM and HRTEM micrographs on GaN NWs. According to the HRTEM analysis, GaN NWs have wurtzite structure with hexagonal symmetry belonging to  $P6_3mc$  space group, and they are grown in  $[0001]$  direction. Lateral facets, as indicated by red arrows, are  $(10\text{-}10)$ ,  $(\text{-}1010)$ ,  $(01\text{-}10)$ ,  $(0\text{-}110)$ ,  $(1\text{-}100)$ , and  $(\text{-}1100)$  which are non-polar as at the surface always both Ga and N are present with same quantity.

As discussed above, one of the advantages of diamond substrate is the



**Figure 5.6** HRTEM micrograph of a GaN NW from the top view showing the WZ structure, prismatic cross-section, and lateral facets



**Figure 5.7** Z-contrast images of a GaN NW associated with EELS compositional maps

epitaxial growth of the GaN NWs with almost no buffer layer. To study the interface, a cross-section TEM sample was prepared. Diamond is a hardest material and it cannot be easily cut and polished by conventional cross-section TEM sample preparation methods. Therefore focused ion beam (FIB) sample preparation was a reasonable and appropriate method to this end. Figure 5.7 shows a Z-contrast image of a NW associated with EELS compositional maps. Firstly, the map on the whole NW reveals the homogeneity of the chemical composition, and secondly, the magnified map of the interface shows that Ga and N abruptly start on the substrate. In the few first atomic monolayers both C and N can be seen which is attributed to the slope of the substrate due to the  $5^\circ$  offcut.

Furthermore, we also performed cross-sectional HRTEM analysis. In Figure 5.8 the interface is clearly seen. Right on diamond GaN starts to grow. The steps

of the diamond monolayers due to the offcut are indicated with red arrows. It is observed that GaN adapts to these monoatomic steps and grows vertically. The power spectra in red and green refer to GaN and diamond, respectively. The overlap of these two power spectra reveals the relaxed structure of wurtzite GaN. The (2-20) planes reflection of diamond is quite close to (2-200) one of GaN. Plane distances in the case of  $(2-20)_{\text{Diamond}}$  and  $(2-200)_{\text{GaN}}$  are 1.261 Å and 1.369 Å, respectively, which theoretically bring 7.89% mismatch, meaning within every 12 or 13 (2-20) planes we should have one misfit dislocation. This is in good agreement with the experimental results shown in Figure 5.9. The HRTEM micrograph at left is frequency-filtered by masking the obtained power spectrum in a way that only  $(2-20)_{\text{Diamond}}$  and  $(2-200)_{\text{GaN}}$  reflections remain. To assign different colors to different structures, these two reflections are taken separately. In this figure, the diamond/GaN interface is indicated by a dot line, coinciding  $(2-20)_{\text{Diamond}}$  and  $(2-200)_{\text{GaN}}$  planes by dash lines, and misfit dislocations with yellow arrows.

In order to see whether the GaN structure is relaxed, we performed geometric phase analysis (GPA) as seen in Figure 5.10. The color of the GPA map on GaN is almost smooth, meaning no strain is observed. There are some

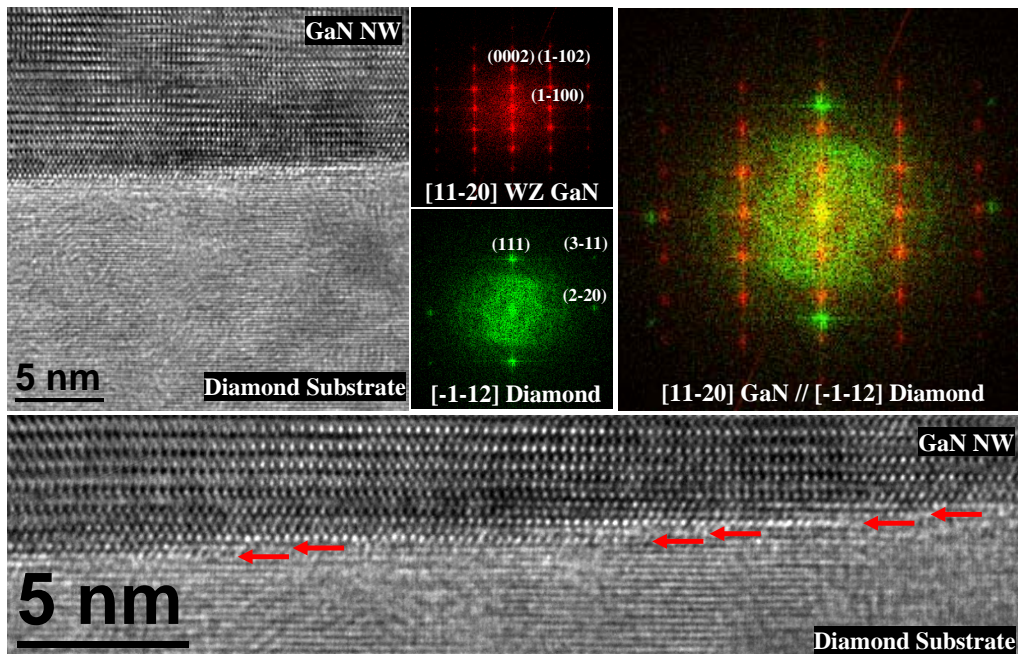


**Figure 5.8** Cross-sectional HRTEM analysis of GaN NW interface with diamond substrate

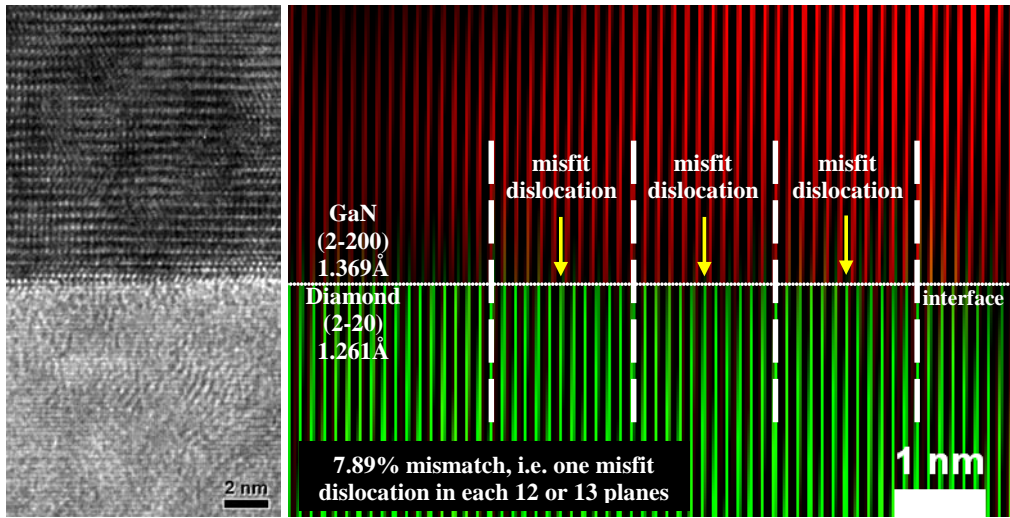


**Figure 5.9** Mismatch analysis on frequency-filtered HRTEM image of a GaN/diamond interface

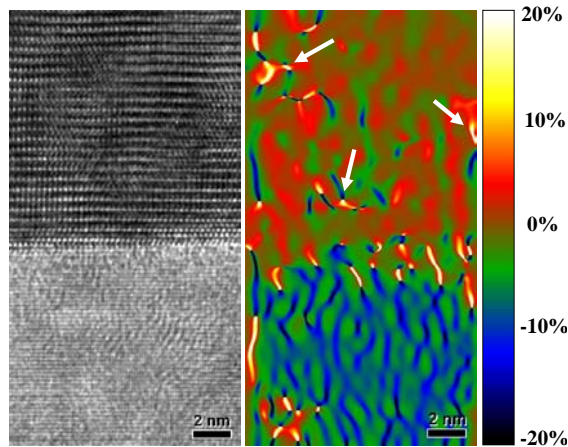


**Figure 5.10** Geometric phase analysis (GPA) on the interface of a GaN/diamond interface

points that are indicated but white arrows which seem like strain points, but indeed, they are artifacts due to the overlap of the structure with the Pt particles. Pt particles come from FIB sample preparation process, deposited to protect the sample in front of the ion beam. In addition, in the interface also some strain-like points are observed which are due to the presence of misfit dislocations.

In Figure 5.11 this Interface is also studied with 3D atomic models created by virtue of Rhodius software package. As a matter of fact, the same mismatch

is observed in the interface. Besides, Ga-N pair orientation is visualized from two different zone axes,  $[11-20]$  and  $[1-210]$ . Here it is shown that the lateral facets are non-polar as Ga and N are present with equal quantity. In contrast, one can see (in both  $[11-20]$  and  $[1-210]$  zone axes) that the last atomic layer consists of only N atoms and Ga-N dumbbells are pointing upwards, meaning the NWs are N-polar. The major difference between these two zone axes is the way the dumbbells are seen. From  $[1-210]$  direction they are vertically oriented whereas from  $[11-20]$  direction they are oriented diagonally. The problem with vertically-aligned dumbbells is that firstly, it can hinder polarity determination as the distance between the anion and cation is shorter in the TEM images ( $0.63 \text{ \AA}$ ). In  $[11-20]$  maximum cation-anion distance ( $0.89 \text{ \AA}$ ) can be seen. Secondly, twin defect cannot be observed and as a consequence wurtzite and zinc-blende structures are not distinguishable. In WZ GaN, the distance between a Ga atom and the four surrounding N atoms,  $d$  is  $1.89 \text{ \AA}$  and the angle between the bonds,  $\theta$ , is  $109.48^\circ$ . Therefore, the dumbbell length from  $[11-20]$  zone axis is:

$$\frac{d}{2} \cos\theta = 0.89 \text{ \AA}$$

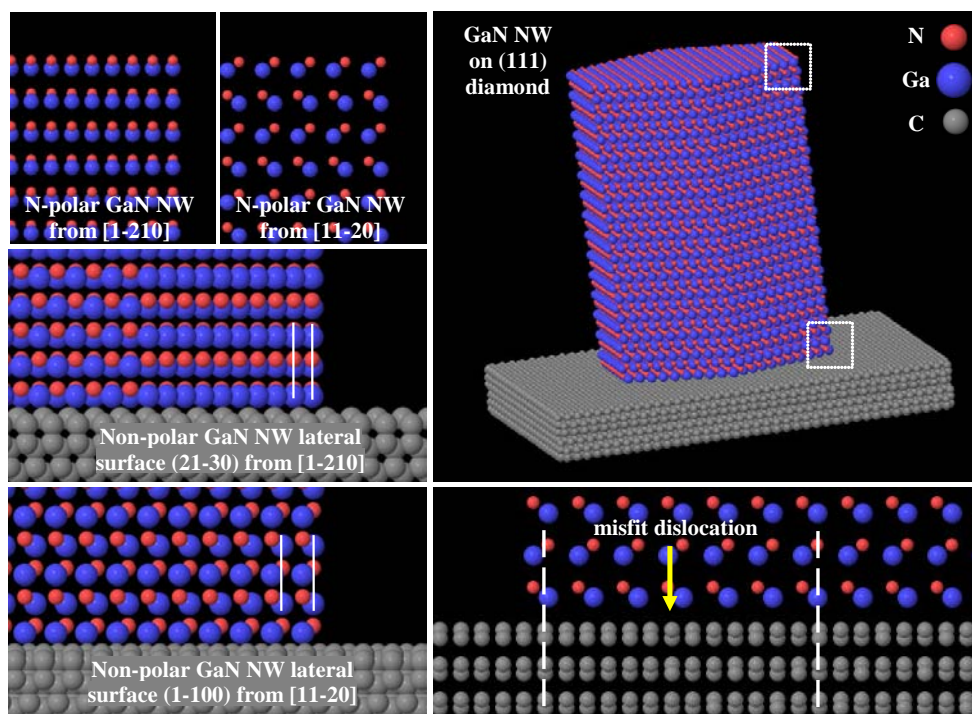


**Figure 5.11** 3D atomic models of a GaN NW grown on diamond substrate, general view, interface and polarity from  $[11-20]$  and  $[1-210]$  zone axes

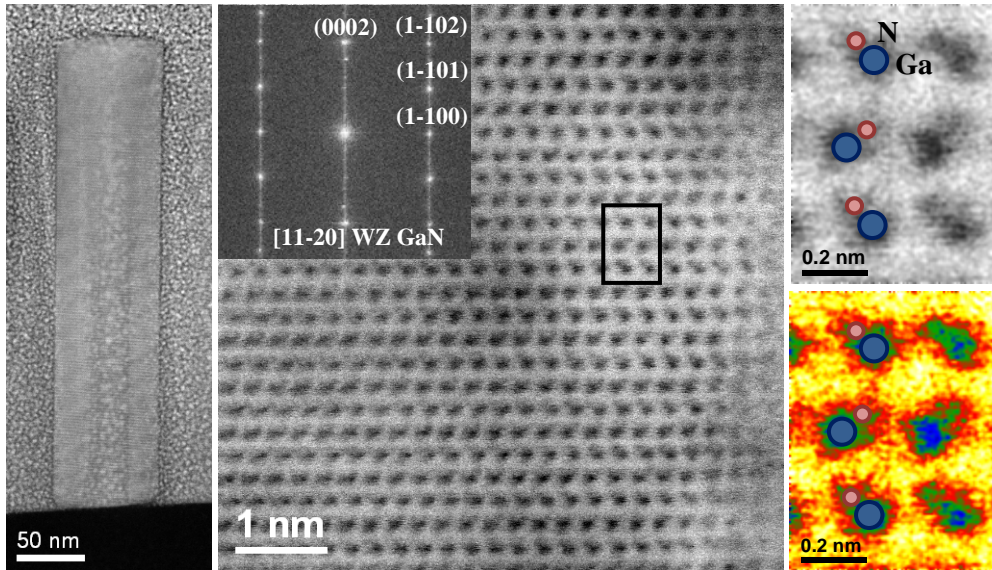


**Figure 5.12** Annular bright-field (ABF)-STEM micrograph of a GaN NW showing N-polarity

and from [1-210] zone axis is:

$$d\sin\theta = 0.63 \text{ \AA}$$

Therefore, in order to determine the polarity by means of high-angle annular dark-field (HAADF) and annular bright-field (ABF) techniques, one should use [11-20] (or [01-10] and [10-10] which are equivalent) zone axis. In Figure 5.12 we reveal an ABF-STEM image of GaN NW by means of an aberration-corrected microscope. ABF is a novel technique<sup>60</sup> that allows visualizing light atoms such as H,<sup>61</sup> O<sup>62</sup> and N<sup>6,45</sup> and thus polarity of compounds like ZnO and GaN with atomic resolution. One of the advantages of this technique is any polarity inversion within the atomic layers can be interpreted directly from the micrographs.

GaN NWs grown on diamond substrate showed impressive optical properties. In Figure 5.13, the photoluminescence (PL) of an ensemble of as-grown GaN NWs on diamond (Figure 5.13(a)) is presented which was recorded at liquid-helium temperature. The spectra are compared with the one of GaN NWs grown on Si (Figure 5.13(b) and (c)). Further, the spectra were recorded at different temperatures ranging from liquid-helium to room temperature.

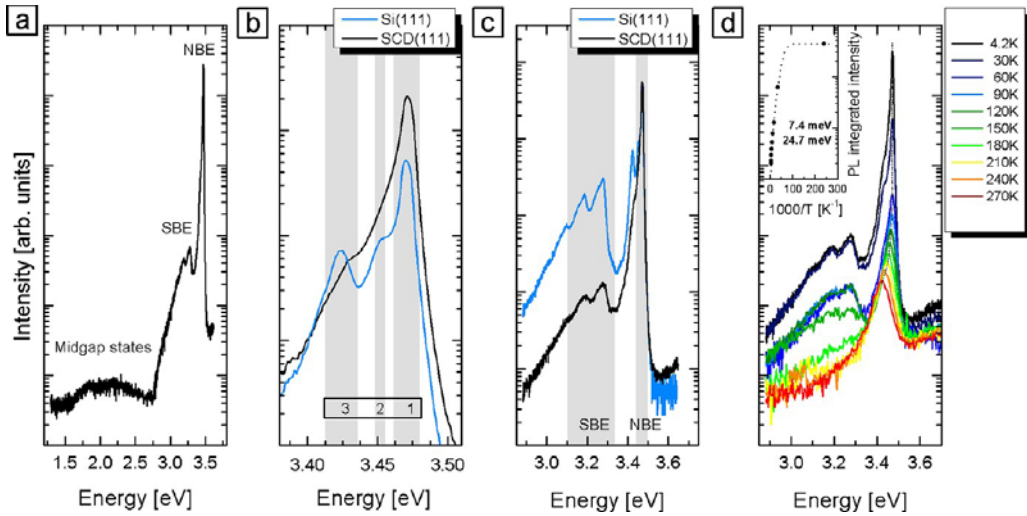


**Figure 5.13** PL analysis of GaN NWs: (a) the entire spectrum, (b) NBE region of NWs grown on diamond (black) and Si (blue), (c) SBE comparison by shifting the NBW maximum, (d) spectrum shift at different temperatures due to GaN band gap shrinkage<sup>45</sup>

The PL spectrum consists of a pronounced excitonic near-band-gap emission (NBE) at 3.4-3.5 eV, a sub-band-gap emission (SBE) at 3.2-3.3 eV and defect recombination forming midgap states. The yellow luminescence, which is a well-known problem in GaN films due to structural imperfections,<sup>63</sup> is almost 5 orders of magnitude weaker with respect to the NBE, undermining the qualitative superiority of NWs with respect to two-dimensional films. In recent years, PL spectra of GaN NWs on silicon substrates have been discussed in detail.<sup>64</sup> Here the same discussion is used as it seems reasonable to assume the same recombination processes in GaN NWs grown on diamond with the exception of a different substrate/NW interface. Low-temperature PL spectra of as-grown GaN NWs on diamond (111) and silicon (111) substrates are compared in Figure 5.13(b) and (c). On silicon substrates, three contributions to the NBE can be distinguished which are highlighted in Figure 5b: 3.470 eV (1), 3.452 eV (2), and 3.424 eV (3). These emission lines have been attributed to (1) excitons bound to neutral shallow donor impurities ( $D^0X$ ), (2) excitons bound to point defects induced by the N-rich growth conditions, for example, gallium vacancies, and (3) excitons bound to structural defects such as stacking faults from the bottom interface of the NW.<sup>65</sup> Emissions (2) and (3) are not resolved,

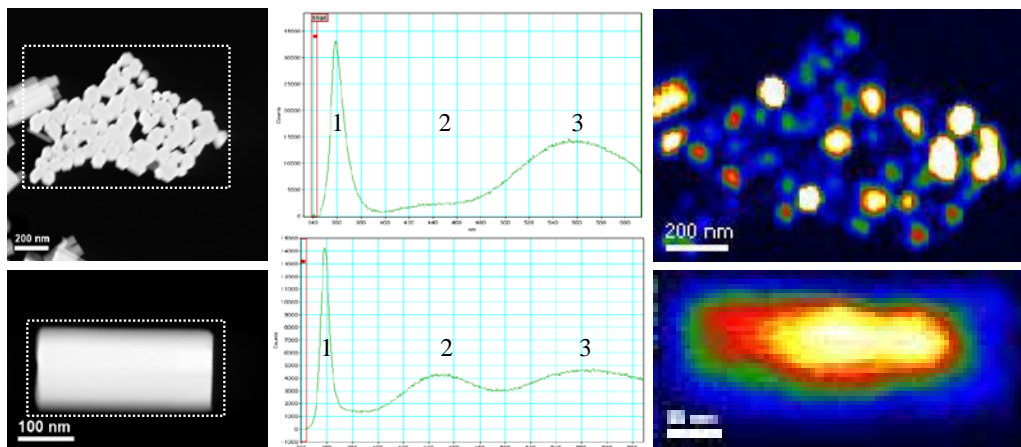
suggesting a lower defect density as well as a highly ordered substrate/NW interface, as confirmed by HRTEM measurements. The origin of the emission at about 3.43 eV is so far unknown.<sup>45</sup>

Figure 5.13(c) is a comparison between the intensity of SBE in PL spectrum of GaN NWs on diamond and the one of the NWs grown on Si. The spectra are fit by considering the maximum of the NBE at the same height. Thus, the reduction of SBE in the case of diamond substrate (over one order of magnitude) is explicitly shown. A well-known origin for SBE is formation of GaN with zinc-blende structure. However, following the HRTEM analysis, this structure with an excitonic band gap of 3.27-3.28 eV does not occur in the NWs,<sup>51</sup> so it can be partially excluded as possible origin of this emission. It can be attributed to the twin defects in wurtzite structure which indeed create some zinc-blende atomic monolayers within the structure. Moreover, this emission can also be assigned to a donor-acceptor pair (DAP) recombination<sup>65</sup> that is very pronounced due to a strong interdiffusion of silicon into the GaN NW, resulting in a highly n-type doped NW base.

Finally, in Figure 5.13(d) temperature dependence of the emissions is shown by performing PL measurement in different temperatures ranging from 4 to 270 K. By reducing the temperature, a redshift of the NBE position due to the temperature-induced shrinkage of the band gap occurs. The intensity drop of the excitonic NBE can be modeled by a two-step dissociation mechanism, consisting of (i) the release of excitons from localization centers and (ii) exciton dissociation, which both lead to a decrease in radiative recombination. As the NWs exhibit excellent structural quality, surface states are expected to act as localization centers for the excitons.<sup>45</sup>

In the end, cathodoluminescence (CL) measurement in TEM was performed in order to evaluate the optical properties with higher spatial resolution. The experiment was carried out in the temperature of liquid nitrogen (90 K) to reduce the noise and obtain clearer signals. This method is quite delicate as high potential of the electron beam can introduce defects in the structure in a way that no light will be emitted. Hence, the experiment was performed at 80 kV with cryostat sample holder to reduce the sample temperature to 90 K.

In Figure 5.14 Z-contrast micrographs (left) are associated with corresponding CL spectra (center) and NBE intensity maps in color (right). The upper one shows CL analysis on a bunch on GaN NWs which are looking through the monitor, and the lower one refers to a GaN NW from the side view.



**Figure 5.14** CL analysis: Z-contrast images (left) associated with CL spectra (center) and CL intensity map from region 1 of the spectra

On the CL spectra three regions are indicated by numbers. Region 1 corresponds to the NBE region which has the maximum at 358 nm (equal to 3.46 eV), in good agreement with PL results. The colored maps correspond to this region. As observed in the upper image, luminescence is stronger in the case of bigger NWs. However, smaller NWs also emit. In the lower image, it is shown that the NBE intensity in the middle of the NW is much stronger than the regions close to the external surfaces. In both cases this can be attributed to Ga-vacancies as point defects in the surface which take place as a consequence of highly N-rich growth conditions which deteriorate the NBE and at the same time give rise to yellow-band emission (region 3).<sup>66,67</sup>

On the other hand, some studies have been performed on emission through, polar, semi-polar, and non-polar surfaces of GaN. As a matter of fact, we also observed that there are some differences between the spectrum taken from standing NWs (upper images in Figure 5.14) and the one related to the lying NW (lower images in the same figure). In the latter, the peak in the second region of the spectrum is significantly higher, which in the literature is attributed to the non-polar (11-20) surface of GaN.<sup>67,68</sup> Note that the CL detector has a concave mirror placed above of the sample holder with a hole to avoid obstructing the transmitted beam. Thus, only the emissions that come through the mirror are collected. This can account for the appearance of the peak of region 2 that is attributed to non-polar surfaces of GaN. In the second case, the NW is lying down on the carbon grid with a non-polar (11-20) surface looking

directly through the mirror which enhances the peak of region 2. Additionally, strength of region 3 in the first spectrum is attributed to the emission of c-facets (i.e. (0001) and (000-1) facets) which are polar. As the NWs are not on the substrate, we cannot determine whether they are N-polar or Ga-polar.

In general, CL in TEM is an advanced technique which can assist for some particular characterizations of different materials. For instance, it can be used to analyze radiative recombination properties of the sample and image material defects. However it has some disadvantages. The range of the materials that can be analyzed by CL is rather small, comprising the ones that emit photons when excited with high-energy electrons, so in other words, they should be nonmetallic. In the case of narrow-band-gap semiconductors or some insulators, it is rather complicated to obtain the desired results. Moreover, the phenomena of luminescence are extremely complex since the type and amount of impurities or defects have dramatic trace on luminescence properties of the material.<sup>69</sup> Therefore, a precise and complete theoretical and experimental study is required in order to understand all the emissions in detail.

To sum up, in this section we studied the structure and optical properties of high-quality GaN NWs grown on diamond substrates. These NWs were epitaxially grown on the substrate which makes them promising for novel applications in optoelectronic devices, or quantum computation and single-spin magnetometry. In optoelectronics, the high-quality GaN NWs can be used as UV-range LEDs, while in quantum computation and single-spin magnetometry nitrogen-vacancy defects in diamond play the main role. The novel properties of this heterojunction (NW/substrate) were proved by advanced structure study by means of newly developed TEM techniques. 3D atomic models revealed the situation of the interface corroborating the epitaxial growth and strain-free analysis performed in the experiment. Polarity determination was carried out directly from the ABF micrographs. This method provide straightforward and reliable results on polarity as it allows us to see even light atoms like O and N and consequently the polarity in every single atomic layer.

Likewise, PL analysis showed the excellent quality of the NWs which proves their promise in the field of optoelectronics. A significant improvement in optical emission of the GaN NWs was observed which was in good agreement with CL analysis performed in TEM in liquid-nitrogen temperature.

After analyzing bare GaN NWs, in the following section, heterostructures based on p-GaN/n-ZnO NWs will be studied. There an interesting phenomenon

takes place: polarity inversion; a phenomenon that seldom occurs and can cause dramatic changes in physical properties of the compounds if occurs.

### 5.3.2 p-GaN/n-ZnO heterostructure nanowires

In this section a study on axial p-GaN/n-ZnO heterostructure NWs is carried out. The idea was originally motivated by the desire to create an appropriate epitaxial heterostructure. GaN and ZnO NWs both usually have wurtzite structure with hexagonal symmetry in  $P6_3mc$  space group. Cell parameters of wurtzite GaN are:  $a = b = 3.162 \text{ \AA}$  and  $c = 5.142 \text{ \AA}$ , while wurtzite ZnO unit cell has rather similar size:  $a = b = 3.265 \text{ \AA}$  and  $c = 5.219 \text{ \AA}$ . The crystal structures are shown in Figure 5.15.

As NWs of both structures grow in [0001] direction, it is assumed that (0001) planes of ZnO lie on the same planes of GaN, and thus epitaxial relationship occurs in (11-20) plane families. These atomic planes in GaN and ZnO are of  $2.738 \text{ \AA}$  and  $2.827 \text{ \AA}$ , respectively, and consequently 3.25% mismatch is expected. Therefore, the epitaxial relationship in this heterostructure is far better than the one of ZnO with usual substrates (e.g. Si and sapphire). On the other hand, although n-doping of ZnO is quite common, this material cannot be easily doped with p-type impurities and this fact confines its applications. Hence, GaN as a perfect p-type supplement can open new ways towards further applications.

In order to create p-GaN/n-ZnO heterostructure, p-GaN nanowires were overgrown by intrinsically n-type ZnO to form a p-n junction which can be used as LED emitting in the UV-spectral range. A scheme is shown in Figure 5.16.

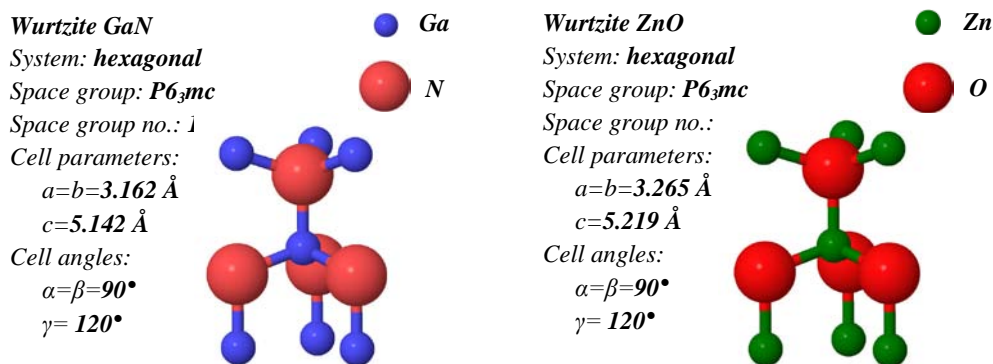


**Figure 5.15** Crystal structure of wurtzite GaN (left) and ZnO (right) with hexagonal symmetry belonging to  $P6_3mc$  space group

Here GaN is doped with Mg.

Figure 5.17 shows scanning electron microscopy (SEM) images of GaN:Mg NWs deposited on p-type silicon (111) before (Figure 5.17(a) and (b)) and after (Figure 5.17(c) and (d)) deposition of n-ZnO cap. The dimensions of the highly p-type doped GaN NWs were determined to be  $40 \pm 8$  nm in diameter and  $360 \pm 30$  nm in length. The heterostructure NWs were fabricated in a two-step growth procedure using two different MBE systems. After the second growth step, ZnO coverage can clearly be seen while maintaining the NW geometry by high axial and low radial growth rates. STEM studies reveal the formation of ZnO caps

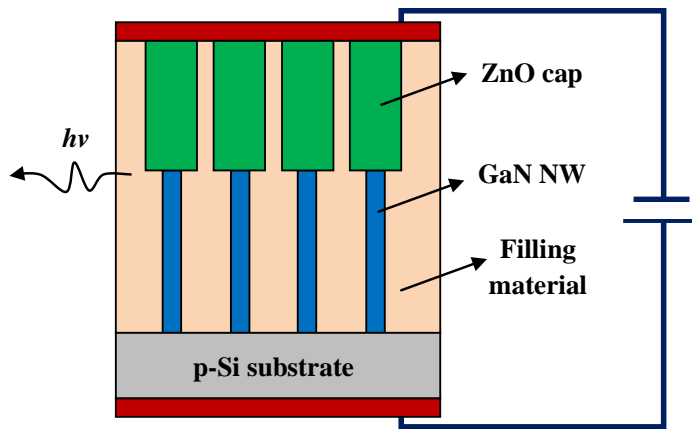


**Figure 5.16** Scheme of p-GaN/n-ZnO heterostructure NWs as a UV-LED

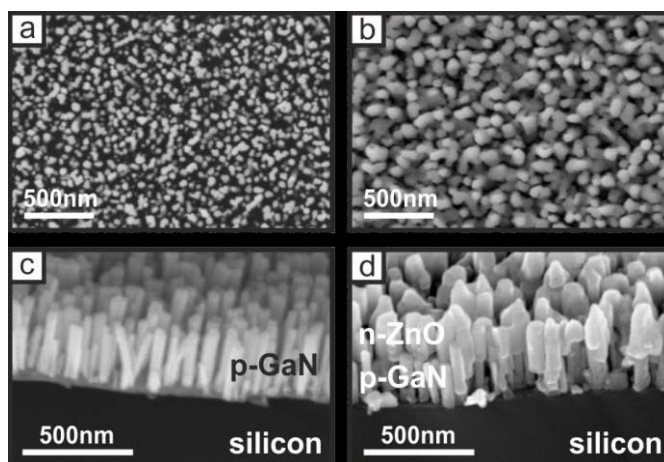


**Figure 5.17** SEM micrographs showing the GaN NWs (a), (b) before and (c), (d) after being covered with ZnO cap

with a mean height of 200 nm observed on almost all polar GaN NW top facets. However, only a short part of the non-polar side facets are covered by a complete ZnO shell with thicknesses up to 20 nm, extending towards the bottom of the NW. Also in STEM images the formation of a homogeneous  $\gamma\text{-Ga}_2\text{O}_3$  layer (crystalline  $\gamma\text{-Ga}_2\text{O}_3$  with cubic symmetry belonging to  $Fd3m$  space group) of several nanometers (1-5 nm) is observed which seems to prevent ZnO nucleation.

Figure 5.18 reveals high-resolution STEM images of a GaN NW without ZnO cap associated with EELS compositional maps and power spectra

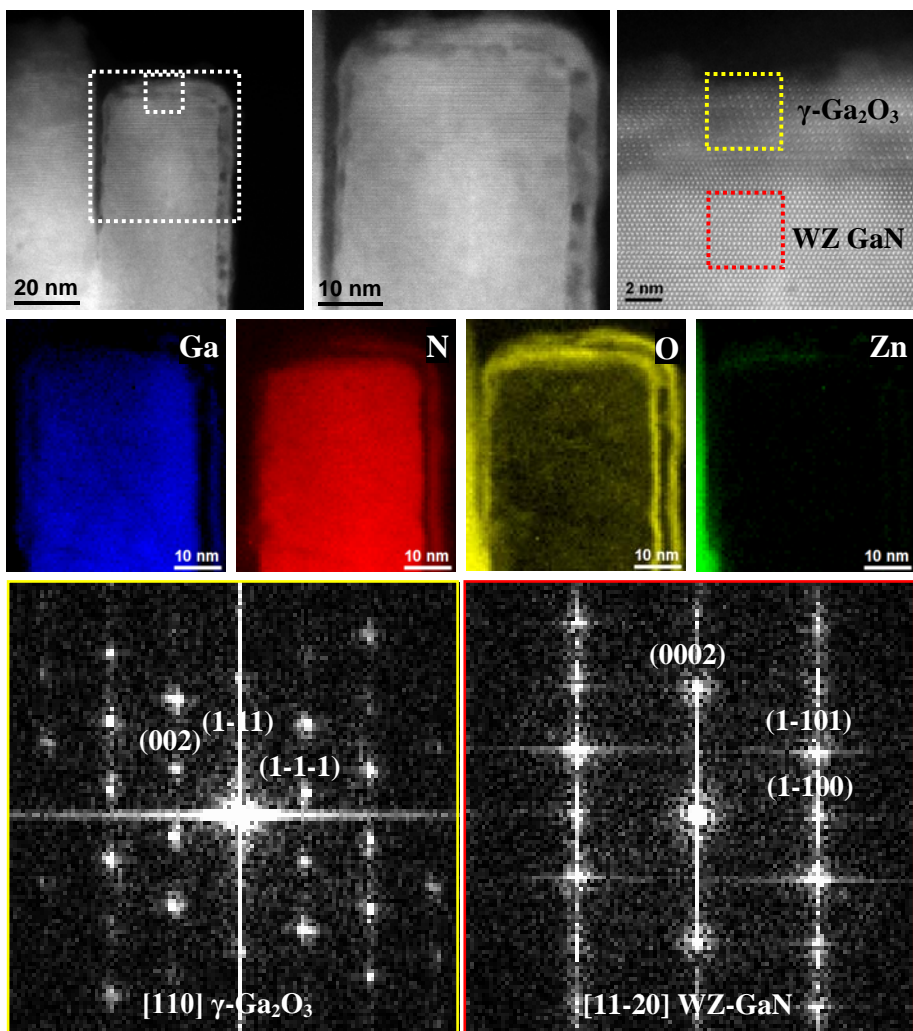


**Figure 5.18** High-resolution STEM images associated with EELS compositional maps and corresponding power spectra

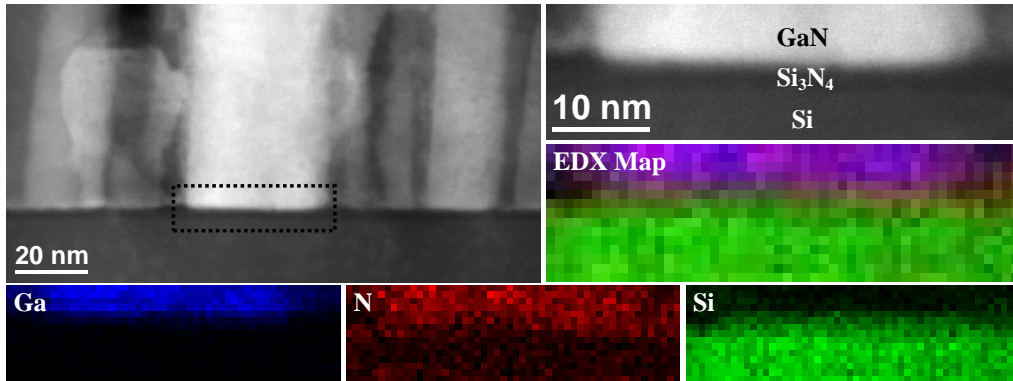


**Figure 5.19** HAADF-STEM image of the interface between a GaN NW and the Si substrate, associated with EDX maps showing the formation of Si<sub>3</sub>N<sub>4</sub> buffer layer

corresponding to the Ga<sub>2</sub>O<sub>3</sub> layer and the GaN NW in yellow and red, respectively. The power spectra in this figure shows that Ga<sub>2</sub>O<sub>3</sub> layer has epitaxial relationship with the GaN NW: (0-11)[110]<sub>Ga<sub>2</sub>O<sub>3</sub></sub> // (0001)[11-20]<sub>GaN</sub>. In the EELS compositional maps of this figure one can see that some content of N can be found in the Ga<sub>2</sub>O<sub>3</sub> layer. Therefore we believe that this layer can be a mixture of oxide and nitride.

In Figure 5.19 STEM analysis associated with EDX compositional maps is performed in the interface between the GaN NW and the Si substrate. As mentioned in the previous section, a thin buffer layer made of amorphous Si<sub>3</sub>N<sub>4</sub> is formed in the interface between the as-grown NWs and the Si substrate. In the middle of the map, there is a zone that Si and N overlap in the absence of Ga. The stoichiometry of Si<sub>3</sub>N<sub>4</sub> is confirmed by EDX quantification.

A detailed analysis of the p-GaN/n-ZnO heterointerface is performed and presented in Figure 5.20. Here, a sample with thinner ZnO coverage was used for a better access to the interface region. The polar top facet of an exemplary GaN NW is covered with a ZnO cap which is larger in diameter. Interestingly, the ZnO cap does not sit exclusively on the GaN top facet, but surrounds the GaN NW for about 10 nm. The NW sidewalls are not covered with ZnO, but with a 1-5 nm thick crystalline Ga<sub>2</sub>O<sub>3</sub> layer with a nitrogen content of up to 20%. This indicates that the mobility of the impinging Zn atoms is high enough to reach the polar top facet of the GaN NWs, whereas the impinging oxygen radicals are incorporated also on the non-polar sidewalls and form Ga<sub>2</sub>O<sub>3</sub>. The heterointerface in the HAADF-STEM image is smooth and abrupt with no

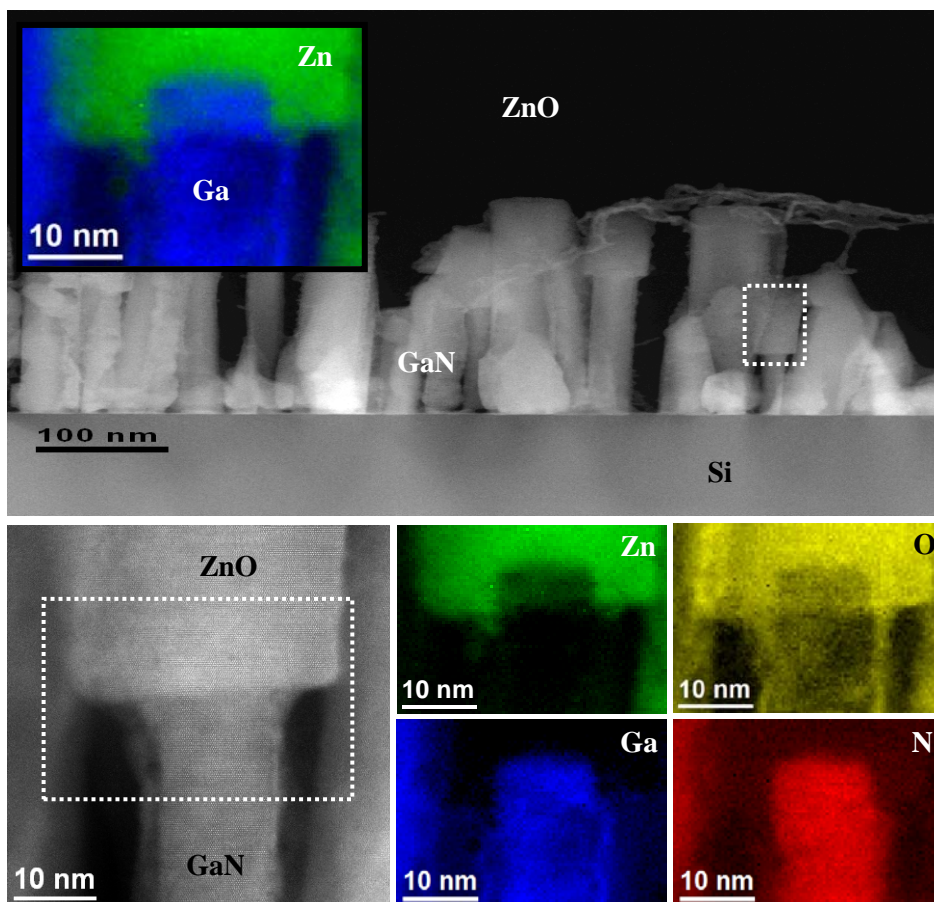


**Figure 5.20** HAADF-STEM micrographs on p-GaN/n-ZnO heterostructure NWs, associated with EELS compositional maps

defects to be seen in the vicinity, what is clearly a result of the low lattice mismatch of the two materials.

As discussed previously, it is of paramount importance to know the polarity configuration to model the electronic band structure across the heterostructure. To this end, the polarities of GaN and ZnO were determined directly by virtue of aberration-corrected ABF-STEM as described in the previous section. The results in Figure 5.21 reveal the characteristic atomic layers in polar direction where the single dumbbell units are clearly resolved. Accordingly, the polarity can be determined to be N-polar for GaN and Zn-polar for ZnO. This polarity inversion from anion to cation was found to occur for all investigated heterojunction NWs. The attempt to influence the ZnO polarity by the growth

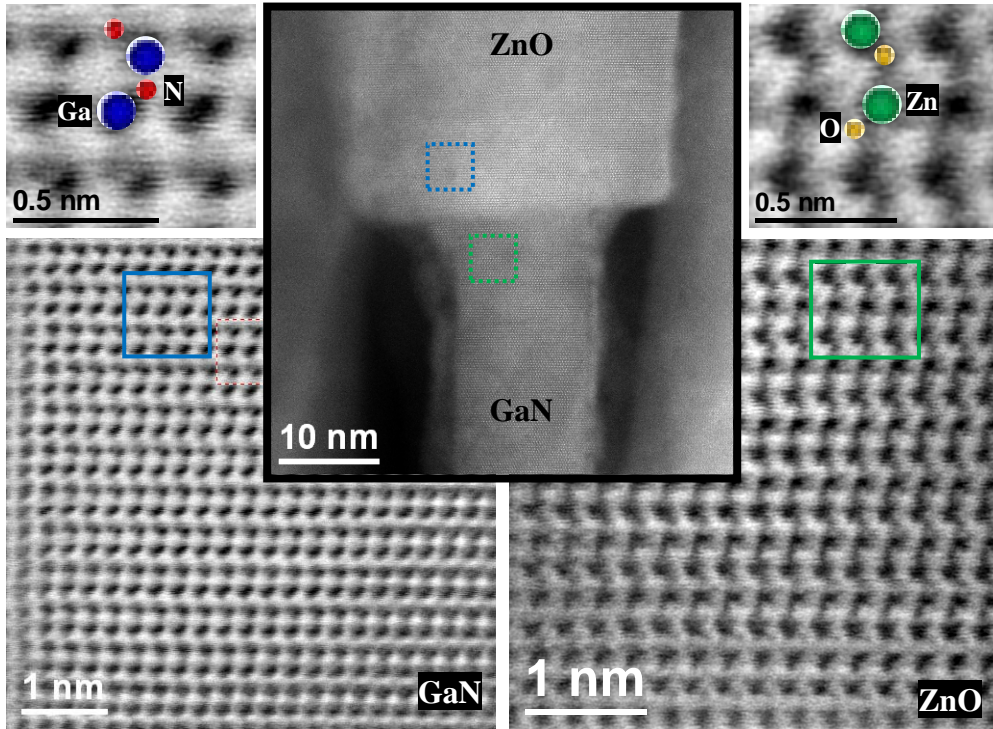


**Figure 5.21** Aberration-corrected ABF-STEM images of a GaN/ZnO heterostructure NW determining N-polarity and Zn-polarity in GaN and ZnO, respectively

procedure, i.e. starting the growth with Zn or O pre-exposure, was investigated in two additional samples but showed no effect on the polarity configuration. This can be assigned to the high binding energy of the N-O bonds which seem to be responsible for the observed polarity inversion. Due to the overlap of ZnO cap on GaN NWs, it cannot be precisely observed where exactly the polarity changes, however, N-polarity in GaN and Zn-polarity in ZnO can be seen explicitly, in good agreement with previously-obtained results by the group.<sup>6,45,50</sup> Figure 5.22 also reveals the same results although the attempt was to obtain O-polar ZnO caps and it failed. The only difference was the undesired morphology of ZnO cap which in some cases covered some of the lateral facets of GaN NWs.

Additionally, theoretical study is performed on band structure taking into account the different possibilities of polarity in the interface. In other words, GaN: Ga- or N-polar, and ZnO: Zn- or O-polar give the combination of four

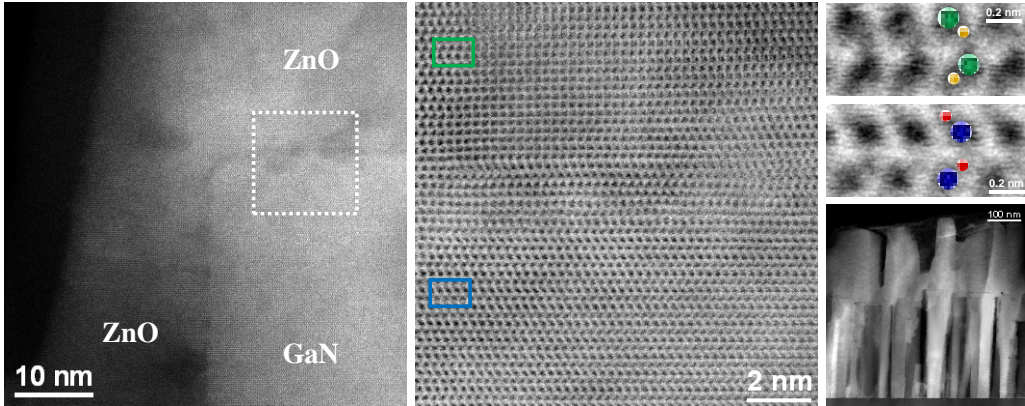


**Figure 5.22** Failure in ZnO polarity change, aberration-corrected ABF-STEM images of a GaN/ZnO heterostructure NW determining N-polarity and Zn-polarity in GaN and ZnO, respectively

different p-GaN/n-ZnO heterostructures: N-polar/O-polar, N-polar/Zn-polar, Ga-polar/O-polar, Ga-polar/Zn-polar. It is useful to add non-polar band structure as a reference.

The electronic band structure of the p-GaN/n-ZnO heterointerface was simulated by means of the *nextnano*<sup>3</sup> software package which is a simulation tool for prediction and understanding electronic and optical properties of semiconductor nanodevices.<sup>70</sup> The simulation sequence was started by the input of the strain tensor to evaluate piezoelectric charges as well as spontaneous polarization charges at the interface. Then the Schrödinger and Poisson equation were solved self-consistently with applied Neumann boundary conditions  $\partial\phi/\partial z = 0$ , where  $z$  is the growth direction, to enforce a vanishing electric field on both sides towards the bulk. The thermally activated free charge carriers are modeled according to an effective mass approach with Neumann boundary conditions. In all simulations, the Fermi energy ( $E_F$ ) is set to zero indicated by the green dash-dotted line.<sup>47</sup>

In Figure 5.23(a) the basic type-II band lineup of the two materials is shown, based on the theoretical valence band offset (VBO) of 1.3 eV<sup>71</sup> (this parameter contains some uncertainty). Nevertheless, the theoretical value was used for the simulation, since the experimental reports do not account for interface effects. To form a p-n heterodiode the following doping levels were assumed: Mg acceptors in GaN with a density of and an activation energy of 150 meV and intrinsic donors in ZnO with a density of  $10^{17}$  cm<sup>-3</sup> and an

activation energy of 35 meV, e.g. hydrogen. To account for the strain present in the vicinity of such a heterointerface, which induces piezoelectric charges, the growth of ZnO on GaN is considered here. Therefore, ZnO is assumed to grow pseudomorphically for the first monolayers and then relax its biaxial strain linearly over the following 100 nm. The strain tensor components for the growth in a polar direction can be seen in Figure 5.23(a). Note that in order to keep it simple, strain was not considered for non-polar directions, which is a reasonable assumption as no piezoelectric effect is present.<sup>47</sup>

The calculated 1D band structure, namely the lowest conduction band energy level and the highest valence band (heavy hole), are presented together

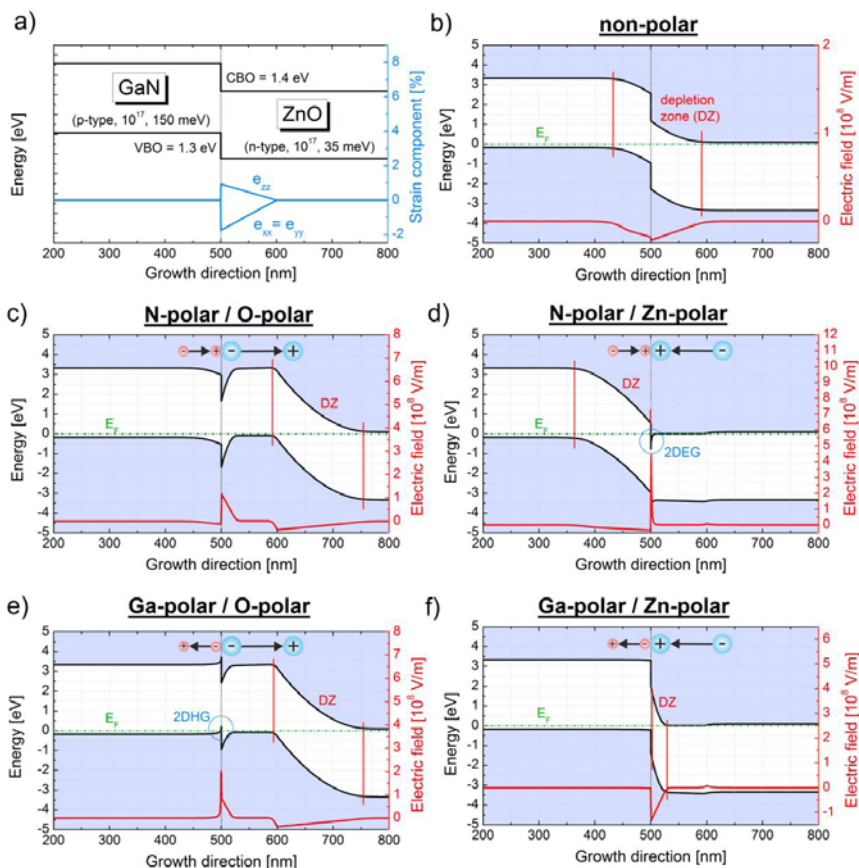


**Figure 5.23** (a) Basic band lineup of a GaN/ZnO heterostructure with the valence band offset (VBO), (b)-(f) simulated 1D band structure and electric field for different polarity configurations of the heterostructure, where interface charges due to spontaneous polarization are additionally illustrated. The Fermi levels and depletion zones (DZ) are indicated by green and red lines, respectively.<sup>47</sup>

with the electric field across the heterointerface in Figure 5.23(b)-(f) for different polarity configurations. First of all, the results obtained for a non-polar p-GaN/n-ZnO heterostructure are depicted in Figure 5.23(b). The interface in this heterostructure is dominated by the type-II alignment of the two materials, where CBO and VBO form energetic barriers for electrons and holes to cross the interface. As these barriers have nearly the same height, the depletion zone (DZ) is formed almost symmetrically on both sides of the heterointerface.

The situation becomes more complicated for polar heterostructures as shown in Figure 5.23(b)-(f). As GaN can be either N-polar or Ga-polar and ZnO either O-polar or Zn-polar, interface charges occur due to both piezoelectricity and spontaneous polarization. The details of the simulations are revealed elsewhere.<sup>47</sup> However, it is already sufficient for showing the high importance of polarity in physical properties of the heterostructures.

As a conclusion, the theoretical analysis and simulation of the p-GaN/n-ZnO heterointerface reveals various possibilities of the band structure, mainly depending on the polarity and strain of the two wurtzite materials. For potential applications it is therefore crucial to choose an optimal polarity configuration according to the particular requirements. The realization is then a matter of growth and certainly challenging, but not impossible. In any case, the realization of p-GaN/n-ZnO heterojunctions with all polarity configurations seems to be possible, thus a detailed understanding of the band alignments as presented above can be helpful to understand the experimental results.

In order to obtain experimental proof of the assumption of strain, we performed geometric phase analysis (GPA) on the p-GaN/n-ZnO heterointerface and the region around which is revealed in Figure 5.24. Only one strain concentration point can be found in the interface (indicated by a yellow oval) and the rest of the interface seems to be defect-free. Therefore, ZnO structure tried to adapt to GaN and compensate the 3.25% mismatch due to the difference between (11-20) plane distances of GaN and ZnO ( $(11-20)_{\text{GaN}} = 2.827 \text{ \AA}$ ,  $(11-20)_{\text{ZnO}} = 2.738 \text{ \AA}$ ). It starts with (11-20) plane distance almost the same as the one of GaN. Soon after, it starts to go back to relaxed (11-20) ZnO gradually along the growth direction. Nonlinear curve fit of the intensity profiles (red dash-lines on the intensity profiles of Figure 5.24) reveal that the GaN is relaxed as the intensity average of the GPA map is almost constant, whereas it starts to grow right from the overlap region till the top of the image. This gradual intensity increase is attributed to gradual relaxation along the growth direction. Note that in the fitting, the defect indicated by the yellow oval is excluded.

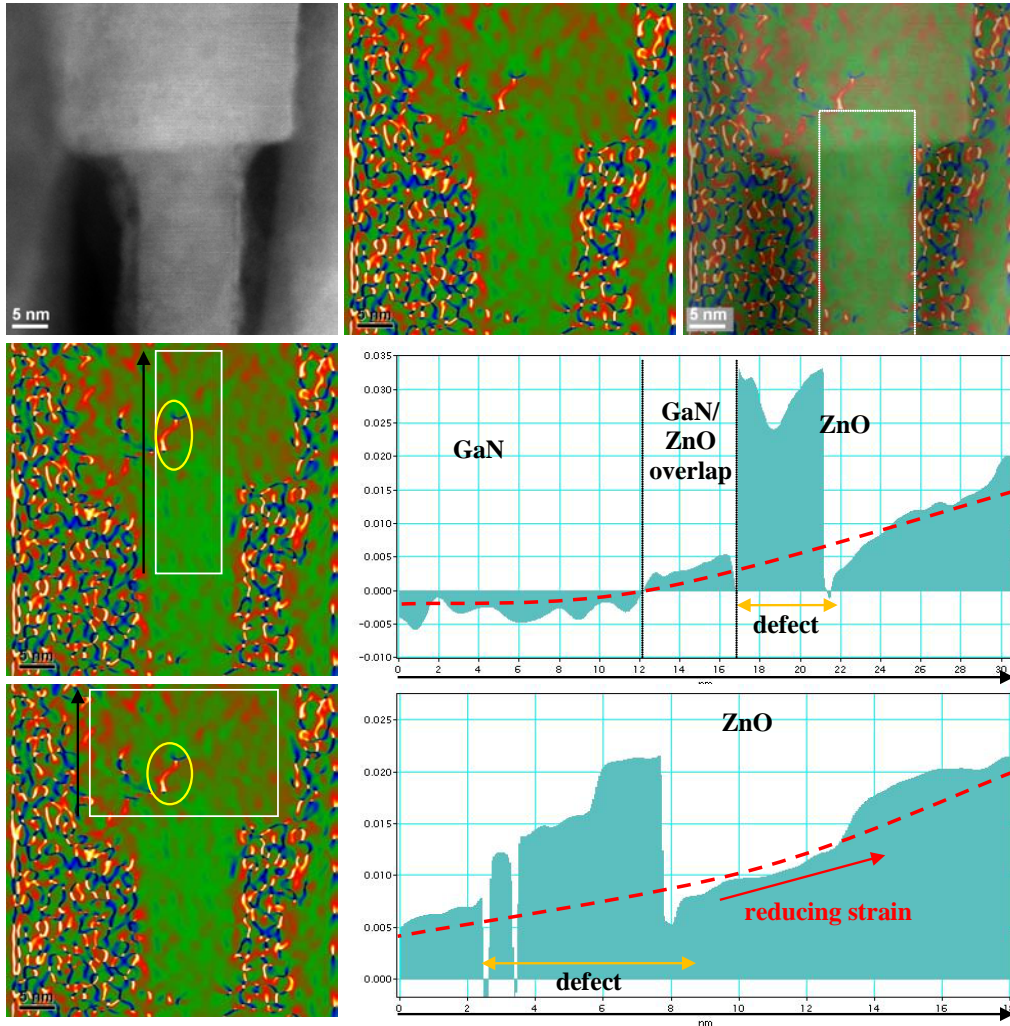


**Figure 5.24** Geometric phase analysis (GPA) on a p-GaN/n-ZnO heterointerface showing the relaxation of ZnO structure along [000-1] direction with intensity profiles

The optical properties of the heterojunction NWs were investigated by ensemble PL in backscattering geometry with an excitation wavelength of 244 nm. The PL spectrum at liquid-helium temperature is presented in Figure 5.25(a) over a wide energy range, where only ZnO-related luminescence is observed due to a complete absorption of the excitation laser in the ZnO caps. The spectrum can be divided in two relevant regions: (i) an intense excitonic near-bandgap emission (NBE, 3.2-3.4 eV) and (ii) defect-related luminescence bands in the energy range of 1.7-2.5 eV, often referred to as red, yellow and green

luminescence bands.<sup>72</sup> As deep states show an intensity over four orders of magnitude lower, a high crystalline quality of the p-GaN/n-ZnO NWs can be confirmed, in accordance with the HAADF and ABF-STEM results presented above.

PL spectra taken in different temperatures ranging from liquid-helium to room temperature are shown in Figure 5.25(b). NBE region is magnified in order to facilitate the visualization of various peaks within. Besides the energy position, the intensity quenching of a PL emission line is characteristic for the responsible recombination process. Intensity dependence to temperature is given by:

$$I(T) = \frac{I_0}{1 + C \cdot \exp\left(-\frac{E_a}{kT}\right)} \quad (5.1)$$

where  $E_a$  is the activation energy of the non-radiative process.<sup>73</sup> Thus, by decreasing the temperature, luminescence and signal-to-noise ratio increase.

The shift of the emission edge in II-VI compounds due to the change of temperature was investigated more than thirty years ago.<sup>74,75</sup> At low temperatures, the most intense emission is located at 3.36 eV which shifts to 3.29 eV at room temperature. This peak can be assigned to neutral donor-bound

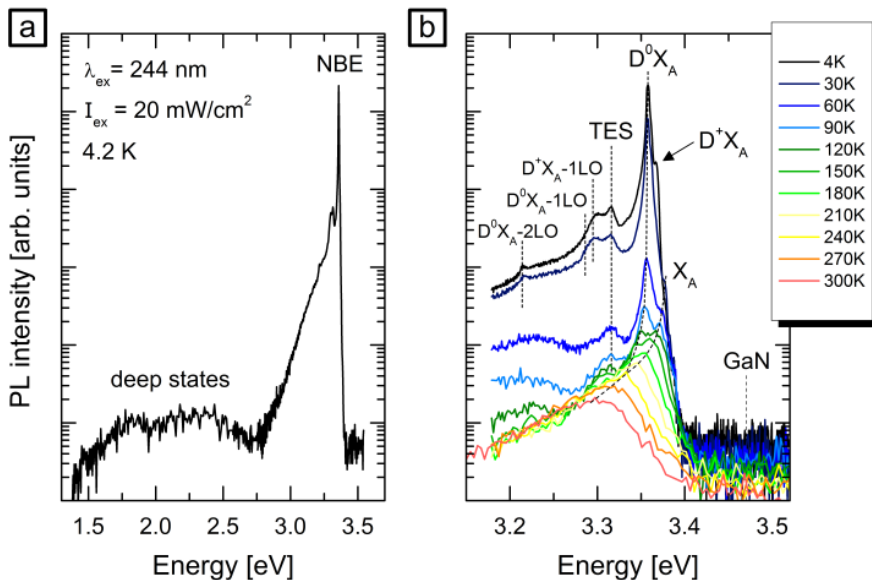


**Figure 5.25** (a) Ensemble PL spectrum at 4.2 K of p-GaN/n-ZnO heterojunction NWs, (b) temperature dependence of the PL emission in the NBE region from 4.2 K to room temperature<sup>47</sup>

exciton recombination ( $D^0X_A$ ). Further detail of the peak assignments and attribution of defects in luminescence can be found elsewhere.<sup>47</sup>

In summary, p-GaN/n-ZnO heterostructure NWs were systematically analyzed in this chapter. The high importance of the polarity determination in such heterostructures was proven by both experimental and theoretical studies. Polarity changes in heterostructures have dramatic influence on electronic band structure of the heterointerfaces and the regions around, which has to be precisely studied in order to understand their behavior in the devices. Such heterostructure NWs have an excellent promise to be used in UV-ranged LEDs or LDs.

## 5.4 Conclusion

In this chapter we proved the importance of epitaxial interfaces in III-V NW-based compounds and how they can be employed for novel applications. III-V NWs, particularly GaN NWs, are wide-band-gap semiconductors which nowadays are widely investigated for optoelectronic devices. They can be doped and heterojunctioned by appropriate materials such as diamond or ZnO and create suitable p-n junctions. GaN is capable of being either p-doped or n-doped, where this characteristic broadens the application possibilities of this material. Additionally, NW morphology has some unique advantages (self-purification, dislocation confinement, strain release, etc) that can bolster the material's functionality.

Epitaxially grown GaN NWs on diamond substrates create a p-n junction at nano scale which is proven to be encouraging for UV-ranged LEDs, quantum computation, and single-spin magnetometry. As the focus in this chapter is on optoelectronic applications, optical properties are measured and justified superior by photoluminescence. Further to optical property study, cathodoluminescence in TEM with higher spatial resolution was conducted and the results were in agreement with the ones of PL.

On the other hand, elaborate structural studies confirmed the high quality of the material. The perfect epitaxial growth and relaxed structure of the GaN NWs were explicitly revealed and further confirmed with theoretical study by means of 3D atomic models. Moreover, GaN NW N-polarity was observed by visualization of GaN dumbbell units in ABF-STEM micrographs. ABF is one of the recently-developed methods that allow local polarity assignment directly from the micrographs with high accuracy and reliance.

In the second part, p-doped GaN NWs were used as the base for deposition of ZnO in order to produce axial GaN/ZnO heterostructure NWs, i.e. another p-n junction at nano scale comprising a p-GaN NW and an n-ZnO cap on top. Interestingly, the polarity of the heterojunction is inversed in the interface, meaning the Zn-polar ZnO cap accommodates on the N-polar GaN NW. As a matter of fact, the polarity influence on electronic band structure was theoretically studied by simulation of the band gap and strain contribution which was corroborated in practice.

## 5.5 References

- 1 S.J. Pearton, F. Ren, A.P. Zhang, K.P. Lee, **'Fabrication and performance of GaN electronic devices'**, *Materials Science and Engineering R* 30, 55-212 (2000)
- 2 M. Stutzmann, O. Ambacher, M. Eickhoff, U. Karrer, A. Lima Pimenta, R. Neuberger, J. Schalwig, R. Dimitrov, P.J. Schuck, R.D. Grober, **'Playing with Polarity'**, *Physica Status Solidi B* 228, 505-512 (2001)
- 3 P.W. Avraam, N.D. M. Hine, P. Tangney, P.D. Haynes, **'Fermi-level pinning can determine polarity in semiconductor nanorods'**, *Physical Review B* 85, 115404 (2012)
- 4 V. Ramachandran, R.M. Feenstra, W.L. Sarney, L. Salamanca-Riba, J.E. Northrup, L.T. Romano, D.W. Greve, **'Inversion of wurtzite GaN(0001) by exposure to magnesium'**, *Applied Physics Letters* 75, 808 (1999)
- 5 Y. Kawaguchi, C.-Y. Huang, Y.-R. Wu, Q. Yan, C.-C. Pan, Y. Zhao, S. Tanaka, K. Fujito, D. Feezell, C.G. Van de Walle, S.P. DenBaars, S. Nakamura, **'Influence of polarity on carrier transport in semipolar (20-2-1) and (20-21) multiple-quantum-well light-emitting diodes'**, *Applied Physics Letters* 100, 231110 (2012)
- 6 M. de la Mata, C. Magen, J. Gazquez, M.I.B. Utama, M. Heiss, S. Lopatin, F. Furtmayr, C.J. Fernandez-Rojas, B. Peng, J.R. Morante, R. Rurali, M. Eickhoff, A. Fontcuberta i Morral, Q. Xiong, J. Arbiol, **'Polarity assignment in ZnTe, GaAs, ZnO and GaN-AlN nanowires from direct dumbbell analysis'**, *Nano Letters* 12, 2579-2586 (2012)
- 7 P. Neumann, R. Kolesov, B. Naydeno, J. Beck, F. Rempp, M. Steiner, V. Jacques, G. Balasubramanian, M.L. Markham, D.J. Twitchen, S. Pezzagna, J. Meijer, J. Twamley, F. Jelezko, J. Wrachtrup, **'Quantum register based on**

---

**coupled electron spins in a room-temperature solid**', *Nature Physics* 6, 249-253 (2010)

8 J.R. Maze, P.L. Stanwix, J.S. Hodges, S. Hong, J.M. Taylor, P. Cappellaro, L. Jiang, M.V.G. Dutt, E. Togan, A.S. Zibrov, A. Yacoby, R.L. Walsworth, M.D. Lukin, '**Nanoscale magnetic sensing with an individual electronic spin in diamond**', *Nature* 455, 644-647 (2008)

9 G. Balasubramanian, P. Neumann, D. Twitchen, M. Markham, R. Kolesov, N. Mizuochi, J. Isoya, J. Achard, J. Beck, J. Tissler, V. Jacques, P.R. Hemmer, F. Jelezko, J. Wrachtrup, '**Ultralong spin coherence time in isotopically engineered diamond**', *Nature Materials* 8, 383 (2009)

10 G. Fasol, '**Room-temperature blue gallium nitride laser diode**', *Science* 272, 1751-1752 (1996)

11 F.A. Ponce, D.P. Bour, '**Nitride-based semiconductors for blue and green light-emitting devices**', *Nature* 386, 351-359 (1997)

12 J.C. Zolper, R.J. Shul, A.G. Baca, R.G. Wilson, S.J. Pearton, R.A. Stall, '**Ion-implanted GaN junction field effect transistor**', *Applied Physics Letters* 68, 2273-2275 (1996)

13 Q. Chen, M. A. Khan, J. W. Wang, C. J. Sun, M. S. Shur, H. Park, '**High transconductance heterostructure field-effect transistors based on AlGaIn/GaN**', *Applied Physics Letters* 69, 794-796 (1996)

14 G.S. Cheng, L.D. Zhang, Y. Zhu, G.T. Fei, L. Li, C.M. Mo, Y.Q. Mao, '**Large-scale synthesis of single crystalline gallium nitride nanowires**', *Applied Physics Letters* 75, 2455-2457 (1999)

15 E. Russo-Averchi, M. Heiss, L. Michelet, P. Krogstrup, J. Nygård, C. Magen, J.R. Morante, E. Uccelli, J. Arbiol, A. Fontcuberta i Morral, '**Suppression of three dimensional twinning for a 100% yield of vertical GaAs nanowires on silicon**', *Nanoscale* 4, 1486-1490 (2012)

16 B. Ketterer, M. Heiss, E. Uccelli, J. Arbiol, A. Fontcuberta i Morral, '**Untangling the electronic band structure of wurtzite GaAs nanowires by resonant Raman spectroscopy**', *ACS Nano* 5, 7585-7592 (2011)

17 Y. Kim, H.J. Joyce, Q. Gao, H.H. Tan, C. Jagadish, M. Paladugu, J. Zou, A.A. Suvorova, '**Influence of nanowire density on the shape and optical properties of ternary InGaAs nanowires**', *Nano Letters* 6, 599-604 (2006)

18 M. Jeppsson, K.A. Dick, J.B. Wagner, P. Caroff, K. Deppert, L. Samuelson, L.-E. Wernersson, '**GaAs/GaSb nanowire heterostructures grown by MOVPE**', *Journal of Crystal Growth* 310, 4115-4121 (2008)

- 
- 19 K.A. Dick, C. Thelander, L. Samuelson, P. Caroff, '**Crystal phase engineering in single InAs nanowires**', *Nano Letters* 10, 3494-3499 (2010)
- 20 P. Caroff, M.E. Messing, B.M. Borg, K.A. Dick, K. Deppert, L.-E. Wernersson, '**InSb heterostructure nanowires: MOVPE growth under extreme lattice mismatch**', *Nanotechnology* 20, 495606 (2009)
- 21 W. Lei, H.H. Tan, C. Jagadish, '**Engineering the composition, morphology, and optical properties of InAsSb nanostructures via graded growth techniques**', *Applied Physics Letters* 102, 033111 (2013)
- 22 J. Johansson, L.S. Karlsson, C.P.T. Svensson, T. Mårtensson, B.A. Wacaser, K. Deppert, L. Samuelson, W. Seifert, '**Structural properties of <111>B-oriented III-V nanowires**', *Nature Materials* 5, 574-580 (2006)
- 23 M.T. Borgström, E. Norberg, P. Wickert, H.A. Nilsson, J. Trägårdh, K.A. Dick, G. Statkute, P. Ramvall, K. Deppert, L. Samuelson, '**Precursor evaluation for in situ InP nanowire doping**', *Nanotechnology* 19, 445602 (2008)
- 24 X. Zhou, J. Chesin, S. Crawford, S. Gradecak, '**Using seed particle composition to control structural and optical properties of GaN nanowires**', *Nanotechnology* 23, 285603 (2012)
- 25 S. Vaddiraju, A. Mohite, A. Chin, M. Meyyappan, G. Sumanasekera, B.W. Alphenaar, M.K. Sunkara, '**Mechanisms of 1D crystal growth in reactive vapor transport: indium nitride nanowires**', *Nano Letters* 5, 1625-1631 (2005)
- 26 L. Rigutti, J. Teubert, G. Jacopin, F. Fortuna, M. Tchernycheva, A. De Luna Bugallo, F.H. Julien, F. Furtmayr, M. Stutzmann, M. Eickhoff, '**Origin of energy dispersion in  $\text{Al}_x\text{Ga}_{1-x}\text{N}/\text{GaN}$  nanowire quantum discs with low Al content**', *Physical Review B* 82, 235308 (2010)
- 27 P. Caroff, J.B. Wagner, K.A. Dick, H.A. Nilsson, M. Jeppsson, K. Deppert, L. Samuelson, L.R. Wallenberg, L.-E. Wernersson, '**High-quality InAs/InSb nanowire heterostructures grown by metal-organic vapor-phase epitaxy**', *Small* 4, 878-882 (2008)
- 28 F. Furtmayr, J. Teubert, P. Becker, S. Conesa-Boj, J.R. Morante, A. Chernikov, S. Schäfer, S. Chatterjee, J. Arbiol, M. Eickhoff, '**Carrier confinement in  $\text{GaN}/\text{Al}_x\text{Ga}_{1-x}\text{N}$  nanowire heterostructures ( $0 < x < 1$ )**', *Physical Review B* 84, 205303 (2011)
- 29 M. Heiss, Y. Fontana, A. Gustafsson, G. Wüst, C. Magen, D.D. O'Regan, J.W. Luo, B. Ketterer, S. Conesa-Boj, A.V. Kuhlmann, J. Houel, E. Russo-Averchi, J.R. Morante, M. Cantoni, N. Marzari, J. Arbiol, A. Zunger, R.

---

J. Warburton, A. Fontcuberta i Morral, '**Self-assembled quantum dots in a nanowire system for quantum photonics**', *Nature Materials* 12, 439-444 (2013)

30 J. Arbiol, C. Magen, P. Becker, G. Jacopin, A. Chernikov, S. Schäfer, F. Furtmayr, M. Tchernycheva, L. Rigutti, J. Teubert, S. Chatterjee, J.R. Morante, M. Eickhoff, '**Self-assembled GaN quantum wires on GaN/AlN nanowire templates**', *Nanoscale* 4, 7517-7524 (2012)

31 A. Urban, J. Malindretos, M. Seibt, A. Rizzi, '**Structure and Elemental Distribution of (Ga,Mn)N Nanowires**', *Nano Letters* 11, 398-401 (2011)

32 W. Guo, M. Zhang, A. Banerjee, P. Bhattacharya, '**Catalyst-free InGaN/GaN nanowire light emitting diodes grown on (001) Si by molecular beam epitaxy**', *Nano Letters* 10, 3355-3359 (2010)

33 V. Zeghbroeck, '**p-n junctions**', *Principles of semiconductor devices*, (online book), Ch. 4 (2011)

34 S. Nakamura, '**Current status of GaN-based solid-state lighting**', *MRS Bulletin* 34, 101-107 (2009)

35 D.F. Feezell, M.C. Schmidt, S.P. DenBaars, S. Nakamura, '**Development of nonpolar and semipolar InGaN/GaN visible light-emitting diodes**', *MRS Bulletin* 34, 318-324 (2009)

36 A. Fontcuberta i Morral, '**Synthesis and fundamental properties of semiconductor nanowires**', *Habilitation*, Walter Schottky Institut - Technische Universität München (2009)

37 M.B. Panish, '**Molecular beam epitaxy**', *Science* 208, 916-922 (1980)

38 D. Spirkoska, C. Colombo, M. Heiss, G. Abstreiter, A. Fontcuberta i Morral, '**The use of molecular beam epitaxy for the synthesis of high purity III-V nanowires**', *Journal of Physics: Condensed Matter* 20, 454225 (2008)

39 A. Fontcuberta i Morral, D. Spirkoska, J. Arbiol, M. Heigoldt, J.R. Morante, G. Abstreiter, '**Prismatic quantum heterostructures synthesized on molecular-beam epitaxy GaAs nanowires**', *Small* 4, 899-903 (2008)

40 E. Calleja, M.A. Sánchez-García, F.J. Sánchez, F. Calle, F.B. Naranjo, E. Muñoz, U. Jahn, K. Ploog, '**Luminescence properties and defects in GaN nanocolumns grown by molecular beam epitaxy**', *Physical Review B* 62, 16826-16834 (2000)

41 M.A. Berding, A. Sher, A.-B. Chen, '**Polarity in semiconductor compounds**', *Physical Review B* 36, 7433-7436 (1987)

- 
- 42 J.-P. Faurie, '**Developments and trends in MBE of II-VI Hg-based compounds**', *Journal of Crystal Growth* 81, 483-488 (1987)
- 43 E. Uccelli, J. Arbiol, C. Magen, P. Krogstrup, E. Russo-Averchi, M. Heiss, G. Mugny, F. Morier-Genoud, J. Nygard, J.R. Morante, A. Fontcuberta i Morral, '**Three-dimensional multiple-order twinning of self-catalyzed GaAs nanowires on Si substrates**', *Nano Letters* 11, 3827-3832 (2011)
- 44 M.I.B. Utama, M. de la Mata, C. Magen, J. Arbiol, Q. Xiong, '**Twinning-, Polytypism-, and Polarity-Induced Morphological Modulation in Nonplanar Nanostructures with van der Waals Epitaxy**', *Advanced Functional Materials* 23, 1636-1646 (2013)
- 45 F. Schuster, F. Furtmayr, R. Zamani, C. Magen, J.R. Morante, J. Arbiol, J.A. Garrido, M. Stutzmann, '**Self-assembled GaN nanowires of diamond**', *Nano Letters* 12, 2199-2204 (2012)
- 46 F. Furtmayr, M. Vielemeyer, M. Stutzmann, J. Arbiol, S. Estradé, F. Peiró, J.R. Morante, M. Eickhoff, '**GaN nanorods on Si (111) surfaces by plasma-assisted molecular beam epitaxy - The influence of Si- and Mg-doping**', *Journal of Applied Physics* 104, 034309 (2008)
- 47 F. Schuster, B. Laumer, R. Zamani, C. Magen, J.R. Morante, J. Arbiol, M. Stutzmann, '**p-GaN/n-ZnO heterojunction nanowires for UV-LEDs and laser diodes**', Submitted (2013)
- 48 M.J. Hÿtch, '**Geometric phase analysis of high resolution electron microscope images**', *Scanning microscopy* 11, 53-66 (1997)
- 49 S. Bernal, F.J. Botana, J.J. Calvino, C. Lopez-Cartes, J.A. Perez-Omil, J.M. Rodriguez-Izquierdo, '**The interpretation of HREM images of supported metal catalysts using image simulation: profile view images**', *Ultramicroscopy* 72, 135-164 (1998)
- 50 M.I.B. Utama, F.J. Belarre, C. Magen, B. Peng, J. Arbiol, Q. Xiong, '**Incommensurate van der Waals Epitaxy of Nanowire Arrays: A Case Study with ZnO on Muscovite Mica Substrates**', *Nano Letters* 12, 2146-2152 (2012)
- 51 J. Arbiol, S. Estrade, J.D. Prades, A. Cirera, F. Furtmayr, C. Stark, A. Laufer, M. Stutzmann, M. Eickhoff, M.H. Gass, A.L. Bleloch, F. Peiro, J.R. Morante, '**Triple-twin domains in Mg doped GaN wurtzite nanowires: structural and electronic properties of this zinc-blende-like stacking**', *Nanotechnology* 20, 145704 (2009)
- 52 H. Hirai, M. Terauchi, M. Tanaka, K. Kondo, '**Estimating band gap of amorphous diamond and nanocrystalline diamond powder by electron**

---

**energy loss spectroscopy**', *Diamond and Related Materials* 8, 1703-1706 (1999)

53 C. R. Miskys, J. A. Garrido, C.E. Nebel, M. Hermann, O. Ambacher, M. Eickhoff, M. Stutzmann, '**AlN/diamond heterojunction diodes**', *Applied Physics Letters* 82, 290-292 (2003)

54 G. Vogt, C.R. Miskys, J.A. Garrido, M. Hermann, M. Eickhoff, M. Stutzmann, '**High quality heteroepitaxial AlN films on diamond**', *Journal of Applied Physics* 96, 895-902 (2004)

55 J.R. Rabeau, P. Reichart, G. Tamanyan, D.N. Jamieson, S. Praver, F. Jelezko, T. Gaebel, I. Popa, M. Domhan, J. Wrachtrup '**Implantation of labelled single nitrogen vacancy centers in diamond using  $^{15}\text{N}$** ', *Applied Physics Letters* 88, 023113 (2006)

56 J. Meijer, B. Burchard, M. Domhan, C. Wittmann, T. Gaebel, I. Popa, F. Jelezko, J. Wrachtrup, '**Generation of single color centers by focused nitrogen implantation**', *Applied Physics Letters* 87, 261909 (2005)

57 A. Gruber, A. Dräbenstedt, C. Tietz, L. Fleury, J. Wrachtrup, C. von Borczyskowski, '**Scanning confocal optical microscopy and magnetic resonance on single defect centers**', *Science* 276, 2012-2014 (1997)

58 F. Jelezko, T. Gaebel, I. Popa, A. Gruber, J. Wrachtrup, '**Observation of coherent oscillations in a single electron spin**', *Physical Review Letters* 92, 076401 (2004)

59 M.V. Hauf, B. Grotz, B. Naydenov, M. Dankerl, S. Pezzagna, J. Meijer, F. Jelezko, J. Wrachtrup, M. Stutzmann, F. Reinhard, J.A. Garrido, '**Chemical control of the charge state of nitrogen-vacancy centers in diamond**', *Physical Review B* 83, 081304(R) (2011)

60 E. Okunishi, I. Ishikawa, H. Sawada, F. Hosokawa, M. Hori, Y. Kondo, '**Visualization of Light Elements at Ultrahigh Resolution by STEM Annular Bright Field Microscopy**', *Microscopy and Microanalysis* 15, 164-165 (2009)

61 R. Ishikawa, E. Okunishi, H. Sawada, Y. Kondo, F. Hosokawa, E. Abe, '**Direct imaging of hydrogen-atom columns in a crystal by annular bright-field electron microscopy**', *Nature Materials* 10, 278-281 (2011)

62 S.D. Findlay, S. Azuma, N. Shibata, E. Okunishi, Y. Ikuhara, '**Direct oxygen imaging within a ceramic interface, with some observations upon the dark contrast at the grain boundary**', *Ultramicroscopy* 111, 285-289 (2011)

---

63 E. Calleja, F.J. Sánchez, D. Basak, M.A. Sánchez-García, E. Muñoz, I. Izpura, F. Calle, J.M.G. Tijero, J.L. Sánchez-Rojas, B. Beaumont, P. Lorenzini, P. Gibart, '**Yellow luminescence and related deep states in undoped GaN**', *Physical Review B* 55, 4689-4694 (1997)

64 L.H. Robins, K.A. Bertness, J.M. Barker, N.A. Sanford, J. B. Schlager, '**Optical and structural study of GaN nanowires grown by catalyst-free molecular beam epitaxy. I. Near-band-edge luminescence and strain effects**', *Journal of Applied Physics* 101, 113505 (2007)

65 F. Furtmayr, M. Vilemeyer, M. Stutzmann, A. Laufer, B.K. Meyer, M. Eickhoff, '**Optical properties of Si- and Mg-doped gallium nitride nanowires grown by plasma-assisted molecular beam epitaxy**', *Journal of Applied Physics* 104, 074309 (2008)

66 G. Salviati, M. Albrecht, C. Zanotti-Fregonara, N. Armani, M. Mayer, Y. Shreter, M. Guzzi, Y.V. Melnik, K. Vassilevski, V.A. Dmitriev, H.P. Strunk, '**Cathodoluminescence and transmission electron microscopy study of the influence of crystal defects on optical transitions in GaN**', *Physica Status Solidi A* 171, 325-339 (1999)

67 T. Günhe, Z. Bougrioua, P. Vennéguès, M. Leroux, M. Albrecht, '**Cathodoluminescence spectroscopy of epitaxial-lateral-overgrown nonpolar (11-20) and semipolar (11-22) GaN in relation to microstructural characterization**', *Journal of Applied Physics* 101, 113101 (2007)

68 C. Wetzel, M. Zhu, J. Senawiratne, T. Detchprohma, P.D. Persans, L. Liu, E.A. Preble, D. Hanser, '**Light-emitting diode development on polar and non-polar GaN substrates**', *Journal of Crystal Growth* 310, 3987-3991 (2008)

69 D.R. Pendse, A.K. Chin, '**Cathodoluminescence and Transmission Cathodoluminescence**', *Encyclopedia of Materials: Science and Technology*, 1-7 (2001)

70 S. Birner, T. Zibold, T. Andlauer, T. Kubis, M. Sabathil, A. Trellakis, P. Vogl, '**nextnano: General purpose 3-D simulations**', *IEEE Transactions on Electron Devices* 54, 2137-2142 (2007)

71 Chris G. Van de Walle, J. Neugebauer, '**Universal alignment of hydrogen levels in semiconductors, insulators and solutions**', *Nature* 423, 626-628 (2003)

72 Ü. Özgür, Ya. I. Alivov, C. Liu, A. Teke, M. A. Reshchikov, S. Doğan, V. Avrutin, S.-J. Cho, H. Morkoç, '**A comprehensive review of ZnO materials and devices**', *Journal of Applied Physics* 98, 041301 (2005)

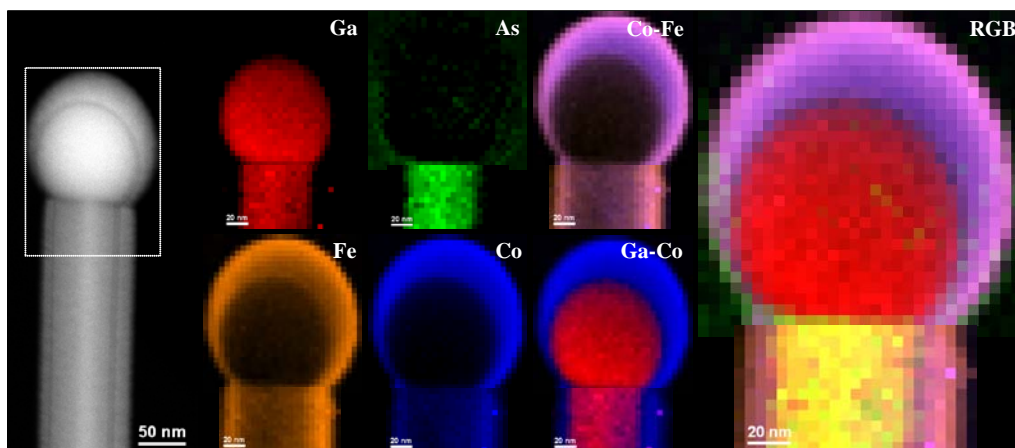
73 D. Bimberg, M. Sondergeld, E. Grobe, '**Thermal dissociation of excitons bounds to neutral acceptors in high-purity GaAs**', *Physical Review B* 4, 3451-3455 (1971)

74 B.G. Yacobi, '**Temperature shift of the emission edge in ZnS and CdS**', *Physical Review B* 22, 1007-1009 (1980)

75 L. Samuel, Y. Brada, A. Burger, M. Roth, '**Temperature shift of the absorption edge in mixed single crystals of  $Zn_xCd_{1-x}Se$** ', *Physical Review B* 36, 1174-1177 (1987)

# CHAPTER VI

## CONCLUSION AND OUTLOOK



CHAPTER VI: CONCLUSION AND OUTLOOK

## 6.1 Let's sum up!

After having three adventurous journeys towards the '*nanoland*' (which was a kind of '*wonderland*'), through the '*rooms at the bottom*', we sum up our achievements in a few pages. There is a lot to talk about, but this part is supposed to be kept short. So we avoid the details.

In the first journey (Chapter 3) we went through the chemical, structural, and morphological details of the complex chalcogenides. Nanoengineering of the compounds, starting with the simple studies and ending with the challenging issues, was carried out by various TEM characterization methodologies. Cu-based ternary and quaternary chalcogenide (CTSe, CZTSe, CZGSe, CHTSe) NCs with ZB-like structures were engineered in a way that the chemical composition changes led to structural defects (twin boundaries) and emergence of WZ or polytypic WZ-ZB structures (CGSe, CHGSe, CCTSe NCs). It was shown that such structural changes have a dramatic influence on physical properties of the compounds, and thus enhance their functionality in the applications such as thermoelectrics. Further, we studied different issues playing around with the crystal structure, chemical composition and morphology through synthetic routes, which may have influence on various properties of the compounds. Polytypism, branching, and 'polytypic branching', cation ordering, and polarity were the different aspects of our structural analyses. We proved how polarity determines the morphology and drives the branching mechanism. On the other hand, the influence of polytypism and cation ordering on the electronic band structure was studied. *Ab-initio* studies showed that the WZ branches, which do not have cation ordering, are metallic.

In the same journey, the coaxial heterostructuring approach was utilized to produce core-shell NPs with two materials which are dissimilar but have close

crystal structures. In this way, epitaxial relationship can be achieved while taking advantage of chemical stability of the core and surface properties of the shell. PbTe@PbS core-shell NPs were used to create PbTe-PbS nanocomposites for thermoelectric devices and they showed dramatic improvement in the thermoelectric figure of merit comparing to bare PbTe and PbS structures.

The latter approach was used in the second journey (Chapter 4), but this time for oxide NWs. In fact two different ways of heterostructuring were chosen in this chapter with the aim of functionality enhancement: core-shell (coaxial), and NP-on-NW. In the case of ZnO NWs, polycrystalline shells of ZnS and TiO<sub>2</sub> improved the photocurrent density and PEC properties as well as the efficiency of DSC devices. The same results were obtained by accommodation of a hongqiite TiO shell on rutile TiO<sub>2</sub> NWs. In this case perfect epitaxial relationship was found between the core and the shell which was in fact the reason that hongqiite TiO phase emerged.

Furthermore, a precise study was conducted on crystal structure of titanium, vanadium, and titanium-vanadium oxides as shells on SnO<sub>2</sub> NWs. Epitaxial relationship between the core and the shell played a paramount role in formation of structures that were seldom reported before. Ti<sub>2</sub>O shell with cubic structure was observed which in bulk is not chemically stable. Also, TiVO<sub>3</sub> mixed oxide with karelianite structure was found which can be justified by mismatch study of TiVO<sub>3</sub>-SnO<sub>2</sub> interface. The latter shell can be a good candidate for sensing applications as it has a quite low mismatch with the core and contains titanium oxide which is known for suitable photocatalytic properties.

Moreover, in this chapter, p-CuO NP/n-SnO<sub>2</sub> NW heterostructures were created in order to have p-n junctions at nanoscale. These nanojunctions exhibited a dramatic enhancement in H<sub>2</sub>S gas sensing response as they take advantage of two sensing mechanisms simultaneously. In the case of the second mechanism which is due to the formation of the heterostructure, breakup of the p-n junction causes the considerable change in electrical resistivity of the NW and thus sensing response.

However, the story did not end here. In the third journey (Chapter 5) another heterostructuring approach, i.e. NW-on-NW or formation of axial heterostructure was followed where the heteroepitaxy in the interface played the key role. In this case, the heterostructures were based on III-V nanostructured materials, particularly on GaN NWs. GaN as a wide-band-gap semiconductor behaves nicely in optoelectronic devices.

Epitaxially grown GaN NWs on diamond substrates create a p-n junction at nano scale which is proven to be encouraging for UV-ranged LEDs, quantum computation, and single-spin magnetometry. As the focus in this chapter was on optoelectronic applications, optical properties are measured and justified superior by photoluminescence. Further to optical property study, cathodoluminescence in TEM with higher spatial resolution was conducted and the results were in agreement with the ones of PL.

On the other hand, elaborate structural studies confirmed the high quality of the material. The perfect epitaxial growth and relaxed structure of the GaN NWs were explicitly revealed and further confirmed with theoretical study by means of 3D atomic models. Moreover, GaN NW N-polarity was observed by visualization of GaN dumbbell units in ABF-STEM micrographs. ABF is one of the recently-developed methods that allow local polarity assignment directly from the micrographs with high accuracy and reliance.

In the second part, p-doped GaN NWs were used as the base for deposition of ZnO in order to produce axial GaN/ZnO heterostructure NWs, i.e. another p-n junction at nano scale comprising a p-GaN NW and an n-ZnO cap on top. Interestingly, the polarity of the heterojunction is inversed in the interface, meaning the Zn-polar ZnO cap accommodates on the N-polar GaN NW. As a matter of fact, the polarity influence on electronic band structure was theoretically studies by simulation of the band gap and strain contribution which was corroborated in practice.

## 6.2 Outlook

One can imagine that the mentioned approaches can open tones of new possibilities for further improvements. Still there is a lot of room for more structure nanoengineering. Many heterostructures with different approaches (axial, coaxial, NP-on-NW, NW-on-NW, quantum structures, etc) and different materials can be designed. Moreover, other physical properties and applications can be examined.

In the case of copper-based chalcogenide NCs, their plasmonic properties can be studied. Such experiment can be carried out by means of low-loss EELS, where the plasmon peaks appear.

Moreover, as the branching mechanism in CCTSe NCs is studied, same experimental situations can be applied in the case of other complex compounds in order to make them branch out. It can take place in the case of the compounds

that their WZ polytypes are thermodynamically and kinetically possible to occur.

Study of polarity and ionicity of the other compounds is also in hand. Such investigation can lead us to a global conclusion on occurrence of cation-/anion-polarity and whether polarity can confine/define the morphology of the NCs.

Furthermore, we should limit the applications of these NCs to thermoelectric devices. Such semiconductors can be used for photovoltaics devices, and in some cases their plasmonic properties are quite promising. The CCTSe polytops can additionally be used as Schottky diodes as their branches are metallic.

In the case of oxide NWs, the core-shell NWs can be used for gas sensing applications. It is expected to obtain better response from the core-shell structures. The challenge would be connecting a single core-shell NW by FIB where before Pt deposition some parts of the shell should be removed in order to have a direct contact with the core materials. On the other hand, multiple overlayers can further improve the response. An intermediate shell can facilitate the accommodation of a secondary shell on the system. Core-double-shell structures are in hand, and by playing around with the type of the shell materials and their thickness one can enhance the functionality of the devices. In this context, environmental TEM (ETEM) experiments are promising, as the behavior of the system and sensing mechanism can be studied online.

Additionally, the NWs can be decorated with many different NPs including QDs, metallic and oxide NPs and expand their range of applications. With adequate QDs, one can improve the charge transfer in the surface of the system and fortify the electrical conductivity when exposed to the target gases and thus the sensing response.

Finally, in the case of III-V NWs, beside GaN, there are other III-nitrides which are used for optoelectronics. For example GaN-AlN heterostructures of quantum structures can be useful for optoelectronic devices as their band structure can be engineered by the arrangements and thicknesses of each compound. Such structures can be precisely characterized by CL in TEM as the structures can be scanned with a reasonable spatial resolution.

There are lots of possibilities. The periodic table is large enough and contains many elements. At the same time, powerful electron microscopes in the hands of researchers, have gradually improved and arrived to this point that provide information from different properties of the materials and allow us to visualize the structures at atomic scale. New methods and technologies are

developed with high accuracy, and now they are more on hand than ever. The ways towards further studies are always open. It's a never-ending story...

CHAPTER VI: CONCLUSION AND OUTLOOK

# **A**PPENDICES

APPENDICES

# APPENDIX A

## ABBREVIATIONS AND SYMBOLS

## APPENDIX A: ABBREVIATIONS AND SYMBOLS

**Abbreviations**

0D	zero-dimensional
1D	one-dimensional
3D	three-dimensional
ABF	annular bright-field
ADF	annular dark-field
AES	Auger electron spectroscopy
BF	bright-field
BFP	back focal plane
CBED	convergent-beam electron diffraction
CBM	conduction band minimum
CBO	conduction band offset
CCD	charge-coupled device
CCTSe	$\text{Cu}_2\text{CdSnSe}_4$
CGSe	$\text{Cu}_2\text{GeSe}_3$
CHGSe	$\text{Cu}_2\text{HgGeSe}_4$
CHTSe	$\text{Cu}_2\text{HgSnSe}_4$
CL	cathodoluminescence
CLEN	clinoenstatite
CTEM	conventional transmission electron microscopy
CTSe	$\text{Cu}_2\text{SnSe}_3$
CVD	chemical vapor deposition
TACVD	thermally activated CVD
PECVD	plasma-enhanced CVD
PACVD	photo-assisted CVD
LACVD	laser-assisted CVD

## APPENDIX A: ABBREVIATIONS AND SYMBOLS

FACVD	flame-assisted CVD
MB-CVD	molecule-based CVD
MOCVD	metal-organic CVD
EVD	electrochemical vapor deposition
CZGSe	$\text{Cu}_2\text{ZnGeSe}_4$
CZTSe	$\text{Cu}_2\text{ZnSnSe}_4$
DAP	donor-acceptor pair
DC	direct-current
DF	dark-field
DOS	density of state
DP	diffraction pattern
DSC	dye synthesized solar cell
DZ	depletion zone
ECU	electrically conducting unit
ED	electron diffraction
EDS	energy-dispersive X-ray spectroscopy
EDX	energy-dispersive X-ray spectroscopy
EEL	electron energy loss
EELS	electron energy loss spectroscopy
EFTEM	energy-filtered transmission electron microscopy
EIS	electrochemical impedance spectroscopy
EIU	electrically insulating unit
EM	electron microscopy
ETEM	environmental transmission electron microscopy
fcc	face-centered cubic
FEG	field-emission gun
FET	field-effect transistor
FFT	fast Fourier transform
FIB	focused ion beam
GIF	Gatan image filter
GIS	gas-injection system
GPA	geometric phase analysis
HAADF	high-angle annular dark-field
HCI	hollow-cone illumination
hcp	hexagonal close-packed
HPHT	high-pressure/high-temperature

## APPENDIX A: ABBREVIATIONS AND SYMBOLS

HR-STEM	high-resolution scanning transmission electron microscopy
HRTEM	high-resolution transmission electron microscopy
IFFT	inversed fast Fourier transform
ICPE	incident photon to current conversion efficiency
IR	infrared
KS	kesterite
LD	laser diode
LED	light emitting diode
MAADF	medium-angle annular dark-field
MBE	molecular beam epitaxy
PAMBE	plasma-assisted MBE
MOX	metal oxide
MSA	multivariate statistical analysis
NBE	near-band-gap emission
NC	nanocrystal
NP	nanoparticle
NR	nanorod
NW	nanowire
OREN	orthoestatite
PCA	principal component analysis
PEC	photoelectrochemical
PF	power factor
PL	photoluminescence
PLD	pulsed laser deposition
QD	quantum dot
RH	relative humidity
SAED	selected-area electron diffraction
SBE	sub-band-gap emission
SE	secondary electron
SEM	scanning electron microscope
SK	Stranski-Krastanov
SLS	solution-liquid-solid
SPM	scanning probe microscope
ST	stannite
STEM	scanning transmission electron microscopy
TE	thermoelectrics

## APPENDIX A: ABBREVIATIONS AND SYMBOLS

TEM	transmission electron microscope
TVO	TiVO <sub>3</sub>
UHV	ultrahigh vacuum
UV	ultraviolet
VBM	valence band maximum
VBO	valence band offset
VLM	visible-light microscope
VLS	vapor-liquid-solid
VS	vapor-solid
WZ	wurtzite
XRD	X-ray diffraction
ZB	zinc-blende
ZT	thermoelectric figure of merit

### Notations

(x y z)	crystallographic plane
[x y z]	crystallographic direction
{x y z}	crystallographic plane family
xxx@yyy	core-shell structure, 'xxx' as core and 'yyy' as shell

### Symbols

$\alpha$	Seebeck coefficient
$\delta$	resolution
$\Delta f_{Sch}$	Scherzer defocus
$\kappa$	thermal conductivity
$\lambda$	wavelength
$\Pi$	Peltier coefficient
$\sigma$	electrical conductivity
$C_c$	chromatic aberration
$C_s$	spherical aberration
$(D/A)^{(0/+/-)}$	neutral/ionized impurity (donor/acceptor)
$e^-$	electron
$E_c$	conduction band energy
$E_f$	Fermi level

## APPENDIX A: ABBREVIATIONS AND SYMBOLS

$E_g$	band gap energy
$E_v$	valence band energy
$g_{hkl}$	reciprocal lattice vector
$h^+$	hole
$J_{sc}$	short-circuit current
$S$	Seebeck coefficient
$V_{oc}$	open-circuit voltage
$X$	free-exciton recombination
$Z$	atomic number
$ZT$	thermoelectric figure of merit

## APPENDIX A: ABBREVIATIONS AND SYMBOLS

# **A**PPENDIX **B**

ABSTRACT IN ENGLISH

APPENDIX B: ABSTRACT IN ENGLISH

In this report novel materials for advanced applications are studied by means of the latest microscopy technologies and methodologies which have had a dramatic impact on progress in materials science. The aim was to study phenomena such as polytypism, unusual morphologies, polytypic branching, band gap engineering, cation ordering, polarity, epitaxial growth and interface, accommodation of a secondary structure on a base, etc, in order to find adequate explanations for the influence of the phenomena on the properties and applications such as thermoelectricity, p-n junction functionality, photovoltaic efficiency, optoelectronic properties, and sensing response. Various semiconducting materials, i.e. complex chalcogenides, metal oxides, and III-V nanostructures were characterized for this purpose. Here, nanoengineered structures of functional materials at nanoscale are studied by means of advanced electron microscopy methods ranging from imaging and diffraction to spectroscopy techniques.

Chapter 1 gives a brief introduction to the report; the main purpose of the work, state-of-the-art, challenges and possibilities. In chapter 2 the methodology is described. Chapter 3, 4, and 5 are the results, and chapter 6 is the general conclusions and the outlook. Note that each chapter of results (chapters 3 to 5) has its own introduction and conclusion. Therefore, chapter 1 consists of just a short introduction to the general idea of the study, its importance and the state-of-the-art, and a preface of the thesis.

In chapter 2, after a brief history and the basic concepts of EM (i.e. electron-matter interaction, diffraction, resolution, aberration and aberration correction), the TEM methodology is described; the advanced TEM techniques used to study the nanostructured semiconductors at atomic scale. In general, it consists of brief descriptions of basic principles of TEM, techniques, and the cons and pros to them. Note that in order to keep the report short, details are

avoided, hence excellent references are provided for further details. Each section starts with conventional use of the method(s) and ends with the state-of-the-art which is applied for novel materials science studies. As experimental results are corroborated by theoretical studies and simulations, these procedures (image processing, simulations, etc) are also described shortly. Here is a list of the described techniques:

- Diffraction methods: SAED,
- Imaging methods: BF-TEM, DF-TEM, HRTEM, ADF/HAADF-STEM, BF-STEM, ABF-STEM,
- Spectroscopy methods: EELS, EDX, CL,
- Quantitative analysis, image processing and simulation: GPA, MSA, Rhodius/Eje-Z, JEMS,
- Specimen preparation methods.

Chapter 3 is dedicated to nanoengineering crystal structure and morphology of nanocrystals of complex copper-based chalcogenide. Several materials are studied from binaries to complex ternary and quaternary compounds. In this chapter it is shown that there is a wide range of possibilities for engineering, as many elements can be substituted with the primary cations and anions, and each element has unique influence on the properties of the compound. Mostly these compounds are based on copper-selenide with additional cations substituting copper which are excellent candidates for thermoelectric devices. Advanced TEM studies are performed in order to figure out the physics behind the property modifications. Phenomena such as morphology change, polytypism, ordering, polarity, electronic band change, strain, etc are elaborately studied, and correlated to the physical properties such as thermoelectricity.

The results section in this chapter starts with single-phased compounds: CTSe, CZTSe, CZGSe, and CHTSe NCs. Then we continue with multi-phased (polytypic) structures, CGSe, CHGSe, CCTSe NCs, and CCTSe polypods. And finally, we move on to the core-shell heterostructured NPs: FePt@PbTe, BiTe@PbTe, and PbTe@PbS core-shell NPs. In most of the cases thermoelectric properties of the compounds were measured and the improvement was observed.

CCTSe polypods are the case of a complete structure study to understand the branching mechanism. Therefore, by means of an aberration-corrected TEM (with three  $C_c$  and  $C_s$  correctors) the polarity and cation ordering was

determined. Polarity-driven morphology and branching mechanism is explained. Moreover, electronic band structure in this polytypic structure is simulated.

Chapter 4 is based on the study of nanojunctions in metal oxide heterostructured NWs, structures that can enhance the functionality of the targeted devices, such as photovoltaic cells, or gas sensors. Metal oxide semiconductors showed their promise since a few decades ago, and still a considerable amount of research is dedicated to them in order to optimize their properties. Production of nanojunctions is one of the most successful approaches in this context. In chapter 4 it is shown how coaxial heterostructuring of NWs, i.e. formation of core-shell structures and other types increase the efficiency of the solar cells or enhance the sensitivity and selectivity of the gas sensors. Here is a list of the materials that we studied in this chapter:

- Bare ZnO NWs doped with Cl, and ZnO:Cl@ZnS and ZnO:Cl@TiO<sub>2</sub> core-shell NWs,
- Bare TiO<sub>2</sub> NRs and NWs, and TiO<sub>2</sub>(rutile)@TiO(hongquiiite) core-shell NWs
- Bare SnO<sub>2</sub> NWs, SnO<sub>2</sub>@Ti<sub>2</sub>O, SnO<sub>2</sub>@V<sub>2</sub>O<sub>3</sub>, and SnO<sub>2</sub>@TiVO<sub>3</sub> core-shell NWs
- SnO<sub>2</sub> NWs decorated with CuO NPs

In chapter 5 almost the same approach was followed, nevertheless, this time with III-V NWs. Also there the importance of axial heterostructures and fully-epitaxial and relaxed structure are emphasized. The optoelectronic properties of the GaN NWs, such promising p-n junctions, are examined. Polarity issue, as a remarkably influencing parameter, is precisely studied in practice and also its effect on electronic band structure in the heterointerface is proven by the theoretical simulations.

Two heterostructures are studied in this chapter: GaN NWs on diamond substrate, and ZnO caps on GaN NWs. Both systems can act like p-n junctions as they consist of a p-type and an n-type semiconductor with epitaxial interfaces. In the case of GaN NWs on diamond, besides the characteristics of GaN which make it a suitable candidate for optoelectronic devices in UV range, diamond can also be used for applications like quantum computation and spin magnetometry. In this chapter, nonetheless, we only focused on optoelectronic properties and examined them by means of PL and CL analyses.

The interesting issue in the case of GaN/ZnO axial heterostructures was the inversion of polarity. ZnO caps were Zn-polar although they were

accommodated on N-polar GaN NWs. Therefore, the band structures of different possibilities of the interface, i.e. Zn-polar/N-polar, Zn-polar/Ga-polar, O-polar/N-polar, O-polar/Ga-polar interfaces of ZnO/GaN heterostructures were simulated. GPA is also performed in both cases in order to observe the strain at the interfaces.

In the end, a general conclusion of the whole work and room for further study and future work is discussed in chapter 6. The ample freedom of structural nanoengineering in the materials, together with development of novel electron microscopy techniques, opens the way towards the new possibilities for the future work. On the other side, we mention some works in hand which have not arrived to the final results yet. They are in the way of nanoengineering as they seem quite feasible and encouraging for novel applications.

# APPENDIX C

## RESUMEN EN ESPAÑOL

APPENDIX C: RESUMEN EN ESPAÑOL

En este trabajo hemos estudiado materiales avanzados con las últimas tecnologías y metodologías de microscopía electrónica, las que tienen un impacto importante en el desarrollo de la ciencia de materiales. El objetivo principal ha sido estudiar fenómenos como el politipismo, morfologías inusuales, ramificación, ‘ramificación politípica’, manipulación de la estructura de banda, ordenación de los cationes, polaridad, crecimiento e interfase epitaxial, alojamiento de una fase secundaria en una base, etc. para razonar la influencia de aquellos fenómenos en las propiedades y aplicaciones, por ejemplo la termoelectricidad, el funcionamiento de unión p-n, la eficiencia de las celdas solares, las propiedades optoelectrónicas, la respuesta de los sensores, etc. Distintos semiconductores han sido caracterizados: nanopartículas de calcogenuros complejos, nanohilos de óxidos de metales, y nanohilos del grupo III-V.

En este informe hemos estudiado los materiales funcionales en escala nanométrica por medio de métodos avanzados de microscopía electrónica incluyendo métodos de difracción, captura de imágenes (*imaging*) y espectroscopía.

El capítulo 1 es una breve introducción a la tesis, en la que se exponen los objetivos principales del trabajo, los últimos avances (*state-of-the-art*), los retos, y las nuevas posibilidades. El capítulo 2 consiste en la descripción de la metodología. Los capítulos 3, 4, y 5 se componen de los resultados, y el capítulo 6 incluye las conclusiones y la perspectiva del trabajo futuro. Se debe tener en cuenta que los capítulos de resultados (capítulos 3 a 5) contienen una introducción y conclusión completa. Por lo tanto, la introducción a la tesis (capítulo 1) y su conclusión (capítulo 6) no son muy extensas. El capítulo 1 expone la idea general de este trabajo, su importancia, la última generación, y un prefacio de la tesis.

El capítulo 2 se inicia con los conceptos básicos de microscopía electrónica, concretamente la interacción de los electrones con la materia, difracción, resolución, aberración y corrección de aberración. Después de esto, se explica la metodología de microscopía electrónica de transmisión (MET o TEM), y los métodos avanzados utilizados para estudiar los semiconductores en la escala atómica, sus ventajas y desventajas. En general las descripciones son breves. No obstante, hemos provisto excelentes referencias en las que se puede encontrar información complementaria. En este capítulo, cada sección empieza con métodos convencionales y termina con la última generación apropiada para estudiar los materiales avanzados. Los resultados experimentales están corroborados con estudios teóricos y simulaciones. Por lo tanto, también explicamos estos procedimientos.

A continuación se listan los métodos explicados en el capítulo 2:

- Los métodos de difracción: SAED
- Los métodos de captura de imagen: BF-TEM, DF-TEM, HRTEM, ADF/HAADF-STEM, BF-STEM, ABF-STEM
- Los métodos de espectroscopia: EELS, EDX, CL
- Análisis cuantitativo, procesar los imágenes y simulación: GPA, MSA, Rhodius/Eje-Z, JEMS
- Métodos de preparación de muestras

Estos son los métodos que se han utilizado para obtener los resultados de los capítulos 3, 4, y 5.

El capítulo 3 está basado en el análisis de la estructura y morfología de las nanopartículas de calcogenuros complejos. Se estudian varios compuestos binarios, ternarios y cuaternarios. Se demuestra que hay un rango amplio de posibilidades para modular la estructura química de las nanopartículas porque hay muchos elementos en la tabla periódica que se substituyen en los sitios de los aniones y cationes. Y cada elemento tiene una única influencia en las propiedades físicas de los compuestos. La mayoría de estos compuestos están basados en el selenio de cobre, agregando más cationes que substituyen el cobre y forman compuestos ternarios y cuaternarios. De hecho, empleamos la microscopía avanzada para analizar y comprender la física detrás de estos cambios en las propiedades. Fenómenos como cambio de morfología, politipismo, ordenación de los cationes, polaridad, cambio de la posición de las bandas electrónicas, estrés, y las propiedades físicas correlacionadas como termoelectricidad.

La sección de resultados en este capítulo contiene tres partes. En la primera, los compuestos monoestructurados están analizados: nanopartículas de CTSe, CZTSe, CZGSe, y CHTSe. En la segunda parte se estudian los compuestos multiestructurados, politípicos con defectos cristalográficos: CGSe, CHGSe, CCTSe. Y finalmente se da un paso adelante y se estudian nanopartículas heteroestructuradas de tipo *core-shell*: FePt@PbTe, BiTe@PbTe, y PbTe@PbS *core-shell* nanopartículas. En la mayoría de los casos en las tres partes, la propiedad termoeléctrica de los compuestos se examina y la mejora de la figura de mérito (ZT) queda demostrada.

En caso de nanopartículas cuaternarias de CCTSe, las nanopartículas ramifican y forman polipodos (dependiendo del número de las ramas forman monopodos, bipodos, trípodos y tetrapodos), que es el caso de un estudio elaborado porque el mecanismo de la ramificación es interesante. Por lo tanto, se estudia el material por medio de un microscopio con tres correctores de aberraciones y se justifica la morfología de pentatetrahedral y el mecanismo de ramificación con el concepto de polaridad. Además se llevan a cabo las simulaciones de la estructura de las bandas electrónicas en las dos situaciones en las que los cationes son ordenados o desordenados.

En capítulo 4 se trabaja con los nanohilos de óxidos de metales que sirven para muchas aplicaciones como celdas solares o sensores de gas. Los semiconductores de óxidos de metal son definitivamente prometedores y han sido utilizados ampliamente durante estas últimas décadas. En nuestro caso, con el objetivo de mejorar la funcionalidad de los aparatos, hemos estudiado heteroestructuras tipo *core-shell*, y nanohilos decorados con nanopartículas. En este capítulo se enseña que con esta aproximación se pueden crear heteroestructuras de óxidos distintos para optimizar el funcionamiento del aparato, por ejemplo la eficiencia de las celdas solares, la sensibilidad y selectividad de los sensores de gas, etc. A continuación se listan los materiales que han sido estudiados en este capítulo:

- Nanohilos simples de ZnO dopados con Cl, y nanohilos de ZnO:Cl cubiertos con ZnS o TiO<sub>2</sub>: ZnO:Cl@ZnS y ZnO:Cl@TiO<sub>2</sub> *core-shell*
- Nanohilos simples de TiO<sub>2</sub> NWs, y nanohilos de TiO<sub>2</sub> rutilo cubiertos con TiO hongquite: TiO<sub>2</sub>(rutilo)@TiO(hongquite) *core-shell*
- Nanohilos simples de SnO<sub>2</sub> rutilo, y nanohilos de SnO<sub>2</sub> cubiertos con una capa de Ti<sub>2</sub>O, V<sub>2</sub>O<sub>3</sub>, o TiVO<sub>3</sub>: SnO<sub>2</sub>@Ti<sub>2</sub>O, SnO<sub>2</sub>@V<sub>2</sub>O<sub>3</sub>, y SnO<sub>2</sub>@TiVO<sub>3</sub> *core-shell*
- Nanohilos de SnO<sub>2</sub> decorados con nanopartículas de CuO

En el capítulo 5 prácticamente la misma aproximación está escogida, pero esta vez con nanohilos del grupo III-V. Aquí hemos enfatizado la importancia del crecimiento epitaxial de heteroestructuras, porque este asunto tiene un impacto muy fuerte en las propiedades. Este tipo de heteroestructuras se usan para crear uniones p-n, y como los nanohilos de GaN son muy prometedores en los sistemas optoelectrónicos, se han hecho las medidas ópticas. El asunto de polaridad en este caso tiene una influencia notable. Por lo tanto, el material está precisamente analizado ambos experimentalmente y teóricamente. Hemos estudiado el efecto de la polaridad, como un parámetro impactante en las interfases, en la estructura de las bandas electrónicas con simulaciones de *ab-initio*.

Dos heteroestructuras están estudiadas en este capítulo: nanohilos de GaN crecidos en sustrato de diamante, y nanohilos de GaN con capuchas. En el primer caso, por un lado GaN funciona de forma excelente en los sistemas optoelectrónicos en rango de ultravioleta, y por otro lado, en esta unión p-n, el diamante puede ser utilizado para otras aplicaciones como computación cuántica y magnetometría de espín. En este capítulo sólo nos enfocamos en las propiedades optoelectrónicas y las examinamos en medio de análisis de fotoluminiscencia y catodoluminiscencia.

El aspecto más interesante en el caso de la heteroestructura de GaN/ZnO ha sido la inversión de la polaridad. Es decir, las capuchas de ZnO con polaridad Zn crecen sobre nanohilos de GaN con polaridad N. Por lo tanto, para ver la influencia de la polaridad, hemos simulado la estructura de las bandas electrónicas en la interfase en cuatro casos distintos: Zn-polar/N-polar, Zn-polar/Ga-polar, O-polar/N-polar, O-polar/Ga-polar en la interfase de heteroestructura de ZnO/GaN. Además, hemos desempeñado el análisis geométrico de fase (GPA) para verificar si hay estrés en la interfase o si las estructuras están relajadas.

Por último, en el capítulo 6 hemos hablado de las conclusiones generales y las perspectivas para la investigación futura. La amplia libertad de manejar la estructura química y cristalográfica, acompañada del desarrollo de los métodos nuevos y avanzados de la microscopía electrónica, nos abre las puertas hacia nuevas posibilidades de mejorar el funcionamiento de los sistemas avanzados. Por otro lado, también hablamos de unos trabajos que aún no han llegado a los resultados finales. De todas formas, aún hay muchas oportunidades que parecen totalmente factibles para desarrollar nuevas aplicaciones y aumentar la eficiencia de los sistemas.

# APPENDIX D

## RESUM EN CATALÀ

## APPENDIX D: RESUM EN CATALÀ

En aquest treball hem estudiat els materials avançats amb les últimes tecnologies i metodologies de microscòpia electrònica, les que tenen un impacte important en el desenvolupament de la ciència de materials. L'objectiu principal ha estat estudiar fenòmens com el politipisme, les morfologies inusuals, la ramificació, 'ramificació politípica', modulació de les bandes electròniques, l'ordenació dels cations, la polaritat, el creixement i la interfície epitaxial, allotjament d'una fase secundària en un base, etc. per raonar la influència d'aquests fenòmens en les propietats i aplicacions, per exemple en la termoelectricitat, el funcionament de les unions p-n, l'eficiència de les cel·les solars, les propietats optoelectròniques, la resposta dels sensors, etc. Diferents semiconductors han estat caracteritzats: nanopartícules de calcògens complexos, nanofils d'òxids metàl·lics, i nanofils semiconductors dels grups III-V.

En aquest informe hem estudiat els materials funcionals a escala nanomètrica per mitjà de mètodes avançats de microscòpia electrònica incloent mètodes de difracció, presa d'imatges (*imaging*) i espectroscòpia.

El capítol 1 és una breu introducció de la tesi, on s'exposen els objectius principals del treball, les últimes novetats (*state-of-the-art*), els reptes i les noves possibilitats. El capítol 2 consisteix en la descripció de la metodologia. En els capítols 3,4 i 5 es troben els resultats i en el capítol 6 s'inclouen les conclusions i la perspectiva del treball futur. S'haurà de tenir en compte que els capítols de resultats (capítols 3 al 5) contenen una introducció i una conclusió complerta. Per tant, la introducció a la tesi (capítol 1) i la seva conclusió (capítol 6) no son excessivament extenses.

Al capítol 1 s'exposa la idea general d'aquest treball, la seva importància, l'última generació i un prefaci de la tesi.

El capítol 2 s'inicia amb els conceptes bàsics de la microscòpia electrònica, concretament amb la interacció dels electrons amb la matèria, la difracció,

resolució, aberració i correcció de l'aberració. Després d'això, s'explica la metodologia de la microscòpia electrònica de transmissió (MET o TEM) i els mètodes avançats utilitzats per estudiar els semiconductors a escala atòmica, els seus avantatges i desavantatges. En general les descripcions són breus. No obstant això, hem proveït el capítol d'excel·lents referències en les quals es pot trobar informació complementària. En aquest capítol, cada secció comença amb els mètodes convencionals i acaba amb l'última generació apropiada per estudiar els materials avançats. Els resultats experimentals estan corroborats amb estudis teòrics i simulacions. Per tant, també expliquem aquests procediments.

A continuació es llisten els mètodes explicats al capítol 2:

- Els mètodes de difracció: SAED
- Els mètodes de prendre imatges: BF-TEM, DF-TEM, HRTEM, ADF/HAADF-STEM, BF-STEM, ABF-STEM
- Els mètodes d'espectroscòpia: EELS, EDX, CL
- Anàlisi quantitatiu, processar les imatges i simulació: GPA, MSA, Rhodius/Eje-Z, JEMS
- Mètodes de preparació de mostres

Aquests són els mètodes que s'han utilitzat per obtenir els resultats dels capítols 3,4 i 5.

El capítol 3 està basat en l'anàlisi de l'estructura i la morfologia de les nanopartícules de calcògens complexes. S'estudien diferents compostos de binaris a ternaris i quaternaris. Es demostra que hi ha un ampli rang de possibilitats per modular l'estructura química de les nanopartícules perquè hi han molts elements a la taula periòdica que es substitueixen en llocs les posicions dels anions i cations. I cada element té una única influència en les propietats físiques dels compostos. La majoria d'aquests compostos es basen en el seleniur de coure, agregant més cations que substitueixen el coure i formen ternaris i quaternaris. De fet, realitzem l'anàlisi avançat de TEM per comprendre la física darrere d'aquests canvis en les propietats. Fenòmens com el canvi de morfologia, el politipisme, l'ordenació dels cations, la polaritat, el canvi de posició de les bandes electròniques, l'estrés i les propietats físiques correlacionades amb la termoelectricitat.

La secció de resultats en aquest capítol conté tres parts. A la primera, els compostos monoestructurats estan analitzats: nanopartícules de CTSe, CZTSe, CZGSe i CHTSe. A la segona part s'estudien els compostos multiestructurats, politips amb defectes cristal·logràfics: CGSe, CHGSe, CCTSe. I finalment es dona un pas endavant i s'estudien nanopartícules heteroestructurades de tipus

nucli-capa (*core-shell*): nanopartícules *nucli-capa* de FePt@PbTe, BiTe@PbTe, i PbTe@PbS . En la majoria dels casos, a les tres parts, la propietat termoelèctrica dels compostos s'examina i la millora de la figura de mèrit (ZT) queda demostrada.

En el cas de nanopartícules quaternàries de CCTSe, les nanopartícules ramifiquen i formen polípodes (depenent del número de rames formen monòpodes, bípedes, trípedes i tetràpedes), que és el cas d'un estudi elaborat pel gran interès del mecanisme de la ramificació. Per tant, s'estudia el material per mitjà d'un microscopi amb tres correctors d'aberracions i es justifica la morfologia de pentatetraedre i el mecanisme de ramificació amb el concepte de polaritat. A més es duen a terme les simulacions de l'estructura de les bandes electròniques en les dues situacions en les que els cations son ordenats o desordenats.

Al capítol 4 es treballa amb nanofils d'òxids de metàl·lics que serveixen per moltes aplicacions com les cel·les solars o els sensors de gas. Els semiconductors d'òxids de metàl·lics són definitivament prometedors i han estat utilitzats àmpliament durant les últimes dècades. En el nostre cas, amb l'objectiu de millorar la funcionalitat dels dispositius, hem estudiat heteroestructures del tipus *nucli-capa*, i nanofils decorats amb nanopartícules. En aquest capítol s'ensenya que amb aquesta aproximació es poden crear heteroestructures d'òxids diferents per optimitzar el funcionament del dispositiu, per exemple l'eficiència de les celdes solars, la sensibilitat i selectivitat dels sensors de gas, etc.

A continuació es llisten els materials que han sigut estudiats en aquest capítol:

- Nanofils simples de ZnO dopats amb Cl, i nanofils de ZnO:Cl coberts amb ZnS o TiO<sub>2</sub>: ZnO:Cl@ZnS i ZnO:Cl@TiO<sub>2</sub> *core-shell*
- Nanofils simples de TiO<sub>2</sub>, i nanofils de TiO<sub>2</sub> rutil coberts amb TiO hongquiite: TiO<sub>2</sub>(rutile)@TiO(hongquiite) *core-shell*
- Nanofils simples de SnO<sub>2</sub> rutil, i nanofils de SnO<sub>2</sub> coberts amb una capa de Ti<sub>2</sub>O, V<sub>2</sub>O<sub>3</sub>, o TiVO<sub>3</sub>: SnO<sub>2</sub>@Ti<sub>2</sub>O, SnO<sub>2</sub>@V<sub>2</sub>O<sub>3</sub>, i SnO<sub>2</sub>@TiVO<sub>3</sub> *core-shell*
- Nanofils de SnO<sub>2</sub> decorats amb nanopartícules de CuO

En el capítol 5 s'escull pràcticament la mateix aproximació, però aquesta vegada amb nanofils del grup III-V. Aquí hem emfatitzat la importància del creixement epitaxial d'heteroestructures, perquè aquest assumpte té un impacte molt fort en les propietats. Aquest tipus d'heteroestructures s'usen per crear unions p-n, i com els nanofils de GaN són molt prometedors en els sistemes

optoelectrònics, s'han fet les mides òptiques. L'assumpte de polaritat en aquest cas té una influència notable. Per tant, el material està precisament analitzat experimental i teòricament. Hem estudiat l'efecte de la polaritat, com un paràmetre impactant en les unions, en l'estructura de les bandes electròniques amb simulacions *ab-initio*.

Dues heteroestructures s'estudien en aquest capítol: nanofils de GaN crescuts sobre un substrat de diamant, i nanofils de GaN amb caputxons de ZnO. En el primer cas, per una banda, el GaN funciona de forma excel·lent en els sistemes optoelectrònics en el rang ultraviolat, i per l'altra banda, en aquesta unió p-n, el diamant pot ser utilitzat per altres aplicacions com en la computació quàntica i la magnetometria d'espí. En aquest capítol només ens enfoquem en les propietats optoelectròniques i les examinem en mig de l'anàlisi de la fotoluminescència i la catodoluminescència.

L'aspecte més interessant en el cas de l'heteroestructura de GaN/ZnO ha estat la inversió de la polaritat. És a dir, els caputxons de ZnO amb polaritat Zn creixen sobre nanofils de GaN amb polaritat N. Per tant, per veure la influència de la polaritat, hem simulat l'estructura de les bandes electròniques a l'unió en quatre casos diferents: Zn-polar/N-polar, Zn-polar/Ga-polar, O-polar/N-polar, O-polar/Ga-polar a la unió de l'heteroestructura de ZnO/GaN. A més, hem realitzat l'anàlisi geomètric de fase (GPA) per verificar si hi ha estrès a la unió o si les estructures estan relaxades.

Per últim, al capítol 6 parlem de les conclusions generals i les perspectives per a la investigació futura. L'àmplia llibertat de modular i/o manipular l'estructura química i cristal·logràfica, acompanyada del desenvolupament de nous mètodes avançats de la microscòpia electrònica, ens obre les portes cap a noves possibilitats de millorar el funcionament dels sistemes avançats. Per altra banda, també parlem d'uns treballs que encara no han arribat als resultats finals. De totes maneres, encara hi han moltes oportunitats que semblen totalment factibles per desenvolupar noves aplicacions i augmentar l'eficiència dels sistemes.

# **A**PPENDIX **E**

## PUBLICATIONS

## APPENDIX E: PUBLOCATIONS

## Composition Control and Thermoelectric Properties of Quaternary Chalcogenide Nanocrystals: The Case of Stannite $\text{Cu}_2\text{CdSnSe}_4$

Maria Ibáñez,<sup>†</sup> Doris Cadavid,<sup>‡</sup> Reza Zamani,<sup>‡,§</sup> Nuria García-Castelló,<sup>†</sup> Victor Izquierdo-Roca,<sup>‡</sup> Wenhua Li,<sup>‡</sup> Andrew Fairbrother,<sup>‡</sup> Joan Daniel Prades,<sup>†</sup> Alexey Shavel,<sup>†</sup> Jordi Arbiol,<sup>§,||</sup> Alejandro Pérez-Rodríguez,<sup>†,‡</sup> Joan Ramon Morante,<sup>†,‡</sup> and Andreu Cabot<sup>\*,†,‡</sup>

<sup>†</sup>Departament Electronica, Universitat de Barcelona, Barcelona 08028, Spain

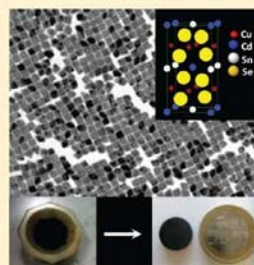
<sup>‡</sup>Catalonia Energy Research Institute (IREC), Jardí de les Dones de Negre 1, Planta 2, E-08930, Sant Adria del Besos, Barcelona 08930, Spain

<sup>§</sup>Institut de Ciència de Materials de Barcelona (ICMAB-CSIC), Campus de la UAB, Bellaterra 08193, Spain

<sup>||</sup>Institució Catalana de Recerca i Estudis Avançats (ICREA), Barcelona 08010, Spain

**ABSTRACT:** A high-yield and upscalable colloidal synthesis route for the production of quaternary I<sub>2</sub>–II–IV–VI<sub>4</sub> nanocrystals, particularly stannite  $\text{Cu}_{2-x}\text{Cd}_{1-x}\text{SnSe}_4$ , with narrow size distribution and precisely controlled composition is presented. It is also shown here how the diversity of valences in the constituent elements allows an effective control of their electrical conductivity through the adjustment of the cation ratios. At the same time, while the crystallographic complexity of quaternary chalcogenides is associated with intrinsically low thermal conductivities, the reduction of the lattice dimensions to the nanoscale further reduces the materials thermal conductivity. In the specific case of the stannite crystal structure, a convenient slab distribution of the valence band maximum states permits a partial decoupling of the p-type electrical conductivity from both the Seebeck coefficient and the thermal conductivity. Combining these features, we demonstrate how an initial optimization of the nanocrystals Cd/Cu ratio allowed us to obtain low-temperature solution-processed materials with ZT values up to 0.71 at 685 K.

**KEYWORDS:** nanocrystal, chalcogenide, thermoelectric, colloidal synthesis, stannite, semiconductor nanoparticle



### INTRODUCTION

Thermoelectric devices, allowing the solid-state conversion between thermal and electrical energy, have long been considered a very attractive technology for cooling and waste heat recovery. However, the low conversion efficiencies of actual thermoelectric devices have prevented them from entering most of their potential application markets. Over the last 15 years, advances in the fields of materials science and nanotechnology have restored an intense interest for such an energy conversion technology. Today's main strategy to produce materials with high thermoelectric figures of merit is to trigger phonon scattering at multiple length scales without disturbing the charge carrier transport.<sup>1–9</sup> The goal is to minimize the lattice thermal conductivity in highly electrically conductive materials: the so-called electron-crystal phonon-glass paradigm. This strategy is implemented by two main approaches: (i) the scattering of phonons at the atomic length scale by the synthesis of complex crystal phases that include one dimensional (1D) phonon scattering centers, such as vacancies or rattling atoms,<sup>4</sup> and/or two dimensional (2D) layered crystallographic structures<sup>5</sup> and (ii) the scattering of phonons at the 1–100 nm scale by reducing the crystal domain dimensions to the nanoscale.<sup>6–9</sup> An additional advantage of the confinement of the lattice dimensions to the nanometer scale is the potential decoupling of the Seebeck coefficient from

electrical conductivity.<sup>10,11</sup> In this regard, the increase of the electronic density of states near the Fermi level in quantum confined nanostructures has been predicted to enhance the Seebeck coefficient.<sup>9,12,13</sup> At the same time, energy filtering at nanocrystal interfaces may further enhance the thermopower of nanostructured material by selectively scattering low energy charge carriers.<sup>14–17</sup>

In this scenario, colloidal synthesis routes are particularly well suited for the production of thermoelectric materials. Solution-processing methods have a high potential for the production of low-cost, high-yield, large-scale, high-output, and shape-adaptable devices. Moreover, bottom-up approaches allow to directly obtain materials with reduced crystal domain size and controlled geometry.<sup>18–20</sup> In this regard, while the fabrication of solar cells from solution-processed semiconductors generally has the downside of requiring a thermal treatment to crystallize the absorbent layers, the huge interface densities of the solution-processed nanocrystalline materials represent an advantage in the thermoelectrics field.<sup>21–23</sup>

Some quaternary chalcogenides and, in particular, I<sub>2</sub>–II–IV–VI<sub>4</sub> adamantines have the required attributes to be potentially

Received: October 24, 2011

Revised: January 6, 2012

Published: January 31, 2012

## Extending the Nanocrystal Synthesis Control to Quaternary Compositions

Maria Ibáñez,<sup>†</sup> Reza Zamani,<sup>‡,§</sup> Wenhua Li,<sup>‡</sup> Alexey Shavel,<sup>‡</sup> Jordi Arbiol,<sup>§,||</sup> Joan Ramon Morante,<sup>†,‡</sup> and Andreu Cabot<sup>\*,†,‡</sup>

<sup>†</sup>Departament Electronica, Universitat de Barcelona, Barcelona 08028, Spain

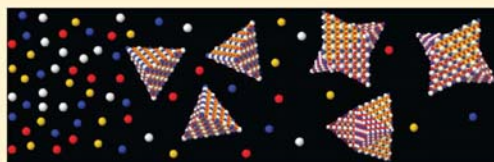
<sup>‡</sup>Catalonia Energy Research Institute—IREC, Jardí de les Dones de Negre 1, Planta 2, Sant Adria del Besos, Barcelona 08930, Spain

<sup>§</sup>Institut de Ciència de Materials de Barcelona, ICMAB-CSIC, Campus de la UAB, Bellaterra 08193, Spain

<sup>||</sup>Institució Catalana de Recerca i Estudis Avançats (ICREA), 08010 Barcelona, Spain

### Supporting Information

**ABSTRACT:** The ample chemical and structural freedom of quaternary compounds permits engineering materials that fulfill the requirements of a wide variety of applications. In this work, the mechanisms to achieve unprecedented size, shape, and composition control in quaternary nanocrystals are detailed. The described procedure allows obtaining tetrahedral and penta-tetrahedral quaternary nanocrystals with tuned size distributions and controlled compositions from a plethora of  $I_2-II-IV-VI_4$  semiconductors.



Colloidal synthesis routes have proven successful in obtaining elemental and binary nanocrystals with controlled size and shape distributions. One step beyond that, the production of ternary and quaternary nanocrystals with precisely controlled characteristics remains a challenge. Owing to their recognized interest, significant efforts are currently underway to accomplish this step-change in the potential of solution-processing methods to produce functional nanomaterials. These efforts pay off with the strong added value that ternary and quaternary compositions bring in.

The numerous possibilities for chemical substitutions and structural modifications in quaternary materials allow significant range in tuning their fundamental chemical and physical properties.<sup>1–4</sup> For instance, compositional control in these quaternary semiconductors offers an accessible method to tune their valence balance, thereby adjusting their Fermi level. This intrinsic doping strategy to control the semiconductor electronic properties is especially interesting in the bottom-up processing of nanomaterials, where the introduction of extrinsic dopants has not proven significantly feasible. Such ample chemical and structural freedom permits engineering quaternary chalcogenides, potentially made of abundant and nontoxic elements, to fulfill the requirements of a wide variety of applications. As an example,  $Cu_2ZnSn(S,Se)_4$ , having a direct band gap in the visible spectrum and a high absorption coefficient, has recently attracted much attention in the field of photovoltaics as alternative absorber materials to  $CdTe$  and  $Cu(In,Ga)Se_2$ .<sup>5–7</sup> On the other hand, some quaternary diamond-like chalcogenides have been proven excellent thermoelectric materials because of their layered structures and intrinsically low lattice thermal conductivities.<sup>8</sup> Quaternary

$I_2-II-IV-VI_4$  semiconductors are also excellent candidates for nonlinear optic applications.<sup>9</sup> Furthermore, some of these compounds have been very recently demonstrated to be topological insulators with large nontrivial band gaps.<sup>10,11</sup>

A few reports have already detailed successful preliminary synthesis procedures to obtain particularly interesting quaternary nanostructured chalcogenides:  $Cu_2ZnSnS_4$ ,<sup>12,13</sup> and  $Cu_2ZnSnSe_4$ .<sup>6</sup> However, the complexity of the thermodynamics and kinetics of nucleation and growth of such complex structures has resulted up to now in irregular shapes and broad size distributions. The very limited control over the size, geometry, and composition of the nanocrystals previously obtained precludes a systematic investigation of their fundamental properties and limits their range of potential applications. Moreover, the synthesis of nanocrystals of new potentially useful quaternary chalcogenides, e.g.  $Cu_2CdGeSe_4$  and  $Cu_2ZnGeSe_4$ , has not yet been attempted.

In the present work, the mechanisms to achieve unprecedented size, shape, and composition control in quaternary  $I_2-II-IV-VI_4$  nanocrystals are detailed. While the presented procedures are illustrated using  $Cu_2CdSnSe_4$  nanocrystals as the prototypical system, this synthetic route is proven successful for the production of a plethora of other quaternary chalcogenide nanoparticles. Furthermore, in the present approach, particular care was taken in designing a cost-effective and up-scalable process to ensure its relevance in a future industrial implementation. The potential for large scale

Received: December 27, 2011

Revised: January 20, 2012

Published: February 8, 2012

## Cu<sub>2</sub>ZnGeSe<sub>4</sub> Nanocrystals: Synthesis and Thermoelectric Properties

Maria Ibáñez,<sup>†</sup> Reza Zamani,<sup>‡,§</sup> Aaron LaLonde,<sup>||</sup> Doris Cadavid,<sup>‡</sup> Wenhua Li,<sup>‡</sup> Alexey Shavel,<sup>‡</sup> Jordi Arbiol,<sup>§,⊥</sup> Joan Ramon Morante,<sup>†,‡</sup> Stéphane Gorsse,<sup>#</sup> G. Jeffrey Snyder,<sup>||</sup> and Andreu Cabot<sup>\*,†,‡</sup>

<sup>†</sup>Departament Electronica, Universitat de Barcelona, Barcelona 08028, Spain

<sup>‡</sup>Catalonia Energy Research Institute (IREC), Jardí de les Dones de Negre 1, Sant Adria del Besos, Barcelona 08930, Spain

<sup>§</sup>Institut de Ciència de Materials de Barcelona (ICMAB-CSIC), Campus de la UAB, Bellaterra 08193, Spain

<sup>||</sup>Materials Science, California Institute of Technology, 1200 East California Boulevard, Pasadena, California 91125, United States

<sup>⊥</sup>Institució Catalana de Recerca i Estudis Avançats (ICREA), Barcelona 08010, Spain

<sup>#</sup>CNRS, Université de Bordeaux, ICMCB, 87 avenue du Docteur Albert Schweitzer, 33608 Pessac Cedex, France

**S** Supporting Information

**ABSTRACT:** A synthetic route for producing Cu<sub>2</sub>ZnGeSe<sub>4</sub> nanocrystals with narrow size distributions and controlled composition is presented. These nanocrystals were used to produce densely packed nanomaterials by hot-pressing. From the characterization of the thermoelectric properties of these nanomaterials, Cu<sub>2</sub>ZnGeSe<sub>4</sub> is demonstrated to show excellent thermoelectric properties. A very preliminary adjustment of the nanocrystal composition has already resulted in a figure of merit of up to 0.55 at 450 °C.

The ample chemical and structural freedom of quaternary diamond-like chalcogenides allows their use in multiple applications, such as photovoltaics,<sup>1,2</sup> nonlinear optics,<sup>3</sup> thermoelectrics,<sup>4,5</sup> and even topological insulators, as recently demonstrated.<sup>6,7</sup> In particular, in the field of photovoltaics, copper-based quaternary diamond-like semiconductors of the family I<sub>2</sub>-II-IV-VI<sub>4</sub> have recently gained a great deal of attention as alternatives to CdTe and Cu(In,Ga)Se<sub>2</sub> for use as absorber materials. The possibility of engineering quaternary semiconductors made of relatively low cost, abundant, and nontoxic elements having an optimum direct band gap has drawn high interest in the preparation and characterization of this class of materials, particularly Cu<sub>2</sub>ZnSn(S,Se)<sub>4</sub>.<sup>1,2,8</sup>

On the other hand, the complexity of the crystallographic structures of quaternary compounds is associated with intrinsically low thermal conductivities. In addition, the control of their composition allows for the tuning of their charge carrier concentration. Moreover, in the particular case of compositionally layered structures such as stannite, high electrical conductivities can coexist with large Seebeck coefficients and intrinsically low thermal conductivities. Thus, these quaternary compounds are also potentially excellent thermoelectric materials.<sup>4,5,9</sup>

While in photovoltaics the reduction of the lattice dimensions to the nanoscale allows for low-cost solution processing of devices, in the thermoelectrics field, nanostructuring further allows improvement of their efficiency.<sup>10,11</sup> Mainly, the reduction of the crystal domains to the nanoscale introduces a high density of phonon scattering centers, which

reduce the material's thermal conductivity and enhance its thermoelectric figure of merit.

Cu<sub>2</sub>ZnGeSe<sub>4</sub> (CZGS) is a p-type semiconductor with a direct band gap between 1.21 and 1.63 eV, as determined experimentally and theoretically.<sup>12–15</sup> Its ideal band gap makes it an alternative indium- and cadmium-free absorber material for photovoltaics.<sup>15–18</sup> CZGS crystallizes in a non-centered tetragonal structure with space group  $\bar{I}42m$ .<sup>19–21</sup> Its quaternary nature, variety of ionic valences, and particular crystallographic structure suggest that CZGS should be characterized by intrinsically low thermal conductivities and potentially high electrical conductivities and Seebeck coefficients. This combination of properties qualifies CZGS as a potentially outstanding thermoelectric material.

In this communication, a synthetic route for producing CZGS nanoparticles with narrow size distributions and controlled composition is presented. This is the first presented synthetic route for the production of CZGS nanocrystals. Furthermore, the potential of CZGS as a thermoelectric material is demonstrated by characterizing the thermoelectric properties of CZGS nanocrystals with two different compositions.

CZGS nanoparticles were prepared by reacting metal complexes with an excess of selenium in octadecene. In a typical synthesis, 0.50 mmol of CuCl, 0.50 mmol of ZnO, 0.25 mmol of GeCl<sub>4</sub>, 5 mM hexadecylamine, 0.1 mmol of *n*-tetradecylphosphonic acid, and 10 mL of octadecene were placed in a four-neck flask and heated to 200 °C under and argon flow. Separately, a 0.8 M selenium solution was prepared under argon by dissolving selenium dioxide in octadecene at 180 °C. A 4 mL aliquot of the precursor Se solution was injected into the heated solution containing the metal complexes at 295 °C. The solution was kept at this temperature for 5 min to allow the nanoparticles to grow. Finally, the flask was rapidly cooled to room temperature.

Figure 1 shows a representative transmission electron microscopy (TEM) micrograph of CZGS nanoparticles produced by the procedure detailed here. Narrow size distributions, with dispersions below 10%, were systematically

Received: December 22, 2011

Published: February 14, 2012

Crystallographic Control at the Nanoscale To Enhance Functionality: Polytypic  $\text{Cu}_2\text{GeSe}_3$  Nanoparticles as Thermoelectric Materials

Maria Ibáñez,<sup>†</sup> Reza Zamani,<sup>‡,§</sup> Wenhua Li,<sup>‡</sup> Doris Cadavid,<sup>‡</sup> Stéphane Gorsse,<sup>¶</sup> Nebil A. Katcho,<sup>||</sup> Alexey Shavel,<sup>‡</sup> Antonio M. López,<sup>⊥</sup> Joan Ramon Morante,<sup>†,‡</sup> Jordi Arbiol,<sup>\*,§,∇</sup> and Andreu Cabot<sup>\*,†,‡</sup>

<sup>†</sup>Departament d'Electrònica, Universitat de Barcelona, Barcelona 08028, Spain

<sup>‡</sup>Catalonia Energy Research Institute (IREC), Jardins de les Dones de Negre 1, Sant Adria del Besos, Barcelona 08930, Spain

<sup>§</sup>Institut de Ciència de Materials de Barcelona, ICMAB-CSIC, Campus de la UAB, Bellaterra 08193, Spain

<sup>||</sup>LITEN, CEA-Grenoble, 17 rue des Martyrs, 38054 Grenoble Cedex 9, France

<sup>⊥</sup>Departament d'Enginyeria Electrònica, Universitat Politècnica de Catalunya, EPSEVG, Avenida Victor Balaguer s/n, 08800 Barcelona, Spain

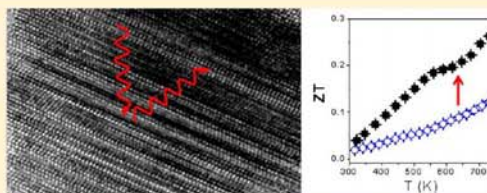
<sup>∇</sup>Institució Catalana de Recerca i Estudis Avançats (ICREA), 08010 Barcelona, Spain

<sup>\*</sup>CNRS, Université de Bordeaux, ICMCB, 87 avenue du Docteur Albert Schweitzer, 33608 Pessac Cedex, France

**S** Supporting Information

**ABSTRACT:** The potential to control the composition and crystal phase at the nanometer scale enable the production of nanocrystalline materials with enhanced functionalities and new applications. In the present work, we detail a novel colloidal synthesis route to prepare nanoparticles of the ternary semiconductor  $\text{Cu}_2\text{GeSe}_3$  (CGSe) with nanometer-scale control over their crystal phases. We also demonstrate the structural effect on the thermoelectric properties of bottom-up-prepared CGSe nanomaterials. By careful adjustment of the nucleation and growth temperatures, pure orthorhombic CGSe nanoparticles with cationic order or polytypic CGSe nanoparticles with disordered cation positions can be produced. In this second type of nanoparticle, a high density of twins can be created to periodically change the atomic plane stacking, forming a hexagonal wurtzite CGSe phase. The high yield of the synthetic routes reported here allows the production of single-phase and multiphase CGSe nanoparticles in the gram scale, which permits characterization of the thermoelectric properties of these materials. Reduced thermal conductivities and a related 2.5-fold increase of the thermoelectric figure of merit for multiphase nanomaterials compared to pure-phase CGSe are systematically obtained. These results are discussed in terms of the density and efficiency of phonon scattering centers in both types of materials.

**KEYWORDS:** polytypic nanocrystals, thermoelectrics, chalcogenide, nanocomposite, wurtzite, orthorhombic, zinc blende,  $\text{Cu}_2\text{GeSe}_3$ , ternary semiconductor



**■ INTRODUCTION**

The numerous possibilities for chemical substitutions and structural modifications of ternary and quaternary chalcogenides allow a significant degree of engineering of their fundamental chemical and physical properties, including the band gap and carrier concentration.<sup>1–3</sup> Besides, the possibility of tailoring the material properties by the preparation of metastable crystallographic phases has recently generated a great deal of attention. The metastable wurtzite phases recently identified in many compounds and particularly in some copper-based ternary and quaternary semiconductors deserve special mention.<sup>4–7</sup>

A particularly attractive ternary chalcogenide is  $\text{Cu}_2\text{GeSe}_3$  (CGSe). CGSe is a p-type semiconductor with a direct band gap in the IR ( $E_g = 0.78$  eV).<sup>8,9</sup> It has a low melting temperature (770 °C), a relatively low density ( $\rho = 5.6$  g cm<sup>-3</sup>),<sup>10</sup> and a high diffraction index,  $n \sim 3.2$ .<sup>8,9,11</sup> Different crystal structures have

been described for this compound: cubic (zinc-blende-like),<sup>12</sup> tetragonal chalcopyrite,<sup>13–15</sup> and orthorhombic with space group *Imm2*.<sup>16,17</sup> CGSe has a thermal expansion coefficient of  $8.4 \times 10^{-6}$  K<sup>-1</sup>, a heat capacity of about  $0.34$  J g<sup>-1</sup> K<sup>-1</sup>, and a relatively low thermal conductivity of  $2.4$  W m<sup>-1</sup> K<sup>-1</sup> at 300 K.<sup>11,18</sup> These properties make it a promising thermoelectric material.<sup>19–21</sup>

One main strategy to increase the figure of merit of thermoelectric materials is to decrease their thermal conductivity by promoting phonon scattering. This goal can be achieved by reducing the size of the crystal domains to the nanoscale.<sup>22–27</sup> In this direction, the ball milling of crystalline ingots into a nanopowder and its posterior reconsolidation into bulk nano-

Received: October 8, 2012

Revised: November 11, 2012

Published: November 14, 2012

Colloidal synthesis and thermoelectric properties of  
 $\text{Cu}_2\text{SnSe}_3$  nanocrystalsCite this: *J. Mater. Chem. A*, 2013, **1**,  
1421Maria Ibáñez,<sup>†a</sup> Doris Cadavid,<sup>†b</sup> Umberto Anselmi-Tamburini,<sup>c</sup> Reza Zamani,<sup>bd</sup>  
Stéphane Gorsse,<sup>e</sup> Wenhua Li,<sup>b</sup> Antonio M. López,<sup>f</sup> Joan Ramon Morante,<sup>ab</sup>  
Jordi Arbiol<sup>dg</sup> and Andreu Cabot<sup>\*ab</sup>

Copper-based selenides are attracting increasing interest due to their outstanding optoelectronic and thermoelectric properties. Herein a novel colloidal synthetic route to prepare  $\text{Cu}_2\text{SnSe}_3$  nanocrystals with controlled size, shape and composition is presented. The high yield of the developed procedure allowed its up-scaling to the production of grams of colloidal  $\text{Cu}_2\text{SnSe}_3$  nanocrystals. These nanocrystals were used as building blocks for the production of  $\text{Cu}_2\text{SnSe}_3$  bulk nanostructured materials by spark plasma sintering. The thermoelectric properties of the prepared nanocrystalline  $\text{Cu}_2\text{SnSe}_3$  pellets were characterized in the temperature range from 300 to 720 K. The obtained results show the bottom-up production of nanocrystalline materials from solution-processed nanocrystals to be a potentially advantageous alternative to conventional methods of production of efficient thermoelectric materials.

Received 24th September 2012  
Accepted 15th November 2012

DOI: 10.1039/c2ta00419d

www.rsc.org/MaterialsA

## Introduction

The numerous possibilities for chemical substitutions and structural modifications in ternary diamond-like chalcogenides allow a significant range in engineering their fundamental chemical and physical properties. Such ample chemical and structural freedom permits the use of ternary chalcogenides in multiple applications. Ternary diamond-like semiconductors of the family  $\text{I}_2\text{-IV-VI}_3$  (I = Cu, Ag; IV = Ge, Sn; VI = S, Se, Te) find applications in the fields of photovoltaics,<sup>1</sup> Li-ion batteries,<sup>2,3</sup> thermoelectrics,<sup>4</sup> and in acousto-optic devices.<sup>5</sup>

In particular,  $\text{Cu}_2\text{SnSe}_3$  (CTSe) is a p-type semiconductor with a direct band gap of 0.84 eV and a high optical absorption coefficient  $>10^4 \text{ cm}^{-1}$ .<sup>6-8</sup> CTSe monocrystals are characterized by relatively high hole mobilities ( $870 \text{ cm}^2 \text{ V}^{-1} \text{ s}^{-1}$ )<sup>9</sup> and a hole effective mass of  $1.2m_0$ .<sup>8</sup> CTSe has been reported to crystallize in a cubic sphalerite-like phase (space group  $F\bar{4}3m$ )<sup>10,11</sup> or in the monoclinic structure, the space group  $Cc$ , with a sphalerite superstructure.<sup>8,12-14</sup>

CTSe is an interesting candidate for acousto-optic applications in the IR region because of its low melting temperature (690 °C), relative low energy band gap, high mean atomic weight and high refractive indices.<sup>8</sup> It has been also extensively studied as an important ternary phase in the processing of  $\text{Cu}_2\text{ZnSnSe}_4$ , which is a potential low-cost solar cell absorber.<sup>15,16</sup>

Furthermore, like other copper-based ternary and quaternary selenides,<sup>4,17-24</sup> CTSe shows excellent thermoelectric properties. In CTSe the Cu-Se bond network stabilizes the structure and forms an electrically conductive framework. While Cu-Se bonds play the dominant role in controlling hole transport, Sn orbitals do not contribute much to the p-type carrier transport but allow tuning electrical conductivity by their partial substitution by a group III element.<sup>17</sup> At the same time, ionic substitutions create atomic mass fluctuations that promote phonon scattering, thus reducing thermal conductivities.<sup>4,17,25</sup> These properties have allowed the production of bulk CTSe with figures of merit up to 1.14 at 850 K and 0.41 at 716 K when doped with In or Mn atoms.<sup>17,26</sup>

Thermal conductivities can be further reduced by confining the material crystal domains to the nanoscale.<sup>27-34</sup> The ball-milling of crystalline ingots into small pieces and their posterior reconsolidation into bulk nanocrystalline materials by hot-pressing or spark plasma sintering is currently the most used approach in this direction.<sup>35</sup> Nevertheless, in the very last few years, the bottom-up processing of nanocrystalline materials from solution-processed nanoparticles is becoming a serious alternative to produce efficient thermoelectric nanomaterials.<sup>33,34,36-38</sup>

In this scenario, while a high degree of control over the solution processing of binary chalcogenide nanocrystals exists,<sup>36,37</sup> the synthesis of ternary and quaternary nanocrystals

<sup>a</sup>Departament d'Electrònica, Universitat de Barcelona, 08028 Barcelona, Spain<sup>b</sup>Catalonia Institute for Energy Research, IREC, 08930 Sant Adrià del Besos, Barcelona, Spain. E-mail: acabot@irec.cat<sup>c</sup>Dipartimento di Chimica, Università di Pavia, V.le Taramelli, 16, 27100 Pavia, Italy<sup>d</sup>Institut de Ciència de Materials de Barcelona, ICMAB-CSIC, Campus de la UAB, Bellaterra, 08193, Spain<sup>e</sup>CNRS, Université de Bordeaux, ICMCB, 87 avenue du Docteur Albert Schweitzer, 33608 Pessac Cedex, France<sup>f</sup>Departament d'Enginyeria Electrònica, Universitat Politècnica de Catalunya, EPSEVG, Av. Víctor Balaguer s/n, 08800 Barcelona, Spain<sup>g</sup>Institució Catalana de Recerca i Estudis Avançats (ICREA), 08010 Barcelona, Spain

† These authors contributed equally.

## Metal Ions To Control the Morphology of Semiconductor Nanoparticles: Copper Selenide Nanocubes

Wenhua Li,<sup>‡</sup> Reza Zamani,<sup>‡,||</sup> Maria Ibáñez,<sup>†</sup> Doris Cadavid,<sup>‡</sup> Alexey Shavel,<sup>‡</sup> Joan Ramon Morante,<sup>†,‡</sup> Jordi Arbio,<sup>||,§</sup> and Andreu Cabot<sup>\*,†,‡</sup>

<sup>‡</sup>Catalonia Energy Research Institute - IREC, Jardí de les Dones de Negre, 1, 08930 Sant Adria del Besos, Barcelona, Spain

<sup>||</sup>Institut de Ciència de Materials de Barcelona, ICMAB-CSIC, Campus de la UAB, 08193 Bellaterra, Spain

<sup>†</sup>Departament d'Electrònica, Universitat de Barcelona, Martí i Franques 1, 08028 Barcelona, Spain

<sup>§</sup>Institució Catalana de Recerca i Estudis Avançats (ICREA), 08010 Barcelona, Spain

### Supporting Information

**ABSTRACT:** Morphology is a key parameter in the design of novel nanocrystals and nanomaterials with controlled functional properties. Here, we demonstrate the potential of foreign metal ions to tune the morphology of colloidal semiconductor nanoparticles. We illustrate the underlying mechanism by preparing copper selenide nanocubes in the presence of Al ions. We further characterize the plasmonic properties of the obtained nanocrystals and demonstrate their potential as a platform to produce cubic nanoparticles with different composition by cation exchange.

It is in large part through the surface that nanocrystals (NCs) interact with neighboring NCs and the medium. Catalytic, electronic, optoelectronic and thermoelectric performance of NCs and nanocrystalline materials strongly rely on the chemical and energy exchange in the form of ions, charge carriers or phonons that take place between NCs themselves and between NCs and the medium. In this sense, numerous applications depend on the organization of the NC last atomic layers. That is, on the type and ratio of the NC facets, i.e., its morphology.

Morphology also controls NC assembly into macroscopic superstructures. In this regard, a particularly interesting geometry for technological applications is that of cubes.<sup>1</sup> Nanocubes can maximize NC packing and produce highly compact films or bulk nanostructured materials. At the same time, nanocubes can form lattice-matched superstructures where all crystallographic domains are oriented in the same direction.<sup>2</sup> This may be an important asset in magnetic, electronic, optoelectronic, and thermoelectric applications, where charge carrier or phonon exchange is fundamental.

To control NC morphology, organic molecules that selectively bind to different NC facets are generally used. There are countless examples on the use of aliphatic chains with carboxylic acid, phosphonic acid and amine functional groups to control the morphology of elemental, binary, ternary, and quaternary nanoparticles.<sup>3</sup> Some metal ions have also been proved as efficient directors of NC morphology, especially for metal nanoparticles. A particularly illustrative example is that of Pt-based nanocubes. Tungsten,<sup>4</sup> iron,<sup>5</sup> cobalt,<sup>6</sup> and chromium<sup>7</sup> carbonyls and also iron chloride,<sup>8</sup> silver nitrate<sup>9</sup> and silver

acetylacetonate<sup>10</sup> have been used to produce Pt nanocubes by manipulating NC nucleation and growth rate in the different crystallographic directions. In many cases, these metal ions did not incorporate in the NC structure and were not detected on the surface or within the final NCs. They just catalyzed the nanocube formation, returning afterward to the solution or precipitating as a salt.

Previous studies on the use of foreign metal ions to control NC morphology were focused on metal NCs. However, because the underlying mechanism is a general one, we believe metal ions should be also included in our tool bench as potential morphology drivers of semiconductor NCs.

Here, we report an example of the influence of foreign metal ions to control the morphology of a chalcogenide semiconductor: Cu<sub>x</sub>Se. In particular, we detail a synthetic route to produce Cu<sub>x</sub>Se nanocubes by the incorporation of Al ions in the initial precursor solution. We also characterize the plasmonic properties of the new copper selenide geometry obtained and demonstrate the potential of the produced Cu<sub>x</sub>Se NCs to prepare nanocubes of other semiconductor chalcogenides by cation exchange. This is exemplified by preparing Ag<sub>2</sub>Se nanocubes.

We produced Cu<sub>x</sub>Se NCs by reacting CuCl with an excess of selenium precursor in the presence of hexadecylamine (HDA). In a typical preparation, 0.0495 g of CuCl (0.5 mmol, 99.99%, Aldrich), 5 mmol HDA (90% Aldrich) and 10 mL of octadecene (ODE, 90%, Aldrich) were introduced inside a four-neck flask and heated to 200 °C under argon flow until all precursors were dissolved. The yellowish transparent solution produced was maintained under Ar flow at 200 °C for an additional hour to remove oxygen, water and other low-boiling point impurities. Afterward, the solution was cooled to 180 °C and 4 mL of a 0.8 M ODE-Se solution was injected through a septum (detailed information on the selenium precursor preparation and the nanocrystal synthesis can be found in the Supporting Information, SI). The mixture was maintained at 180 °C for 5 min. Afterward, the solution was rapidly cooled down to room temperature. The NCs were isolated and purified using the standard solvent/nonsolvent precipitation/redispersion procedure. The reaction yield was around 80% for

Received: January 15, 2013

Published: March 7, 2013

## CuTe Nanocrystals: Shape and Size Control, Plasmonic Properties, and Use as SERS Probes and Photothermal Agents

Wenhua Li,<sup>†</sup> Reza Zamani,<sup>‡,‡</sup> Pilar Rivera Gil,<sup>||</sup> Beatriz Pelaz,<sup>||</sup> Maria Ibáñez,<sup>‡</sup> Doris Cadavid,<sup>†</sup> Alexey Shavel,<sup>†</sup> Ramon A. Alvarez-Puebla,<sup>#,v,§</sup> Wolfgang J. Parak,<sup>||</sup> Jordi Arbiol,<sup>‡,§</sup> and Andreu Cabot<sup>\*,†,‡</sup>

<sup>†</sup>Catalonia Energy Research Institute–IREC, Barcelona 08930, Spain

<sup>‡</sup>Institut de Ciència de Materials de Barcelona, ICMAB-CSIC, Campus de la UAB, Bellaterra 08193, Spain

<sup>||</sup>Philipps Universität Marburg, 35037 Marburg, Germany

<sup>‡</sup>Departament d'Electrònica, Universitat de Barcelona, Barcelona 08028, Spain

<sup>#</sup>Department of Electronic Engineering, Universitat Rovira i Virgili, Tarragona 43007, Spain

<sup>v</sup>Center for Chemical Technology of Catalonia, Tarragona 43007, Spain

<sup>§</sup>Institució Catalana de Recerca i Estudis Avançats, 08010 Barcelona, Spain

### Supporting Information

**ABSTRACT:** We report a procedure to prepare highly monodisperse copper telluride nanocubes, nanoplates, and nanorods. The procedure is based on the reaction of a copper salt with trioctylphosphine telluride in the presence of lithium bis(trimethylsilyl)amide and oleylamine. CuTe nanocrystals display a strong near-infrared optical absorption associated with localized surface plasmon resonances. We exploit this plasmon resonance for the design of surface-enhanced Raman scattering sensors for unconventional optical probes. Furthermore, we also report here our preliminary analysis of the use of CuTe nanocrystals as cytotoxic and photothermal agents.

Copper-based chalcogenides are used in a wide range of applications, from thermoelectrics to batteries, including photonics, photovoltaics, and photothermal therapy.<sup>1,2</sup> They are usually p-type semiconductors, due to the presence of copper vacancies. Copper vacancies not only determine charge transport properties but also provide copper chalcogenides with a particularly attractive property: a composition-dependent localized surface plasmon resonance (LSPR) in the near-infrared (NIR).<sup>3</sup> In particular, copper telluride is characterized by a large thermal power, a direct band gap between 1.1 and 1.5 eV, and superionic conductivity. Copper telluride can exist in a wide range of compositions and phases, which allows tuning its properties by just adjusting the Cu:Te ratio. These properties provide it with both high fundamental interest and technological potential. However, in spite of its relevance, little is known about its properties at the nanoscale, e.g., plasmonics, and a synthetic route to produce uniform copper telluride nanoparticles (NPs) is yet to be reported. While a variety of procedures to prepare sulfide and selenide NPs with excellent uniformity are available,<sup>3,4</sup> one main constraint to produce telluride NPs and particularly copper telluride is the reduced number of tellurium sources available, which narrows the range of accessible reaction conditions to direct telluride NPs nucleation and growth.

In the present work, we demonstrate the potential of lithium bis(trimethylsilyl)amide to control the growth of copper telluride NPs and detail a simple synthetic route to produce highly uniform copper telluride nanocubes, nanoplates, and nanorods. We further demonstrate how copper telluride NPs provide a new and unique optical platform for the design of plasmonic sensors of a wide family of molecules that cannot be conventionally analyzed with surface-enhanced Raman scattering (SERS).<sup>5</sup> Furthermore, we report preliminary results on the use of copper telluride NPs for photothermal destruction of cells.

Copper telluride NPs were prepared by reacting copper(I) chloride with trioctylphosphine telluride (TOPTe) in the presence of trioctylphosphine (TOP), trioctylphosphine oxide (TOPO), lithium bis(trimethylsilyl)amide (LiN(SiMe<sub>3</sub>)<sub>2</sub>), and oleylamine (OLA). In a typical synthesis, 0.25 mmol of CuCl was mixed with 1 mmol of TOPO and 6 mL of OLA in a 25 mL three-neck flask. The mixture was heated under vacuum to 100 °C to obtain a clear blue solution and kept at this temperature for 30 min to remove low-boiling-point impurities. The temperature was then increased to 160 °C, and 0.125 mL of TOP was added. In parallel, a tellurium precursor solution was prepared inside a glovebox by mixing 0.125 mL of a 2 M TOPTe solution with 0.5 mL of a 0.5 M LiN(SiMe<sub>3</sub>)<sub>2</sub> solution in dried octadecene (ODE). The tellurium solution was rapidly injected into the copper solution maintained at 160 °C. Upon injection, the solution color immediately changed to deep green, and the temperature dropped to 152 °C. Just after injection, the temperature was set to 220 °C, and NPs were allowed to grow for 30 min. During cooling, when the temperature reached 70 °C, 2 mL of oleic acid was added to replace the weakly bound OLA molecules.

Figure 1A shows representative transmission electron microscopy (TEM) and high-resolution TEM (HRTEM) micrographs of the copper telluride NPs obtained by the procedure described above. NPs displayed a cubic geometry

Received: February 7, 2013

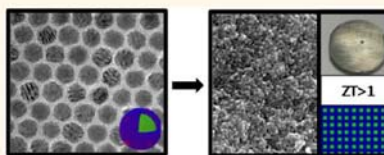
Published: April 30, 2013

# Core–Shell Nanoparticles As Building Blocks for the Bottom-Up Production of Functional Nanocomposites: PbTe–PbS Thermoelectric Properties

Maria Ibáñez,<sup>†</sup> Reza Zamani,<sup>\*,5</sup> Stéphane Gorsse,<sup>‡</sup> Jiandong Fan,<sup>‡</sup> Silvia Ortega,<sup>†</sup> Doris Cadavid,<sup>‡</sup> Joan Ramon Morante,<sup>†,\*</sup> Jordi Arbiol,<sup>5,||</sup> and Andreu Cabot<sup>†,\*</sup>

<sup>†</sup>Departament d'Electrònica, Universitat de Barcelona, Barcelona 08028, Spain, <sup>‡</sup>Catalonia Institute for Energy Research—IREC, Jardí de les Dones de Negre 1, Sant Adrià de Besòs, Barcelona, 08930, Spain, <sup>§</sup>Institut de Ciència de Materials de Barcelona, ICMAB-CSIC, Campus de la UAB, Bellaterra, 08193, Spain, <sup>||</sup>CNRS, Université de Bordeaux, ICMCB, 87 Avenue du Docteur Albert Schweitzer, 33608 Pessac Cedex, France, and <sup>||</sup>Institució Catalana de Recerca i Estudis Avançats (ICREA), 08010 Barcelona, Spain

**ABSTRACT** The bottom-up assembly of nanocrystals provides access to a three-dimensional composition control at the nanoscale not attainable by any other technology. In particular, colloidal nanostructures, with intrinsic multiphase organization, are especially appealing building blocks for the bottom-up production of nanocomposites. In the present work, we use PbTe–PbS as the model material system and thermoelectricity as the paradigmatic application to investigate the potential of the bottom-up assembly of core–shell nanoparticles to produce functional nanocomposites. With this goal in mind, a rapid, high-yield and scalable colloidal synthetic route to prepare grams of PbTe@PbS core–shell nanoparticles with unprecedented narrow size distributions and exceptional composition control is detailed. PbTe@PbS nanoparticles were used as building blocks for the bottom-up production of PbTe–PbS nanocomposites with tuned composition. In such PbTe–PbS nanocomposites, synergistic nanocrystal doping effects result in up to 10-fold higher electrical conductivities than in pure PbTe and PbS nanomaterials. At the same time, the acoustic impedance mismatch between PbTe and PbS phases and a partial phase alloying provide PbTe–PbS nanocomposites with strongly reduced thermal conductivities. As a result, record thermoelectric figures of merit (ZT) of  $\sim 1.1$  were obtained from undoped PbTe and PbS phases at 710 K. These high ZT values prove the potential of the proposed processes to produce efficient functional nanomaterials with programmable properties.



**KEYWORDS:** colloidal nanoparticles · thermoelectricity · nanomaterial · nanocomposite · heterostructures · core–shell nanoparticles

To control material properties and to understand mechanisms and phenomena at the atomic scale are two main ambitious goals of the current research and development of advanced functional materials. One step above that, industrial innovation requires the development of cost-effective processes able to transform this control and understanding into optimized or novel products. In this context, the bottom-up assembly of nanoparticles (NP) offers a unique potential not only to perform fundamental studies with precisely controlled material parameters but also to produce artificial materials with functional properties by design in a cost-effective manner. In this scenario, the

outstanding degree of control over size, shape, phase, and composition that colloidal synthesis methods have achieved makes colloidal NPs particularly suitable building blocks to prepare functional nanomaterials.<sup>1–6</sup> At the same time, the advantageous processability, low synthesis temperatures, large production rates, and high production yields of solution-processing methods offer unpaired opportunities to fabricate low-cost devices.

An especially attractive application for nanomaterials and nanotechnology researchers and developers is thermoelectricity. Thermoelectric energy conversion comprises two very appealing attributes: an enormous potential for economical and social impact, and the need for material control at the

\* Address correspondence to acabot@irec.cat.

Received for review December 24, 2012 and accepted February 28, 2013.

Published online February 28, 2013  
10.1021/nn305971v

© 2013 American Chemical Society

Available online at [www.sciencedirect.com](http://www.sciencedirect.com)

Acta Materialia 59 (2011) 6790–6800

[www.elsevier.com/locate/actamat](http://www.elsevier.com/locate/actamat)

## Control of the doping concentration, morphology and optoelectronic properties of vertically aligned chlorine-doped ZnO nanowires

Jiandong Fan<sup>a</sup>, Alexey Shavel<sup>a</sup>, Reza Zamani<sup>b,c</sup>, Cristian Fábrega<sup>c</sup>, Jean Rousset<sup>d</sup>,  
 Servane Haller<sup>d</sup>, Frank Güell<sup>a</sup>, Alex Carrete<sup>a,c</sup>, Teresa Andreu<sup>c</sup>, Jordi Arbiol<sup>b,e</sup>,  
 Joan Ramón Morante<sup>a,c</sup>, Andreu Cabot<sup>a,c,\*</sup>

<sup>a</sup> *Departament Electronica, Universitat de Barcelona, Barcelona 08028, Spain*<sup>b</sup> *Institut de Ciència de Materials de Barcelona, ICMAB-CSIC, Campus de la UAB, Bellaterra 08193, Spain*<sup>c</sup> *Catalonia Institute for Energy Research, IREC, Sant Adria del Besos, Barcelona 08930, Spain*<sup>d</sup> *Institute for Research and Development of Photovoltaic Energy (IRDEP), UMR 7174 CNRS-EDF-Chimie Paristech, 6 quai Watier, Paris 78401, France*<sup>e</sup> *Institució Catalana de Recerca i Estudis Avançats, ICREA, Barcelona 08010, Spain*

Received 2 April 2011; received in revised form 15 July 2011; accepted 15 July 2011

Available online 9 August 2011

### Abstract

Vertically aligned single-crystal and chlorine-doped ZnO nanowires (NWs) were grown by a low-cost, high-yield and seed-free electrochemical route. The effects of the applied potential and the concentration of ammonium chloride (NH<sub>4</sub>Cl) on the morphology, structural and optoelectronic properties of the ZnO:Cl NWs were comprehensively investigated. The amount of Cl ions introduced in the ZnO structure increased almost linearly with both the concentration of NH<sub>4</sub>Cl in solution, and the electrodeposition potential. As side-effects, the presence of NH<sub>4</sub>Cl in the growth solution slowed down the electrodeposition rate and resulted in closer packed and lower aspect ratio NWs, but having a higher degree of vertical alignment and less defective surfaces. The NW tip morphology also changed with the NH<sub>4</sub>Cl concentration, from pyramidal to flat tips. By changing the amount of NH<sub>4</sub>Cl in the growth solution, the carrier concentration of such ZnO:Cl NWs could be tuned in the range between  $5 \times 10^{17}$  and  $4 \times 10^{20} \text{ cm}^{-3}$ . The optical gap of the heavily doped NWs increased due to the Moss–Burstein effect. At the same time, a band gap narrowing was detected from photoluminescence measurements.

© 2011 Acta Materialia Inc. Published by Elsevier Ltd. All rights reserved.

**Keywords:** Nanowire; Electrodeposition; Morphology; Optical spectroscopy; Electrical properties

### 1. Introduction

Zinc oxide is an important technological material with a broad range of applications which take advantage of its abundance, stability, biocompatibility and a unique combination of chemical and physical properties [1]. Among other fields, ZnO is used in the rubber industry, in paints and sunscreens, as a gas sensor and as a biosensor [2–4]. Its piezoelectric properties make it a suitable material for

mechanical actuators, piezoelectric sensors and for energy scavenging [5–7]. ZnO wide direct band gap (3.37 eV) and large exciton binding energy (60 meV) make it an excellent candidate for particular optoelectronic applications, such as light-emitting diodes [8], laser diodes [9] and solar cells [10].

While ZnO is an intrinsic n-type semiconductor, an increase of its electrical conductivity is necessary in those applications where ZnO has an active electronic role, especially when used as a transparent conductive oxide [11,12] and in transistors [13–16]. Extrinsic doping is the main strategy to increase ZnO electrical conductivity and/or change it to p-type. In particular, cationic doping obtained by the replacement of Zn by Al [17,18], Co [19] or Ag

\* Corresponding author at: Departament Electronica, Universitat de Barcelona, Barcelona 08028, Spain. Tel.: +34 933562615; fax: +34 933563802.

E-mail address: [acabot@irec.cat](mailto:acabot@irec.cat) (A. Cabot).

# Solution-growth and optoelectronic performance of ZnO : Cl/TiO<sub>2</sub> and ZnO : Cl/Zn<sub>x</sub>TiO<sub>y</sub>/TiO<sub>2</sub> core-shell nanowires with tunable shell thickness

Jiandong Fan<sup>1</sup>, Reza Zamani<sup>2,3</sup>, Cristian Fábrega<sup>2</sup>, Alexey Shavel<sup>2</sup>, Cristina Flox<sup>2</sup>, Maria Ibáñez<sup>1</sup>, Teresa Andreu<sup>2</sup>, Antonio M López<sup>4</sup>, Jordi Arbiol<sup>3,5</sup>, Joan Ramón Morante<sup>1,2</sup> and Andreu Cabot<sup>1,2</sup>

<sup>1</sup> Departament Electronica, Universitat de Barcelona, 08028 Barcelona, Spain

<sup>2</sup> Catalonia Institute for Energy Research, IREC, 08930 Sant Adria del Besos (Barcelona), Spain

<sup>3</sup> Institut de Ciència de Materials de Barcelona, ICMA-B-CSIC, Campus de la UAB, 08193 Bellaterra, Spain

<sup>4</sup> Departament d'Enginyeria Electrònica, Universitat Politècnica de Catalunya, EPSEVG, Av. Victor Balaguer s/n, 08800 Barcelona, Spain

<sup>5</sup> Institució Catalana de Recerca i Estudis Avançats, ICREA, 08010 Barcelona, Spain

E-mail: [acabot@irec.cat](mailto:acabot@irec.cat)

Received 13 April 2012, in final form 30 July 2012

Published 27 September 2012

Online at [stacks.iop.org/JPhysD/45/415301](http://stacks.iop.org/JPhysD/45/415301)

## Abstract

Arrays of vertically aligned ZnO : Cl/TiO<sub>2</sub> and ZnO : Cl/Zn<sub>x</sub>TiO<sub>y</sub>/TiO<sub>2</sub> core-shell nanowires (NWs) were prepared by means of the combination of two solution-growth processes. First, single-crystal ZnO NWs with controlled n-type doping were grown on conducting substrates by a low-cost, high-yield and seed-free electrochemical route. These NWs were covered by a titanium oxide shell of tunable thickness mediating successive adsorption-hydrolysis-condensation steps. Using this atomic-layer growth procedure, titania shells with controlled thickness and the anatase TiO<sub>2</sub> phase were obtained after sintering at 450 °C. Higher sintering temperatures resulted in the formation of ZnO : Cl/Zn<sub>x</sub>TiO<sub>y</sub>/TiO<sub>2</sub> core-shell NWs by the interdiffusion of Zn and Ti ions at the ZnO-TiO<sub>2</sub> interface. The performance of ZnO : Cl/TiO<sub>2</sub> and ZnO : Cl/Zn<sub>x</sub>TiO<sub>y</sub>/TiO<sub>2</sub> core-shell NWs towards photoelectrochemical (PEC) water splitting was investigated as a function of the titania shell thickness. Furthermore, the performance of such core-shell NWs as photoelectrodes in dye-sensitized solar cells was also characterized. The TiO<sub>2</sub> presence at the ZnO : Cl surface promoted a two-fold increase on the produced photocurrent densities, probing their potential for PEC and optoelectronic applications. Electrochemical impedance spectroscopy was used to corroborate the lower resistance for charge transfer between the NWs and the electrolyte in the presence of the TiO<sub>2</sub> shell.

(Some figures may appear in colour only in the online journal)

## 1. Introduction

Semiconductor nanowires (NWs) find multiple applications in the fields of optoelectronics and photoelectrocatalysis. The NW geometry habituates the combined optimization of both charge carrier injection/separation and charge transport. On

the other hand, the NW composition needs to satisfy the strong demands on the materials' qualities usually required, especially in terms of surface chemistry and electrical conductivities. In this scenario, core-shell nanostructures allow the synergic combination of two different materials to take full advantage of the NW geometry.



## Solution-growth and optoelectronic properties of ZnO:Cl@ZnS core-shell nanowires with tunable shell thickness

Jiandong Fan<sup>a</sup>, Cristian Fábrega<sup>b</sup>, Reza Zamani<sup>b,c</sup>, Alexey Shavel<sup>b</sup>, Frank Güell<sup>a</sup>, Alex Carrete<sup>b</sup>, Teresa Andreu<sup>b</sup>, Antonio M. López<sup>d</sup>, Joan Ramón Morante<sup>a,b</sup>, Jordi Arbiol<sup>c,e</sup>, Andreu Cabot<sup>a,b,\*</sup>

<sup>a</sup> *Departament Electrònica, Universitat de Barcelona, Barcelona 08028, Spain*

<sup>b</sup> *Catalonia Institute for Energy Research, IREC, Sant Adria del Besos, Barcelona 08930, Spain*

<sup>c</sup> *Institut de Ciència de Materials de Barcelona, ICMA-B-CSIC, Campus de la UAB, Bellaterra 08193, Spain*

<sup>d</sup> *Departament d'Enginyeria Electrònica, Universitat Politècnica de Catalunya, EPSEVG, Av. Víctor Balaguer s/n, Barcelona 08800, Spain*

<sup>e</sup> *Institució Catalana de Recerca i Estudis Avançats, ICREA, Barcelona 08010, Spain*

### ARTICLE INFO

#### Article history:

Received 10 August 2012

Received in revised form 12 November 2012

Accepted 22 November 2012

Available online 14 December 2012

#### Keywords:

Nanostructured materials

Photoconductivity and photovoltaics

Luminescence

### ABSTRACT

Arrays of vertically aligned ZnO:Cl@ZnS core-shell nanowires (NWs) were grown by a facile low-cost, high-yield and seed-free two-step process. These NWs were used to demonstrate the potential of 3D electrodes based on core-shell heterostructures to enhance charge carrier separation and transfer. With this goal in mind, the photocurrent density of ZnO:Cl@ZnS NWs was characterized as a function of the shell thickness. Although no significant variations in the absorption and photoluminescence spectra were found with the presence of the shell, the photocurrent measured from the core-shell NWs was highly enhanced with respect to bare ZnO:Cl NWs. These photocurrent variations are associated with the control of the band bending in the core-shell NW surface, which modifies the efficiency of charge carrier transfer between the NW and the electrolyte.

© 2012 Elsevier B.V. All rights reserved.

### 1. Introduction

Aligned nanowire (NW) arrays allow the concurrence of high efficiencies of charge carrier transport with large interface areas for charge separation and/or transfer with the surrounding species/material/electrolyte. Therefore, NW- and nanotube-based electrodes are widely used to improve the efficiency of a plethora of applications where both charge carrier transport and separation/transfer are fundamental. In this scenario, core-shell NWs are ideal candidates to independently optimize both properties.

In particular, ZnO and ZnS are well studied II–VI semiconductors with direct band gaps of 3.37 and 3.73 eV, respectively [1,2]. They find multiple applications in the fields of photonics, optoelectronics, photocatalysts and also piezoelectrics [3–6]. At the same time, ZnO–ZnS heterostructures are used as photocatalysts, [7] efficient UV emitters and photodetectors, [8,9] chemical sensors, [10] n-type support/transparent-electrode/buffer layer in dye-sensitized [11] and CIGS solar cells, [12,13] and they have been also proposed as absorber material in a new class of stable and low-cost photovoltaic solar cells [14,15].

Recently, the production of ZnO@ZnS heterostructured NWs has been attempted by various techniques including chemical vapor deposition, [15,16] thermal evaporation, [6] and ion exchange [11]. Nevertheless, an especially convenient and efficient approach for the synthesis of arrays of vertically aligned ZnO@ZnS heterostructured NWs, owing to its simplicity and potential for large scale and low cost production, is the successive ionic layer adsorption and reaction (SILAR). SILAR deposition routes have been rarely reported for the synthesis of ZnO@ZnS heterostructured NWs [17]. At the same time, to the best of our knowledge, a study on the photoelectrochemical properties of ZnO@ZnS core-shell NWs is not yet available in the literature.

In the present work, we present a novel approach to produce ZnO:Cl@ZnS core-shell NWs prepared by a facile two step process at low temperature and ambient pressure. The proposed approach allows adjusting the core conductivity of the nanowires by means of controlling the chlorine concentration. The ZnO:Cl electrodeposition parameters allow also tuning the NW density, thickness and length. Likewise, the SILAR procedure offers a precise control of the thickness and characteristics of the shell. These ZnO:Cl@ZnS NWs were used to demonstrate the potential of core-shell heterostructures to enhance the photoelectrochemical properties of ZnO NWs. The obtained experimental results are discussed here in view of the energy band alignment and the depletion regions created in the formed heteronanostructures. We believe such core-shell NWs

\* Corresponding author at: Catalonia Institute for Energy Research, IREC, Sant Adria del Besos, Barcelona 08930, Spain. Tel: +34 934039154; fax: +34 934021148.  
E-mail address: [acabot@irec.cat](mailto:acabot@irec.cat) (A. Cabot).



## Catalyst size limitation in vapor–liquid–solid ZnO nanowire growth using pulsed laser deposition

A. Marcu<sup>a,\*</sup>, L. Trupina<sup>b</sup>, R. Zamani<sup>c,d</sup>, J. Arbiol<sup>c,e</sup>, C. Grigoriu<sup>a</sup>, J.R. Morante<sup>d,f</sup>

<sup>a</sup> National Institute for Laser Plasma and Radiation Physics, Laser Department, Atomistilor 409, P.O. Box MG 36, Bucharest-Magurele, Romania

<sup>b</sup> National Institute of Materials Physics, Atomistilor 105 bis, P.O. Box MG 67, Bucharest-Magurele, Romania

<sup>c</sup> Institut de Ciència de Materials de Barcelona ICMA-B-CMAB-CSIC, 08193 Bellaterra, CAT, Spain

<sup>d</sup> Catalonia Institute for Energy Research (IREC), E-08019 Barcelona, CAT, Spain

<sup>e</sup> Institució Catalana de Recerca i Estudis Avançats (ICREA) E-08010 Barcelona, CAT, Spain

<sup>f</sup> Departament d'Electrònica, Universitat de Barcelona, E-08028 Barcelona, CAT, Spain

### ARTICLE INFO

Available online 28 October 2011

#### Keywords:

Vapor–liquid–solid  
Catalyst size  
ZnO nanowire  
VLS/PLD  
PLD/PR system  
PLD with plasma reflection

### ABSTRACT

Using a pulsed laser deposition system in a plane reflector configuration, we have grown single crystal ZnO nanowires using different gold catalyst quantities and different local particle fluxes. The number of ZnO nanowire over the square micrometer substrate surface proved to depend on both gold quantity and particle flux, in specific conditions. If for a “low particle flux” the nanowire density seems to strongly depend on the gold quantity, for a “high particle flux”, the dependence is no longer observable. The results were interpreted in terms of the catalyst absorbed particle concentration dependence on the catalyst droplet size and incident particle flux.

© 2011 Elsevier B.V. All rights reserved.

### 1. Introduction

Zinc Oxide (ZnO) is a direct band-gap ( $E_g = 3.37$  eV) semiconductor with a large excitation binding energy (60 meV), exhibiting near UV emission, transparent conductivity and piezoelectricity. Various applications of ZnO nano materials such as ultraviolet detectors and field emission display devices are under way. Moreover, ZnO is biocompatible and can be used for biomedical applications without coating so biosensors are also a promising opportunity for the ZnO nanostructure. With the Bottom-Up burst in nanotechnology development, ZnO-based nanowire devices become technically possible [1–7] but morphology control remains a challenge for the present technologies. One approach in morphology control is to use the vapor–liquid–solid technique (VLS) where the dimensions are generally controlled by the catalyst size. This technique became a common technique for nanostructure fabrication, particularly for oxide materials [8–13], but not exclusively [14,15]. Since the fabricated nanostructures are requested to be smaller and smaller with controlled material properties, pushing the technique to its limits requires a better understanding and control of technique elementary processes. However, most of the experimental investigations of the VLS elementary processes and optimizations covered the temperature related process dependences [16–18] while the catalyst size related problems were drawn less attention and the present

knowledge on the related interactions is still rather scarce. Catalyst size related processes were theoretically investigated by some papers [19–21] and there are just a few reports [22] on experimental work involved in distinguishing and controlling the catalyst size related processes.

In this paper, we are using a Pulsed Laser Deposition (PLD) system in a special geometry setup for growing ZnO nanowires based on the VLS technique. The investigations focus on the catalyst and particle flux limitations and their possible applications in nanowire diameter and nanowire density control respectively.

### 2. Experimental details

Pulsed Laser Deposition (PLD) system used for these experiments consisted of a picosecond Nd:YAG pulsed laser and a vacuum chamber. Laser wavelength was 355 nm, frequency 500 kHz and laser power 1.5 W. The target was a sintered ZnO material and the substrate a 11–20 single crystal  $Al_2O_3$ . We used gold droplets as liquid catalyst. The catalyst was deposited on the substrate surface by sputtering. The substrate conditions were specific to PLD/VLS ZnO nanowire growing process, respectively substrate temperature  $\sim 800$  °C and ambient oxygen pressure  $\sim 1$  Pa. Substrate pre-annealing time at the working temperature was in the range of several minutes.

The particularity of the experimental setup (Fig. 1) is the presence of a plane reflector between target and substrate in a so called pulsed laser deposition with plasma reflector [23]. While it has been previously proved that the clusters and big particles inhibit the VLS growing process [24], the main role of the reflector is to filter the big particles

\* Corresponding author. Fax: +40 21 457 4027.  
E-mail address: [marcu@ifin.nipne.ro](mailto:marcu@ifin.nipne.ro) (A. Marcu).

## Enhanced Photovoltaic Performance of Nanowire Dye-Sensitized Solar Cells Based on Coaxial TiO<sub>2</sub>@TiO Heterostructures with a Cobalt(II/III) Redox Electrolyte

Jiandong Fan,<sup>†</sup> Cristian Fábrega,<sup>\*,†</sup> Reza Zamani,<sup>†,‡</sup> Yan Hao,<sup>§</sup> Andres Parra,<sup>†</sup> Teresa Andreu,<sup>†</sup> Jordi Arbiol,<sup>‡,⊥</sup> Gerrit Boschloo,<sup>§</sup> Anders Hagfeldt,<sup>§</sup> Joan Ramon Morante,<sup>†,||</sup> and Andreu Cabot<sup>\*,†,||</sup>

<sup>†</sup>Catalonia Institute for Energy Research (IREC), Sant Adrià de Besòs 08930, Spain

<sup>||</sup>Departament d'Electrònica, Universitat de Barcelona, Barcelona 08028, Spain

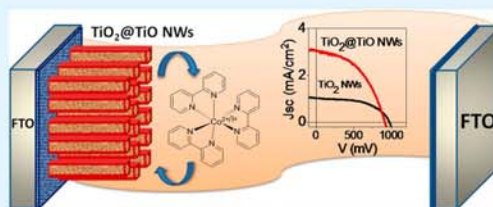
<sup>‡</sup>Institut de Ciència de Materials de Barcelona, ICMAB-CSIC, Campus de la UAB, Bellaterra 08193, Spain

<sup>§</sup>Ångström Laboratory, Department of Chemistry, Uppsala University, Box 523, 75120 Uppsala, Sweden

<sup>⊥</sup>Institució Catalana de Recerca i Estudis Avançats (ICREA), Barcelona 08010, Spain

**ABSTRACT:** The growth of a TiO shell at the surface of TiO<sub>2</sub> nanowires (NWs) allowed us to improve the power conversion efficiency of NW-based dye-sensitized solar cells (DSCs) by a factor 2.5. TiO<sub>2</sub>@TiO core-shell NWs were obtained by a two-step process: First, rutile-phase TiO<sub>2</sub> NWs were hydrothermally grown. Second, a hongquite-phase TiO shell was electrochemically deposited at the surface of the TiO<sub>2</sub> NWs. Bare TiO<sub>2</sub> and heterojunction TiO<sub>2</sub>@TiO NW-based DSCs were obtained using a cobalt(II/III) redox electrolyte and LEG4 as the dye. With this electrolyte/dye combination, DSCs with outstanding  $V_{oc}$  values above 900 mV were systematically obtained. While TiO<sub>2</sub>@TiO NW-based DSCs had slightly lower  $V_{oc}$  values than bare TiO<sub>2</sub> NW-based DSCs, they provided 3-fold higher photocurrents, overall reaching 2.5-fold higher power conversion efficiencies. The higher photocurrents were associated with the larger surface roughness and an enhanced charge-carrier separation/transfer at the NW/dye interface.

**KEYWORDS:** hydrothermal deposition, electrochemical deposition, nanowires, TiO<sub>2</sub>, cobalt(II/III) electrolyte, dye-sensitized solar cells



### INTRODUCTION

Oriented one-dimensional nanostructures with direct charge-transport paths from reaction/injection sites to the electrode are excellent architectures to improve efficiency in multiple electrocatalytic, electronic, and optoelectronic applications.<sup>1–3</sup> While the nanowire (NW) geometry habitates the combined optimization of both charge-carrier transport and charge-carrier injection/separation, its composition also needs to satisfy strong demands in terms of the surface chemistry and electrical transport properties. In this scenario, core-shell nanostructures permit one to independently optimize both processes and to further take advantage of the synergic combination of two different materials.<sup>4–7</sup>

TiO<sub>2</sub> NWs find numerous technological uses, e.g., gas sensing,<sup>8,9</sup> photovoltaics,<sup>10,11</sup> photodetection,<sup>12</sup> photocatalysis,<sup>13,14</sup> and photoelectrocatalysis.<sup>15,16</sup> In all of these applications, TiO<sub>2</sub> plays multiple roles: (i) it supports the photoactive or catalytically active species; (ii) it plays a catalytic/photocatalytic role itself; (iii) it collects/separates charge carriers from photoactive or catalytically active sites and species; (iv) it provides avenues for charge-carrier transportation between reaction sites or between reaction/photogeneration/recombination sites and the electrodes. Such

multifunctional character requires very demanding material qualities, for which independent optimization is frequently incompatible with the limited degrees of freedom available in a single material.

Compositionally graded and core-shell nanostructures are interesting architectures able to provide higher levels of control over the material's functional properties.<sup>17–19</sup> Shells can provide higher chemical stability and surface passivation to prevent recombination, and they can extend the electric field region for charge-carrier separation.<sup>4–6</sup> Shells of lower-band-gap materials are also able to extend the NW's core optical absorption to lower energies, thus promoting charge-carrier photogeneration.<sup>20–22</sup>

However, to grow defect-free coaxial heterojunctions, a major challenge needs to be overcome: the lattice mismatch.<sup>23</sup> Lattice mismatches generally introduce a significant density of interface defects that strongly deteriorate the optoelectronic properties of the formed heterostructure.

Received: June 17, 2013

Accepted: September 11, 2013

Cite this: *CrystEngComm*, 2012, 14, 3882–3887

www.rsc.org/crystengcomm

PAPER

## Pt doping triggers growth of TiO<sub>2</sub> nanorods: nanocomposite synthesis and gas-sensing properties†

Mauro Epifani,<sup>\*a</sup> Teresa Andreu,<sup>bc</sup> Reza Zamani,<sup>cd</sup> Jordi Arbiol,<sup>de</sup> Elisabetta Comini,<sup>f</sup> Pietro Siciliano,<sup>a</sup> Guido Faglia<sup>f</sup> and Joan R. Morante<sup>bc</sup>

Received 16th December 2011, Accepted 5th March 2012

DOI: 10.1039/c2ce06690d

TiO<sub>2</sub> nanocrystals were prepared by solvothermal treatment in oleic acid at 250 °C of amorphous TiO<sub>2</sub> nanoparticles. The latter were prepared by sol–gel processing in dodecylamine at 100 °C of starting solutions synthesized from TiCl<sub>4</sub>. For preparing Pt/TiO<sub>2</sub> nanocomposites, with Pt/Ti nominal atomic ratio of 0.05, the required amount of Pt precursor was added to the amorphous TiO<sub>2</sub> nanoparticles before heating at 250 °C. Control synthesis experiments, evaluated by X-ray diffraction and X-ray photoelectron spectroscopy showed Pt(acac)<sub>2</sub> as the best Pt precursor, and 250 °C as the optimum temperature for simultaneous TiO<sub>2</sub> crystallization and efficient Pt nucleation. Transmission electron microscopy observations evidenced Pt nanocrystals dispersed in the surrounding TiO<sub>2</sub> host, with a mean size of 4 nm. The TiO<sub>2</sub> host was constituted of rod-shaped anatase nanocrystals. Comparison with pure TiO<sub>2</sub> showed that the rod shape was favored by the presence of Pt species. As an example of application, the nanocomposites were used for preparing ethanol-sensing devices. The Pt addition remarkably improved the response with respect to pure TiO<sub>2</sub> sensors, and electrical characterization of the sensors helped in establishing that the effect of Pt was due to spillover rather than electronic sensitization.

### Introduction

The addition of noble metals to metal oxides is of crucial importance in such fields as gas sensors and catalysis.<sup>1</sup> The promoting action of the catalyst is typically attributed to: (1) electronic sensitization, where the catalyst modifies the intrinsic electronic properties of the host material or (2) spillover effect, where the catalyst is able of creating intermediate more reactive species, which are then transferred to the surface of the host material. In both cases, it is important to achieve an intimate mixing of the catalyst with the host material, avoiding early separations between the two components. In a previous work,<sup>2</sup> we have investigated the dispersion of Pd in SnO<sub>2</sub> nanocrystals

depending on the Pd insertion route. We had shown that the addition of Pd to pre-formed SnO<sub>2</sub> nanocrystals favored the dispersion of Pd without forming isolated Pd nanoparticles. It would be of interest to extend the synthesis procedure to a system such as Pt/TiO<sub>2</sub>, of enormous interest in catalysis,<sup>3</sup> gas-sensors,<sup>4</sup> and photocatalytic applications,<sup>5</sup> for investigating alternative procedures that avoid the usual impregnation step for introducing Pt. The synthesis of TiO<sub>2</sub> raises an additional difficulty since it is not crystallized as easily as SnO<sub>2</sub>. It is known that crystallization of TiO<sub>2</sub> nanoparticles may require high heating temperatures and/or heating times, which can be detrimental to the growth of nanocrystalline Pt species. In this paper we show that a suitable choice of the Pt precursor is able to delay the formation of the Pt nanocrystals. In this way, we could add the Pt precursor in the crystallization step of TiO<sub>2</sub> nanoparticles, obtaining Pt nanocrystals dispersed in the co-growing TiO<sub>2</sub> host. Moreover, comparison with pure TiO<sub>2</sub> nanocrystals showed that Pt addition favored the formation of TiO<sub>2</sub> nanorods. There are a large number of papers in the literature concerning the investigation of Pt/TiO<sub>2</sub> systems, but the observation that Pt may influence the shape evolution is novel. Moreover, while many reports can be found about the deposition of Pt nanocrystals onto larger species such as nanofibres or nanowires, the coexistence of Pt nanocrystals with TiO<sub>2</sub> nanorods is a different and intriguing material configuration, due to the more intimate contact between the two components.

The resulting Pt/TiO<sub>2</sub> nanorod nanocomposites were used as active materials in gas-sensing devices. The response enhancement

<sup>a</sup>Consiglio Nazionale delle Ricerche Istituto per la Microelettronica ed I Microsistemi (CNR-IMM), via Monteroni clo Campus Universitario, I-73100, Lecce, Italy. E-mail: mauro.epifani@le.imm.cnr.it

<sup>b</sup>EMEI/XaRMAE/IN2UB, Departament d'Electrònica, Universitat de Barcelona, C/Martí i Franquès 1, E-08028 Barcelona, Spain

<sup>c</sup>Institut de Recerca en Energia de Catalunya (IREC), C/Josep Pla 2, B3, Ground Floor, E-08019 Barcelona, Spain

<sup>d</sup>Institut de Ciència de Materials de Barcelona, ICMAB-CSIC, Campus de la UAB, 08193 Bellaterra, CAT, Spain

<sup>e</sup>Institució Catalana de Recerca i Estudis Avançats (ICREA), Passeig Lluís Companys, 23, 08010 Barcelona, CAT, Spain

<sup>f</sup>CNR-IDASC, SENSOR Lab, Department of Chemistry and Physics, Brescia University, Via Valotti 9, 25133, Brescia, Italy

† Electronic supplementary information (ESI) available: Further HRTEM images. See DOI: 10.1039/c2ce06690d



## Soft chemistry routes to transparent metal oxide thin films. The case of sol–gel synthesis and structural characterization of Ta<sub>2</sub>O<sub>5</sub> thin films from tantalum chloromethoxide

Mauro Epifani<sup>a,\*</sup>, Reza Zamani<sup>b,c</sup>, Jordi Arbiol<sup>c,d</sup>, Cristian Fabrega<sup>b</sup>, Teresa Andreu<sup>b</sup>, Giovanni Battista Pace<sup>a</sup>, Pietro Siciliano<sup>a</sup>, Joan R. Morante<sup>b,e</sup>

<sup>a</sup> Istituto per la Microelettronica e i Microsistemi, IMM-CNR, Via Monteroni, 73100 Lecce, Italy

<sup>b</sup> Catalonia Institute for Energy Research, IREC c/Jardins de les Dones de Negre, 1, 08930-Sant Adria del Besos, Barcelona, Spain

<sup>c</sup> Institut de Ciència de Materials de Barcelona, ICMAB-CSIC, 08193 Bellaterra, CAT, Spain

<sup>d</sup> Institutio Catalana de Recerca i Estudis Avançats, ICREA, 08010, Barcelona, Spain

<sup>e</sup> M2E-INZUB-XarMAE, Departament d'Electrònica, Universitat de Barcelona, C. Martí i Franquès 1, 08028 Barcelona, CAT, Spain

### ARTICLE INFO

Available online xxx

#### Keywords:

Sol–gel  
Tantalum pentoxide  
Spin-coating  
Inorganic precursors  
Microstructure

### ABSTRACT

Ta<sub>2</sub>O<sub>5</sub> thin films were prepared by spin-coating methanol solutions of Ta chloromethoxide. It was prepared by reacting TaCl<sub>5</sub> with methanol, followed by water addition (H<sub>2</sub>O: Ta molar ratio was 16). Thin films were deposited by spin-coating onto SiO<sub>2</sub>/Si substrates, followed by drying at 90 °C and heat-treatment up to 700 °C. The films were characterized by X-ray diffraction, transmission electron microscopy and field emission scanning electron microscopy. Crystallization was obtained only after heating at 700 °C, in the Ta<sub>2</sub>O<sub>5</sub> orthorhombic phase. The resulting films had a thickness of 100 nm. Their structure was constituted by porous crystals with size up to 50 nm, while the pores had a size of about 10 nm. The results demonstrated that TaCl<sub>5</sub> is very convenient precursor for the wet chemical synthesis of Ta<sub>2</sub>O<sub>5</sub> thin films.

© 2013 Elsevier B.V. All rights reserved.

### 1. Introduction

Tantalum pentoxide (Ta<sub>2</sub>O<sub>5</sub>) is a candidate material for several applications, such as dielectric for capacitors [1], gate oxide in thin films transistors [2], optical and anti-reflection coatings [3], RF-MEMS (radio frequency microelectromechanical systems) switches [4], integrated circuits insulator [5]. For this reason a wide variety of preparation techniques have been used for the deposition of Ta<sub>2</sub>O<sub>5</sub> thin films. Among these, solution techniques like the sol–gel process [6–10] have many attractive features, in particular the simple and inexpensive deposition apparatus. On the other hand, the precursor used in the just mentioned works [6–10] is tantalum ethoxide, which has very high cost, is highly sensitive to moisture and must be carefully handled in order to exclude water from the environment and increase its time stability. It is then of interest to develop alternative precursors, which should be cheaper and more stable. In a series of works [11–14], we have proposed metal chloroalkoxides as convenient alternative precursors to pure alkoxides. In this paper we show that it is possible to extend this class of precursors by synthesizing Ta chloroalkoxide from TaCl<sub>5</sub>. By using this precursor, it is possible to

carry out deposition of very uniform Ta<sub>2</sub>O<sub>5</sub> thin films in a simple apparatus not needing complex environment control.

### 2. Experimental details

All the chemicals were provided by Sigma-Aldrich in analytical grade or, as concerns TaCl<sub>5</sub>, with 99.8% purity. For preparing the starting Ta<sub>2</sub>O<sub>5</sub> precursor sols, 10 ml of methanol were slowly added to 1 g of TaCl<sub>5</sub> in a glove-box with < 1 ppm of H<sub>2</sub>O. After 1 hour, H<sub>2</sub>O was added dropwise with H<sub>2</sub>O:Ta molar ratio of 16. After further stirring for 24 hr, 30 mg of cetyltrimethylammonium bromide (CTAB) were added, in order to improve the film adhesion on the substrates. The substrates for film deposition were <100> silicon wafers with a 560 nm SiO<sub>2</sub> overlayer. One day after CTAB addition, the solution was spin-coated at 2000 rpm for 30 s onto the substrates, pre-cleaned for 2 min in boiling isopropanol. The films were dried for 3 min at 80 °C in air, then heat-treated for 1 hour at temperatures ranging from 100 °C to 700 °C in air atmosphere in a tubular furnace, with heating rate of 5 °C/min. The thickness of films heat-treated at 500 °C was about 100 nm, as measured with a profilometer (Tencor Instruments, Alpha-Step IQ) and confirmed by transmission electron microscopy.

Fourier Transform Infrared Spectroscopy (FTIR) measurements were carried out in diffuse reflectance mode with a Nicolet 6700 spectrometer, after mixing one drop of the starting solution with KBr. X-Ray

\* Corresponding author.

E-mail address: [mauro.epifani@le.imm.cnr.it](mailto:mauro.epifani@le.imm.cnr.it) (M. Epifani).

## Oxide–oxide nanojunctions in coaxial SnO<sub>2</sub>/TiO<sub>2</sub>, SnO<sub>2</sub>/V<sub>2</sub>O<sub>3</sub> and SnO<sub>2</sub>/(Ti<sub>0.5</sub>V<sub>0.5</sub>)<sub>2</sub>O<sub>3</sub> nanowire heterostructures†

Cite this: *CrystEngComm*, 2013, 15, 4532

Reza Zamani,<sup>ab</sup> Raquel Fiz,<sup>c</sup> Jun Pan,<sup>c</sup> Thomas Fischer,<sup>c</sup> Sanjay Mathur,<sup>\*c</sup> Joan Ramon Morante<sup>\*bcd</sup> and Jordi Arbiol<sup>\*ae</sup>

A single-crystalline shell based on titanium and vanadium binary oxides with karelianite structure (Ti<sub>1-x</sub>V<sub>x</sub>)<sub>2</sub>O<sub>3</sub> was successfully deposited onto SnO<sub>2</sub> nanowires by sequential chemical vapor deposition (CVD). In comparison to single titanium or vanadium oxide shells, the binary Ti–V metal oxide overlayer overcomes the problems related to lattice mismatch and thermochemical stability, which usually take place in coaxial oxide–oxide heterostructures due to the atomic diffusion between core and shell. The modulation of the titanium content in the binary (Ti<sub>1-x</sub>V<sub>x</sub>)<sub>2</sub>O<sub>3</sub> karelianite shell results in a lower mismatch (~1.5%) and improves the epitaxial relationship with the rutile lattice of SnO<sub>2</sub> core nanowires. Therefore, the presence of defects such as dislocations and strain fields, which in principle limit the carrier transport properties affecting the electrical, optical and photocatalytic performance, is strongly reduced. Atomic model simulations confirm that structural characteristics related to lattice mismatch and strain accommodation at the heterojunction influence the thermochemical stability and were corroborated by detailed high resolution transmission electron microscopy analyses of the different core–shell systems.

Received 12th October 2012,  
Accepted 25th March 2013

DOI: 10.1039/c3ce26672a

www.rsc.org/crystengcomm

### A. Introduction

Metal oxide nanowires (NWs) have attracted a dramatic surge of interest. Their novel properties, which are distinctive from conventional bulk and thin film materials, carry promising potential for new applications<sup>1</sup> such as thermoelectrics,<sup>2–4</sup> electronics and photonics,<sup>5–12</sup> biosensing<sup>13–17</sup> and gas sensing devices.<sup>18–21</sup>

Since the first synthesis of 1-dimensional (1D) tin oxide nanostructures,<sup>22</sup> considerable efforts have been carried out to investigate and improve their applications.<sup>20</sup> In addition to their physical characteristics, their surface activity driven by the presence of residual groups such as dangling bonds and defects make them interesting systems to implement in

nanodevices.<sup>22–24</sup> Usually, the use of 1D structures in nanodevices provides a more efficient charge carrier transfer due to their unique geometry. The direct electrical pathways provided along the axial direction ensure the rapid and efficient transfer to the external electrical contact. On the other hand, holes move across the radial direction towards their surface and/or interface under the effects of the electrical field associated with the surface depletion zone, despite the short diffusion length. Therefore, the surface properties of nanostructures become especially important to the overall charge collection efficiency since they can influence the recombination rate and the chemical reaction dynamics taking place at the surface. The method chosen to synthesize nanostructures significantly influences their surface states. Hence, their coating with an overlayer shell provides outstandingly efficient charge performances related to the heterostructure properties: allowing the control over the surface recombination as well as the chemical reaction kinetics and the charge transfer through the coaxial formed junction.

In this scenario, core–shell coaxial 1D nanostructures based on metal oxides, and particularly based on SnO<sub>2</sub> cores, allow:

(i) The use of cores with predetermined properties, mainly related to free carrier concentration and optical band gap of nano-SnO<sub>2</sub>.

(ii) The control over core and/or shell doping, which determines, on the one hand, the global electrical properties

<sup>a</sup>Institut de Ciència de Materials de Barcelona, ICMA-B-CMAB, E-08193 Bellaterra, CAT, Spain. E-mail: arbiol@icrea.cat

<sup>b</sup>Catalonia Institute for Energy Research (IREC), E-08930 Sant Adrià del Besòs, CAT, Spain. E-mail: jrmorante@irec.cat

<sup>c</sup>Institute of Inorganic Chemistry, University of Cologne, Cologne, Germany. E-mail: sanjay.mathur@uni-koeln.de

<sup>d</sup>Departament d'Electrònica, Universitat de Barcelona, E-08028 Barcelona, CAT, Spain

<sup>e</sup>Institució Catalana de Recerca i Estudis Avançats (ICREA), E-08010 Barcelona, CAT, Spain

† Electronic supplementary information (ESI) available: Atomic simulation of the interfaces between rutile SnO<sub>2</sub> NW core and different shells: Ti<sub>2</sub>O, Ti<sub>2</sub>O<sub>3</sub>, TiO<sub>2</sub> rutile and TiO<sub>2</sub> anatase, sketch on the formation mechanism of SnO<sub>2</sub>-based heterostructures and *in situ* mass spectrometric analysis of the gas phase during the deposition process. See DOI: 10.1039/c3ce26672a



Contents lists available at SciVerse ScienceDirect

## Sensors and Actuators B: Chemical

journal homepage: [www.elsevier.com/locate/snb](http://www.elsevier.com/locate/snb)Heterostructured p-CuO (nanoparticle)/n-SnO<sub>2</sub> (nanowire) devices for selective H<sub>2</sub>S detectionF. Shao<sup>a</sup>, M.W.G. Hoffmann<sup>a,b</sup>, J.D. Prades<sup>b</sup>, R. Zamani<sup>a,c</sup>, J. Arbiol<sup>c,d</sup>, J.R. Morante<sup>a,b</sup>, E. Varechkina<sup>e</sup>, M. Rumyantseva<sup>e</sup>, A. Gaskov<sup>e</sup>, I. Giebelhaus<sup>f</sup>, T. Fischer<sup>f</sup>, S. Mathur<sup>f</sup>, F. Hernández-Ramírez<sup>a,b,\*</sup><sup>a</sup> Catalonia Institute for Energy Research (IREC), E-08930 Sant Adrià del Besòs, Spain<sup>b</sup> Department of Electronics, University of Barcelona, E-08028 Barcelona, Spain<sup>c</sup> Institut de Ciència de Materials de Barcelona, ICMA-B-CMAB-CSIC, Campus de la UAB, E-08193 Bellaterra, Spain<sup>d</sup> Institució Catalana de Recerca i Estudis Avançats (ICREA), E-08010 Barcelona, Spain<sup>e</sup> Chemistry Department, Moscow State University, 119991 Moscow, Russia<sup>f</sup> Institute of Inorganic Chemistry, University of Cologne, D-50939 Cologne, Germany

## ARTICLE INFO

## Article history:

Received 2 October 2012

Received in revised form

30 December 2012

Accepted 14 January 2013

Available online xxx

## Keywords:

H<sub>2</sub>S

Sensor

Heterostructure

Metal oxide

CuO

SnO<sub>2</sub>

## ABSTRACT

Dihydrogen sulphide (H<sub>2</sub>S) is a dangerous pollutant released in fossil combustion processes. Here, p-CuO (particle)/n-SnO<sub>2</sub> (nanowire) heterostructures were evaluated as selective H<sub>2</sub>S sensors, and the working principle behind their good performance was qualitatively modelled. It was concluded that the main sensing mechanism was dissimilar to standard redox reactions typical of simple metal oxide devices, but ascribable to the sulphurization of CuO and the consequent variation of the pn-junction band structure at the CuO–SnO<sub>2</sub> interfaces. Experimental data showed that these H<sub>2</sub>S sensors suit well for alarm applications with extremely high selectivity and sensitivity to this gas for concentrations between 1 ppm and 10 ppm.

© 2013 Elsevier B.V. All rights reserved.

## 1. Introduction

Fossil combustion processes play a key role in the worldwide production of air pollutants due to the release of dust particles, greenhouse gases (CO<sub>2</sub>) and highly toxic gas species (e.g. NO<sub>x</sub>, CO and H<sub>2</sub>S). Main sources such as power plants and car engines usually operate in direct proximity to urban areas, which makes the control and optimization of combustion processes essential to guarantee a high environmental quality [1–3]. Amongst all pollutants, dihydrogen sulphide (H<sub>2</sub>S) is identified as a major threat for the human health even at low concentrations of 10 ppm [4]. Therefore, the search of new and highly selective methods for the detection of H<sub>2</sub>S has attracted a huge interest within the past years [5].

Metal oxides (MOX) have shown outstanding sensing properties to different chemical species with simple and cost effective device configurations [6,7]. Nevertheless, a major drawback of this

technology is the unspecific interaction of the MOX surface with the surrounding atmosphere, which is based on redox processes involving surface bound oxygen species (combustion), and a consequent modulation of the electrical resistance [8]. The integration of MOX heterostructures [9–11] in sensors is considered a promising alternative to reach partial improvements in terms of both selectivity and sensitivity. For H<sub>2</sub>S detection, CuO/SnO<sub>2</sub> heterostructures revealed an extraordinary performance in these domains [12–15]. This is usually explained by two different but complementary contributions; (i) the particular interaction of CuO and H<sub>2</sub>S and (ii) the intrinsic properties of the CuO/SnO<sub>2</sub> interface.

The interaction of CuO with H<sub>2</sub>S does not follow a conventional redox reaction, but undergoes a thermal activated anion exchange to form CuS. This transformation is reversible in oxygen-rich atmosphere [16–19], and it is summarized by:



The stoichiometric chemical path shown in Eq. (1) facilitates thus a selective detection of H<sub>2</sub>S and an effective discrimination towards other gases.

\* Corresponding author at: Catalonia Institute for Energy Research (IREC), E-08930 Sant Adrià del Besòs, Spain. Tel.: +34 933 562 615; fax: +34 933 563 802.  
E-mail address: [hermandez@irec.cat](mailto:hermandez@irec.cat) (F. Hernández-Ramírez).



## Preparation of copper oxide nanowire-based conductometric chemical sensors

D. Zappa<sup>a,\*</sup>, E. Comini<sup>a</sup>, R. Zamani<sup>b,c</sup>, J. Arbiol<sup>b,d</sup>, J.R. Morante<sup>c,e</sup>, G. Sberveglieri<sup>a</sup><sup>a</sup> SENSOR, University of Brescia and CNR-IDASC, Via Valotti 9, 25133 Brescia, Italy<sup>†</sup><sup>b</sup> Institut de Ciència de Materials de Barcelona, ICMA-B-CMAB-CSIC, Campus de la UAB, Bellaterra 08193, Spain<sup>c</sup> Catalonia Institute for Energy Research, IREC, Jardins de les Dones de Negre 1, Sant Adria del Besos, Barcelona 08930, Spain<sup>d</sup> Institut Catalana de Recerca i Estudis Avançats, ICREA, Barcelona 08010, Spain<sup>e</sup> MZE University of Barcelona, Martí i Franques 1, Barcelona 08028, Spain

## ARTICLE INFO

## Article history:

Received 23 June 2012

Received in revised form 25 January 2013

Accepted 19 February 2013

Available online xxx

## Keywords:

Nanostructures

Metal-oxides

Chemical sensing

CuO nanowires

## ABSTRACT

CuO nanowires (NWs) were grown by thermal oxidation of metallic Cu thin layer deposited by sputtering on different substrates. Optimal growth parameters were found, studying the influence of the oxidizing temperature and the atmosphere during the oxidation process. A strong relation between oxidation parameters and morphology has been detected. The preliminary response of this sensing material, using nanowire's mat-based device, to various oxidizing and reducing target gases has been evaluated, in order to corroborate the functional properties of the CuO NWs as potential sensing material under certain conditions and to confirm the p-type conductometric response of the material.

© 2013 Elsevier B.V. All rights reserved.

## 1. Introduction

Nanostructured materials are subject of an intensive scientific research because of their interesting properties and potential technological applications, compared to their bulk or micro-sized counterparts, due to the efficient transport of carriers and excitons within the smallest dimension. Among the most promising nanostructures, metal oxide nanowires (NWs), nanobelts and nanorods deserve a special mention. Due to the high surface area/volume ratio and high crystallinity [1], nanostructured materials, in particular metal oxide NWs, are promising in the field of gas sensing [2–5], for third generation solar cells [6,7] and as field emitters sources [8,9].

So far the research in this field focused on the investigation of n-type semiconductor materials, such as ZnO [6,10], SnO<sub>2</sub> [11–13], TiO<sub>2</sub> [14,15], and so on. Few studies have been reported on the use of p-type material NWs as chemical sensors, like for example copper oxide [16,17].

Oxygen can interact with copper forming two different structures: CuO and Cu<sub>2</sub>O. Copper (II) oxide, or cupric oxide (CuO), is an intrinsically p-type semiconductor mainly due to Cu vacancies [18] with a narrow bandgap of 1.2 eV, has monoclinic crystal

structure and black color. It can be found in nature as tenorite rocks. It's currently used in field emission sources [19,20], magnetic storage media [21], high-T superconductors [22], solar cells [23,24] and heterogeneous catalysis [25].

Copper (I) oxide, or cuprous oxide (Cu<sub>2</sub>O), a p-type semiconductor as well, has an energy gap of 2.1 eV and a cubic crystal structure. It's mainly used for water photodecomposition [26], photodegradation of organic pollutants and as electrode in lithium ion batteries [27,28]. It's found as red mineral called cuprite. It's less stable than CuO, and usually degrades to that form in moist air. Both oxides have been poorly studied for gas sensing applications [29,30] in spite of the potential interest that p-type sensing materials have owing to the transduction mechanisms changes originated by the carrier availability and surface band bending potential values.

In literature several different techniques were presented to prepare CuO NWs including wet chemical methods [31,32], templating method [33], thermal decomposition [34], anodization [35], thermal oxidation [36–38] and electrospinning [39]. Among these methods, CuO NWs prepared via thermal oxidation seem more crystalline and with higher aspect ratios compared to those prepared via other methods. In this study, CuO NWs were prepared grown by thermal oxidation of metallic Cu thin layer deposited by sputtering on various substrates. Then, the preliminary response of this sensing material, using nanowire's mat-based device, to various oxidizing and reducing target gases has been evaluated, in order to corroborate the functional properties of the CuO NWs as potential sensing material under certain conditions.

\* Corresponding author at: SENSOR Laboratory, Faculty of Engineering, University of Brescia, Via Valotti 9, 25133 Brescia, Italy.

E-mail address: [dario.zappa@ing.unibs.it](mailto:dario.zappa@ing.unibs.it) (D. Zappa).

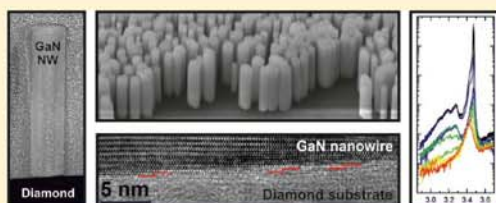
<sup>†</sup> <http://sensor.ing.unibs.it>.

## Self-Assembled GaN Nanowires on Diamond

Fabian Schuster,<sup>\*,†</sup> Florian Furtmayr,<sup>†</sup> Reza Zamani,<sup>‡,||</sup> Cesar Magén,<sup>§</sup> Joan R. Morante,<sup>||,⊥</sup> Jordi Arbiol,<sup>‡,¶</sup> Jose A. Garrido,<sup>†</sup> and Martin Stutzmann<sup>†</sup><sup>†</sup>Walter Schottky Institut, Technische Universität München, Am Coulombwall 4, 85748 Garching, Germany<sup>‡</sup>Institut de Ciència de Materials de Barcelona, ICMAB-CSIC, Campus de la UAB, 08193 Bellaterra, Spain<sup>§</sup>Laboratorio de Microscopías Avanzadas, Instituto de Nanociencia de Aragon-ARAID and Departamento de Física de la Materia Condensada, Universidad de Zaragoza, 50018 Zaragoza, Spain<sup>||</sup>Catalonia Institute for Energy Research, IREC, 08930 Sant Adrià del Besòs, Spain<sup>⊥</sup>Department d'Electrònica, Universitat de Barcelona, 08028 Barcelona, Spain<sup>¶</sup>Institució Catalana de Recerca i Estudis Avançats (ICREA), 08010 Barcelona, Spain

**ABSTRACT:** We demonstrate the nucleation of self-assembled, epitaxial GaN nanowires (NWs) on (111) single-crystalline diamond without using a catalyst or buffer layer. The NWs show an excellent crystalline quality of the wurtzite crystal structure with *m*-plane faceting, a low defect density, and axial growth along the *c*-axis with N-face polarity, as shown by aberration corrected annular bright-field scanning transmission electron microscopy. X-ray diffraction confirms single domain growth with an in-plane epitaxial relationship of (1010)<sub>GaN</sub> || (011)<sub>Diamond</sub> as well as some biaxial tensile strain induced by thermal expansion mismatch. In photoluminescence, a strong and sharp excitonic emission reveals excellent optical properties superior to state-of-the-art GaN NWs on silicon substrates. In combination with the high-quality diamond/NW interface, confirmed by high-resolution transmission electron microscopy measurements, these results underline the potential of p-type diamond/n-type nitride heterojunctions for efficient UV optoelectronic devices.

**KEYWORDS:** Nanowires, GaN, nitrides, diamond, molecular beam epitaxy, heteroepitaxy



It is now almost ten years since the idea of combining the III-nitride material system with diamond substrates was investigated, mainly motivated by the lack of efficient p-type doping in the nitrides, especially with high aluminum content, and n-type doping in diamond, respectively. The complementary configuration of these wide bandgap materials, namely p-type boron-doped diamond and n-type silicon-doped AlGaN, is promising to form efficient heterodiodes with high carrier mobilities. Driven by this motivation, the growth of heteroepitaxial AlN films on diamond substrates was reported,<sup>1,2</sup> resulting in the fabrication of the first heterobipolar diode emitting in the UV spectral range.<sup>2</sup> However, the performance of these light-emitting diodes stayed behind the expectations due to numerous structural imperfections in the nitride films, especially in the interface region. Up to now, direct nucleation of GaN and AlN films on diamond remains challenging due to the high difference in the thermal expansion coefficients of GaN and diamond,<sup>3,4</sup> which leads to cracking of the epitaxial film during cooling down of the samples from growth to room temperature. To circumvent this problem, an AlN nucleation layer is most commonly used,<sup>5,6</sup> sometimes even followed by a strain engineering stack of AlN/GaN multilayers.<sup>7,8</sup> As a consequence, the use of diamond substrates is currently limited to applications that do not benefit from diamond doping, but only use its high thermal conductivity. For

instance, AlGaN/GaN high-electron-mobility transistors (HEMTs) show an improved performance when prepared on diamond substrates.<sup>7–11</sup>

A new approach for defect-free AlGaN on diamond is the growth of nanowires, which are expected to yield much better structural quality and do not suffer from thermal mismatch. This nucleation of high-quality nitrides directly on a diamond substrate represents a major step forward toward the fabrication of efficient p-diamond/n-nitride heterostructures. We currently explore two possible applications of nitride NWs on diamond. First, efficient optoelectronic devices operating in the UV spectral range, benefiting from the effective p-type doping as well as the high thermal conductivity of diamond. The NW configuration does not only provide defect-free AlGaN with excellent luminescence properties but can also be used as intrinsic cavities for strong light-matter coupling. Second, we target the field of quantum computation, where nitrogen-vacancy (NV) centers in diamond currently attract much attention as potential qubits.<sup>12,13</sup> To electrically control single NV centers, nitride NWs are ideal local contacts for applying

Received: November 3, 2011

Revised: April 16, 2012

Published: April 16, 2012

## Active nano-CuPt<sub>3</sub> electrocatalyst supported on graphene for enhancing reactions at the cathode in all-vanadium redox flow batteries

Cristina Flox <sup>a,\*</sup>, Javier Rubio-Garcia <sup>a</sup>, Raquel Nafria <sup>a</sup>, Reza Zamani <sup>a,b</sup>,  
Marcel Skoumal <sup>a</sup>, Teresa Andreu <sup>a</sup>, Jordi Arbiol <sup>b,c</sup>, Andreu Cabot <sup>a,d</sup>,  
Joan Ramon Morante <sup>a,d</sup>

<sup>a</sup> Catalonia Institute for Energy Research, IREC, Barcelona 08930, Spain

<sup>b</sup> Institut de Ciència de Materials de Barcelona, ICMAB-CSIC, Bellaterra 08193, Spain

<sup>c</sup> Institució Catalana de Recerca i Estudis Avançats, ICREA, Barcelona 08010, Spain

<sup>d</sup> Departament d'Electrònica, Universitat de Barcelona, Barcelona 08028, Spain

### ARTICLE INFO

#### Article history:

Received 13 October 2011

Accepted 19 January 2012

Available online 28 January 2012

### ABSTRACT

Graphene-supported monometallic (Pt) and bimetallic (CuPt<sub>3</sub>) cubic nanocatalysts have been investigated as new positive electrode materials for improving the VO<sub>2</sub><sup>+</sup>/VO<sup>2+</sup> redox process occurring in the vanadium redox flow batteries (VRB). High-resolution transmission electron microscopy (HRTEM) and scanning electron microscopy (SEM) have been employed to characterize the electrodes. The presence of the CuPt<sub>3</sub> nanocubes on graphene conferred higher electrocatalytic activity due to the much higher electroactive area compared to that obtained with the Pt nanoparticles. The electrochemical surface area of the nano-(CuPt<sub>3</sub>)-decorated graphene electrode was 105% higher compared to non-decorated graphene, being then a promising alternative for improving the VRB.

© 2012 Elsevier Ltd. All rights reserved.

Among all the new large-scale energy storage technologies currently under development, the vanadium redox flow battery (VRB) appears to be very promising [1]. In contrast with other batteries, the amount of energy storage in the VRB is determined by the concentration of the vanadium species and the volume of the reservoirs. On the other hand, the system power is determined by the rate of reaction of the vanadium species at each electrode and the total surface area. Since a sulfuric acid solution is used as the supporting electrolyte in VRB, carbon materials are preferably chosen and generally used as electrodes. But, these materials have been proven to show poor kinetic reversibility [2]. The two redox couples of VO<sub>2</sub><sup>+</sup>/VO<sup>2+</sup> and V<sup>2+</sup>/V<sup>3+</sup> are used for the positive and negative half-cell reactions, respectively. In comparison with the negative electrode, the positive redox couple sustains a relatively slow dynamic reaction, due to the rearrangement of the coordination structures of the vanadium ions, resulting in a significant influence on the performance of the cell. This rearrangement consists in the transfer of electrons, the exchange of protons, and the formation of a number of intermediate complexes, according to the pH of the electrolyte and the electrical potential; hence, it is the positive

half-cell reaction of the VRB what dominates the electrochemical kinetic limitation [2]. Therefore, much attention has been paid to the modification of the positive electrode materials to enhance the electrochemical activity in order to obtain a battery that has high power density and is energy efficient. In this framework, this work is focused on the study of characteristics and performance of a novel electrode for the cathodic reaction of a VRB, using graphene-support such as electrode material decorated with bimetallic (CuPt<sub>3</sub>) nanoparticles in order to provide stable active sites, high-conductivity and long cyclic life for the electrode in sulfuric acid. This effect has been compared with that of Pt nanocubes. CuPt<sub>3</sub> bimetallic nanoparticles have been chosen as a preliminary stoichiometric combination, shape and size to show a catalyst that has been applied in other systems [3,4] but for the first time into VRB.

A graphene oxide (GO)-based thin film was printed by inkjet printing onto an inert substrate (geometric area of 1 cm<sup>2</sup>). Hereafter, the resulting electrode is called GO. The GO, which exhibited low electrical conductivity, was reduced with hydrazine. The resulting electrode henceforth referred to as hydrazine treated graphene oxide (HTGO). The Pt (or CuPt<sub>3</sub>/HTGO)

\* Corresponding author. Fax: +34 93 3563802.

E-mail address: cflox@irec.cat (C. Flox).

0008-6223/\$ - see front matter © 2012 Elsevier Ltd. All rights reserved.

doi:10.1016/j.carbon.2012.01.060

Cite this: *RSC Advances*, 2012, 2, 9643–9650

www.rsc.org/advances

PAPER

## Tailored graphene materials by chemical reduction of graphene oxides of different atomic structure

Cristina Botas,<sup>a</sup> Patricia Álvarez,<sup>a</sup> Clara Blanco,<sup>a</sup> M. Dolores Gutiérrez,<sup>b</sup> Pablo Ares,<sup>c</sup> Reza Zamani,<sup>d</sup> Jordi Arbiol,<sup>e</sup> Joan R. Morante<sup>d</sup> and Rosa Menéndez<sup>\*a</sup>

Received 13th July 2012, Accepted 10th August 2012

DOI: 10.1039/c2ra21447d

Graphene materials with different characteristics in terms of sheet size and defects (structural and/or functional groups) were obtained by the reduction with hydrazine of two graphene oxides with similar oxygen content, but with functional groups of different type and location. The oxides were prepared from two synthetic graphites with distinct crystalline structure. Our research has obtained experimental evidence of a greater reactivity of the oxygen functional groups located in the interior of the aromatic domains on the basal planes (mainly epoxy) and a lower reactivity of oxygen functional groups located at the edges (mainly carboxyl and OH). Furthermore, these edge-located groups were found to be responsible for hydrogen bonding lateral interactions between sheets (these occur through the residual OH groups), which cause a substantial increase in the size of the reduced graphene oxide with respect to that of the parent graphene oxide. These results offer a way to tailor the characteristics of graphene materials for diverse applications.

### 1. Introduction

A great deal of effort has been devoted in recent years to the synthesis of graphene by various methods<sup>1,2</sup> and especially to the study of its electronic behavior<sup>3</sup> with the aim of tuning it to specific potential applications.<sup>4</sup> The preparation of graphene by chemical methods, such as the graphene oxide route, offers the possibility of producing it on a large scale and, at the same time, of controlling its quality, depending on: i) the properties of the parent graphite,<sup>5,6</sup> ii) the oxidation method used<sup>7</sup> and iii) the final reduction of the graphene oxide (GO).<sup>8</sup> GOs and reduced graphene oxides (rGOs) are graphene derivatives that exhibit a structure decorated with defects resulting from the oxidation and/or reduction processes.<sup>9</sup> These materials are of great interest for applications that involve catalytic processes, among others.<sup>10</sup> However, the complexity of the reactions involved in the overall process (oxidation, exfoliation, reduction), in addition to the numerous variables that may affect the bonding of the carbon atoms of the parent graphite, make it very difficult to achieve strict control of the yield and quality of the products.

Oxygen functionalities of four kinds are known to be present in GO: epoxy, hydroxyl, carbonyl and carboxyl.<sup>11</sup> Generally speaking, epoxy and hydroxyl, located on the basal plane of GO,

are considered to be the main functionalities, whereas carbonyl and carboxyl, distributed at the edges, are regarded as minor, although this largely depends on the initial parent graphite crystalline structure. The chemical structure of GO has been the subject of considerable debate for a number of years, and even now no definitive model exists.<sup>8,9</sup> After reduction with hydrazine, the oxygen atoms in GO are removed to a large extent<sup>12</sup> and the resultant rGO differs markedly from a defect-free graphene.<sup>13</sup> Besides, the structural disorder and defects inherited from the GO, the rGO still includes residual oxygen functional groups and N-containing species. The mechanisms involved in the reduction of GO with hydrazine have been proposed in the case of the epoxy groups by Stankovich<sup>14</sup> and further investigated by Gao *et al.*,<sup>12</sup> who employed the density functional theory method for this purpose. However, the processes involved in the case of the hydroxyl and carboxyl groups are still unclear. Further experimental evidences are necessary to support these theoretical studies. It is thought that the position of the oxygen functional groups in the interior of the aromatic domains or at the edges conditions the reactivity of GO during reduction.<sup>12</sup> This would also have a strong influence on the final chemical/catalytic properties of the graphene materials and would determine their applications.

The aim of this paper is to obtain graphenes of different characteristics by chemical reduction with hydrazine of two GOs of similar oxygen content, but with rather different types and different distributions of the oxygen functional groups. The GOs were characterized in detail at the atomic level by aberration-corrected low energy high resolution transmission electron microscopy (HRTEM), and both GOs and the corresponding

<sup>a</sup>Instituto Nacional del Carbón, INCAR-CSIC, Apdo. 73, 33080, Oviedo, Spain. E-mail: rosmenen@incar.csic.es<sup>b</sup>Universidad de Oviedo, Julian Clavería 8, 33006, Oviedo, Spain<sup>c</sup>Nanotec Electrónica S.L. Ronda de Poniente, 12, 28760, Tres Cantos, Madrid, Spain<sup>d</sup>Catalonia Institute for Energy Research, IREC, 08930, Barcelona, Spain<sup>e</sup>Institució Catalana de Recerca i Estudis Avançats, ICREA, 08010, Barcelona, Spain

## APPENDIX E: PUBLOCATIONS

# APPENDIX F

## AUTHOR'S CURRICULUM VITAE

APPENDIX F: AUTHOR'S CV

**REZA ZAMANI**

**Address:** Institut de Ciència de Materials de  
Barcelona (ICMAB-CSIC), Campus de  
la UAB, Bellaterra 08193, Spain  
P.O. Box: 114

**Phone:** +34-935 801 853 (ext. 302)

**Cell Phone:** +34-608 60 50 61

**E-mail:** rzamani@icmab.es  
reza.r.zamani@gmail.com



**Date of Birth:** December 30, 1982

**Place of Birth:** Tehran, Iran

**Gender:** Male

**SUMMARY OF QUALIFICATIONS**

- **Education:** PhD candidate in Nanoscience specialized in Electron Microscopy of Nanostructured Materials - 2010-2013, MS in Nanoscience and Nanotechnology - 2009, and BS in Materials Science and Engineering - 2007
- **Courses:** Participating in TEM training courses, e.g. UCA-TEM summer school, UB-EELS/Crystallography course, EMAT-TEM/EELS winter school, 5<sup>th</sup> SuperSTEM summer school, etc.
- **Scientific Output:** 21 papers already published, some in high impact-factor journals, e.g. Nano Letters, ACS Nano, Journal of the American Chemical Society, and Chemistry of Materials; 1 proceeding, and 5 other publications in process
- **Public Appearance:** 28 participations many of them in important international congresses in the field of microscopy (EMC 2012, MFS 2011 and 2013, MCM 2011) and Materials Science (MRS and E-MRS 2010-2013), attending with oral presentations or posters
- Participating in various scientific projects, European and National (Spanish)

## SUMMARY OF SKILLS

- ***Electron Microscopy Experience:*** different TEMs and SEMs, such as Jeol 2010F and Jeol 2100 (University of Barcelona), Zeiss Libra 120+ (IREC-Barcelona), Philips CM300 and Jeol 2200FS (EPFL), Tecnai G<sup>2</sup> (EMAT-University of Antwerp), Tecnai F30 and Aberration Corrected microscopes TITAN (LMA-University of Zaragoza), TITAN PICO and TITAN HOLO (ER-C Jülich); different microscopy techniques mostly focused on HRTEM, EELS, EDX, STEM, HAADF, ABF, EFTEM, CL, computation of strain analysis by using GPA and PPA
- ***Materials Science Experience:*** characterizing a wide range of materials, mostly nanostructured (nanowires, nanorods, nanoparticles) and thin film semiconductors (e.g. metal oxides, III-Vs, III-nitrides, chalcogenides)
- ***Software:*** Digital Micrograph, CaRIne, FEI ES Vision, INCA, Rhodius, Eje-Z, JEMS, PPA, GPA, MSA, Photoshop, Minitab
- ***Management Skill:*** four years of experience in automotive industry, working as quality manager, director's representative in quality, and counselor of quality management systems based on ISO 9001 and ISO/TS 16949, and able to use related techniques, e.g. FMEA, APQP, SPC, MSA, SQFE, COQ
- ***Languages:*** Persian (Native), English (Fluent), Spanish (Fluent), Catalan (Basic)

## PROFESSIONAL BACKGROUND

### EDUCATION

- **PhD Candidate in Nanoscience**, 2010-present (to be finished in October 2013)  
Institute of Materials Science of Barcelona (ICMAB-CSIC) and Catalonia Institute for Energy Research (IREC), Barcelona, Spain
- **MS in Nanoscience and Nanotechnology**, 2008-2009  
University of Barcelona (UB), Barcelona, Spain
- **BS in Materials Engineering-Extractive Metallurgy**, 2001-2007  
Sharif University of Technology (SUT), Tehran, Iran



## APPENDIX F: AUTHOR'S CV

- **Workshop:** Course of Microscopy, EELS, and Electronic Crystallography  
*Theme:* Course of Transmission Electron Microscopy (TEM) and Electron Energy Loss Spectroscopy (EELS), Precession and Electronic Crystallography  
*Duration:* 3 days *Organizer:* SCT, University of Barcelona (UB)  
*Place:* Barcelona, Spain *Date:* November 2010
  
- **Workshop:** Workshop on Transmission Electron Microscopy - TEM 2011  
*Theme:* Transmission Electron Microscopy (TEM)  
*Duration:* 1 day *Organizer:* ICMAB  
*Place:* Bellaterra, Spain *Date:* October 2010
  
- **Workshop:** European Summer Workshop: Transmission Electron Microscopy of Catalytic Materials and Nanoparticles (TEM-UCA 2010)  
*Theme:* Workshop on Transmission Electron Microscopy (TEM) and Electron Energy Loss Spectroscopy (EELS), and Theoretical Simulation and Modeling  
*Duration:* 1 week *Organizer:* University of Cadiz (UCA)  
*Place:* Cadiz, Spain *Date:* June 2010
  
- **Workshop:** MOX Semiconductors Gas Sensor Technology  
*Theme:* Course Fundamentals of Gas Sensing and Metal Oxide Gas Sensors  
*Duration:* 1 week *Organizer:* CNR-IDASC SENSOR Lab (ITA)  
*Place:* Rimini, Italy *Date:* May 2010

## ACHIEVEMENTS

- Awards:
  - IFSM Young Scientist Award at the EMC 2012 in Manchester, UK
- Grants:
  - PhD Scholarship from Catalonia Institute for Energy Research (IREC)
- Congress Grants:
  - Scholarship to attend MSF 2013 Congress
  - Scholarship to attend MSF 2011 Congress
  - Scholarship to attend TEM-UCA summer school

## RESEARCH INTERESTS

- Advanced Electron Microscopy
- Nanostructured Materials
- Semiconductors and Metal Oxides

## PUBLICATIONS

Totally *21 papers* already published, *1 Proceeding*, and 5 others in hand (submitted, under revision, etc)

### 2013

1. J.D. Fan, C. Fabrega, R.R. Zamani, Y. Hao, A. Parra, T. Andreu, J. Arbiol, G. Boschloo, A. Hagfeldt, J.R. Morante, A. Cabot, '**Enhanced photovoltaic performance of nanowire dye-sensitized solar cells based on coaxial TiO<sub>2</sub>@TiO heterostructures with a cobalt (II/III) redox electrolyte**', *ACS Applied Materials and Interfaces*, DOI: 10.1021am402344d (2013)
2. M. Epifani, R. Zamani, J. Arbiol, C. Fabrega, T. Andreu, G. Battista Pace, P. Siciliano, J.R. Morante, '**Soft chemistry routes to transparent metal oxide thin films. The case of sol-gel synthesis and structural characterization of Ta<sub>2</sub>O<sub>5</sub> thin films from tantalum chloromethoxide**', *Thin Solid Films*, DOI: 10.1016/j.tsf.2013.05.139 (2013)
3. R. Zamani, R. Fiz, J. Pan, T. Fischer, S. Mathur, J.R. Morante, J. Arbiol, '**Oxide-oxide nanojunctions in coaxial SnO<sub>2</sub>/TiO<sub>2</sub>, SnO<sub>2</sub>/V<sub>2</sub>O<sub>3</sub> and SnO<sub>2</sub>/(Ti<sub>0.5</sub>V<sub>0.5</sub>)<sub>2</sub>O<sub>3</sub> nanowire heterostructures**', *CrystEngComm* 15, 4532-4539 (2013)
4. W.H. Li, R. Zamani, P. Rivera Gil, B. Pelaz, M. Ibáñez, D. Cadavid, A. Shavel, R.A. Alvarez-Puebla, W.J. Parak, J. Arbiol, A. Cabot, '**CuTe nanocrystals: Shape and size control, plasmonic properties, and use as SERS probes and photothermal agents**', *Journal of the American Chemical Society* 135, 7098-7101 (2013)
5. W.H. Li, R. Zamani, M. Ibáñez, D. Cadavid, A. Shavel, J.R. Morante, J. Arbiol, A. Cabot, '**Metal ions to control the morphology of semiconductor nanoparticles: Copper selenide nanocubes**', *Journal of the American Chemical Society* 135, 4664-4667 (2013)

6. M. Ibáñez, R. Zamani, S. Gorsse, J.D. Fan, S. Ortega, D. Cadavid, J.R. Morante, J. Arbiol, A. Cabot, '**Core-shell nanoparticles as building blocks for the bottom-up production of functional nanocomposites: PbTe-PbS thermoelectric properties**', *ACS Nano* 7, 2573-2586, (2013)
7. D. Zappa, E. Comini, R. Zamani, J. Arbiol, J.R. Morante, G. Sberveglieri, '**Preparation of copper oxide nanowire-based conductometric chemical sensors**', *Sensors and Actuators B: Chemical* 182, 7-15 (2013)
8. F. Shao, M.W.G. Hoffmann, J.D. Prades, R. Zamani, J. Arbiol, J.R. Morante, E. Varechkina, M. Rumyantseva, A. Gaskov, I. Giebelhaus, T. Fischer, S. Mathur, F. Hernández-Ramírez '**Heterostructured p-CuO (nanoparticle) / n-SnO<sub>2</sub> (nanowire) devices for selective H<sub>2</sub>S detection**', *Sensors and Actuators B: Chemical* 181, 130-135 (2013)
9. J.D. Fan, C. Fábrega, R. Zamani, A. Shavel, F. Güell, A. Carrete, T. Andreu, A.M. López, J.R. Morante, J. Arbiol, A. Cabot, '**Solution-growth and optoelectronic properties of ZnO:Cl@ZnS core-shell nanowires with tunable shell thickness**', *Journal of Alloys and Compounds* 555, 213-218 (2013)
10. M. Ibáñez, D. Cadavid, U. Anselmi-Tamburini, R. Zamani, S. Gorsse, W.H. Li, A.M. López, J.R. Morante, J. Arbiol, A. Cabot, '**Colloidal synthesis and thermoelectric properties of Cu<sub>2</sub>SnSe<sub>3</sub> nanocrystals**', *Journal of Materials Chemistry A* 1, 1421-1426 (2013)

## 2012

11. M. Ibáñez, R. Zamani, W.H. Li, D. Cadavid, S. Gorsse, N.A. Katcho, A. Shavel, A.M. López, J.R. Morante, J. Arbiol, A. Cabot, '**Crystallographic control at the nanoscale to enhance functionality: Cu<sub>2</sub>GeSe<sub>3</sub> nanoparticles as thermoelectric materials**', *Chemistry of Materials* 24, 4615-4622 (2012)
12. J.D. Fan, R. Zamani, C. Fábrega, A. Shavel, C. Flox, M. Ibáñez, T. Andreu, A.M. López, J. Arbiol, J.R. Morante, A. Cabot, '**Solution-growth and optoelectronic performance of ZnO:Cl/TiO<sub>2</sub> and ZnO:Cl/Zn<sub>x</sub>TiO<sub>y</sub>/TiO<sub>2</sub> core-shell nanowires with tunable shell thickness**', *Journal of Physics D: Applied Physics* 45, 415301 (2012)

13. C. Botas, P. Alvarez, C. Blanco, M.D. Gutiérrez Álvarez, P. Ares, R. Zamani, J. Arbiol, J.R. Morante, R. Menéndez, '**Tailored graphene materials by chemical reduction of graphene oxide of different atomic structure**', *RSC Advances* 2, 9643-9650 (2012)
14. M. Epifani, T. Andreu, R. Zamani, J. Arbiol, E. Comini, P. Siciliano, G. Faglia, J.R. Morante, '**Pt doping triggers growth of TiO<sub>2</sub> nanorods. Nanocomposite synthesis and gas-sensing properties**', *CrystEngComm* 14, 3882-2887 (2012)
15. F. Schuster, F. Furtmayr, R. Zamani, C. Magén, J.R. Morante, J. Arbiol, J.A. Garrido, M. Stutzmann, '**Self-assembled GaN nanowires on diamond**', *Nano Letters* 12, 2199-2204 (2012)
16. A. Marcu, L. Trupina, R. Zamani, J. Arbiol, C. Grigoriu, J.R. Morante, '**Catalyst size limitation in vapor-liquid-solid ZnO nanowire growth using pulsed laser deposition**', *Thin Solid Films* 520, 4626-4631 (2012)
17. M. Ibáñez, R. Zamani, A. LaLonde, D. Cadavid, W.H. Li, A. Shavel, J. Arbiol, J.R. Morante, S. Gorsse, G. Snyder, A. Cabot, '**Cu<sub>2</sub>ZnGeSe<sub>4</sub> nanocrystals: Synthesis and thermoelectric properties**', *Journal of the American Chemical Society* 134, 4060-4063 (2012)
18. M. Ibáñez, R. Zamani, W.H. Li, A. Shavel, J. Arbiol, J.R. Morante, A. Cabot, '**Extending the nanocrystal synthesis control to quaternary compositions**', *Crystal Growth and Design* 12, 1085-1090 (2012)
19. C. Flox, J. Rubio-García, R. Nafria, R. Zamani, M. Skoumal, T. Andreu, J. Arbiol, A. Cabot, J.R. Morante, '**Active nano-CuPt<sub>3</sub> electrocatalyst supported on graphene for enhancing reactions at the cathode in all-vanadium redox flow batteries**', *Carbon* 50, 2372-2374 (2012)
20. M. Ibáñez, D. Cadavid, R. Zamani, N. Garcia-Castello, V. Izquierdo-Roca, W.H. Li, A. Fairbrother, J.D. Prades, A. Shavel, J. Arbiol, A. Pérez-Rodríguez, J.R. Morante, A. Cabot, '**Composition control and thermoelectric properties of quaternary chalcogenide nanocrystals: The case of stannite Cu<sub>2</sub>CdSnSe<sub>4</sub>**', *Chemistry of Materials* 24, 562-570 (2012)

**2011**

21. J.D. Fan, A. Shavel, R. Zamani, C. Fábrega, J. Rousset, S. Haller, F. Güell, A. Carreté, T. Andreu, J. Arbiol, J. R. Morante, A. Cabot, '**Control of the doping concentration, morphology and optoelectronic properties of vertically aligned chlorine-doped ZnO nanowires**', *Acta Materialia* 59, 6790-6800 (2011)

**PAPERS IN HAND**

1. R.R. Zamani, M. Ibáñez, M. Luysberg, N. Garcia-Castello, L. Houben, J.D. Prades, R. Dunin-Borkowski, J.R. Morante, A. Cabot, J. Arbiol, '**Polytypic and polarity-directed branching in Cu-based quaternary nanostructures**', To be submitted, (2013)
2. M. Epifani, R. Díaz, C. Force, E. Comini, T. Andreu, R.R. Zamani, J. Arbiol, P. Siciliano, G. Faglia, J.R. Morante, '**The colloidal counterpart of the TiO<sub>2</sub>-supported V<sub>2</sub>O<sub>5</sub> system: a case study of oxide-on-oxide deposition by wet chemical techniques, synthesis, vanadium speciation and gas-sensing enhancement**', *Journal of Physical Chemistry C*, Revised version submitted (2013)
3. F. Schuster, B. Laumer, R.R. Zamani, C. Magén, J.R. Morante, J. Arbiol, M. Stutzmann, '**p-GaN/n-ZnO heterojunction nanowires for UV-LEDs and laser diodes**', Submitted (2013)
4. W.H. Li, M. Ibáñez, D. Cadavid, R.R. Zamani, J. Rubio-Garcia, S. Gorsse, J.R. Morante, J. Arbiol, A. Cabot, '**Colloidal synthesis and functional properties of quaternary Cu-based semiconductors: Cu<sub>2</sub>HgGeSe<sub>4</sub>**', Submitted (2013)
5. W.H. Li, M. Ibáñez, R.R. Zamani, N. García-Castelló, S. Gorsse, D. Cadavid, J.D. Prades, J. Arbiol, A. Cabot, '**I<sub>2</sub>-II-IV-VI<sub>4</sub> nanoparticles: the case of Cu<sub>2</sub>HgSnSe<sub>4</sub>**', Submitted (2013)

## PROCEEDINGS

- D. Zappa, E. Comini, R. Zamani, J. Arbiol, J.R. Morante, G. Sberveglieri, **‘Copper oxide nanowires prepared by thermal oxidation for chemical sensing’**, *Procedia Engineering* 25, 753-756 (2011)  
Conference: *Euroensors XXV*, Athens-Greece, September 2011

## CONGRESSES

- R. Zamani, M. Ibáñez, J.R. Morante, A. Cabot , J. Arbiol, **‘Structure study of complex ternary and quaternary copper-selenide based nanocrystals for thermoelectrics’**  
*Microscopy at the Frontiers of Science (MFS 2013)*, Tarragona, Spain, September 2013  
*Type of Participation: Oral*
- R. Zamani, M. Ibáñez, J.R. Morante, A. Cabot , J. Arbiol, **‘Functional nanocomposites made of PbTe-PbS core-shell nanocrystals for thermoelectrics: structure study’**  
*Microscopy at the Frontiers of Science (MFS 2013)*, Tarragona, Spain, September 2013  
*Type of Participation: Poster*
- R. Zamani, M. Ibáñez, D. Cadavid, J.R. Morante, A. Cabot, J. Arbiol, **‘Structure influence in complex ternary and quaternary chalcogenide nanoparticles for thermoelectric applications’**  
*E-MRS Spring Meeting 2013*, Strasbourg, France, May 2013  
*Type of Participation: Oral*
- M. de la Mata, R. Zamani, C. Magen, M.I.B. Utama, M. Heiss, B. Peng, J.R. Morante, R. Rurali, M. Eickhoff, A. Fontcuberta i Morral, Q. Xiong, J. Arbiol, **‘Direct dumbbell analyses for polarity assignment in semiconductor nanostructures by means of aberration-corrected STEM techniques’**  
*E-MRS Spring Meeting 2013*, Strasbourg, France, May 2013  
*Type of Participation: Oral*

- M. Ibáñez, S. Ortega, R. Zamani, S. Gorsse, D. Cadavid, J.R. Morante, J. Arbiol, A. Cabot, '**Core-shell nanoparticles as building blocks for the bottom-up**'  
*E-MRS Spring Meeting 2013*, Strasbourg, France, May 2013  
*Type of Participation: Oral*
- A. Casadei, E. Russo Averchi, J. Schwendeeer, D. Ruffer, R. Zamani, J. Arbiol, A. Fontcuberta i Morral, '**Electrical properties of carbon doped GaAs nanowires and related heterostructures**'  
*E-MRS Spring Meeting 2013*, Strasbourg, France, May 2013  
*Type of Participation: Oral*
- W. Li, R. Zamani, A. Shavel, M. Ibáñez, J. Arbiol, A. Cabot, '**Synthesis and characterization of shape-controlled Cu<sub>x</sub>Te nanoparticles**'  
*E-MRS Spring Meeting 2013*, Strasbourg, France, May 2013  
*Type of Participation: Poster*
- M. Epifani, T. Andreu, J. Arbiol, R. Zamani, L. Francioso, P. Siciliano, J.R. Morante, '**Solution synthesis of metal oxide thin films: different synthetic approaches and microelectronic processing of gas-sensing devices**'  
*2013 MRS Spring Meeting*, San Francisco, USA, April 2013  
*Type of Participation: Oral*
- J. Arbiol, M. de la Mata, R. Zamani, J.R. Morante, '**Visualization of light atoms (O and N) in semiconductor NWs: direct way to determine the polarity in 1D nanostructures**'  
*37<sup>th</sup> International Conference and Expo on Advanced Ceramics and Composites (ICACC'13)*, Dayton Beach, USA, January 2013  
*Type of Participation: Invited Communication*
- R. Zamani, C. Magén, F. Schuster, F. Furtmayr, D.T.L. Alexander, C. Hébert, J.A. Garrido, M. Stutzmann, J.R. Morante, J. Arbiol, '**Self-assembled GaN nanowires diamond: direct polarity measurements, epitaxy and luminescence properties**'  
*2012 MRS Fall Meeting*, Boston, USA, November 2012  
*Type of Participation: Oral*

- M. de la Mata, R. Zamani, J. Gazquez, C. Magén, M.I.B. Utama, M. Heiss, B. Peng, J.R. Morante, R. Rurali, M. Eickhoff, A. Fontcuberta i Morral, Q. Xiong, J. Arbiol, **'Polarity assignment in ZnTe, GaAs, ZnO and GaN-AlN nanowires from direct dumbbell analysis by means of aberration corrected HAADF and ABF STEM'**  
*2012 MRS Fall Meeting, Boston, USA, November 2012*  
*Type of Participation: Oral*
- A. Marcu, R. Zamani, J.R. Morante, C.P. Lungu, C. Grigoriu, J. Arbiol, **'Laser pulse parameters influences on nanowire morphology in vapor-liquid-solid growing by pulsed laser ablation'**  
*2012 MRS Fall Meeting, Boston, USA, November 2012*  
*Type of Participation: Poster*
- R. Zamani, C. Magén, F. Schuster, F. Furtmayr, D. Alexander, C. Hébert, J.A. Garrido, M. Stutzmann, J.R. Morante, J. Arbiol, **'Self-assembled GaN nanowires nucleated on diamond substrate: direct polarity measurements, epitaxy and luminescence properties'**  
*The 15<sup>th</sup> European Microscopy Congress (EMC 2012), Manchester, UK, September 2012*  
*Type of Participation: Oral*
- R. Zamani, M. Ibáñez, W. Li, D. Cadavid, J.R. Morante, A. Cabot, J. Arbiol, **'Structural and morphological changes in I<sub>2</sub> II IV VI<sub>4</sub> adamantines for thermoelectric applications'**  
*The 15<sup>th</sup> European Microscopy Congress (EMC 2012), Manchester, UK, September 2012*  
*Type of Participation: Poster*
- A. Casadei, P. Krogstrup, E. Russo Averchi, C. Colombo, M. Heiss, R. Zamani, E. Uccelli, D. Ruffer, S. Conesa-Boj, J. Nygard, J.R. Morante, J. Arbiol, A. Fontcuberta i Morral, **'Doping mechanism in GaAs nanowires'**  
*31<sup>st</sup> International Conference on the Physics of Semiconductors (ICPS 2012), Zurich, Switzerland, July-August 2012*  
*Type of Participation: Poster*
- R. Zamani, M. Ibáñez, W. Li, D. Cadavid, J.R. Morante, A. Cabot, J. Arbiol, **'Structural and morphological changes in I<sub>2</sub> II IV VI<sub>4</sub> adamantines for thermoelectric applications'**  
*Nanoselect Annual Meeting 2012, Costa Brava, Spain, July 2012*  
*Type of Participation: Poster*

- F. Schuster, F. Furtmayr, R. Zamani, C. Magén, J.R. Morante, J. Arbiol, J.A. Garrido, M. Stutzmann, '**Nucleation of self-assembled GaN nanowires on diamond**'  
*6<sup>th</sup> Nanowire Growth Workshop*, St. Petersburg, Russia, June 2012  
*Type of Participation: Oral*
- A. Marcu, R. Zamani, I. Enculescu, S. Vizireanu, J.R. Morante, R. Birjega, C.P. Lungu, C. Grigoriu, J. Arbiol, '**Nanoparticle-nanowire interface influence on ZnO nanostructure luminescence shifting**'  
*E-MRS Spring Meeting 2012*, Strasbourg, France, May 2012  
*Type of Participation: Poster*
- M. Ibáñez, D. Cadavid, R. Zamani, J. Arbiol, N. Garcia, J.D. Prades, J.R. Morante, A. Cabot, '**Copper-based diamond-like semiconductors as thermoelectric materials**'  
*E-MRS Spring Meeting 2012*, Strasbourg, France, May 2012  
*Type of Participation: Oral*
- R. Zamani, M. Ibáñez, D. Cadavid, J.R. Morante, A. Cabot, J. Arbiol, '**Structural and morphological changes in I<sub>2</sub> II IV VI<sub>4</sub> adamantines for thermoelectric applications**'  
*Microscopy at the Frontiers of Science (MFS 2011)*, Aveiro, Portugal, October 2011  
*Type of Participation: Oral*
- M. Ibáñez, D. Cadavid, R. Zamani, N. Garcia, J. Arbiol, D. Prades, J. Morante, A. Cabot, '**Thermoelectric properties of nanostructured I<sub>2</sub> II IV VI<sub>4</sub> adamantines**'  
*9<sup>th</sup> European Conference on Thermoelectrics (ECT2011)*, Thessaloniki, Greece, September 2011  
*Type of Participation: Oral*
- D. Zappa, E. Comini, R. Zamani, J. Arbiol, J.R. Morante, G. Sberveglieri, '**Copper oxide nanowires prepared by thermal oxidation for chemical sensing**'  
*Eurosensors XXV*, Athens, Greece, September 2011  
*Publication: Procedia Engineering*, Volume 25, 2011, Pages 753-756  
*Type of Participation: Oral*

- R. Zamani, M. Epifani, P. Siciliano, J.R. Morante, J. Arbiol, '**Anatase TiO<sub>2</sub> nanorods for gas sensor applications: high-resolution transmission electron microscopy and strain analysis**'  
*10<sup>th</sup> Multinational Congress on Microscopy (MCM 2011)*, Urbino, Italy, September 2011  
*Type of Participation: Poster*
- R. Menéndez, C. Botas, P. Alvarez, R. Zamani, C. Magén, J. Arbiol, J.R. Morante, '**Local chemical structure of graphene oxides and reduced graphene oxides obtained from graphites of different crystallinity**'  
Congress: *Carbon 2011*, Shanghai, China, July 2011  
*Type of Participation: Oral*
- R. Zamani, F. Hernández-Ramírez, J. Pan, T. Fischer, S. Mathur, J.R. Morante, J. Arbiol, '**Metal oxide nanowires for energy and gas sensing applications, electron nanoscopy overviews**'  
*Nanoselect Annual Meeting 2011*, Costa Brava, Spain, June 2011  
*Type of Participation: Poster*
- R. Zamani, F. Hernández-Ramírez, J. Pan, T. Fischer, S. Mathur, J.R. Morante, J. Arbiol, '**Insight on the crystalline matching in SnO<sub>2</sub>/TiO<sub>2</sub> based core-shell nanowires for energy and sensor applications**'  
*E-MRS Spring Meeting 2011*, Nice, France, May 2011  
*Type of Participation: Poster*
- T. Chávez-Capilla, M. Epifani, T. Andreu, R. Zamani, J. Palma, J. Arbiol, P. Siciliano, J.R. Morante, R. Díaz, '**Synthesis of TiO<sub>2</sub>/V<sub>2</sub>O<sub>5</sub> core/shell nanocrystals for supercapacitors**'  
*E-MRS Spring Meeting 2011*, Nice, France, May 2011  
*Type of Participation: Poster*
- R. Zamani, F. Hernandez-Ramirez, J. Pan, T. Fischer, S. Mathur, J.R. Morante, J. Arbiol, '**Insight on the crystalline matching between Ti<sub>1-x</sub>V<sub>x</sub>O<sub>y</sub> shell and SnO<sub>2</sub> core nanowires**'  
*2010 MRS Fall Meeting*, Boston, USA, December 2010  
*Type of Participation: Oral*

## RESEARCH PROJECTS

- *Project Title:* Surface ionization and novel concepts in nano-MOX gas sensors with increased Selectivity, Sensitivity and Stability for detection of low concentrations of toxic and explosive agents (S3)  
*Financing Firm/Administration:* European Union (EU)  
*Reference:* FP7-247768 *Amount:* 1.550.000 €  
*Participants:* Kurchatov Institute (Russia), EADS Deutschland GmbH (Germany), Catalonia Institute for Energy Research, IREC (Spain), University of Tuebingen (Germany), University of Cologne (Germany), Moscow State University (Russia), Moscow Institute of Physical Engineering (Russia), Research Institute of Electron Technique (Russia), CNR-IDASC SENSOR Lab (Italy)  
*Number of Participants:* >50 *Period:* 1/9/2009 - 31/8/2012  
*Main Researcher:* Prof. Joan Ramon Morante
  
- *Project Title:* Nanoscopias Electrónicas Avanzadas aplicadas a MAteriales Nanoestructurados (NEAMAN)  
*Financing Firm/Administration:* Consejo Superior de Investigaciones Científicas (CSIC) / MICINN  
*Reference:* 200960I199 *Amount:* 50.000 €  
*Participants:* Institut de Ciencia de Materials de Barcelona, ICMAB-CSIC  
*Number of Participants:* 2 *Period:* 1/1/2010 - 31/12/2010  
*Main Researcher:* Prof. Jordi Arbiol
  
- *Project Title:* Correlation of the Electronic and Optical Properties in Functional Nanowires through Advanced Electron Nanoscopy (COPEON)  
*Financing Firm/Administration:*  
*Reference:* MAT2010-15138 *Amount:* 72.600 €  
*Participants:* Institut de Ciencia de Materials de Barcelona (ICMAB-CSIC), École Polytechnique Fédérale de Lausanne (EPFL)  
*Number of Participants:* 8 (6 in EPFL) *Period:* 1/1/2011 - 31/12/2013  
*Main Researcher:* Prof. Jordi Arbiol
  
- *Project Title:* Desarrollo de catalizadores más eficientes para el diseño de procesos químicos sostenibles y producción limpia de energía (MULTICAT)  
*Financing Firm/Administration:* CONSOLIDER / MICINN  
*Reference:* CSD2009-00050 *Amount:* 3.500.000 €  
*Participants:* INCAR-CSIC, IREC, ITQ-UPV-CSIC, UniZar, IQOG-CSIC, ICTP-CSIC, UCLM

*Number of Participants:* > 50

*Period:* 2009 - 2014

*Main Researcher:* Prof. Joan Ramon Morante (Coordinator: A. Corma ITQ-UPV-CSIC)

- *Project Title:* SYNthesis and NanoCharacterization of Advanced Metal Oxide Nanostructures (SYNCAMON)  
*Financing Firm/Administration:* Consejo Superior de Investigaciones Científicas (CSIC)  
*Reference:* 2010IT0001 *Amount:* 8.000 €  
*Participants:* CNR, Institut de Ciència de Materials de Barcelona (ICMAB-CSIC)  
*Period:* 1/1/2011 - 31/12/2012  
*Main Researcher:* Prof. Jordi Arbiol
  
- *Project Title:* Integration of compound semiconductors and silicon in nanowires (InCoSiN)  
*Financing Firm/Administration:* Ministerio de Economía y Competitividad (MINECO)  
*Reference:* PRI-PIMERU-2011-1422 *Amount:* 30.000 €  
*Program:* ERA.Net RUS *Period:* 1/9/2012 - 1/9/2014  
*Main Researcher:* Prof. Jordi Arbiol

## PROFESSIONAL AFFILIATIONS

- Institut de Ciència de Materials de Barcelona (ICMAB-CSIC) and Catalonia Institute for Energy Research (IREC), Spain; PhD Candidate, 2010-present
  
- MIND/IN2UB Departament d'Electronica, Universitat de Barcelona, Martí i Franques 1, Barcelona 08028, Spain; Master Student, 2008-2009